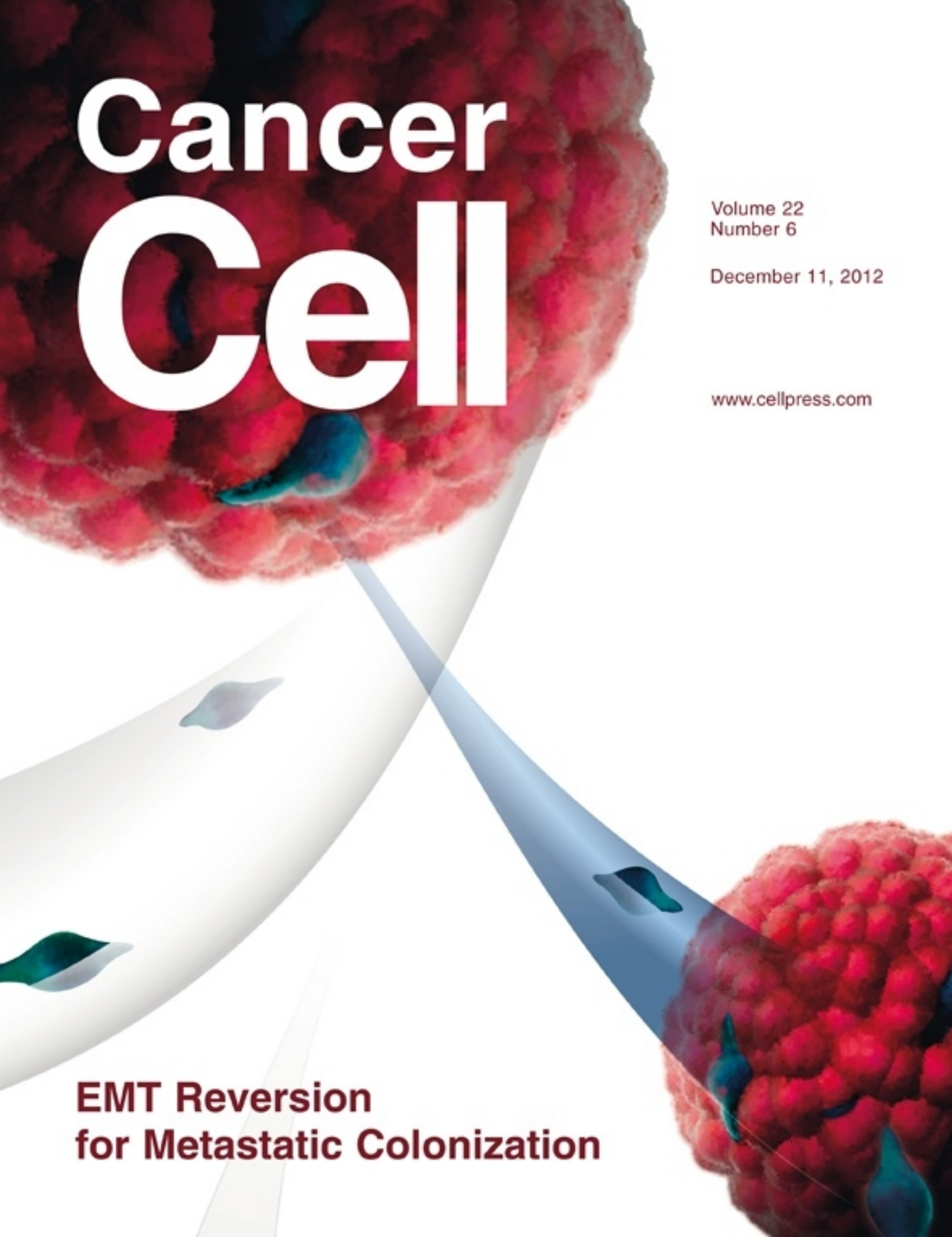

Cancer Cell

Volume 22
Number 6

December 11, 2012

www.cellpress.com

EMT Reversion for Metastatic Colonization

Cancer Cell
Article

Spatiotemporal Regulation of Epithelial-Mesenchymal Transition Is Essential for Squamous Cell Carcinoma Metastasis

Jeff H. Tsai,[1] Joana Liu Donaher,[3] Danielle A. Murphy,[4] Sandra Chau,[1] and Jing Yang[1,2,*]
[1]Department of Pharmacology
[2]Department of Pediatrics
University of California, San Diego, School of Medicine, 9500 Gilman Drive, La Jolla, CA 92093-0636, USA
[3]Whitehead Institute for Biomedical Research, 9 Cambridge Center, Cambridge, MA 02142, USA
[4]The Sanford Burnham Medical Research Institute, La Jolla, CA 92037, USA
*Correspondence: jingyang@ucsd.edu
http://dx.doi.org/10.1016/j.ccr.2012.09.022

SUMMARY

Epithelial-mesenchymal transition (EMT) is implicated in converting stationary epithelial tumor cells into motile mesenchymal cells during metastasis. However, the involvement of EMT in metastasis is still controversial, due to the lack of a mesenchymal phenotype in human carcinoma metastases. Using a spontaneous squamous cell carcinoma mouse model, we show that activation of the EMT-inducing transcription factor Twist1 is sufficient to promote carcinoma cells to undergo EMT and disseminate into blood circulation. Importantly, in distant sites, turning off Twist1 to allow reversion of EMT is essential for disseminated tumor cells to proliferate and form metastases. Our study demonstrates in vivo the requirement of "reversible EMT" in tumor metastasis and may resolve the controversy on the importance of EMT in carcinoma metastasis.

INTRODUCTION

During metastasis, epithelial tumor cells invade surrounding extracellular matrix (ECM), disseminate into the systemic circulation, and then establish secondary tumors in distant sites. A developmental program termed epithelial-mesenchymal transition (EMT) has been implicated in giving rise to the dissemination of single carcinoma cells. During EMT, stationary epithelial cells lose their epithelial characteristics, including adherent junctions and apical-basal polarity, and acquire a mesenchymal morphology and the ability to migrate and invade (Hay, 1995). Biochemically, cells switch off the expression of epithelial markers, such as adherens junction proteins E-cadherin and catenins, and turn on mesenchymal markers, including vimentin and fibronectin. Studies using cell culture and tumor xenograft models show that activation of EMT promotes carcinoma cells to dissociate from each other and metastasize to distant organs (Hay, 1995; Kalluri and Weinberg, 2009; Thiery, 2002, 2009).

However, the involvement of EMT in tumor metastasis in vivo is still hotly debated (Garber, 2008; Ledford, 2011; Tarin et al., 2005; Thompson et al., 2005). In human carcinoma, although primary tumors show many morphological and molecular features of EMT in subpopulations of invasive cells, distant metastases present an epithelial morphology (Peinado et al., 2007). This phenomenon contradicts the assumption that activation of EMT in tumor cells should result in metastases with a mesenchymal phenotype, therefore casting doubts on the occurrence of EMT during metastasis. This discrepancy could be due to the interpretation of the EMT program as a permanent nonreversible course during tumor metastasis. A reversible EMT model has been proposed to explain this apparent paradox: carcinoma cells undergo EMT to invade and disseminate from the primary tumor; once reaching distant sites, tumor cells need to revert to an epithelial identity to form macrometastases (Thiery, 2002). However, this hypothesis has not been attested in vivo.

Significance

EMT features are frequently observed in many types of primary human carcinoma, but not their corresponding metastases. Our findings indicate that reversible EMT likely represents a key driving force in human carcinoma metastasis. Delayed onset of metastasis following primary tumor removal is thought to be due to resurrection of latent carcinoma cells in distant organs. Our study raises the possibility that tumor dormancy could be due to the inability of disseminated tumor cells to revert EMT and proliferate. The dynamic involvement of EMT in metastasis cautions that therapies inhibiting EMT could be counterproductive in preventing distant metastases when patients already present circulating tumor cells. Instead, blocking EMT reversion may prevent dormant tumor cells from establishing metastases.

The EMT program is orchestrated through a network of transcription factors, including Twist1 (Yang et al., 2004), Snail1/2 (Batlle et al., 2000; Cano et al., 2000; Hajra et al., 2002), Zeb1/2 (Comijn et al., 2001; Eger et al., 2005), and FOXC2 (Mani et al., 2007). Our previous study found that Twist1 is a potent inducer of EMT and invadopodia-mediated ECM degradation (Eckert et al., 2011; Yang et al., 2004). In mouse and human breast tumor xenograft models, Twist1 expression can promote tumor metastasis (Yang et al., 2004). Clinical studies have also associated expression of Twist1 in primary tumors with disease aggressiveness and poor survival in many types of human cancers, such as squamous cell carcinoma, breast cancer, prostate cancer, and gastric cancer (Eckert et al., 2011; Kallergi et al., 2011; Peinado et al., 2007; Watson et al., 2007).

Unlike human carcinoma metastases, most established metastatic tumor cell lines present a permanent mesenchymal phenotype (Blick et al., 2008) and cannot be used to address the dynamic EMT process during tumor metastasis in vivo. Recent elegant studies using autochthonous mouse tumor models observed the occurrence of EMT in primary carcinoma, but how EMT spatiotemporally regulates metastasis has not been investigated in these models (Hüsemann et al., 2008; Rhim et al., 2012). The chemical carcinogenesis mouse skin model has been shown to recapitulate the multistep process of human carcinoma progression, including initiation, growth, invasion, and metastasis (Kemp, 2005; Perez-Losada and Balmain, 2003). At the molecular and genetic levels, the skin carcinogenesis model shares strong similarities with a number of carcinoma in humans, including activating mutations in Ras family members, activation of PI3K- and Stat3-mediated signaling pathways, elevated expression of transforming growth factor β1 (TGFβ1), and activation of the TGFβ/Smad signaling pathways and, at later stages, *Trp53* mutations (DiGiovanni, 1992; Kemp, 2005). Importantly, like human squamous cell carcinoma, this model develops distant metastases with an epithelial morphology in lymph nodes and lungs (Han et al., 2005), making it a suitable model to study the involvement of EMT in vivo. Furthermore, extensive studies have shown that expression of Twist1 in primary human squamous cell carcinoma, including esophageal cancer (Sasaki et al., 2009; Xie et al., 2009; Yuen et al., 2007) and head and neck cancer (Ou et al., 2008; Wushou et al., 2012), correlates with distant metastasis and poor prognosis. In this study, we investigate the importance of the dynamic EMT process in metastasis in vivo using the skin carcinogenesis model.

RESULTS

Induction of Twist1 Promotes Invasive Carcinoma Conversion

Previous studies have demonstrated the necessary role of Twist1 as an inducer of EMT. To understand the contribution of Twist1 in metastatic carcinoma, we analyzed 99 primary human carcinomas with patient-matched lymph node metastases for Twist1 expression. Of the 20 cases with high Twist1 expression in the primary tumor, we found 16 cases with over 50% drop in Twist1 levels in the lymph node metastases (Figures S1A and S1B available online), suggesting Twist1 is activated in the primary tumor but not distant metastases. To study how dynamic activation of Twist1 directly impacts carcinoma progression, we generated skin-specific Twist1 Tet-on inducible mice by crossing transgenic mice carrying a single copy of a TetOP-Twist1 transgene with Keratin 5 promoter-driven reverse tetracycline-controlled transactivator mice (K5-rtTA) (Diamond et al., 2000). Bitransgenic mice (referred to as K5-Twist1 mice) showed specific expression of Twist1 protein in the basal epidermal layer upon doxycycline (dox) treatment (Figure S1C). Long-term induction of Twist1 alone in K5-Twist1 mice did not result in visible skin abnormalities (data not shown). To generate squamous cell carcinoma (SCC), K5-Twist1 mice and control single transgene littermates were treated with a single dose of 7,12-dimethylbenz[a]anthracene (DMBA) followed by weekly applications of 12-O-tetradecanoylphorbol-13-acetate (TPA) for 20 weeks to allow skin tumor development (Abel et al., 2009; Kemp, 2005; Sun et al., 2007) (Figure 1A). At the end of TPA treatment, when all mice have developed multiple papillomas, we randomly divided these mice into two groups. One group of mice received doxycycline in the drinking water to allow continuous Twist1 expression in K5-positive tumor cells, even if tumor cells have migrated out of the skin and disseminated throughout the body. We used this systemic Twist1 induction group as the model for "irreversible EMT." The second group of mice received doxycycline topically on the dorsal skin area containing papillomas to induce Twist1 only at the primary tumor site, such that tumor cells would lose Twist1 expression once they have disseminated from the skin. This local induction of Twist1 was used as the model for "reversible EMT" (Figures 1A and S1D).

Within 7 days of doxycycline treatment through either oral or topical routes, papillomas on the K5-Twist1 mice began to invaginate into the skin and converted to SCCs at similar rates in both groups (Figures 1B and 1C). By three weeks, both groups of K5-Twist1 mice presented over 3-fold higher conversion frequencies than their control littermates (Figure 1C). Importantly, induction of Twist1 by oral or topical doxycycline resulted in similar conversion rates and frequencies of papillomas to SCCs (52% for oral treatment versus 40% for topical treatment; Figures 1C and 1D), demonstrating similar efficacy of Twist1 induction at the primary site using both doxycycline delivery methods. Histological analysis confirmed that papillomas have converted to poorly differentiated SCCs, with many regions presenting a spindle-cell phenotype in both groups of K5-Twist1 mice, while the naturally converted SCCs in the control group showed a well- to moderately differentiated epithelial morphology (Figure 1E). In Twist1-induced SCCs, tumor cells invaded through the underlying basement membrane, demonstrating a role of Twist1 in matrix degradation (Figure 1F). Together, these data indicate that Twist1 is sufficient to promote invasive carcinoma progression in vivo.

Reversible Induction of Twist1 Promotes Carcinoma Metastasis

To understand how irreversible versus reversible induction of Twist1 impacts metastasis, we examined individual mice for distant metastases by macroscopic and histological analysis. Starting at 5 weeks after doxycycline induction, mice with heavy metastasis burden were sacrificed together with mice in the comparison groups, and all mice were terminated by 8 weeks.

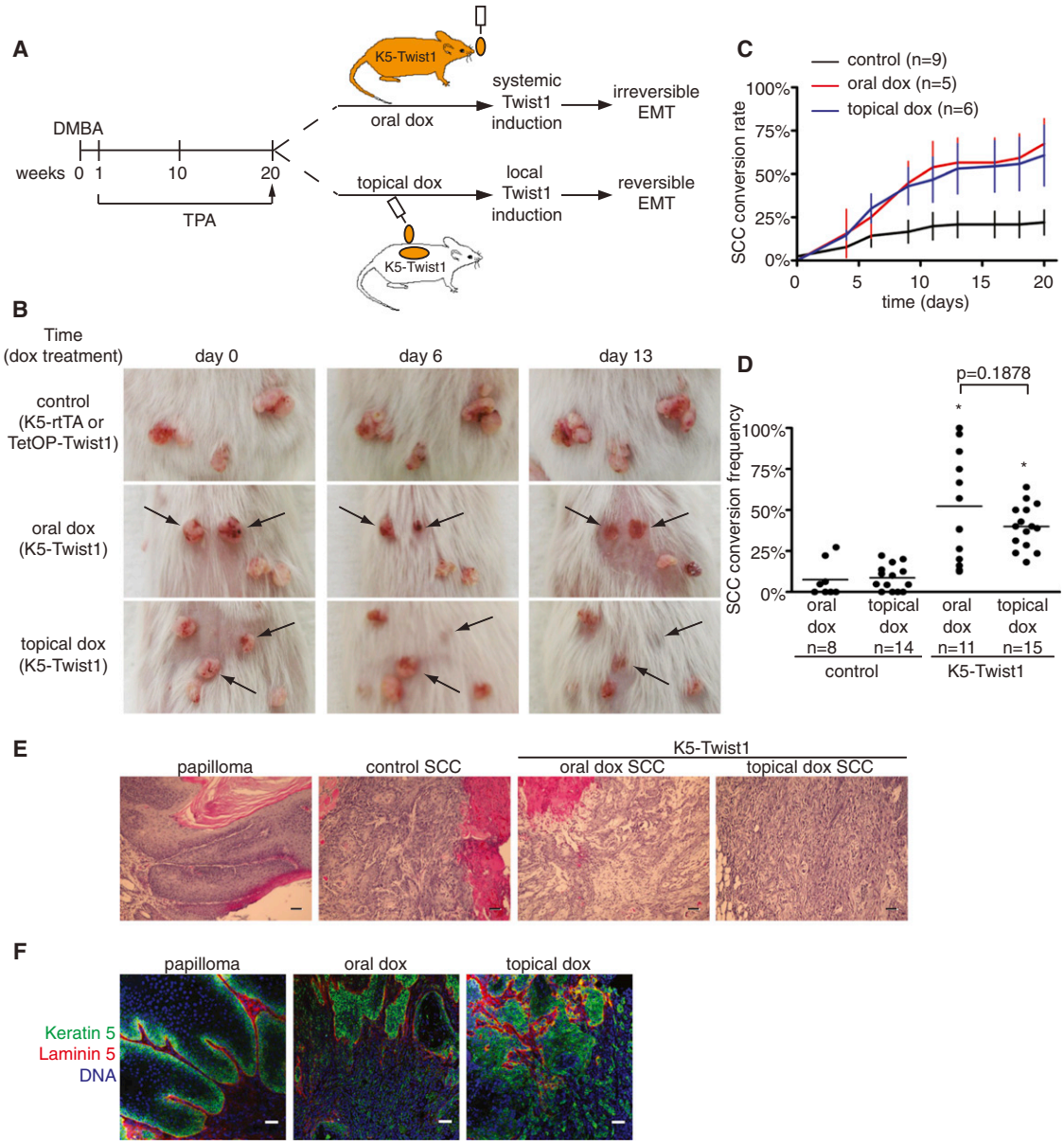

Figure 1. Induction of Twist1 Promotes Invasive Carcinoma Conversion

(A) A schematic of the DMBA/TPA skin tumor model and two doxycycline (dox) induction approaches in K5-Twist1 mice.

(B) Representative images of tumor lesions in control and doxycycline-treated K5-Twist1 mice over time. Control mice are single transgene littermates that received oral or topical doxycycline.

(C) Graph of conversion rates from papillomas to SCCs over time for a representative cohort ± SEM at each time point.

(D) Scatter plot of SCC conversion frequency in control and doxycycline-treated K5-Twist1 mice. Each dot represents one mouse, and the bar represents the mean of each group. *$p < 0.0001$ compared to control group, Student's t test.

(E) Histologic sections of tumors stained with hematoxylin and eosin. Papillomas have well-defined cellular organization, whereas control SCCs are well- to moderately differentiated. In contrast, doxycycline-treated tumors are disorganized and poorly differentiated. Bar = 50 μm.

(F) Frozen tumor sections were costained for tumor cells (K5, green), basement membrane (laminin 5, red), and nuclei stain (blue) to examine the breachment of basement membrane by tumor cells. Bar = 50 μm.

See also Figure S1.

Consistent with published data, 27%–33% of control SCC-bearing mice developed distant metastases in the lymph node and/or the lung (Abel et al., 2009; Kemp, 2005). Strikingly, 12 out of 14 K5-Twist1 mice (86%) receiving topical doxycycline developed distant metastases. In contrast, only three out of 13 K5-Twist1 mice (23%) receiving oral doxycycline developed distant metastases (Figure 2A). K5-Twist1 mice receiving topical doxycycline also developed significantly more metastatic

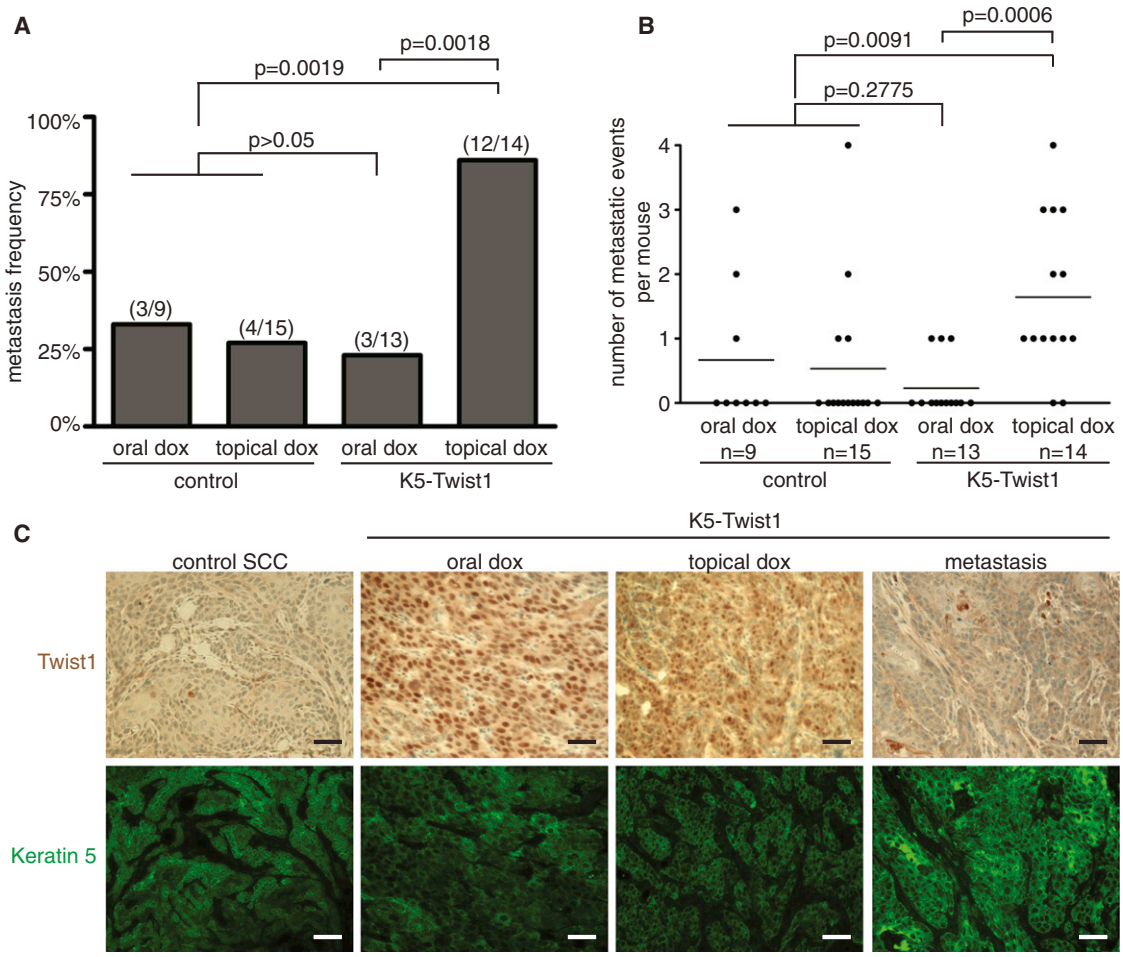

Figure 2. Reversible Induction of Twist1 Promotes Carcinoma Metastasis

(A) A histogram showing metastasis frequencies in control and K5-Twist1 mice group receiving oral or topical doxycycline. The fraction of mice developing metastases in individual groups is represented above each bar. Fisher's exact test analysis was performed to determine statistical significance.

(B) An event was defined as a tumor nodule in an individual lymph node and/or the presence of at least a single nodule in the lung tissue. Each dot represents a single mouse. Student's t test statistical analysis was performed to compare average events per group.

(C) Representative images of tumor sections costained for Twist1 (brown) and K5 (green). Paraffin-embedded tumor sections were stained for Twist1 using immunohistochemistry (brown) followed by immunofluorescent staining for K5 (green) on the same section to identify tumor cells. Bar = 50 μm.

lesions per mouse than mice receiving oral doxycycline, highlighting the drastic difference in metastasis incidences between these two groups (Figure 2B). It is also important to note that this difference is not due to nonspecific effects of doxycycline, since control mice receiving oral or topical doxycycline presented similar metastasis frequencies (Figures 2A and 2B).

We next examined the expression of Keratin 5 and Twist1 in the primary tumors and metastatic nodules. We found that all skin tumor cells express Keratin 5 both with and without Twist1 induction, suggesting that Keratin 5 can be used to specifically mark skin tumor cells in this model. Importantly, we detected robust nuclear Twist1 expression in the primary tumors following both oral and topical doxycycline treatment; in contrast, all distant metastatic lesions showed no Twist1 expression (Figure 2C). Together, these results indicate that only reversible, but not irreversible, induction of Twist1 significantly promotes distant metastasis.

Twist1 Regulates EMT in a Reversible Fashion during Metastasis In Vivo

To understand whether Twist1 indeed regulates EMT in a reversible manner during metastasis, we examined both primary tumors and metastatic nodules for the expression of Twist1 and key EMT markers. In control mice, the naturally converted SCCs showed strong expression of epithelial markers, including E-cadherin, β-catenin, and γ-catenin (Figures 3A–3C and S2A) and no expression of mesenchymal marker vimentin in the tumor cells (Figure 3D). Primary tumors from K5-Twist1 mice receiving either oral or topical doxycycline presented diminished epithelial markers and strong vimentin expression, indicating that Twist1 can effectively induce EMT in primary tumors (Figures 3, S2A, and S2B). In contrast, all corresponding distant metastases in the topical induction group present an epithelial morphology with no vimentin expression and strong E-cadherin staining (Figures 3C, 3D, and S2C). The fact that topical induction of

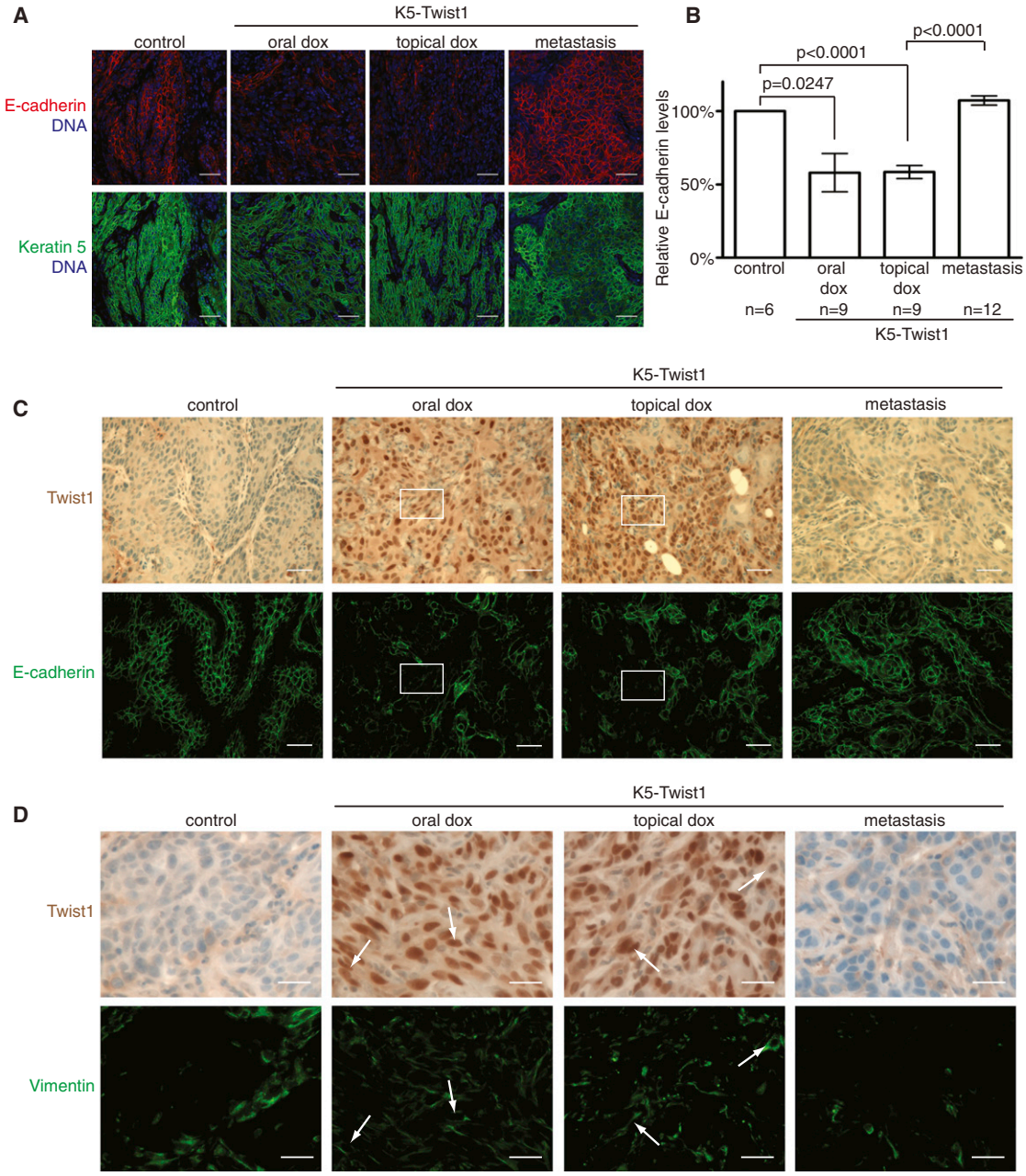

Figure 3. Twist1 Regulates EMT in a Reversible Fashion during Metastasis

(A) Primary and metastatic tumor samples were costained for E-cadherin (red) and K5 (green) to identify tumor cells undergoing EMT. Bar = 50 μm.

(B) The relative E-cadherin levels in $K5^+$ tumor cells were quantified in individual tumor samples from (A). Values were normalized to control samples and plotted on a histogram ± SEM. Student's t test statistical analysis was performed.

(C) Representative images of tumor sections from control and K5-Twist1 mice costained for Twist1 (brown) and E-cadherin (green) expression. Boxed regions highlight areas of Twist1-positive tumor cells with disrupted or absent E-cadherin expression. Bar = 50 μm.

(D) Representative images of tumor sections from control and K5-Twist1 mice costained for Twist1 (brown) and vimentin (green) expression. Arrows indicate Twist1-positive tumor cells that express vimentin. Bar = 25 μm.

See also Figure S2.

Twist1 drastically increased metastasis incidence and that distant metastases presented an epithelial phenotype indicates that "reversible EMT" can effectively promote tumor metastasis. To our surprise, while oral doxycycline induction of Twist1 reduced E-cadherin expression and induced EMT in primary tumors in all 13 mice (Figure 3), the rare metastatic nodules developed in three mice also presented an epithelial morphology (Figure S2D). Immunostaining analyses of these metastases showed strong E-cadherin along with weak Twist1 expression in the tumor cells (Figure S2E), suggesting that these rare

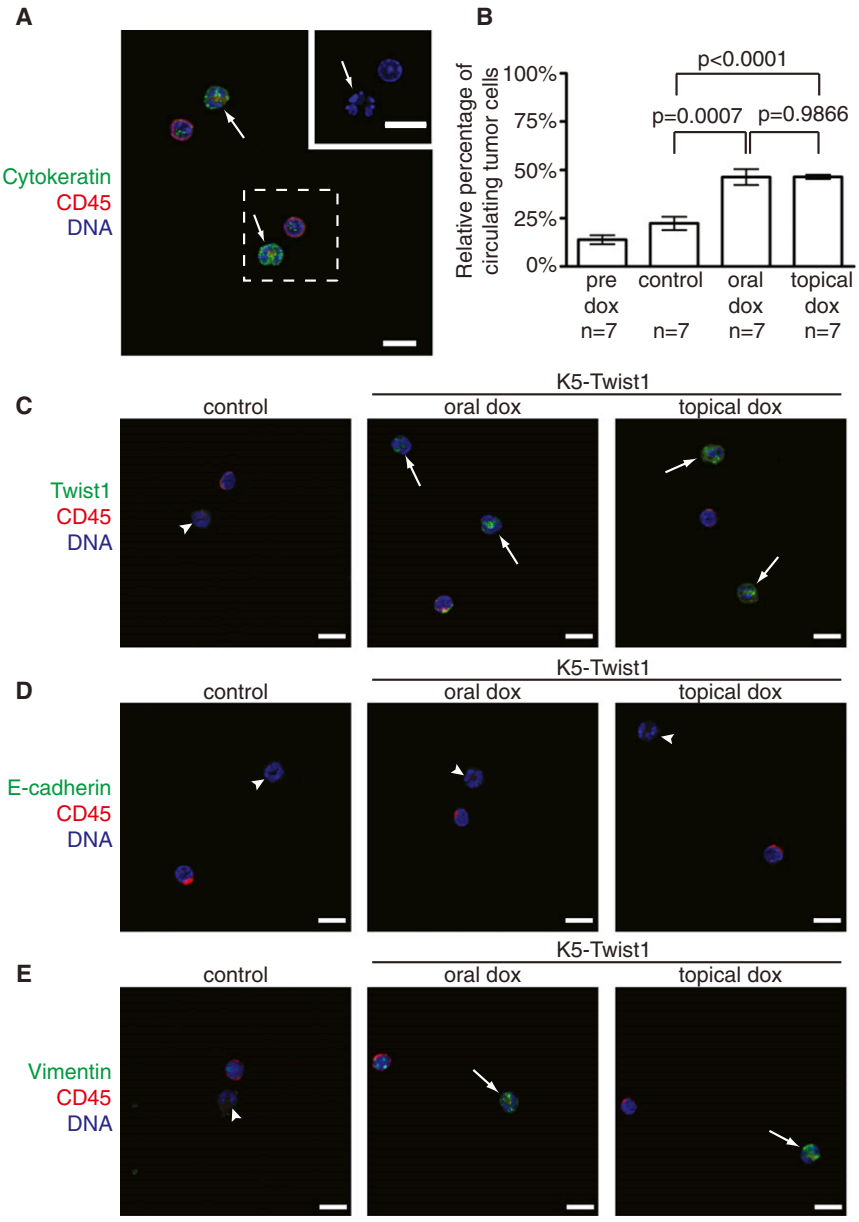

Figure 4. Activation of EMT Promotes Tumor Cell Intravasation

(A) Representative image of circulating tumor cells (CTCs). CTCs are defined as cells that are $CD45^-$ (red) and CK^+ (green) and present irregular nuclear shape (arrows). Inset shows magnified irregular nucleus in CTC. Bar = 10 μm.

(B) Quantification of CTCs in K5-Twist1 mice prior to doxycycline treatment (pre dox) in control mice and K5-Twist1 mice receiving oral and topical doxycycline. The percentages of CTCs among all nucleated cells were plotted on a histogram ± SEM. Student's t test statistical analysis was performed.

(C) CTCs from control and doxycycline-treated K5-Twist1 mice were examined for Twist1 expression. Representative images of CTCs costained for Twist1 (green), CD45 (red), and nuclei (blue). Arrows represent CTCs that are Twist1-positive; arrowheads represent CTCs that are Twist1-negative. Bar = 10 μm.

(D) Representative images of CTCs costained for E-cadherin (green), CD45 (red), and nuclei (blue). Arrowheads represent CTCs that are E-cadherin-negative. All CTCs show no E-cadherin expression. Bar = 10 μm.

(E) Representative images of CTCs stained for vimentin (green), CD45 (red), and nuclei (blue). Arrows represent CTCs that are vimentin-positive; arrowheads represent CTCs in the control littermates that are vimentin-negative. Bar = 10 μm.

See also Figure S3.

metastases are likely due to additional selective genetic and/or epigenetic changes that circumvent Twist1-induced EMT to allow the formation of epithelial metastases. Together, these results strongly support a requirement for the reversion of EMT in forming distant metastases in vivo.

Activation of EMT in Primary Tumors Promotes Intravasation

To successfully metastasize, carcinoma cells need to complete distinct steps, including invasion, intravasation, extravasation, and growth at distant sites. To investigate how activation of EMT impacts tumor cell intravasation into the blood circulation, we isolated circulating tumor cells (CTCs) from peripheral blood of K5-Twist1 and control mice. CTCs are defined as cells that are $CD45^-$ and pan-cytokeratin $(CK)^+$ and present irregular nuclear shape (Figure 4A). The percentages of CTCs in the blood increased over 2-fold in K5-Twist1 mice following oral or topical doxycycline treatment, compared to samples from control mice or from K5-Twist1 mice prior to doxycycline treatment (Figure 4B). Importantly, upon Twist1 induction, these CTCs were positive for Twist1 and mesenchymal marker vimentin, but negative for epithelial markers E-cadherin and β-catenin (Figures 4C–4E and S3), indicating an EMT phenotype in the CTCs. This result is consistent with studies showing that CTCs from human cancer patients present many features of EMT (Hou et al., 2011; Kallergi et al., 2011; Min et al., 2009) and that the presence of CTCs in human squamous cell carcinoma cancer patients is associated with distant metastasis and poor survival (Jatana et al., 2010; Pajonk et al., 2001; Winter et al., 2009). Our data show that both reversible and irreversible activation of EMT are equally effective in promoting tumor cell intravasation, and therefore the ability to disseminate is not the cause of different metastasis rates.

Activation of EMT Promotes Tumor Cell Extravasation

To examine the impact of EMT on tumor cell extravasation in distant organs, we isolated primary tumor cells from a K5-Twist1 mouse and treated them in culture with doxycycline for 7–11 days to induce Twist1 and EMT (Figures 5A and S4). These cells were then labeled with a fluorescent cell tracker and injected via tail vein into wild-type mice receiving doxycycline

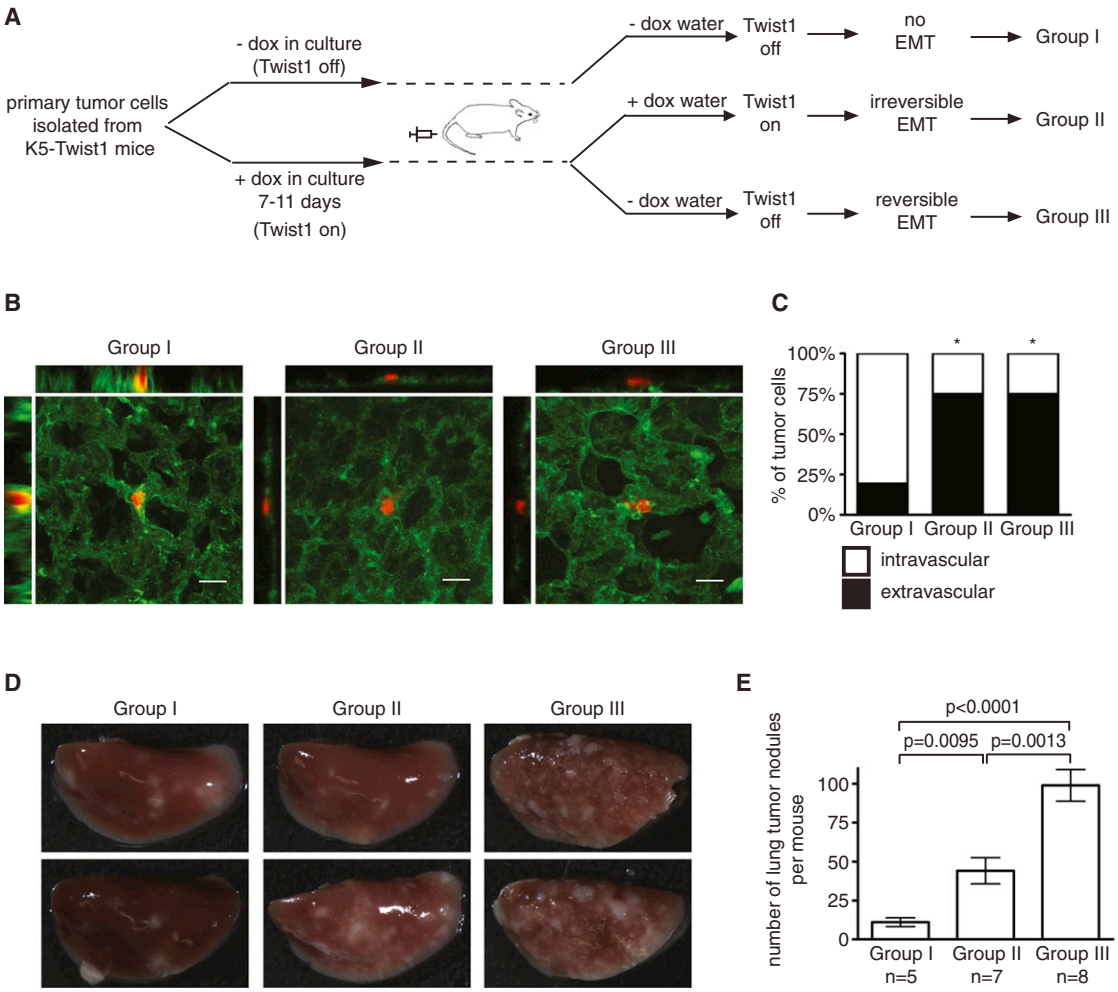

Figure 5. Activation of EMT Promotes Tumor Cell Extravasation

(A) A schematic of the experimental lung metastasis design.

(B) Confocal images of tumor cell (red) extravasation from lung vasculature (green). Bar = 20 μm.

(C) Quantification of tumor cell extravasation at 36 hr post tail vein injection. The number of tumor cells inside or outside of the vasculature was counted and then divided by the total number of cells assayed (n = 28–32 cells per group). The percentage of tumor cells inside (intravascular) or outside (extravascular) of the vessel was plotted on a stacked bar graph. *p < 0.0001 as determined by Fisher's exact test, compared to control group I.

(D and E) Images of lung tissues and quantification of average lung nodules per mouse ± SEM 4 weeks after tail vein injection. Student's t test statistical analysis was performed.

See also Figure S4.

or no doxycycline in drinking water, mimicking "irreversible" versus "reversible" EMT, respectively. The parental primary tumor cells were also injected as the "no EMT" control (Figure 5A). At 36 hr after injection, we quantified the number of tumor cells extravasated from the lung vasculature. While only 20% of "no EMT" control cells (Group I) extravasated out of the lung vasculature, induction of Twist1 promoted 75% of tumor cells to extravasate under both "irreversible" and "reversible" conditions (Group II and III) (Figures 5B and 5C). Supporting these results, 4 weeks after tail vein injection, the "no EMT" group (Group I) resulted in very few lung metastases compared to the other two groups (Group II and III) (Figures 5D and 5E). This strongly indicates that activation of Twist1 and EMT is critical to promote extravasation. Furthermore, consistent with previous studies (Cameron et al., 2000; Mendoza et al., 2010), tumor cells in circulation can extravasate from the blood within 1–2 days, much shorter than the time required for EMT reversion (~5 days). Therefore, these data also show that reversible activation of EMT in tumor cells can persist long enough to allow effective extravasation from the vasculature into distant organs before EMT reversion.

Reversion of EMT Promotes Colonization in Distant Sites

Since reversible and irreversible activation of EMT can both effectively promote local invasion, intravasation, and extravasation, the ability to grow in distant organs is likely to be the critical step regulated by the reversion of EMT. Because cell

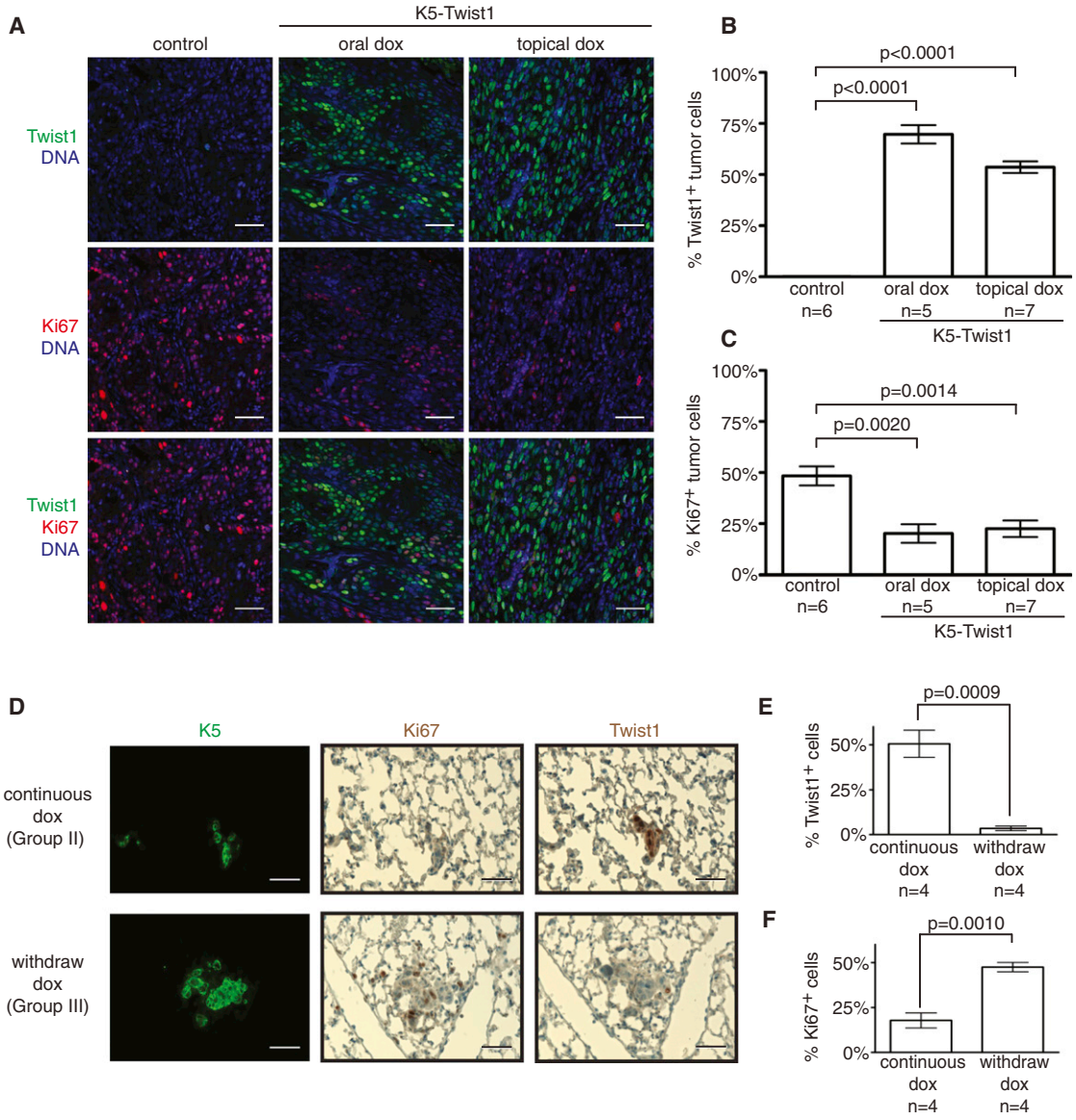

Figure 6. Reversion of EMT Promotes Colonization in Distant Sites

(A) Representative images of tumor sections costained with Twist1 (green), Ki67 (red), and nuclear stain (blue). Tumor sections from control and doxycycline-treated K5-Twist1 mice were costained for Twist1 and Ki67 to identify proliferation tumor cells. Bar = 50 μm.

(B and C) Relative levels of Twist1 and Ki67 expression in primary tumors from control and doxycycline-treated K5-Twist1 mice. Values were plotted on a histogram ± SEM. Student's t test statistical analysis was performed. n = tumor samples per group.

(D–F) Representative images of lung sections costained for K5 (green), Twist1 (brown) or Ki67 (brown), and quantification of Twist1 and Ki67 expression at 7 days post tail vein injection. Values were plotted on a histogram ± SEM. Student's t test statistical analysis was performed. n = mice per group.

proliferation is essential for establishing macrometastases and EMT-inducing factors are shown to reduce cell proliferation (Evdokimova et al., 2009; Vega et al., 2004), we analyzed the effect of Twist1 on tumor cell proliferation. Indeed, individual primary tumor cells expressing Twist1 showed very low to nondetectable expression of the proliferation marker Ki67 (Figure 6A). Tumor cell proliferation appeared to be negatively correlated with Twist1 expression (Figures 6B and 6C). To demonstrate that reversion of EMT to promote cell proliferation at distant sites is the essential step in establishing early metastatic colonies, we performed experimental lung metastasis studies, as described in Figure 5A, and examined cell proliferation and Twist1 expression in early metastatic lesions in the lung (7 days postinjection). Remarkably, early metastatic colonies showed strong positive Ki67 expression and low Twist1 expression under "reversible" EMT condition, while "irreversible" EMT resulted in colonies with high Twist1 expression and low Ki67 (Figures 6D–6F). This demonstrates that reversion of EMT promotes proliferation and establishment of early metastatic colonies in distant sites. Consistent with this result, 4 weeks after tail injection, mice in

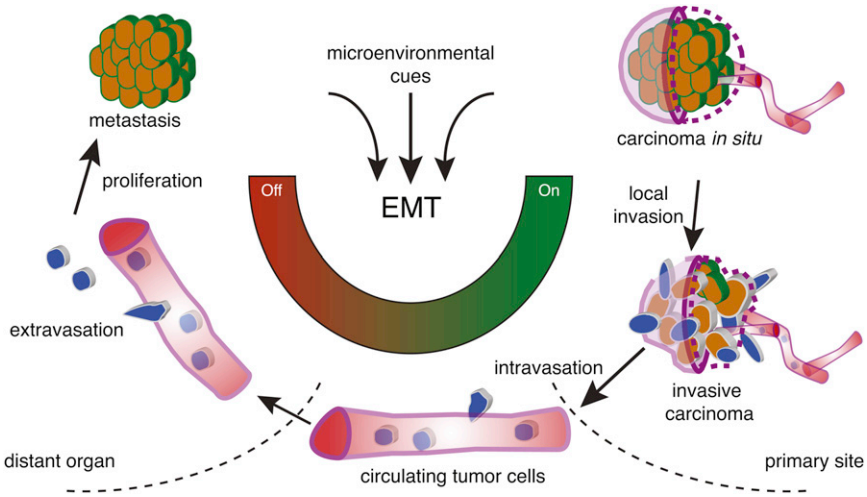

Figure 7. Reversible EMT Model for Tumor Metastasis

During tumor progression, local microenvironmental cues in the primary tumor activate the EMT program. This triggers local tumor cell invasion and intravasation into the blood vessels. Circulating tumor cells maintain an EMT phenotype and travel to a distant site, after which the cells extravasate into the tissue parenchyma. The loss of EMT activating signals is essential for tumor cells to reverse phenotype and proliferate to form macrometastases.

the reversible EMT group (Group III) developed significantly more metastatic lung nodules than the irreversible group (Group II) (Figures 5D and 5E). Combined with our results above, these data show that disseminated tumor cells need to turn off Twist1 to reverse the EMT program, thus allowing proliferation to facilitate colonization in distant sites.

DISCUSSION

The in vivo role of EMT in tumor metastasis has been under intense debate, due to conflicting observations in human primary carcinoma and their corresponding distant metastases. In a spontaneous squamous cell carcinoma mouse model, we demonstrate the dynamic requirement of EMT in tumor metastasis: activation of EMT promotes local tumor invasion, intravasation, and extravasation of the systemic circulation; while reversion of EMT is essential to establish macrometastases (Figure 7). This mouse model mimics many genetic, molecular, and cellular features of human carcinoma. Our study, together with other clinical studies in breast, ovarian, and prostate cancers (Chao et al., 2010; Hudson et al., 2008; Hugo et al., 2007), indicates that EMT is activated in many types of primary human carcinoma, but not in their distant metastases. Therefore, the reversible EMT model demonstrated in the mouse squamous cell carcinoma is likely a general principle applicable to human carcinoma metastasis.

The "reversible" EMT model implies a level of cellular plasticity in the tumor cells. In other words, it is rather unlikely that genes involved in the EMT program will be permanently altered on the genome level, thus being unable to revert in distant sites during metastasis. This is supported by the fact that key EMT-inducing transcription factors and other key genes involved in the EMT pathway have not been reported to be prime targets for genomic deletion or mutation in various human cancer genome sequencing and mouse tumor model studies. Instead, the EMT program is largely controlled at the transcriptional and translational level in response to various proinvasion signals in the local tumor microenvironment, such as hypoxia, inflammation, and nutrient conditions. TGFβ1, one such EMT-inducing signal from tumor stroma, has been examined for its role in promoting invasion and metastasis in the skin carcinogenesis model. Interestingly, the inducible TGFβ1 mice used in the study required topical induction to activate the TGFβ1 transgene. In these mice, topical activation of TGFβ1 signaling promoted invasive SCCs with spindle cell morphology and resulted in distant metastases with epithelial characteristics (Han et al., 2005; Weeks et al., 2001). These results could also be due to tumor cells undergoing a reversible EMT to form epithelial metastases, as demonstrated in our Twist1 mouse model.

An alternative model of EMT in tumor metastasis proposes that epithelial tumor cells can seed metastasis without undergoing EMT in the presence of mesenchymal tumor cells that have undergone EMT (Celià-Terrassa et al., 2012; Tsuji et al., 2008). Our results, showing that circulating tumor cells express no E-cadherin (Figure 4D), would argue that these epithelial cells might have undergone a transient EMT, perhaps in response to an inducing signal from coexisting mesenchymal tumor cells in primary tumors to metastasize.

The transient nature of EMT requires a delicate balance between the maintenance and loss of epithelial traits to promote efficient metastasis in vivo. In culture, epithelial cells undergoing a complete EMT lose epithelial markers, including cytokeratin expression. Our data suggests carcinoma cells in vivo may only need to undergo a partial EMT for dissemination, as evident by detectable cytokeratin expression in the CTCs (Figure 4). This is supported by observations that human cytokeratin-positive CTCs also present an EMT signature (Hou et al., 2011; Kallergi et al., 2011; Min et al., 2009; Rhim et al., 2012). A partial EMT would be sufficient to promote tumor cell dissemination, but also facilitate disseminated mesenchymal tumor cells to quickly revert to an epithelial phenotype for proliferation and colonization in distant organs.

The ability to proliferate at distant sites is essential for the establishment of early metastatic lesions. Previous studies have shown that EMT-inducing factors can reduce cell proliferation in various tumor cells (Bierie and Moses, 2006; Evdokimova et al., 2009; Vega et al., 2004). Independent studies also found that invasive tumor cells also present a gene signature that implicates decreased cellular proliferation and increased motility (Goswami et al., 2004; Wang et al., 2004). Our study demonstrates that Twist1 expression decreased cell proliferation in vivo and turning off Twist1 at distant sites promoted metastatic growth, therefore suggesting that tumor cells need to toggle

proliferation and migration to achieve efficient metastasis. This is consistent with a recent report that reversion of EMT in MDA-MB-231 cells is associated with increased proliferation during lung colonization (Gao et al., 2012). However, given that colonization, a rate-limiting step in metastasis, has been shown to require numerous cellular and molecular events to accomplish (Chambers et al., 2002; Luzzi et al., 1998; Sugarbaker, 1993; Weiss, 1990), it is evident that reversion of EMT to increase proliferation in distant sites alone is not sufficient for colonization. Indeed, the results from our spontaneous skin tumor model show that the number of metastatic lesions in individual mice is still much lower (average two lesions per mouse) compared to the abundant circulating tumor cells detected in the blood upon Twist1 induction. Therefore, future studies are needed to identify additional molecular events that contribute to colonization in this tumor model.

Cancer patients can develop metastases from dormant tumor cells years after primary tumor resection (Chambers et al., 2002; Goss and Chambers, 2010; Meng et al., 2004). Although it is technically challenging to detect single dormant tumor cells in distant organs in our spontaneous tumor model and in cancer patients, both our study and several clinical studies found that circulating tumor cells in the blood present many molecular features of EMT (Hou et al., 2011; Kallergi et al., 2011; Min et al., 2009; Rhim et al., 2012). Therefore, our study raises the possibility that dormant tumor cells are in an EMT state and need to revert EMT to regain proliferation. Therapeutic agents that inhibit EMT have been proposed as a treatment option against tumor metastasis (Garber, 2008). The transient nature of EMT in carcinoma metastasis cautions that such an approach alone could be counterproductive and promote metastatic colonization when patients already present circulating tumor cells. Instead, inhibiting the reversion of EMT could be a logical approach to prevent resurrection of dormant tumor cells.

EXPERIMENTAL PROCEDURES

Generation of Inducible Twist1 Mice and Tumor Model

All animal care and experiments were approved by the Institutional Animal Care and Use Committee of the University of California, San Diego. TetOP-Twist1 mice were generated using a site-specific single copy integration strategy (Beard et al., 2006). Mice were backcrossed over nine generations onto the FVB/N strain. Skin-specific inducible Twist1 mice were generated by crossing TetOP-Twist1 mice with K5-rtTA mice (Diamond et al., 2000) (kindly provided by Dr. Stuart Yuspa, NCI, Bethesda, MD). The DMBA/TPA multistage chemical carcinogenesis model was performed as previously described (Abel et al., 2009; Sun et al., 2007). Briefly, 20 μg of DMBA was applied topically on the dorsal skin of transgenic mice. Mice were then treated with 12.5 μg of TPA twice a week for 20 weeks. Papilloma-bearing mice were then randomly divided to receive doxycycline (2 mg/ml) in the drinking water or topically on the dorsal skin.

The conversion rate from papilloma to squamous cell carcinoma (SCC) was calculated by dividing the number of ulcerated tumors by the total number of papillomas plus ulcerated tumors per mouse. Ulcerated tumors were defined as nodules that were previously papillomas and have invaginated into the dorsal skin. Mice with heavy metastasis burden were sacrificed together with mice in the comparison groups, and all mice were examined for macrometastases. A metastatic event was defined as a tumor nodule in an individual lymph node and/or the presence of at least a single nodule in the lung tissue.

Biochemistry and Immunohistological Staining and Analysis

Paraffin-embedded tumor sections were stained with a mouse anti-Twist1 antibody (Santa Cruz Biotech, Santa Cruz, CA), rabbit anti-Keratin 5 antibody (K5, Covance, Princeton, NJ), rabbit anti-pan-cytokeratin antibody (pan-CK, Abcam, Cambridge, MA), rabbit anti-E-cadherin (Abcam), mouse anti-β-catenin (BD Biosciences, San Diego, CA), mouse anti-γ-catenin (BD Biosciences), rabbit anti-vimentin (GeneTex, Irvine, CA), or rabbit anti-Ki67 antibody (Abcam). Endogenous mouse antigen was blocked using Mouse on Mouse blocking agent (Vector labs, Burlingame, CA). Immunohistochemistry was performed using the ABC kit (Vector labs) and developed with 3,3′ diaminobenzidine chromogen (Vector labs). Frozen tumor sections were stained with a chicken anti-K5 antibody (gift from Dr. Colin Jamora) and rabbit anti-laminin 5 antibody (gift from Dr. Monique Aumailley) to identify K5 tumor cells and basement membranes. Alexafluor dyes (Invitrogen, Carlsbad, CA) conjugated to the appropriate species were used as secondary antibodies. Hoechst 33258 dye or DAPI were used for nuclear stain. Western blot analysis for Twist1, E-cadherin, β-catenin, and glyceraldehyde-3-phosphate dehydrogenase protein expression was performed as previously described (Eckert et al., 2011).

Images were collected using an Olympus FV-1000 confocal microscope or Nikon E600 upright microscope. For quantification of Twist1 and Ki67 expression, at least three fields were collected for each tumor and at least five tumors from each group were examined. Twist1-positive cells, Ki67-positive cells, and the total number of cells (nuclear stain positive) from each field were counted using Volocity software (PerkinElmer, Waltham, MA). For quantification of relative E-cadherin levels, images were analyzed for E-cadherin expression by measuring the threshold level of staining using Image J software (National Institutes of Health), then divided by the area of positive K5 staining to calculate relative E-cadherin levels in tumor regions. Values were normalized to E-cadherin levels in control tumors.

Circulating Tumor Cell Staining and Analysis

Peripheral blood was obtained from tumor-bearing mice via submandibular bleeding or intracardiac puncture at the termination of the experiment. Red blood cells (RBCs) were removed by incubating whole blood in RBC lysis solution. Remaining cells were spun down and fixed in 4% paraformaldehyde. Cells were then spun onto slides using a cytospin and stained with rat anti-CD45 (BD Biosciences) and rabbit anti-pan-CK (Abcam) antibodies, followed by DAPI nuclear stain. Circulating tumor cells (CTCs) were identified as irregularly shaped nucleated cells that were CD45-negative, CK-positive cells. All cells in at least five high-powered fields were counted, and the relative percentage of CTCs was calculated and plotted on a histogram.

Experimental Lung Metastasis Assay

Primary inducible Twist1 skin tumor cells were isolated from a tumor-bearing K5-Twist1 mouse according to manufacturer's protocol for Defined Keratinocyte Serum-Free Media protocol (Invitrogen). Briefly, tumors were removed and incubated in PBS with 2X antibiotic cocktail solution (Invitrogen) for 1–2 hr at 4°C. Tumors were transferred to dispase solution supplemented with 2X antibiotic cocktail solution and incubated at 4°C overnight. Tumors were then minced in 0.5% Trypsin solution and incubated at 37°C for about 15 min. A soybean trypsin inhibitor (Invitrogen) was used to stop the trypsinization. Cells were maintained in serum-free keratinocyte media. To induce Twist1 in culture, doxycycline (1 μg/ml) was added into the media. After 7–11 days, 1–1.5 × 10^6 cells were injected via tail vein injection into mice receiving no doxycycline water or 2 mg/ml doxycycline water. Mice were monitored and euthanized when breathing appeared difficult. Lung tissue was perfused with and fixed in 4% paraformaldehyde. Tumor nodules on the surface of every lung lobe were counted, and the numbers were plotted on a histogram. For tumor cell proliferation analysis, mice were euthanized 7 days postinjection of cells. Lung tissue was perfused and embedded in paraffin. Tissue sections were stained for K5, Twist1, and Ki67, as previously mentioned.

For tumor cell extravasation analysis, cells were labeled with CellTracker-Red (Invitrogen) according to manufacturer's recommendation. A total of 1–1.5 × 10^6 cells were injected into mice via tail vein, and mice were euthanized after 36 hr. To label lung vasculature, mice were injected with Fluorescein-labeled Lycopersicon Esculentum Lectin (Vector Labs) 30 min prior to euthanasia. Thick lung tissue sections were obtained by manually slicing the tissue and were then mounted on slides for viewing. Confocal z-stack images were obtained using an Olympus FV-1000 microscope and analyzed using FluoView (Olympus) and Image J software.

Human Breast Cancer Tissue Microarray

Tissue microarray (TMA) of 99 human breast carcinoma and matched metastases were purchased from US Biomax Inc. The TMA contained human tissues obtained with informed consent according to US federal law and are exempt from Institutional Review Board review by the University of California, San Diego Human Research Protections Program. Staining for Twist1 and cytokeratin was performed as described above. All samples were analyzed for Twist1 expression, and patient samples were considered positive for Twist1 expression only if >10% of tumor cells in the primary tumor stained positive for nuclear Twist1. Out of 99 matched samples, only 20 samples met our criteria for being positive for Twist1. Cells were counted using the cell counter function in Image J software.

Statistical Analysis

Statistical analysis was performed using GraphPad Prism Software (La Jolla, CA). Student's t test was applied for comparisons between two groups. The Fisher's exact test was applied to analyze the metastasis frequency and tumor cell extravasation rate using a contingency table. The one-tailed exact binomial test was performed for statistical analysis of Twist1 expression in human breast cancer TMA.

SUPPLEMENTAL INFORMATION

Supplemental Information includes four figures and can be found with this article online at http://dx.doi.org/10.1016/j.ccr.2012.09.022.

ACKNOWLEDGMENTS

We thank Konrad Hochedlinger, Colin Jamora, Caroline Beard, Edward Vizcarra, Ferenc Reinhardt, Esmeralda Casas, Naoto Yoshizuka, and Monique Aumailley for reagents and invaluable technical help. We thank Robert Weinberg for his initial support on this work, members of the Yang lab for helpful discussions, and Sylvia Evans and Ittai Ben-Porath for critically reading the manuscript. We thank the Shared Microscope Facility and UCSD Cancer Center Specialized Support Grant P30 CA23100. This work was supported by grants from American Cancer Society (RSG-09-282-01-CSM), NIH (DP2 OD002420-01), the Sidney Kimmel Foundation for Cancer Research, and the University of California Cancer Research Coordinating Committee to J.Y. J.H.T. was supported by NIH (T32CA121938) and the California Breast Cancer Program postdoctoral fellowship (16FB-0009).

Received: May 15, 2012
Revised: July 25, 2012
Accepted: September 14, 2012
Published online: November 29, 2012

REFERENCES

Abel, E.L., Angel, J.M., Kiguchi, K., and DiGiovanni, J. (2009). Multi-stage chemical carcinogenesis in mouse skin: fundamentals and applications. Nat. Protoc. *4*, 1350–1362.

Batlle, E., Sancho, E., Francí, C., Domínguez, D., Monfar, M., Baulida, J., and García De Herreros, A. (2000). The transcription factor snail is a repressor of E-cadherin gene expression in epithelial tumour cells. Nat. Cell Biol. *2*, 84–89.

Beard, C., Hochedlinger, K., Plath, K., Wutz, A., and Jaenisch, R. (2006). Efficient method to generate single-copy transgenic mice by site-specific integration in embryonic stem cells. Genesis *44*, 23–28.

Bierie, B., and Moses, H.L. (2006). Tumour microenvironment: TGFbeta: the molecular Jekyll and Hyde of cancer. Nat. Rev. Cancer *6*, 506–520.

Blick, T., Widodo, E., Hugo, H., Waltham, M., Lenburg, M.E., Neve, R.M., and Thompson, E.W. (2008). Epithelial mesenchymal transition traits in human breast cancer cell lines. Clin. Exp. Metastasis *25*, 629–642.

Cameron, M.D., Schmidt, E.E., Kerkvliet, N., Nadkarni, K.V., Morris, V.L., Groom, A.C., Chambers, A.F., and MacDonald, I.C. (2000). Temporal progression of metastasis in lung: cell survival, dormancy, and location dependence of metastatic inefficiency. Cancer Res. *60*, 2541–2546.

Cano, A., Pérez-Moreno, M.A., Rodrigo, I., Locascio, A., Blanco, M.J., del Barrio, M.G., Portillo, F., and Nieto, M.A. (2000). The transcription factor snail controls epithelial-mesenchymal transitions by repressing E-cadherin expression. Nat. Cell Biol. *2*, 76–83.

Celià-Terrassa, T., Meca-Cortés, Ó., Mateo, F., de Paz, A.M., Rubio, N., Arnal-Estapé, A., Ell, B.J., Bermudo, R., Díaz, A., Guerra-Rebollo, M., et al. (2012). Epithelial-mesenchymal transition can suppress major attributes of human epithelial tumor-initiating cells. J. Clin. Invest. *122*, 1849–1868.

Chambers, A.F., Groom, A.C., and MacDonald, I.C. (2002). Dissemination and growth of cancer cells in metastatic sites. Nat. Rev. Cancer *2*, 563–572.

Chao, Y.L., Shepard, C.R., and Wells, A. (2010). Breast carcinoma cells re-express E-cadherin during mesenchymal to epithelial reverting transition. Mol. Cancer *9*, 179.

Comijn, J., Berx, G., Vermassen, P., Verschueren, K., van Grunsven, L., Bruyneel, E., Mareel, M., Huylebroeck, D., and van Roy, F. (2001). The two-handed E box binding zinc finger protein SIP1 downregulates E-cadherin and induces invasion. Mol. Cell *7*, 1267–1278.

Diamond, I., Owolabi, T., Marco, M., Lam, C., and Glick, A. (2000). Conditional gene expression in the epidermis of transgenic mice using the tetracycline-regulated transactivators tTA and rTA linked to the keratin 5 promoter. J. Invest. Dermatol. *115*, 788–794.

DiGiovanni, J. (1992). Multistage carcinogenesis in mouse skin. Pharmacol. Ther. *54*, 63–128.

Eckert, M.A., Lwin, T.M., Chang, A.T., Kim, J., Danis, E., Ohno-Machado, L., and Yang, J. (2011). Twist1-induced invadopodia formation promotes tumor metastasis. Cancer Cell *19*, 372–386.

Eger, A., Aigner, K., Sonderegger, S., Dampier, B., Oehler, S., Schreiber, M., Berx, G., Cano, A., Beug, H., and Foisner, R. (2005). DeltaEF1 is a transcriptional repressor of E-cadherin and regulates epithelial plasticity in breast cancer cells. Oncogene *24*, 2375–2385.

Evdokimova, V., Tognon, C., Ng, T., Ruzanov, P., Melnyk, N., Fink, D., Sorokin, A., Ovchinnikov, L.P., Davicioni, E., Triche, T.J., and Sorensen, P.H. (2009). Translational activation of snail1 and other developmentally regulated transcription factors by YB-1 promotes an epithelial-mesenchymal transition. Cancer Cell *15*, 402–415.

Gao, D., Joshi, N., Choi, H., Ryu, S., Hahn, M., Catena, R., Sadik, H., Argani, P., Wagner, P., Vahdat, L.T., et al. (2012). Myeloid progenitor cells in the premetastatic lung promote metastases by inducing mesenchymal to epithelial transition. Cancer Res. *72*, 1384–1394.

Garber, K. (2008). Epithelial-to-mesenchymal transition is important to metastasis, but questions remain. J. Natl. Cancer Inst. *100*, 232–233, 239.

Goss, P.E., and Chambers, A.F. (2010). Does tumour dormancy offer a therapeutic target? Nat. Rev. Cancer *10*, 871–877.

Goswami, S., Wang, W., Wyckoff, J.B., and Condeelis, J.S. (2004). Breast cancer cells isolated by chemotaxis from primary tumors show increased survival and resistance to chemotherapy. Cancer Res. *64*, 7664–7667.

Hajra, K.M., Chen, D.Y., and Fearon, E.R. (2002). The SLUG zinc-finger protein represses E-cadherin in breast cancer. Cancer Res. *62*, 1613–1618.

Han, G., Lu, S.L., Li, A.G., He, W., Corless, C.L., Kulesz-Martin, M., and Wang, X.J. (2005). Distinct mechanisms of TGF-beta1-mediated epithelial-to-mesenchymal transition and metastasis during skin carcinogenesis. J. Clin. Invest. *115*, 1714–1723.

Hay, E.D. (1995). An overview of epithelio-mesenchymal transformation. Acta Anat. (Basel) *154*, 8–20.

Hou, J.M., Krebs, M., Ward, T., Sloane, R., Priest, L., Hughes, A., Clack, G., Ranson, M., Blackhall, F., and Dive, C. (2011). Circulating tumor cells as a window on metastasis biology in lung cancer. Am. J. Pathol. *178*, 989–996.

Hudson, L.G., Zeineldin, R., and Stack, M.S. (2008). Phenotypic plasticity of neoplastic ovarian epithelium: unique cadherin profiles in tumor progression. Clin. Exp. Metastasis *25*, 643–655.

Hugo, H., Ackland, M.L., Blick, T., Lawrence, M.G., Clements, J.A., Williams, E.D., and Thompson, E.W. (2007). Epithelial—mesenchymal and mesenchymal—epithelial transitions in carcinoma progression. J. Cell. Physiol. *213*, 374–383.

Hüsemann, Y., Geigl, J.B., Schubert, F., Musiani, P., Meyer, M., Burghart, E., Forni, G., Eils, R., Fehm, T., Riethmüller, G., and Klein, C.A. (2008). Systemic spread is an early step in breast cancer. Cancer Cell *13*, 58–68.

Jatana, K.R., Balasubramanian, P., Lang, J.C., Yang, L., Jatana, C.A., White, E., Agrawal, A., Ozer, E., Schuller, D.E., Teknos, T.N., and Chalmers, J.J. (2010). Significance of circulating tumor cells in patients with squamous cell carcinoma of the head and neck: initial results. Arch. Otolaryngol. Head Neck Surg. *136*, 1274–1279.

Kallergi, G., Papadaki, M.A., Politaki, E., Mavroudis, D., Georgoulias, V., and Agelaki, S. (2011). Epithelial to mesenchymal transition markers expressed in circulating tumour cells of early and metastatic breast cancer patients. Breast Cancer Res. *13*, R59.

Kalluri, R., and Weinberg, R.A. (2009). The basics of epithelial-mesenchymal transition. J. Clin. Invest. *119*, 1420–1428.

Kemp, C.J. (2005). Multistep skin cancer in mice as a model to study the evolution of cancer cells. Semin. Cancer Biol. *15*, 460–473.

Ledford, H. (2011). Cancer theory faces doubts. Nature *472*, 273.

Luzzi, K.J., MacDonald, I.C., Schmidt, E.E., Kerkvliet, N., Morris, V.L., Chambers, A.F., and Groom, A.C. (1998). Multistep nature of metastatic inefficiency: dormancy of solitary cells after successful extravasation and limited survival of early micrometastases. Am. J. Pathol. *153*, 865–873.

Mani, S.A., Yang, J., Brooks, M., Schwaninger, G., Zhou, A., Miura, N., Kutok, J.L., Hartwell, K., Richardson, A.L., and Weinberg, R.A. (2007). Mesenchyme Forkhead 1 (FOXC2) plays a key role in metastasis and is associated with aggressive basal-like breast cancers. Proc. Natl. Acad. Sci. USA *104*, 10069–10074.

Mendoza, A., Hong, S.H., Osborne, T., Khan, M.A., Campbell, K., Briggs, J., Eleswarapu, A., Buquo, L., Ren, L., Hewitt, S.M., et al. (2010). Modeling metastasis biology and therapy in real time in the mouse lung. J. Clin. Invest. *120*, 2979–2988.

Meng, S., Tripathy, D., Frenkel, E.P., Shete, S., Naftalis, E.Z., Huth, J.F., Beitsch, P.D., Leitch, M., Hoover, S., Euhus, D., et al. (2004). Circulating tumor cells in patients with breast cancer dormancy. Clin. Cancer Res. *10*, 8152–8162.

Min, A.L., Choi, J.Y., Woo, H.Y., Kim, J.D., Kwon, J.H., Bae, S.H., Yoon, S.K., Shin, S.H., Chung, Y.J., and Jung, C.K. (2009). High expression of Snail mRNA in blood from hepatocellular carcinoma patients with extra-hepatic metastasis. Clin. Exp. Metastasis *26*, 759–767.

Ou, D.L., Chien, H.F., Chen, C.L., Lin, T.C., and Lin, L.I. (2008). Role of Twist in head and neck carcinoma with lymph node metastasis. Anticancer Res. *28* (2B), 1355–1359.

Pajonk, F., Schlessmann, S., Guttenberger, R., and Henke, M. (2001). Epithelial cells in the peripheral blood of patients with cancer of the head and neck: incidence, detection and possible clinical significance. Radiother. Oncol. *59*, 213–217.

Peinado, H., Olmeda, D., and Cano, A. (2007). Snail, Zeb and bHLH factors in tumour progression: an alliance against the epithelial phenotype? Nat. Rev. Cancer *7*, 415–428.

Perez-Losada, J., and Balmain, A. (2003). Stem-cell hierarchy in skin cancer. Nat. Rev. Cancer *3*, 434–443.

Rhim, A.D., Mirek, E.T., Aiello, N.M., Maitra, A., Bailey, J.M., McAllister, F., Reichert, M., Beatty, G.L., Rustgi, A.K., Vonderheide, R.H., et al. (2012). EMT and dissemination precede pancreatic tumor formation. Cell *148*, 349–361.

Sasaki, K., Natsugoe, S., Ishigami, S., Matsumoto, M., Okumura, H., Setoyama, T., Uchikado, Y., Kita, Y., Tamotsu, K., Sakamoto, A., et al. (2009). Significance of Twist expression and its association with E-cadherin in esophageal squamous cell carcinoma. J. Exp. Clin. Cancer Res. *28*, 158.

Sugarbaker, P.H. (1993). Metastatic inefficiency: the scientific basis for resection of liver metastases from colorectal cancer. J. Surg. Oncol. Suppl. *3*, 158–160.

Sun, P., Yoshizuka, N., New, L., Moser, B.A., Li, Y., Liao, R., Xie, C., Chen, J., Deng, Q., Yamout, M., et al. (2007). PRAK is essential for ras-induced senescence and tumor suppression. Cell *128*, 295–308.

Tarin, D., Thompson, E.W., and Newgreen, D.F. (2005). The fallacy of epithelial mesenchymal transition in neoplasia. Cancer Res. *65*, 5996–6000.

Thiery, J.P. (2002). Epithelial-mesenchymal transitions in tumour progression. Nat. Rev. Cancer *2*, 442–454.

Thiery, J.P., Acloque, H., Huang, R.Y., and Nieto, M.A. (2009). Epithelial-mesenchymal transitions in development and disease. Cell *139*, 871–890.

Thompson, E.W., Newgreen, D.F., and Tarin, D. (2005). Carcinoma invasion and metastasis: a role for epithelial-mesenchymal transition? Cancer Res. *65*, 5991–5995, discussion 5995.

Tsuji, T., Ibaragi, S., Shima, K., Hu, M.G., Katsurano, M., Sasaki, A., and Hu, G.F. (2008). Epithelial-mesenchymal transition induced by growth suppressor p12CDK2-AP1 promotes tumor cell local invasion but suppresses distant colony growth. Cancer Res. *68*, 10377–10386.

Vega, S., Morales, A.V., Ocaña, O.H., Valdés, F., Fabregat, I., and Nieto, M.A. (2004). Snail blocks the cell cycle and confers resistance to cell death. Genes Dev. *18*, 1131–1143.

Wang, W., Goswami, S., Lapidus, K., Wells, A.L., Wyckoff, J.B., Sahai, E., Singer, R.H., Segall, J.E., and Condeelis, J.S. (2004). Identification and testing of a gene expression signature of invasive carcinoma cells within primary mammary tumors. Cancer Res. *64*, 8585–8594.

Watson, M.A., Ylagan, L.R., Trinkaus, K.M., Gillanders, W.E., Naughton, M.J., Weilbaecher, K.N., Fleming, T.P., and Aft, R.L. (2007). Isolation and molecular profiling of bone marrow micrometastases identifies TWIST1 as a marker of early tumor relapse in breast cancer patients. Clin. Cancer Res. *13*, 5001–5009.

Weeks, B.H., He, W., Olson, K.L., and Wang, X.J. (2001). Inducible expression of transforming growth factor beta1 in papillomas causes rapid metastasis. Cancer Res. *61*, 7435–7443.

Weiss, L. (1990). Metastatic inefficiency. Adv. Cancer Res. *54*, 159–211.

Winter, S.C., Stephenson, S.A., Subramaniam, S.K., Paleri, V., Ha, K., Marnane, C., Krishnan, S., and Rees, G. (2009). Long term survival following the detection of circulating tumour cells in head and neck squamous cell carcinoma. BMC Cancer *9*, 424.

Wushou, A., Pan, H.Y., Liu, W., Tian, Z., Wang, L.Z., Shali, S., and Zhang, Z.Y. (2012). Correlation of increased twist with lymph node metastasis in patients with oral squamous cell carcinoma. J. Oral Maxillofac. Surg. *70*, 1473–1479.

Xie, F., Li, K., and Ouyang, X. (2009). Twist, an independent prognostic marker for predicting distant metastasis and survival rates of esophageal squamous cell carcinoma patients. Clin. Exp. Metastasis *26*, 1025–1032.

Yang, J., Mani, S.A., Donaher, J.L., Ramaswamy, S., Itzykson, R.A., Come, C., Savagner, P., Gitelman, I., Richardson, A., and Weinberg, R.A. (2004). Twist, a master regulator of morphogenesis, plays an essential role in tumor metastasis. Cell *117*, 927–939.

Yuen, H.F., Chan, Y.P., Wong, M.L., Kwok, W.K., Chan, K.K., Lee, P.Y., Srivastava, G., Law, S.Y., Wong, Y.C., Wang, X., and Chan, K.W. (2007). Upregulation of Twist in oesophageal squamous cell carcinoma is associated with neoplastic transformation and distant metastasis. J. Clin. Pathol. *60*, 510–514.

Cancer Cell
Article

Metastatic Colonization Requires the Repression of the Epithelial-Mesenchymal Transition Inducer Prrx1

Oscar H. Ocaña,[1] Rebeca Córcoles,[1,5] Ángels Fabra,[2,5] Gema Moreno-Bueno,[3,4] Hervé Acloque,[1,6] Sonia Vega,[1] Alejandro Barrallo-Gimeno,[1,7] Amparo Cano,[3] and M. Angela Nieto[1,*]
[1]Instituto de Neurociencias CSIC-UMH, Avda. Ramón y Cajal s/n, 03550 San Juan de Alicante, Spain
[2]IDIBELL (Bellvitge Biomedical Research Institute), Centre d' Oncologia Molecular, Gran Via de L'Hospitalet, 199 Barcelona, Spain
[3]Departamento de Bioquímica, UAM. Instituto de Investigaciones Biomédicas "Alberto Sols" CSIC-UAM, IdiPAZ, Arturo Duperier, 4, 28029 Madrid, Spain
[4]Fundación MD Anderson Internacional, Arturo Soria 270, 28033 Madrid, Spain
[5]These authors equally contributed to this work
[6]Present address: UMR 444, INRA-ENVT, Génétique Cellulaire, F-31706 Toulouse, France
[7]Present address: Deptartamento de Ciències Fisiològiques - II, Facultat de Medicina i Odontologia, Universitat de Barcelona, Feixa Llarga, s/n, 08907 L'Hospitalet Llobregat, Barcelona, Spain
*Correspondence: anieto@umh.es
http://dx.doi.org/10.1016/j.ccr.2012.10.012

SUMMARY

The epithelial-mesenchymal transition (EMT) is required in the embryo for the formation of tissues for which cells originate far from their final destination. Carcinoma cells hijack this program for tumor dissemination. The relevance of the EMT in cancer is still debated because it is unclear how these migratory cells colonize distant tissues to form macrometastases. We show that the homeobox factor Prrx1 is an EMT inducer conferring migratory and invasive properties. The loss of Prrx1 is required for cancer cells to metastasize in vivo, which revert to the epithelial phenotype concomitant with the acquisition of stem cell properties. Thus, unlike the classical EMT transcription factors, Prrx1 uncouples EMT and stemness, and is a biomarker associated with patient survival and lack of metastasis.

INTRODUCTION

Metastasis is still the cause of 90% of deaths from carcinomas (Gupta and Massagué, 2006) and despite the efforts devoted to understand the mechanisms that drive disseminated tumor cells to colonize distant tissues, it remains the least understood step of tumor progression. To form distant metastasis, cancer cells must first dissociate from the primary tumor, invade adjacent tissues, and intravasate into lymphatic and blood vessels to later colonize lymph nodes and distant organs. For invasion to occur, there is evidence that carcinoma cells can undergo a phenotypic transformation, the epithelial-mesenchymal transition (EMT; Nieto, 2011), which enables them to invade, intravasate, and navigate through a network of thin vessels while acquiring stem cell-like properties (Mani et al., 2008; Morel et al., 2008; Wellner et al., 2009). Still, it is not clear how these individual mesenchymal cells can then form distant macrometastases, in particular because carcinoma metastases usually present a well-differentiated epithelial phenotype. Clues as to how this mesenchymal-to-epithelial plasticity may arise have come from the study of embryonic development, where several rounds of EMT and the reverse process, mesenchymal-epithelial transition (MET), are responsible for the formation of many tissues and organs (Yang and Weinberg, 2008; Thiery et al., 2009). Indeed, although experimental evidence is still scarce, some indications suggest that this might indeed occur in vivo

Significance

Metastasis is the cause of the vast majority of cancer-associated deaths, but the underlying mechanisms remain poorly understood. The invasion and dissemination steps during carcinoma progression have been associated with EMT, which endows cells with invasive abilities and the stem cell-like properties required to initiate the formation of a secondary tumor. However, it is unclear how these migratory cells colonize distant territories. Here, we show that abrogation of the EMT is important for metastatic colonization. The loss of the EMT inducer Prrx1 allows cancer cells to revert EMT while acquiring tumor-initiating abilities. Our results help reevaluate the potential benefits of current therapeutic strategies aimed at targeting the EMT while supporting those aimed at targeting stem cell properties in cancer cells.

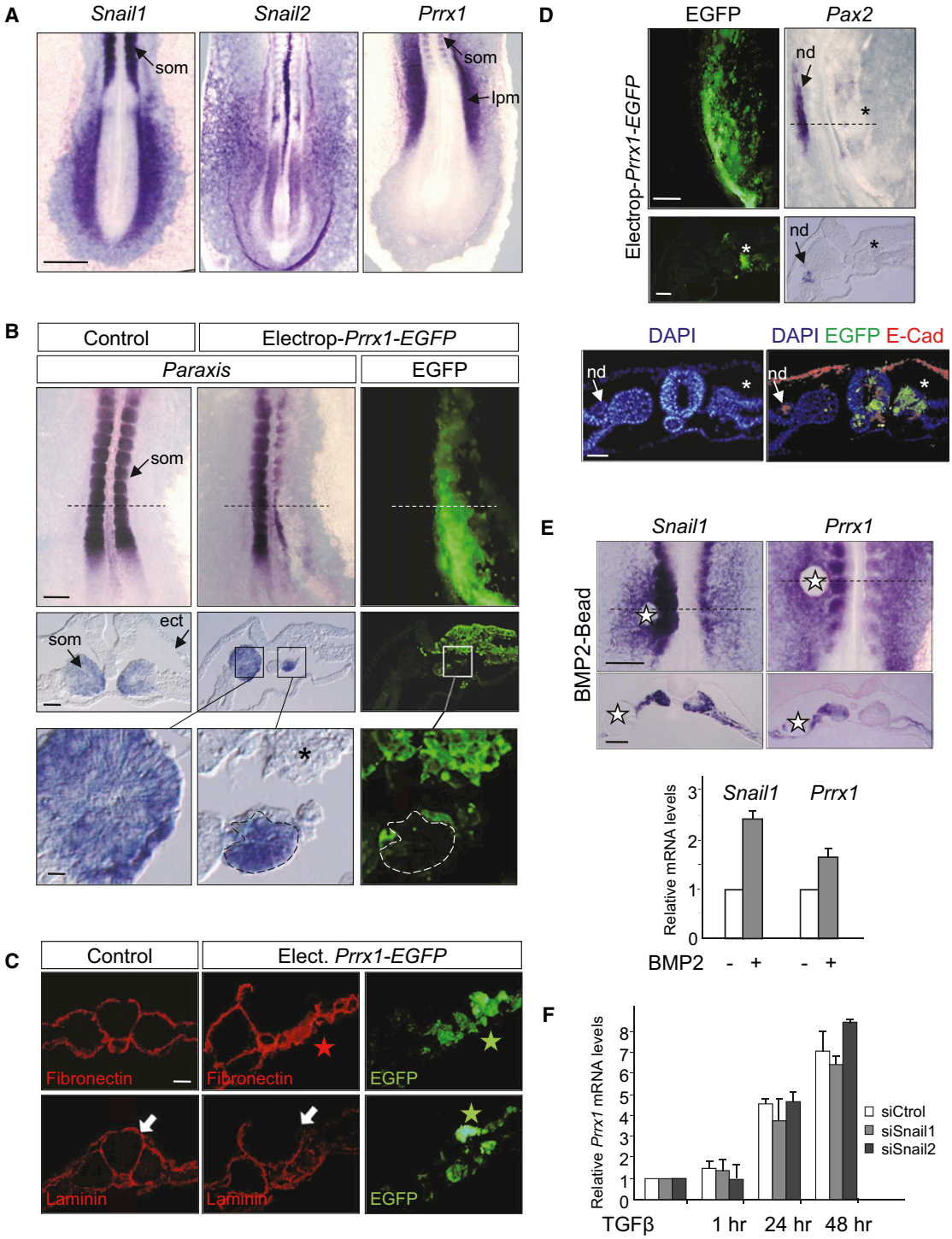

Figure 1. The Prrx1 Transcription Factor Induces a Full EMT In Vivo

(A) Dorsal view of the posterior region of stage HH10-11 chick embryos. The expression of *Snail1*, *Snail2*, and *Prrx1* was detected by ISH. Note the complementary expression patterns. Lpm, lateral plate mesoderm; som, somites. Scale bar: 500 μm.

(B) Chick embryos were coelectroporated on the right hand side with an EGFP expressing construct and a vector expressing *Prrx1* or an empty control vector at stage HH4 and examined at stage HH10-11. The expression of *Paraxis* was detected by ISH and the expression of EGFP by immunofluorescence staining. Top panels show the dorsal views and the middle panels show transverse sections taken at the level of the dotted lines after the ectopic expression of Prrx1. The bottom panels show high power images of boxed areas. Note that the loss of the epithelial somite marker *Paraxis* (black asterisk) occurs only in the electroporated (EGFP) cells. Ect, ectoderm.; Som, somites Scale bars: 250, 50, and 10 μm for upper, middle, and lower panels, respectively.

(C) Expression of fibronectin and laminin and EGFP detection in transverse frozen sections of chick embryos electroporated with *Prrx1* or the control vector. Note the excess of fibronectin (red star) and the disruption of the basement membrane (white arrows) in the electroprated areas (green stars). Scale bar: 50 μm.

during tumor progression (Chaffer et al., 2006; Dykxhoorn et al., 2009).

The similarities between developmental and pathologic EMT validate the embryo as an excellent model to find new clues regarding the events driving tumor progression. Indeed, the EMT has developed during evolution to allow cells to migrate to their final target destination, which they colonize before contributing to the formation of definitive differentiated organs (Nieto and Cano, 2012), a concept very similar to the process of metastatic colonization. Therefore, the reactivation of a developmental program such as the EMT can make tumor cells competent to respond to internal and external cues that confer them with a high degree of epithelial plasticity. The aim of this study was to take advantage of the vertebrate embryo to get further insight into the mechanisms of metastatic colonization, focusing on epithelial plasticity and the acquisition of stem cell properties.

RESULTS

Prrx1 Induces Full EMT in Embryos and Cancer Cells

In search for EMT inducers, we performed expression screening for transcription factors associated with early mesodermal tissues in the chick embryo. We previously showed that upon delamination from the primitive streak, the subdivision of mesodermal territories was accompanied by the distribution of *Snail1* and *Snail2* expression (Sefton et al., 1998). However, we have now found a subset of lateral plate mesodermal cells that did not express either *Snail1* or *Snail2*, but rather express the paired-related homeobox transcription factor *Prrx1* (Figure 1A). *Prrx1* is also expressed in the somites. Interestingly, the somites also express *Snail* genes but, as in the lateral plate mesoderm, they also show complementary expression patterns (Figure S1A).

Prrx1 had previously been implicated in several developmental processes and aspects of fibroblast behavior (Cserjesi et al., 1992; McKean et al., 2003), we therefore examined whether Prrx1 could be an EMT inducer. Ectopic expression of Prrx1 in the chicken embryo, as Snail1, caused failure of epithelial somite development, as assessed by morphology and by the loss of expression of the somitic epithelial markers *Paraxis* (Figures 1B and S1B) and *Uncx4.1* (Figure S1C). This defective epithelialization occurred in a cell autonomous manner (Figure 1B) and was accompanied by the increase in fibronectin deposition and the disappearance of the basement membrane as assessed by laminin staining (Figure 1C), all hallmarks of an EMT.

In addition to the paraxial (somitic mesoderm), *Prrx1* ectopic expression also prevented the epithelialization of the intermediate mesoderm precluding the formation of its derivative, the nephric duct (nd), as assessed by morphologic analysis and by the absence of expression of both its specific marker *Pax2* (Figure 1D, upper panels) and of the epithelial marker E-cadherin (Figure 1D, lower panels).

Like *Snail1*, *Prrx1* expression was induced by BMP2 in the embryo (Figure 1E) and ectopic expression of either *Snail1* or *Prrx1* did not influence that of the other gene (Figure S1D). Therefore, BMP2 seems to induce Snail1 and Prrx1 in an independent manner. The existence of two parallel activation pathways triggered by members of the tumor growth factor (TGF)-β superfamily was confirmed in MDCK cells after treatment with TGF-β, the main inducer of EMT transcription factors in epithelial cells (EMT-TFs; Thiery et al., 2009). Accordingly, interfering with Snail1 or Snail2 expression in MDCK cells did not prevent the induction of *Prrx1* by TGF-β (Figure 1F).

Because TGF-β could induce *Prrx1* expression in MDCK cells, we examined whether *Prrx1* could induce EMT in these cultured cells. Indeed, *Prrx1*-expressing MDCK cells adopted a mesenchymal morphology concomitant with loss of E-cadherin expression and gain of vimentin (Figure 2A). In cultured wound-healing assays, these MDCK-Prrx1 cells healed the wound much faster than control cells (Figure 2B) and they could migrate through collagen gels (Figure 2C). Unlike MDCK-mock cells that formed prototypical epithelial ducts, MDCK-Prrx1 cells grown in 3D matrigel cultures instead formed a network of mesenchymal cells (Figure 2D). Moreover, these cells had downregulated epithelial markers and they had gained the expression of mesenchymal markers, including some EMT-TFs (Figure 2E). Interestingly, as already observed in living embryos, Prrx1 did not influence *Snail1* expression, as MDCK-Prrx1 cells are devoid of *Snail1* transcripts (Figure 2E).

Given the relationship between EMT and Prrx1, we analyzed the expression of this factor in a panel of human cancer cell lines and we found that it was associated with the mesenchymal phenotype and invasive properties (Figures 2F and S2). Furthermore, when compared to the expression of other EMT-TFs in these cell lines, we noted that *PRRX1* expression was frequently associated with that of *TWIST1* in invasive cell lines, indicating that both factors could cooperate in the induction of EMT (Figures 2F and S2; data not shown).

To further characterize Prrx1 as an EMT inducer in vivo and to explore its relationship with Twist1, we moved to the zebrafish embryo, which is very amenable to gain and loss of function studies. We found that among the Prrx and Twist family members in the fish, *prrx1a* and *twist1b* show an expression pattern very similar to that observed in the chick for *Prrx1* and *Twist1*. In particular, these two genes were also coexpressed in the lateral plate mesoderm (lpm) (Figures 3A and 3B). The

(D) Prrx1 electroporation was carried out as in (B). Upper panels show the expression of *Pax2* detected by ISH. Note the absence of *Pax2* on the right hand side (asterisk), more evident on the sections (middle panels). The bottom panels show DAPI stainings (blue) to visualize nuclei and E-cadherin detected by immunofluorescence (red). Note the presence of the epithelial nephric duct (nd) at the left side but it is missing at the right side (asterisk). Scale bars: 500 μm (upper and middle panels) and 50 μm (bottom panels).

(E) BMP2-soaked beads (white stars) were implanted in the left lpm of chick embryos at stage HH7 that were examined 5 hr later. Note both in the whole mounts and in the sections that the expression of *Snail1* and *Prrx1* is stronger and expanded close to the beads. The bar graph shows the result of real-time RT-PCR (bottom). Scale bars: 250 μm (upper panels) and 100 μm (lower panels).

(F) The expression of *Prrx1* in TGF-β-treated MDCK cells transfected with the indicated siRNAs was measured by real-time PCR analysis.

Histograms in (E) and (F) show one representative of three independent experiments and include the mean ± SD of technical triplicates.

See also Figure S1.

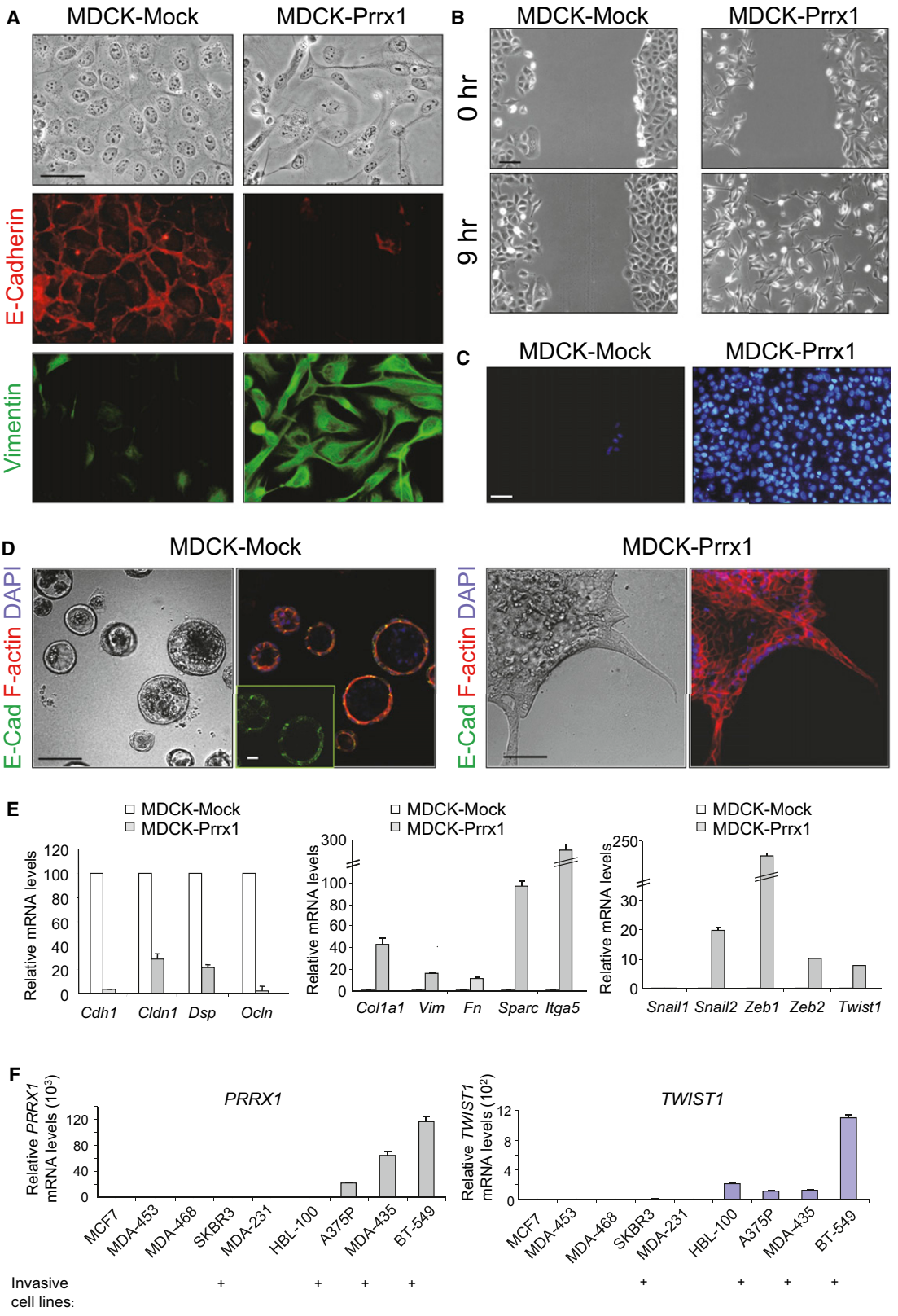

Figure 2. Prrx1 Induces a Full EMT in MDCK Cells Concomitant with the Acquisition of Migratory and Invasive Properties

(A) Phase-contrast images and images of immunofluorescence staining of indicated proteins of MDCK clones expressing Prrx1 or an empty vector (mock). Scale bar: 50 μm.

gain of function induced by injecting *prrx1a* mRNA into embryos produced a dramatic phenotype, whereby lpm cells became invasive and violated the embryonic boundaries to enter the extraembryonic tissues. The position of the cells could be readily detected by examining the expression of *twist1b*, with cells found all around the yolk (Figure 3C, lower panels). Knockdown of *prrx1a* by antisense morpholino oligonucleotide (MO) injection (*prrx1a*^{MO1}) produced the opposite effect to that of *prrx1a* mRNA injection, with cells being retained very close to the neural tube, failing to migrate and colonize their normal territory (Figure 3D; see also Figure S3 for morpholino specificity and efficiency). A different MO against *prrx1a* (*prrx1a*^{MO2}, see Figure S3) was also tested giving similar results (not shown). We decided to continue our experiments with MO1, which will be hereafter referred to as *prrx1a*^{MO}. The observed defects were specific to Prrx1a silencing as this phenotype could be rescued by coinjection of *prrx1a*^{MO} and *prrx1a*^{mRNA} (Figures 3E and 3G). Interestingly, injection of *twist1b*^{MO} could also rescue the Prrx1a overexpression phenotype, suggesting that these genes cooperate to induce the invasive phenotype observed in the lpm, the tissue in which they are coexpressed (Figures 3F and 3G). Indeed, this is compatible with the finding that tissues other than the lpm did not seem to be affected when *prrx1a* alone was overexpressed (Figure 3C; *prrx1a*^{mRNA}). These results indicate that Prrx1a also behaves as an EMT inducer in the fish embryo and that its upregulation induces a prominent invasive phenotype in vivo when acting in cooperation with Twist1b.

To further investigate the cooperation between Prrx1 and Twist in conferring invasive properties, we examined the effect of their downregulation in the invasive BT-549 human cancer cell line, which expresses significant levels of both factors (Figure 2F) and lacks SNAI1 expression (Moreno-Bueno et al., 2011). We found that transient RNA interference of *PRRX1* or *TWIST1* compromised the ability of BT-549 cells to degrade collagen, which was further diminished when both factors were knocked-down simultaneously (Figure 3H). Three independent siRNA sequences were tested in these experiments (not shown). Conversely, in the TWIST1-positive, PRRX1-negative, and noninvasive HBL-100 cells, *PRRX1* transfection renders them invasive, a phenotype that was diminished when the endogenous expression of *TWIST1* was downregulated (Figure 3I). Together, our data indicate that PRRX1 also confers invasive properties to cancer cells in cooperation with TWIST1.

Cells Must Lose Prrx1 to Metastasize

We next investigated the role of Prrx1 in tumorigenesis by injecting MDCK-Prrx1 and control cells into the tail vein of immunocompromised mice and we failed to detect metastatic lung foci (not shown). Moreover, when PRRX1-positive BT-549 breast tumor cells were similarly injected, we did not detect lung colonization either (Figure 4A; shC). However, when PRRX1 was stably silenced by short-hairpin interference mediated by lentiviral infection, BT-549 cells consistently colonized the lung in all animals, inducing metastatic foci (Figure 4A; shPR1). Likewise, silencing both PRRX1 and TWIST1 in BT-549 cells induced lung metastasis in 100% of animals and the number of foci increased significantly (Figure 4A; shPR1-shTW1), indicating that TWIST1 downregulation also favors metastasis formation. However, TWIST1 silencing alone (shTW1) was not sufficient to induce metastatic colonization in the presence of PRRX1 (Figure 4A). The lack of colonization of control or shTWIST1 cells was not due to a failure in extravasation, since single GFP-positive cells were detected 24–30 hr after intravenous injection in the lung parenchyma in all conditions (Figure S4A). Quantification of GFP-positive lesions in the lungs at necropsy on day 60 together with a fluorescence and histologic analysis confirmed the presence of metastasis in mice injected with BT-549 cells knocked-down for PRRX1 alone or for PRRX1 and TWIST1, together with the absence of metastasis in mice injected with control cells or knocked-down for TWIST1 alone (Figure 4B). Interestingly, cardiac and mediastinal metastasis were also observed at necropsy in one mouse in which both PRRX1 and TWIST1 were downregulated (Figure S4B). Cells in which PRRX1 alone was silenced still express TWIST1 (Figure S4C), indicating that PRRX1 silencing in BT-549 cells is sufficient for these cells to engraft the lung and therefore, for colonization in experimental metastasis assays.

To test the role of PRRX1 in primary tumor formation and in distant metastatic colonization in vivo, we orthotopically implanted the BT-549 cells into the right and left inguinal mammary fat pads of athymic nude mice. The generation of primary tumors closely paralleled the capacity of these cells to metastasize in the previous experiments. Thus, while BT-549 control cells or those in which only TWIST1 was downregulated never generated tumors, downregulation of PRRX1 and TWIST1 or even of PRRX1 alone was sufficient to enable tumor growth (Figure 4C). The tumors that developed in mice bearing BT-549 cells lacking both PRRX1 and TWIST1 were detected earlier than those with PRRX1-defective BT-549 cells, although the growth rate was similar in both cases (not shown). Primary tumors were always confined to the mammary gland, with the fatty tissue facing the tumor being almost intact and with a remarkable absence of invasive cells at the tumor margin (Figure 4D). Consistent with their deficient invasive ability (Figure S4D), no metastatic foci

(B) The migratory properties of MDCK-Prrx1 cells were tested in wound healing assays. Scale bar: 100 μm.
(C) Invasive behavior of MDCK-Prrx1 cells in collagen-type-IV gels, as observed in Boyden chamber invasion assays. Nuclei of invasive cells are visualized with DAPI. Scale bar: 100 μm.
(D) Phase-contrast images showing the morphology of control and Prrx1-expressing MDCK cells in 3D culture. Cells were stained with phalloidin for F-actin and E-cadherin (E-Cad) antibodies, and counterstained with DAPI. Scale bar: 50 μm (main pictures) and 15 μm (inset).
(E) Real-time RT-PCR analysis of control and Prrx1-expressing MDCK cells show the repression of epithelial markers genes (*Cdh1, E-cadherin*; *Cldn1*, *claudin 1*; *Dsp*, *desmoplakin*; and *Ocln*, *occludin*) and the activation of mesenchymal markers (*Col1a1*, *collagen I*; *Vim*, *vimentin*; *Fn*, *fibronectin*; *Sparc;* and *Itga5*, *integrin* α*5*) together with several EMT-TFs (*Snail1, Snail2, Zeb1, Zeb2*, and *Twist1*) upon Prrx1 ectopic expression.
(F) Expression of *PRRX1* and *TWIST1* in a panel of human cancer cell lines and its relationship with invasive properties.
Histograms in (E) and (F) show one representative of three independent experiments and include the mean ± SD of technical triplicates.
See also Figure S2.

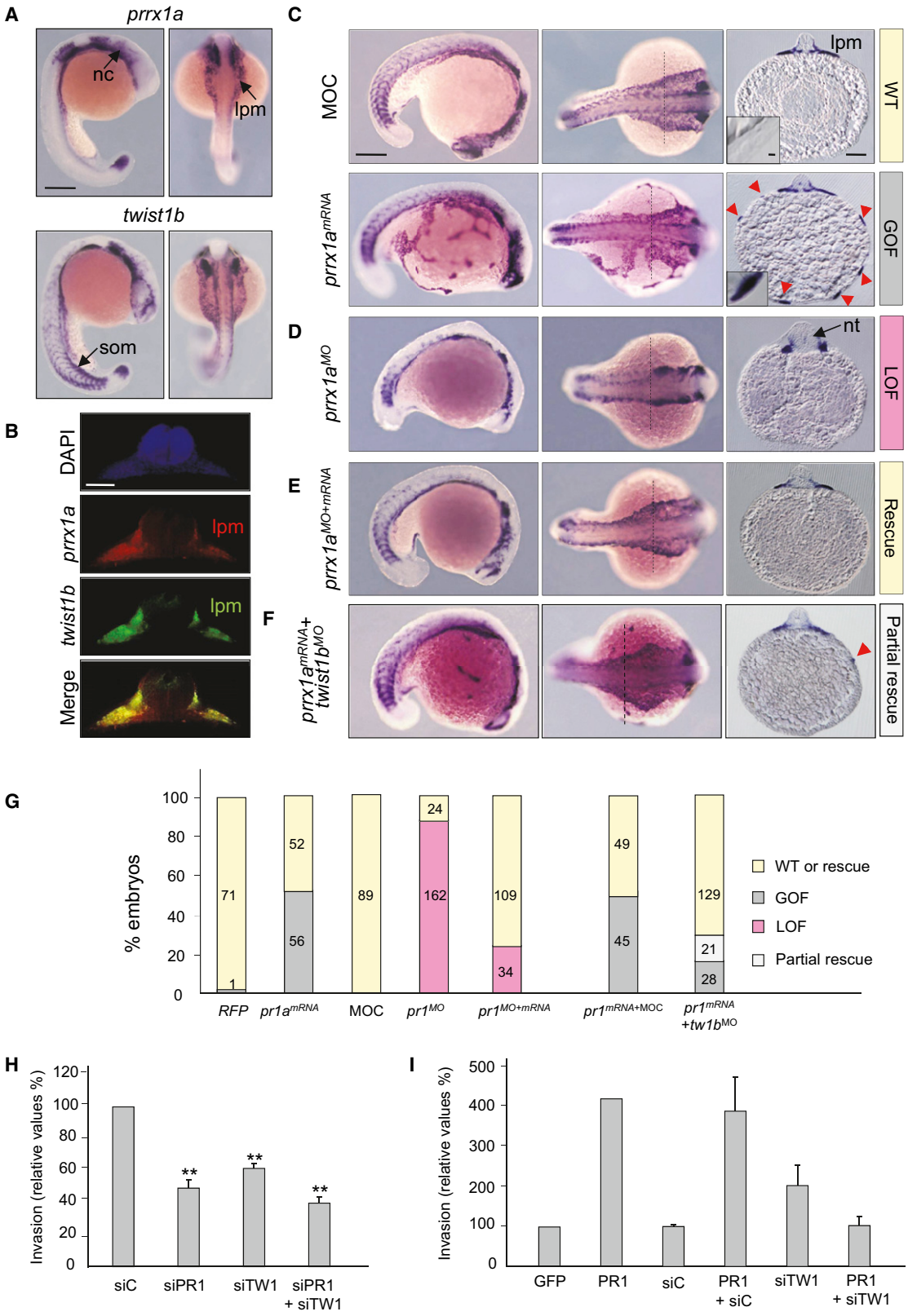

Figure 3. Prrx1 Overexpression Induces Massive Invasion in Zebrafish Embryos

(A) Expression of *prrx1a* and *twist1b* in zebrafish embryos at the 22-somite stage (lateral and dorsal views). nc, neural crest; lpm, lateral plate mesoderm; som, somites. Scale bar: 200 μm.

were detected in any organ at necropsy, even 4 months after inoculation of BT-549 cells where PRRX1 alone or PRRX1 and TWIST1 were downregulated. This is again reminiscent of the situation in embryos, where PRRX1 loss prevents cells from migrating to then colonize their normal territories. Interestingly, metastatic growth was found in axillary lymph nodes in two out six mice bearing BT-549 PRRX1- and TWIST1-deficient cells (Figure 4C), compatible with the proposal that lymph node colonization does not require EMT. As such, although individual mesenchymal cells can invade lymph nodes, their colonization can also occur through collective cell migration (Giampieri et al., 2009).

The Loss of PRRX1 Reverts EMT and Induces Stem Cell Properties

Having shown that the loss of PRRX1 was sufficient for metastatic colonization, but that PRRX1 expression was important for invasion, we examined the impact of its downregulation on the behavior of cancer cells. We first found that the loss of PRRX1 was indeed sufficient for BT-549 cells to revert EMT, undergoing a MET in culture, evidenced by the changes in morphology and actin filament reorganization (Figure 5A). When grown in 3D Matrigel cultures, PRRX1-deficient BT-549 cells did not form mesenchymal networks like control cells, but rather they formed spheroids that had lost vimentin expression, expressed significant levels of E-cadherin and β-catenin at the cell membrane and that secreted laminin I, indicative of the formation of a basement membrane-like structure (Figure 5B). A similar phenotype was observed in cells in which both PRRX1 and TWIST1 were downregulated (Figure 5B). However, TWIST1 downregulation in BT-549 cells was unable to revert the EMT (Figure 5B). It is worth noting here that these cells still express high levels of PRRX1 (Figure S4C). In summary, it appears that the loss of PRRX1 is sufficient to revert the EMT, even in the presence of other EMT inducers such as TWIST1.

We next asked whether the altered phenotype and the ability of BT-549 cells to form metastasis in vivo following *PRRX1* loss was at least partially due to a modification in the tumor-initiating properties of the nontumorigenic BT-549 cells. Soft agar cultures and mammosphere formation assays in ultralow attachment plates were used to examine the cells' ability to support attachment-independent growth and to self-renew, respectively, taken as indicators of tumor-initiating capacity. While BT-549 control cells were unable to grow in soft agar, silencing of *PRRX1* or of both *PRRX1* and *TWIST1* enabled these cells to form colonies (Figures 6A and 6B), and facilitated secondary mammosphere formation (Figures 6C and 6D). The number of mammospheres increased when *TWIST1* was additionally silenced, compatible again with a cooperation between these two factors. However, TWIST1 downregulation alone was not able to induce BT-549 cells to grow in soft agar or to form mammospheres (Figures 6A–6D). This is compatible with the previous finding that TWIST1 expression can endow cells with stem cell properties (Mani et al., 2008; Morel et al., 2008). Importantly, PRRX1 loss was sufficient to sustain mammosphere growth up to at least six consecutive passages (not shown).

It has been shown that EMT inducers attenuate proliferation, which may also compromise tumor growth (Vega et al., 2004; Mejlvang et al., 2007). Similarly, we found that PRRX1 loss enhanced cell division, like Snail1 loss, as evident both by the increase in cell number and the expression of the mitotic marker phospho-histone 3 (PH3; Prigent and Dimitrov, 2003) (Figures 6E and 6F). A similar effect was observed when both PRRX1 and TWIST1 were silenced. Again, in the presence of PRRX1, TWIST1 downregulation was not able to significantly alter cell growth (Figures 6E and 6F).

To further characterize the impact of PRRX1 loss, we examined the expression of the CD44 and CD24 cell surface markers, given that their relative expression and the $CD44^{high}/CD24^{low}$ profile in particular, has been associated with stemness in both normal mammary and breast cancer cells (Sleeman et al., 2006). Silencing PRRX1 or PRRX1 and TWIST1 converted BT-549 cells (mostly $CD44^{+}/CD24^{+}$ double-positive) into $CD44^{high}$ cells (Figure 6G), indicative of a stem cell phenotype (Marotta et al., 2011). Therefore, PRRX1 downregulation was sufficient to shift cells toward a population of $CD44^{+}$ single-positive cells. By contrast, TWIST1 downregulation decreased CD44 expression. As CD24 was almost abrogated from the cell surface after PRRX1 silencing, we wondered whether PRRX1 could regulate its expression. We found that PRRX1 loss leads to an almost complete downregulation of *CD24* transcription. By contrast, TWIST1 downregulation increases the levels of *CD24* transcripts, pointing again to an antagonistic role between PRRX1 and TWIST1 in relation to the acquisition of stem cell properties (Figure 6H).

If PRRX1 loss is sufficient to induce stem cell properties in a non-tumorigenic cell line, ectopic expression of PRRX1 in tumorigenic PRRX1-negative cells may have a negative impact on their stem cell properties. To test it, we chose the tumorigenic and highly metastatic MDA-MB-231 cell line (from now on

(B) Double fluorescent ISH of transverse gelatin sections taken at the mid trunk level shows the coexpression of *prrx1a* and *twist1b* in the lpm. Scale bar: 50 μm. (C–F) ISH for *twist1b* to detect lpm cells in zebrafish embryos. Lateral (left), dorsal (middle), and transverse gelatin sections (at the level of the dotted lines, right) view of lpm cells of zebrafish embryos microinjected with a control morpholino (MOC) or *prrx1a* mRNA ($prrx1a^{mRNA}$) (C), a *prrx1a* morpholino oligonucleotide ($prrx1a^{MO}$) (D), $prrx1a^{mRNA}$ together with $prrx1a^{MO}$ (E), or $twist1b^{MO}$ together with $prrx1a^{mRNA}$ (F). nt, neural tube. Red arrowheads indicate invasive cells in extraembryonic territories. A color code was assigned to the different phenotypes (boxes on the right) as follows: yellow, WT (wild-type) and rescue; gray, GOF (gain of function); pink, LOF (loss of function/knockdown), pale gray, partial rescue. This color code was also used for the quantification of phenotypes shown in (G), Scale bar: 200 μm in left and middle, 100 μm in the right, and 10 μm in the insets.

(G) Quantitative analysis of the fish phenotypes shown in (C–F) and that of microinjection of a control mRNA (*RFP*). (H) Invasive properties of BT-549 human cancer cells after transient downregulation of *PRRX1* and/or *TWIST1* by siRNA transfection. Invasion is represented relative to that observed in control (siC-treated) BT-549 cells. Histograms represent the mean ± SD of three independent experiments (**$p < 0.01$ compared to the control condition).

(I) Analysis of cell invasion of collagen matrices after ectopic PRRX1 expression (PR1) and/or downregulation of endogenous TWIST1 expression (siTW1) in HBL-100 cells. Histograms represent the mean ± SD of four independent experiments ($p = 0.083$ PR1+siC versus siC; $p = 0.082$ PR1+siTW1 versus PR1+siC). PR or pr, PRRX or prrx; TW or tw, TWIST1 or twist, respectively.

See also Figure S3.

A

BT-549 cells	Inoculation	n mice	Sacrifice	Lung Metastatic Colonization	number of foci /single mice
shC	iv	11	60 days	none	none
shPR1	iv	9	60 days	100 %	1-12
shPR1-shTW1	iv	10	60 days	100 %	17-40
shTW	iv	10	60 days	none	none

B

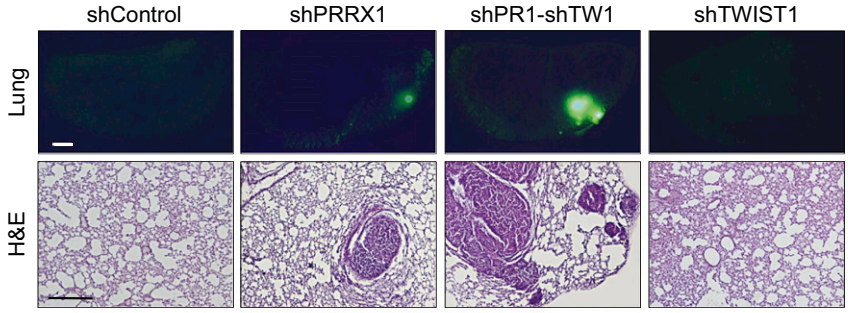

C

BT-549 cells	Inoculation	n mice	Tumor detection	Tumor development Incidence	Lymph node Incidence
shC	i.m.f.p.	3 double injections	none (0/6) at 138 days	none	none
shPR1	i.m.f.p.	3 double injections	day 31-40 (6/6)	100 %	none (0/6) at 138 days
shPR1-shTW1	i.m.f.p.	6 double injections	day 21-29 (11/12)	91.6 %	2/6 at 90 days
shTW1	i.m.f.p.	3 double injections	none (0/6) at 138 days	none	none

D

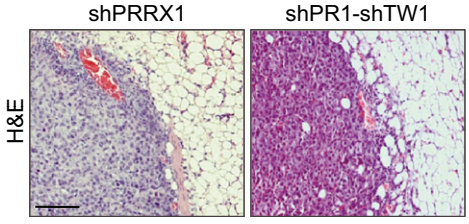

Figure 4. PRRX1 Expression Regulates the Tumorigenic and Metastatic Potential

(A) Experimental lung metastasis in Balb/c nude mice 60 days after injection of BT-549 cells.

(B) Representative GFP-positive foci in lungs (upper panels) and H&E sections of the lungs (lower panels). Scale bars: 1 mm (upper panels) and 200 μm (lower panels).

(C) Primary xenografts generated from BT-549 cells on the days indicated after double inguinal intramammary fat pad (i.m.f.p.) injection (1×10^6 cells/injection site).

(D) Representative H&E sections of tumors from mice injected with BT-549 shPRRX1 (left) or shPRRX1-shTWIST1 cells (right). Scale bar: 100 μm.

C, control; PR, PRRX; TW, TWIST.

See also Figure S4.

MDA-231), which expresses EMT-TFs but is devoid of PRRX1 and TWIST1 (Figures 2F and S2). As expected, stable PRRX1 ectopic expression in MDA-231 cells alone or together with TWIST1 (Figure 7A) did not have any impact on the morphology of these already mesenchymal cells (Figure 7B). However, both the number of colonies formed in soft agar cultures and particularly, the number of secondary and tertiary mammospheres significantly decreased upon PRRX1 ectopic expression (Figures 7C–7F). Interestingly, all these effects were reinforced by the additional ectopic expression of TWIST1 (Figures 7C–7F). Furthermore, MDA-231 cells (mostly $CD44^+$ single positive) lose CD44 expression and shift toward a $CD44^-/CD24^-$ double-negative population (Figure 7G). Hence, as hypothesized, the effect of ectopically expressing PRRX1 in MDA-231 cells is opposite to that found after PRRX1 downregulation in BT-549 cells.

Collectively, our data indicate that the loss of PRRX1 alone is sufficient to revert EMT, inducing a MET accompanied by the acquisition of stem cell properties and increased proliferation, all important events for metastatic colonization.

PRRX1 Expression Is Associated with Good Prognosis and Metastasis-Free Disease

Our data from the studies in mice indicate that the loss of PRRX1 is associated with the development of metastases. Therefore, we wanted to know whether there was any relationship between the level of *PRRX1* expression and metastasis in human patients. We analyzed publically available data sets and found that low *PRRX1* transcription was associated with a poor relapse-free survival (RFS) in breast adenocarcinoma (Chin et al., 2006) (Figure 8A) and lung squamous cell carcinoma (SCC) (Raponi et al., 2006) (Figure 8A). Furthermore, low expression of both *PRRX1* and *TWIST1* associate with a lower RFS in lung SCC (Figure 8B). In contrast, there was no association between RFS and expression of *TWIST1* alone or of *SNAI1* (Figure S5A).

Consistent with our data in embryos and cancer cell lines, a statistically significant association was found between *PRRX1* and *TWIST1* expression in human breast adenocarcinoma and in two series of lung SCC (Chin et al., 2006; Raponi et al., 2006; Larsen et al., 2007) (Figure 8C). Similarly, and again as in embryos and tumor cells, no association was found between *PRRX1* and *SNAI1* expression (Figure 8C). Furthermore, significant correlations were evident between strong *PRRX1* expression and increased RFS either alone or in

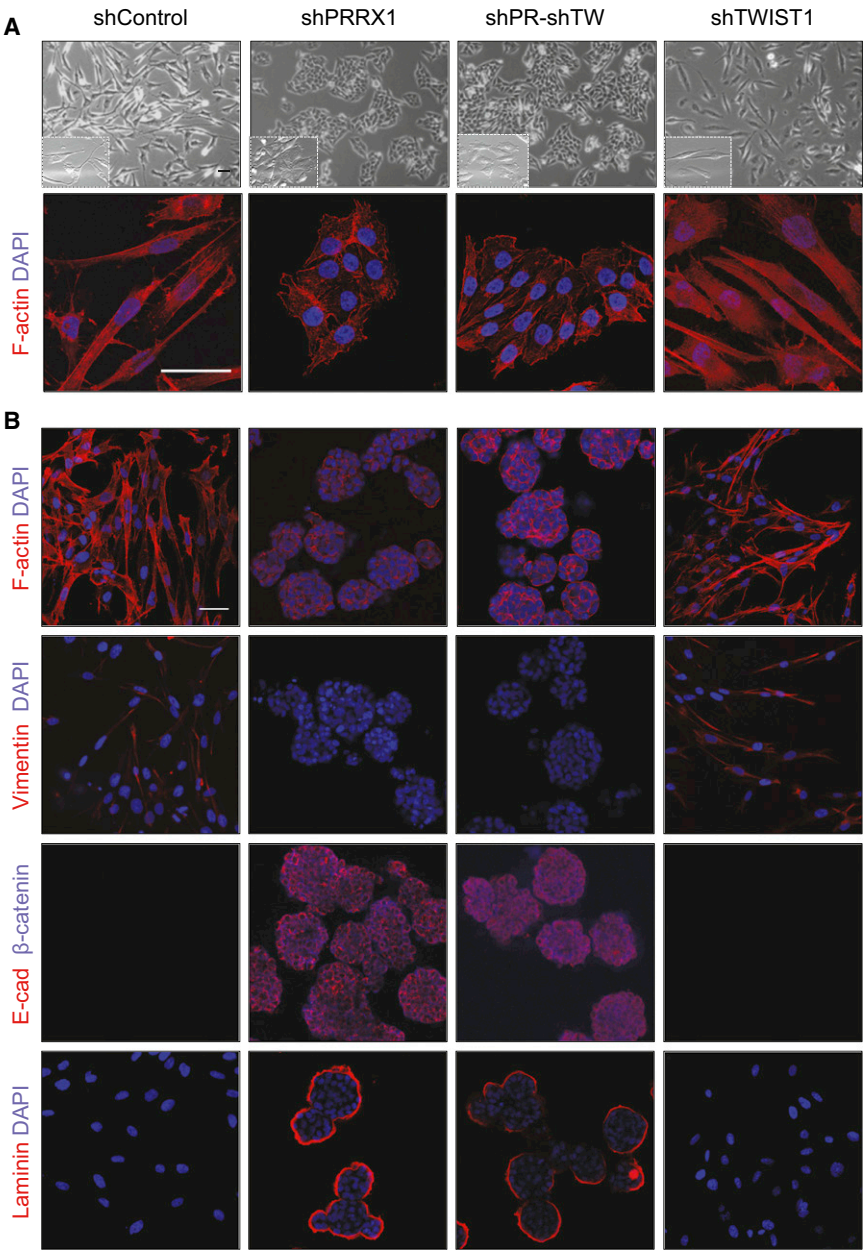

Figure 5. PRRX1 Knockdown in Cancer Cells Induces a Mesenchymal-to-Epithelial Transition and Spheroid Formation

(A) Phase-contrast and phalloidin staining images showing the phenotype of BT-549 cells transfected with indicated shRNAs. Scale bars: 50 μm. (B) Confocal images depicting the phenotype of the different BT-549 cells transfected with indicated shRNAs grown in 3D matrigel cultures and assessed for the presence of epithelial (E-cadherin and β-catenin), mesenchymal (vimentin), and extracellular matrix (laminin I) markers. DAPI staining (blue) was used as a nuclei reporter. Scale bar: 50 μm. PR, PRRX; TW, TWIST.

combination with *TWIST1* expression in breast carcinoma using a Log-rank-p-value method in the breast and lung series mentioned and in an additional breast series (Pawitan et al., 2005). The analysis of the Ur-Rehman (2011) data set available at the Online Breast Cancer Knowledgebase (ROCK) (Experimental Procedures) including 1570 human samples (Table S1) confirmed these findings.

We also observed a statistical correlation between *PRRX1* downregulation and progression to the metastatic disease. Analyzing the Chin's breast adenocarcinoma data set (Chin et al., 2006) we found that remarkably, metastasis did not develop in close to 90% of the tumors with medium/strong *PRRX1* expression (Figure 8D). The combination of strong *TWIST1* expression with strong *PRRX1* expression did not increase the percentage of metastasis-free tumors.

Finally, after the analyses of the different data sets, we examined the expression of *PRRX1* in 113 high-grade infiltrating breast ductal carcinoma (IDC) included in a tissue microarray (TMA). We found that around one third of the tumors analyzed showed significant *PRRX1* expression (Figures 8E and S5B) and interestingly, that metastasis did not develop in over 90% of these tumors (Figure 8F). These data are fully consistent with those found in our analyses of the data sets mentioned above. Thus, considering that all the data sets and the tissue microarrays used correspond to primary tumors, our observations indicate that strong *PRRX1* expression could be considered as an independent marker of good disease prognosis.

DISCUSSION

We have identified an EMT inducer that can trigger the full process in living embryos and human cancer cells. There are several features that make Prrx1 unique when compared to other well-known EMT-TFs, which expand our understanding of the complexity underlying metastatic processes, and help to reconcile conflicting results that have challenged the significance of EMT and stemness.

Prrx1 induces EMT in a manner independent of Snail1. Both during embryonic development and tumor progression, a temporal activation hierarchy drives the onset and maintenance of the mesenchymal program, with Snail1 situated high in the list. While Snail1 is required for the triggering of the EMT, other EMT-TFs reinforce and maintain the mesenchymal state (Peinado et al., 2007; Olmeda et al., 2008; Casas et al., 2011; Tran et al., 2011). However, we found that Snail1 does not influence *Prrx1* expression nor does Prrx1 modulate the expression of *Snail1*. Interestingly, we have observed that the same signaling molecule induces *Prrx1* and *Snail1* either in the embryo (BMP) or in epithelial cells (TGF-β). Hence, a single signal can

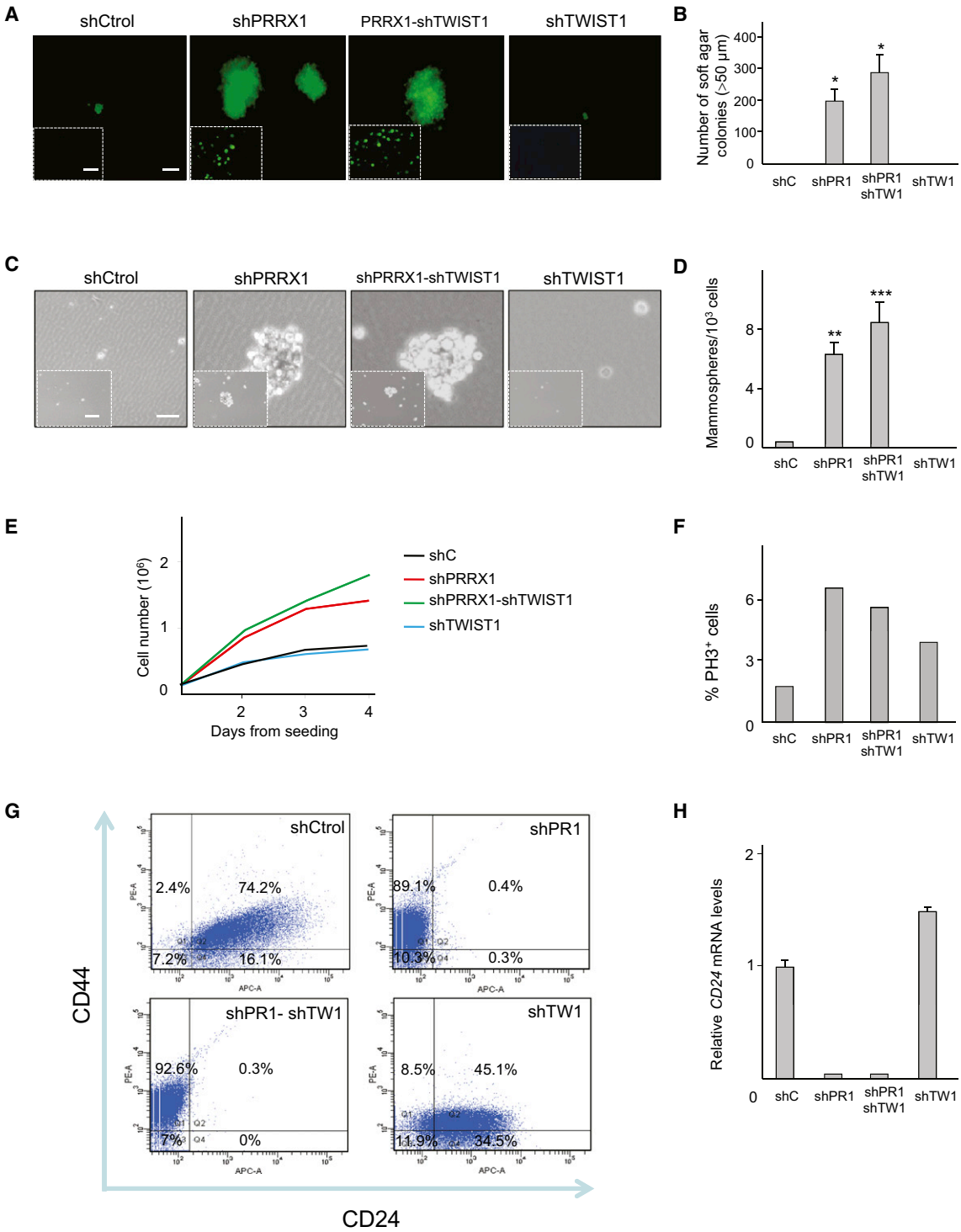

Figure 6. PRRX1 Knockdown Induces the Acquisition of Stem Cell Properties in Cancer Cells

(A) Representative fluorescence images showing the ability to induce colony formation in soft agar 15 days after seeding. Insets are low magnification images. Scale bars: 100 μm (main pictures) and 500 μm (inset).

(B) Quantification of soft agar colonies above 50 μm in diameter. Histograms represent the mean ± SD of three independent experiments (*$p < 0.05$, compared to the control condition).

(C) Phase-contrast images showing the mammosphere-forming capacity of different BT-549 cells. Scale bars: 50 μm (main pictures) and 200 μm (inset).

(D) Quantification of secondary mammospheres as the number formed/10^3 cells seeded. Histograms represent the mean ± SD of three independent experiments (**$p < 0.01$; ***$p < 0.001$ compared to the control condition).

(E) Growth curve of different BT-549 cells. Graphics shows a representative experiment (n = 3).

simultaneously and independently activate Prrx1 and Snail1 expression, and therefore, trigger parallel and probably nonredundant EMT pathways.

Our data show that Prrx1 is essential for the acquisition of invasive properties and indeed, when silenced in embryos, lpm cells fail to migrate. Similarly, there is no sign of cellular or local invasion in primary tumors generated by PRRX1-deficient BT-549 cells, even though both lpm cells and PRRX1-deficient human cells still express other EMT-TFs, including Twist1. Our data show that Prrx1 is essential for the acquisition of invasive properties and that Prrx1 cooperates with Twist1 in driving invasion in embryos and cancer cells. This is consistent with the described role of Twist in invasion and particularly, in the formation of invadopodia (Yang et al., 2004; Eckert et al., 2011). Once more, these findings support the cooperation between EMT-TFs, both during development and in cancer (Olmeda et al., 2008; Tran et al., 2011). Our data also reinforce the concept that EMT is important for the invasive behavior of the primary tumor, generating individual delaminating cells and subsequent tumor progression. Indeed, the loss of PRRX1 in BT-549 cells results in the formation of primary tumors without invasion and distant metastasis when orthotopically injected in the inguinal mammary fat pads. This is in agreement with the finding that abrogating classical EMT-TFs such as Snail1and Snail2 prevents individual cell migration and therefore attenuates invasion and subsequent distant metastasis when tested in similar experiments (Olmeda et al., 2008). Interestingly, albeit not commonly, lymph node metastases were found in PRRX1-TWIST1-deprived cells, consistent with the proposal that the EMT is not required for lymph node metastasis (Giampieri et al., 2009), albeit individual cells generated by EMT can also populate the lymph nodes.

A crucial difference between Prrx1 and other EMT-TFs is that Prrx1-induced EMT does not concur with the described induction of stem cell-like properties concomitant with Snail-, Twist-, or Zeb-mediated mesenchymal transitions (Mani et al., 2008; Morel et al., 2008; Wellner et al., 2009). On the contrary, it is PRRX1 loss rather than gain in cancer cells that is accompanied by the acquisition of stemness-related capabilities, including anchorage-independent growth, mammosphere formation, increased cell proliferation, and the conversion from a mostly $CD44^{+}/CD24^{+}$ double-positive population to $CD44^{high}$ single-positive cells. $CD44^{high}/CD24^{low}$ is the described profile for breast cancer stem cells associated with the most aggressive and metastatic types (Marotta et al., 2011).

Importantly, the loss of PRRX1 in mesenchymal cancer cells induces a complete reversion to the epithelial phenotype, even in the presence of classical EMT inducers. As such, our data show that abrogation of the EMT is important for metastatic colonization and this phenotype reversion concurrent with the aforementioned acquisition of stem cell-like properties upon PRRX1 downregulation favors metastatic colonization. This observation is similar to the finding that the MET process is essential for fibroblasts to acquire stem cell properties during cellular reprogramming (Li et al., 2010, Samavarchi-Tehrani et al., 2010), linking MET and stemness rather than EMT and stemness as described during the mesenchymal transition triggered by classical EMT-TFs. Our data also show that EMT and stemness can be independently regulated, but it is clear that they can coexist in some contexts such as in the migrating cancer stem cells and in early embryonic development. Indeed, EMT can induce the loss of epithelial characteristics of trophoblast stem cells while maintaining self-renewal and pluripotency (Abell et al., 2011), as shown for the classical EMT-TFs during tumor progression. However, it is worth noting that Snail2 (Slug) and Sox9 cooperate in the acquisition of the mesenchymal mammary stem cell state, with Snail2 essentially inducing the EMT and Sox9 facilitating entry into the stem cell state (Guo et al., 2012). All these findings indicate that EMT-TFs, or at least, the mesenchymal phenotype and stemness can coexist, as initially proposed following studies on colon carcinomas from which the concept of "migrating cancer stem cells" arose (Brabletz et al., 2005). However, the coexistence of these combined traits also implies phenotypic plasticity, because our data indicate that mesenchymal cells must revert to the epithelial phenotype to form the typical well-differentiated metastases while maintaining stemness, as suggested previously (Chaffer et al., 2006; Dykxhoorn et al., 2009; Celià-Terrassa et al., 2012; Brabletz, 2012). If MET is required for metastatic colonization, the loss of classical EMT-TFs would also convey the potential loss of stem cell properties associated with tumor-initiating capacity, thereby impairing metastatic colonization. Our findings showing that *PRRX1* loss induces both MET and stemness, and provides a mechanism that favors metastatic progression.

The fact that EMT and stemness are uncoupled in PRRX1-induced EMT again supports the existence of a parallel nonredundant EMT pathway mediated by PRRX1 in cancer cells and the requirement of PRRX1 loss for the development of distant macrometastases. As already mentioned, PRRX1 loss promotes stemness, thereby favoring tumor-initiating capacities when PRRX1 itself and the other EMT-TFs are downregulated after extravasation at the secondary organ to favor MET. By contrast, high PRRX1 expression can preclude progression to the metastatic state due to both a deficiency in tumor-initiating capacity and the persistence of an EMT state. As such, the unique association of strong PRRX1 expression in primary tumors with metastatic-free disease and good RFS in patients with different types of carcinoma, such as breast adenocarcinomas and lung SCC supports this proposal. On the one hand this suggests that strong PRRX1 expression in primary tumors could be used as diagnostic of good prognosis and on the other hand, that therapies aimed at targeting EMT might in fact promote metastatic colonization once cells have already delaminated from the primary tumor. Finally, the independent regulation of EMT

(F) Quantification of cells undergoing mitosis as assessed by PH3 staining 16 hr after cell seeding. Histograms shows a representative experiment (n = 3).
(G) BT-549 control cells and those in which PRRX1, TWIST1, or both had been downregulated were evaluated for their surface expression of CD44 and CD24 by FACS.
(H) *CD24* transcript levels observed in BT-549 control cells or in those where PRRX1, TWIST1 or both were downregulated. Histograms represent the mean ± SD of three independent experiments.
C or Ctrol, control; PR, PRRX; TW, TWIST.

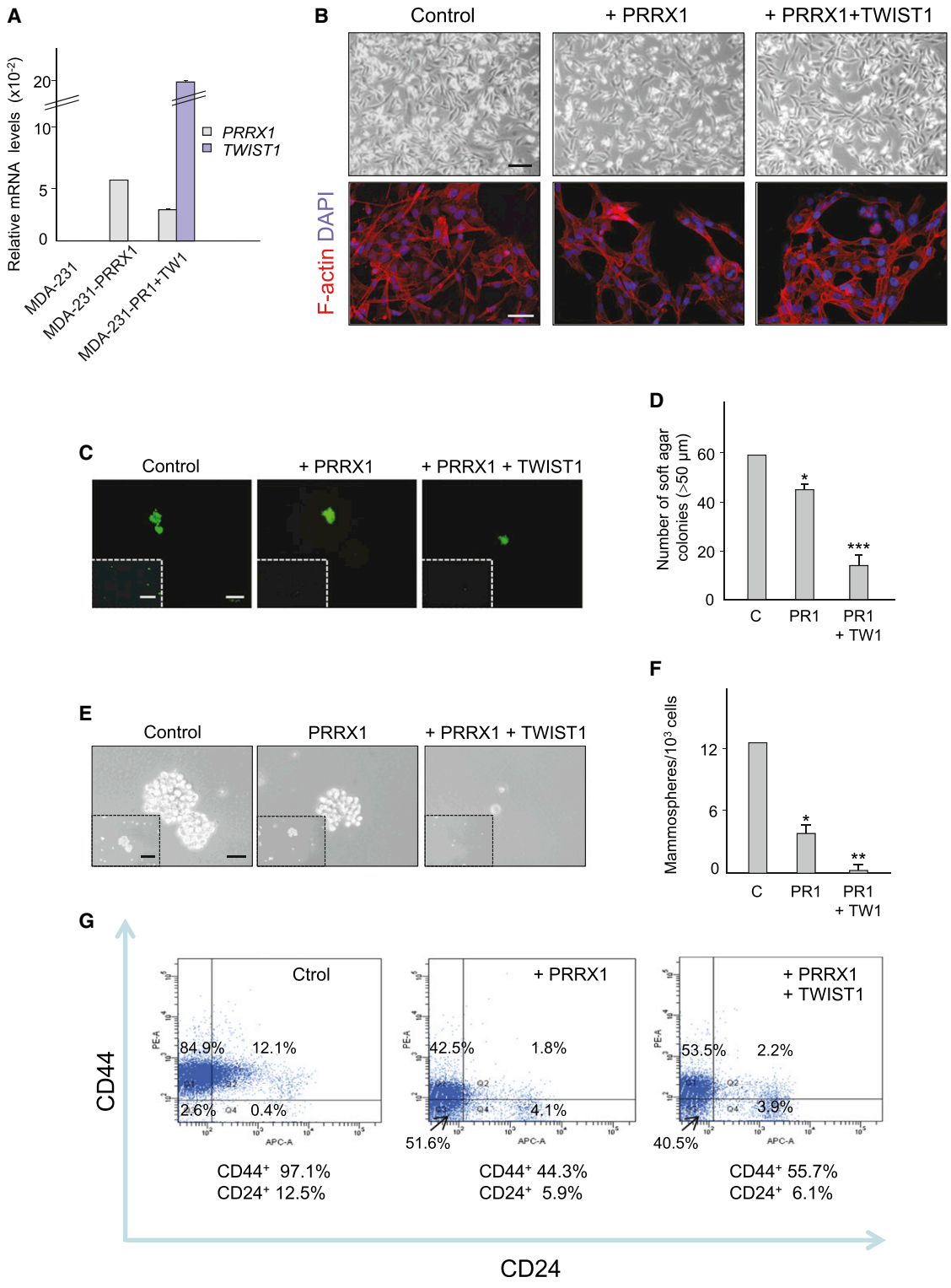

Figure 7. PRRX1 Ectopic Expression Impairs Stem Cell Properties in Cancer Cells

(A) Relative expression of *PRRX1* and *TWIST1* in MDA-231 control cells and in those transduced with viruses to ectopically express either PRRX1 or PRRX1 plus TWIST1. One representative of three independent experiments is shown and includes the mean ± SD of technical triplicates.

(B) Phase-contrast and phalloidin staining images showing the phenotype of control MDA-231 cells or of those in which PRRX1 has been ectopically expressed alone or together with TWIST1. Scale bars: 100 µm (upper panel) and 50 µm (lower panel).

(C) Representative fluorescence images showing the ability of MDA-231 control cells and that of those with ectopic expression of PRRX1 or PRRX1 plus TWIST1 to form colonies in soft agar 30 days after seeding. Insets are low magnification images. Scale bars: 100 µm (main pictures) and 500 µm (inset).

and stem cell properties supports the development of therapeutic strategies aimed at targeting stemness.

EXPERIMENTAL PROCEDURES

Human Breast Cancer

The analysis of *PRRX1* expression was performed using a total of 113 retrospective IDC from the Pathology Department of MD Anderson Cancer Center (MDACC) Madrid, Spain. All samples were grade 3. Patients underwent surgery between 2005 and 2006. Two different tumor areas from each sample were included into a tissue microarray (TMA) according to manufacturer's procedures. The mean patient age at surgery was 57.2 years (range, 38–85 years). The *HsPRRX1* probe was amplified by PCR from total cDNA and subcloned into a pGEMT-easy vector (Promega). In situ hybridization (ISH) of TMA sections was performed as described previously (Nieto et al., 1996) with some modifications. Briefly, 5 μm sections were deparaffinized in xylene and rehydrated in descending ethanol series. Slides were permeabilized with 10 ug/ml of proteinase K for 5 min at room temperature and prehybridized in hybridization buffer without probe for 3 hr and incubated with digoxigenin-labeled riboprobe overnight at 60°C. The following day, sections were washed in 2X SSC/50% formamide for 4 hr at 60°C. Hybridized probes were detected using an alkaline phosphatase-conjugated anti-digoxigenin antibody (Roche, 1:1000) in the presence of substrate nitroblue tetrazolium (NBT) 5-bromo-4-chloro-3-indolyl phosphate (BCIP) to produce a blue precipitate at the site of hybridization. Sections were photographed under a Leica DMR microscope (Leica, Wetzlar, Germany).

This study was performed following standard ethical procedures of the Spanish regulation (Ley de Investigación Orgánica Biomédica, 14 July 2007). All participants in this study gave written informed consent, and the study was approved by the Institutional Review Boards of MDACC Madrid.

Embryos

AB and Tup-Lof wild-type zebrafish strains were maintained at 28°C under standard conditions and the embryos were staged as described previously (Kimmel et al., 1995). Fertilized hen eggs were purchased from the Granja Gilbert (Tarragona, Spain) and incubated in a humidified incubator at 37.5°C. Chick embryos were staged according to Hamburger and Hamilton, 1951 (HH).

Cell Lines

MCF7, MDA-MB-231, MDA-MB-435S, A375P, HBL-100, MDA-MB-468, SKBR3, and BT-549 human tumor cell lines and MDCK dog kidney cells were purchased from the ATCC (Virginia, USA) and were cultured as described in Supplemental Experimental Procedures. The names of MDA cell lines have been reduced in the text for convenience.

Electroporation of Chicken Embryos and BMP2 Treatment

Chick embryos were electroporated with different expression constructs at stage HH4 as described previously (Acloque et al., 2011). In all experiments, the nonelectroporated side of the embryo served as a control. Human recombinant BMP2 protein (obtained from R&D Systems) was loaded onto heparin acrylic beads at a concentration of 0.2 mg/ml. See also Supplemental Experimental Procedures.

Morpholino Oligonucleotide and mRNA Injections

All MOs were obtained from Gene Tools and they were used as described elsewhere (Nasevicius and Ekker, 2000). The dose was chosen after testing the efficiency of MO1 in preventing splicing (Figure S3). The specificity of the MOs was checked by cloning the MO sequence in front of the EGFP coding sequence and assessing the decrease in GFP expression after coinjection with the corresponding MO. For overexpression analyses, embryos were injected with mRNAs synthesized for *prrx1a* coding sequence. Rescue experiments were performed by coinjecting mRNA plus MOs. See Supplemental Experimental Procedures for details.

Whole-Mount In Situ Hybridization

Whole-mount ISH was carried out essentially as described previously (Nieto et al., 1996). See Supplemental Experimental Procedures for details of the probes used.

Viral Production and Cell Infections

Human cDNA containing the coding sequence of *PRRX1* was subcloned in the pBABE-neo retroviral vector. Retroviral production and infection were carried out as previously described (Mani et al., 2008). After infection, MDA-231 or HBL-100 cells expressing either pBabe-neo (empty vector) or pBabe-neo-PRRX1 were selected with 400 μg/ml G418 for 2 weeks. The lentiviral vector containing the human *TWIST1* ORF sequence was obtained from Open Biosystems (OHS5898-101004920). Lentiviral plasmids containing shRNAs were purchased from Open Biosystems and are listed as the following: Human shPRRX1 (RHS3979-9588052 and RHS3979-9588055), and Human shTWIST1 (RHS3979-9587949 and RHS3979-9587951). Lentiviral supernatants were produced using a viral packaging system that includes the psPAX2 and pM2DG plasmids (purchased from Open Biosystems). Two days after transfection, the viral supernatants were collected and used to infect BT-549 and MDA-231 cells, which were then selected with 2 μg/ml puromycine. The empty pLKO.1 vector was used as a control and in all cases, the cells were also infected with the empty pGIPZ vector (obtained from Open Biosystems) as a reporter of EGFP expression. For BT-549 cells, at least two independent pools were generated in each case and the cultured cells were initially tested for changes in morphology, expression, and invasive properties. Different pools behaved similarly and for each condition, one was chosen for the in vivo experiments.

Total RNA Extraction, cDNAs Isolation, and QRT-PCR Analysis

All the protocols are described in detail in the Supplemental Experimental Procedures.

Generation and Characterization of Prrx1-Expressing Stable Cell Lines

Stable transfectants were generated in MDCK cells and selected for 2 weeks with 400 μg/ml G418. Five independent clones were analyzed for pcDNA3-mPrrx1 and three for pcDNA3 alone (mock). Where indicated, cells were transfected with siRNAs using Lipofectamine RNAiMAX according to the manufacturer's instructions (Invitrogen). Three independent siRNA sequences were tested. See Supplemental Experimental Procedures for more details and primer sequences.

Immunofluorescence

The methods used are described in the Supplemental Experimental Procedures.

Tumor Growth and Histologic Studies

Mouse studies were carried out with the approval of the IDIBELL Animal Ethics Committee (Procedure 4587 AFF) and in accordance with the Spanish National Health and Medical Research Council's guidelines and the AALAC for the care and use of laboratory animals. Details are provided in the Supplemental Experimental Procedures.

(D) Quantification of soft agar colonies above 50 μm in diameter. Histograms represent the mean ± SD of three independent experiments (*$p < 0.05$, ***$p < 0.001$ compared to the control condition).
(E) Phase-contrast images showing the ability to form mammospheres of the different MDA-231 cells. Scale bars: 50 μm (main pictures) and 200 μm (inset).
(F) Quantification of tertiary mammospheres as the number formed/10^3 cells seeded. Histograms represent the mean ± SD of three independent experiments (*$p < 0.05$; **$p < 0.01$ compared to the control condition).
(G) Analysis of CD44 and CD24 surface expression by FACS.
C, control; PR, PRRX; TW, TWIST.

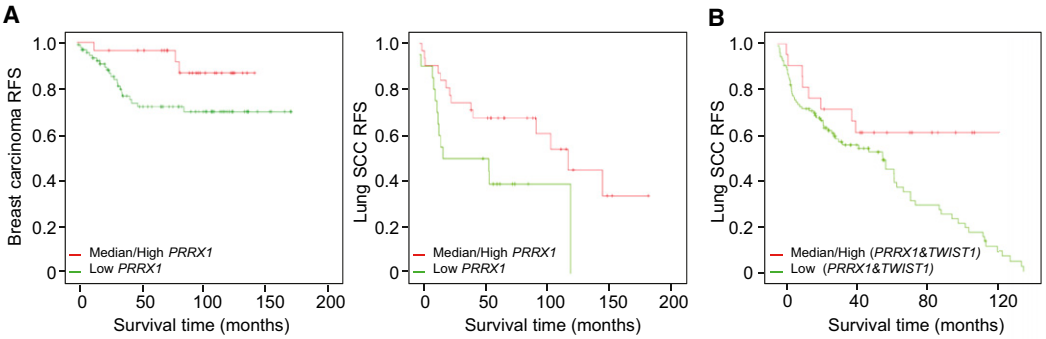

C

PRRX1 expression *n (%)	LOW	MEDIAN/HIGH
Breast dataset Chin et al., 2006		
***TWIST1* expression** LOW (n=74) MEDIAN/HIGH (n=43)	23 (31.1) 6 (13.9)	51 (68.9) 37 (86.1) p=0.033
***SNAI1* expression** LOW (n=38) MEDIAN/HIGH (n=79)	10 (26.3) 19 (24.1)	28(73.3) 60(75.9) ns
Lung dataset Raponi et al., 2006		
***TWIST1* expression** LOW (n=95) MEDIAN/HIGH (n=33)	76 (80.0) 12 (36.4)	19 (20.0) 21(63.6) p<0.001
***SNAI1* expression** LOW (n=88) MEDIAN/HIGH (n=40)	63(71.6) 25(62.5)	25(28.4) 15(37.5) ns
Lung dataset Larsen et al., 2007		
***TWIST1* expression** LOW (n=24) MEDIAN/HIGH (n=27)	13(54.2) 7(25.9)	11(45.8) 20(74.1) p=0.039
***SNAI1* expression** LOW (n=29) MEDIAN/HIGH (n=22)	10 (34.5) 10 (45.5)	19 (65.5) 12 (54.5) ns

D

	METASTASIS NO	METASTASIS YES
Breast dataset Chin et al., 2006		
***PRRX1* expression** LOW (n=29) MEDIAN/HIGH (n=88)	7 (24.1) **77 (87.5)**	22 (75.9) 11 (12.5) p=0.027

	METASTASIS NO	METASTASIS YES
Breast dataset Chin et al, 2006		
***PRRX1* and *TWIST1* expression** LOW (n=32) MEDIAN/HIGH (n=85)	8 (25) **76 (89.4)**	24 (75) 9 (10.6) p<0.001

E

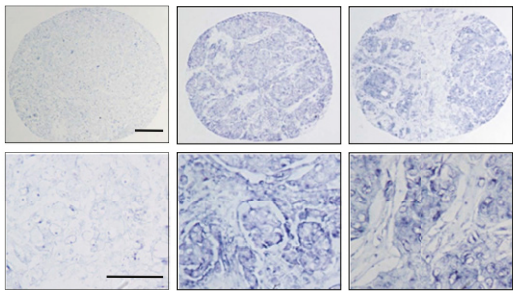

F

	METASTASIS NO	METASTASIS YES
TMA MD-Anderson		
***PRRX1* expression** Negative (n=78) Positive (n=35)	60 (76.9) **32 (91.4)**	18 (23.1) 3 (8.6) p=0.05

Figure 8. Strong PRRX1 Expression in Breast Carcinomas and Lung SCC Is Correlated with the Lack of Metastases and Increased RFS

(A) Kaplan-Meier plots showing the association between *PRRX1* expression and RFS using data sets from the Chin breast adenocarcinoma series (Chin et al., 2006) and from a series of lung SCC (Raponi et al., 2006).

(B) Kaplan-Meier plots showing the association between combined high *PRRX1* and high *TWIST1* expression with increased RFS from the lung SCS database in (A).

(C) Correlation between *PRRX1* and *TWIST1* expression in a breast adenocarcinoma and two independent lung SCC data sets.

(D) Statistical association between either *PRRX1* alone or *PRRX1* and *TWIST1* together with metastasis.

(E) Representative examples of ISH for *PRRX1* in a retrospective grade 3 infiltrating ductal breast carcinoma series (n = 113) included in a tumor microarray (TMA). Lower panels show high power images. Scale bars: 200 μm (upper panels) and 50 μm (lower panels).

(F) Statistical association between *PRRX1* expression and metastasis formation from the expression analysis of the TMA shown in (E).

*n (%), number of cases (percentage); ns, nonsignificant.

See also Figure S5 and Table S1.

Migration and Invasion Assays

For migration assays cells were seeded in six-well culture dishes at a density of 1×10^6 cells/well. A wound was made in the center of the culture 24 hr later, and phase-contrast pictures were taken at different intervals. Invasion assays on collagen type-IV gels were performed as described previously (Cano et al., 2000). Briefly, 35,000–50,000 cells of each type were seeded onto the upper surface of the filters in modified Boyden chambers. After 7 or 16 hr incubation for BT-549 and HBL-100 respectively, cells attached to the lower part of the filters were fixed in methanol, stained with 4,6-diamidinophenylindole (DAPI), and counted. Longer incubation times for HBL-100 cells were required because they are noninvasive.

Soft Agar Assays and Mammosphere Cultures

For details, see the Supplemental Experimental Procedures.

Cell Proliferation and Cell Cytometry Analysis

Analyses of cell proliferation and cell cytometry were carried out as described in the Supplemental Experimental Procedures.

Metanalysis

To validate the metastatic prediction model, several independent data sets of breast carcinoma (See Chin et al., 2006; Pawitan et al., 2005) and lung SCC series (Raponi et al., 2006; Larsen et al., 2007) were analyzed. The breast and lung microarrays, and the clinical data were obtained from ICR and GEO databases, respectively. In addition, the Ur-Rehman data set, publicly available in ROCK (http://www.rock.icr.ac.uk) was also used in the analysis. The Ur-Rehman data set was a collection of independent published breast cancer data sets containing 1,570 samples analyzed with the U133 Affymetrix platform arrays, all of them were normalyzed using the same Robust Multi-array Average method. The statistical survival analysis associated to the breast and lung samples was performed using ROCK (http://www.rock.icr.ac.uk) and SPSS software (SPSS), respectively. Kaplan-Meier plots of the RFS curves are represented using log-rank tests. The expression values of *PRRX1, TWIST1*, and *SNAI1* was categorized using upper quartile (25% against rest). The Chi-square contingency test Yates correction, or Fisher's exact test, was used to determine the statistical significance of the relationships between *PRRX1* expression and *TWIST1* expression, and metastasis. Values of $p < 0.05$ were considered statistically significant. These analyses were carried out using the SPSS 17.0 for statistical software.

SUPPLEMENTAL INFORMATION

Supplemental Information includes five figures, one table, and Supplemental Experimental Procedures and can be found with this article online at http://dx.doi.org/10.1016/j.ccr.2012.10.012.

ACKNOWLEDGMENTS

We would like to thank members of Angela Nieto's lab for their helpful suggestions, Antonio Caler for the flow cytometry analyses, Antònia Vinyals for her help with the cell extravasation experiments, Diana Abad for excellent care of the zebrafish facility, and Giovanna Exposito for her invaluable assistance with the confocal microscopes. This work has been supported by grants from the Spanish Ministry of Science and Innovation BFU2008-01042 (to M.A.N.), SAF2010-21143 (to A.C.), and CONSOLIDER-INGENIO 2010 CSD2007-00017 to both labs. A grant from the Spanish Fondo de Investigaciones Sanitarias (FIS PS09/00373) supports Á.F.'s lab and CONSOLIDER-INGENIO 2010 CSD2007-00023 and Generalitat Valenciana (Prometeo 2008/049 and ISIC/2012/010) also support M.A.N.'s lab.

Received: June 7, 2012
Revised: September 17, 2012
Accepted: October 22, 2012
Published online: November 29, 2012

REFERENCES

Abell, A.N., Jordan, N.V., Huang, W., Prat, A., Midland, A.A., Johnson, N.L., Granger, D.A., Mieczkowski, P.A., Perou, C.M., Gomez, S.M., et al. (2011). MAP3K4/CBP-regulated H2B acetylation controls epithelial-mesenchymal transition in trophoblast stem cells. Cell Stem Cell *8*, 525–537.

Acloque, H., Ocaña, O.H., Matheu, A., Rizzoti, K., Wise, C., Lovell-Badge, R., and Nieto, M.A. (2011). Reciprocal repression between Sox3 and snail transcription factors defines embryonic territories at gastrulation. Dev. Cell *21*, 546–558.

Brabletz, T. (2012). To differentiate or not—routes towards metastasis. Nat. Rev. Cancer *12*, 425–436.

Brabletz, T., Jung, A., Spaderna, S., Hlubek, F., and Kirchner, T. (2005). Opinion: migrating cancer stem cells - an integrated concept of malignant tumour progression. Nat. Rev. Cancer *5*, 744–749.

Cano, A., Pérez-Moreno, M.A., Rodrigo, I., Locascio, A., Blanco, M.J., del Barrio, M.G., Portillo, F., and Nieto, M.A. (2000). The transcription factor snail controls epithelial-mesenchymal transitions by repressing E-cadherin expression. Nat. Cell Biol. *2*, 76–83.

Casas, E., Kim, J., Bendesky, A., Ohno-Machado, L., Wolfe, C.J., and Yang, J. (2011). Snail2 is an essential mediator of Twist1-induced epithelial mesenchymal transition and metastasis. Cancer Res. *71*, 245–254.

Celià-Terrassa, T., Meca-Cortés, O., Mateo, F., de Paz, A.M., Rubio, N., Arnal-Estapé, A., Ell, B.J., Bermudo, R., Díaz, A., Guerra-Rebollo, M., et al. (2012). Epithelial-mesenchymal transition can suppress major attributes of human epithelial tumor-initiating cells. J. Clin. Invest. *122*, 1849–1868.

Cserjesi, P., Lilly, B., Bryson, L., Wang, Y., Sassoon, D.A., and Olson, E.N. (1992). MHox: a mesodermally restricted homeodomain protein that binds an essential site in the muscle creatine kinase enhancer. Development *115*, 1087–1101.

Chaffer, C.L., Brennan, J.P., Slavin, J.L., Blick, T., Thompson, E.W., and Williams, E.D. (2006). Mesenchymal-to-epithelial transition facilitates bladder cancer metastasis: role of fibroblast growth factor receptor-2. Cancer Res. *66*, 11271–11278.

Chin, K., DeVries, S., Fridlyand, J., Spellman, P.T., Roydasgupta, R., Kuo, W.L., Lapuk, A., Neve, R.M., Qian, Z., Ryder, T., et al. (2006). Genomic and transcriptional aberrations linked to breast cancer pathophysiologies. Cancer Cell *10*, 529–541.

Dykxhoorn, D.M., Wu, Y., Xie, H., Yu, F., Lal, A., Petrocca, F., Martinvalet, D., Song, E., Lim, B., and Lieberman, J. (2009). miR-200 enhances mouse breast cancer cell colonization to form distant metastases. PLoS ONE *4*, e7181.

Eckert, M.A., Lwin, T.M., Chang, A.T., Kim, J., Danis, E., Ohno-Machado, L., and Yang, J. (2011). Twist1-induced invadopodia formation promotes tumor metastasis. Cancer Cell *19*, 372–386.

Giampieri, S., Manning, C., Hooper, S., Jones, L., Hill, C.S., and Sahai, E. (2009). Localized and reversible TGFbeta signalling switches breast cancer cells from cohesive to single cell motility. Nat. Cell Biol. *11*, 1287–1296.

Guo, W., Keckesova, Z., Donaher, J.L., Shibue, T., Tischler, V., Reinhardt, F., Itzkovitz, S., Noske, A., Zürrer-Härdi, U., Bell, G., et al. (2012). Slug and Sox9 cooperatively determine the mammary stem cell state. Cell *148*, 1015–1028.

Gupta, G.P., and Massagué, J. (2006). Cancer metastasis: building a framework. Cell *127*, 679–695.

Hamburger, V., and Hamilton, H. (1951). A series of normal stages in the development of the chick embryo. J. Morphol. *88*, 49–92.

Kimmel, C.B., Ballard, W.W., Kimmel, S.R., Ullmann, B., and Schilling, T.F. (1995). Stages of embryonic development of the zebrafish. Dev. Dyn. *203*, 253–310.

Larsen, J.E., Pavey, S.J., Passmore, L.H., Bowman, R., Clarke, B.E., Hayward, N.K., and Fong, K.M. (2007). Expression profiling defines a recurrence signature in lung squamous cell carcinoma. Carcinogenesis *28*, 760–766.

Li, R., Liang, J., Ni, S., Zhou, T., Qing, X., Li, H., He, W., Chen, J., Li, F., Zhuang, Q., et al. (2010). A mesenchymal-to-epithelial transition initiates and is required for the nuclear reprogramming of mouse fibroblasts. Cell Stem Cell *7*, 51–63.

Mani, S.A., Guo, W., Liao, M.J., Eaton, E.N., Ayyanan, A., Zhou, A.Y., Brooks, M., Reinhard, F., Zhang, C.C., Shipitsin, M., et al. (2008). The epithelial-mesenchymal transition generates cells with properties of stem cells. Cell *133*, 704–715.

Marotta, L.L., Almendro, V., Marusyk, A., Shipitsin, M., Schemme, J., Walker, S.R., Bloushtain-Qimron, N., Kim, J.J., Choudhury, S.A., Maruyama, R., et al. (2011). The JAK2/STAT3 signaling pathway is required for growth of $CD44^{+}CD24^{-}$ stem cell-like breast cancer cells in human tumors. J. Clin. Invest. *121*, 2723–2735.

McKean, D.M., Sisbarro, L., Ilic, D., Kaplan-Alburquerque, N., Nemenoff, R., Weiser-Evans, M., Kern, M.J., and Jones, P.L. (2003). FAK induces expression of Prx1 to promote tenascin-C-dependent fibroblast migration. J. Cell Biol. *161*, 393–402.

Mejlvang, J., Kriajevska, M., Vandewalle, C., Chernova, T., Sayan, A.E., Berx, G., Mellon, J.K., and Tulchinsky, E. (2007). Direct repression of cyclin D1 by SIP1 attenuates cell cycle progression in cells undergoing an epithelial mesenchymal transition. Mol. Biol. Cell *18*, 4615–4624.

Morel, A.P., Lièvre, M., Thomas, C., Hinkal, G., Ansieau, S., and Puisieux, A. (2008). Generation of breast cancer stem cells through epithelial-mesenchymal transition. PLoS ONE *3*, e2888.

Moreno-Bueno, G., Salvador, F., Martín, A., Floristán, A., Cuevas, E.P., Santos, V., Montes, A., Morales, S., Castilla, M.A., Rojo-Sebastián, A., et al. (2011). Lysyl oxidase-like 2 (LOXL2), a new regulator of cell polarity required for metastatic dissemination of basal-like breast carcinomas. EMBO Mol. Med. *3*, 528–544.

Nasevicius, A., and Ekker, S.C. (2000). Effective targeted gene 'knockdown' in zebrafish. Nat. Genet. *26*, 216–220.

Nieto, M.A. (2011). The ins and outs of the epithelial to mesenchymal transition in health and disease. Annu. Rev. Cell Dev. Biol. *27*, 347–376.

Nieto, M.A., and Cano, A. (2012). The epithelial-mesenchymal transition under control: Global programs to regulate epithelial plasticity. Semin. Cancer Biol. *22*, 361–368.

Nieto, M.A., Patel, K., and Wilkinson, D.G. (1996). In situ hybridization analysis of chick embryos in whole mount and tissue sections. Methods Cell Biol. *51*, 219–235.

Olmeda, D., Montes, A., Moreno-Bueno, G., Flores, J.M., Portillo, F., and Cano, A. (2008). Snai1 and Snai2 collaborate on tumor growth and metastasis properties of mouse skin carcinoma cell lines. Oncogene *27*, 4690–4701.

Pawitan, Y., Bjöhle, J., Amler, L., Borg, A.L., Egyhazi, S., Hall, P., Han, X., Holmberg, L., Huang, F., Klaar, S., et al. (2005). Gene expression profiling spares early breast cancer patients from adjuvant therapy: derived and validated in two population-based cohorts. Breast Cancer Res. *7*, R953–R964.

Peinado, H., Olmeda, D., and Cano, A. (2007). Snail, Zeb and bHLH factors in tumour progression: an alliance against the epithelial phenotype? Nat. Rev. Cancer *7*, 415–428.

Prigent, C., and Dimitrov, S. (2003). Phosphorylation of serine 10 in histone H3, what for? J. Cell Sci. *116*, 3677–3685.

Raponi, M., Zhang, Y., Yu, J., Chen, G., Lee, G., Taylor, J.M., Macdonald, J., Thomas, D., Moskaluk, C., Wang, Y., and Beer, D.G. (2006). Gene expression signatures for predicting prognosis of squamous cell and adenocarcinomas of the lung. Cancer Res. *66*, 7466–7472.

Samavarchi-Tehrani, P., Golipour, A., David, L., Sung, H.K., Beyer, T.A., Datti, A., Woltjen, K., Nagy, A., and Wrana, J.L. (2010). Functional genomics reveals a BMP-driven mesenchymal-to-epithelial transition in the initiation of somatic cell reprogramming. Cell Stem Cell *7*, 64–77.

Sefton, M., Sánchez, S., and Nieto, M.A. (1998). Conserved and divergent roles for members of the Snail family of transcription factors in the chick and mouse embryo. Development *125*, 3111–3121.

Sleeman, K.E., Kendrick, H., Ashworth, A., Isacke, C.M., and Smalley, M.J. (2006). CD24 staining of mouse mammary gland cells defines luminal epithelial, myoepithelial/basal and non-epithelial cells. Breast Cancer Res. *8*, R7.

Thiery, J.P., Acloque, H., Huang, R.Y., and Nieto, M.A. (2009). Epithelial-mesenchymal transitions in development and disease. Cell *139*, 871–890.

Tran, D.D., Corsa, C.A., Biswas, H., Aft, R.L., and Longmore, G.D. (2011). Temporal and spatial cooperation of Snail1 and Twist1 during epithelial-mesenchymal transition predicts for human breast cancer recurrence. Mol. Cancer Res. *9*, 1644–1657.

Vega, S., Morales, A.V., Ocaña, O.H., Valdés, F., Fabregat, I., and Nieto, M.A. (2004). Snail blocks the cell cycle and confers resistance to cell death. Genes Dev. *18*, 1131–1143.

Wellner, U., Schubert, J., Burk, U.C., Schmalhofer, O., Zhu, F., Sonntag, A., Waldvogel, B., Vannier, C., Darling, D., zur Hausen, A., et al. (2009). The EMT-activator ZEB1 promotes tumorigenicity by repressing stemness-inhibiting microRNAs. Nat. Cell Biol. *11*, 1487–1495.

Yang, J., and Weinberg, R.A. (2008). Epithelial-mesenchymal transition: at the crossroads of development and tumor metastasis. Dev. Cell *14*, 818–829.

Yang, J., Mani, S.A., Donaher, J.L., Ramaswamy, S., Itzykson, R.A., Come, C., Savagner, P., Gitelman, I., Richardson, A., and Weinberg, R.A. (2004). Twist, a master regulator of morphogenesis, plays an essential role in tumor metastasis. Cell *117*, 927–939.

Cancer Cell
Article

Cell-type, Dose, and Mutation-type Specificity Dictate Mutant p53 Functions In Vivo

Ming Kei Lee,[1] Wei Wei Teoh,[1] Beng Hooi Phang,[1] Wei Min Tong,[2] Zhao Qi Wang,[3,4] and Kanaga Sabapathy[1,5,6,*]
[1]Division of Cellular and Molecular Research, Humphrey Oei Institute of Cancer Research, National Cancer Centre, 11, Hospital Drive, Singapore 169610, Singapore
[2]Institute of Basic Medical Sciences School of Basic Medicine, Chinese Academy of Medical Sciences, Peking Union Medical College 5, Dong Dan San Tiao, 100005, Beijing, China
[3]Leibniz Institute for Age Research, Fritz Lipmann Institute e.V., Beutenbergstrasse 11, 07745 Jena, Germany
[4]Biology and Pharmacy Faculty, Friedrich-Schiller-University, 07745 Jena, Germany
[5]Cancer and Stem Cell Biology Program, Duke-NUS Graduate Medical School, 8, College Road, Singapore 169857, Singapore
[6]Department of Biochemistry, National University of Singapore, 8, Medical Drive, Singapore 117597, Singapore
*Correspondence: cmrksb@nccs.com.sg
http://dx.doi.org/10.1016/j.ccr.2012.10.022

SUMMARY

The specific roles of mutant p53's dominant-negative (DN) or gain-of-function (GOF) properties in regulating acute response and long-term tumorigenesis is unclear. Using "knockin" mouse strains expressing varying R246S mutant levels, we show that the DN effect on transactivation is universally observed after acute p53 activation, whereas the effect on cellular outcome is cell-type specific. Reducing mutant p53 levels abrogated the DN effect. Mutant p53's DN effect protected against radiation-induced death but did not accentuate tumorigenesis. Furthermore, the R246S mutant did not promote tumorigenesis compared to *p53*$^{-/-}$ mice in various models, even when MDM2 is absent, unlike the R172H mutant. Together, these data demonstrate that mutant p53's DN property only affects acute responses, whereas GOF is not universal, being mutation-type specific.

INTRODUCTION

Mutations in *p53* occur in over 50% of all human cancers, and in the other cases, alterations in the p53 pathway have been observed, indicating that the functional inactivation of the p53 pathway is a critical step in tumor formation (Robles and Harris, 2010; Zilfou and Lowe, 2009). Most of the mutations are missense mutations—often in the DNA-binding domain—and therefore lead to loss of target gene transactivation (Olivier et al., 2010). Mutations in *p53* often occur during the course of tumorigenesis, and hence, the mutant allele coexists with the wild-type allele in the cell for a time period until the latter is lost because of loss-of-heterozygozity (LOH), leaving behind the mutant allele in some cancers (Levine et al., 1991; Robles and Harris, 2010). Mutant *p53* is also found in the germline in the case of Li-Fraumeni syndrome (LFS) patients, resulting in higher rate of tumorigenesis. Interestingly, LOH is not observed in all LFS patients, suggesting that mutant p53 may exhibit dominant-negative (DN) activities or reduced p53 activity per se may be sufficient to drive carcinogenesis (haploid insufficiency) (Palmero et al., 2010; Varley et al., 1997). Regardless of the sporadic or familial nature of cancers, the observation of LOH of the wild-type allele in some cancers indicates that complete loss of wild-type p53 further promotes turmorigenesis, and cells expressing only mutant p53 may have additional advantages through acquired gain-of-functions (GOF) (Brosh and Rotter, 2009; Oren and Rotter, 2010).

A large body of in vitro work using overexpressed mutant p53 has demonstrated mutant p53's ability to bind and inhibit wild-type p53 activity when both coexist, in a phenomenon termed as the DN effect (Kern et al., 1992; Milner and Medcalf, 1991; Petitjean et al., 2007). However, the relevance of DN

Significance

Mutant p53 has been shown to exhibit dominant-negative (DN) effects and gain-of-function (GOF) properties in vitro, though the in vivo relevance is relatively unclear. Using knockin mouse strains expressing varying levels of the R246S mutant, we show that the DN effect is exhibited in vivo in a cell-type-specific and dose-dependent manner, being observed only after acute p53 activation and preventing radiosensitivity but not contributing to long-term tumorigenesis. GOF, however, was not observed in various cancer/cellular models, even when MDM2 is absent. These data therefore signify the need for the evaluation of p53 status during cancer therapy, which often activates p53 acutely, leading possibly to DN effects. Moreover, the GOF property appears not to be a universal phenomenon of p53 mutants.

activity in vivo in the context of tumor formation has been questionable. The initial generation of knockin mice and cells expressing mutant p53 has indicated that DN activity is displayed in some tissues, such as embryonic stem cells, breast and lung epithelium, but not in others, such as the skin epithelium, unless UV irradiated, indicating a contextual setting in which such activity can be manifested (Jackson et al., 2005; Lee and Sabapathy, 2008; Wijnhoven et al., 2005, 2007). However, detailed characterization of mutant p53's DN activity in multiple tissues after p53 activation and in the context of concomitant tumorigeneis has not been performed, and its significance is not well understood. Given that tumors would generally retain the wild-type allele in mutant p53 expressing cells in the early phases—during which chemo- and radiotherapies may be administered—the impact of mutant p53's DN effect can be expected to be a crucial factor in determining successful therapeutic and hence survival outcome. Studies on human follicular lymphoma have shown that heterozygote status with the presence of one mutant *p53* allele leads to poor overall survival and shortened time of disease progression (O'Shea et al., 2008), supporting this hypothesis.

Similarly, a substantial amount of evidence exists for the oncogenic GOF of mutant p53, which has been shown to be capable of transactivating novel noncanonical target genes that confer additional growth advantage, migratory potential, and drug resistance (Muller et al., 2009; Weisz et al., 2007, Yeudall et al., 2012). We and others have also demonstrated that cancer cells become addicted to mutant p53 expression, abrogation of which leads to cell death and reduced tumor formation in scid mice (Bossi et al., 2006; Vikhanskaya et al., 2007). Moreover, mutant p53 interacts with a variety of cellular proteins, such as p63, p73, and NF-Y, thereby altering the activities of these proteins to prevent proliferation or interfere with apoptosis (Oren and Rotter, 2010). Consistently, analysis of two strains of knockin mice expressing hot spot mutants R172H and R270H revealed that these mutants were capable of inhibiting p63/73 function, supporting the case for GOF (Lang et al., 2004; Olive et al., 2004). Subsequent experiments with other cancer models using these knockin mice confirmed this phenomenon (Jackson et al., 2005; Morton et al., 2010), elevating enthusiasm that all p53 mutants may generally exhibit GOF that could be amenable to therapeutic targeting. However, it remains unclear whether GOF is a universal property of all hot spot p53 mutants. Furthermore, the manifestation of GOF has been correlated to conditions in which mutant p53 is "hyperstable," such as in the "cancer-cell context" or in the absence of Mdm2, where basal mutant p53 levels are elevated, leading to enhanced spontaneous tumor formation (Terzian et al., 2008), suggesting a requirement for increased stability for phenotypic manifestation of GOF. However, current data are not conclusive enough to confirm the universality of this requirement.

Hence, we have embarked on addressing the role of DN and GOF in detail, through the use of knockin mice strains expressing different levels of the R246S mutant, equivalent of the hot spot human R249S mutant, to understand the effect of its presence in various tissues upon pathological and nonpathological p53 activating conditions, some of which lead to tumorigenesis over time.

RESULTS

Mutant p53 Exhibits Dominant Negative Effect on Cellular Viability in a Cell-type-Dependent Manner

To determine the effects of mutant p53 over its wild-type counterpart in an endogenous setting in various tissues, we generated a knockin mouse strain that carries the *R246S* mutation (human *R249S* equivalent) through germline targeting (Figure S1A available online) and analyzed a variety of cell types after exposure to γ-irradiation (IR) or treatment with the p53-activating agent nutlin (Vassilev et al., 2004). Whole-body irradiation showed that thymocytes were expectedly highly sensitive to IR in vivo and die in a p53-dependent manner, as $p53^{-/-}$ thymocytes were almost completely resistant to cell death (Figure 1A; Figure S1B). $p53^{+/-}$ thymocytes were also very sensitive, though less than $p53^{+/+}$ cells. By contrast, $p53^{+/R246S}$ thymocytes were significantly more resistant to death than $p53^{+/-}$ cells, being almost similar to $p53^{-/-}$ cells, indicating DN activity of the mutant protein over the wild-type protein (percentage of cell viability- $p53^{+/R246S}$ versus $p53^{+/-}$: 90.17 ± 4.22 versus 62.47 ± 1.76; $p < 0.001$) (Figure 1A). To confirm the cell-autonomous nature of this effect, we isolated thymocytes from various genotypes of mice and irradiated or treated them with nutlin ex vivo. Irradiation with 5 Gy and analysis over time indicated that $p53^{+/R246S}$ thymocytes were indeed more resistant than $p53^{+/-}$ (percentage of cell viability at 15 hr- $p53^{+/R246S}$ versus $p53^{+/-}$: 66.37 ± 3.11 versus 36.84 ± 1.45; $p < 0.001$) (Figure 1B). Similar results were obtained with various doses of irradiation (percentage of cell viability at 5 Gy- $p53^{+/R246S}$ versus $p53^{+/-}$: 62.70 ± 2.24 versus 33.86 ± 1.33; $p < 0.001$) (Figure 1C). Moreover, treatment with nutlin also led to the exhibition of DN effect of the mutant p53, as thymocytes from $p53^{+/R246S}$ mice were more resistant than $p53^{+/-}$ cells (percentage of cell viability at 15 hr- $p53^{+/R246S}$ versus $p53^{+/-}$: 45.52 ± 3.77 versus 19.50 ± 1.63; $p < 0.001$) (Figure 1D).

Detailed analysis of several lymphoid organs revealed that cell death was less pronounced in thymus, spleen, and lymph nodes of $p53^{+/R246S}$ mice compared to $p53^{+/-}$ mice after whole-body irradiation (Figure 1E). However, cell death was similar in bone marrow (BM) cells from these two genotypes. To confirm that DN effect is lacking in BM cells, we purified and used Lin^{-ve} progenitor cells from BM, which confirmed the lack of DN effect in this cell type (percentage of cell viability- $p53^{+/R246S}$ versus $p53^{+/-}$: 31.65 ± 3.34 versus 22.40 ± 2.40; $p > 0.05$) (Figure 1F). Thus, to determine if the DN effect seen in the other organs is attributable to specialized cell types, we analyzed T and B cells from lymph nodes and spleen after staining with anti-CD3 and anti-B220 antibodies, respectively. Ex vivo irradiation led to a significant DN effect in $p53^{+/R246S}$ $CD3^{+ve}$ cells from both spleen and lymph nodes ($p < 0.05$) (Figure 1G). Similarly, nutlin treatment also led to DN effect in $p53^{+/R246S}$ $CD3^{+ve}$ cells, in which cell death was less compared to their $p53^{+/-}$ counterparts (percentage of cell viability- $p53^{+/R246S}$ versus $p53^{+/-}$: 61.45 ± 3.38 versus 42.69 ± 2.46 for 10 μM nutlin; $p < 0.001$ and 53.73 ± 1.63 versus 33.69 ± 0.77 at 5 Gy, $p < 0.001$) (Figures 1H, S1C, and S1D). $B220^{+ve}$ cells from $p53^{+/R246S}$ mice were also significantly more resistant to cell death than $p53^{+/-}$ cells upon nutlin treatment and irradiation, though the difference was less pronounced at a higher dose of irradiation (percentage of cell

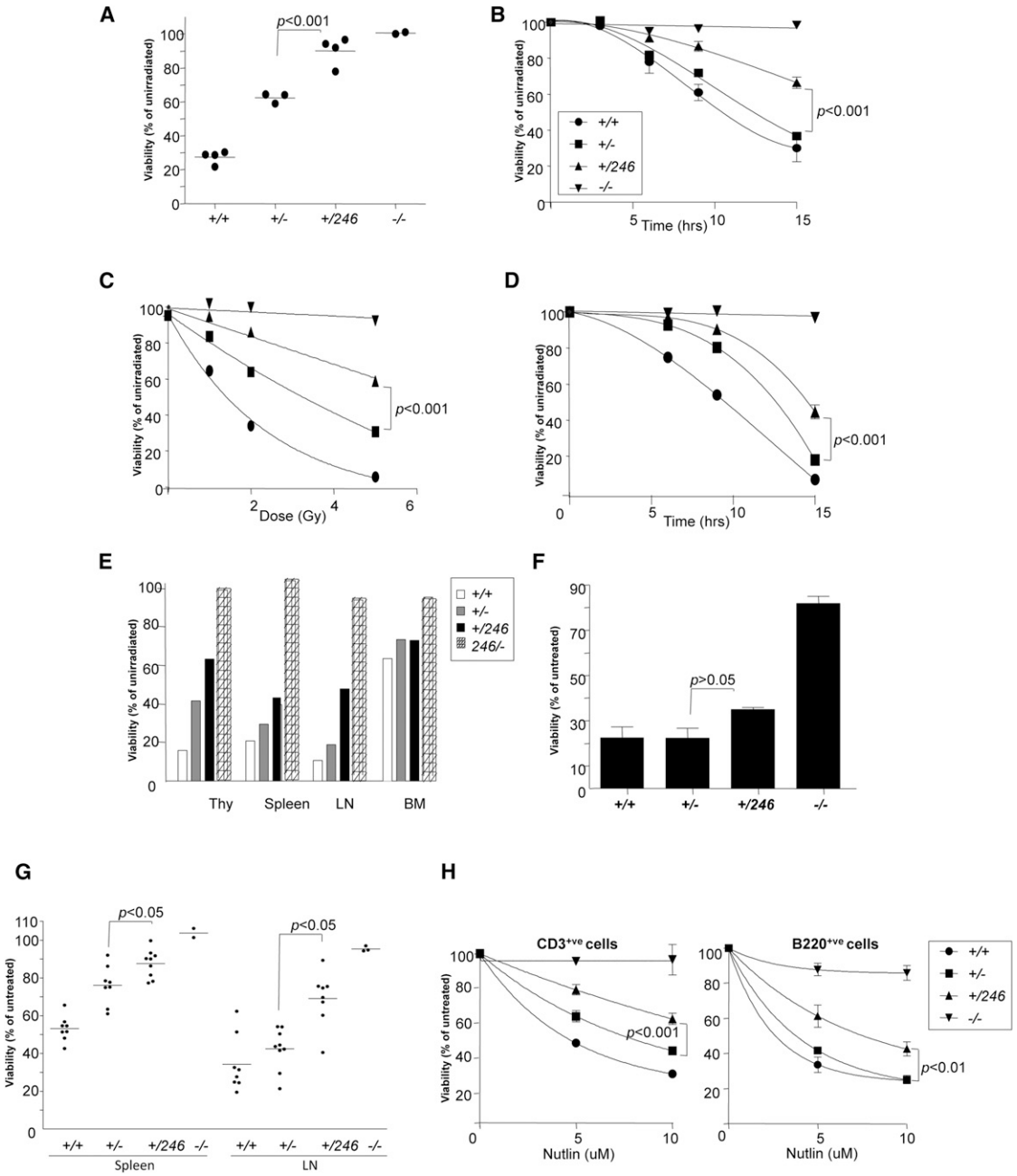

Figure 1. DN Effect of Mutant p53 on Cell Death Is Cell-type Specific

(A) Thymocytes of whole-body irradiated (5 Gy) 5-week-old mice were harvested 12 hr later for flow cytometric determination of viability after annexin-V/propidium iodide (PI) staining. Mean viability for each genotype (–) and thymocyte viability of each individual mouse (●) are shown.

(B–D) Thymocytes were irradiated ex vivo (5 Gy or otherwise indicated) (B and C) or treated with 10 μM nutlin (D) for 15 hr (or otherwise indicated), and cellular viability was determined by normalizing against unirradiated samples for each time point. Data represents mean ± SEM with 2–8 mice/genotype.

(E–H) Thymocytes, splenocytes, lymph node (LN), and bone marrow (BM) cells were irradiated (5 Gy) ex vivo (E–G) or treated with nutlin (H), and viability was determined 12–15 hr later. Lineage negative (Lin^{-ve}) cells were purified from BM and assayed similarly (F). Viability of $CD3^{+ve}$ and $B220^{+ve}$ cells were determined by staining with FITC-annexin-V and PE-conjugated CD3 or B220 antibody double staining, respectively, followed by flow cytometric analysis (G, $CD3^{+}$ cells only) and (H, $CD3^{+}$ or $B220^{+}$ cells). Mean viability (–) for each genotype and the viability of cells from each individual mouse (●) are represented by dots (G). Data represents mean ± SEM with three mice/genotype.

See also Figure S1.

viability- $p53^{+/R246S}$ versus $p53^{+/-}$: for nutlin, 61.24 ± 6.33 versus 41.73 ± 2.00 at 5 μM, $p < 0.001$; and 42.52 ± 4.01 versus 25.06 ± 2.37 at 10 μM, $p < 0.01$ and 47.54 ± 0.89 versus 29.53 ± 1.61 at 2 Gy, $p < 0.01$; and 17.84 ± 0.21 versus 10.61 ± 0.17 at 5 Gy) (Figures 1H and S1C). Collectively, these results demonstrate the cell-type-specific exhibition of DN effect of mutant p53.

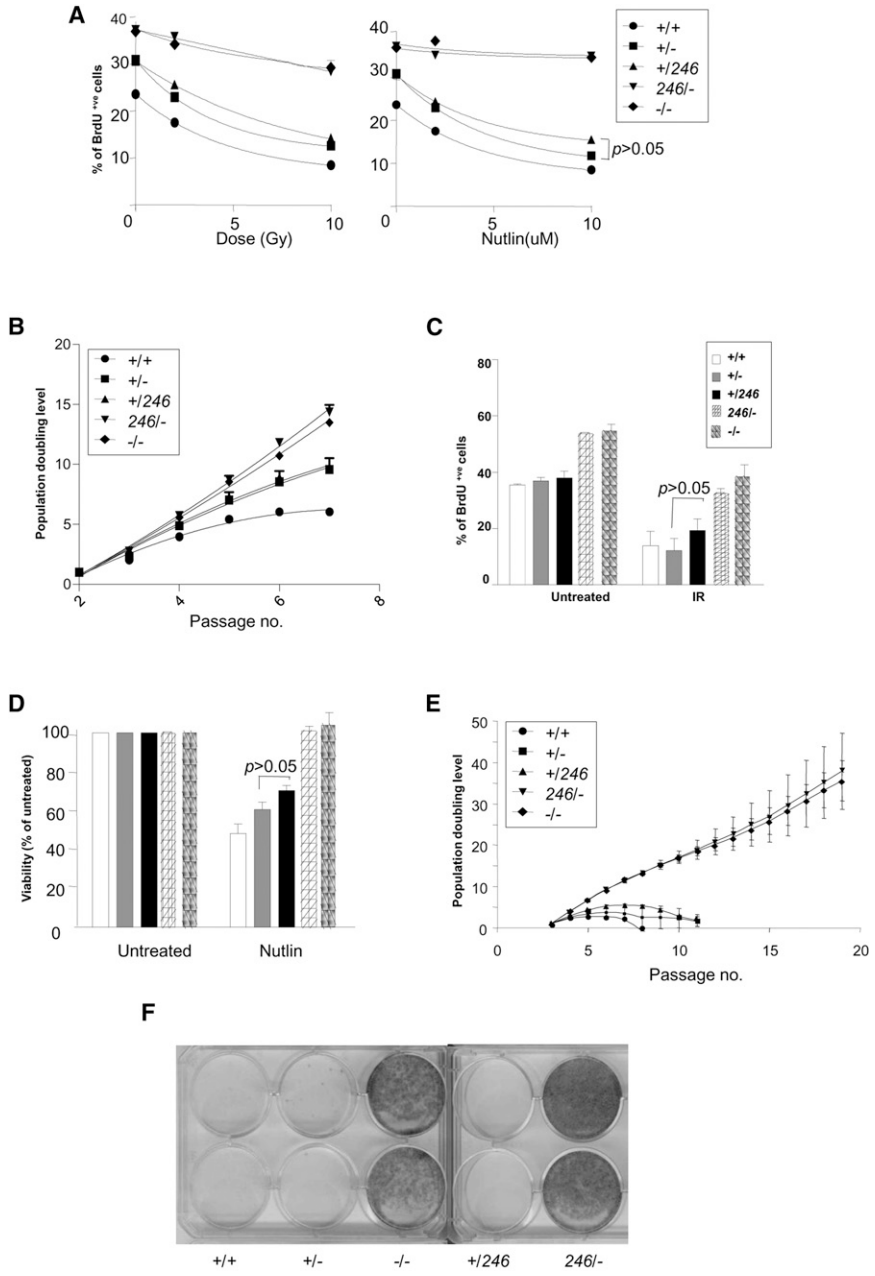

Figure 2. Cellular Predisposition to Cell Death or Cell-Cycle Arrest Does Not Dictate Mutant p53's DN Effect

(A) Primary MEFs (same passage) of different *p53* genotypes were γ-irradiated or nutlin treated and pulsed with 10 μM BrdU 24 hr after treatment for 1 hr. $BrdU^+$ cells were detected by flow cytometric analysis.

(B) Growth potential of primary MEFs was determined by population doubling in culture over seven passages. Data represents mean ± SEM with 3–4 clones of MEFs/genotype.

(C and D) Early passage E1A/Ras-transformed MEFs were γ-irradiated (5 Gy) or nutlin treated (10 mM), and the proportion of $BrdU^+$ cells was determined (C). Cell death of E1A/Ras-transformed MEFs was determined by annexin-V/PI staining (D). Data represents mean ± SEM with 3–4 mice/genotype.

(E) Spontaneous transformation/replicative senescence of primary MEFs was determined by growing cells in accordance with the 3T3 protocol. Data represents mean ± SEM with two clones of MEFs/genotype.

(F) Primary MEFs were transduced with oncogenic mutant Ras-V12-expressing retrovirus and selected for 2 weeks with puromycin. Viable cell colonies were stained with crystal violet, and representative data of three independent replicates are shown.

Lack of DN Effect Is Not due to Cellular Predisposition to Cell Death or Cellular Senescence

As the DN effect on cellular survival appears to be only seen in some cell types, we utilized primary mouse embryonic fibroblasts (MEFs) to determine DN effects on cellular proliferation and senescence. Treatment with nutlin or irradiation led to a reduction in BrdU incorporation in a p53-dependent manner (Figure 2A). However, $p53^{+/R246S}$ fibroblasts were as sensitive as the $p53^{+/+}$ and $p53^{+/-}$ cells, suggesting that the mutant p53 does not have a negative effect of the remaining wild-type protein (percentage of Brdu incorporation- $p53^{+/R246S}$ versus $p53^{+/-}$: 14.33 ± 0.22 versus 12.63 ± 0.24; $p > 0.05$ at 10 Gy and 15.53 ± 0.56 versus 11.75 ± 0.09; $p > 0.05$ at 10 μM nutlin). Moreover, growth rates were similar between $p53^{+/R246S}$ fibroblasts and $p53^{+/-}$ cells and lower than the $p53^{-/-}$ cells (Figure 2B). As primary fibroblasts generally undergo cell-cycle arrest upon irradiation, we utilized MEFs that have been transformed by the expression of E1A+Ras oncogenes, which have been shown to sensitize MEFs to cell death (Lowe et al., 1993). E1A/Ras-transformed $p53^{+/R246S}$ fibroblasts did not also exhibit any significant DN effects upon irradiation on cellular proliferation (percentage of BrdU incorporation- $p53^{+/R246S}$ versus $p53^{+/-}$: 19.40 ± 4.00 versus 12.24 ± 4.36; $p > 0.05$) (Figure 2C) or cell death (percentage of cell viability- $p53^{+/R246S}$ versus $p53^{+/-}$: 70.38 ± 2.59 versus 60.52 ± 3.86; $p > 0.05$) (Figure 2D). Basal BrdU incorporation for primary and E1A/Ras-transformed MEFs were also not significantly different ($p53^{+/R246S}$ versus $p53^{+/-}$: primary - 30.70 ± 1.21 versus 30.93 ± 0.43; $p > 0.05$ and E1A/Ras - 38.00 ± 2.43 versus 36.95 ± 1.25; $p > 0.05$) (Figures 2A and 2C). These data indicate that lack of DN effect in MEFs is regardless of their predisposition to cell-cycle arrest (primary MEFs) or death (transformed cells).

We next explored the DN potential during cellular senescence and transformation in MEFs. Primary MEFs were grown in the 3T3 protocol and development of spontaneous transformation was assayed. As shown in Figure 2E, $p53^{-/-}$ and $p53^{R246S/-}$ cells

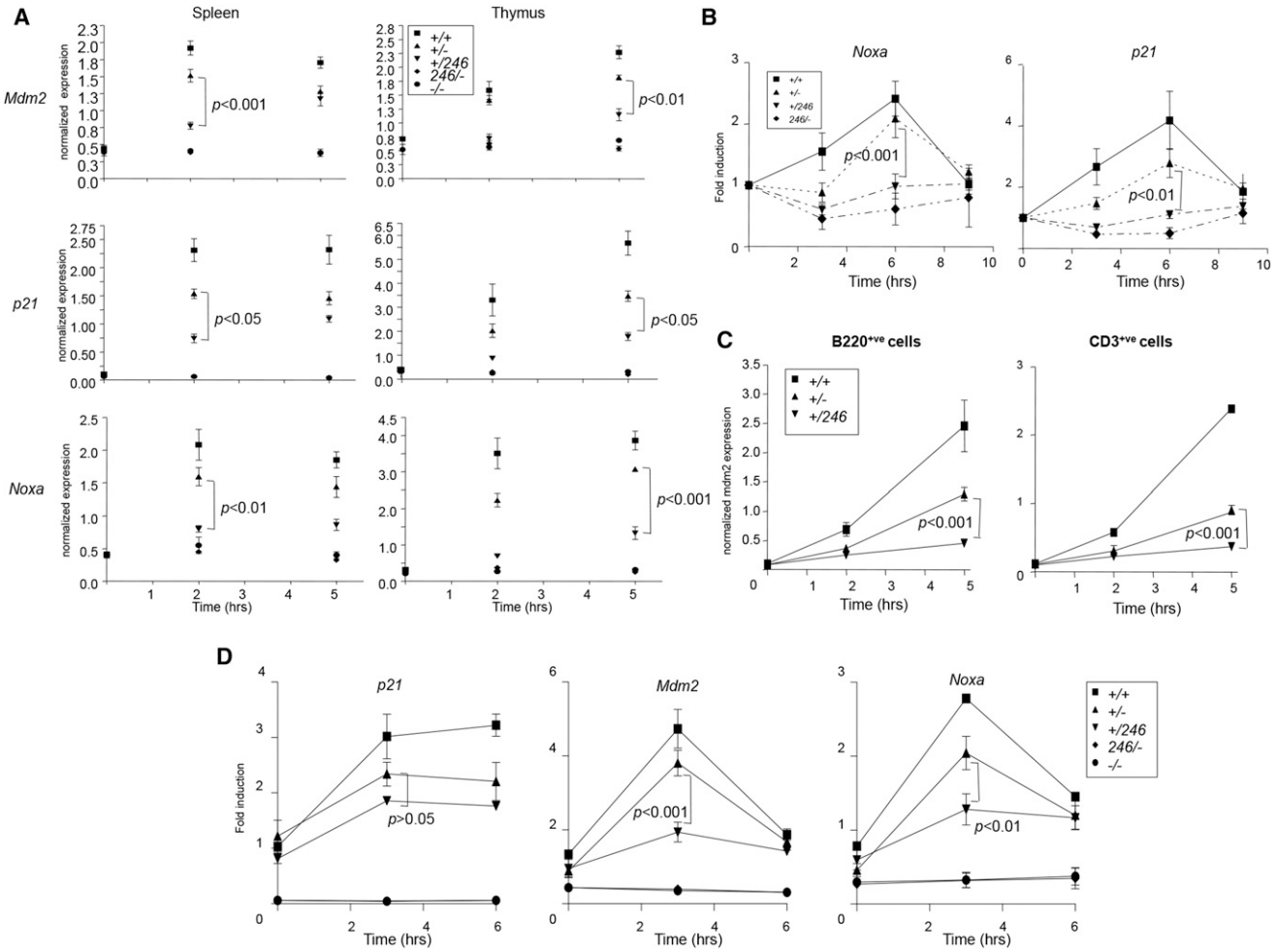

Figure 3. DN Effect of Mutant p53 on Transactivation of p53-Target Genes

(A) Various tissues from whole-body irradiated (10 Gy) mice were harvested at the times indicated for determination of p53 target gene expression by quantitative real-time RT-PCR (normalized against actin). Data represents mean ± s.e.m. with 4-8 mice/genotype, except where only 2 $p53^{-/-}$ mice were used.

(B) Thymocytes were irradiated (5Gy) ex vivo prior to analysis of p53 target genes. Fold induction was calculated based on unirradiated samples. Data represents mean ± s.e.m. with 4-8 mice/genotype, except where only 2 $p53^{246/-}$ mice were used.

(C) $CD3^+$ and $B220^+$ cells from spleens of 6-8 week old mice were purified and irradiated (5Gy) prior to determination of expression of p53 target genes. Data represents mean ± SEM with 2–3 mice/genotype.

(D) Early passage (<passage 4) MEFs of different *p53* genotypes were irradiated (10 Gy), and p53 target gene expression was determined. Data represents mean ± SEM with 3–4 mice/genotype.

readily transformed spontaneously in culture without undergoing replicative senescence, whereas $p53^{+/+}$, $p53^{+/-}$, and $p53^{+/R246S}$ MEFs did not, suggesting that the R246S mutant is incapable of exhibiting DN effects to overcome barriers of transformation. In addition, we utilized oncogenic Ras to induce oncogene-induced senescence, which again revealed the lack of DN effect, as only $p53^{-/-}$ and $p53^{R246S/-}$ cells were transformed, unlike the others (Figure 2F), demonstrating the absence of a DN effect during both spontaneous and Ras-induced senescence/transformation of MEFs in culture.

These data together demonstrate that the coexistence of endogenous mutant p53 and wild-type p53 leads to a DN effect on p53-mediated cell survival only in some cell types upon p53 activation.

Mutant p53 Exhibits DN Effect on p53-Mediated Transactivation in Both Sensitive and Insensitive Cell Types

We next examined if p53-mediated target gene transactivation is sensitive to DN effects of mutant p53 in various cell types by performing quantitative real-time PCR analysis. Whole-body irradiation led to maximal p53 target gene activation around 2 hr in spleen and 5 hr in thymus (Figure 3A). *Mdm2*, *p21*, and *Noxa* levels were highest at these time points, respectively, in the $p53^{+/+}$ case, whereas it was slightly reduced in $p53^{+/-}$ cells. However, target gene activation was significantly reduced in tissues from the $p53^{+/R246S}$ mice, almost similar to the $p53^{-/-}$ case (Figure 3A). It is noteworthy that the difference between $p53^{+/-}$ and $p53^{+/R246S}$ cases were maximal and significant at

the highest point of activation (normalized *Mdm2* expression - $p53^{+/-}$ versus $p53^{+/R246S}$: 1.512 ± 0.094 versus 0.776 ± 0.050 for spleen, $p < 0.001$ and 1.814 ± 0.041 versus 1.148 ± 0.108 for thymus, $p < 0.01$; *p21* expression - 1.534 ± 0.085 versus 0.741 ± 0.077 for spleen, $p < 0.05$ and 3.466 ± 0.219 versus 1.781 ± 0.166 for thymus, $p < 0.05$; *Noxa* expression - 1.590 ± 0.136 versus 0.799 ± 0.050 for spleen, $p < 0.01$ and 3.073 ± 0.027 versus 1.324 ± 0.178 for thymus, $p < 0.001$).

p53 target gene activation in thymocytes and purified T and B cells from spleen after irradiation ex vivo was also examined. Similar to the in vivo case, p53-dependent *p21* and *Noxa* activation was maximal around 6 hr after irradiation in thymocytes, at which point the difference between $p53^{+/-}$ and $p53^{+/R246S}$ was most obvious and significant (normalized *Noxa* expression - $p53^{+/-}$ versus $p53^{+/R246S}$: 2.088 ± 0.313 versus 0.982 ± 0.205, $p < 0.001$; *p21* expression - 2.787 ± 0.468 versus 1.110 ± 0.135, $p < 0.01$) (Figure 3B). Importantly, these targets were minimally activated in $p53^{+/R246S}$ cells. Purified T and B cells also showed a similar trend, where the *Mdm2* activation was markedly reduced in $p53^{+/R246S}$ cells compared to $p53^{+/-}$ cells (normalized *Mdm2* expression - $p53^{+/-}$ versus $p53^{+/R246S}$: 1.288 ± 0.116 versus 0.450 ± 0.053, $p < 0.001$ for $B220^{+}$ cells; 0.739 ± 0.068 versus 0.369 ± 0.032, $p < 0.001$ for $CD3^{+}$ cells at 5 hr) (Figure 3C), highlighting that the presence of mutant p53 was indeed affecting the wild-type p53-dependent target gene activation in sensitive cells.

Because we noted the absence of a DN effect on cell death and proliferation in MEFs, we evaluated if p53-dependent target gene activation is at all affected by the presence of mutant p53. Whereas *p21* activation was not compromised in $p53^{+/R246S}$ MEFs, indicating the lack of a DN effect, *Noxa* and *Mdm2* activation was significantly compromised (normalized *Mdm2* expression - $p53^{+/-}$ versus $p53^{+/R246S}$: 3.808 ± 0.344 versus 1.934 ± 0.267, $p < 0.001$; *Noxa* expression – 2.044 ± 0.224 versus 1.280 ± 0.210, $p < 0.01$; *p21* expression – 2.341 ± 0.215 versus 1.858 ± 0.009, $p > 0.05$ at 3 hr) (Figure 3D). *Mdm2* and *Noxa* activation in $p53^{+/R246S}$ MEFs was minimal and significantly lower than in $p53^{+/-}$ cells. These data indicate that the DN effect on transactivation can indeed be observed in MEFs on some target genes, despite the lack of effect on the biological outcome (Figure 2). Altogether, the data highlight that the DN effect of mutant p53 on wild-type p53-mediated transactivation is observed in both sensitive tissues, such as thymus and lymphoid cells, and selectively on some target genes in insensitive cells, like the MEFs.

Threshold Level of Mutant p53 Is Required for DN Effect In Vivo

Another knockin mouse strain that carries the same R246S mutation but which also retains the neomycin resistance cassette in intron 6 of the *p53* locus, therefore making it a potential hypomorphic allele ($p53^{+/R246SNeo}$) (Figure S2), was generated. Analyzing transcript levels revealed that the mutant *p53* levels were considerably lower in $p53^{+/R246SNeo}$ thymocytes compared to $p53^{+/R246S}$ thymocytes (Figure 4A). Irradiation of thymocytes and splenocytes led to an increase in total p53 levels in cells from all *p53* genotypes but was maximal in the $p53^{+/R246S}$ case (Figure 4B). By contrast, p53 levels were lower in $p53^{+/R246SNeo}$ cells, confirming that the mutant p53 is indeed expressed at a higher steady-state level and that the presence of the neomycin cassette leads to a hypomorphic state, resulting in reduced expression (Figure 4B).

Irradiation of thymocytes revealed that the cells from $p53^{+/R246SNeo}$ mice were as sensitive as the $p53^{+/-}$ cells and not as resistant as the $p53^{+/R246S}$ cells, suggesting a lack of the DN effect in the $p53^{+/R246SNeo}$ case (percentage of cell viability at 5 Gy- $p53^{+/R246S}$ versus $p53^{+/R246Sneo}$: 62.50 ± 3.03 versus 45.71 ± 1.75, $p < 0.001$) (Figure 4C). To confirm if this loss of the DN effect on cell viability is also observed on p53-target gene transactivation, *p21* and *Noxa* induction was analyzed. As shown in Figure 4D, both the target genes were induced to a greater extent in the $p53^{+/R246SNeo}$ cells, compared to the $p53^{+/R246S}$ cells that showed minimal activation. Importantly, the level of induction was comparable between $p53^{+/R246SNeo}$ cells and $p53^{+/-}$ cells, thereby confirming the lack of a DN effect in the former cells (normalized *p21* expression - $p53^{+/-}$ versus $p53^{+/R246SNeo}$ versus $p53^{+/R246S}$ 3.042 ± 0.188 versus 3.168 ± 0.114 versus 1.666 ± 0.124, $p > 0.05$ for $p53^{+/-}$ versus $p53^{+/R246SNeo}$ and $p < 0.001$ for $p53^{+/-}$ versus $p53^{+/R246S}$; *Noxa* expression – 4.757 ± 0.35 versus 4.203 ± 0.465 versus 0.712 ± 0.21, $p > 0.05$ for $p53^{+/-}$ versus $p53^{+/R246SNeo}$ and $p < 0.001$ for $p53^{+/-}$ versus $p53^{+/R246S}$, at 5 hr). Similar results were obtained using splenocytes on cellular viability (percentage of cell viability at 5 Gy- $p53^{+/R246S}$ versus $p53^{+/R246SNeo}$: 71.439 ± 4.104 versus 43.591 ± 1.545, $p < 0.001$) (Figure 4E) and target gene activation (normalized *Mdm2* expression - $p53^{+/-}$ versus $p53^{+/R246SNeo}$ versus $p53^{+/R246S}$ 1.608 ± 0.307 versus 1.618 ± 0.329 versus 0.891 ± 0.074, $p > 0.05$ for $p53^{+/-}$ versus $p53^{+/R246SNeo}$ and $p < 0.01$ for $p53^{+/-}$ versus $p53^{+/R246S}$; *p21* expression – 1.883 ± 0.244 versus 1.832 ± 0.237 versus 0.790 ± 0.082, $p > 0.05$ for $p53^{+/-}$ versus $p53^{+/R246SNeo}$ and $p < 0.001$ for $p53^{+/-}$ versus $p53^{+/R246S}$, at 5 hr) (Figure 4F). These data together demonstrate that a threshold level of mutant p53 expression is required for the manifestation of DN effects, below which the effect is abrogated.

Mutant p53's DN Effect Affects Acute Response but Does Not Accentuate Tumor Formation

Low-dose (≤5 Gy) whole-body irradiation sensitizes p53 heterozygous mice to tumor formation (lymphomas and thymomas) (Kemp et al., 1994). Hence, we investigated if the DN effect on cellular survival seen in thymocytes and lymphocytes can lead to accentuation of tumor formation after low-dose whole-body irradiation. Analysis of $CD3^{+ve}$ cell count from peripheral blood a day after irradiation showed a reduction in mice of all *p53* genotypes, although the decrease appeared to be less pronounced in $p53^{+/R246S}$ mice and almost negligible in $p53^{-/-}$ mice (Figure 5A). To analyze this effect in detail, we performed a time-course analysis of $CD3^{+ve}$ cell numbers, which showed a dramatic decrease in cell numbers following the first day after irradiation, but which recovered starting from about day 4 onward (Figure 5A). The decrease was most significant in $p53^{+/+}$ mice, followed by the $p53^{+/-}$ mice. However, the decrease was less pronounced in $p53^{+/R246S}$ and $p53^{-/-}$ mice, indicative of DN activity during the acute response phase of radiosensitivity (for 24 hr after whole-body irradiation, absolute count of $CD3^{+}$ cells/μl of peripheral blood - $p53^{+/R246S}$ versus $p53^{+/-}$: 2,190.42 ± 60.10 versus 1,065.67 ± 164.00, $p < 0.05$). It is noteworthy that the

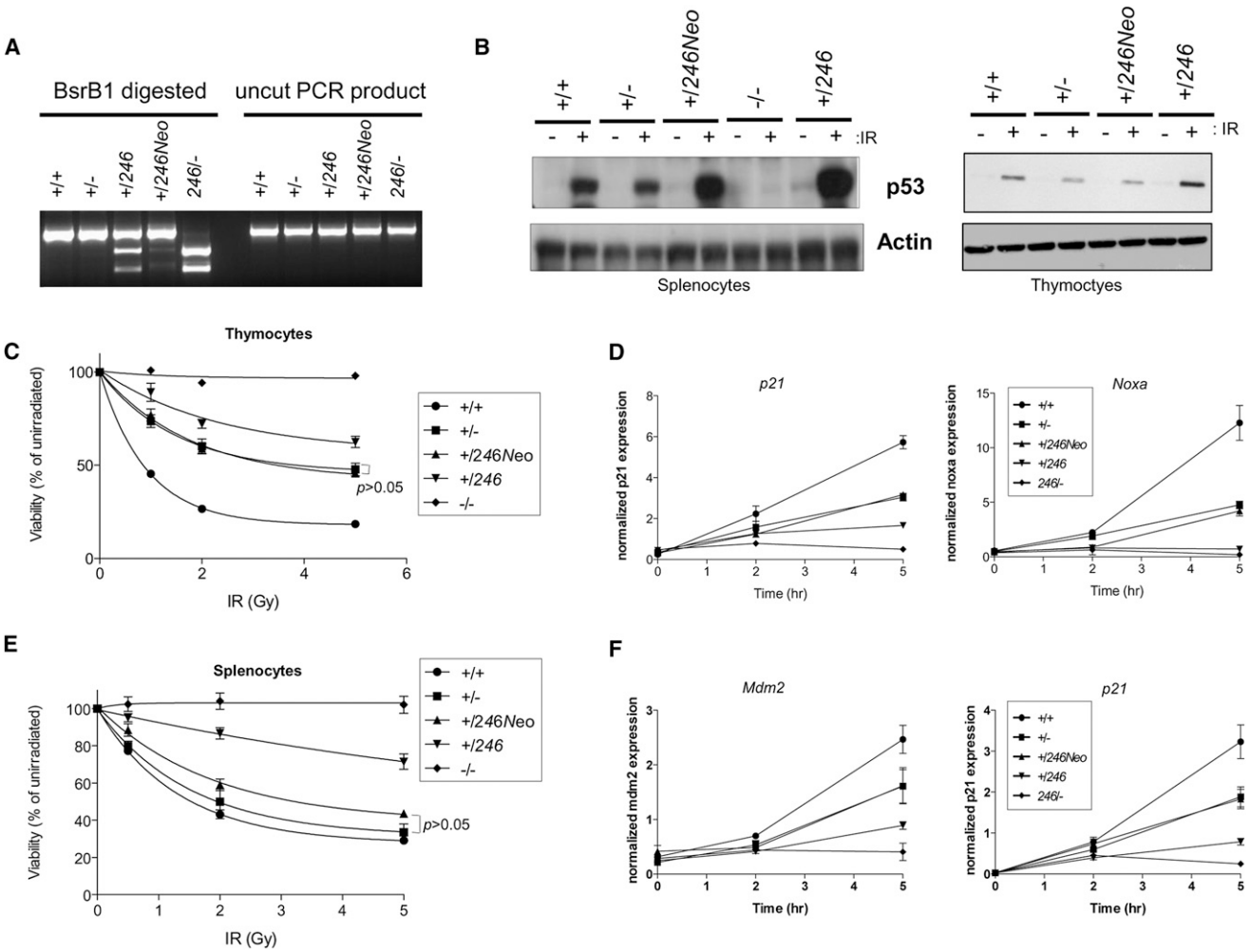

Figure 4. DN Effects Are Abrogated in Hypomorphic Mutant p53-Expressing $p53^{+/R246SNeo}$ Mice

(A) Expression of different *p53* alleles was determined by restriction fragment length polymorphism using thymocyte cDNA. *p53* transcript was amplified by RT-PCR, and 1 μg of purified RT-PCR product was digested with the *BsrB1* restriction enzyme—because of the generation of this site by the introduced R246S mutation—and analyzed by agarose gel electrophoresis. The relative intensity of the cleaved products indicates the expression levels of the knockin allele.

(B) Irradiated (5 Gy) splenocytes and thymocytes were harvested, and p53 protein levels were determined by immunoblotting. Representative blot of two independent experiments are shown.

(C–F) Viability of thymocytes (C) and splenocytes (E) was determined after irradiation. Expression of p53 target genes after irradiation (5 Gy) of thymocytes (D) and splenocytes (F) were determined. Data represents mean ± SEM with 3–4 (C and E) or 2–3 (D and F) mice/genotype, except for the $p53^{-/-}$ case in which one mouse was used for thymocytes. p values are shown for differences between the $p53^{+/246Neo}$ and $p53^{+/-}$ genotypes.

See also Figure S2.

numbers returned to almost baseline levels about 2 weeks after irradiation and that there was no elevation beyond the baseline values in both in $p53^{+/R246S}$ and $p53^{-/-}$ mice (Figure 5A).

Long-term monitoring of these irradiated cohorts of mice expectedly led to thymoma/lymphoma/sarcoma formation in a p53-dependent manner (median tumor-free survival of $p53^{+/-}$ versus $p53^{-/-}$ mice is 33.43 weeks versus 16.65 weeks, $p < 0.01$) (Figure 5B). However, tumor formation rate was not accentuated in $p53^{+/R246S}$, which were almost identical to the $p53^{+/-}$ case (median tumor-free survival of $p53^{+/R246S}$ versus $p53^{+/-}$ mice is 35.43 weeks versus 33.43 weeks, $p = 0.835$), indicating that the initial DN effect on cell death after acute DNA damage did not have any impact on tumor formation rates. Analysis of tumor spectrum revealed that majority of both $p53^{+/R246S}$ and $p53^{+/-}$ mice developed sarcomas primarily and lymphomas to a lesser extent (data not shown), confirming the lack of DN effect on carcinogenesis.

To further confirm that the mutant p53-mediated DN effect is indeed only observed at the initial acute phase but is not contributory to tumor formation, we utilized the Myc-induced B cell lymphoma model (*Eμ-Myc* transgenics) to follow the fate of B cells that develop lymphomas in a p53-dependent manner (Schmitt et al., 1999). First, we purified B cells from *Eμ-Myc* transgenic mice of the various *p53* genotypes at an early age, where LOH has not taken place (Figures S3A and S3B), to determine the effect of irradiation. The analysis revealed that the

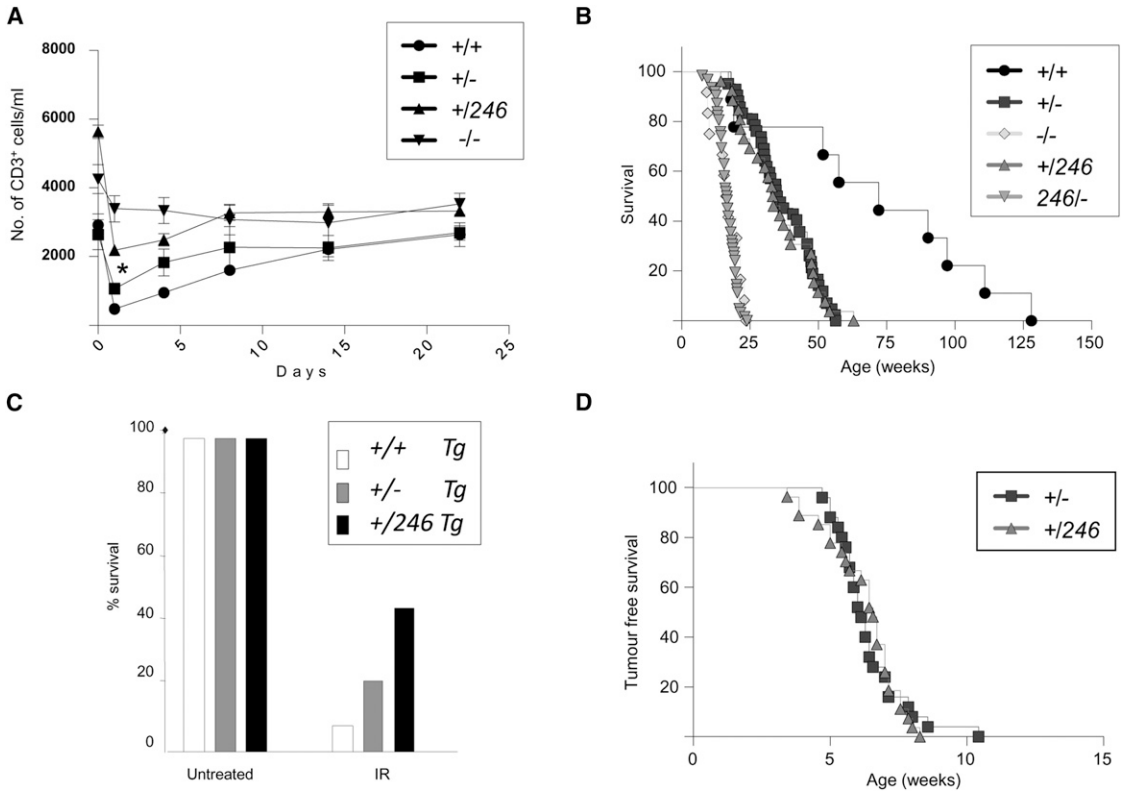

Figure 5. DN Effect Contributes to Acute p53-Mediated Response but Does Not Promote Tumorigenesis

(A) Absolute counts of peripheral $CD3^+$ lymphocytes from 20 μl of blood collected from 8-week-old mice were determined before and up to 3 weeks after whole-body γ-irradiation (2.5 Gy). Data represents mean ± SEM with three mice/genotype. * represents $p < 0.05$ for differences between the $p53^{+/246}$ and $p53^{+/-}$ genotypes.

(B) Kaplan-Meier survival curves of γ-irradiated (single dose, at 5–8 weeks) mice are shown.

(C) $B220^+$ cells were purified from splenocytes of 4 weeks old *Eμ-Myc* transgenic mice of various *p53* genotypes and irradiated (5 Gy), prior to determination of cellular viability. Data represents the percent viability normalized against unirradiated control.

(D) Kaplan-Meier survival curves of Eμ-Myc transgenic mice of various *p53* genotypes are shown.

See also Figure S3.

presence of the mutant protein led to resistance to cell death compared to the $p53^{+/-}$ cells (percentage of cell viability-$p53^{+/R246S}$ versus $p53^{+/-}$: 42.26 versus 20.29 with Myc) (Figure 5C), indicating the presence of DN activity on cellular survival upon acute p53 activation. Monitoring these mice over time indicated that both the *Eμ-Myc*;$p53^{+/R246S}$ mice and *Eμ-Myc*;$p53^{+/-}$ mice succumbed to tumor formation at the same rate, with the median tumor-free survival being 6.57 and 6.14 weeks, respectively ($p = 0.973$) (Figure 5D). These results suggest that the DN effect seen after acute p53 activation on cell death during the radiosensitive phase does not lead to enhanced tumorigenesis.

DN Effect Is neither Exhibited during Spontaneous Tumor Formation in the Absence of Stress Stimuli nor Evident during Embryonic Lethality Because of Mdm2 Absence

In order to further investigate if a DN effect is exhibited in the absence of exposure to acute stress signals, we first monitored a cohort of mice of various *p53* genotypes for spontaneous tumor formation. Similar to the irradiated cohorts, the median survival of $p53^{+/-}$ and $p53^{+/R246S}$ mice was comparable, indicating a lack of DN effects on overall tumorigenesis (median survival of $p53^{+/-}$ and $p53^{+/R246S}$ mice: 63.43 versus 59.86 weeks, $p = 0.46$) (Figure 6A; Table 1). Furthermore, there was no difference in the spectrum of tumors arising from mice of $p53^{+/-}$ and $p53^{+/R246S}$ genotypes (comparison of tumor spectrum by genotype, $p53^{+/-}$ *versus* $p53^{+/R246S}$ mice: 2 lymphoma and 19 sarcoma versus 8 lymphoma and 15 sarcoma, $p = 0.0725$ by Fisher's exact test) (Table 1). However, when we focused on the incidence of lymphoma alone, there is a slight but statistically significant decrease in the lymphoma incidence in $p53^{+/R246S}$ mice (lymphoma-bearing $p53^{+/R246S}$ versus $p53^{+/-}$ mice: 2/20 versus 8/19, $p = 0.031$ by Fisher's exact test) (Table 1). Nonetheless, there was no significant difference in survival between $p53^{+/-}$ and $p53^{+/R246S}$ mice in terms of spontaneous or IR-induced tumor formation, as well as in the *Eμ-Myc* lymphoma model (Figure 5; Table 1), suggesting that though the DN effect of mutant p53 may affect the type of cancers because of cell-type specificity, it does not affect overall tumor susceptibility. Supporting this idea, no significant difference was noted in the lymphoma incidence between the $p53^{+/R246S}$ versus $p53^{-/-}$ mice (lymphoma-bearing $p53^{+/R246S}$

versus $p53^{-/-}$ mice: 8/19 versus 29/42, p = 0.054, Fisher's exact test), although the rate of tumorigenesis was markedly different between the genotypes (Table 1), indicating that the mutant allele may have an effect on tissue specificity, though not having any DN effect on overall tumorigenesis.

Second, we investigated if embryonic lethality due to Mdm2 deficiency—that can be rescued by inactivation of p53 (Jones et al., 1995)—can be rescued by the DN effect of mutant p53. To that end, we intercrossed the $p53^{+/R246S}$;$Mdm2^{+/-}$ double heterozygotes and found no viable $Mdm2^{-/-}$ mice with $p53^{+/+}$ or $p53^{+/R246S}$ genotypes, in contrast to $Mdm2^{-/-}$;$p53^{R246S/R246S}$ double homozygous mice, which were viable at birth (number of $Mdm2^{-/-}$;$p53^{+/+}$, $Mdm2^{-/-}$;$p53^{+/R246S}$, and $Mdm2^{-/-}$;$p53^{R246S/R246S}$ mice found at the time of weaning: 0, 0, and 22, respectively) (Table 2). These results indicated that the R246S mutant is a completely nonfunctional mutant, reflecting the $p53^{-/-}$ case when homozygous but does not confer DN effects to rescue $Mdm2^{-/-}$ lethality.

These data therefore show that the DN effect of mutant p53 is only manifested during the acute p53 activation phase and does not contribute in any significant way to accelerate tumor formation in the three models studied here, as well as during embryogenesis.

Elevated Mutant p53 Expression in the Absence of Mdm2 or in Tumors Is Insufficient to Confer GOF Properties

We next explored if the R246S mutant possesses oncogenic GOF properties, by first analyzing the tumor formation rates in several models. As shown in Figure 5B and Figure 6A, the median survival of $p53^{-/-}$, $p53^{R246S/-}$, and $p53^{R246S/R246S}$ mice are comparable during both spontaneous and IR-induced cancer formation (spontaneous cancers - $p53^{-/-}$ versus $p53^{R246S/-}$ versus $p53^{R246S/R246S}$: 21.29 versus 20.86 versus 19.71 weeks, p = 0.375, for IR-induced cancer $p53^{-/-}$ versus $p53^{R246S/-}$: 16.64 versus 16.5 weeks, p = 0.23), suggesting that the R246S mutant may not possess GOF properties. Detailed analysis indicated that the $p53^{-/-}$, $p53^{R246S/-}$, and $p53^{R246S/R246S}$ mice developed mainly lymphomas and sarcomas with similar incidence, much more than the $p53^{+/R246S}$ and $p53^{+/-}$ mice, during both spontaneous and IR-induced cancer formation (proportion of $p53^{-/-}$ versus $p53^{R246S/R246S}$ mice developing spontaneous tumors that are lymphoma and sarcoma: 69% and 23.9% versus 78.3% and 21.7%, p = 0.3846 by Fisher's exact test) (Table 1 and data not shown). Unlike the case of other hot spot mutant p53 - R172H, metastasis was not observed in the tumor-bearing $p53^{R246S/-}$ and $p53^{R246S/R246S}$ mice (data not shown), further suggesting a lack of GOF properties of the R246S mutant.

Terzian and colleagues have suggested that the manifestation of the GOF of mutant p53 can be elevated by increasing the abundance of the mutant p53 protein, in the $Mdm2^{-/-}$ background (Terzian et al., 2008). To investigate this aspect, we first analyzed the status of mutant p53 in normal thymus and thymoma of $p53^{R246S/-}$ mice by immunoblotting, which indicated that the stabilization of the protein only in the tumorigenic state (Figure 6B), similar to the observation with other hot spot mutant p53 knockin mice (Lang et al., 2004; Olive et al., 2004). Immunohistochemical staining of tumors of $p53^{R246S/R246S}$ mice also confirmed the elevation of R246S mutant protein only in tumor cells (Figures S4A–S4D), altogether implying that the abundance of R246S mutant in tumors alone is insufficient to confer GOF. Moreover, the stabilized mutant p53 was found to be S18 phosphorylated (Figure 6B), suggesting elevated basal DNA damage in tumors that may contribute to its increased abundance.

We thus evaluated if the R246S mutant p53 would be capable of exhibiting GOF properties in the $Mdm2^{-/-}$ background, by generating cohorts of $p53^{R246S/R246S}$ mice with different *Mdm2* genotypes. As shown in Figure 6C, the median survival of $p53^{R246S/R246S}$ mice with different *Mdm2* genotypes were similar (median survival of $p53^{R246S/R246S}$ mice with *Mdm2* genotypes +/+ versus +/− versus −/−: 16 versus 17.5 versus 17.57 weeks, p = 0.577). Analysis of the tumor spectrum of these mice also revealed no significant differences among the various *Mdm2* genotypes, suggesting that the R246S mutant does not possess oncogenic GOF properties (proportion of $Mdm2^{+/+}$ versus $Mdm2^{+/-}$ versus $Mdm2^{-/-}$ mice with $p53^{R246S/R246S}$ harboring lymphoma: 71.4% versus 54.2% versus 58.3% and sarcoma: 28.6% versus 37.5% versus 25%, p = 0.9039 by chi-square test) (Table S1A). Examination of mutant p53 expression in normal tissues (spleen and thymus) revealed that the level of R246S mutant protein was indeed elevated in the absence of Mdm2 (Figure 6D, left panel). Furthermore, the R246S mutant protein levels were much higher in tumors compared to normal tissues lacking Mdm2 (Figure 6D, right panel), implying that phosphorylation of mutant p53 in the tumor context may prevent its degradation. Immunohistochemical staining of tumors of $p53^{R246S/R246S}$; $Mdm2^{-/-}$ mice also confirmed the elevated levels of R246S mutant in tumors and in normal tissues (Figures S4E–S4H). These data therefore indicate that elevation of mutant p53 levels alone by Mdm2 absence or by the DNA damage context in tumors is insufficient to confer GOF properties to the R246S mutant.

GOF Is a Phenomenon Exhibited by the R172H Mutant but Not by the R246S Mutant

Although we did not observe any biological differences between $p53^{-/-}$ and $p53^{R246S/R246S}$ mice with and without Mdm2, one cannot exclude the possibility that there may be subtle differences that cannot be revealed by macroscopic analysis. Transcriptome profiling was thus performed using normal thymus from $p53^{-/-}$ and $p53^{R246S/R246S}$ mice with/without Mdm2. The principal component analysis (PCA) of normal thymi indicated the transcriptome profiles were nearly identical among different genotypes (data not shown). In order to detect differential gene expression based on different *p53* genotypes, we performed ANOVA and compared the transcriptomes of $p53^{-/-}$ and $p53^{R246S/R246S}$ samples. As shown by the volcano plot in Figure S4I (left panel), most genes showed high p values and low fold changes, suggesting they are not significantly differentially expressed, indicating the lack of GOF in normal tissues. A similar trend was also noted in the absence of Mdm2, implying that Mdm2 loss per se does not confer GOF to the R246S mutant p53 (Figure S4I, right panel).

To determine if the "tumor context" is a prerequisite for the manifestation of GOF, we performed additional microarray analyses using B cells (primary or *Eμ-myc*-induced lymphoma) and MEFs (E1A/Ras transformed). For B lymphoma analysis, only cells that have lost the wild-type allele were used so that the

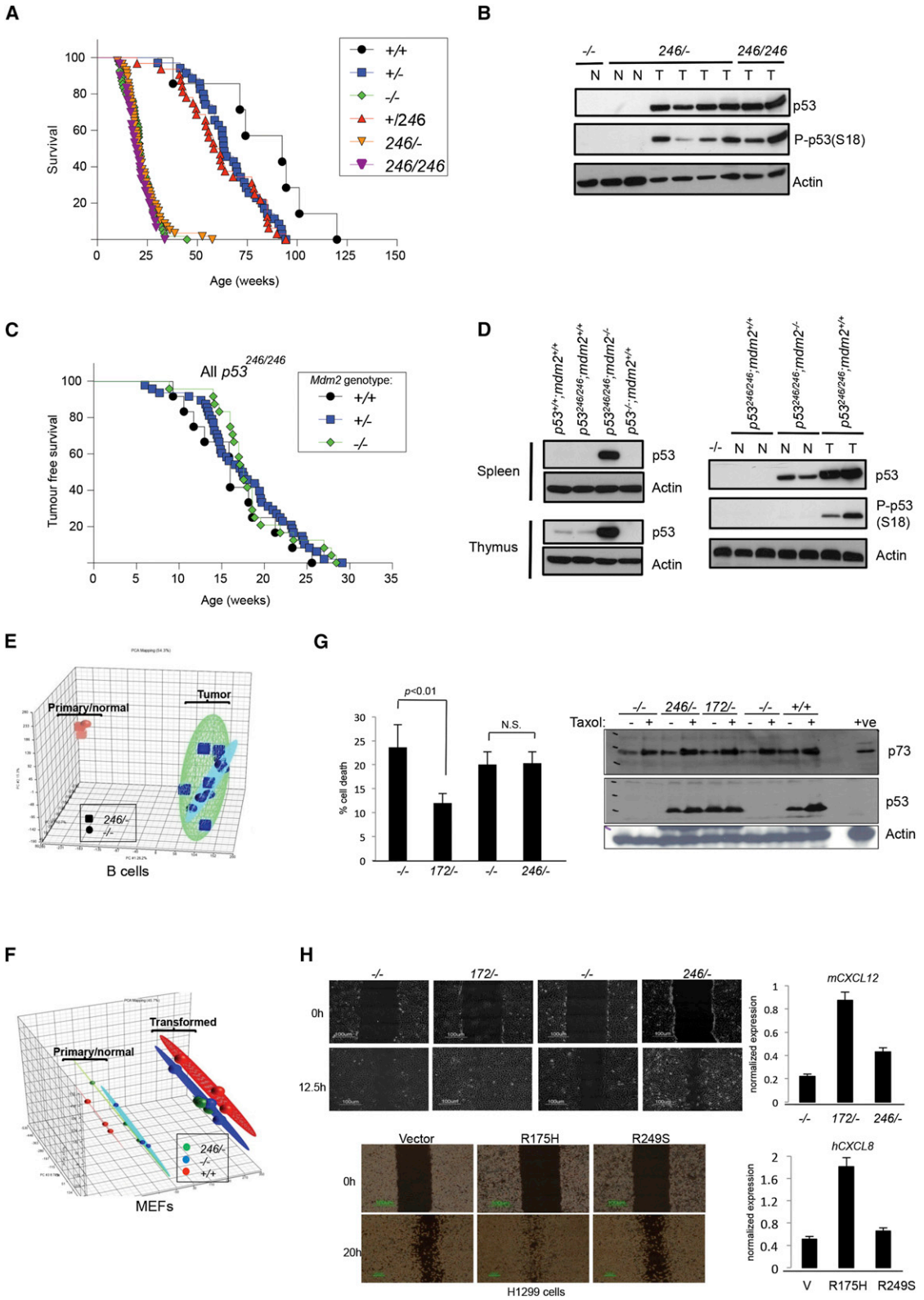

Figure 6. Mutant p53 GOF Properties Are Mutation-type Specific

(A) Kaplan-Meier survival curves of untreated mice of various *p53* genotypes are shown.

(B) Abundance and phosphorylation status of p53 protein in thymoma (T) and normal (N) thymi of mice of various *p53* genotypes were analyzed by western blotting.

Table 1. Characterization of Spontaneous Tumors in Various *p53* Genotypic Backgrounds

p53 Genotype	+/+	+/−	*+/246*	−/−	*246/246*
Lymphoma (%)	nd	2/20 (10)	8/19 (42.1)	29/42 (69)	18/23 (78.3)
Sarcoma (%)	nd	19/20 (95)	15/19 (78.9)	10/42 (23.9)	5/23 (21.7)
Other (%)	nd	0/20 (0)	0/19 (0)	3/42 (7.1)	0/23 (0)
Median survival (weeks)	92.43	63.43	59.86	21.29	19.71

Cohorts of mice of various *p53* genotypes were aged, and spontaneous tumor formation was monitored. Moribund mice were sacrificed, and necropsy was performed to determine the type of tumor developed. Stats – (2×2) contingency table of (+/−, *+/246*) × (lymphoma, sarcoma) (Fisher's exact test): +/− versus *+/246*, p = 0.0725. Stats – (2×2) contingency table of (+/−, *+/246*) × (lymphoma, nonlymphoma) (Fisher's exact test): +/− versus *+/246*, p = 0.031. nd, not detected.

p53 status of the lymphoma cells will be $p53^{-/-}$ and $p53^{R246S/-}$ (Figure S4J). For MEFs, the level of p53 and p19ARF of primary and E1A/Ras-transformed MEFs were determined to ensure transformation was successful (Figure S4K). PCA analyses revealed that the lymphoma cells were distinctly separated from the normal primary B cells (Figure 6E). However, the p53 null and R246S mutant expressing samples were clustered together and not segregated, suggesting the global transcriptome profiles were almost identical. As shown in the volcano plots, the detailed ANOVA comparing p53 null and mutant cells also indicated most genes were not differentially expressed between these two genotypes (Figure S4L). Similar results were obtained using both primary and transformed MEFs, suggesting a lack of GOF properties of the R246S mutant (Figures 6F and S4M). To rule out the possibility that there may be a small collection of genes that may be differentially expressed because of the GOF of the R246S mutant, we determined the expression of genes showing the highest fold changes in the microarray study by qRT-PCR, which did not reveal any differences (Table S1B).

At the cellular level, the viability of $p53^{R246S/-}$ thymocytes was nearly identical to that of $p53^{-/-}$ thymocytes upon irradiation and lacked transactivation potential (Figures 3 and S1D). Moreover, $p53^{R246S/-}$ and $p53^{-/-}$ MEFs always respond similarly to all stresses tested (Figures 2 and 3), further suggesting a lack of GOF at cellular and biochemical levels. Given that the $p53^{R172H/-}$ MEFs have been shown to display GOF properties through the inhibition of its family members (Lang et al., 2004; Olive et al., 2004), we studied the effect on p73-mediated transactivation of target genes upon ectopic expression of p73 in $p53^{R246S/-}$ or $p53^{R172H/-}$ MEFs. Expression of *Mdm2* was much less induced by p73 in $p53^{R172H/-}$ cells compared to $p53^{R246S/-}$ MEFs (Figure S4N). Similarly, p73-mediated upregulation of *p21*-promoter luciferase activity was consistently reduced by the R175H but not the R249S mutant, the human equivalents of the mouse mutants examined here (Figure S4O), as previously shown (Gaiddon et al., 2001), suggesting that the R246S mutant p53 is not capable of efficiently inhibiting p73 activity. In order to confirm the lack of this inhibitory activity, we performed two additional experiments. First, we took advantage of the fact that taxol-induced cell death is highly p73-dependent (and not p53-dependent) (Toh et al., 2010) and compared sensitivity of $p53^{-/-}$, $p53^{R246S/-}$, and $p53^{R172H/-}$ MEFs to taxol. Both $p53^{-/-}$ and $p53^{R246S/-}$ MEFs were found to be equally sensitive to taxol treatment, whereas $p53^{R172H/-}$ MEFs were more resistant (percentage of cell death- $p53^{-/-}$ versus $p53^{R246S/-}$ versus $p53^{R172H/-}$: 23.67 or 20.0 versus 20.0 versus 12.0), although p73 induction was similar in all cells (Figure 6G). Next, we analyzed ras-induced cellular transformation, which was shown to be more efficient in $p53^{R172H/-}$ MEFs compared to p53 null cells (Lang et al., 2004). Expectedly, ras-mediated transformation was more efficient in $p53^{R172H/-}$, but not in $p53^{R246S/-}$ MEFs, compared to $p53^{-/-}$ MEFs, resulting in at least 2-fold more colonies in the former case (Figure S4P). Altogether, these data suggest that the inability of R246S mutant to inhibit p73 appears to be one reason for the lack of GOF.

Given that p53 mutants can also exhibit GOF through activation of novel target genes and promote cellular migration (Muller et al., 2009; Weisz et al., 2007, Yeudall et al., 2012), we further examined the effect of R246S mutant on cellular migration. Scratch assays indicated that although the $p53^{R172H/-}$ MEFs were able to close the wounded area fully by 12.5 hr, both $p53^{-/-}$ and $p53^{R246S/-}$ MEFs had only partially migrated (Figure 6H). Similarly, human H1299 cells stably expressing the R175H mutant (Vikhanskaya et al., 2007) were able to close

(C) Kaplan-Meier survival curves of $p53^{R246S/R246S}$ mice on various *Mdm2* genotypic backgrounds are shown.
(D) Western blot analysis of p53 protein levels in normal spleen and thymus (left), and the comparison of p53 levels and phosphorylation status of normal thymi and thymoma from $p53^{R246S/R246S}$ mice of different *Mdm2* genotypes (right) are shown.
(E and F) Transcriptome profiling of tissues/cells of various *p53* genotypes were performed by Affymetrix mouse exon array. Principal component analysis (PCA) is shown for normal and B lymphoma cells from *Eμ-Myc* transgenic mice (E) and for primary and E1A/Ras-transformed MEFs (F). Each data point represents one sample, and the ellipsoids represent the zone within two SD of an experimental group.
(G) Viability of E1A/Ras-transformed MEFs of various *p53* genotypes was determined 48 hr after 400 nM taxol treatment by Annexin v and PI staining (left panel). Respective sibling $p53^{-/-}$ MEFs from the R172H or R246S crosses were used as controls for each mutant-p53 expressing MEF line. Cellular lysates from parallel cultures were used after 24 hr treatment for western blot analysis of p53. p73 expression was determined by immunoprecipitation followed by immunoblotting (right panels). Cells transfected with *p73* was used as a positive control (+ve). Data represents mean ± SEM.
(H) MEFs from the indicated genotypes (top panel) and human H1299 cells stably expressing the indicated p53 mutants (lower panel) were used in wound-healing scratch assays, and photographs taken at 0 hr (at scratch) or the indicated time points thereafter are shown to determine extent of cellular migration. Real-time PCR analysis of mouse (m) *CXCL12* or human (h) *CXCL8* were determined in these cell lines. Data represents mean ± SEM.
See also Figure S4 and Table S1.

Table 2. *Mdm2*$^{-/-}$ Lethality Rescue: Offspring Analysis

$p53^{+/246}Mdm2^{+/-}$ Intercross		*p53* +/+	*+/246*	*246/246*
Mdm2	+/+	32	77	26
	+/−	78	170	52
	−/−	0	0	22

$p53^{+/R246S};Mdm2^{+/-}$ mice were intercrossed to generate mice of various *p53* and *Mdm2* genotypes. Mice were weaned at 3 weeks old, and genotypes were determined by PCR. Numbers in the table indicate number of offspring at 3 weeks of age.

the wounds by 20 hr, at which time the empty vector or R249S mutant p53-expressing counterparts had only partially closed the wounded area (Figure 6H, lower panel). Consistent with these effects, the expression of the chemokines *CXCL12* or *CXCL8*, shown to be novel targets of mutant p53 with GOF (Yeudall et al., 2012), were much more elevated in the $p53^{R172H/-}$ MEFs and R175H-expressing H1299 cells, respectively, compared to $p53^{R246S/-}$ MEFs and R249S-expressing H1299 cells. These results collectively demonstrate that the R246S p53 mutant, unlike the other hot spot R172H mutant, does not exhibit GOF properties in various cell types, both in the primary and transformed tissues, and even in the absence of Mdm2.

DISCUSSION

The data presented here demonstrate that the DN activity of mutant p53 is indeed operative in vivo. It is apparent after acute p53 activation and affects target gene transactivation and short-term biological outcomes, such as sensitivity to irradiation, in a cell-type-specific manner but does not affect long-term tumorigenesis. Importantly, it is dependent on the dose of the mutant p53, as hypomorphic mice expressing reduced levels of mutant p53 do not exhibit the DN effects. In addition, this study also highlights that the GOF properties of mutant p53 are not a universal phenomenon. It is specific to the mutation and cannot be induced by absence of Mdm2, demonstrating the differences in properties of even the common hot spot mutants found in human cancers. These data raise several interesting points that merit consideration.

First, the DN effect is seen in a cell-type-specific manner, as the biological outcome was affected in embryonic stem cells (Lee and Sabapathy, 2008), T and B lymphoid cells (referred to here as sensitive cell types) but not in Lin$^-$ progenitor cells and MEFs (referred to here as insensitive cell types). Interestingly, transactivation was also affected in the insensitive MEFs, indicating that in these cells, p53-mediated target gene transactivation alone may not be sufficient to determine biological outcome, as opposed to the sensitive cell types, in which the p53-dependent target gene activation may the dominant mechanism regulating cellular survival. These findings highlight that mutant p53 is capable of inhibiting the wild-type counterpart at the molecular and biochemical level, although the effect is not translated onto the cellular outcome in all cases. This further suggests that other cell-type-specific and cell fate regulating signaling pathways may be operating in conjunction with p53 pathway, and hence, the manifestation of DN effects on cellular outcome reflect the reliance of cells on the p53 pathway. Though the identity and nature of factors that discriminate between the cell-type specificity is at present unclear, it appears that the generally observed predisposition of a cell to p53 activation, such as cell-cycle arrest versus apoptosis, is not the determining factor. For example, E1A/Ras-transformed MEFs did not exhibit a DN effect and underwent cell death or cell-cycle arrest upon nutlin treatment and IR, respectively. Moreover, primary MEFs underwent cell-cycle arrest upon nutlin treatment, which induced apoptosis in their transformed counterparts, although a DN effect was not observed in both cases. The manifestation of the DN effect also appears to be independent of cellular "stemness" as the effects were observed in ES cells (Lee and Sabapathy, 2008) but not Lin^{-ve} hematopoietic progenitors, whereas mature splenic and peripheral lymphocytes displayed the effects.

Second, the DN effect is seen only after acute activation of p53, being able to negate radiosensitivity, but does not appear to contribute to long-term tumorigenesis after irradiation, thereby defining the perimeters for exhibition of the DN effect in vivo. This suggests that the transient activation of p53 activity, which regulates acute cellular survival, is the time point at which the DN effect is manifested, in contrast to baseline activity, which appears to be critical for prevention of tumor formation. The DN effect may therefore be important during therapeutic p53 activation phases, such as during chemo- or radiotherapy. Inducible p53 expression in mice has also supported the notion that p53 activity during acute DNA damage is not sufficient to prevent tumor formation (Christophorou et al., 2006; Junttila and Evan, 2009), emphasizing that the p53 burst in the acute phase of activation is neither relevant nor required for tumor suppressive properties. Supporting this conclusion, a recent study on familial cancer prone patients with different *p53* mutations revealed no differences in the distribution of the clinical subclasses in patients carrying a perceived DN or a severely defective nonfunctional (SD) *p53* allele, suggesting that haploinsufficiency, rather than a DN effect, is the major factor contributing to cancer predisposition (Monti et al., 2011). Interestingly, patients carrying these DN alleles tended to develop brain tumors in contrast to SD allele carriers, who were at a higher risk of developing breast cancers, suggesting tissue specificity of the DN effects in vivo (Monti et al., 2011), as noted in the study presented here.

Another salient point to emerge is that the DN effect is dependent on the dose of mutant p53 protein present in the cells. The DN effect was completely abolished in sensitive cell types in the hypomorphic strain used here, clearly demonstrating the requirement for sufficient levels of mutant p53 to inhibit wild-type p53 function. This is again consistent with the observation that the DN effect is generally seen upon acute p53 activation, when the p53 levels are elevated. While this manuscript was in preparation, Lozano and colleagues showed that reducing wild-type p53 levels in $p53^{+(Neo)/R172H}$ mice also led to the manifestation of DN effects in tissues and cell types that generally do not exhibit it (insensitive tissues) (Wang et al., 2011). For example, spontaneous tumor formation was affected by the presence of a weaker wild-type allele. These data provide proof of principle that DN can exist in vivo and are consistent with the fact that the ratio of mutant to wild-type p53 determines the

manifestation of DN effects in sensitive cells, as has also been implied from in vitro work (Chan et al., 2004). In addition, this also suggests that the different mutant p53's may have different properties, including different degrees of the DN effect in the same tissue.

The work presented here implies that the coexistence of mutant *p53* with the wild-type allele prior to LOH will have an impact during acute p53 activation, as shown with the case of radiosensitivity, and thus in cases of therapeutic treatment. Hence, mutant p53 may affect the outcome of treatment, likely leading to reduced or poor response and the eventual relapse of tumors. Though direct clinical evidence for this is unavailable, presence of mutant p53 has been correlated with poor prognosis after treatment (Robles and Harris, 2010). However, one could not be precisely sure if this was due to mutant p53's GOF in tumors that have lost the wild-type allele or to the DN effect of the mutant, as the early sequencing efforts would have not excluded the presence of stromal compartments in evaluating *p53* status (which would contain wild-type *p53* and therefore lead to contamination). We have not been able to directly test the hypothesis that mutant p53's DN effect is indeed contributory to poor response to therapy in mice, as LOH is predominant in tumors arising in the irradiation and the Myc-induced models (data not shown). Nonetheless, evidence from Lozano and colleagues indicate that although wild-type p53 activation in mutant p53-expressing tumors could arrest tumor growth, this is not as efficient as in the case in which mutant p53 is absent, suggesting that mutant p53's presence can indeed prevent complete functionality of wild-type p53 when activated (Wang et al., 2011). Thus, the existence of mutant p53 certainly has a negative impact on cellular survival and hence therapeutic efficacy, either through the DN effect or GOF.

The most convincing evidence by far supporting the existence of GOF in vivo are derived from the analysis of mutant p53 knockin mice harboring other hot spot mutants, such as R172H and R270H, which showed higher incidence of carcinoma and higher metastatic potential than the p53 null mice (Lang et al., 2004; Olive et al., 2004). GOF was attributed to the ability of the mutant p53 protein to inhibit its family members, p73 and p63. However, it is still unclear if GOF properties are universal for all major hot spot mutants and if there are any differences in the degree and spectrum of biological activities of GOF among different mutants. Here, we provide extensive evidence that a particular hot spot mutant may not exhibit GOF in multiple cell types and even when its levels are elevated because of Mdm2 deficiency, challenging the belief that elevated mutant p53 levels alone are sufficient for GOF of all mutants. The lack of GOF properties of the R246S mutant p53 is consistent with its lack of ability to inhibit p73 (this report and Gaiddon et al., 2001), supporting the notion that inhibition of p73 is one mechanism by which GOF is manifested, and highlights the importance of our knockin model in understanding human cancers. Moreover, our data also imply the presence of other negative regulators of p53 abundance, which could be deactivated in the tumor context, leading to further stabilization.

In conclusion, mutant p53 is shown here to have DN effects in a cell-type and dose-dependent manner, especially during acute p53 activation, and hence highlights the need for consideration during cancer therapy. Furthermore, GOF properties appear not to be a universal phenomenon for all hot spot p53 mutants.

EXPERIMENTAL PROCEDURES

Generation and Breeding of $p53^{+/R246S}$ Knockin Mice

The targeting construct, screening strategy, targeted mouse generation, and genotyping methodology have been previously described (Lee and Sabapathy, 2008; Lee et al., 2011). All animal experiments were approved by and performed in accordance with the guidelines of the Singhealth's Animal Care and Use Committee.

Cell Culture and Biochemical Analysis

Details of cell/tissue isolation, culture and treatment, cell-cycle and cell death analysis, immunoblotting, flow cytometric, and quantitative real-time PCR analysis are described in detail in the Supplemental Experimental Procedures.

Statistical Analysis

ANOVA was used to determine statistical significance in all experiments, except cancer formation cohorts. Fisher's exact test was used to analyze the difference in incidences of different types of tumor. For cancer formation cohorts, the "Log-rank (Mantel-Cox) test" was used.

ACCESSION NUMBERS

The microarray data reported in this paper have been deposited in the Gene Expression Omnibus (GEO) database (http://www.ncbi.nlm.nih.gov/geo). The accession number is GSE40417.

SUPPLEMENTAL INFORMATION

Supplemental Information includes four figures, one table, and Supplemental Experimental Procedures and can be found with this article online at http://dx.doi.org/10.1016/j.ccr.2012.10.022.

ACKNOWLEDGMENTS

We thank Dr. Deepa Subramanian for assistance in the revision stages, Dr. Geoff Wahl for constructive comments, and Dr. David Lane for the $p53^{R172H/-}$ MEFs. W.M.T. is supported in part by the Natural Sciences Foundation of China (30970602) and 111 Project (B08007). This work was supported by grants from the National Medical Research Council of Singapore and the Singapore Millennium Foundation to K.S. and L.M.K. L.M.K. designed the experiments, performed the research work, analyzed the data, and helped with writing of the manuscript. T.W.W. performed the microarray-related work. P.B.H. performed the experiments with human p53 mutants. W.M.T. and Z.Q.W. helped with ES cell targeting and generation of the chimeric mice. K.S. designed the experiments, analyzed the data, and wrote the manuscript.

Received: May 28, 2011
Revised: January 27, 2012
Accepted: October 28, 2012
Published: December 10, 2012

REFERENCES

Bossi, G., Lapi, E., Strano, S., Rinaldo, C., Blandino, G., and Sacchi, A. (2006). Mutant p53 gain of function: reduction of tumor malignancy of human cancer cell lines through abrogation of mutant p53 expression. Oncogene *25*, 304–309.

Brosh, R., and Rotter, V. (2009). When mutants gain new powers: news from the mutant p53 field. Nat. Rev. Cancer *9*, 701–713.

Chan, W.M., Siu, W.Y., Lau, A., and Poon, R.Y. (2004). How many mutant p53 molecules are needed to inactivate a tetramer? Mol. Cell. Biol. *24*, 3536–3551.

Christophorou, M.A., Ringshausen, I., Finch, A.J., Swigart, L.B., and Evan, G.I. (2006). The pathological response to DNA damage does not contribute to p53-mediated tumour suppression. Nature *443*, 214–217.

Gaiddon, C., Lokshin, M., Ahn, J., Zhang, T., and Prives, C. (2001). A subset of tumor-derived mutant forms of p53 down-regulate p63 and p73 through a direct interaction with the p53 core domain. Mol. Cell. Biol. *21*, 1874–1887.

Jackson, E.L., Olive, K.P., Tuveson, D.A., Bronson, R., Crowley, D., Brown, M., and Jacks, T. (2005). The differential effects of mutant p53 alleles on advanced murine lung cancer. Cancer Res. *65*, 10280–10288.

Jones, S.N., Roe, A.E., Donehower, L.A., and Bradley, A. (1995). Rescue of embryonic lethality in Mdm2-deficient mice by absence of p53. Nature *378*, 206–208.

Junttila, M.R., and Evan, G.I. (2009). p53—a Jack of all trades but master of none. Nat. Rev. Cancer *9*, 821–829.

Kemp, C.J., Wheldon, T., and Balmain, A. (1994). p53-deficient mice are extremely susceptible to radiation-induced tumorigenesis. Nat. Genet. *8*, 66–69.

Kern, S.E., Pietenpol, J.A., Thiagalingam, S., Seymour, A., Kinzler, K.W., and Vogelstein, B. (1992). Oncogenic forms of p53 inhibit p53-regulated gene expression. Science *256*, 827–830.

Lang, G.A., Iwakuma, T., Suh, Y.A., Liu, G., Rao, V.A., Parant, J.M., Valentin-Vega, Y.A., Terzian, T., Caldwell, L.C., Strong, L.C., et al. (2004). Gain of function of a p53 hot spot mutation in a mouse model of Li-Fraumeni syndrome. Cell *119*, 861–872.

Lee, M.K., and Sabapathy, K. (2008). The R246S hot-spot p53 mutant exerts dominant-negative effects in embryonic stem cells in vitro and in vivo. J. Cell Sci. *121*, 1899–1906.

Lee, M.K., Tong, W.M., Wang, Z.Q., and Sabapathy, K. (2011). Serine 312 phosphorylation is dispensable for wild-type p53 functions in vivo. Cell Death Differ. *18*, 214–221.

Levine, A.J., Momand, J., and Finlay, C.A. (1991). The p53 tumour suppressor gene. Nature *351*, 453–456.

Lowe, S.W., Ruley, H.E., Jacks, T., and Housman, D.E. (1993). p53-dependent apoptosis modulates the cytotoxicity of anticancer agents. Cell *74*, 957–967.

Milner, J., and Medcalf, E.A. (1991). Cotranslation of activated mutant p53 with wild type drives the wild-type p53 protein into the mutant conformation. Cell *65*, 765–774.

Monti, P., Perfumo, C., Bisio, A., Ciribilli, Y., Menichini, P., Russo, D., Umbach, D.M., Resnick, M.A., Inga, A., and Fronza, G. (2011). Dominant-negative features of mutant TP53 in germline carriers have limited impact on cancer outcomes. Mol. Cancer Res. *9*, 271–279.

Morton, J.P., Timpson, P., Karim, S.A., Ridgway, R.A., Athineos, D., Doyle, B., Jamieson, N.B., Oien, K.A., Lowy, A.M., Brunton, V.G., et al. (2010). Mutant p53 drives metastasis and overcomes growth arrest/senescence in pancreatic cancer. Proc. Natl. Acad. Sci. USA *107*, 246–251.

Muller, P.A., Caswell, P.T., Doyle, B., Iwanicki, M.P., Tan, E.H., Karim, S., Lukashchuk, N., Gillespie, D.A., Ludwig, R.L., Gosselin, P., et al. (2009). Mutant p53 drives invasion by promoting integrin recycling. Cell *139*, 1327–1341.

O'Shea, D., O'Riain, C., Taylor, C., Waters, R., Carlotti, E., Macdougall, F., Gribben, J., Rosenwald, A., Ott, G., Rimsza, L.M., et al. (2008). The presence of TP53 mutation at diagnosis of follicular lymphoma identifies a high-risk group of patients with shortened time to disease progression and poorer overall survival. Blood *112*, 3126–3129.

Olive, K.P., Tuveson, D.A., Ruhe, Z.C., Yin, B., Willis, N.A., Bronson, R.T., Crowley, D., and Jacks, T. (2004). Mutant p53 gain of function in two mouse models of Li-Fraumeni syndrome. Cell *119*, 847–860.

Olivier, M., Hollstein, M., and Hainaut, P. (2010). TP53 mutations in human cancers: origins, consequences, and clinical use. Cold Spring Harb. Perspect. Biol. *2*, a001008.

Oren, M., and Rotter, V. (2010). Mutant p53 gain-of-function in cancer. Cold Spring Harb. Perspect. Biol. *2*, a001107.

Palmero, E.I., Achatz, M.I., Ashton-Prolla, P., Olivier, M., and Hainaut, P. (2010). Tumor protein 53 mutations and inherited cancer: beyond Li-Fraumeni syndrome. Curr. Opin. Oncol. *22*, 64–69.

Petitjean, A., Mathe, E., Kato, S., Ishioka, C., Tavtigian, S.V., Hainaut, P., and Olivier, M. (2007). Impact of mutant p53 functional properties on TP53 mutation patterns and tumor phenotype: lessons from recent developments in the IARC TP53 database. Hum. Mutat. *28*, 622–629.

Robles, A.I., and Harris, C.C. (2010). Clinical outcomes and correlates of TP53 mutations and cancer. Cold Spring Harb. Perspect. Biol. *2*, a001016.

Schmitt, C.A., McCurrach, M.E., de Stanchina, E., Wallace-Brodeur, R.R., and Lowe, S.W. (1999). INK4a/ARF mutations accelerate lymphomagenesis and promote chemoresistance by disabling p53. Genes Dev. *13*, 2670–2677.

Terzian, T., Suh, Y.A., Iwakuma, T., Post, S.M., Neumann, M., Lang, G.A., Van Pelt, C.S., and Lozano, G. (2008). The inherent instability of mutant p53 is alleviated by Mdm2 or p16INK4a loss. Genes Dev. *22*, 1337–1344.

Toh, W.H., Nam, S.Y., and Sabapathy, K. (2010). An essential role for p73 in regulating mitotic cell death. Cell Death Differ. *17*, 787–800.

Varley, J.M., Evans, D.G., and Birch, J.M. (1997). Li-Fraumeni syndrome—a molecular and clinical review. Br. J. Cancer *76*, 1–14.

Vassilev, L.T., Vu, B.T., Graves, B., Carvajal, D., Podlaski, F., Filipovic, Z., Kong, N., Kammlott, U., Lukacs, C., Klein, C., et al. (2004). In vivo activation of the p53 pathway by small-molecule antagonists of MDM2. Science *303*, 844–848.

Vikhanskaya, F., Lee, M.K., Mazzoletti, M., Broggini, M., and Sabapathy, K. (2007). Cancer-derived p53 mutants suppress p53-target gene expression—potential mechanism for gain of function of mutant p53. Nucleic Acids Res. *35*, 2093–2104.

Wang, Y., Suh, Y.A., Fuller, M.Y., Jackson, J.G., Xiong, S., Terzian, T., Quintás-Cardama, A., Bankson, J.A., El-Naggar, A.K., and Lozano, G. (2011). Restoring expression of wild-type p53 suppresses tumor growth but does not cause tumor regression in mice with a p53 missense mutation. J. Clin. Invest. *121*, 893–904.

Weisz, L., Oren, M., and Rotter, V. (2007). Transcription regulation by mutant p53. Oncogene *26*, 2202–2211.

Wijnhoven, S.W., Zwart, E., Speksnijder, E.N., Beems, R.B., Olive, K.P., Tuveson, D.A., Jonkers, J., Schaap, M.M., van den Berg, J., Jacks, T., et al. (2005). Mice expressing a mammary gland-specific R270H mutation in the p53 tumor suppressor gene mimic human breast cancer development. Cancer Res. *65*, 8166–8173.

Wijnhoven, S.W., Speksnijder, E.N., Liu, X., Zwart, E., vanOostrom, C.T., Beems, R.B., Hoogervorst, E.M., Schaap, M.M., Attardi, L.D., Jacks, T., et al. (2007). Dominant-negative but not gain-of-function effects of a p53.R270H mutation in mouse epithelium tissue after DNA damage. Cancer Res. *67*, 4648–4656.

Yeudall, W.A., Vaughan, C.A., Miyazaki, H., Ramamoorthy, M., Choi, M.Y., Chapman, C.G., Wang, H., Black, E., Bulysheva, A.A., Deb, S.P., et al. (2012). Gain-of-function mutant p53 upregulates CXC chemokines and enhances cell migration. Carcinogenesis *33*, 442–451.

Zilfou, J.T., and Lowe, S.W. (2009). Tumor suppressive functions of p53. Cold Spring Harb. Perspect. Biol. *1*, a001883.

Cancer Cell
Article

JAK2/STAT5 Inhibition Circumvents Resistance to PI3K/mTOR Blockade: A Rationale for Cotargeting These Pathways in Metastatic Breast Cancer

Adrian Britschgi,[1] Rita Andraos,[2] Heike Brinkhaus,[1] Ina Klebba,[1] Vincent Romanet,[2] Urs Müller,[1] Masato Murakami,[2] Thomas Radimerski,[2] and Mohamed Bentires-Alj[1,*]
[1]Friedrich Miescher Institute for Biomedical Research, Basel, CH-4058, Switzerland
[2]Novartis Institutes for Biomedical Research, Disease Area Oncology, Basel, CH-4057, Switzerland
*Correspondence: bentires@fmi.ch
http://dx.doi.org/10.1016/j.ccr.2012.10.023

SUMMARY

Hyperactive PI3K/mTOR signaling is prevalent in human malignancies and its inhibition has potent antitumor consequences. Unfortunately, single-agent targeted cancer therapy is usually short-lived. We have discovered a JAK2/STAT5-evoked positive feedback loop that dampens the efficacy of PI3K/mTOR inhibition. Mechanistically, PI3K/mTOR inhibition increased IRS1-dependent activation of JAK2/STAT5 and secretion of IL-8 in several cell lines and primary breast tumors. Genetic or pharmacological inhibition of JAK2 abrogated this feedback loop and combined PI3K/mTOR and JAK2 inhibition synergistically reduced cancer cell number and tumor growth, decreased tumor seeding and metastasis, and also increased overall survival of the animals. Our results provide a rationale for combined targeting of the PI3K/mTOR and JAK2/STAT5 pathways in triple-negative breast cancer, a particularly aggressive and currently incurable disease.

INTRODUCTION

Detailed understanding of the genetic abnormalities that drive subsets of cancer has led to the development of highly specific inhibitors targeting key oncogenic pathways. The clinical efficacy and low toxicity of some of these mechanism-based therapies raised hopes for a new era in the treatment of cancer (Haber et al., 2011; Sellers, 2011). This is illustrated by several therapeutic successes, including imatinib in chronic myelogenous leukemia carrying the *BCR-ABL* fusion gene (O'Brien et al., 2003), and targeting V600E mutant B-RAF in metastatic melanoma (Flaherty et al., 2010). At the same time, it became evident that genetic and adaptive resistance are major obstacles in translating therapeutic efficacy into curative cancer therapy due to the evolutionary nature of cancer and the instable genome of some cancers. A thorough understanding of the "wiring diagram" of cancer cells and the mechanisms of resistance to targeted therapy is of paramount importance for designing multidrug combinations (Haber et al., 2011; Sellers, 2011).

The phosphatidylinositol 3-kinase (PI3K) signaling axis is vital for cell metabolism, proliferation, survival, and motility (Engelman et al., 2006). Class I PI3Ks phosphorylate phosphatidylinositol-4,5-bisphosphate and generate phosphatidylinositol-3,4,5-trisphosphate downstream of growth factor receptors and G protein-coupled receptors. This leads to activation of several kinases, including protein kinase B (PKB/AKT), mammalian target of rapamycin (mTOR), and p70 ribosomal protein S6 kinase (S6K) (Engelman et al., 2006). Studies in *Drosophila melanogaster* and in mammalian cells have revealed a PI3K regulatory negative feedback in which activation of S6K dampens IGF1-receptor (IGF-1R)/PI3K signaling via suppression of IRS1 (Harrington et al., 2004; Haruta et al., 2000; Radimerski et al., 2002).

The PI3K signaling cascade is one of the most frequently hyperactivated pathways in human cancer (Samuels et al., 2004). Not surprisingly, different classes of PI3K, AKT, and mTOR inhibitors have been developed and 26 compounds are presently in clinical trials (Engelman, 2009; Sheppard et al., 2012). Early results show limited efficacy of allosteric mTOR complex 1

Significance

The PI3K/mTOR pathway is very often subverted during tumorigenesis and contributes to numerous hallmarks of cancer. Twenty-six inhibitors of this pathway are currently in clinical trials. Using various cell lines and primary tumor models of triple-negative breast cancer, we have discovered that PI3K/mTOR inhibition elicits a positive feedback loop by activating JAK2/STAT5. This induces secretion of the pro-metastatic cytokine IL-8, which in turn feeds back into JAK2/STAT5, thereby completing the loop. Notably, inhibition of JAK2 abrogated this feedback, reduced tumor seeding and metastasis and increased overall survival of the animals. These data suggest IL-8 as a predictor of the efficacy of PI3K/mTOR inhibition and provide a rationale for combined inhibition of the PI3K/mTOR and JAK2/STAT5 pathways in triple-negative breast cancer.

(mTORC1) inhibition, most likely because it abrogates S6K-mediated negative feedback, leading to reactivation of PI3K/AKT signaling (O'Reilly et al., 2006). Similarly, allosteric AKT inhibition reactivates several RTKs that attenuate the beneficial effect of the inhibitor (Chandarlapaty et al., 2011). These studies stress the urgent need to identify mechanisms of resistance to PI3K pathway inhibition in order to rationally design optimal drug combinations.

The Janus family of kinases (JAKs) and their associated signal transducers and activators of transcription (STATs) also play a key role in cancer. Activation of JAKs/STATs stimulates cell proliferation, differentiation, migration, and survival (Harry et al., 2012). The JAK/STAT pathway is activated upon binding of hormones and cytokines (e.g., prolactin and interleukins) to their receptors. In neoplasia, the ligands are secreted by cancer cells and/or by cells from the tumor microenvironment (Bissell and Radisky, 2001). JAKs/STATs can also be activated by gain-of-function mutations like the JAK2 V617F mutation in myeloproliferative neoplasms, for which JAK2 inhibitors have shown promising activity (Harrison et al., 2012).

Given the many inhibitors of the PI3K pathway currently being evaluated, we sought to understand the effects of inhibiting this pathway on signaling in order to anticipate potential mechanisms of resistance. We assessed the effects of PI3K/mTOR inhibition in triple-negative breast cancer (TNBC), which is characterized by the absence of expression of estrogen and progesterone as well as ERBB2/HER2 receptors, is associated with a dismal prognosis, and still lacks effective targeted therapies (Hudis and Gianni, 2011).

RESULTS

PI3K/mTOR Inhibition Activates JAK2/STAT5

As PI3K/mTOR is a crucial oncogenic signaling node, its inhibition would be expected to activate compensatory mechanisms. To test this, we assessed the effects of inhibiting the PI3K/mTOR pathway in PTEN-deficient MDA-MB468 (MDA468) and RAS-mutated MDA-MB231 LM2 (MDA231 LM2) human breast cancer cells and in the mouse breast cancer line 4T-1. Single doses of BEZ235, a dual PI3K/mTOR inhibitor currently in clinical trials (Maira et al., 2008; Serra et al., 2008), were applied and the phosphorylation levels of several signaling proteins measured. BEZ235 reduced pAKT and completely blocked pS6 levels up to 20 hr in vitro and in vivo (Figure 1A; Figure S1A available online). Surprisingly, we also detected considerable upregulation of pJAK2 and pSTAT5, but not consistently of pSTAT3, after BEZ235 treatment (Figures 1A and S1A).

To elucidate which arm of the dual PI3K/mTOR inhibitor BEZ235 was responsible for the observed crosstalk to JAK2/STAT5, we applied the pan-PI3K inhibitor BKM120 and the mTORC1 inhibitor RAD001. Individual inhibition of either PI3K and mTORC1 upregulated pJAK2 and pSTAT5. Notably, although RAD001 readily activated JAK2/STAT5 after 4 hr treatment, BKM120 induced JAK2/STAT5 only after 8 hr (Figure S1B).

Both JAK1 and JAK2 signal to STAT5 and STAT3 depending on cell type and the receptor with which they are associated (Desrivières et al., 2006). Thus, we examined whether JAK1 and/or JAK2 are responsible for STAT5 activation upon PI3K/mTOR inhibition. siRNA depletion of each JAK isoform revealed that JAK2 activates STAT5 while JAK1 is upstream of STAT3 in our models (Figure 1B). Furthermore, siRNA depletion and inhibition of JAK2 by the JAK2-specific inhibitor NVP-BSK805 (Baffert et al., 2010) both counteracted the BEZ235-mediated upregulation of pSTAT5 (Figure 1C). As found in other models (Andraos et al., 2012), JAK2 inhibition by NVP-BSK805 efficiently blocked phosphorylation of STAT5 but did not reduce phosphorylation of JAK2.

Combined PI3K/mTOR and JAK2 Inhibition Induces Cell Death

Notably, we observed rapid recovery of pAKT after treatment with BEZ235 in all models, whereas pS6 remained inhibited (Figures 1A and S1A). We found that PHLPP, the phosphatase that targets Ser473 of AKT (Gao et al., 2005), was downregulated after 8 hr of BEZ235 treatment (Figure S2A). In addition, mTORC2 inhibition by siRNA-mediated depletion of RICTOR combined with BEZ235 treatment prevented the recovery of pAKT Ser473 (Figure S2B). As JAK2 is known to activate PI3K (Jin et al., 2008; Yamauchi et al., 1998), it was conceivable that BEZ235-induced JAK2 activation contributed to AKT reactivation. To test this, we examined whether combined inhibition of JAK2 and PI3K/mTOR prolongs inhibition of pAKT. Indeed, although blocking JAK2 alone did not impact on pAKT levels, the combination of BEZ235 and NVP-BSK805 prolonged pAKT suppression (Figure 2A).

To determine effects of blocking JAK2/STAT5 signaling on cell viability, we treated breast cancer lines with NVP-BSK805 or BEZ235 alone or in combination at concentrations that inhibit their respective targets. Although NVP-BSK805 alone had no impact on cell viability, it significantly decreased the number of living cells when combined with BEZ235. Combination of NVP-BSK805 and BEZ235 also significantly reduced colony formation capacity compared with DMSO or the single drug treatments (Figure 2B). Similar results were obtained with combinations of a doxycycline-inducible shRNA against JAK2 or siRNA-mediated depletion of STAT5A and B and BEZ235 treatment (Figure S2C).

To assess effects on cell death, we performed FACS analysis of propidium iodide- and/or AnnexinV-stained cells (Figures 2C, left panel, and S2D). Addition of NVP-BSK805 to BEZ235-treated cells resulted in a 25%–41% decrease in cells in S-phase and an ~1.8-fold increase in cells in sub-G1 (Figure S2D). Interestingly, cell death was not induced by individual treatments but increased significantly after combined inhibition of PI3K/mTOR and JAK2/STAT5 (Figure 2C, left panel). Immunoblotting revealed upregulation and increased electrophoretic mobility of the BH3-only protein BIM and, thus, its activation following treatment with NVP-BSK805 alone or in combination with BEZ235 (Figure 2C, right panel). Because BIM is inhibited by ERK1/2 (Ley et al., 2003), we assessed ERK1/2 phosphorylation levels in cells treated with BEZ235 and/or NVP-BSK805 but found no consistent changes in pERK1/2 (Figure S2E). It was reported previously that activation of BIM and downregulation of the pro-survival BCL2-family member MCL1 are both required for induction of cell death (Certo et al., 2006). In line with this, immunoblotting showed degradation of MCL1 only in cells treated with both BEZ235 and NVP-BSK805 (Figure 2C, right panel). Consistently, we found an increase in cleaved PARP only after combined BEZ235/NVP-BSK805 treatment (Figure 2C, right panel).

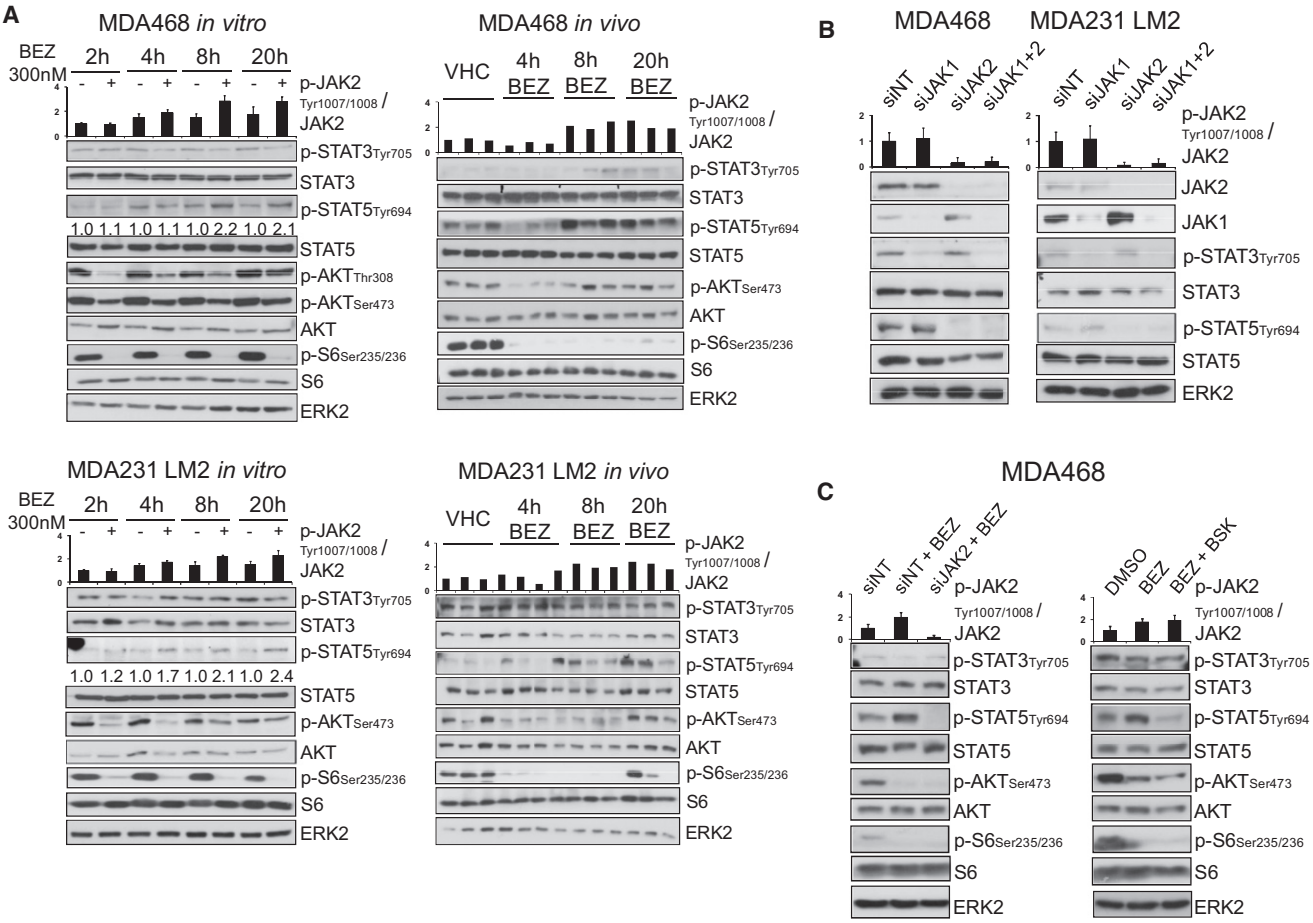

Figure 1. Dual PI3K/mTOR Inhibition by BEZ235 Activates JAK2/STAT5

(A) Immunoblots of lysates from breast cancer cells grown as monolayer cultures or as xenografts and treated with BEZ235 (BEZ). Mice bearing xenografts were treated with vehicle (VHC) or 30 mg/kg BEZ and dissected as indicated. The numbers indicate the ratios of pSTAT5/STAT5 as measured by densitometry. pJAK2 levels were measured in triplicate by ELISA and normalized to total JAK2 levels (y axis). ERK2 levels were used as a loading control.

(B) Immunoblots of lysates from breast cancer cells in which JAK2 and/or JAK1 were depleted by siRNA (siJAK). siNT, nontargeting control siRNA.

(C) Immunoblots of lysates from 8 hr BEZ-treated MDA468 cells in which JAK2/STAT5 signaling was blocked by JAK2 siRNA (left panel) or by the JAK2-specific inhibitor NVP-BSK805 (BSK) (right panel). ELISA data are means ± SD (n = 3).

See also Figure S1.

Given the involvement of the PI3K/AKT pathway in the regulation of several BH3-only proteins (Parcellier et al., 2008), we assessed the levels and activation states of BAD, BCL2, and BCL-XL. Both BCL2 and BCL-XL declined upon JAK2 inhibition or the combination treatment, whereas inactive pBAD decreased following PI3K/mTOR inhibition or the combination treatment (Figure 2C, right panel). These data indicate a pivotal involvement of decreased MCL1 in cell death induction by the combination of BEZ235 and NVP-BSK805.

Dual PI3K/mTOR Inhibition Triggers Secretion of IL-8

To determine whether the observed activation of JAK2/STAT5 upon BEZ235 treatment occurs via secretion of a soluble factor, we collected conditioned medium from cells treated for 20 hr with BEZ235, applied this to untreated cells, and lysed them 1 hr later. Medium supplemented with BEZ235 was used as a control. pJAK2 and pSTAT5 were both upregulated upon incubation with the conditioned medium compared with the control treatments, suggesting that a soluble factor mediated activation of JAK2/STAT5 (Figure 3A).

As JAKs are crucial transducers of cytokine signaling, we analyzed cytokine profiles after BEZ235 treatment, either in supernatants of cultured cells or lysates of tumor xenografts. Considerable changes in several cytokines were found, the most consistent being upregulation of IL-8 (Figure 3B).

To gain further insight into the kinetics of this response, we performed ELISA for IL-8 on supernatants of cells treated with BEZ235 (Figure 3C, left). A significant increase in IL-8 secretion was found after 20 hr of treatment. This secretion pattern was mirrored by upregulation of IL-8 mRNA, which suggested transcriptional regulation of the cytokine (Figure 3C, right).

To determine whether secreted IL-8 activated JAK2/STAT5 in breast cancer cells, we assessed whether these cells express its cognate receptors, CXCR1 and CXCR2. There was a 2.8- to 3-fold higher expression of CXCR1 than CXCR2 on both MDA468 and MDA231 LM2 cells (Figure S3A). Stimulation with cytokines

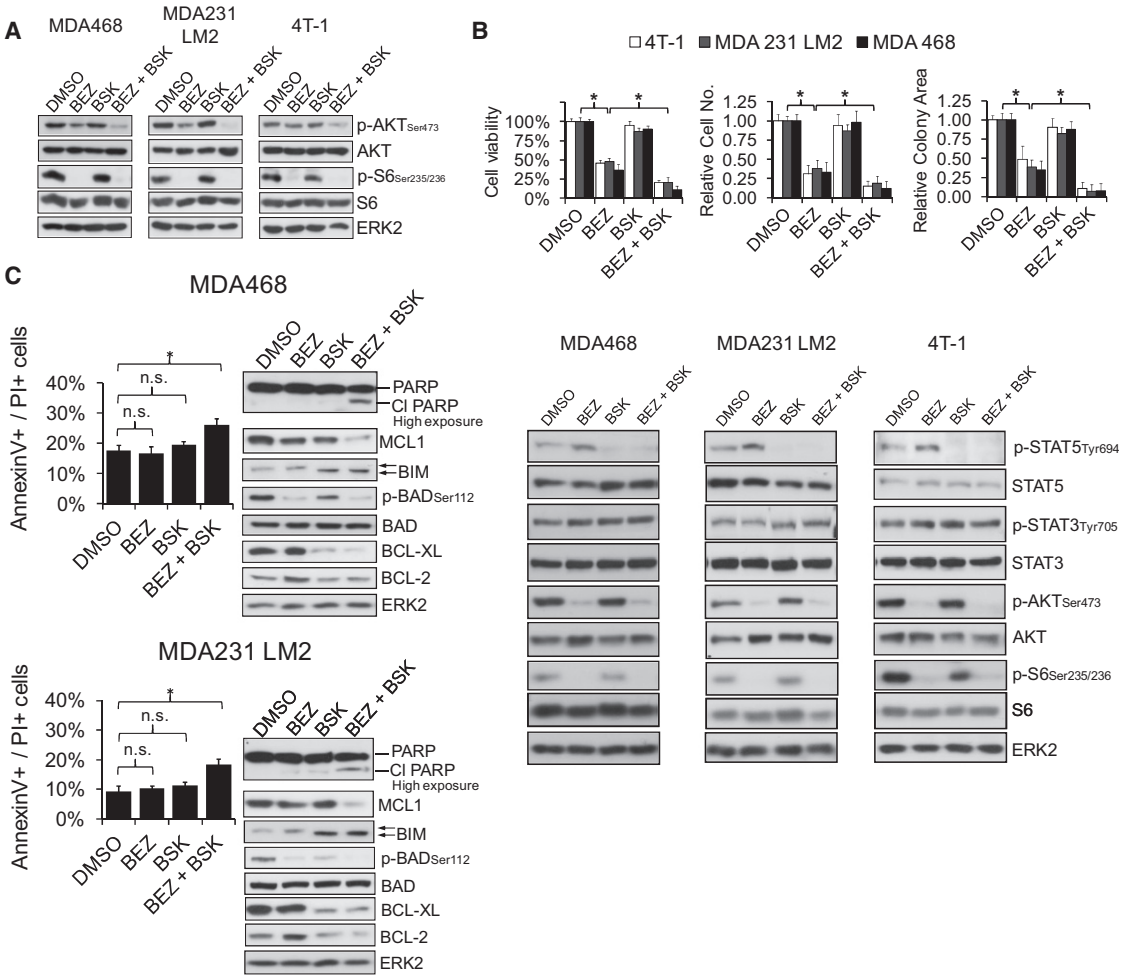

Figure 2. Cotargeting PI3K/mTOR and JAK2 Reduces Cell Viability

(A) Immunoblots of lysates of breast cancer cells after 20 hr of treatment with BEZ or BSK alone or in combination. DMSO, lysates of cells treated with 0.005% DMSO for 20 hr.

(B) Bar graphs showing the mean percentage of cell viability measured by the WST-1 assay (upper left) and by Trypan Blue cell counts (upper middle) of cell lines grown under 0.5% serum and treated with 300 nM BEZ and/or 350 nM BSK for 72 hr. Bar graph representing colony formation frequencies of cells treated as indicated (upper right). Immunoblots of lysates from the same cell lines after 8 hr of treatment as indicated are shown in the lower panel. Data are means ± SEM (n = 4, *p < 0.05).

(C) Bar graphs showing the mean percentage of apoptotic and dead cells after 48 hr of treatment as measured by FACS analysis of AnnexinV and PI stained cells treated with 300 nM BEZ and/or 350 nM BSK as indicated (left panel). Immunoblots of lysates from cells treated with 300 nM BEZ and/or 350 nM BSK for 24 hr (right panel). Data are means ± SEM (n = 5, *p < 0.05).

See also Figure S2.

known to activate JAK2/STAT5 in different cellular settings revealed strong activation of JAK2/STAT5 by IL-8 (Figure S3B).

Chemotherapy can induce senescence-associated secretion of cytokines, including IL-8 (Rodier and Campisi, 2011). We tested whether BEZ235 induces senescence by treating cells with the inhibitor for 5 days and then stained for β-galactosidase activity. We found that BEZ235 did not induce senescence in breast cancer cell lines (Figure S3C).

Activation of JAK2/STAT5/IL-8 Is Frequent in BEZ235-Insensitive TNBC Models

To assess the generality of our findings, we treated a panel of 18 breast cancer lines with BEZ235 and measured JAK2/STAT5 activation and IL-8 secretion. TNBC lines showed a higher baseline of pJAK2 and pSTAT5 than luminal cell lines and enhanced secretion of IL-8. Importantly, pJAK2, pSTAT5, and/or IL-8 secretion increased in 11 of the 18 lines upon BEZ235 treatment. Notably, the significant correlation found between BEZ235-triggered activation of JAK2 and IL-8 secretion strongly supports the generality of the crosstalk demonstrated between PI3K/mTOR and JAK2/STAT5/IL-8 in TNBC (Figure 3D; Table S1).

Our data suggested that activation of JAK2/STAT5 counteracts BEZ235-mediated reduction in cell viability (see Figures 2B and S2D). Therefore, we asked whether the upregulation of JAK2/STAT5/IL-8 upon BEZ235 treatment is correlated with

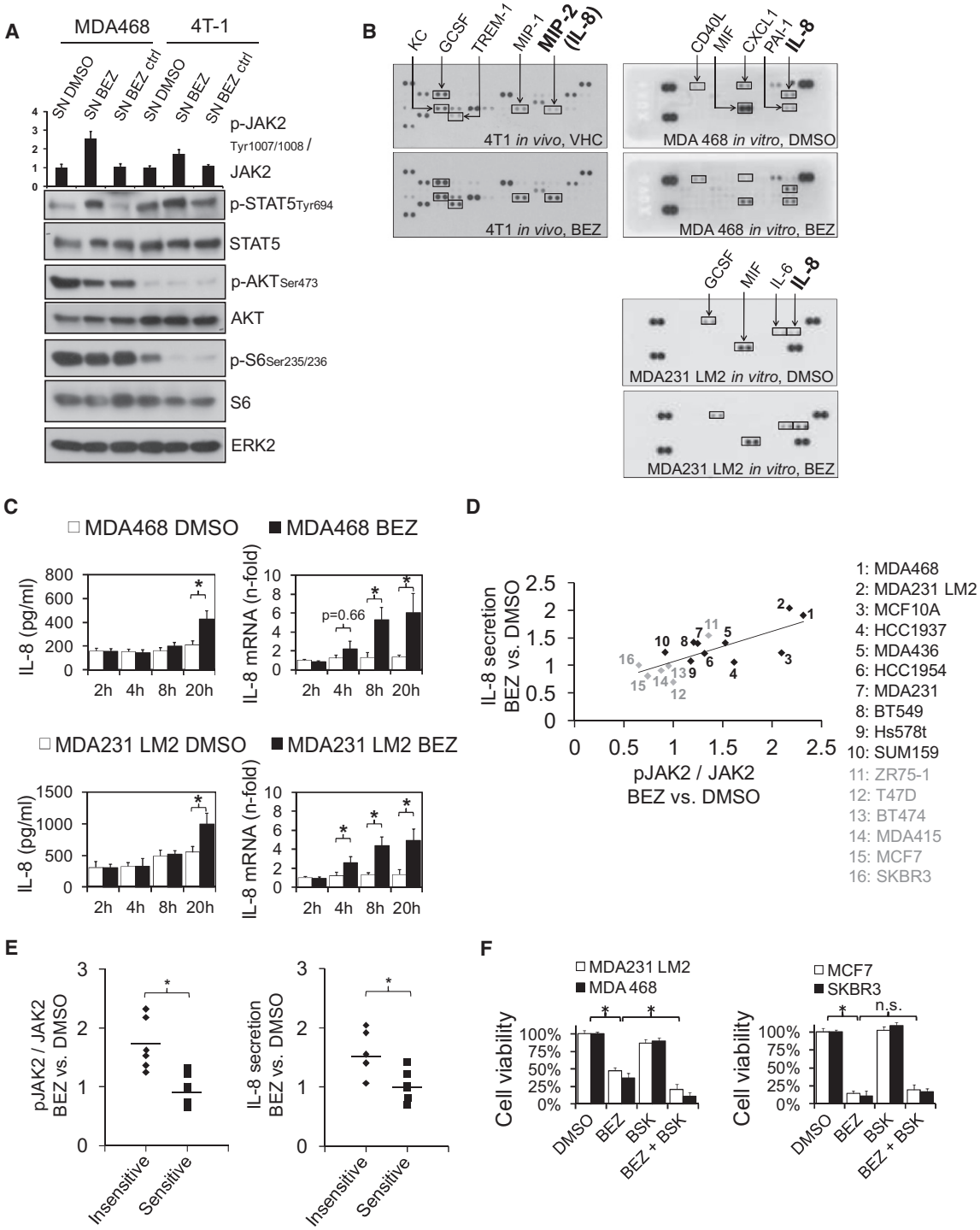

Figure 3. Dual PI3K/mTOR Inhibition Induces IL-8 Secretion in BEZ235-Insensitive Breast Cancer Cells

(A) Immunoblots of lysates from cells treated for 1 hr with conditioned media from cells treated with 300 nM BEZ for 20 hr. Lysates of cells treated with medium containing BEZ (SN BEZ ctrl) were used as a control for the BEZ present in the conditioned media. ELISA data are means ± SD (n = 3).

(B) Cytokine arrays showing expression of the indicated cytokines in supernatants of cells treated with 300 nM BEZ for 24 hr (upper panel) or in tumors from mice treated with 30 mg/kg BEZ for 10 days (lower panel). Mouse MIP2 is the functional homolog of human IL-8.

(C) Bar graphs showing the levels of IL-8 secretion (left panel) and mRNA (right panel) in cells treated with 300 nM BEZ as indicated. Levels of IL-8 were measured by ELISA and RT-qPCR and are shown as means ± SEM (n = 4, *p < 0.05).

(D) Scatter plot showing correlation in breast cancer lines between IL-8 secretion and the ratios of pJAK2/JAK2 upon BEZ treatment for 20 hr and 8 hr, respectively. Grey: luminal-like lines. Black: TNBC lines. Values from BEZ-treated relative to DMSO cells are shown (see also Table S1). Data are means of three independent experiments (n = 16, correlation = 0.77, p = 0.0006).

the sensitivity of cell lines to this inhibitor. Comparison of pJAK2 and IL-8 levels in 12 breast cancer cell lines to their reported sensitivity to BEZ235 (Brachmann et al., 2009) revealed higher activation of JAK2 and upregulation of IL-8 in BEZ235-insensitive than in sensitive lines (Figure 3E). Combined inhibition of PI3K/mTOR and JAK2 reduced the viability of BEZ235-insensitive lines further, underscoring the relevance of the crosstalk between the PI3K and JAK2/STAT5 pathways for the response to PI3K/mTOR inhibition (Figure 3F).

Biphasic Activation of JAK2/STAT5 upon PI3K/mTOR Inhibition

To test whether IL-8 is necessary and sufficient for activation of JAK2/STAT5, we blocked CXCR1, and thus IL-8 signaling, at different time points after BEZ235 treatment using a CXCR1-neutralizing antibody. As predicted, blocking CXCR1 reduced pFAK (Figure S4A) (Ginestier et al., 2010). More importantly, CXCR1 inhibition efficiently blocked the induction of pJAK2/pSTAT5 after 20 hr of BEZ235 treatment but, surprisingly, failed to prevent activation after only 8 hr (Figure 4A). Furthermore, we found that depletion of CXCR1 by siRNA did not affect BEZ235-induced upregulation of pJAK2/pSTAT5 after 8 hr of treatment, but abrogated it after 20 hr of treatment (Figures S4B and S4C). This suggests a biphasic activation of JAK2/STAT5 upon PI3K/mTOR inhibition, the first phase being IL-8/CXCR1-independent and the second being IL-8/CXCR1-dependent. This is in line with the increase in IL-8 secretion observed after 20 hr of BEZ235 treatment (Figure 3C).

These results raised the question of how JAK2 and STAT5 are activated at earlier time points of PI3K/mTOR inhibition. Epidermal growth factor receptor (EGFR) activates JAK2 in some models (Yamauchi et al., 1997) and, as EGFR has been shown to be activated upon PI3K/mTOR inhibition (Muranen et al., 2012), we tested whether EGFR is important for the activation of JAK2/STAT5 upon PI3K/mTOR blockade. Cells were treated for 8 hr with BEZ235 and/or the EGFR inhibitor AEE788 (Traxler et al., 2004). Although inhibition of EGFR indeed reduced pSTAT5 levels, it did not block the upregulation following BEZ235 treatment (Figure S4D).

Components of the insulin receptor (IR)/IGF-1R signaling pathways have been shown to interact with JAK/STAT (Gual et al., 1998; Le et al., 2002) and the same pathways are upregulated and activated upon mTOR (Haruta et al., 2000) and AKT inhibition (Chandarlapaty et al., 2011). Hence, there appears to be crosstalk between activation of the IR/IGF-1R pathways induced by AKT/mTOR inhibition and JAK2/STAT5. Indeed, IR and IGF-1R were upregulated and underwent increased phosphorylation upon BEZ235 treatment for 8 and 20 hr; IRS1 accumulated and showed increased phosphorylation after 2–20 hr of treatment (Figure 4B).

These data showed that accumulation of IRS1 preceded and possibly accounted for the first wave of pJAK2/pSTAT5 activation. Coimmunoprecipitation studies revealed association of both JAK2 and STAT5 with IRS1 in BEZ235- as well as DMSO-treated cells, but only weak association of JAK1 and STAT3 with IRS1 (Figure 4C). Our data thus showed that JAK2/STAT5 bind to IRS1 but not whether binding accounts for the first phase of BEZ235-induced pJAK2/pSTAT5. To address this question, we depleted IRS1 prior to BEZ235 treatment and found that this abrogated JAK2/STAT5 activation (Figure 4D, upper panel); thus, the first phase of JAK2/STAT5 activation appears to be IRS1-dependent.

Next, we examined whether the first phase of JAK2/STAT5 activation accounts for IL-8 upregulation and secretion by measuring IL-8 levels in the supernatant of cells expressing IRS1 siRNA and which were also treated with BEZ235. Depletion of IRS1 abrogated secretion of IL-8 upon BEZ235 treatment (Figure 4D, lower panel). In addition, knockdown of STAT5 or inhibition of JAK2 decreased BEZ235-evoked IL-8 transcription and secretion (Figures 4E and 4F), demonstrating that IL-8 upregulation is JAK2/STAT5-dependent.

Taken together, these data show that BEZ235-evoked activation of IR/IGF-1R/IRS1 triggered phosphorylation of JAK2/STAT5, which led to upregulation of IL-8 and induced the second phase of JAK2/STAT5 activation, thus completing a positive feedback loop.

Combined Inhibition of PI3K/mTOR and JAK2 Reduces Tumor Growth

That PI3K/mTOR inhibition triggers activation of JAK2/STAT5 and upregulation of IL-8 raises the possibility that this feedback loop could reduce the efficacy of PI3K/mTOR inhibitors in vivo. Using two independent orthotopic xenograft models and one orthotopic allograft model of breast cancer, we examined whether interfering with this feedback loop by inhibiting JAK2 affects the growth of tumors. Palpable tumors were treated with BEZ235 and/or inducible shRNA targeting JAK2, or with BEZ235 and/or NVP-BSK805. Single inhibition of JAK2 had no impact on tumor growth (Figures 5A–5D, left panels). However, tumor growth was reduced by treatment with BEZ235 and a synergistic reduction in tumor growth was seen when BEZ235 was combined with JAK2 inhibition (Figures 5A–5D, left panels). Tumor weight at the end of the treatments mirrored differences in tumor volume (Figures S5A and S5B). Notably, a synergistic effect was observed at lower doses of BEZ235 and NVP-BSK805 when combined than as individual treatments. Lower doses of the inhibitors were applied to avoid possible side-effects and potential drug-drug interaction of the combination. Indeed, there was no significant reduction in mouse body weight after any of the treatments (Figure S5C).

We then assessed the efficiency of PI3K/mTOR and JAK2 inhibition (Figures 5A–5D, right panels, and S5D). Both BEZ235 and NVP-BSK805 potently blocked their targets, as judged by the levels of pAKT/pS6 and pSTAT5, respectively. In addition, consistent with our previous results, pSTAT5 was strongly upregulated by BEZ235 treatment in all models, cleaved PARP

(E) Scatter plots showing breast cancer lines as in (D), depicted based on the ratios of pJAK2/JAK2 (left panel), the levels of secreted IL-8 (right panel) upon BEZ treatment, and sensitivity toward BEZ. The horizontal lines represent mean values (n = 3, *p < 0.05).
(F) Bar graphs showing the mean percentages of cell viability as measured by the WST-1 assay of two BEZ-insensitive lines (left panel) and two BEZ-sensitive lines (right panel) grown under 0.5% serum and treated with 300 nM BEZ and/or 350 nM BSK for 72 hr. Data are means ± SEM (n = 4, *p < 0.05).
See also Figure S3 and Table S1.

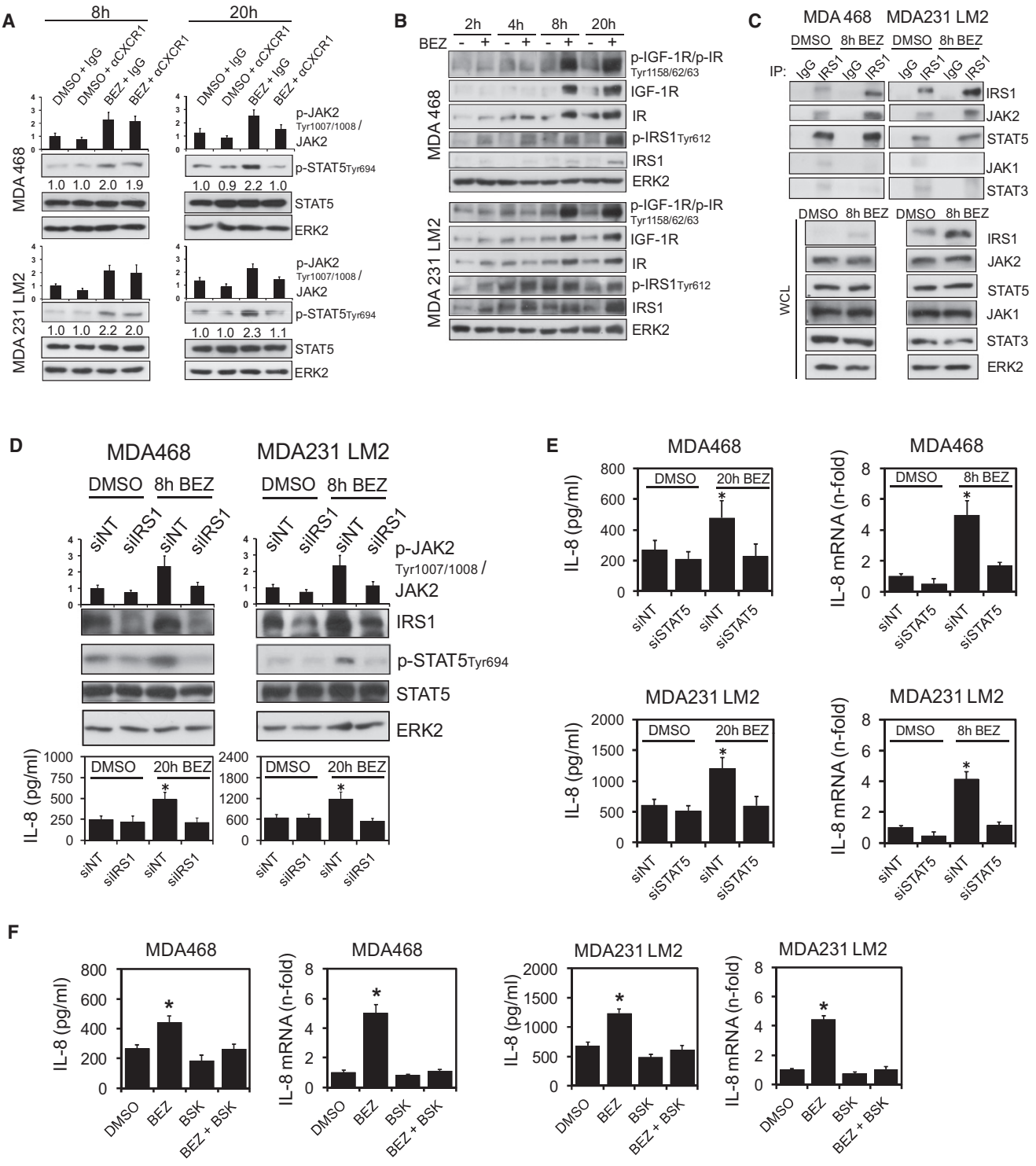

Figure 4. Cotargeting PI3K/mTOR Induces Biphasic Activation of JAK2/STAT5

(A) Immunoblots of lysates from cells treated with DMSO or 300 nM BEZ alone or in combination with IgG or a CXCR1-blocking antibody added 1 hr before lysis. The numbers indicate the ratios of pSTAT5/STAT5 as measured by densitometry. ELISA data are means ± SD (n = 3).

(B) Immunoblots of lysates from cells treated with 300 nM of BEZ as indicated.

(C) Immunoprecipitation (IP) and immunoblotting of lysates from cells treated with DMSO or 300 nM BEZ for 8 hr. WCL, whole cell lysates.

(D) Immunoblots of lysates from cells in which IRS1 was depleted by siRNA before treatment with DMSO or 300 nM BEZ for 8 hr. ELISA data are means ± SD (n = 3) (upper panel). Bar graphs showing the levels of IL-8 secretion upon treatment with 300 nM BEZ for 20 hr (lower panel). Levels of IL-8 were measured by ELISA and are shown as means ± SEM (n = 4, *p < 0.05).

increased in the combination treatment regime only, and proliferation declined in the BEZ235 and combination treatment groups (Figures 5A–5D, right panels, and S5E).

Combined Inhibition of PI3K/mTOR and JAK2 Reduces Metastasis

Metastasis is a multistep process that culminates with growth of tumor cells at distant sites. We analyzed the effects of targeting PI3K/mTOR alone or in combination with JAK2 inhibition on metastasis in mice injected with GFP-expressing MDA231 LM2 or 4T-1 metastatic cell lines. FACS analysis showed a slight reduction in the number of circulating GFP+ tumor cells (CTC) in the blood of mice following BEZ235 treatment, but a dramatic reduction after JAK2 inhibition or combined inhibition of PI3K/mTOR and JAK2 (Figure S5F). To test whether the reduction in CTCs was a consequence of reduced primary tumor volume, we calculated the CTC index upon PI3K/mTOR or JAK2 inhibition alone or in combination (Figure 5E). The CTC index was not affected by BEZ235 alone, but was significantly reduced by the combination of PI3K/mTOR and JAK2 inhibition or by JAK2 inhibition alone (Figure 5E). Next, we analyzed effects of the treatment on lung metastasis (Figure 5F). Importantly, although BEZ235 alone had no effect, the combination of BEZ235 and JAK2 inhibition or JAK2 inhibition alone reduced the metastatic index in all models (Figures 5G, 5H, S5G, and S5H).

To test whether this reduction in metastasis was due to cell-autonomous and/or noncell autonomous effects, we treated mice bearing tumors expressing shJAK2 either with vehicle or NVP-BSK805. No further reduction in the lung metastatic index was observed compared with single inhibition of JAK2 (Figure S5I). Thus, NVP-BSK805 mainly reduces metastatic burden in a cell-autonomous fashion.

Inhibition of JAK2 Blocks the BEZ235-Evoked IL-8/CXCR1 Pro-Metastatic Axis

To elucidate the mechanism underlying the reduction in metastasis observed upon combined PI3K/mTOR and JAK2 inhibition, we evaluated the impact of BEZ235 or NVP-BSK805 or their combination on IL-8 transcription and secretion in vitro and in vivo. Basal levels of active JAK2/STAT5 were higher in the highly metastatic breast cancer sublines 4T-1 and MDA231 LM2 than in the cognate poorly metastatic parental lines 168FARN and MDA231, respectively (Figure S6A). Consistently, the metastatic MDA231 LM2 cells exhibited stronger transcription and secretion of IL-8 (Figure S6B) and higher expression of the IL-8 surface receptor CXCR1 (Figure S6C) than the parental MDA231 cell line. Moreover, we found a correlation between IL-8 secretion, the triple-negative subtype and invasiveness in luminal and TNBC lines (Neve et al., 2006) (Figure S6D). We then compared CXCR1 expression levels in invasive, BEZ235-resistant cell lines and in noninvasive, BEZ235-sensitive cell lines. A striking correlation between CXCR1 expression and the invasive, BEZ235-resistant phenotype was observed, suggesting the involvement of CXCR1 signaling in invasion and adaptive resistance toward BEZ235 (Figure S6E; see also Figure 3E).

Given that IL-8 was induced by PI3K/mTOR inhibition and reduced by blockade of JAK2 in vitro (Figure 4F), we examined whether this was also the case in vivo. We found IL-8 to be elevated in tumors (Figure 6A) and in the plasma of BEZ235-treated mice (Figure 6B); this was reduced by inhibition of JAK2 or both JAK2 and PI3K/mTOR. To address the consequences of increased IL-8 secretion, we inhibited the IL-8 receptor in vitro using a CXCR1-blocking antibody and in vivo by Repertaxin, a noncompetitive allosteric CXCR1/2 inhibitor (Bertini et al., 2004). Combined inhibition of IL-8 and PI3K/mTOR reduced invasion as well as the CTC and metastatic indices. Notably, inhibition of IL-8 did not enhance the effects of JAK2 inhibition in these assays, further supporting roles for IL-8/CXCR1/JAK2 in invasion, tumor seeding and metastasis (Figures 6C–6E and S6F).

IL-8 and CXCR1 have been shown to be important for tumor-initiating cells (Ginestier et al., 2010). We confirmed this observation using limiting dilution transplantation of $CXCR1^+$ and $CXCR1^-$ cell populations (Figure S6G). FACS analysis of dissociated tumor cells, CTCs and lungs from vehicle-treated mice bearing xenografts revealed that only 3% of primary tumor cells were $CXCR1^+$ but CTCs were almost exclusively $CXCR1^+$ (96%). Furthermore, 20.5% of lung metastases cells expressed the receptor at high levels (Figure 6F). In the primary tumor, the $CXCR1^+$ population increased 1.9-fold upon PI3K/mTOR inhibition and decreased 2-fold upon inhibition of JAK2 alone or in combination with PI3K/mTOR inhibition (Figure 6G). Notably, JAK2 inhibition preferentially triggered cell death in the $CXCR1^+$ subpopulation (Figure 6H). Consistently, limiting dilution transplantation experiments revealed a decrease in tumor-initiating cell frequency upon JAK2 inhibition alone or in combination with PI3K/mTOR inhibition (Figures 6I and S6H).

Collectively, our data demonstrate that inhibition of the JAK2/STAT5/IL-8 positive feedback loop triggered by PI3K/mTOR blockade reduced tumor growth and seeding as well as lung metastasis due to its impact on the tumorigenic and metastatic $CXCR1^+$ subpopulation of cancer cells. This strongly suggests that the combination of PI3K and JAK2 inhibitors may be more effective in the neoadjuvant setting than either inhibitor alone.

PI3K/mTOR Inhibition Activates JAK2/STAT5/IL-8 in Primary Human Breast Tumors

We next assessed whether interfering with PI3K/mTOR in human primary breast tumors also triggered a JAK2/STAT5/IL-8 positive feedback loop. BEZ235 treatment of human primary TNBCs grown as xenografts increased pJAK2 and pSTAT5 (Figure 7A). Moreover, IL-8 in the tumors and in the plasma of the mice also increased upon treatment with BEZ235 (Figure 7B). These

(E) Bar graphs showing the levels of IL-8 secretion (left panel) and mRNA (right panel) upon treatment with 300 nM BEZ for 20 hr (left panel) or 8 hr (right panel). Levels of IL-8 were measured by ELISA and RT-qPCR, and are shown as means ± SEM (n = 4, *p < 0.05). For immunoblots of lysates from siSTAT5 depleted cells see Figure S2B.

(F) Bar graphs showing the levels of IL-8 secretion (left panel) and mRNA (right panel) upon treatment with 300 nM BEZ and/or 350 nM BSK for 20 hr (left panel) or 8 hr (right panel). Levels of IL-8 were measured by ELISA and RT-qPCR, and are shown as means ± SEM (n = 4, *p < 0.05).

See also Figure S4.

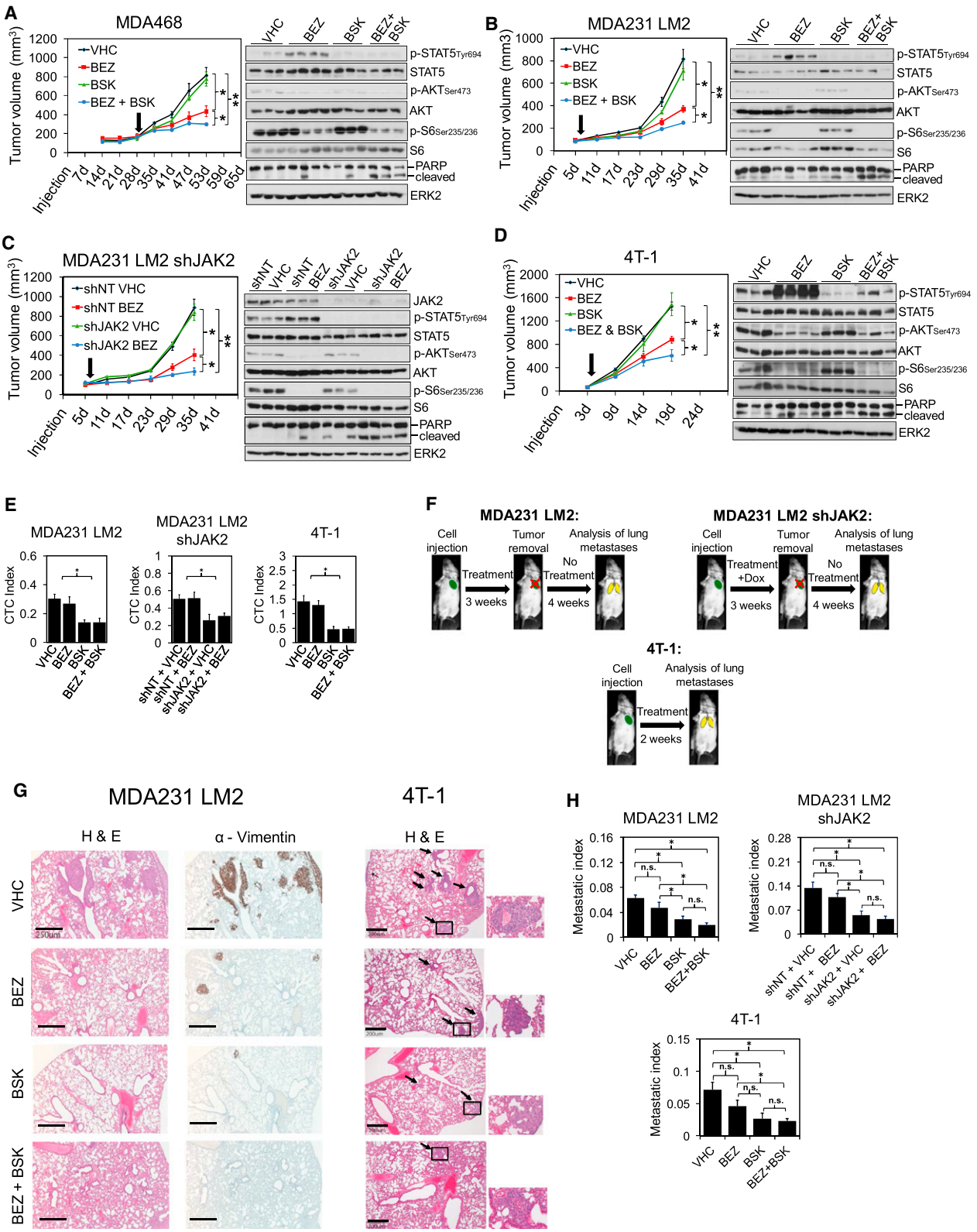

Figure 5. Cotargeting PI3K/mTOR and JAK2/STAT5 Reduces Primary Tumor Growth, Tumor Seeding, and Metastasis

(A–D) Growth curves of tumors and immunoblots of tumor lysates from mice treated with VHC, 30 mg/kg BEZ, 120 mg/kg BSK, or 25 mg/kg BEZ and 100 mg/kg BSK. In (C) JAK2 was depleted in tumors by doxycycline (dox) administration to induce expression of a JAK2-targeting shRNA (shJAK2). shNT, nontargeting shRNA. Injection refers to orthotopic cell injection and the arrows indicate initiation of treatment and/or administration of dox. Immunoblotting was performed on

data showed that the identified positive feedback loop mediated by PI3K/mTOR inhibition is also active in human primary breast tumors and suggest that targeting JAK2 in addition to PI3K/mTOR should block this resistance mechanism and enhance the efficacy of the inhibitors.

Combined PI3K/mTOR and JAK2 Inhibition Increases Survival in a Preclinical Setting

To leverage the mechanistic understanding gained from our experiments into a preclinical setting and to assess the therapeutic relevance of our findings, we performed survival studies using two different metastatic models. We treated tumor-bearing mice with BEZ235 and/or NVP-BSK805 and scored the time at which primary tumors reached 1 cm^3 (event-free survival) (Figure 8A). To mimic the neoadjuvant setting, we treated tumor-bearing mice with BEZ235 and/or NVP-BSK805, dissected the primary tumors, treated mice again, and then monitored them for signs of distress (overall survival) (Figure 8B). We found that BEZ235 treatment reduced primary tumor volume in both models and that JAK2 inhibition, although not affecting event-free survival, significantly enhanced overall survival. Most important, combination of BEZ235 and NVP-BSK805 enhanced preclinical benefit in terms of both event-free and overall survival of the animals.

DISCUSSION

Targeted anticancer drugs have greatly increased the hope of more effective and better tolerated therapies. Although some targeted therapies constitute a breakthrough and have changed the treatment landscape, in numerous cases they have not yet lived up to their promise, with the sobering realization that resistance can emerge within a few months (Engelman et al., 2008; Solit and Rosen, 2011). Delineation of these resistance mechanisms will pave the way for rationally designed and hopefully long-lasting combinations of targeted therapies. In the present study, we found that PI3K/mTOR inhibition elicits a positive feedback response in TNBC that leads to biphasic activation of JAK2/STAT5 and IL-8 secretion, thus dampening the response to the PI3K inhibitors. Our data suggest the following model (Figure 8C): in the untreated tumor (left), PI3K and mTOR are active and support survival and proliferation; JAK2/STAT5 signaling induces IL-8 production and contributes to metastasis. Upon PI3K/mTOR inhibition (middle), IRS1 as well as IGF-1R and IR accumulate and lead to the first wave of JAK2/STAT5 hyperactivation. JAK2/STAT5 activity in turn restores pAKT and blocks cell death, thereby offsetting the impact of BEZ235 on cell viability. JAK2/STAT5 activation also leads to an increase in IL-8 secretion, which activates the second wave of JAK2/STAT5 and completes the feedback loop. Moreover, IL-8 increases the relative number of $CXCR1^+$ cells. The efficacy of PI3K/mTOR inhibition can be improved dramatically by simultaneous JAK2 inhibition (right), which reduces the viability of $CXCR1^+$ tumor-initiating cells, the number of CTCs, and metastatic spread as well as increase the overall survival of the animals.

Identification of a Multimodal Mechanism of Resistance to PI3K/mTOR Inhibition

Mechanisms of resistance to targeted therapy often involve mutation of the target (Engelman and Jänne, 2008), reactivation of the targeted pathway (vertical resistance) (Chandarlapaty et al., 2011; Engelman et al., 2007), or activation of alternative survival pathways (horizontal resistance) (Turke et al., 2010). Activation of the PI3K pathway accounts for vertical and horizontal resistance to several targeted therapies, including inhibitors of EGFR, ERBB2, NOTCH, and MEK1 (Berns et al., 2007; Engelman et al., 2007; Palomero et al., 2007; Wee et al., 2009). But how does resistance to PI3K pathway inhibition occur? Notably, all reported mechanisms leading to escape from inhibition of this pathway comprise vertical resistance. Indeed, treatment with mTOR or AKT inhibitors may lead to reactivation of upstream components of the PI3K pathway (Chandarlapaty et al., 2011; Haruta et al., 2000; O'Reilly et al., 2006).

In the present study, we have uncovered a multimodal mechanism of resistance to targeting PI3K/mTOR. Biphasic activation of JAK2/STAT5 stifles the actions of PI3K/mTOR inhibition by reactivating AKT and increasing cell survival (vertical resistance), while at the same time increasing the systemic levels of the pro-metastatic cytokine IL-8 (horizontal resistance).

As expected, vertical cotargeting of the PI3K/mTOR pathway using dual inhibitors circumvented the IR/IGF-1R/IRS1-evoked reactivation of PI3K arising after mTOR inhibition, which most likely accounts for the limited success of rapalogs as single-agent anticancer therapies. Nevertheless, although dual PI3K/mTOR inhibition reduces reactivation of PI3K, the IR/IGF-1R/IRS1 axis remains active. The consequences of the sustained activity of this axis on other pathways and on the sensitivity to dual PI3K/mTOR inhibitors remain ill-defined. Our findings that PI3K/mTOR inhibition-mediated reactivation of

tumors harvested after 14 days of treatment for MDA468, 10 days of treatment for MDA231 LM2, and 6 days of treatment for 4T-1. Results are mean tumor volume ± SEM (three independent experiments, total n = 4–8, *$p < 0.05$, **$p < 0.01$).

(E) Bar graphs showing the circulating tumor cell (CTC) index. The number of CTCs was measured by FACS analysis of GFP+ cells in tail vein blood performed 21 days (MDA231 LM2) or 5 days (4T-1) after initiation of the treatment as in (B)–(D). The CTC index was calculated by dividing the total number of GFP+ CTCs per 100 μl peripheral blood by tumor volume. Data represent the means ± SEM (for MDA231 LM2 shJAK2 in two independent experiments, total of n = 4 mice, and for the other models in three independent experiments, with a total n = 7 mice; *$p < 0.05$).

(F) Drawings of the experimental setup.

(G) Representative IHC pictures of lungs from VHC-, BEZ-, BSK- and BEZ/BSK-treated animals. Left panel: H&E- (left) and Vimentin-(right) stained lungs from MDA231 LM2-bearing animals, treated as described in (B) and (F). Scale bar represents 250 μm. Right panel: H&E-stained lungs from 4T-1-bearing animals, treated as described in (D) and (F). Arrows indicate metastases; the images to the right are magnifications of single metastatic foci. Scale bar represents 200 μm.

(H) Bar graphs showing the metastatic index of mice treated as in (B–D) calculated by dividing the total number of visible lung metastases nodules by tumor volume. Data are means ± SEM (for MDA231 LM2 shJAK2 from two independent experiments, total n = 4, for the other models from three independent experiments, total n = 10, *$p < 0.05$).

See also Figure S5.

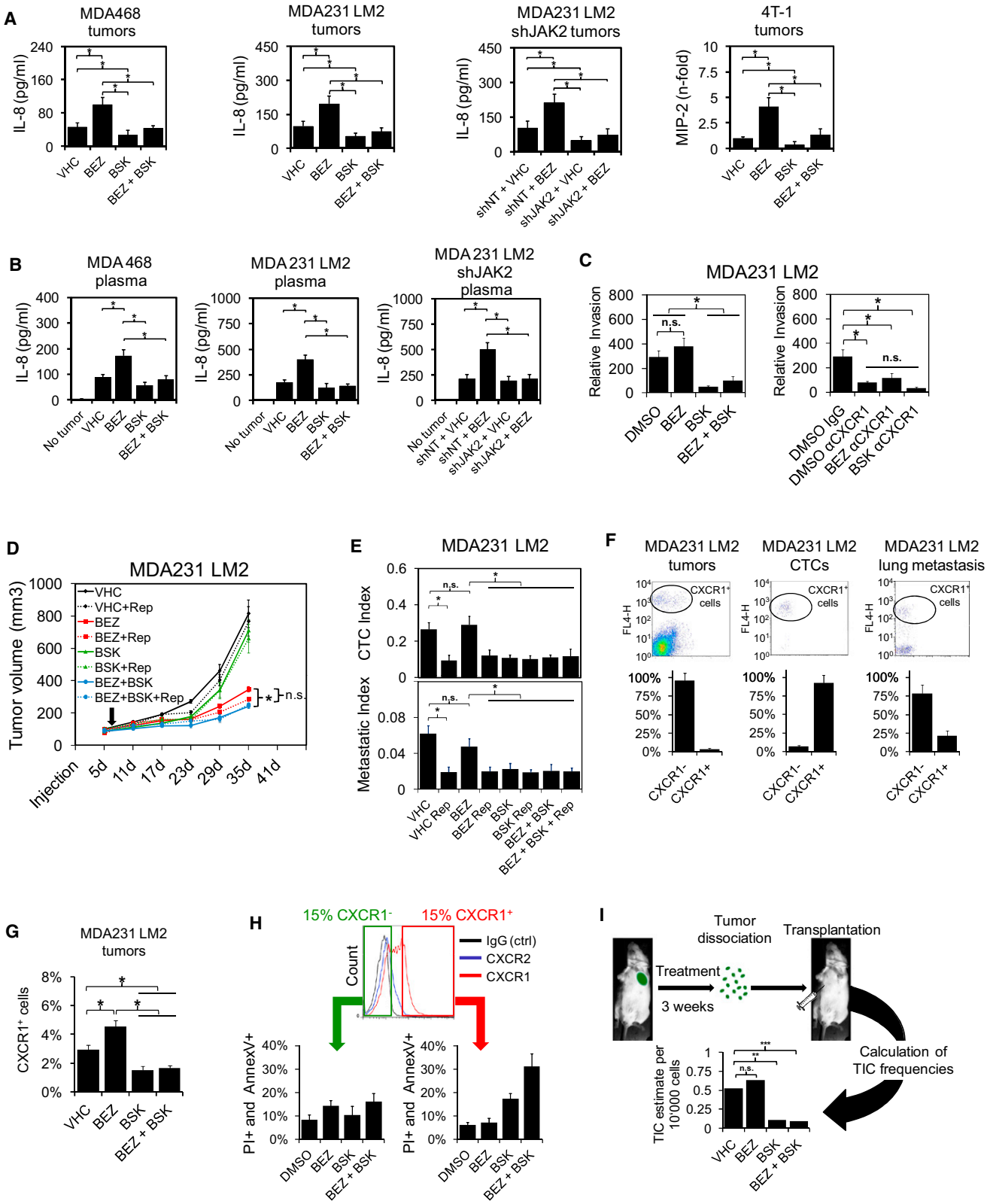

Figure 6. PI3K/mTOR Inhibition Increases, whereas JAK2 Inhibition Blocks IL-8 Secretion and Reduces the Tumor-Initiating CXCR1$^+$ Subpopulation

(A) Bar graphs showing IL-8 levels measured by ELISA (left and middle panels) or quantification of dots of cytokine arrays (right panel) from tumors of mice treated as in Figures 5A–5D. Data are means ± SEM (n = 3–8, *p < 0.05).

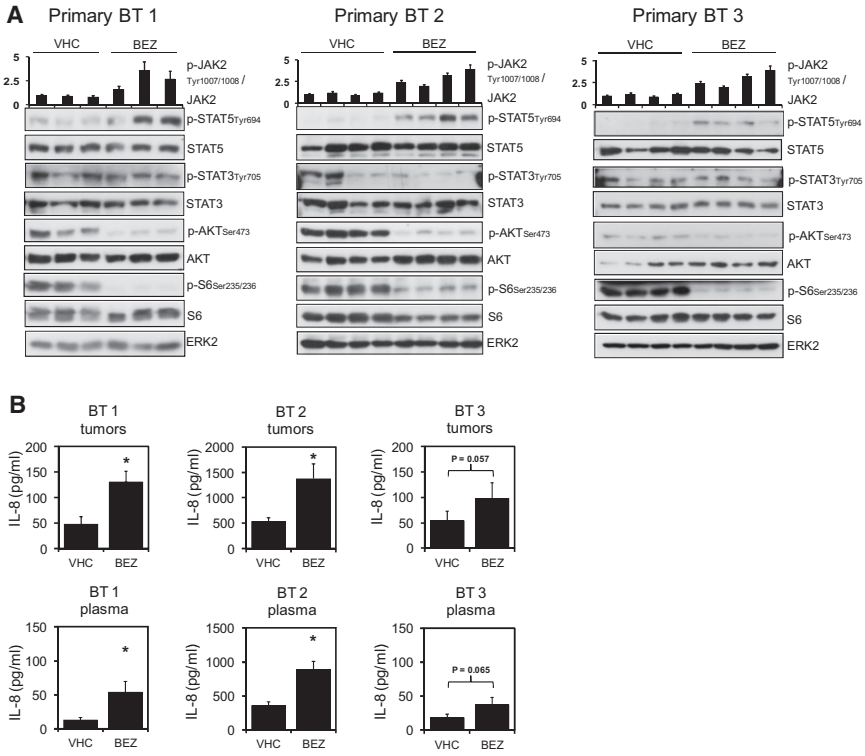

Figure 7. BEZ235 Treatment Activates JAK2/STAT5 and IL-8 Secretion in Primary Human TNBC Xenografts

(A) Immunoblots of lysates from primary TNBC xenografts treated for 4 days with 30 mg/kg BEZ or VHC. ELISA data are means ± SD (n = 3).

(B) Bar graphs showing IL-8 levels measured by ELISA in the dissected tumors from or in the plasma of mice at day 3 of treatment with 30 mg/kg BEZ or VHC. Data are means ± SEM (n = 3–4, *p < 0.05).

IR/IGF-1R/IRS1 induces a first wave of active JAK2/STAT5, which in turn contributes to rephosphorylation of AKT, shed light on this question. We further found that BEZ235 reduces the expression of the AKT Ser473 phosphatase PHLPP and that it inefficiently targets the mTORC2 complex. Genetic inhibition of mTORC2 blocked the recovery of pS473 AKT upon treatment with BEZ235, consistent with previous studies showing that inhibition of S6K-induced mTORC2/AKT (Dibble et al., 2009). These different feedback mechanisms may explain the limited efficacy of dual PI3K/mTOR inhibition in some cancer models. These results and our observation that individual PI3K or mTOR inhibition also causes JAK2/STAT5 activation raise the possibility that other inhibitors of the PI3K pathway may elicit similar crosstalk.

Cotargeting PI3K/mTOR and JAK2 Increases Cell Death and Reduces Tumor Growth

The PI3K and JAK2 pathways activate the prosurvival protein MCL1 and suppress the pro-apoptotic protein BIM at the transcriptional and posttranslational levels (Ewings et al., 2007; Opferman, 2006). We found that combined inhibition of PI3K/mTOR and JAK2 activates BIM and concomitantly downregulates MCL1, causing an increase in apoptosis. Notably, this latter effect was not observed upon single inhibition of PI3K/mTOR or JAK2/STAT5, suggesting that activation of either pathway prevents cell death. Combined PI3K and MEK inhibition similarly decreased MCL1 and increased BIM, thereby triggering cell death in EGFR mutant lung cancer (Faber et al., 2009). The moderate levels of cell death detected upon combined PI3K/mTOR and JAK2 inhibition, both in vitro and in vivo, can be explained by the fact that cell death was mainly induced in the small subpopulation of CXCR1$^+$ tumor-initiating cells.

Genetic depletion of JAK2 after overt tumor development was shown to have no effect on tumor growth (Sakamoto et al., 2009). Similarly, we found no effect of single JAK2 inhibition on tumor growth. However, (Hedvat et al., 2009; Xin et al., 2011) showed that a different JAK inhibitor reduced primary tumor growth of xenografts of MDA468 and 4T-1, two cell lines that we also

(B) Bar graphs showing IL-8 levels measured by ELISA in plasma of mice bearing tumors treated as in Figures 5A–5C. Data are means ± SEM (n = 4, *p < 0.05).

(C) Bar graphs showing relative invasion of MDA231 LM2 cells seeded on Matrigel-coated Boyden chambers and treated with 300 nM BEZ, 350 nM BSK and/or CXCR1 blocking antibody. Invasion was assessed after 48 hr. Data represent relative invasion values normalized to cell number and are means ± SEM (n = 4, *p < 0.05).

(D) Growth curves of tumors from mice treated with VHC, 30 mg/kg BEZ, 120 mg/kg BSK, 20 mg/kg Repertaxin (Rep), or 25 mg/kg BEZ, 100 mg/kg BSK and 20 mg/kg Rep. Injection refers to orthotopic cell injection and the arrow indicates initiation of treatment. Data are mean tumor volume ± SEM (n = 4–8, *p < 0.05).

(E) Bar graphs showing CTC (upper panel) and lung metastatic (lower panel) indices of mice treated as in Figure 5F. Rep was administered at 20 mg/kg. Data are means ± SEM (n = 3–4, *p < 0.05).

(F) Upper: representative images of FACS dot plots of CXCR1-stained tumors, CTCs and lungs. Lower: bar graphs showing the percentage of CXCR1$^+$ cells. Data are means ± SEM (n = 6).

(G) Bar graph showing percentages of CXCR1$^+$ cells in MDA231 LM2 tumors of mice treated as in Figure 5B. Data are means ± SEM (n = 4–6, *p < 0.05).

(H) Representative dot plot of FACS analyses performed on CXCR1- (upper panel), AnnexinV-, and PI-stained (lower panel) MDA231 LM2 cells treated with inhibitors as in Figure 2C. Bar graphs show the mean percentages of apoptotic and dead cells after 48 hr of treatment. Data are means ± SEM (n = 4, *p < 0.05).

(I) Upper: drawing of the experimental setup. Mice bearing MDA231 LM2 tumors were treated as in Figure 5B. The tumors were dissected, dissociated, and retransplanted at different dilutions. Cell viability prior to retransplantation was analyzed by PI-FACS staining and was found to be equal in all treatment groups (data not shown). Lower: bar graph showing the TIC frequencies after treatment as in Figure 5B. Data are mean estimates from three independent experiments, total n = 7 mice, *p < 0.05, ***p < 0.0001.

See also Figure S6.

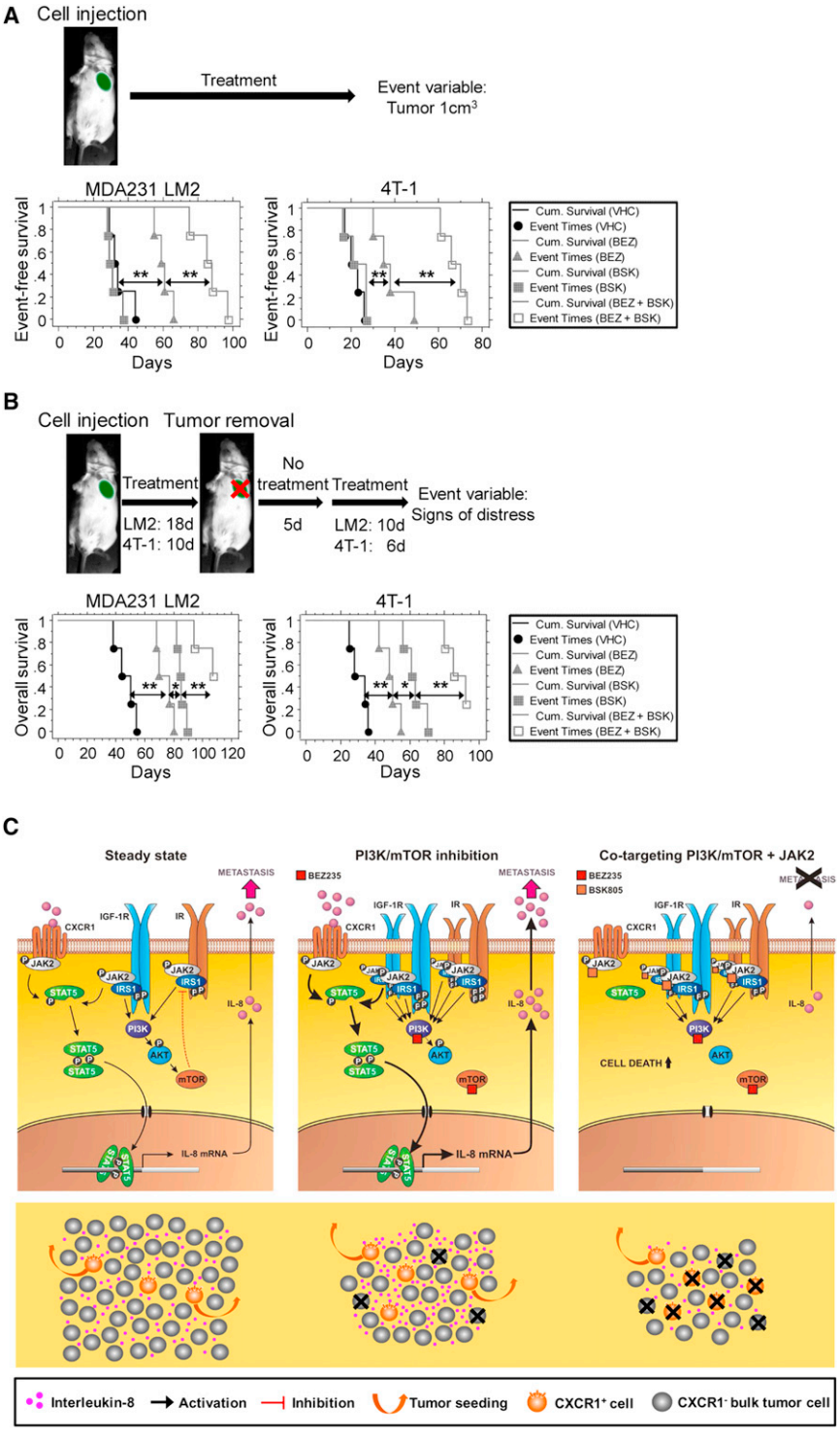

Figure 8. Cotargeting PI3K/mTOR and JAK2 Increases Event-Free and Overall Survival in Two Models of Metastatic Breast Cancer

(A) Upper: drawing of the experimental setup. Lower: Kaplan-Meier survival curves of MDA231 LM2 (left) and 4T-1 (right) tumor-bearing mice treated with BEZ and/or BSK as in Figures 5B and 5D. An event was scored when a tumor reached 1 cm^3 (n = 4, *p < 0.05, **p < 0.01).

(B) Upper: drawing of the experimental setup. Lower: Kaplan-Meier survival curves of MDA231 LM2 (left) and 4T-1 (right) tumor-bearing mice treated with BEZ and/or BSK as in Figures 5B and 5D. An event was scored when a mouse showed any sign of distress; (n = 4, *p < 0.05, **p < 0.01).

(C) Schematics illustrating the identified positive feedback loop triggered by inhibition of PI3K/mTOR and offset by JAK2/STAT5 inhibition. Upper: effects of PI3K/mTOR inhibition and/or JAK2 inhibition at the cellular level. Lower: effects of PI3K/mTOR and/or JAK2 inhibition at the tumor level.

used in the present study. This inhibitor (Hedvat et al., 2009) displayed a spectrum of JAK kinase selectivity different to NVP-BSK805, which is biased toward JAK2 within the JAK family (Baffert et al., 2010). Different inhibitors also display divergent spectra of overall kinase selectivity, which may also account for some of the tumor growth effects observed by (Hedvat et al., 2009). Of note, the focus of some of the other studies has been on oncogenic STAT3 signaling in breast cancer models (Hedvat et al., 2009; Marotta et al., 2011), whereas our present work has revealed an important role for JAK2/STAT5 signaling. RNAi experiments in our models showed that JAK2 is required for STAT5 phosphorylation, whereas JAK1 predominantly signals to STAT3. Hence, dual JAK1/2 inhibitors may have additional antitumor effects due to suppression of both STAT3 and STAT5 phosphorylation.

Inhibition of PI3K/mTOR and JAK2 or JAK2 Alone Reduces Metastasis and Increases Overall Survival

Consistent with the multimodal nature of the identified feedback, cotargeting PI3K/mTOR and JAK2/STAT5 also reduced tumor seeding and metastasis. These effects can be explained by the fact that targeting JAK2 abrogated this feedback loop, decreasing STAT5 activation and IL-8 transcription and secretion, which culminated in death of the $CXCR1^+$ cells. The observation that $CXCR1^+$ cells were a minor subpopulation in the primary tumor but constitute the majority of CTCs and ~20% of lung metastases raises the intriguing possibility that CXCR1 and its associated downstream signaling are crucial for intravasation and/or survival of the cells in the periphery, but less critical once cells have reached the metastatic site. Consistently, IL-8 inhibition alone or in combination with PI3K/mTOR inhibition reduced tumor seeding and metastasis. Indeed, IL-8 has been shown to play crucial roles

in the stimulation of tumor-initiating cells, invasion, and metastasis (Charafe-Jauffret et al., 2009; Ginestier et al., 2010; Waugh and Wilson, 2008), and a role for JAK2 in cells with the cancer stem cell phenotype has also been suggested (Marotta et al., 2011).

To gain insights into a potential clinical benefit of combined inhibition of PI3K/mTOR and JAK2, we performed survival studies in a preclinical setting. We found that single JAK2 inhibition increased overall survival, while having no benefit on event-free survival. Notably, combination of BEZ235 and NVP-BSK805 increased both event-free and overall survival of animals. Our findings potentially have direct clinical implications, given that 26 PI3K pathway inhibitors are currently undergoing clinical evaluation (Sheppard et al., 2012). These results urge assessment of the activation of the JAK2/STAT5/IL-8 positive feedback loop before therapy and/or upon PI3K inhibition, and the testing of the efficacy of cotargeting PI3K/mTOR and JAK2 in TNBC and other cancers.

EXPERIMENTAL PROCEDURES

Compounds

BEZ235, NVP-BSK805, NVP-BKM120, and RAD001 were from Novartis (Basel, Switzerland). Repertaxin L-lysine salt was obtained from WuXi AppTec (Shanghai, China). Daunorubicin was obtained from Sigma Aldrich. Compounds were prepared as 10 mM stock solutions in DMSO and stored protected from light at −20°C. NVP-BSK805 was freshly formulated in NMP/PEG300/Solutol HS15 (5%/80%/15%) and BEZ235 in NMP/PEG300 (10%/90%), and both were administered to mice by oral gavage at 10 ml/kg. Repertaxin was freshly formulated in PBS and administered subcutaneously at 20 mg/kg.

Primary Human Breast Tumors

Primary breast cancer specimens were obtained from the consented patients: two specimens were provided by the Cooperative Human tissue Network which is funded by the National Cancer institute, and one was obtained at and approved by the board of the Saint-Louis Clinic (France). All studies were approved by the Ethikkommission beider Basel.

Animal Experiments

SCID/beige, SCID/NOD, and Balb/c mice (Jackson Laboratories) were used in compliance with the Swiss laws on animal welfare and the animal protocols were approved by the Swiss Cantonal Veterinary Office of Basel. For orthotopic engraftment of breast cancer cell lines, 1×10^6 MDA468, 1×10^6 MDA231 LM2, and 0.5×10^6 4T-1 or 4T-1-GFP cells were suspended in a 100 μl mixture of Basement Membrane Matrix Phenol Red-free (BD Biosciences) and PBS 1:1 and injected into mouse mammary gland. Primary breast tumors were cut into 1 mm^3 pieces and transplanted into mouse mammary gland. Tumor-bearing mice were randomized based on tumor volume prior to the initiation of treatment, which started when average tumor volume was at least 100 mm^3. BEZ235 and NVP-BSK805 were given orally on each of 6 consecutive days followed by 1 day without the drug; Repertaxin was administered daily. Expression of shRNAs was induced by adding doxycycline in the drinking water (2 g/l in a 5% sucrose solution), which was refreshed every 48 hr. Tumors were measured every 3–4 days and tumor volumes calculated by the formula 0.5 × (larger diameter) × (smaller diameter)^2. End point tumor sizes were analyzed for synergism using the formula $AB/C < A/C \times B/C$, where C is tumor volume VHC, A is tumor volume compound 1, B is tumor volume compound 2, and AB is tumor volume combination (Clarke, 1997). For survival studies, animals were sacrificed when tumors reached 1 cm^3 or when they showed any signs of distress (e.g., breathing disorders, weight loss, or immobility).

Statistical Analysis

Each value reported represents the mean ± SEM of at least three independent experiments. Data were tested for normal distribution and Student's t test, ANOVAs, or nonparametric Mann-Whitney U/Wilcoxon tests were applied. To account for multiple comparisons, Tukey HSD and Wilcoxon tests were performed. StatView 5.0.1 was used for Kaplan-Meier survival analysis and log rank Mantel-Cox tests were applied to test statistical significance (SAS). Programs JMP4 and JMP9 were used for all other statistical tests (SAS). The p values < 0.05 were considered to be statistically significant.

SUPPLEMENTAL INFORMATION

Supplemental Information includes six figures, one table, and Supplemental Experimental Procedures and can be found with this article online at http://dx.doi.org/10.1016/j.ccr.2012.10.023.

ACKNOWLEDGMENTS

We thank N. Hynes (FMI) for providing the 4T-1 and 168FARN cells and J. Massagué (MSKCC) and C. Kuperwasser (Tufts University) for providing the MDAMB 231 LM2 and SUM159 cells, respectively. We are grateful to W. Sellers (Novartis, ONC) for helpful discussions, M. Maira and C. Fritsch (Novartis, ONC) for supplying BEZ235 and BKM120, and H. Gao and F. Baffert (Novartis, ONC) and Y. Kuhn and C. Peters (Saint-Louis Clinic) for providing primary tumors. Tissue samples were provided by the Cooperative Human Tissue Network, which is funded by the National Cancer Institute. Other investigators may have received specimens from the same subjects. Thanks to H. Kohler, M. Stadler, R. Thierry, and S. Bourke (FMI) for help with data analysis and to further members of the Bentires-Alj lab for discussions. Research in the lab of M.B-A. is supported by the Novartis Research Foundation and the European Research Council. R.A., V.R., M.M., and T.R. are full-time employees of Novartis Pharma AG.

Received: June 7, 2012
Revised: October 8, 2012
Accepted: October 31, 2012
Published: December 10, 2012

REFERENCES

Andraos, R., Qian, Z., Bonenfant, D.b., Rubert, J.l., Vangrevelinghe, E., Scheufler, C., Marque, F., Régnier, C.H., De Pover, A., Ryckelynck, H., et al. (2012). Modulation of activation-loop phosphorylation by JAK inhibitors is binding mode dependent. Cancer Discov. *2*, 512–523.

Baffert, F., Régnier, C.H., De Pover, A., Pissot-Soldermann, C., Tavares, G.A., Blasco, F., Brueggen, J., Chène, P., Drueckes, P., Erdmann, D., et al. (2010). Potent and selective inhibition of polycythemia by the quinoxaline JAK2 inhibitor NVP-BSK805. Mol. Cancer Ther. *9*, 1945–1955.

Berns, K., Horlings, H.M., Hennessy, B.T., Madiredjo, M., Hijmans, E.M., Beelen, K., Linn, S.C., Gonzalez-Angulo, A.M., Stemke-Hale, K., Hauptmann, M., et al. (2007). A functional genetic approach identifies the PI3K pathway as a major determinant of trastuzumab resistance in breast cancer. Cancer Cell *12*, 395–402.

Bertini, R., Allegretti, M., Bizzarri, C., Moriconi, A., Locati, M., Zampella, G., Cervellera, M.N., Di Cioccio, V., Cesta, M.C., Galliera, E., et al. (2004). Noncompetitive allosteric inhibitors of the inflammatory chemokine receptors CXCR1 and CXCR2: prevention of reperfusion injury. Proc. Natl. Acad. Sci. USA *101*, 11791–11796.

Bissell, M.J., and Radisky, D. (2001). Putting tumours in context. Nat. Rev. Cancer *1*, 46–54.

Brachmann, S.M., Hofmann, I., Schnell, C., Fritsch, C., Wee, S., Lane, H., Wang, S., Garcia-Echeverria, C., and Maira, S.M. (2009). Specific apoptosis induction by the dual PI3K/mTor inhibitor NVP-BEZ235 in HER2 amplified and PIK3CA mutant breast cancer cells. Proc. Natl. Acad. Sci. USA *106*, 22299–22304.

Certo, M., Del Gaizo Moore, V., Nishino, M., Wei, G., Korsmeyer, S., Armstrong, S.A., and Letai, A. (2006). Mitochondria primed by death signals determine cellular addiction to antiapoptotic BCL-2 family members. Cancer Cell *9*, 351–365.

Chandarlapaty, S., Sawai, A., Scaltriti, M., Rodrik-Outmezguine, V., Grbovic-Huezo, O., Serra, V., Majumder, P.K., Baselga, J., and Rosen, N. (2011). AKT inhibition relieves feedback suppression of receptor tyrosine kinase expression and activity. Cancer Cell *19*, 58–71.

Charafe-Jauffret, E., Ginestier, C., Iovino, F., Wicinski, J., Cervera, N., Finetti, P., Hur, M.H., Diebel, M.E., Monville, F., Dutcher, J., et al. (2009). Breast cancer cell lines contain functional cancer stem cells with metastatic capacity and a distinct molecular signature. Cancer Res. *69*, 1302–1313.

Clarke, R. (1997). Issues in experimental design and endpoint analysis in the study of experimental cytotoxic agents in vivo in breast cancer and other models. Breast Cancer Res. Treat. *46*, 255–278.

Desrivières, S., Kunz, C., Barash, I., Vafaizadeh, V., Borghouts, C., and Groner, B. (2006). The biological functions of the versatile transcription factors STAT3 and STAT5 and new strategies for their targeted inhibition. J. Mammary Gland Biol. Neoplasia *11*, 75–87.

Dibble, C.C., Asara, J.M., and Manning, B.D. (2009). Characterization of Rictor phosphorylation sites reveals direct regulation of mTOR complex 2 by S6K1. Mol. Cell. Biol. *29*, 5657–5670.

Engelman, J.A. (2009). Targeting PI3K signalling in cancer: opportunities, challenges and limitations. Nat. Rev. Cancer *9*, 550–562.

Engelman, J.A., and Jänne, P.A. (2008). Mechanisms of acquired resistance to epidermal growth factor receptor tyrosine kinase inhibitors in non-small cell lung cancer. Clin. Cancer Res. *14*, 2895–2899.

Engelman, J.A., Luo, J., and Cantley, L.C. (2006). The evolution of phosphatidylinositol 3-kinases as regulators of growth and metabolism. Nat. Rev. Genet. *7*, 606–619.

Engelman, J.A., Zejnullahu, K., Mitsudomi, T., Song, Y.C., Hyland, C., Park, J.O., Lindeman, N., Gale, C.M., Zhao, X.J., Christensen, J., et al. (2007). MET amplification leads to gefitinib resistance in lung cancer by activating ERBB3 signaling. Science *316*, 1039–1043.

Engelman, J.A., Chen, L., Tan, X., Crosby, K., Guimaraes, A.R., Upadhyay, R., Maira, M., McNamara, K., Perera, S.A., Song, Y., et al. (2008). Effective use of PI3K and MEK inhibitors to treat mutant Kras G12D and PIK3CA H1047R murine lung cancers. Nat. Med. *14*, 1351–1356.

Ewings, K.E., Hadfield-Moorhouse, K., Wiggins, C.M., Wickenden, J.A., Balmanno, K., Gilley, R., Degenhardt, K., White, E., and Cook, S.J. (2007). ERK1/2-dependent phosphorylation of BimEL promotes its rapid dissociation from Mcl-1 and Bcl-xL. EMBO J. *26*, 2856–2867.

Faber, A.C., Li, D., Song, Y., Liang, M.C., Yeap, B.Y., Bronson, R.T., Lifshits, E., Chen, Z., Maira, S.M., García-Echeverría, C., et al. (2009). Differential induction of apoptosis in HER2 and EGFR addicted cancers following PI3K inhibition. Proc. Natl. Acad. Sci. USA *106*, 19503–19508.

Flaherty, K.T., Puzanov, I., Kim, K.B., Ribas, A., McArthur, G.A., Sosman, J.A., O'Dwyer, P.J., Lee, R.J., Grippo, J.F., Nolop, K., and Chapman, P.B. (2010). Inhibition of mutated, activated BRAF in metastatic melanoma. N. Engl. J. Med. *363*, 809–819.

Gao, T., Furnari, F., and Newton, A.C. (2005). PHLPP: a phosphatase that directly dephosphorylates Akt, promotes apoptosis, and suppresses tumor growth. Mol. Cell *18*, 13–24.

Ginestier, C., Liu, S., Diebel, M.E., Korkaya, H., Luo, M., Brown, M., Wicinski, J., Cabaud, O., Charafe-Jauffret, E., Birnbaum, D., et al. (2010). CXCR1 blockade selectively targets human breast cancer stem cells in vitro and in xenografts. J. Clin. Invest. *120*, 485–497.

Gual, P., Baron, V., Lequoy, V., and Van Obberghen, E. (1998). Interaction of Janus kinases JAK-1 and JAK-2 with the insulin receptor and the insulin-like growth factor-1 receptor. Endocrinology *139*, 884–893.

Haber, D.A., Gray, N.S., and Baselga, J. (2011). The evolving war on cancer. Cell *145*, 19–24.

Harrington, L.S., Findlay, G.M., Gray, A., Tolkacheva, T., Wigfield, S., Rebholz, H., Barnett, J., Leslie, N.R., Cheng, S., Shepherd, P.R., et al. (2004). The TSC1-2 tumor suppressor controls insulin-PI3K signaling via regulation of IRS proteins. J. Cell Biol. *166*, 213–223.

Harrison, C., Kiladjian, J.-J., Al-Ali, H.K., Gisslinger, H., Waltzman, R., Stalbovskaya, V., McQuitty, M., Hunter, D.S., Levy, R., Knoops, L., et al. (2012). JAK inhibition with ruxolitinib versus best available therapy for myelofibrosis. N. Engl. J. Med. *366*, 787–798.

Harry, B.L., Eckhardt, S.G., and Jimeno, A. (2012). JAK2 inhibition for the treatment of hematologic and solid malignancies. Expert Opin. Investig. Drugs *21*, 637–655.

Haruta, T., Uno, T., Kawahara, J., Takano, A., Egawa, K., Sharma, P.M., Olefsky, J.M., and Kobayashi, M. (2000). A rapamycin-sensitive pathway down-regulates insulin signaling via phosphorylation and proteasomal degradation of insulin receptor substrate-1. Mol. Endocrinol. *14*, 783–794.

Hedvat, M., Huszar, D., Herrmann, A., Gozgit, J.M., Schroeder, A., Sheehy, A., Buettner, R., Proia, D., Kowolik, C.M., Xin, H., et al. (2009). The JAK2 inhibitor AZD1480 potently blocks Stat3 signaling and oncogenesis in solid tumors. Cancer Cell *16*, 487–497.

Hudis, C.A., and Gianni, L. (2011). Triple-negative breast cancer: an unmet medical need. Oncologist *16*(*Suppl 1*), 1–11.

Jin, H., Lanning, N.J., and Carter-Su, C. (2008). JAK2, but not Src family kinases, is required for STAT, ERK, and Akt signaling in response to growth hormone in preadipocytes and hepatoma cells. Mol. Endocrinol. *22*, 1825–1841.

Le, M.N., Kohanski, R.A., Wang, L.H., and Sadowski, H.B. (2002). Dual mechanism of signal transducer and activator of transcription 5 activation by the insulin receptor. Mol. Endocrinol. *16*, 2764–2779.

Ley, R., Balmanno, K., Hadfield, K., Weston, C., and Cook, S.J. (2003). Activation of the ERK1/2 signaling pathway promotes phosphorylation and proteasome-dependent degradation of the BH3-only protein, Bim. J. Biol. Chem. *278*, 18811–18816.

Maira, S.M., Stauffer, F., Brueggen, J., Furet, P., Schnell, C., Fritsch, C., Brachmann, S., Chène, P., De Pover, A., Schoemaker, K., et al. (2008). Identification and characterization of NVP-BEZ235, a new orally available dual phosphatidylinositol 3-kinase/mammalian target of rapamycin inhibitor with potent in vivo antitumor activity. Mol. Cancer Ther. *7*, 1851–1863.

Marotta, L.L.C., Almendro, V., Marusyk, A., Shipitsin, M., Schemme, J., Walker, S.R., Bloushtain-Qimron, N., Kim, J.J., Choudhury, S.A., Maruyama, R., et al. (2011). The JAK2/STAT3 signaling pathway is required for growth of $CD44^{+}CD24^{-}$ stem cell-like breast cancer cells in human tumors. J. Clin. Invest. *121*, 2723–2735.

Muranen, T., Selfors, L.M., Worster, D.T., Iwanicki, M.P., Song, L., Morales, F.C., Gao, S., Mills, G.B., and Brugge, J.S. (2012). Inhibition of PI3K/mTOR leads to adaptive resistance in matrix-attached cancer cells. Cancer Cell *21*, 227–239.

Neve, R.M., Chin, K., Fridlyand, J., Yeh, J., Baehner, F.L., Fevr, T., Clark, L., Bayani, N., Coppe, J.P., Tong, F., et al. (2006). A collection of breast cancer cell lines for the study of functionally distinct cancer subtypes. Cancer Cell *10*, 515–527.

O'Brien, S.G., Guilhot, F., Larson, R.A., Gathmann, I., Baccarani, M., Cervantes, F., Cornelissen, J.J., Fischer, T., Hochhaus, A., Hughes, T., et al.; IRIS Investigators. (2003). Imatinib compared with interferon and low-dose cytarabine for newly diagnosed chronic-phase chronic myeloid leukemia. N. Engl. J. Med. *348*, 994–1004.

O'Reilly, K.E., Rojo, F., She, Q.B., Solit, D., Mills, G.B., Smith, D., Lane, H., Hofmann, F., Hicklin, D.J., Ludwig, D.L., et al. (2006). mTOR inhibition induces upstream receptor tyrosine kinase signaling and activates Akt. Cancer Res. *66*, 1500–1508.

Opferman, J.T. (2006). Unraveling MCL-1 degradation. Cell Death Differ. *13*, 1260–1262.

Palomero, T., Sulis, M.L., Cortina, M., Real, P.J., Barnes, K., Ciofani, M., Caparros, E., Buteau, J., Brown, K., Perkins, S.L., et al. (2007). Mutational loss of PTEN induces resistance to NOTCH1 inhibition in T-cell leukemia. Nat. Med. *13*, 1203–1210.

Parcellier, A., Tintignac, L.A., Zhuravleva, E., and Hemmings, B.A. (2008). PKB and the mitochondria: AKTing on apoptosis. Cell. Signal. *20*, 21–30.

Radimerski, T., Montagne, J., Hemmings-Mieszczak, M., and Thomas, G. (2002). Lethality of Drosophila lacking TSC tumor suppressor function rescued by reducing dS6K signaling. Genes Dev. *16*, 2627–2632.

Rodier, F., and Campisi, J. (2011). Four faces of cellular senescence. J. Cell Biol. *192*, 547–556.

Sakamoto, K., Lin, W.C., Triplett, A.A., and Wagner, K.U. (2009). Targeting janus kinase 2 in Her2/neu-expressing mammary cancer: Implications for cancer prevention and therapy. Cancer Res. *69*, 6642–6650.

Samuels, Y., Wang, Z., Bardelli, A., Silliman, N., Ptak, J., Szabo, S., Yan, H., Gazdar, A., Powell, S.M., Riggins, G.J., et al. (2004). High frequency of mutations of the PIK3CA gene in human cancers. Science *304*, 554.

Sellers, W.R. (2011). A blueprint for advancing genetics-based cancer therapy. Cell *147*, 26–31.

Serra, V., Markman, B., Scaltriti, M., Eichhorn, P.J., Valero, V., Guzman, M., Botero, M.L., Llonch, E., Atzori, F., Di Cosimo, S., et al. (2008). NVP-BEZ235, a dual PI3K/mTOR inhibitor, prevents PI3K signaling and inhibits the growth of cancer cells with activating PI3K mutations. Cancer Res. *68*, 8022–8030.

Sheppard, K., Kinross, K.M., Solomon, B., Pearson, R.B., and Phillips, W.A. (2012). Targeting PI3 kinase/AKT/mTOR signaling in cancer. Crit. Rev. Oncog. *17*, 69–95.

Solit, D.B., and Rosen, N. (2011). Resistance to BRAF inhibition in melanomas. N. Engl. J. Med. *364*, 772–774.

Traxler, P., Allegrini, P.R., Brandt, R., Brueggen, J., Cozens, R., Fabbro, D., Grosios, K., Lane, H.A., McSheehy, P., Mestan, J., et al. (2004). AEE788: a dual family epidermal growth factor receptor/ErbB2 and vascular endothelial growth factor receptor tyrosine kinase inhibitor with antitumor and antiangiogenic activity. Cancer Res. *64*, 4931–4941.

Turke, A.B., Zejnullahu, K., Wu, Y.L., Song, Y., Dias-Santagata, D., Lifshits, E., Toschi, L., Rogers, A., Mok, T., Sequist, L., et al. (2010). Preexistence and clonal selection of MET amplification in EGFR mutant NSCLC. Cancer Cell *17*, 77–88.

Waugh, D.J., and Wilson, C. (2008). The interleukin-8 pathway in cancer. Clin. Cancer Res. *14*, 6735–6741.

Wee, S., Jagani, Z., Xiang, K.X., Loo, A., Dorsch, M., Yao, Y.M., Sellers, W.R., Lengauer, C., and Stegmeier, F. (2009). PI3K pathway activation mediates resistance to MEK inhibitors in KRAS mutant cancers. Cancer Res. *69*, 4286–4293.

Xin, H., Herrmann, A., Reckamp, K., Zhang, W., Pal, S., Hedvat, M., Zhang, C., Liang, W., Scuto, A., Weng, S., et al. (2011). Antiangiogenic and antimetastatic activity of JAK inhibitor AZD1480. Cancer Res. *71*, 6601–6610.

Yamauchi, T., Ueki, K., Tobe, K., Tamemoto, H., Sekine, N., Wada, M., Honjo, M., Takahashi, M., Takahashi, T., Hirai, H., et al. (1997). Tyrosine phosphorylation of the EGF receptor by the kinase Jak2 is induced by growth hormone. Nature *390*, 91–96.

Yamauchi, T., Kaburagi, Y., Ueki, K., Tsuji, Y., Stark, G.R., Kerr, I.M., Tsushima, T., Akanuma, Y., Komuro, I., Tobe, K., et al. (1998). Growth hormone and prolactin stimulate tyrosine phosphorylation of insulin receptor substrate-1, -2, and -3, their association with p85 phosphatidylinositol 3-kinase (PI3-kinase), and concomitantly PI3-kinase activation via JAK2 kinase. J. Biol. Chem. *273*, 15719–15726.

Cancer Cell
Article

CRL4B Catalyzes H2AK119 Monoubiquitination and Coordinates with PRC2 to Promote Tumorigenesis

Huili Hu,[1] Yang Yang,[1] Qinghong Ji,[1] Wei Zhao,[1] Baichun Jiang,[1] Ruiqiong Liu,[1] Jupeng Yuan,[1] Qiao Liu,[1] Xi Li,[1] Yongxin Zou,[1] Changshun Shao,[1] Yongfeng Shang,[2] Yan Wang,[1,2,*] and Yaoqin Gong[1,*]
[1]Key Laboratory of Experimental Teratology, Ministry of Education, Institute of Molecular Medicine and Genetics, Shandong University School of Medicine, Jinan, Shandong 250012, China
[2]2011 Collaborative Innovation Center of Tianjin for Medical Epigenetics, Tianjin Key Laboratory of Medical Epigenetics, Department of Biochemistry and Molecular Biology, Tianjin Medical University, Tianjin 300070, China
*Correspondence: yanwang@tmu.edu.cn (Y.W.), yxg8@sdu.edu.cn (Y.G.)
http://dx.doi.org/10.1016/j.ccr.2012.10.024

SUMMARY

We reported that Cullin4B-Ring E3 ligase complex (CRL4B) is physically associated with Polycomb-repressive complex 2 (PRC2). We showed that CRL4B possesses an intrinsic transcription repressive activity by promoting H2AK119 monoubiquitination. Ablation of *Cul4b* or depletion of CUL4B, the main component of CRL4B, resulted in loss of not only H2AK119 monoubiquitination but also H3K27 trimethylation, leading to derepression of target genes that are critically involved in cell growth and migration. We demonstrated that CUL4B promotes cell proliferation, invasion, and tumorigenesis in vitro and in vivo and found that its expression is markedly upregulated in various human cancers. Our data indicate that CUL4B promotes tumorigenesis, supporting the pursuit of CUL4B as a target for cancer therapy.

INTRODUCTION

Compared to other histone modifications, ubiquitination represents a very large modification and is mainly found on H2A lysine 119 (K119) and H2B (K120 in human and K123 in yeast) (Kouzarides, 2007). Polycomb group proteins are a family of epigenetic regulators responsible for the repression of an array of genes that are critically implicated in development and cell fate specification (Schuettengruber et al., 2007). Two main Polycomb group complexes exist in mammals: PRC1 and PRC2. PRC1 catalyzes histone H2A K119 monoubiquitylation (H2AK119ub1) and compacts chromatin (Wang et al., 2004), while PRC2 catalyzes trimethylation of histone H3 at K27 (H3K27me3) and also contributes to chromatin compaction (Simon and Kingston, 2009). It is believed that PRC1 and PRC2 interplay and that H2AK119ub1 and H3K27me3 are functionally coordinated in transcriptional repression (Müller and Verrijzer, 2009). Although this premise is still cited in the literature, its operational status is equivocal as there are genes that are targeted by PRC2 without PRC1, and vice versa (Tavares et al., 2012). Clearly, there is still much to be learned about the molecular mechanism underlying the coordination between H2AK119ub1 and H3K27me3.

Cullin 4-Ring E3 ligases (CRL4), assembled with CUL4, DDB1, and ROC1 as the core components, participate in a broad variety of physiologically and developmentally controlled processes such as cell cycle progression, replication, and DNA damage response (Jackson and Xiong, 2009). In mammals, there are two Cullin 4 members, CUL4A and CUL4B. Loss-of-function mutation in the X-linked *CUL4B* causes mental retardation, short statue, absence of speech, and other phenotypes in humans (Zou et al., 2007). In *CUL4B* heterozygotes, the cells in which wild-type (WT) *CUL4B* allele is inactivated are severely selected against, underscoring the functional importance of CUL4B in cellular proliferation (Zou et al., 2007). Accordingly, *Cul4b* knockout mice are embryonically lethal (Jiang et al., 2012). It is interesting that CUL4B, unlike CUL4A and other Cullins, carries a nuclear localization signal (NLS) in its N terminus and is also localized in the nucleus (Nakagawa and Xiong, 2011; Zou et al., 2009), suggesting that CUL4B might be involved in the nucleus-based functions. We addressed these issues using molecular, cellular, and epigenetic approaches plus animal models.

Significance

Cullin 4B (CUL4B) is a scaffold protein of the Cullin4B-Ring E3 ligase complex (CRL4B) that functions in proteolysis. However, recent studies indicate that CUL4B could also be localized in the nucleus, suggesting that CUL4B might be also involved in the nucleus-based functions. In addition, although it was shown that H2AK119 monoubiquitination plays a central role in transcriptional repression by coordinating with H3K27 trimethylation, the underlying mechanisms remains to be clarified. We demonstrated CRL4B is an alternative histone modification enzyme responsible for H2AK119ub1 and that CRL4B and PRC1 bind to PRC2 subunits in a mutually exclusive manner. These data provide a molecular basis for the functional interplay between H2AK119ub1 and H3K27me3 in transcription repression.

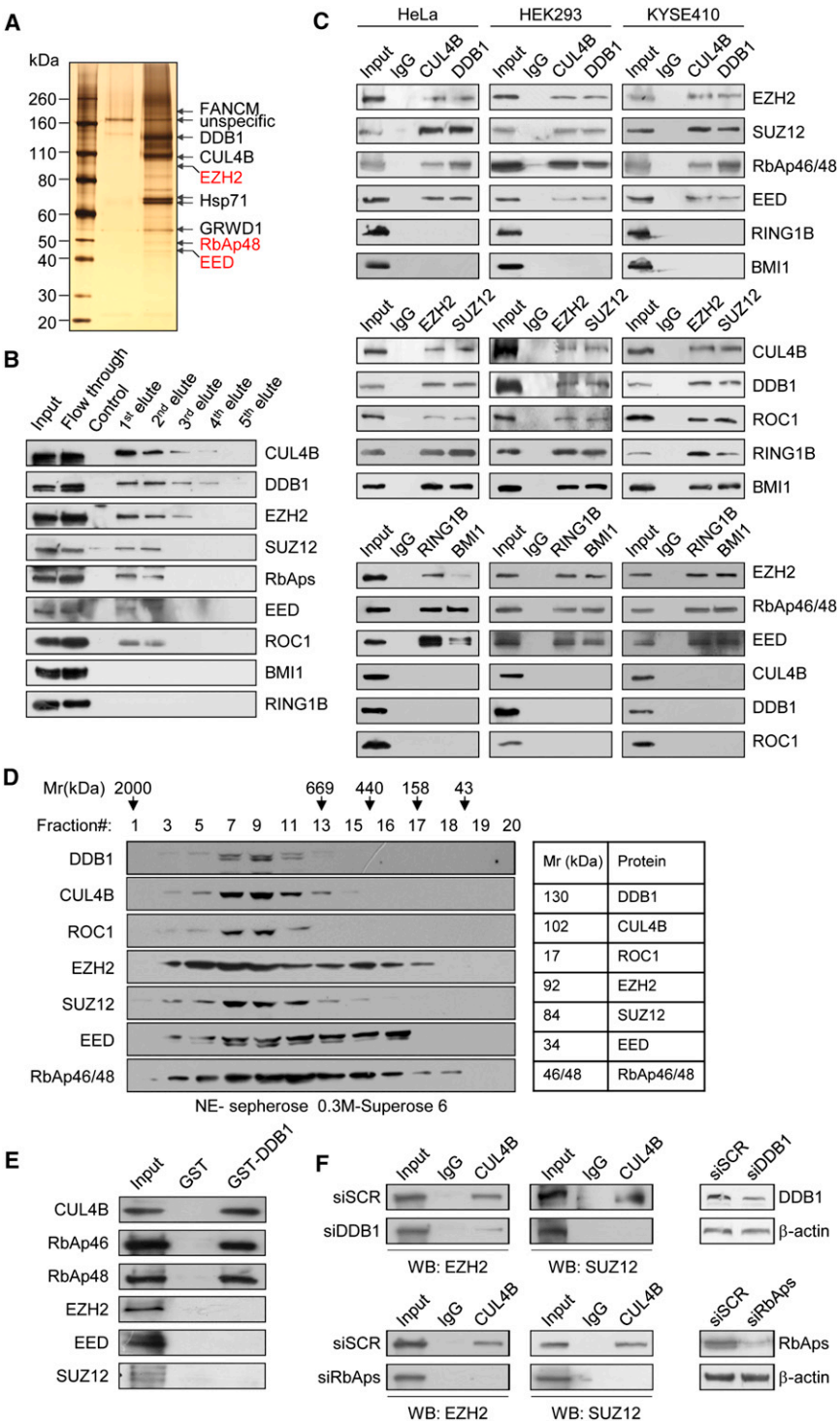

Figure 1. CRL4B Interacts with PRC2

(A) Immunoaffinity purification of CUL4B-containing protein complexes. Cellular extracts from HeLa cells stably expressing FLAG (control) or FLAG-CUL4B were immunopurified with anti-FLAG affinity columns and eluted with FLAG peptide. The eluates were resolved by SDS-PAGE and silver-stained. The protein bands were retrieved and analyzed by mass spectrometry. Detailed results from the mass spectrometric analysis are provided as Table S1.

(B) Western blotting analysis of the purified fractions using antibodies against the indicated proteins.

(C) Association of CRL4B with PRC2 in HeLa, HEK293, and KYSE410 cells. Whole cell lysates were immunoprecipitated with the antibodies against the indicated proteins. Immunocomplexes were then immunoblotted using antibodies against the indicated proteins. IgG served as the negative control.

(D) Cofractionation of the CRL4B complex and the PRC2 complex by fast protein liquid chromatography. Nuclear extracts of HeLa cells were fractionated on a DEAE sepharose column followed by a Superose 6 gel filtration column. The fractions were analyzed by western blotting. Molecular weight standards are shown on top (in kDa). The predicted molecular size of each main component of the CRL4B-PRC2 complex is summarized on the right.

(E) Molecular interaction between DDB1 and PRC2 subunits. GST pull-down experiments with bacterially expressed GST-DDB1 and the in-vitro-transcribed/translated indicated proteins.

(F) IP assays using lysates from HeLa cells transiently expressing DDB1 siRNA or RbAp48 siRNA showing decreased co-IP of CUL4B with EZH2 and SUZ12. The protein expression in these experiments was examined by western blotting using antibodies against the indicated proteins. See also Table S1.

RESULTS

Cullin 4B-RING E3 Ligase Is Physically Associated with PRC2 In Vivo

In an effort to better understand the mechanistic role of CUL4B, we used affinity purification and mass spectrometry to identify the proteins that are associated with CUL4B in vivo. In these experiments, FLAG-tagged CUL4B (FLAG-CUL4B) was stably expressed in HeLa cells. Cellular extracts were prepared and subjected to affinity purification using an anti-FLAG affinity gel. Mass spectrometric analysis indicates that CUL4B copurified with DDB1, GRWD1, COPS3, COPS4, and COPS5, as reported previously (Groisman et al., 2003; Higa et al., 2006). It is interesting that we found that CUL4B also copurified with EZH2, EED, and RbAp48, all of which are the core components of the PRC2 complex (Figure 1A). In addition, heat shock 70 kDa protein 8 (HSP71/73) and Fanconi anemia complementation group M (FANCM) were also detected in the immunocomplex. However, BMI and RING1B, the core components of PRC1 (Cao et al., 2005), did not copurify with CUL4B (Figure 1B, bottom two panels), suggesting that the association of CUL4B with PRC2 is specific. The presence of

EZH2, EED, and RbAp48 in the CUL4B-interacting complex was further confirmed by western blotting analysis (Figure 1B). The detailed results of the mass spectrometric analysis are provided in Table S1 (available online).

To further validate the in vivo interaction between Cullin 4B-RING E3 ligase (CRL4B) and PRC1/2, total proteins from HeLa cells, HEK293 cells (a human embryonic kidney cell line), and KYSE410 cells (a human esophageal squamous cell carcinoma cell line) were extracted and coimmunoprecipitation (co-IP) experiments were performed with antibodies detecting the endogenous proteins. Immunoprecipitation (IP) with antibodies against CUL4B or DDB1 followed by immunoblotting (IB) with antibodies against EZH2, SUZ12, EED, or RbAp46/48 representing PRC2 or against RING1B or BMI representing PRC1 demonstrated that only the PRC2 core components were efficiently coimmunoprecipitated with CUL4B and DDB1 (Figure 1C, upper panels). Reciprocally, IP with antibodies against EZH2 or SUZ12 followed by IB with antibodies against CRL4B subunits CUL4B, DDB1, or ROC1 or against the two PRC1 core components in these three cell lines revealed that both PRC1 and CRL4B complexes were coimmunoprecipitated with PRC2 (Figure 1C, middle panels). However, only PRC2 components could be copurified with PRC1 (Figure 1C, lower panels). These results suggest that CRL4B and PRC1 proteins bind with PRC2 components in a mutually exclusive manner.

To further support the observation that CRL4B complex is associated with PRC2 in vivo, protein fractionation experiments were carried out with nuclear proteins by fast protein liquid chromatography (FPLC). Nuclear extracts derived from HeLa cells were fractionated by DEAE sepharose, followed by superpose 6 gel filtration chromatography. Western blotting revealed a major peak at about 669-1000 kDa for CUL4B, DDB1, and ROC1, and also for PRC2 core components EZH2, SUZ12, EED, and RbAp46/48 (Figure 1D). Significantly, the chromatographic profiles of CUL4B, DDB1, and ROC1 were largely overlapped with that of the components of PRC2, supporting the argument that CRL4B complex is associated with PRC2 in vivo.

In order to further strengthen the argument, we next investigated the molecular basis for the interaction between the CRL4B complex and PRC2. For this purpose, GST pull-down assays were performed using GST-fused CUL4B or GST-fused DDB1 and in-vitro-transcribed/translated EZH2, SUZ12, EED, RbAp46, and RbAp48. These experiments revealed that, although CUL4B interacts directly with DDB1, it did not interact with the PRC2 components that we tested. However, it was shown that DDB1 could interact directly with the two DWD motif (DDB1-binding WD40 protein)-containing molecules, RbAp46 and RbAp48 (Figure 1E), suggesting that DDB1 and RbAp46/48 could act as the bridge molecules in physically linking the CRL4B complex and PRC2. It is interesting that the EED component of PRC2, which also contains a WD40 motif but has no DWD motif, did not show a direct interaction with DDB1, consistent with a previous report (He et al., 2006). The in vitro GST pull-down results were further substantiated by in vivo co-IP experiments in which depletion of either DDB1 or RbAp46/48 could disrupt the interaction between CUL4B and the PRC2 subunits, EZH2 and SUZ12, in HeLa cells (Figure 1F). Taken together, these results provide strong support for a physical association between CRL4B and PRC2 that is bridged by DDB1 and RbAp46/48.

CRL4B Exhibits Transcription Repressive Activity and Promotes H2AK119 Monoubiquitination

The physical association between CRL4B and PRC2 prompted us to investigate the hypothesis that CRL4B might be functionally involved in transcription repression. To this end, we fused CUL4B to Gal4 DNA-binding domain (Gal4-CUL4B) and tested the effect of this construct on the expression of a luciferase reporter gene driven by TK (thymidine kinase) promoter plus five copies of Gal4 binding sequence (Gal4-Luc) in HeLa cells (Figure 2A, upper panel). The results revealed that the expression of Gal4-CUL4B, but not FLAG-CUL4B, led to a drastic decrease in the expression of the reporter gene (Figure 2A, lower panel), indicating that CUL4B has an intrinsic transcriptional repression activity and suggesting that CUL4B could act as a transcription corepressor.

In order to further support this proposition, we investigated the contribution of each of the different domains of CUL4B to its transcriptional repressive function. A series of Gal4-DBD-fused deletion constructs were generated, and the repressor activities of those constructs were monitored using Gal4 UAS luciferase reporter assays (Figure 2B, upper panel). Notably, deletion of the NLS (1–137 amino acids [aa]) (ΔNLS) or NEDD8 neddylation domain (824–895 aa) (ΔNEDD8) did not affect their repressive activities, whereas deletion of either the DID (DDB1-interacting domain) region (137–287 aa) (ΔDID) or Cullin domain (578–718 aa) (ΔCullin) or both resulted in a significant reduction of the transcriptional repressive activity of CUL4B (Figure 2B, lower panel). Thus, it appears that both DID and Cullin domains are required for the transcriptional repressive activity of CUL4B, suggesting that the interaction with DDB1 and ubiquitination function of CUL4B are indispensable for its transcription repressive function.

To further explore the functional connection between CUL4B and PRC2, we performed loss-of-function experiments in the Gal4 UAS luciferase reporter system. As shown in Figure 2C, knockdown of DDB1, EZH2, or RbAps, the components of PRC2, led to a significant reduction of the transcriptional repressive activity of CUL4B, while depletion of BMI or RING1B, the core components of PRC1, had little effect. Again, these experiments suggested that CUL4B functions in transcriptional repression in the context of CRL4B and supported our hypothesis that CRL4B and PRC2 are functionally connected.

H2AK119 monoubiquitination was reported to play a central role in transcriptional repression by coordinating with H3K27me3 (Baarends et al., 2005; Müller and Verrijzer, 2009). Based on our observations that CRL4B and PRC2 are physically and functionally connected, we thus wanted to know whether CRL4B exerts transcriptional repressive activity through H2AK119 monoubiquitination. For this purpose, we performed quantitative chromatin IP (qChIP) assay in HeLa cells that were stably expressing Gal4-UAS reporter (HeLa-Gal4-Luc) to investigate the recruitment of DDB1 and EZH2 to and the changes of H2AK119ub1, H3K27me3, and H3K4me3 on the Gal4 promoter after transfection of these cells with Gal4-CUL4B or control Gal4-DBD. The results showed that artificial recruitment of CUL4B resulted in the recruitment of DDB1 and EZH2,

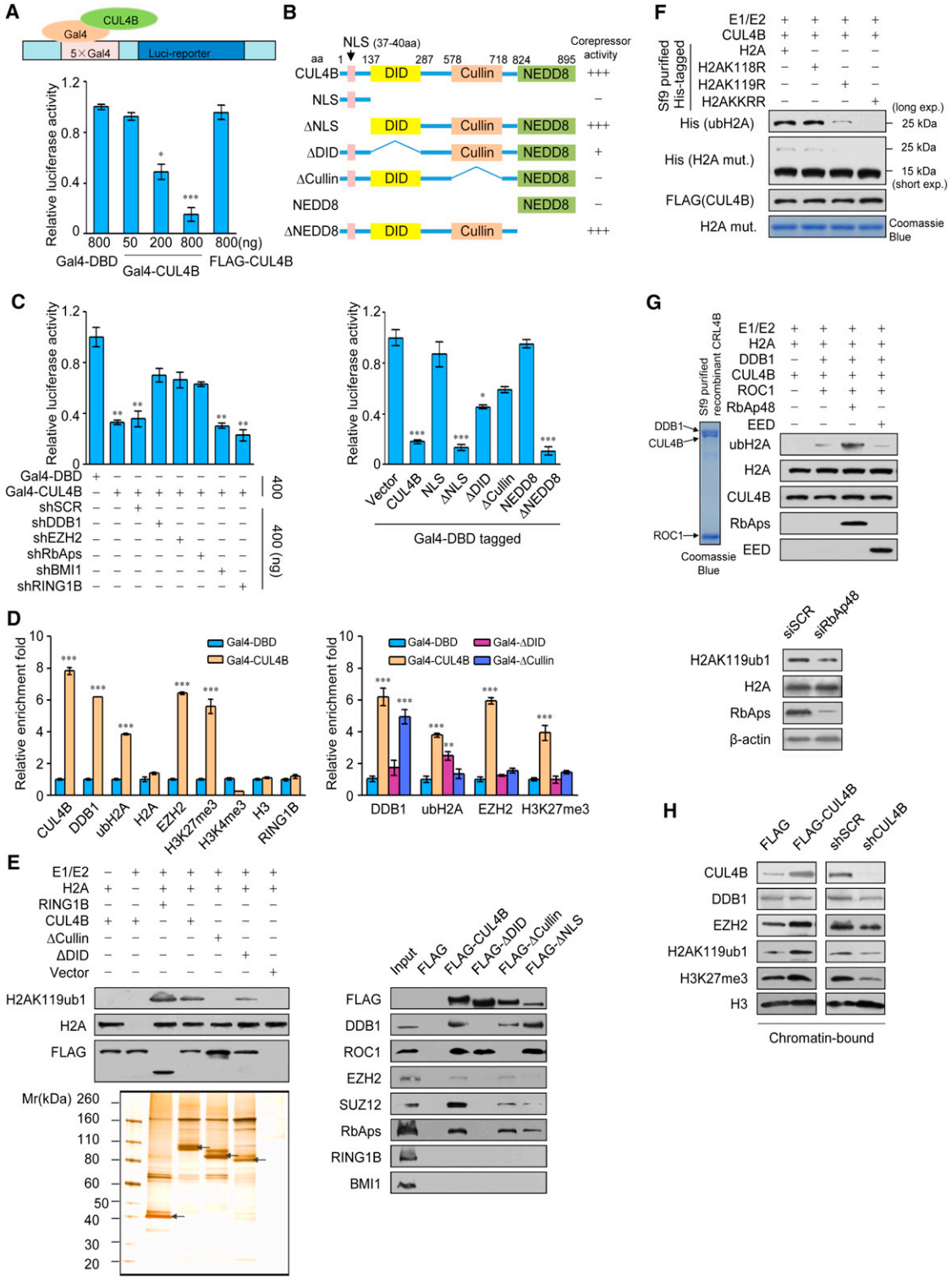

Figure 2. CUL4B Requires Its DID Domain and Cullin Domain for Optimal Repressive Activity

(A) CUL4B possesses an intrinsic transcription repressive activity. Gal4-CUL4B construct or a control vector (containing Gal4-DBD only) was transfected into HeLa cells stably expressing Gal4-UAS reporter (HeLa-Gal4-Luc cells). Gal4 luciferase reporter activity was measured.

(B) Identification of the essential domains required for the transcriptional repressive activity of CUL4B. The upper panel shows the schematic of the CUL4B deletions fused to the C terminus of GAL4 DNA-binding domain. The region fused to Gal4-DBD is graphically depicted. In the lower panel, Gal4 luciferase reporter assay was performed in HeLa-Gal4-Luc cells by transfection of Gal4-DBD-fusion deletion expression vectors. Relative activity is scored with −, +, ++, or +++ corresponding to the significance to facilitate the interpretation of the data.

increased H2AK119ub1 and H3K27me3 levels, and a decreased level of H3K4me3 (Figure 2D, left panel); whereas RING1B, a core component of the PRC1 complex, which was reported to contribute to the monoubiquitination of hisone H2AK119 (de Napoles et al., 2004), was dispensable in this case (Figure 2D, left panel). These experiments support an argument that CRL4B is functionally associated with H2AK119 monoubiquitination. Next, qChIP experiments were performed in HeLa-Gal4-Luc cells that were transfected with Gal4-CUL4B, Gal4-ΔDID, Gal4-ΔCullin, or control Gal4-DBD to investigate the recruitment of DDB1 and EZH2 to and the changes of the H2AK119ub1 and H3K27me3 on the Gal4 promoter. The results showed that, compared to Gal4-CUL4B, ΔDID mutant lost the ability to recruit endogenous DDB1 or EZH2 but still could bind to Gal4-UAS with the artificial recruitment by Gal4-DBD tag and conduct H2AK119 monoubiquitination through classical E1/E2 machinery, resulting in a marginal decrease in monoubiquitination on H2AK119 (Figure 2D, right panel). Although ΔCullin mutant retained the ability to recruit endogenous DDB1, it had no enzymatic activity on H2AK119 (Figure 2D, right panel), thus losing the ability to recruit EZH2 and trimethylate H3K27. These data are in agreement with a functional scheme of CRL4B in which CUL4B relies on its Cullin domain to recruit the enzymatic activity while it uses the DID domain to capture the substrates, favoring our argument that CRL4B promotes H2AK119 monoubiquitination.

To further validate this proposition, we performed in vitro ubiquitination assays. HeLa cells were transfected with FLAG-RING1B, FLAG-CUL4B, FLAG-ΔDID, FLAG-ΔCullin, or FLAG control vector. Cell lysates were affinity purified using FLAG M2 affinity gel, followed by in vitro ubiquitination assays. The results showed that H2AK119 is monoubiquitinated by CRL4B in an E1/E2- and E3-dependent manner (Figure 2E, left panel). It is interesting that, while ΔDID could weakly monoubiquitinate H2A on lysing 119, ΔCullin completely lost such enzymatic activity (Figure 2E, left panel). Co-IP experiments further confirmed that the DID domain is responsible for the formation of the CRL4B-PRC2 machinery, while Cullin domain is responsible for the binding of the ring finger protein ROC1 along with E1/E2/E3 (Figure 2E, right panel). As a positive control, affinity-purified FLAG-RING1B elution was more efficient in the catalysis of H2AK119ub1 than FLAG-CUL4B elution (Figure 2E, left panel). Experiments with H2A and its mutants, K118/R, K119/R, and K118/R+K119/R, indicated that the major ubiquitination site is K119, while residual ubiquitination is found at K118, as reported previously (Richly et al., 2010) (Figure 2F). It is known that Cullins do not directly bind to their substrates directly; they rely on adaptor/receptor proteins in their substrate recognition, such as F-box proteins for CUL1, BTB proteins for CUL3, and WD40 proteins for CUL4 (Zimmerman et al., 2010). To determine which WD40 protein is used for CUL4B to recognize H2AK119, we purified CRL4B subunits CUL4B, DDB1, and ROC1, respectively, from Sf9 insect cells. In vitro ubiquitination assays with the purified proteins showed that the WD40 protein RbAp46/48, not EED, acted as the substrate adaptor/receptor for CUL4B to recognize H2AK119 (Figure 2G, upper panels). Conversely, knocking down RbAp48 resulted in the decrease of H2AK119ub1 (Figure 2G, lower panels). Interestingly, we also found that the amount of chromatin-bound EZH2 was positively correlated with the expression level of CUL4B (Figure 2H) and that the transcription factors such as JARID2 and PHF1 that are essential for PRC2 recruitment (Sarma et al., 2008; Shen et al., 2009) could also interact with CRL4B (Figure S1), further supporting a functional connection between CRL4B and PRC2.

Depletion of CUL4B or Ablation of *Cul4b* Resulted in the Loss of H2AK119ub1 as well as H3K27me3

To further explore the functional relationship between CUL4B and PRC2, we next investigated whether CUL4B depletion would alter H2AK119ub1 and H3K27me3 in vivo. CUL4B-specific shRNA were tagged with enhanced green fluorescent protein (EGFP) and transfected into HeLa cells. Forty-eight hours posttransfection, cells were fixed and stained with antibodies recognizing CUL4B, H2AK119ub1, and H3K27me3. As shown in Figure 3A, although the expression of EZH2 was not affected by CUL4B knockdown, the signals representing H2AK119ub1 and H3K27me3 were significantly reduced in CUL4B-depleted cells, while H3K4me3 signals were slightly increased (marked by arrows). These observations were corroborated by western blotting (Figure 3B).

To further explore the importance of CUL4B in PRC2-mediated gene silencing in vivo, we examined the effect of CUL4B deficiency on the global level of H2AK119ub1 and

(C) Effect of depletion of DDB1, EZH2, BMI, or RING1B on CUL4B repressive activity. HeLa-Gal4-Luc cells were transiently transfected with DBD or DBD-CUL4B constructs along with the indicated shRNAs for 48 hr before luciferase assay. shSCR, control scrambled shRNA.
(D) CUL4B confers repressive activity through H2AK119ub1 catalysis and PRC2 recruitment. ChIP experiments were performed with transient transfection of Gal4-DBD, Gal4-CUL4B, or its deletion constructs. Chromatin was immunoprecipitated with antibodies against the proteins indicated at the bottom. ubH2A, H2AK119 monoubiquitination. DNA enrichment was analyzed at the Gal4 promoter and the results are presented as fold of enrichment over control. In (A–D), all the error bars represent mean ± SD of three independent experiments, and a two-tailed t test was performed (*$p < 0.05$; **$p < 0.01$; ***$p < 0.001$).
(E) The left panel shows in vitro ubiquitination analysis with recombinant CUL4B and CUL4B deletions incubated with different combinations of E1/E2 and recombinant H2A (substrate) along with ubiquitin and ATP. Reactants were subjected to IB with the indicated antibodies. A silver-stained gel on the bottom shows the quality of the isolated complexes. Arrows correspond to the overexpressed FLAG-tagged proteins. In the right panel, HeLa cells were transfected with FLAG-CUL4B or FLAG-tagged mutants, and whole-cell extracts were immunoprecipitated with anti-FLAG M2 resin followed by western blotting with antibodies against DDB1, ROC1, EZH2, SUZ12, RbAps, RING1B, or BMI.
(F) In vitro ubiquitination with recombinant His_6-tagged H2A and its mutants (Mut) purified from Sf9 insect cells. The recombinant substrates were stained by Coomassie blue and shown on the bottom. Exp, exposure.
(G) Upper panels show (left) Coomassie blue staining of CRL4B complex (containing CUL4B, DDB1, and ROC1) purified from Sf9 cells and (right) in vitro ubiquitination analysis using recombinant His_6-tagged CRL4B alone or with WD40 proteins RbAp48 or EED as substrate adaptor/receptors. His_6-tagged CUL4B served as a negative control. In the lower panels, western blotting analysis shows decrease in H2AK119ub1 in HeLa cells upon RbAp48 knockdown.
(H) CUL4B is required for the binding of EZH2 to chromatin and shares the same transcription factors with PRC2. Chromatin-bound fractions were prepared from HeLa cells and analyzed by immunoblotting with the indicated antibodies. Histone H3 served as a loading control.
See also Figure S1.

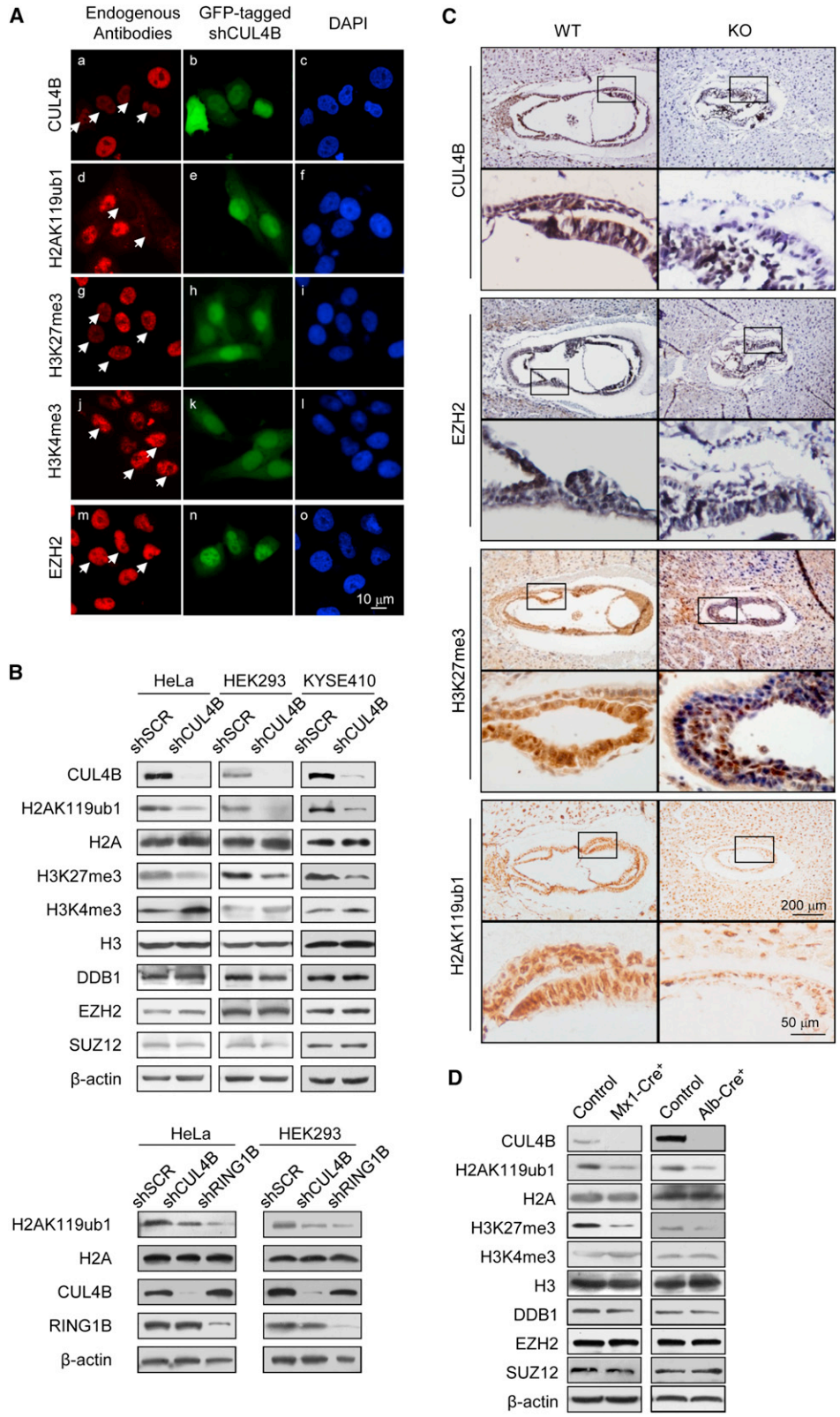

Figure 3. Knockdown of CUL4B or Ablation of Cul4b Resulted in Reduced H2AK119 Monoubiquitination and H3K27 Trimethylation

(A) HeLa cells were transiently transfected with EGFP-carrying CUL4B shRNA and stained with antibodies against CUL4B or EZH2 (red) or against H2AK119ub1, H3K27me3, or H3K4me3 (red). Nucleus was counterstained by DAPI. Significant decrease in H2AK119ub1 and H3K27me3 levels was marked with arrows.

H3K27me3 in *Cul4b* knockout mice. Since *Cul4b* null embryos usually die between 8.5 and 9.5 days postcoitum (dpc), we performed immunostaining on paraffin-embedded *Cul4b* WT and *Cul4b* null (KO) embryos at 7.5 dpc. Immunostaining revealed a significant decrease in H2AK119ub1 and H3K27me3 in the *Cul4b* null embryos, although the level of Ezh2 was comparable to that in WT E7.5 embryos (Figure 3C). These results support a notion that CUL4B is required for the monoubiquitination of H2AK119 and trimethylation of H3K27 during early embryonic development. In addition, examination of the global level of H2AK119ub1 and H3K27me3 in liver from liver-specific *Cul4b* knockout mice [Cul4b (loxp/Y)/Mx-1-Cre(+) and Cul4b (loxp/Y)/Alb-Cre(+)] by western blotting showed a significant reduction of both H2AK119ub1 and H3K27me3 in liver (Figure 3D), further supporting the arguments that CUL4B is required for the trimethylation of H3K27 and that CUL4B and PRC2 are functionally connected.

Genome-wide Identification of Transcription Targets for the CRL4B/PRC2 Complex

To further investigate the functional connection between CRL4B and PRC2 and to explore the biological significance of this connection, we next analyzed the genome-wide transcriptional targets of the CRL4B/PRC2 complex using the ChIP-on-chip (ChIP-on-chip) approach. In these experiments, ChIP experiments were conducted in KYSE410 cells with antibodies against CUL4B, EZH2, or BMI. Following ChIP, CUL4B-, EZH2-, and BMI-associated DNAs were amplified using nonbiased conditions, labeled, and hybridized to an oligonucleotide array covering 2.7 kb (−2.2 kb to +0.5 kb with respect to transcription start sites) of 18,028 annotated transcripts in the NCBI database with a false discovery rate less than 0.05 (GEO accession number: GSE41639). The data from CUL4B antibodies (1,463 genes) were then analyzed with the data from EZH2 (3,705 genes) and BMI antibodies (891 genes) for the identification of common targets, or cotargets (Figure 4A, left panel). The detailed results of the ChIP-on-chip experiments were summarized in Tables S2–S8. A total of 619 unique promoters were found to be cotargeted by CUL4B and EZH2, among which only 53 were overlapped with the 891 targets of BMI, indicating a predominant cooperation between PRC2 and CRL4B, at least in KYSE410 cells. The cotargets of CUL4B/CRL4B and EZH2/PRC2 were then classified into various cellular signaling pathways using Molecule Annotation System software (http://www.capitalbio.com/lifescience/informationsystems/2572.shtml), with a p value cutoff of 10^{-3} (Figure 4A, right panel). These signaling pathways include Wnt, MAPK, focal adhesion, IGF, and apoptosis that are critically involved in cell growth, survival, migration, and invasion. The genes in these pathways include, among others, *PTEN*, *SOCS1*, *AXIN2*, *SIAH1*, *RUXN1*, *FANCB*, *MCM8*, *COL4A1*, *IGFBP3*, and *CDKN2A (p16)*, that are known to be implicated in apoptosis and tumor suppression. Significantly, *FOXO3, E2F1, IGFBP3, p16,* and *TGFBI* have been shown to be transcriptionally repressed by PRC2 (Chen et al., 2009; Tan et al., 2007; Wu et al., 2010). Quantitative ChIP analysis in KYSE410 cells using specific antibodies against CUL4B, EZH2, RING1B, H2AK119ub1, and H3K27me3 on selected genes, including *PTEN*, *SOCS1*, *AXIN2*, *CXCR2*, *FOXO3*, *SIAH1*, *E2F1*, *RUXN1*, *FANCB*, *MCM8*, *NKD2*, *COL4A1*, *IGFBP3*, *p16*, *MLL3*, *CABLES2*, *RNH1*, and *TGFBI*, which represent each of the classified pathways, showed a strong correlation between CUL4B/H2AK119ub1 and EZH2/H3K27me3 enrichments, validating the ChIP-on-chip results (Figures 4B and 4C). Quantitative real-time PCR (qPCR) further showed that the transcription levels of most of the target genes significantly increased in KYSE410 cells upon knockdown of CUL4B or EZH2 (Figure S2).

We next investigated the effect of EZH2 depletion on the recruitment of CUL4B on endogenous target loci and vice versa. To this end, we established KYSE410 cells in which EZH2 expression was knocked down by its shRNA. In these cells, EZH2 was greatly reduced or barely detectable at the promoters of its target genes (Figure 4D, left panel). It is interesting that ChIP experiments with antibodies against CUL4B showed that EZH2 depletion resulted in only marginal or no effect on the recruitment of CUL4B on the target promoters (Figure 4D, right panel). However, in CUL4B-depleted KYSE410 cells, the recruitment of EZH2 to its target promoters was greatly reduced (Figure 4E), although the expression of EZH2 was not affected by CUL4B knockdown (see Figure 3B). In addition, consistent with our earlier observations, the levels of both H2AK119ub1 and H3K27me3 were markedly decreased at all the tested target genes upon CUL4B knockdown (Figure 4F). Collectively, these data suggest that CRL4B may function to promote the recruitment and/or the stabilization of PRC2 onto target promoters, supporting our aforementioned arguments that CUL4B and PRC2 are functionally connected and that CUL4B is required for the trimethylation of H3K27.

Regulation of *p16* and *PTEN* by the CLR4B/PRC2 Complex

Among the common target genes identified earlier, *p16* and *PTEN* are well-established tumor suppressor genes (Lowe and Sherr, 2003; Salmena et al., 2008). We thus further investigated the transcriptional regulation of *p16* and *PTEN* by CUL4B. As expected, CUL4B knockdown in KYSE410, HeLa, HEK293, MCF-7 (human breast adenocarcinoma cell line), and U2OS (human osteosarcoma cell line) led to increased expression of *p16* and *PTEN* at both the transcriptional level (Figure 5A, left panel) and the protein level (Figure 5A, right panel). Significantly, the levels of p16 and PTEN were also elevated in *Cul4b* null embryos (Figure 5B).

We then investigated the regulation of *p16* and *PTEN by* the CLR4B/PRC2 complex. ChIP assays in KYSE410 cells with

(B) Western blotting analysis showing decrease in H2AK119ub1 and H3K27me3 in HeLa, HEK293, and KYSE410 cells upon CUL4B knockdown (upper panels). RING1B knockdown served as a positive control (lower panels).
(C) Immunohistochemical staining of 7.5 dpc in utero embryo sections using antibodies recognizing mouse Cul4b, Ezh2, H3K27me3, and H2AK119ub1 in WT (left panels) and Cul4b KO (right panels) embryos. Different magnifications of the same embryos are presented.
(D) Western blotting analysis showing loss of H2AK119ub1 and H3K27me3 as well as Cul4b protein in conditional liver-specific *Cul4b* ablation mice. Histones H2A and H3 were used as loading controls.

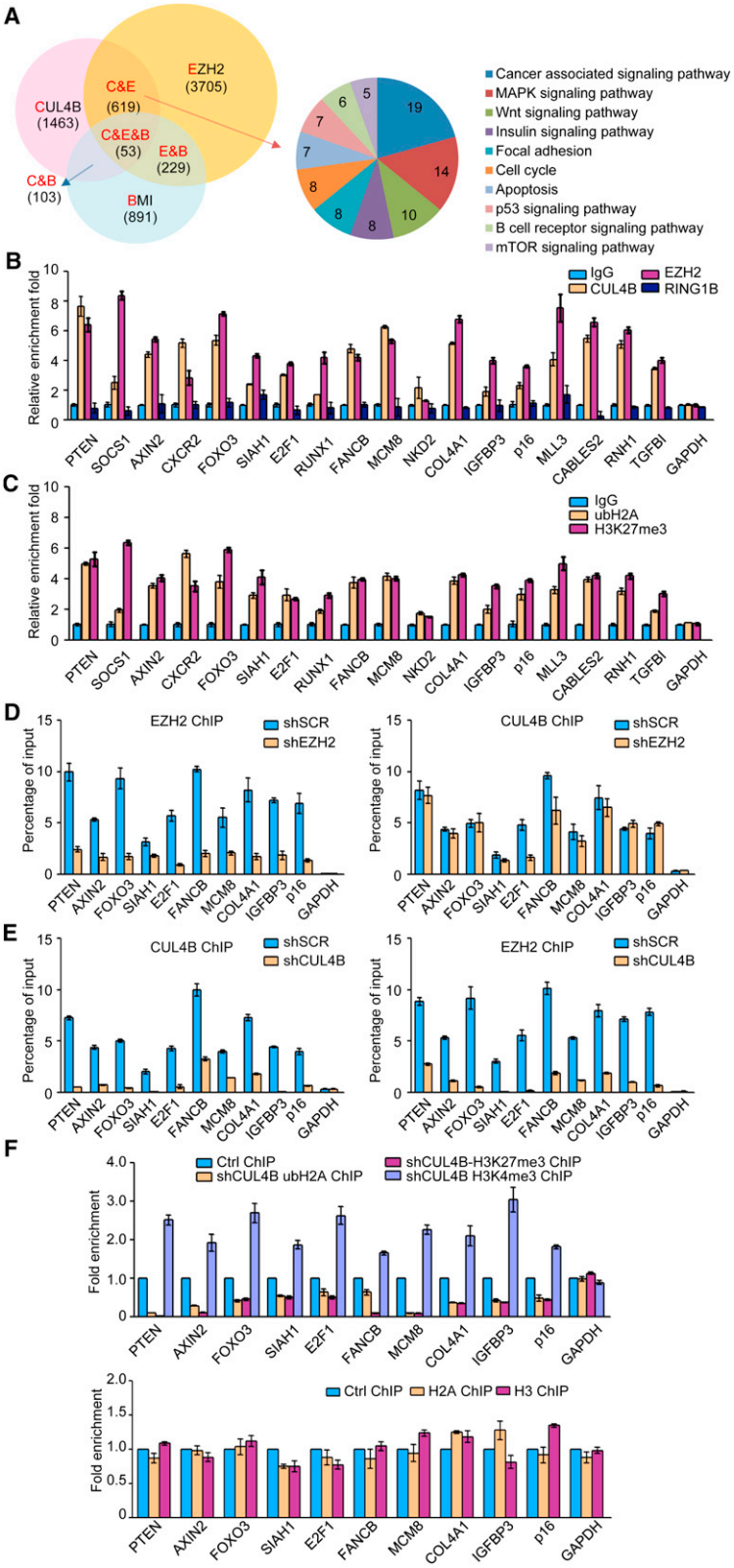

Figure 4. CUL4B/CRL4B and EZH2/PRC2 Co-Occupy Target Genes

(A) The left panel is a Venn diagram showing a statistically significant overlap between promoters bound by CUL4B, EZH2, and BMI in KYSE410 cells. The numbers represent the number of the promoters that were targeted by the indicated proteins. The right panel shows clustering of the 619 overlapping target genes of CUL4B and EZH2 into functional groups.

The detailed results of the ChIP-on-chip experiments are provided in Tables S2–S8.

(B and C) Verification of the ChIP-on-chip results by qChIP analysis of the indicated genes in KYSE410 cells.

(D–F) qChIP analysis of selected promoters in the KYSE410 cells after transfection with control shRNA or shRNAs targeting CUL4B or EZH2 using the indicated antibodies. Results are represented as fold change over control. GAPDH served as a negative control. Error bars represent mean ± SD of three independent experiments. See also Figure S2 and Tables S2–S8.

antibodies against CUL4B, DDB1, EZH2, SUZ12, or control mmnuoglobulin G (IgG) revealed that CRL4B and PRC2 co-occupied the promoters of *p16* and *PTEN* (Figure 5C, upper panels). To further test our proposition that CRL4B and PRC2 function in the same protein complex at *p16* and *PTEN* promoters, sequential ChIP or ChIP/Re-ChIP experiments (Wang et al., 2009) were performed. In these experiments, soluble chromatins were first immunoprecipitated with antibodies against CUL4B, DDB1, EZH2, SUZ12, or H2AK119ub1, while RING1B served as a negative control (Figure 5C, upper panels). The immunoprecipitates were subsequently reimmunoprecipitated with appropriate antibodies. The results showed that, in precipitates, the *p16* and *PTEN* promoters that were immunoprecipitated with antibodies against CUL4B could be reimmunoprecipitated with antibodies against DDB1, EZH2, SUZ12, or H2AK119ub1 (Figure 5C, lower panels). Similar results were obtained when initial ChIP was done with antibodies against DDB1, EZH2, SUZ12, or H2AK119ub1. Furthermore, profiling of the binding patterns of CUL4B, DDB1, EZH2, and SUZ12 by qChIP on a region of ~10 kb upstream and downstream of the transcription start sites of p16 or *PTEN* loci revealed a perfect overlap of the occupancy sites of these proteins, while RING1B/PRC1 binds mainly downstream from the transcription start sites (TSS) of *p16* locus, which is different from CRL4B/PRC2 (Figure 5D). Taken together, these results support the idea that CRL4B and PRC2 occupy the *p16* and *PTEN* promoters in one multiunit complex.

In order to determine a functional connection between CRL4B and PRC2 on *p16* and *PTEN* promoters, KYSE410 cells were transfected with shRNAs specifically against CUL4B, DDB1, EZH2, or SUZ12. Each of these shRNA led to a significant reduction in the expression of its target gene without causing detectable changes of the nontargeted genes (Figure 5E). qChIP analyses showed that knockdown of the expression of CUL4B or DDB1 led to a significant reduction of the binding of EZH2 and SUZ12 to the promoters of *p16* and

PTEN, whereas depletion of EZH2 or SUZ12 expression resulted in only a marginal decrease in the association of CUL4B and DDB1 with the promoters of *p16* and *PTEN* (Figure 5F), which was consistent with the results shown in Figures 4D and 4E. Notably, knockdown of either CUL4B or DDB1 led to a severe decrease in H3K27me3 at the promoters of *p16* and *PTEN*, whereas knockdown of either EZH2 or SUZ12 resulted in a limited reduction in the levels of H2AK119ub1 at the promoters of *p16* and *PTEN* (Figure 5F), suggesting that CRL4B-catalyzed H2AK119ub1 acts sequentially and coordinately with PRC2-mediated H3K27me3.

CUL4B Promotes Cell Proliferation and Invasion

Based on the role of PRC2 in cancer development and progression (Simon and Lange, 2008) and our observation that CRL4B and PRC2 are physically and functionally associated, we next investigated what role, if any, CUL4B plays in tumorigenesis. For this purpose, we first analyzed the effect of gain-of-function and loss-of-function of CUL4B and EZH2 on the cell cycle profile of KYSE410 cells by propidium iodide staining and flow cytometry. KYSE410 cells with stable CUL4B/EZH2 expression or with CUL4B/EZH2 knockdown were synchronized at the G_0/G_1 phases by serum starvation for 24 hr, followed by being released using normal growth media for another 12 hr. Compared with control, CUL4B or EZH2 overexpression was associated with a decreased cell population in G_1 and an increased cell population in the S phases, while KYSE410 cells exposed to CUL4B or EZH2 shRNA exhibited an increase in the proportion of cells in G_1 and a decrease in the proportion of cells in the S phases (Figure 6Aa). Growth curve assays showed that the S-phase accumulation by CUL4B overexpression was not due to S phase arrest (Figure 6Ab). The representative cytometric results from these experiments are shown in Figure S3. Furthermore, western blotting analysis showed that the expression level of CUL4B remained constant at different cell cycle stages, excluding the possibility that proliferation itself increases CUL4B expression (Figure 6B). The cyclin D1 level was low in quiescent cells, and it increased as cells progressed into G1, which served as a control protein (Koepp et al., 1999). These data indicate that CUL4B and EZH2 have similar effect on cell cycle progression in KYSE410 cells, consistent with the role of p16 and PTEN in arresting cells in the G_1 phase (Weng et al., 1999; Zhang et al., 1999). Moreover, colony formation assays further showed that CUL4B overexpression was associated with a marked increase in colony numbers, whereas CUL4B knockdown is associated with a significant decrease in colony numbers (Figure 6C). In addition, while overexpression of WT CUL4B resulted in 1.72-fold increase in colony number, overexpression of CUL4BΔCullin had a dominant negative effect on colony formation (Figure 6D, bars 1–3). Moreover, in agreement with the functional link between CUL4B and p16 described earlier, the positive effect of CUL4B overexpression on colony formation could be partially offset by introduction of exogenous p16 and the decrease in colony formation by CUL4B knockdown could be partially rescued by treatment of cells with p16 shRNA (Figure 6D). In addition, overexpression of CUL4B but knockdown of the expression of EZH2 resulted in a diminished effect of CUL4B on colony formation (Figure 6D, bars 6 and 7). Together, these experiments support a notion that CUL4B promotes esophagus carcinoma cell proliferation and it does so, at least in part, through cooperation with EZH2 and via repression of tumor suppressor p16.

As stated earlier, PRC2 has also been implicated in epithelial-to-mesenchymal transitions (EMT; Herranz et al., 2008). Thus, we next investigated whether CUL4B has a role in EMT and tumor metastasis. For this purpose, CUL4B was overexpressed in KYSE410 cells via stable transfection, and the impact of the gain-of-function of CUL4B on the invasive potential of these cells was assessed using transwell invasion assay. The results showed that, while overexpression of WT CUL4B resulted in more than 3-fold increase in cell invasion, overexpression of the Cullin domain-deleted CUL4B mutant had little effect (Figure 6E, bars 1–3). In addition, the increased invasiveness upon CUL4B overexpression was probably achieved through a concerted action by CRL4B and PRC2, as the effect of CUL4B overexpression was diminished when EZH2 was concomitantly knocked down (Figure 6E, bars 4 and 5). Moreover, the increase in invasiveness associated with CUL4B overexpression could be blocked by PTEN overexpression (Figure 6E, bars 6 and 7). Collectively, these results indicate that CUL4B promotes the invasive potential of KYSE410 cells, possibly by acting in conjunction with PRC2 and by repressing the expression of PTEN.

We next investigated the role of CUL4B in tumor development and progression in vivo by implanting KYSE410 and EC9706 cells that had been engineered to stably express CUL4B shRNA or control scrambled shRNA (shSCR) onto the subcutaneous sites of athymic BALB/c mice. Growth of the implanted tumors was monitored by measuring the tumor sizes every 4 days over a period of 4 weeks. The results showed that tumor growth was greatly suppressed by CUL4B knockdown, indicating that CUL4B had a significant effect on promoting the tumor growth (Figure 6F). Western blotting analysis confirmed the decrease in the levels of H2AK119ub1/H3K27me3 and the increases in the levels of p16 and PTEN proteins in the tumors with CUL4B knockdown (Figure 6G). Immunohistochemical staining for Ki-67, a well-documented marker for cellular proliferation, on serial xenograft tumor sections showed that, compared to the control, tumors with CUL4B knockdown exhibited significantly fewer Ki-67-positive nuclei (Figure 6H). Taken together, these experiments indicate that CUL4B promotes esophageal carcinoma cell proliferation, invasion, and tumorigenesis in vitro and in vivo.

The Expression of CUL4B Is Upregulated in Esophageal Carcinomas and Positively Correlated with Tumor Grade

To further define the role of CUL4B in tumorigenesis, we collected 182 esophageal carcinoma samples, 45 of them with paired adjacent normal tissues, from esophageal cancer patients and performed tissue microarrays by immunohistochemical staining. CUL4B was found to be significantly upregulated in tumors and its expression appeared to be positively correlated with histological grades (Figures 7A and 7B). In 12 of 14 selected paired samples of grade II cancers, the level of *CUL4B* mRNA was found to be higher in tumor tissue than in adjacent tissue, as measured by qPCR (Figure 7C, upper panel) and western blotting (Figure 7C, lower panel), and the levels of p16 and PTEN generally showed an inverse trend with that of CUL4B. Indeed, statistical analysis revealed a significant

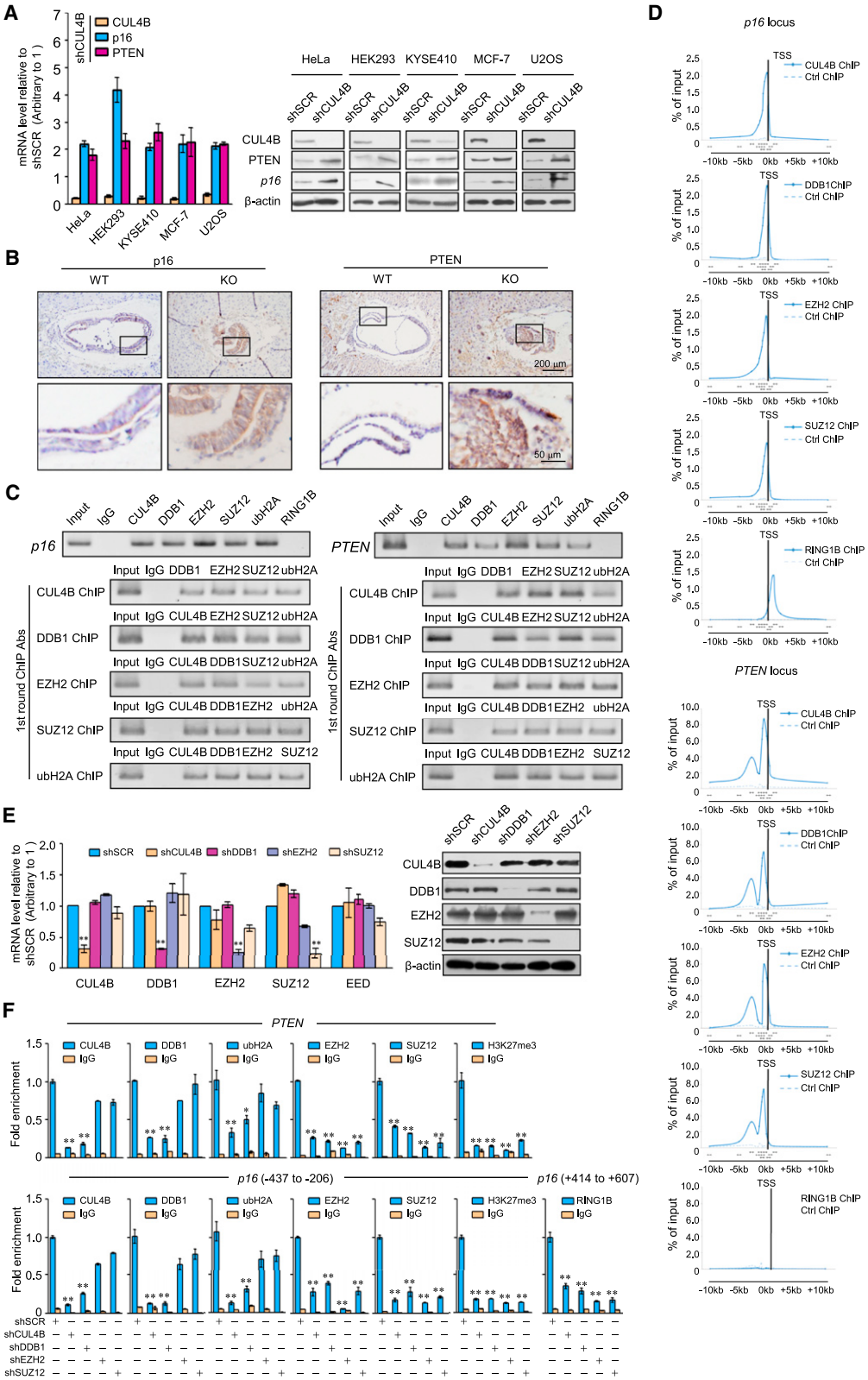

Figure 5. Tumor Suppressor Genes *p16* and *PTEN* Are Cotargeted by CLR4B and PRC2

(A) Clones in which CUL4B was stably knocked down were compared with the parental cell line with respect to the levels of mRNA (left panel) and protein (left panel) of p16 and PTEN in HeLa, HEK293, KYSE410, MCF-7, and U2OS cells. The mRNA levels were normalized to those of GADPH (left panel) and β-actin served as a loading control for the western blotting (right panel).

negative correlation when the relative expression levels of p16 and PTEN were plotted against that of CUL4B in 30 paired samples of grade II (Figure 7D). These data are consistent with a role of CUL4B in promoting carcinogenesis and support the observation that *p16* and *PTEN* are downstream targets of CUL4B.

To investigate whether the tumorigenic effect of CUL4B could be extended to a broader scope of cancers, we collected a series of carcinoma samples from esophageal, lung, gastric, colon, pancreatic, cervical, renal, and bladder cancer patients, with each type of carcinomas having at least three samples paired with adjacent normal tissues. Tissue microarray analysis by immunohistochemical staining showed a statistically significant upregulation of CUL4B expression in carcinomas from multiple tissues compared to the adjacent normal tissues, except for the carcinomas of urinary system (Figure 7E). Since EZH2 has also been reported to be overexpressed in various cancers (Simon and Lange, 2008), we also determined the expression profile of CUL4B and EZH2 using the human cancer survey qPCR gene expression panel (Origene) in tumors originated from breast, colon, kidney, lung, ovary, and thyroid (Figure 7F). The results showed that both CUL4B and EZH2 are overexpressed in all of these cancer groups compared with normal tissue controls except in the kidney. Moreover, the cancer survey cDNA array data also revealed a significant positive correlation between the expression of CUL4B or EZH2 and tumor grade, especially in breast and lung. The expression profiles of CUL4B and EZH2 were very similar. Taken together, these data support a role for CUL4B in promoting tumorigenesis and suggest that CUL4B could serve as a biomarker for cancer diagnosis and a potential target for cancer therapy.

DISCUSSION

Our data indicate CUL4B is a transcriptional corepressor that regulates transcription by recruiting PRC2. The CRL4B subunits do not contain chromatin-binding domains which could contribute to PRC2 recruitment (Figure 7Ga). Although RbAp46/48, two histone binding proteins, were identified to be the bridge molecules for interaction between CRL4B and PRC2, it is more probably that the role of RbAp46/48 in this CRL4B-PRC2 interaction is to recognize and bind histone H2A and H3 (Yoon et al., 2003), thus to further stabilize the binding of this multiunit complex to chromatin rather than to recruit PRC2. To date, PRC2 has been shown to mediate transcription repression by distinct sequence-specific transcription factors. Interestingly, we found that JARID2 and PHF1 could also physically interact with CRL4B in HeLa cells, suggesting that CRL4B and PRC2 may share similar transcription factors thus respond to same signal pathways. Of note, while DNA binding proteins are believed to be responsible for PRC2 recruitment in mammals, recent studies indicated that long noncoding RNA, such as XIST, KCNQ1OT1, and HOTAIR, could also be involved in this process (Maenner et al., 2010; Pandey et al., 2008; Tsai et al., 2010). It is intriguing that Pcu4 and Rik1, the fission yeast homologs of the CUL4 and DDB1, were reported to be involved in noncoding RNA transcription (Hong et al., 2005; Li et al., 2008) (Figure 7Gb). Clearly, future investigations are needed to explore the scope and the variety of the functionality of the CRL4B/PRC2 complex and to determine whether this functionality involves additional elements.

Recent studies showed that there are genes targeted by PRC2 without PRC1, and vice versa (Ku et al., 2008; Tavares et al., 2012). Our findings suggest that CRL4B may function as an alternate histone modification enzyme responsible for H2AK119ub1, providing a molecular basis for the interplay of H2AK119ub1 and H3K27me3 in chromatin remodeling. The replacement of PRC1 by CRL4B could also explain why PRC1 and PRC2 are uncoupled in some instances.

The regulation of *p16* and *PTEN* by CRL4B/PRC2 may have significant physiological implications. In addition to the propositions that CRL4 possibly promotes tumorigenesis through degradation of p53 as well as several cyclin-dependent kinase inhibitors (Banks et al., 2006; Nishitani et al., 2008), our findings add another element to the understanding of the oncogenic potential of CRL4. In this regard, it is interesting to note that CUL4A-DDB1 is reported to cooperate with the MLL1 complex in mediating oncogene-induced p16 activation (Kotake et al., 2009). It appears that CUL4A and CUL4B may have opposite effects on p16 expression and function in a competitive manner. The derepressive effect of CUL4B's loss-of-function combined with the activating effect of CUL4A's gain-of-function resulted in further p16 activation in HeLa and HEK293 cells, in which p16 is highly expressed due to the inactivation of Rb pathway (Kotake et al., 2007). Future studies would clarify whether CRL4 complexes could exert opposite activities depending on the different Cullin member in the complex.

In summary, our study revealed that CRL4B regulates transcription by monoubiquitinating H2AK119 and by coordinating/facilitating PRC2-catalyzed H3K27me3, thus providing a molecular basis for the interplay between histone ubiquitination and methylation in chromatin remodeling. Our data indicate that CUL4B functions as a transcription corepressor and a potential oncogene, supporting the pursuit of CUL4B as a target for cancer therapy.

(B) Different magnifications of immunohistochemical staining using antibodies recognizing mouse p16 and PTEN in WT (left panels) and Cul4B KO (right panels) 7.5 dpc embryos.

(C) The CRL4B and PRC2 complexes exist in the same protein complex on the p16 and PTEN promoters. ChIP and Re-ChIP experiments were performed in KYSE410 cells with the indicated antibodies.

(D) ChIP analysis of the recruitment of CUL4B, DDB1, EZH2, SUZ12, and RING1B on *PTEN* and *p16* gene loci in KYSE410 cells. Rabbit normal IgG served as negative control. ChIP enrichments are presented as percentage of bound/input signal. The position of the qPCR amplicons (arrows) relative to the genes are denoted as black boxes. TSS (dashed line) are also presented in the figure.

(E) The knockdown efficiencies of CUL4B, DDB1, EZH2, and SUZ12 were confirmed by qPCR (left panel) or western blotting (right panel).

(F) qChIP analysis of the recruitment of the indicated proteins on *p16* and *PTEN* promoters in KYSE410 cells after transfection with control shRNA or shRNAs targeting CUL4B, DDB1, EZH2, or SUZ12. RING1B ChIP was also performed on the binding peak shown in Figure 5D. Purified rabbit IgG was used as a negative control. Error bars represent mean ± SD of three independent experiments. *$p < 0.05$ and **$p < 0.01$ (two-tailed unpaired t test).

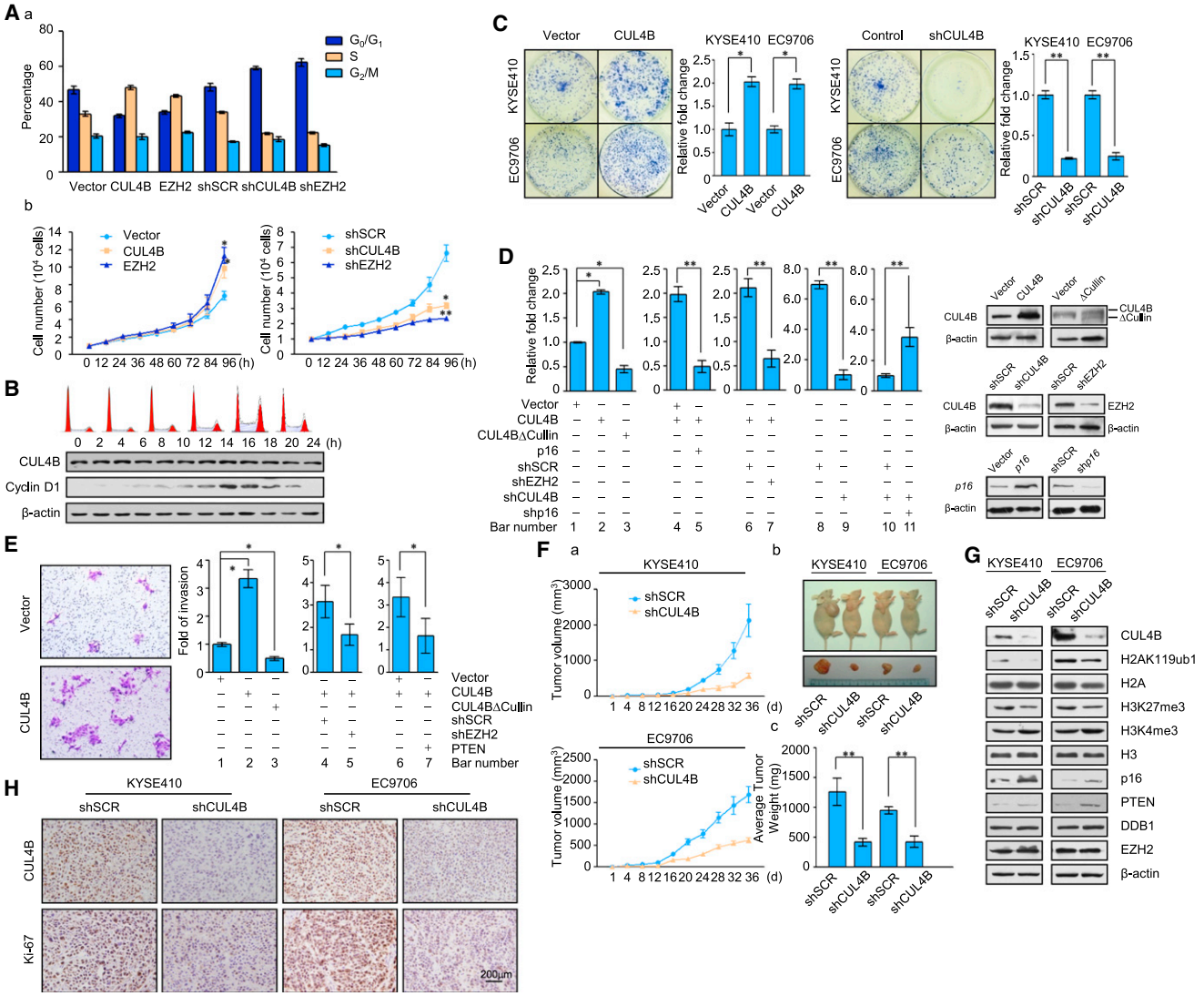

Figure 6. CUL4B Promotes Esophageal Carcinogenesis In Vitro and In Vivo

(A) CUL4B promotes cellular proliferation. KYSE410 cells stably expressing CUL4B/EZH2 or stably transfected with CUL4B/EZH2 shRNA were subjected to cell cycle analysis by flow cytometry (a) and growth curve assay (b). Error bars represent mean ± SD of three independent experiments.

(B) CUL4B remained unchanged throughout the cell cycle in KYSE410 cells. The cells were synchronized at the G0/G1 phases by serum starvation for 24 hr, followed by releasing into normal growth media. Propidium iodide FACS analysis is presented at the top of the panel.

(C) CUL4B enhances the colony-forming efficiency of esophageal cancer cells. KYSE410 cells and EC9706 cells stably expressing corresponding plasmids or shRNA vectors were maintained in culture media for 14 days under the presence of 1 mg/ml G418 prior to being stained with crystal violet.

(D) Enhancement in colony-forming efficiency by CUL4B is p16 and EZH2-dependent. KYSE410 cells were transiently transfected with empty vector, CUL4B expression vector, CUL4ΔCullin expression vector, p16 expression vector, control shRNA, EZH2 shRNA, CUL4B shRNA and p16 shRNA as indicated and maintained in culture media for 14 days under the presence of 1 mg/ml G418 and stained with crystal violet. The protein expression in these experiments was examined by western blotting using antibodies against the indicated proteins.

(E) CUL4B enhances the invasiveness of esophageal cancer cells. KYSE410 cell were transiently transfected with empty vector, CUL4B expression vector, CUL4ΔCullin expression vector, PTEN expression vector, control shRNA, or EZH2 shRNA as indicated and maintained in culture media for 14 days under the presence of 1 mg/ml G418 and assayed for transwell assay. In each experiment in (C–E), at least six randomly selected view fields (40× magnifications) were scored. The number of colonies or transwelled cells in each condition was counted and expressed as mean ± SD from triplicate experiments.

(F) CUL4B promotes esophageal tumorigenesis. KYSE410 and EC9706 cells stably expressing CUL4B shRNA or shRNA were transplanted into athymic mice. Tumors were measured every 4 days using a vernier calliper, and the volume was calculated according to the formula: $1/6 \times \text{length} \times \text{width}^2$. The growth curves of tumors (a), representative images of tumor-bearing mice (b), and their tumors and the average tumor mass of each group (c) are shown. Each point represents the mean ± SEM. *$p < 0.05$ and **$p < 0.01$ (two-tailed unpaired t test).

(G) Western blotting analysis showing loss of H2AK119ub1 and H3K27me3 as well as increase in p16 and PTEN proteins in the tumors.

(H) CUL4B promotes esophageal tumorigenesis through accelerating cell proliferation. Immunohistochemical staining was used, using antibodies against mouse CUL4B and Ki-67 on xenograft tumor sections.

See also Figure S3.

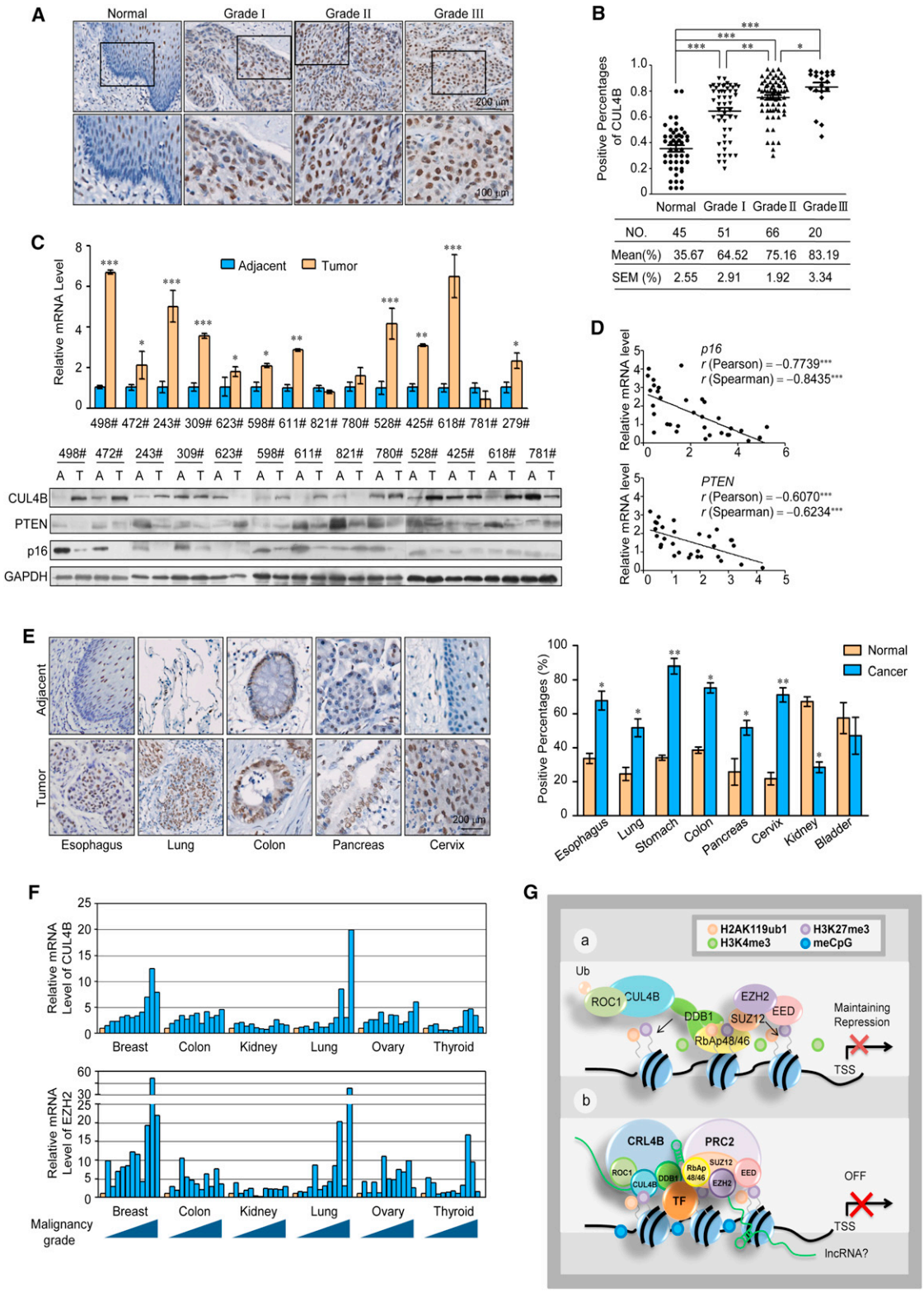

Figure 7. CUL4B Is a Potential Cancer Biomarker

(A) Immunohistochemical staining of CUL4B in normal esophageal tissue and esophageal carcinomas (histological grades I, II, and III). (B) The positively stained nuclei (in percentages) in grouped samples were analyzed by two-tailed unpaired t test (*$p < 0.05$; **$p < 0.01$; ***$p < 0.001$).

(C) The expression of CUL4B mRNA and protein is upregulated in esophageal carcinomas. Total RNAs and proteins in paired samples of esophageal carcinomas versus adjacent normal esophageal tissues were extracted, and the expression of CUL4B was measured by qPCR and western blotting. mRNA levels were

EXPERIMENTAL PROCEDURES

Tumor Xenografts

KYSE410 and EC9706 esophageal cancer cells stably transfected with CUL4B shRNA or scrambled control shRNA were collected, and 2 × 10^6 viable cells in 100 μl PBS were injected subcutaneously into 6- to 8-week-old BALB/c nude mice (Vital River Laboratories, Beijing, China). Eight animals per group (male = 4 and female = 4) were used in each experiment. Tumors were measured every 4 days using a vernier caliper, and the volume was calculated according to the formula: 1/6 × length × square width. All studies were approved by the Animal Care Committee of Shandong University Medical School.

Tissue Specimen and Immunohistochemistry

Esophageal carcinoma tissues were obtained from Qilu Hospital of Shandong University. Samples were frozen in liquid nitrogen immediately after surgical removal and maintained at −80°C until analyzed. Samples were fixed in 4% paraformaldehyde (Sigma-Aldrich) at 4°C overnight, and then embedded in paraffin, sectioned at 8 μm onto Superfrost-Plus Slides, and processed per standard protocols using DAB staining. All human tissue was collected using protocols approved by the Ethics Committee of Shandong University Medical School, and informed consent was obtained from all patients.

ACCESSION NUMBERS

ChIP-on-chip information was deposited at the Gene Expression Omnibus database (http://www.ncbi.nlm.nih.gov/geo/) with the accession number GSE41639.

SUPPLEMENTAL INFORMATION

Supplemental Information includes three figures, eight tables, and Supplemental Experimental Procedures and can be found in this article online at http://dx.doi.org/10.1016/j.ccr.2012.10.024.

ACKNOWLEDGMENTS

This work was supported by the National Natural Science Foundation of China and Ministry of Science and Technology of China (Grant 30830065 to Y.G. and C.S.; Grant 2011CB966201 to Y.W. and C.S.; Grants 90919053 and 31171240 to Y.W.; Grant 81021001 to Y.G. and C.S.; and Grant 2013CB910900 to Y.G.).

Received: May 9, 2012
Revised: August 19, 2012
Accepted: October 31, 2012
Published: December 10, 2012

REFERENCES

Baarends, W.M., Wassenaar, E., van der Laan, R., Hoogerbrugge, J., Sleddens-Linkels, E., Hoeijmakers, J.H., de Boer, P., and Grootegoed, J.A. (2005). Silencing of unpaired chromatin and histone H2A ubiquitination in mammalian meiosis. Mol. Cell. Biol. *25*, 1041–1053.

Banks, D., Wu, M., Higa, L.A., Gavrilova, N., Quan, J., Ye, T., Kobayashi, R., Sun, H., and Zhang, H. (2006). L2DTL/CDT2 and PCNA interact with p53 and regulate p53 polyubiquitination and protein stability through MDM2 and CUL4A/DDB1 complexes. Cell Cycle *5*, 1719–1729.

Cao, R., Tsukada, Y., and Zhang, Y. (2005). Role of Bmi-1 and Ring1A in H2A ubiquitylation and Hox gene silencing. Mol. Cell *20*, 845–854.

Chen, H., Gu, X., Su, I.H., Bottino, R., Contreras, J.L., Tarakhovsky, A., and Kim, S.K. (2009). Polycomb protein Ezh2 regulates pancreatic beta-cell Ink4a/Arf expression and regeneration in diabetes mellitus. Genes Dev. *23*, 975–985.

de Napoles, M., Mermoud, J.E., Wakao, R., Tang, Y.A., Endoh, M., Appanah, R., Nesterova, T.B., Silva, J., Otte, A.P., Vidal, M., et al. (2004). Polycomb group proteins Ring1A/B link ubiquitylation of histone H2A to heritable gene silencing and X inactivation. Dev. Cell *7*, 663–676.

Groisman, R., Polanowska, J., Kuraoka, I., Sawada, J., Saijo, M., Drapkin, R., Kisselev, A.F., Tanaka, K., and Nakatani, Y. (2003). The ubiquitin ligase activity in the DDB2 and CSA complexes is differentially regulated by the COP9 signalosome in response to DNA damage. Cell *113*, 357–367.

He, Y.J., McCall, C.M., Hu, J., Zeng, Y., and Xiong, Y. (2006). DDB1 functions as a linker to recruit receptor WD40 proteins to CUL4-ROC1 ubiquitin ligases. Genes Dev. *20*, 2949–2954.

Herranz, N., Pasini, D., Díaz, V.M., Francí, C., Gutierrez, A., Dave, N., Escrivà, M., Hernandez-Muñoz, I., Di Croce, L., Helin, K., et al. (2008). Polycomb complex 2 is required for E-cadherin repression by the Snail1 transcription factor. Mol. Cell. Biol. *28*, 4772–4781.

Higa, L.A., Wu, M., Ye, T., Kobayashi, R., Sun, H., and Zhang, H. (2006). CUL4-DDB1 ubiquitin ligase interacts with multiple WD40-repeat proteins and regulates histone methylation. Nat. Cell Biol. *8*, 1277–1283.

Hong, E.J., Villén, J., Gerace, E.L., Gygi, S.P., and Moazed, D. (2005). A cullin E3 ubiquitin ligase complex associates with Rik1 and the Clr4 histone H3-K9 methyltransferase and is required for RNAi-mediated heterochromatin formation. RNA Biol. *2*, 106–111.

Jackson, S., and Xiong, Y. (2009). CRL4s: the CUL4-RING E3 ubiquitin ligases. Trends Biochem. Sci. *34*, 562–570.

Jiang, B., Zhao, W., Yuan, J., Qian, Y., Sun, W., Zou, Y., Guo, C., Chen, B., Shao, C., and Gong, Y. (2012). Lack of Cul4b, an E3 ubiquitin ligase component, leads to embryonic lethality and abnormal placental development. PLoS ONE *7*, e37070.

Koepp, D.M., Harper, J.W., and Elledge, S.J. (1999). How the cyclin became a cyclin: regulated proteolysis in the cell cycle. Cell *97*, 431–434.

Kotake, Y., Cao, R., Viatour, P., Sage, J., Zhang, Y., and Xiong, Y. (2007). pRB family proteins are required for H3K27 trimethylation and Polycomb repression complexes binding to and silencing p16INK4alpha tumor suppressor gene. Genes Dev. *21*, 49–54.

Kotake, Y., Zeng, Y., and Xiong, Y. (2009). DDB1-CUL4 and MLL1 mediate oncogene-induced p16INK4a activation. Cancer Res. *69*, 1809–1814.

Kouzarides, T. (2007). Chromatin modifications and their function. Cell *128*, 693–705.

Ku, M., Koche, R.P., Rheinbay, E., Mendenhall, E.M., Endoh, M., Mikkelsen, T.S., Presser, A., Nusbaum, C., Xie, X., Chi, A.S., et al. (2008). Genomewide

normalized to those of GADPH (upper panel) and β-actin served as a loading control for the western blotting (lower panel). Each bar represents the mean ± SD for triplicate experiments (*$p < 0.05$ and ** < 0.01).

(D) CUL4B mRNA level is negatively correlated with the level of p16 and PTEN mRNA. The relative level of CUL4B expression was plotted against the relative level of p16 (upper panel) and PTEN (lower panel) expression (***$p < 0.001$).

(E) CUL4B is unregulated in multiple carcinomas. Immunohistochemical staining of CUL4B in paired samples of esophagus, lung, pancreas, stomach, colon, cervix, kidney, and bladder carcinoma versus adjacent normal tissues. Representative images of 200-fold magnifications of each type of paired tumor section are presented. Each bar represents the mean ± SEM for triplicate experiments (*$p < 0.05$ and ** < 0.01).

(F) Transcript levels of CUL4B and EZH2 are significantly higher in multiple malignant tumor tissues. Relative levels of CUL4B and EZH2 transcripts were normalized to that of GAPDH and calibrated to the mean mRNA level (arbitrary value of 1) in normal tissue (yellow bars). The fold increase in gene expression relative to the mean value for each disease sample is indicated.

(G) Graphic model as discussed in the text. DNA (black line); nucleosomes with single N terminus of H3 and C terminus of H2A (blue ball); transcription factors (TF, orange ball); long noncoding RNA (lncRNA, green line).

analysis of PRC1 and PRC2 occupancy identifies two classes of bivalent domains. PLoS Genet. *4*, e1000242.

Li, F., Huarte, M., Zaratiegui, M., Vaughn, M.W., Shi, Y., Martienssen, R., and Cande, W.Z. (2008). Lid2 is required for coordinating H3K4 and H3K9 methylation of heterochromatin and euchromatin. Cell *135*, 272–283.

Lowe, S.W., and Sherr, C.J. (2003). Tumor suppression by Ink4a-Arf: progress and puzzles. Curr. Opin. Genet. Dev. *13*, 77–83.

Maenner, S., Blaud, M., Fouillen, L., Savoye, A., Marchand, V., Dubois, A., Sanglier-Cianférani, S., Van Dorsselaer, A., Clerc, P., Avner, P., et al. (2010). 2-D structure of the A region of Xist RNA and its implication for PRC2 association. PLoS Biol. *8*, e1000276.

Müller, J., and Verrijzer, P. (2009). Biochemical mechanisms of gene regulation by polycomb group protein complexes. Curr. Opin. Genet. Dev. *19*, 150–158.

Nakagawa, T., and Xiong, Y. (2011). X-linked mental retardation gene CUL4B targets ubiquitylation of H3K4 methyltransferase component WDR5 and regulates neuronal gene expression. Mol. Cell *43*, 381–391.

Nishitani, H., Shiomi, Y., Iida, H., Michishita, M., Takami, T., and Tsurimoto, T. (2008). CDK inhibitor p21 is degraded by a proliferating cell nuclear antigen-coupled Cul4-DDB1Cdt2 pathway during S phase and after UV irradiation. J. Biol. Chem. *283*, 29045–29052.

Pandey, R.R., Mondal, T., Mohammad, F., Enroth, S., Redrup, L., Komorowski, J., Nagano, T., Mancini-Dinardo, D., and Kanduri, C. (2008). Kcnq1ot1 antisense noncoding RNA mediates lineage-specific transcriptional silencing through chromatin-level regulation. Mol. Cell *32*, 232–246.

Richly, H., Rocha-Viegas, L., Ribeiro, J.D., Demajo, S., Gundem, G., Lopez-Bigas, N., Nakagawa, T., Rospert, S., Ito, T., and Di Croce, L. (2010). Transcriptional activation of polycomb-repressed genes by ZRF1. Nature *468*, 1124–1128.

Salmena, L., Carracedo, A., and Pandolfi, P.P. (2008). Tenets of PTEN tumor suppression. Cell *133*, 403–414.

Sarma, K., Margueron, R., Ivanov, A., Pirrotta, V., and Reinberg, D. (2008). Ezh2 requires PHF1 to efficiently catalyze H3 lysine 27 trimethylation in vivo. Mol. Cell. Biol. *28*, 2718–2731.

Schuettengruber, B., Chourrout, D., Vervoort, M., Leblanc, B., and Cavalli, G. (2007). Genome regulation by polycomb and trithorax proteins. Cell *128*, 735–745.

Shen, X., Kim, W., Fujiwara, Y., Simon, M.D., Liu, Y., Mysliwiec, M.R., Yuan, G.C., Lee, Y., and Orkin, S.H. (2009). Jumonji modulates polycomb activity and self-renewal versus differentiation of stem cells. Cell *139*, 1303–1314.

Simon, J.A., and Lange, C.A. (2008). Roles of the EZH2 histone methyltransferase in cancer epigenetics. Mutat. Res. *647*, 21–29.

Simon, J.A., and Kingston, R.E. (2009). Mechanisms of polycomb gene silencing: knowns and unknowns. Nat. Rev. Mol. Cell Biol. *10*, 697–708.

Tan, J., Yang, X., Zhuang, L., Jiang, X., Chen, W., Lee, P.L., Karuturi, R.K., Tan, P.B., Liu, E.T., and Yu, Q. (2007). Pharmacologic disruption of Polycomb-repressive complex 2-mediated gene repression selectively induces apoptosis in cancer cells. Genes Dev. *21*, 1050–1063.

Tavares, L., Dimitrova, E., Oxley, D., Webster, J., Poot, R., Demmers, J., Bezstarosti, K., Taylor, S., Ura, H., Koide, H., et al. (2012). RYBP-PRC1 complexes mediate H2A ubiquitylation at polycomb target sites independently of PRC2 and H3K27me3. Cell *148*, 664–678.

Tsai, M.C., Manor, O., Wan, Y., Mosammaparast, N., Wang, J.K., Lan, F., Shi, Y., Segal, E., and Chang, H.Y. (2010). Long noncoding RNA as modular scaffold of histone modification complexes. Science *329*, 689–693.

Wang, H., Wang, L., Erdjument-Bromage, H., Vidal, M., Tempst, P., Jones, R.S., and Zhang, Y. (2004). Role of histone H2A ubiquitination in Polycomb silencing. Nature *431*, 873–878.

Wang, Y., Zhang, H., Chen, Y., Sun, Y., Yang, F., Yu, W., Liang, J., Sun, L., Yang, X., Shi, L., et al. (2009). LSD1 is a subunit of the NuRD complex and targets the metastasis programs in breast cancer. Cell *138*, 660–672.

Weng, L.P., Smith, W.M., Dahia, P.L., Ziebold, U., Gil, E., Lees, J.A., and Eng, C. (1999). PTEN suppresses breast cancer cell growth by phosphatase activity-dependent G1 arrest followed by cell death. Cancer Res. *59*, 5808–5814.

Wu, Z.L., Zheng, S.S., Li, Z.M., Qiao, Y.Y., Aau, M.Y., and Yu, Q. (2010). Polycomb protein EZH2 regulates E2F1-dependent apoptosis through epigenetically modulating Bim expression. Cell Death Differ. *17*, 801–810.

Yoon, H.G., Chan, D.W., Huang, Z.Q., Li, J., Fondell, J.D., Qin, J., and Wong, J. (2003). Purification and functional characterization of the human N-CoR complex: the roles of HDAC3, TBL1 and TBLR1. EMBO J. *22*, 1336–1346.

Zhang, H.S., Postigo, A.A., and Dean, D.C. (1999). Active transcriptional repression by the Rb-E2F complex mediates G1 arrest triggered by p16INK4a, TGFbeta, and contact inhibition. Cell *97*, 53–61.

Zimmerman, E.S., Schulman, B.A., and Zheng, N. (2010). Structural assembly of cullin-RING ubiquitin ligase complexes. Curr. Opin. Struct. Biol. *20*, 714–721.

Zou, Y., Liu, Q., Chen, B., Zhang, X., Guo, C., Zhou, H., Li, J., Gao, G., Guo, Y., Yan, C., et al. (2007). Mutation in CUL4B, which encodes a member of cullin-RING ubiquitin ligase complex, causes X-linked mental retardation. Am. J. Hum. Genet. *80*, 561–566.

Zou, Y., Mi, J., Cui, J., Lu, D., Zhang, X., Guo, C., Gao, G., Liu, Q., Chen, B., Shao, C., and Gong, Y. (2009). Characterization of nuclear localization signal in the N terminus of CUL4B and its essential role in cyclin E degradation and cell cycle progression. J. Biol. Chem. *284*, 33320–33332.

Cancer Cell
Article

Identification of Sox9-Dependent Acinar-to-Ductal Reprogramming as the Principal Mechanism for Initiation of Pancreatic Ductal Adenocarcinoma

Janel L. Kopp,[1,6] Guido von Figura,[2,6] Erin Mayes,[1] Fen-Fen Liu,[1] Claire L. Dubois,[1] John P. Morris IV,[2] Fong Cheng Pan,[3] Haruhiko Akiyama,[4] Christopher V.E. Wright,[3] Kristin Jensen,[5] Matthias Hebrok,[2,*] and Maike Sander[1,*]
[1]Departments of Pediatrics and Cellular and Molecular Medicine, University of California-San Diego, La Jolla, CA 92093-0695, USA
[2]Diabetes Center, Department of Medicine, University of California-San Francisco, San Francisco, CA 94143, USA
[3]Department of Cell and Developmental Biology, Vanderbilt University, Nashville, TN 37232-8240, USA
[4]Department of Orthopedics, Kyoto University, 54 Kawahara-cho, Shogoin, Sakyo, Kyoto 606-8507, Japan
[5]Department of Pathology, Veterans Affairs Palo Alto Health Care System and Stanford University Hospital, Stanford, CA 94305, USA
[6]These authors contributed equally to this work
*Correspondence: masander@ucsd.edu (M.S.), mhebrok@diabetes.ucsf.edu (M.H.)
http://dx.doi.org/10.1016/j.ccr.2012.10.025

SUMMARY

Tumors are largely classified by histologic appearance, yet morphologic features do not necessarily predict cellular origin. To determine the origin of pancreatic ductal adenocarcinoma (PDA), we labeled and traced pancreatic cell populations after induction of a PDA-initiating Kras mutation. Our studies reveal that ductal and stem-like centroacinar cells are surprisingly refractory to oncogenic transformation, whereas acinar cells readily form PDA precursor lesions with ductal features. We show that formation of acinar-derived premalignant lesions depends on ectopic induction of the ductal gene *Sox9*. Moreover, when concomitantly expressed with oncogenic Kras, *Sox9* accelerates formation of premalignant lesions. These results provide insight into the cellular origin of PDA and suggest that its precursors arise via induction of a duct-like state in acinar cells.

INTRODUCTION

Defining tumor-initiating events is critically important for developing early cancer detection methods and effective treatments. In the past, the cell type responsible for tumor initiation has often been inferred based on the histologic appearance of the tumor. However, morphologic features do not necessarily predict a lineage relationship (Goldstein et al., 2010), which can only be determined by lineage tracing studies.

Invasive pancreatic ductal adenocarcinoma (PDA) is believed to arise from a spectrum of preneoplastic mucinous lesions with ductal morphology, namely pancreatic intraepithelial neoplasias (PanINs), the most common precursor lesions observed in humans, as well as mucinous cystic neoplasias (MCNs) and intraductal papillary mucinous neoplasias (IPMNs) (Hezel et al., 2006). During disease progression, accumulation of genetic mutations in these lesions leads to an increasing degree of atypia and ultimately PDA (Feldmann et al., 2007). The earliest detectable mutations found in preneoplastic lesions are activating mutations of the *KRAS* gene (Kanda et al., 2012). The significance of *Kras* mutations for disease initiation has been demonstrated in mice, where expression of the constitutively active $Kras^{G12D}$ allele induces PanINs and after a significant latency period also PDA (Hingorani et al., 2003). In $Kras^{G12D}$-expressing mice, PanIN formation coincides with, or is preceded by, acinar-to-ductal metaplasia (ADM), characterized by replacement of acinar cells with cells expressing ductal markers, such as *CK19* and the ductal fate determinant *Sox9* (Morris et al., 2010; Zhu et al.,

Significance

PDA has a dismal prognosis, largely because it is mostly diagnosed at an advanced stage. For developing early detection methods and treatments, it is essential to understand the primary events leading to tumor initiation. By tracing specific cell populations in the presence and absence of tissue injury in mice, we demonstrate that oncogenic Kras can readily induce PDA precursor lesions from adult pancreatic acinar cells, but not from ductal or centroacinar cells. Moreover, using loss- and gain-of-function approaches we identify the ductal fate determinant *Sox9* as a critical mediator of Kras-induced premalignant acinar cell reprogramming. Our findings demonstrate a key role for acinar cells in PDA initiation and reveal Sox9 as a potential target for preventing early tumor-initiating events.

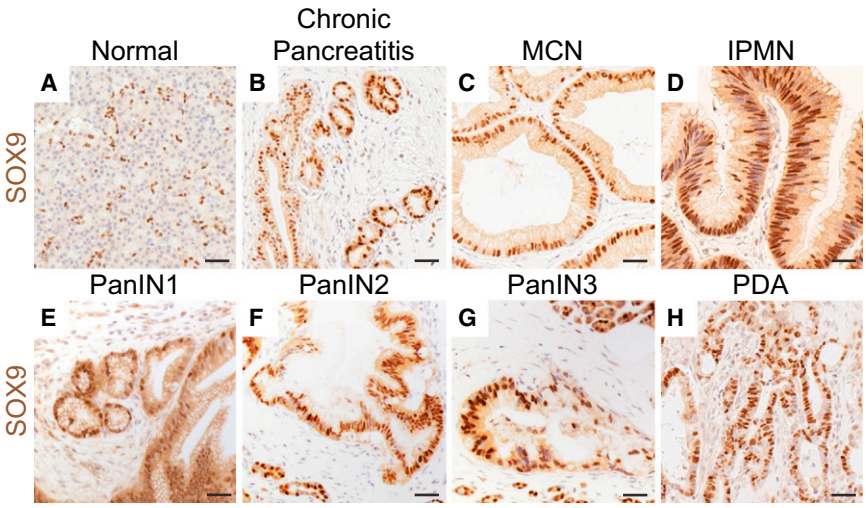

I

Category	Intensity of SOX9 expression		
	Negative	Weak	Strong
Normal	0/16 [0%]	16/16 [100%]	0/16 [0%]
Pancreatitis	2/16 [13%]	13/16 [81%]	1/16 [6%]
MCN	4/22 [18%]	13/22 [59%]	5/22 [23%]
IPMN	1/20 [5%]	13/20 [65%]	6/20 [30%]
PanIN 1-2	1/26 [4%]	12/26 [46%]	13/26 [50%]
PanIN 2-3	2/7 [29%]	2/7 [29%]	3/7 [43%]
PDA	6/19 [32%]	7/19 [37%]	6/19 [32%]

Figure 1. SOX9 Is Expressed in Human Premalignant and Malignant Pancreatic Lesions

(A–H) Immunohistochemistry for SOX9 and hematoxylin counterstain on a tissue microarray spotted with human pancreatic tissue cores. Representative images showing SOX9 expression in normal pancreatic ducts (A), chronic pancreatitis (B), MCN (C), IPMN (D), pancreatic intraepithelial neoplasia 1 (PanIN1) (E), PanIN2 (F), PanIN3 (G), and PDA (H).

(I) Number of tissue cores within each phenotypic category displaying no, weak, or strong SOX9 staining intensity. Scale bars: 100 μm.

2007). ADM is also observed in pancreatitis, which is a significant risk factor for PDA in humans (Lowenfels et al., 1993) and accelerates $Kras^{G12D}$-mediated PanIN and PDA formation in mice (Carrière et al., 2009; Guerra et al., 2007; Morris et al., 2010). These findings imply that oncogenic *Kras* mutations induce ADM, PanINs and ultimately PDA. However, it is still unclear whether ADM and PanINs primarily arise by expansion of ductal cells and secondary replacement of acinar cells or by direct reprogramming of acinar cells into cells with ductal morphology.

Because previous studies have modeled PDA initiation mostly by expressing oncogenic Kras in all cell types of the pancreas (Aguirre et al., 2003; Hingorani et al., 2003, 2005), little is known about its cell of origin. In mice deficient for the tumor suppressor *Pten*, the formation of invasive pancreatic cancer is associated with increased proliferation of centroacinar cells (CACs) (Stanger et al., 2005), which reside at the tips of the ductal tree. CACs express some markers of embryonic pancreatic progenitors and exhibit features of tissue stem cells in vitro (Miyamoto et al., 2003; Rovira et al., 2010). Since numerous tumors have been shown to originate from tissue stem cells (Visvader, 2011), it has been proposed that CACs are the cell of origin for PanINs and PDA (Miyamoto et al., 2003; Stanger et al., 2005). However, this contention has not been directly tested, largely because genetic tools to target ductal and CACs have only recently been generated (Kopp et al., 2011; Solar et al., 2009). Genetic studies, using *CK19* promoter-based alleles to activate oncogenic *Kras* in ductal cells, suggest that PanINs rarely arise from ducts (Brembeck et al., 2003; Ray et al., 2011). Yet, the rather exclusive targeting of larger ducts in these studies precluded assessing susceptibility of CACs to $Kras^{G12D}$-mediated PanIN induction.

Previous studies have shown that oncogenic *Kras* can convert acinar cells into duct-like cells and PanINs (Carrière et al., 2007; De La O et al., 2008; Guerra et al., 2007; Habbe et al., 2008; Morris et al., 2010). While these studies suggest acinar-to-ductal reprogramming (ADR) as a possible mechanism for initiating PanINs, it is unclear whether PanINs are more readily induced after direct oncogenic transformation of ductal or CACs. Moreover, it is unknown whether inducers of ductal cell identity, such as *Sox9* (Delous et al., 2012; Shih et al., 2012), play a role in the induction of PanINs from acinar cells.

In this study, we directly compared the propensity of ductal/CACs and acinar cells to form PanINs and investigated the molecular mechanisms that underlie PanIN formation.

RESULTS

SOX9 Is Expressed in Human Premalignant and Malignant Pancreatic Lesions

Under normal conditions, the transcription factor Sox9 is expressed in ductal and CACs, but not acinar cells (Seymour et al., 2007). In addition, Sox9 is induced during ADM and expressed in PanINs and PDA (Morris et al., 2010; Prevot et al., 2012). To comprehensively examine SOX9 expression in the human pancreas, we used a tissue microarray for immunohistochemical analysis of SOX9 expression in different pancreatic lesions (Figures 1A–1H). SOX9 was expressed in chronic pancreatitis, as well as premalignant and malignant lesions, including MCNs, IPMNs, PanINs, and PDA. Low-grade PanINs were uniformly $SOX9^+$, whereas higher-grade PanIN2/3 lesions and PDA displayed heterogeneous SOX9 expression (Figure 1L; 72% of PanIN2/3 and 69% of PDA were $SOX9^+$). These findings suggest that a $SOX9^+$ state is associated with PDA initiation.

$Kras^{G12D}$-Induced PanINs Predominantly Arise from Acinar but Not Ductal/Centroacinar Cells

To determine whether PanINs arise from Sox9-expressing ductal/CACs or from acinar-derived duct-like cells ectopically

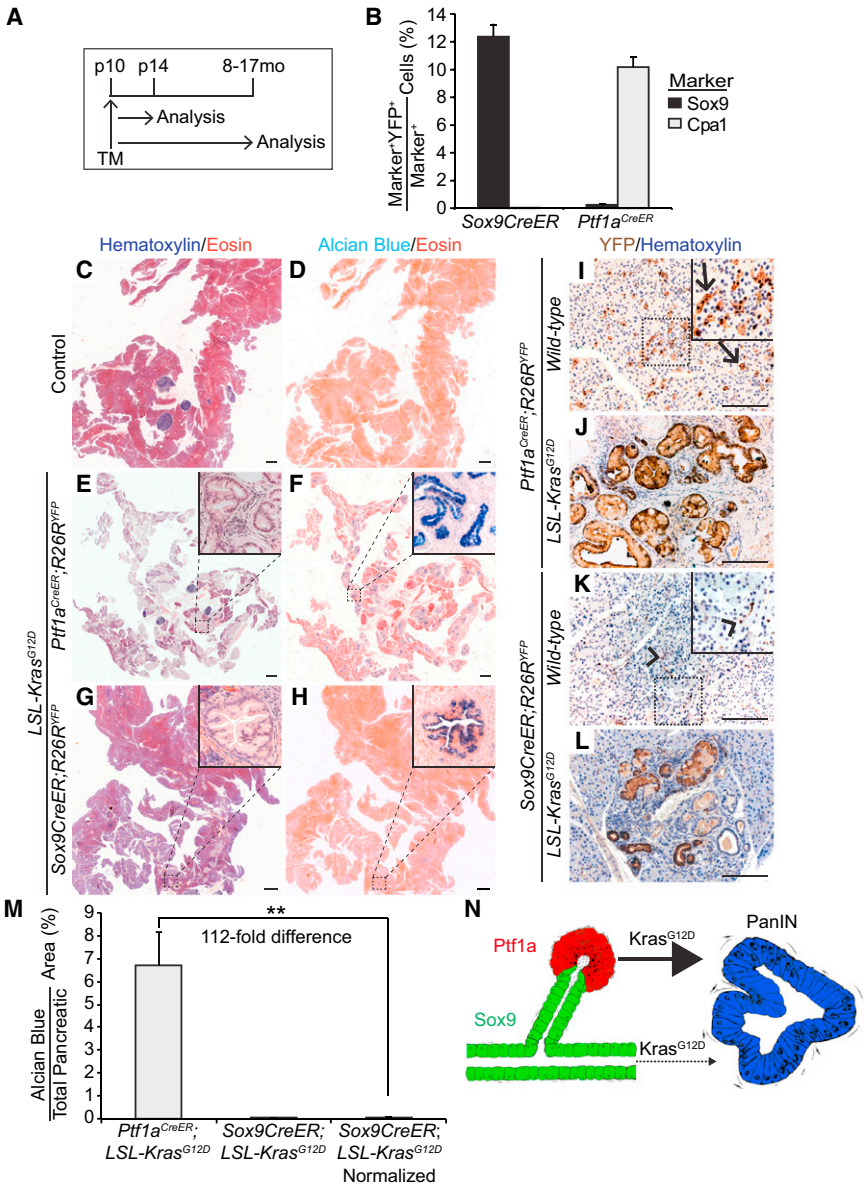

Figure 2. *Kras*^{G12D} Expression in Acinar, but not in Ductal/Centroacinar Cells, readily Induces PanIN Formation

(A) *Sox9CreER;R26R*^{YFP} and *Ptf1a*^{CreER}*;R26R*^{YFP} mice were injected once with tamoxifen (TM) at postnatal day (p) 10 and analyzed at p14 or at 8 to 17 months (mo) of age.

(B–H) Quantification of Sox9^{+} or Cpa1^{+} cells expressing YFP at p14 (n = 4; B). H&E (C, E, and G) or Alcian blue and eosin (D, F, and H) staining of pancreatic sections from 8- to 17-month-old control (C and D), *Ptf1a*^{CreER}*;LSL-Kras*^{G12D}*; R26R*^{YFP} (E and F), or *Sox9CreER;LSL-Kras*^{G12D}*; R26R*^{YFP} (G and H) mice reveals abundant Alcian blue^{+} PanINs only in *Ptf1a*^{CreER}*;LSL-Kras*^{G12D}*; R26R*^{YFP} mice.

(I–L) Immunohistochemistry of YFP in 8- to 17-month-old mice shows expression of YFP in acinar cells in *Ptf1a*^{CreER}*;R26R*^{YFP} mice (I), arrows) and ductal/CACs in *Sox9CreER;R26R*^{YFP} mice (K), arrowheads). PanINs in *Ptf1a*^{CreER}*;LSL-Kras*^{G12D}*; R26R*^{YFP} (J) and *Sox9CreER;LSL-Kras*^{G12D}*; R26R*^{YFP} (L) mice are YFP^{+}, indicating an acinar or ductal/CAC origin, respectively.

(M) Quantification of Alcian blue^{+} pancreatic area in 8- to 17-month-old mice (n = 9 in *Ptf1a*^{CreER}*; LSL-Kras*^{G12D} mice; n = 6 in *Sox9CreER; LSL-Kras*^{G12D} mice). The Alcian blue^{+} area in *Sox9CreER;LSL-Kras*^{G12D}*;R26R*^{YFP} mice was multiplied by 4.6 (normalized) to account for the greater total number of recombined cells in *Ptf1a*^{CreER}*;R26R*^{YFP} mice (see Figure S1L).

(N) Schematic showing the predominantly acinar origin of PanINs after expression of oncogenic Kras. Values are shown as mean ± SEM. **p < 0.01. Scale bars: 1 mm (C–H) and 100 μm (I–L). See also Figure S1.

expressing Sox9, we directly compared the propensity of ductal/CACs and acinar cells to form PanINs in response to oncogenic Kras. To inducibly recombine the *LSL-Kras*^{G12D} allele (hereafter referred to as the *Kras*^{G12D} allele) in ductal/CAC or acinar cells, we used *Sox9CreER* or *Ptf1a*^{CreER} mice, respectively. The Cre-dependent *R26R*^{YFP} reporter allele was included to assess recombination efficiency and map the fate of Kras-active cells. Four days after induction of recombination by tamoxifen at postnatal day 10 (p10), we analyzed pancreatic labeling specificity and efficiency by quantifying the percentage of ductal and acinar cells expressing YFP (Figure 2A; Figure S1A available online). As previously reported (Kopp et al., 2011), the *Sox9CreER* transgene labeled cells throughout the entire ductal tree, including CACs (Figures S1B and S1C; data not shown). On average, we labeled 12% of all Sox9^{+} cells with the *Sox9CreER* transgene and 10% of Cpa1^{+} acinar cells with the *Ptf1a*^{CreER} allele (Figures 2B, S1D, and S1E). Quantification of nonlineage-specific recombination events revealed *R26R*^{YFP} recombination in 0.02% of acinar cells by *Sox9CreER* and 0.23% of Sox9^{+} cells by *Ptf1a*^{CreER} (Figure 2B). A similar pattern of YFP expression was observed after 8 months or longer (Figures 2I and 2K), confirming that acinar and ductal cells do not spontaneously convert into other pancreatic cell types (Desai et al., 2007; Kopp et al., 2011; Solar et al., 2009; Strobel et al., 2007). Overall, this analysis shows that the *Sox9CreER* transgene and *Ptf1a*^{CreER} allele specifically target the ductal/CAC and acinar cell compartments, respectively. Moreover, the *Kras*^{G12D} allele was effectively recombined by both *Ptf1a*^{CreER} and *Sox9CreER* (Figure S1F).

To assess the frequency of PanINs arising from acinar or ductal/CACs after Kras activation, we examined pancreata from *Ptf1a*^{CreER}*;Kras*^{G12D}*;R26R*^{YFP} and *Sox9CreER;Kras*^{G12D}*; R26R*^{YFP} mice 8 to 17 months after *Kras*^{G12D} induction (Figure 2A). Corroborating previous studies, showing that Kras activation in acinar cells can induce PanINs (Carrière et al., 2007; De La O et al., 2008; Gidekel Friedlander et al., 2009; Guerra et al., 2007; Habbe et al., 2008), all *Ptf1a*^{CreER}*; Kras*^{G12D}*;R26R*^{YFP} mice displayed abundant lesions with histologic and molecular characteristics of PanINs, including high

Table 1. Quantification of PanIN Frequency in *Ptf1a^{CreER};LSL-Kras^{G12D};R26R^{YFP}* and *Sox9CreER;LSL-Kras^{G12D};R26R^{YFP}* Mice

Genotype	n	Tamoxifen Injection Age (days)	Analysis Age (months)	Additional Treatment	Number of Mice with PanINs (% of Total Mice)
Ptf1a^{CreER}; LSL-Kras^{G12D};R26R^{YFP}	12	10	8–17	None	12 (100)
Sox9CreER; LSL- Kras^{G12D};R26R^{YFP}	14	10	8–16	None	8 (57)
Ptf1a^{CreER}; LSL-Kras^{G12D};R26R^{YFP}	4	10	2	Caerulein	4 (100)
Ptf1a^{CreER}; LSL-Kras^{G12D};R26R^{YFP}	4	10	2	Saline	4 (100)
Sox9CreER; LSL-Kras^{G12D};R26R^{YFP}	5	10	2	Caerulein	3 (40)
Sox9CreER; LSL-Kras^{G12D};R26R^{YFP}	9	10	2	Saline	1 (11)

See also Table S1.

acidic mucin content, indicated by Alcian blue staining, and expression of Muc5AC and Claudin18 (Figures 2C–2F, S1G, and S1H; Table 1). Expression of YFP further confirmed that the PanINs originated from acinar cells (Figure 2J).

In contrast to *Ptf1a^{CreER};Kras^{G12D};R26R^{YFP}* mice, pancreatic histology was largely normal in *Sox9CreER;Kras^{G12D};R26R^{YFP}* mice and PanINs were rarely observed (Figures 2C and 2G). Of 14 mice, no PanINs were detected in six mice and the remaining mice had no more than ten PanINs per mouse (Tables 1 and S1). As seen in PanINs originating from acinar cells (Figures 2F, S1G, and S1H), the duct-derived lesions were Alcian blue$^+$ (Figure 2H, inset), and expressed Muc5AC and Claudin18 (Figures S1I and S1J) and the lineage marker YFP (Figure 2L). However, unlike acinar-derived PanINs, the duct-derived lesions were not randomly distributed throughout the pancreas, but were more often associated with large ducts (Figure S1J, arrow).

To thoroughly compare the extent of PanIN formation from acinar and ductal/CACs, we quantified the Alcian blue$^+$ area in *Ptf1a^{CreER};Kras^{G12D};R26R^{YFP}* and *Sox9CreER;Kras^{G12D};R26R^{YFP}* mice on sections spaced every 140 μm throughout the entire pancreas (Figure 2M). Notably, Alcian blue staining can be present in duct-like lesions devoid of neoplastic features and conversely, can be absent from high-grade PanIN lesions (Cornish and Hruban, 2011; Strobel et al., 2007). Since the majority of Alcian blue$^+$ lesions in *Ptf1a^{CreER};Kras^{G12D};R26R^{YFP}* and *Sox9CreER;Kras^{G12D};R26R^{YFP}* mice exhibited neoplastic characteristics of PanINs and Alcian blue$^-$ PanINs were rarely observed (Figure S1K and data not shown), Alcian blue staining appeared to be an accurate measure of PanIN frequency in these models. In *Ptf1a^{CreER};Kras^{G12D};R26R^{YFP}* mice, on average 6.7 ± 1.5% of the pancreas was Alcian blue$^+$. In contrast, only 0.013 ± 0.004% of the pancreas exhibited Alcian blue staining in *Sox9CreER;Kras^{G12D};R26R^{YFP}* mice (Figure 2M). While this result suggests a striking difference in the propensity of acinar and ductal/CACs to give rise to PanINs, this quantification likely overestimates the difference, because acinar cells are more abundant than ductal cells and therefore a larger overall number of cells will express *Kras^{G12D}* in *Ptf1a^{CreER};Kras^{G12D};R26R^{YFP}* than in *Sox9CreER;Kras^{G12D};R26R^{YFP}* mice. To account for this difference, we quantified the total number of recombined YFP$^+$ cells in *Sox9CreER;R26R^{YFP}* and *Ptf1a^{CreER};R26R^{YFP}* mice 4 days after tamoxifen injection. After accounting for the 4.6-fold difference (Figure S1L), *Ptf1a^{CreER}*-induced Kras activation still resulted in a 112-fold higher frequency of PanINs than *Sox9CreER*-mediated Kras activation (Figure 2M). These data show that acinar cells have a much greater propensity than ductal/CACs to form PanINs in response to oncogenic Kras (Figure 2N).

Acute Pancreatitis Promotes *Kras^{G12D}*-Mediated PanIN Formation from Acinar, but Not Ductal Cells

Previous studies have shown that caerulein-induced acute or chronic pancreatitis accelerates *Kras^{G12D}*-mediated PanIN and PDA formation (Carrière et al., 2009; Gidekel Friedlander et al., 2009; Guerra et al., 2007; Morris et al., 2010). In the absence of oncogenic Kras, acute pancreatitis induces transient ADM followed by reversion to normal acinar cell morphology (Jensen et al., 2005; Morris et al., 2010). By contrast, acute pancreatitis in the presence of oncogenic Kras leads to persistent ADR and accelerated PanIN formation (De La O and Murtaugh, 2009; Morris et al., 2010). To compare how pancreatitis affects PanIN formation after ductal or acinar cell-specific Kras activation, we induced caerulein-mediated acute pancreatitis in 6-week-old *Ptf1a^{CreER};Kras^{G12D};R26R^{YFP}*, *Sox9CreER;Kras^{G12D};R26R^{YFP}* and control mice and analyzed pancreatic tissue 2 or 21 days later (Figures 3A and S2A). As reported (Morris et al., 2010), 2-day post-caerulein treatment control mice exhibited widespread ADM with characteristic degranulation of acinar cells and appearance of cuboidal to columnar duct-like structures with enlarged lumens (Figures 3B and 3C), which were replaced by normal acini within 21 days (Figures 3D and 3E). In *Ptf1a^{CreER};Kras^{G12D};R26R^{YFP}* mice treated with saline, pancreas morphology was largely normal, although small areas of ADM and occasional PanINs were already evident by 9 weeks of age (Figure 3F, inset). Similar to control mice, caerulein induced widespread ADM within 2 days (Figures 3F and 3G). However, these changes were not transient and duct-like structures were replaced by PanINs after 21 days (Figures 3H and 3I). These

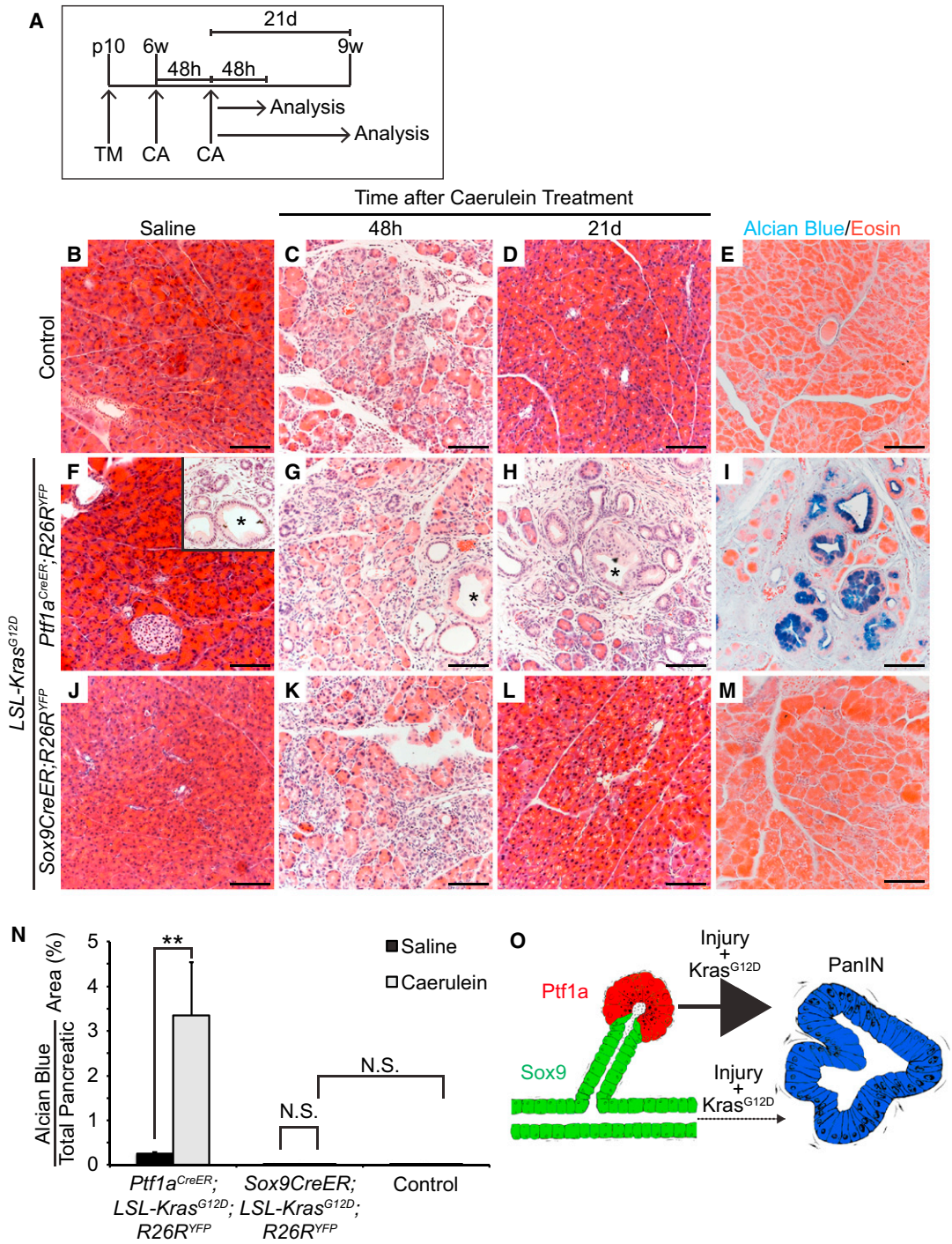

Figure 3. Acute Pancreatitis Promotes PanIN Formation from *Kras*^{G12D}-Expressing Acinar Cells, but not Ductal/Centroacinar Cells

(A) *Ptf1a*^{CreER};*LSL-Kras*^{G12D};*R26R*^{YFP}, *Sox9CreER;LSL-Kras*^{G12D};*R26R*^{YFP} and control mice were injected once with tamoxifen (TM) at postnatal day (p) 10. At 6 weeks (w) of age, mice were treated with two sets of caerulein (CA) or saline injections on alternating days and analyzed 48 hr (h) or 21 days (d) later.

(B–D, F–H, and J–L) H&E staining reveals occasional PanINs in 9-week-old *Ptf1a*^{CreER};*LSL-Kras*^{G12D};*R26R*^{YFP} mice (F, inset) and persistent ADM and PanINs 21d after CA (H), but normal pancreas morphology in *Sox9CreER;LSL-Kras*^{G12D};*R26R*^{YFP} and control mice (D and L). Asterisks denote PanINs.

(E, I, and M) Alcian blue and eosin staining of pancreatic sections from mice 21 days after CA treatment.

(N) Quantification of Alcian blue^{+} pancreatic area reveals a significant increase in PanINs after CA in *Ptf1a*^{CreER};*LSL-Kras*^{G12D};*R26R*^{YFP} (n = 4), but not in *Sox9CreER;LSL-Kras*^{G12D};*R26R*^{YFP} mice (n = 5).

(O) Schematic showing that pancreatic injury promotes PanIN formation from *Kras*^{G12D}-expressing acinar, but not ductal/centroacinar cells. N.S., not significant. Values are shown as mean ± SEM. **p < 0.01. Scale bars: 100 μm.

See also Figure S2.

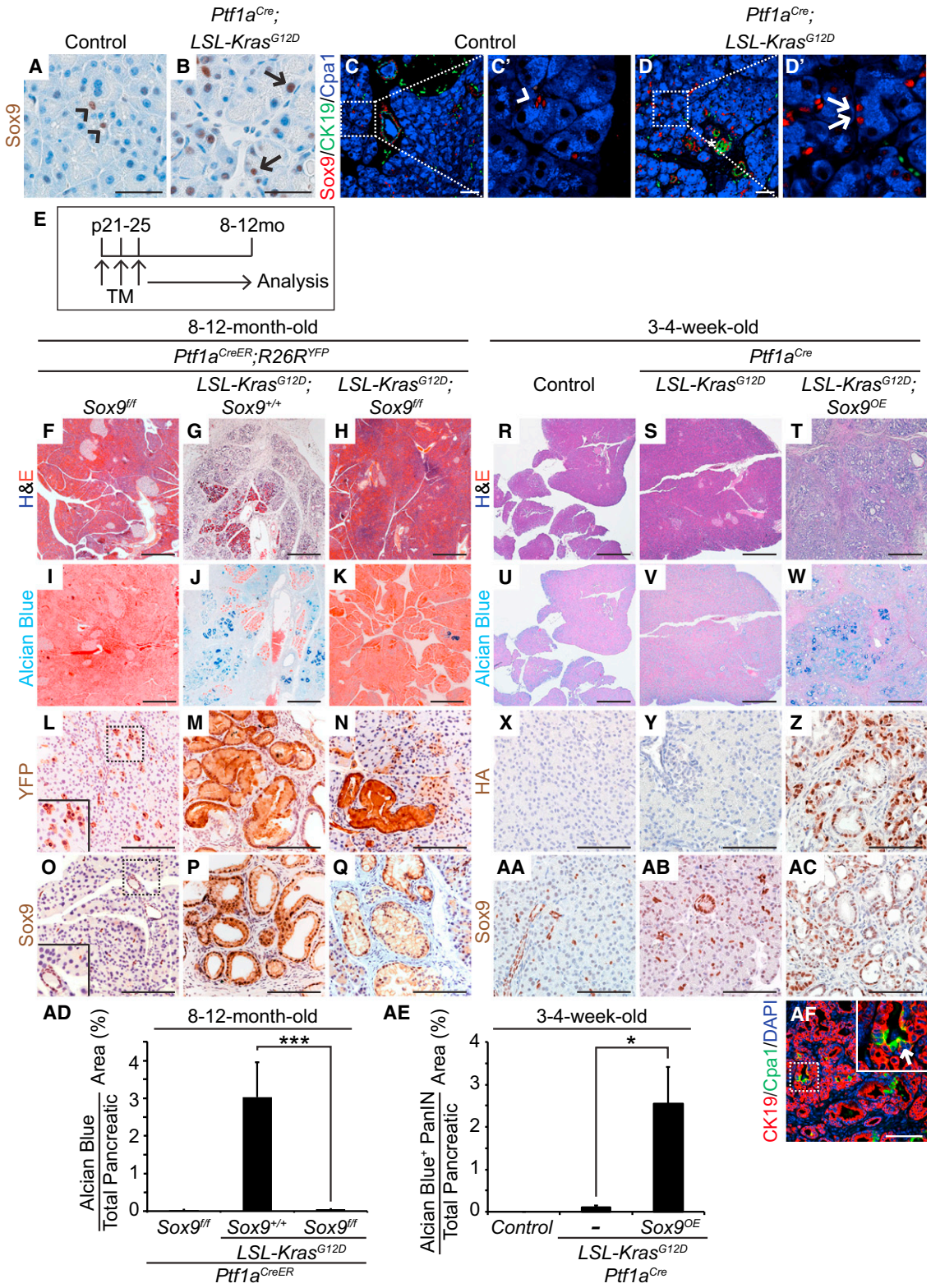

Figure 4. *Sox9* Is Necessary for and Accelerates *Kras*^{G12D}-Induced PanIN Formation

(A and B) Immunohistochemistry shows Sox9 expression in ductal/centroacinar (CAC) (A, arrowheads), but not acinar cells in control mice. In 2-month-old *Ptf1a*^{Cre};*LSL-Kras*^{G12D} mice, Sox9 is also detected in some acinar cells (B, arrows).

(C and D) Co-immunofluorescence staining for Sox9, CK19 and Cpa1 confirms Sox9 expression in ductal/CACs (C', arrowhead points to CAC) in control mice and shows Sox9^{+}Cpa1^{+}CK19^{-} acinar cells in *Ptf1a*^{Cre};*LSL-Kras*^{G12D} mice (D', arrowheads).

observations are consistent with previous findings (Morris et al., 2010) and confirm that acute pancreatitis promotes PanIN formation from $Kras^{G12D}$-expressing acinar cells. In contrast to $Ptf1a^{CreER};Kras^{G12D};R26R^{YFP}$ mice, virtually no PanINs were observed 21 days after caerulein treatment of *Sox9CreER; $Kras^{G12D};R26R^{YFP}$* mice (Figures 3J–3M; Tables 1 and S1) and pancreas morphology was similar to control mice not expressing oncogenic Kras (Figures 3D and 3E). These results suggest that $Kras^{G12D}$-expressing ductal cells have a low propensity to form PanINs even when exposed to pro-neoplastic insults, such as acute pancreatitis.

To directly compare how pancreatitis affects PanIN formation from $Kras^{G12D}$-expressing acinar and ductal/CACs, we quantified the Alcian blue$^+$ area, which was predominately composed of PanIN lesions (data not shown and Figure S2B), in *Sox9CreER;$Kras^{G12D};R26R^{YFP}$* and *$Ptf1a^{CreER};Kras^{G12D};R26R^{YFP}$* mice 21 days after caerulein treatment (Figure 3N). In mice expressing $Kras^{G12D}$ in acinar cells, caerulein induced a significant 20.9-fold increase in Alcian blue$^+$ area. By contrast, no significant increase was observed in *Sox9CreER;$Kras^{G12D};R26R^{YFP}$* mice. Examination of individual mice revealed an increase in the overall number of mice exhibiting Alcian blue$^+$ PanINs in caerulein-treated compared to saline-treated *Sox9CreER;$Kras^{G12D};R26R^{YFP}$* mice (Table 1; three of five mice had PanINs after caerulein treatment versus one of nine mice after saline treatment). However, in mice with PanINs a total of only one to two PanINs were found per pancreas (Table S1). Overall, the Alcian blue$^+$ area in caerulein-treated *Sox9CreER; $Kras^{G12D};R26R^{YFP}$* mice was similar to controls not expressing the *Kras* oncogene (Figure 3N). Together, these data demonstrate that acute pancreatitis potentiates PanIN formation from $Kras^{G12D}$-expressing acinar cells, but not from $Kras^{G12D}$-expressing ductal/CACs (Figure 3O).

Sox9 Is Necessary for $Kras^{G12D}$-Mediated PanIN Induction

Given that ADM and early PanINs are Sox9$^+$ (Figure 1; Morris et al., 2010; Prevot et al., 2012), but Sox9$^+$ ductal cells are not the predominant source of PanINs, we examined whether Sox9 is induced in $Kras^{G12D}$-expressing acinar cells prior to ADM. In control mice, Sox9 expression was restricted to ductal and CACs (Figures 4A and 4C, arrowheads). In $Ptf1a^{Cre};Kras^{G12D}$ mice, Sox9 was additionally detected in a subset of cells with acinar morphology, expressing the acinar marker Cpa1, but not the ductal marker CK19 (Figures 4B and 4D, arrows). These data indicate that Sox9 expression is initiated before Kras-active acinar cells progress to a duct-like state and become PanINs.

Since *Sox9* is important for ductal cell development and regulates critical ductal genes (Shih et al., 2012), we examined whether *Sox9* plays a role in the transformation of acinar cells into ductal structures and premalignant lesions. To test if *Sox9* is required for PanIN formation, we concomitantly induced $Kras^{G12D}$ expression and deleted *Sox9* in acinar cells in 3-week-old $Ptf1a^{CreER};Kras^{G12D};Sox9^{f/f};R26R^{YFP}$ mice (Figures 4E and S3A). Consistent with the lack of Sox9 expression in normal acinar cells, acinar cell-specific *Sox9* deletion did not affect gross acinar cell morphology or the pattern of pancreatic Sox9 expression (Figures 4F, 4I, 4L, and 4O). Next, we analyzed 8- to 12-month-old $Ptf1a^{CreER};Kras^{G12D};Sox9^{+/+};R26R^{YFP}$ and $Ptf1a^{CreER};Kras^{G12D};Sox9^{f/f};R26R^{YFP}$ mice for the presence of PanINs. Confirming our previous findings (Figures 2E and 2F), pancreata from $Ptf1a^{CreER};Kras^{G12D};Sox9^{+/+};R26R^{YFP}$ mice contained widespread Alcian blue$^+$ PanIN lesions, expressing the YFP lineage label and Sox9 (Figures 4G, 4J, 4M, and 4P). In striking contrast, pancreas morphology was virtually normal in *Sox9*-deleted mice and very few PanINs were observed (Figures 4F, 4H, 4I, and 4K). Quantification of Alcian blue staining revealed a 153-fold reduction in the Alcian blue$^+$ area in *Sox9*-deleted $Ptf1a^{CreER};Kras^{G12D}$ mice compared to mice with two functional *Sox9* alleles (Figure 4AD). Notably, PanINs that still formed in $Ptf1a^{CreER};Kras^{G12D};Sox9^{f/f};R26R^{YFP}$ mice were YFP$^+$ and Sox9$^+$ (Figures 4N and 4Q), indicating that these PanINs arose from acinar cells that recombined the $R26R^{YFP}$ and $Kras^{G12D}$ alleles, but not the $Sox9^{flox}$ allele. Together, these findings demonstrate that PanIN formation from Kras-active acinar cells requires Sox9 activity (Figure S3R).

Sox9 Promotes $Kras^{G12D}$-Mediated Induction of PanINs

Given the critical role of *Sox9* in PanIN formation and its early induction in Kras-active acinar cells, we next examined whether forced expression of *Sox9* potentiates $Kras^{G12D}$-mediated PanIN formation. To test this idea, we crossed the well-characterized $Ptf1a^{Cre};Kras^{G12D}$ model of PanIN formation (Hingorani et al., 2003) with mice harboring a Cre-inducible *Sox9* transgene (*CAG-Sox9,* hereafter referred to as $Sox9^{OE}$). In $Sox9^{OE}$ mice, *RFP* is ubiquitously expressed in all cells unless Cre-mediated excision removes the *RFP* sequence and induces heritable expression of a bicistronic transcript encoding *GFP* and HA-tagged *Sox9* (Figure S3B). Consistent with the propensity of $Ptf1a^{Cre}$ to mostly target acinar cells (Heiser et al., 2008),

(E–K) Tamoxifen (TM) was administered to $Ptf1a^{CreER};Sox9^{f/f};R26R^{YFP}$, $Ptf1a^{CreER};LSL\text{-}Kras^{G12D};Sox9^{+/+};R26R^{YFP}$ and $Ptf1a^{CreER};LSL\text{-}Kras^{G12D};Sox9^{f/f};R26R^{YFP}$ mice at postnatal day (p) 21, 23, and 25 to simultaneously ablate *Sox9* and induce $Kras^{G12D}$ in acinar cells. Mice were analyzed at 8–12 months (mo) of age. (F–H) H&E and Alcian blue staining (I–K) shows almost no PanINs after *Sox9* deletion.

(L–Q) Immunohistochemistry reveals expression of YFP in PanINs in both $Ptf1a^{CreER};Kras^{G12D};Sox9^{+/+};R26R^{YFP}$ and $Ptf1a^{CreER};LSL\text{-}Kras^{G12D};Sox9^{f/f};R26R^{YFP}$ mice (M,N). Sox9 expression in PanINs in the $Sox9^{f/f}$ background indicates lack of $Sox9^{f}$ recombination (Q).

(R–AC) H&E (R–T) and Alcian blue staining (U–W) reveals abundant ADM and PanINs in $Ptf1a^{Cre};LSL\text{-}Kras^{G12D};Sox9^{OE}$, but not in $Ptf1a^{Cre};LSL\text{-}Kras^{G12D}$ or control mice at 3–4 weeks of age. Immunohistochemistry for HA (X–Z) and Sox9 (AA–AC) shows Sox9$^+$ PanINs originating from cells that recombined the $Sox9^{OE}$ transgene.

(AD and AE) Quantification of Alcian blue$^+$ pancreatic area reveals a significant reduction of PanINs after *Sox9* deletion (n = 9) and conversely, an increase after *Sox9* misexpression (n = 5).

(AF) Immunofluorescence staining shows abundant CK19 and little Cpa1 expression in 4-week-old $Ptf1a^{Cre};LSL\text{-}Kras^{G12D};Sox9^{OE}$ mice. Arrow points to CK19$^+$Cpa1$^+$ cell.

Values are shown as mean ± SEM. *$p < 0.05$ and ***$p < 0.001$. Scale bars: 25 μm (A and B), 50 μm (C and D), 100 μm (L–Q, X–AC, and AF), and 500 μm (F–K and R–W). See also Figure S3.

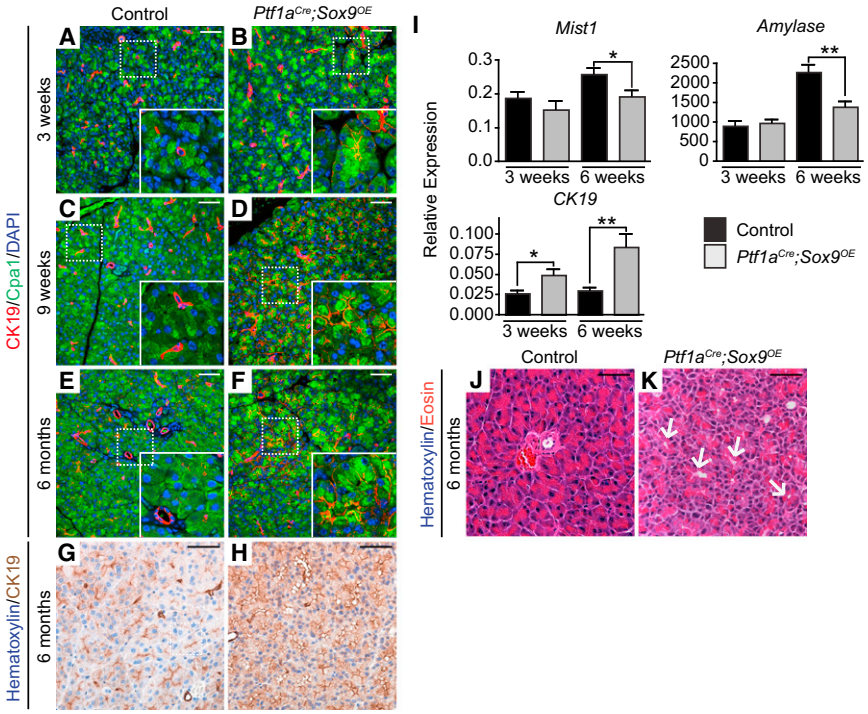

Figure 5. *Sox9* Misexpression Induces Ductal Genes

(A–F) Co-immunofluorescence staining for Cpa1 and CK19 shows CK19$^+$Cpa$^+$ cells in *Ptf1a^{Cre};Sox9^{OE}* mice (B, D, and F), but not in controls (A, C, and E).

(G and H) Immunohistochemistry for CK19 reveals greater staining intensity in 6-month-old *Ptf1a^{Cre};Sox9^{OE}* than in control mice.

(I) QRT-PCR analysis of *Mist1*, *amylase*, and *CK19* in whole pancreas RNA from *Ptf1a^{Cre};Sox9^{OE}* and control mice (n = 5).

(J and K) H&E staining shows acinar clusters with dilated lumens in 6-month-old *Ptf1a^{Cre};Sox9^{OE}* mice (K, arrows). Values are shown as mean ± SEM. *p < 0.05 and **p < 0.01. Scale bars: 50 μm.

Ptf1a^{Cre};Sox9^{OE} mice expressed the HA-tag and Sox9 predominantly in acinar cells, whereas ducts and endocrine clusters remained largely unrecombined and retained RFP (Figures S3E–S3G and S3J–S3L). In 3-week-old *Ptf1a^{Cre};Sox9^{OE}* mice, pancreatic weight, overall tissue morphology and blood glucose levels were similar to control mice (Figures S3C, S3D, S3H, S3I, S3M, and S3N), suggesting that *Ptf1a^{Cre}*-mediated *Sox9* misexpression has no overt effect on pancreatic development.

Similar to *Ptf1a^{Cre};Sox9^{OE}* mice, *Ptf1a^{Cre};Kras^{G12D};Sox9^{OE}* mice also developed normally until 3 weeks of age (data not shown), but thereafter began to exhibit signs of exocrine insufficiency and changes in gross pancreatic morphology not seen in *Ptf1a^{Cre};Kras^{G12D}* or *Ptf1a^{Cre};Sox9^{OE}* mice (Figures S3O–S3Q; data not shown). Synergy between *Sox9* and *Kras^{G12D}* was also observed at a microscopic level, as evidenced by replacement of normal pancreas parenchyma by large areas of Sox9$^+$ ADM and Alcian blue$^+$ PanINs in *Ptf1a^{Cre};Kras^{G12D};Sox9^{OE}* mice (Figures 4T, 4W, and 4AC); a phenotype not seen in age-matched *Ptf1a^{Cre};Kras^{G12D}* or control mice (Figures 4R, 4S, 4U, 4V, 4X, 4Y, 4AA, and 4AB). The pancreatic area occupied specifically by Alcian blue$^+$ PanIN lesions was 17-fold greater in *Ptf1a^{Cre};Kras^{G12D};Sox9^{OE}* than in *Ptf1a^{Cre};Kras^{G12D}* mice (Figure 4AE). Detection of the HA-tag in both ADM and PanIN lesions further demonstrated that they arose from cells expressing the *Sox9^{OE}* transgene (Figure 4Z). Because *Ptf1a^{Cre}* predominantly targets acinar cells (Figures S3K and S3L), these findings suggest that concomitant misexpression of *Sox9* and *Kras^{G12D}* rapidly induces transformation of acinar cells into duct-like cells and subsequent PanIN formation. Consistent with this notion, very few cells retained Cpa1 in *Ptf1a^{Cre};Kras^{G12D};Sox9^{OE}* mice and CK19$^+$ ductal structures were predominant (Figure 4AF). Within these structures, few CK19$^+$ cells coexpressed Cpa1 (Figure 4AF, arrows), indicating that most cells had already transitioned from a CK19$^+$Cpa1$^+$ into a CK19$^+$Cpa1$^-$ state characteristic of ADR (De La O et al., 2008; Morris et al., 2010). Together, these results suggest that *Sox9* accelerates *Kras^{G12D}*-mediated PanIN formation by suppressing a mature acinar cell program and/or promoting a duct-like state (Figure S3R).

Sox9 Induces Ductal Genes in Acinar Cells

To determine whether forced expression of *Sox9* in acinar cells induces a duct-like state in the absence of oncogenic Kras, we examined *Ptf1a^{Cre};Sox9^{OE}* mice for coexpression of CK19 with Cpa1. In *Ptf1a^{Cre};Sox9^{OE}* mice at 3 weeks of age or older, Cpa1 colocalized with CK19, whereas the two domains remained separate in control mice (Figures 5A–5F). QRT-PCR confirmed the increase in *CK19* and also revealed a decrease in acinar cell-specific genes (Figure 5I). While these molecular changes are indicative of acinar cell de-differentiation, the CK19$^+$Cpa1$^+$ cells largely retained acinar morphology and did not form duct-like structures (Figures 5E–5H, 5J, and 5K). This suggests that *Sox9* expression in acinar cells destabilizes the acinar cell state and promotes expression of ductal genes, but is not sufficient to induce complete ductal reprogramming.

Sox9 Promotes Acinar-to-Ductal Reprogramming and Induces Mucinous Metaplasia after Pancreatic Injury

Although Kras activation induces ADM and PanINs, it does so with considerable latency, which is significantly shortened in the presence of pancreatitis (De La O and Murtaugh, 2009; Guerra et al., 2007; Morris et al., 2010). To test whether Sox9, like oncogenic Kras, requires inflammatory cues to initiate widespread ADM, we induced acute pancreatitis in *Ptf1a^{Cre};Sox9^{OE}* mice. Injection with caerulein on consecutive days (Figure 6A) resulted in loss of acinar morphology and induction of Sox9 and CK19 in a subset of Cpa1$^+$ cells 2 days after treatment (Figures 6C, 6I, and 6O). In control mice, normal pancreatic morphology was restored after 7 days and CK19 and Sox9 expression was again restricted to ductal cells (Figures 6B, 6D, 6H, 6J, 6N, and

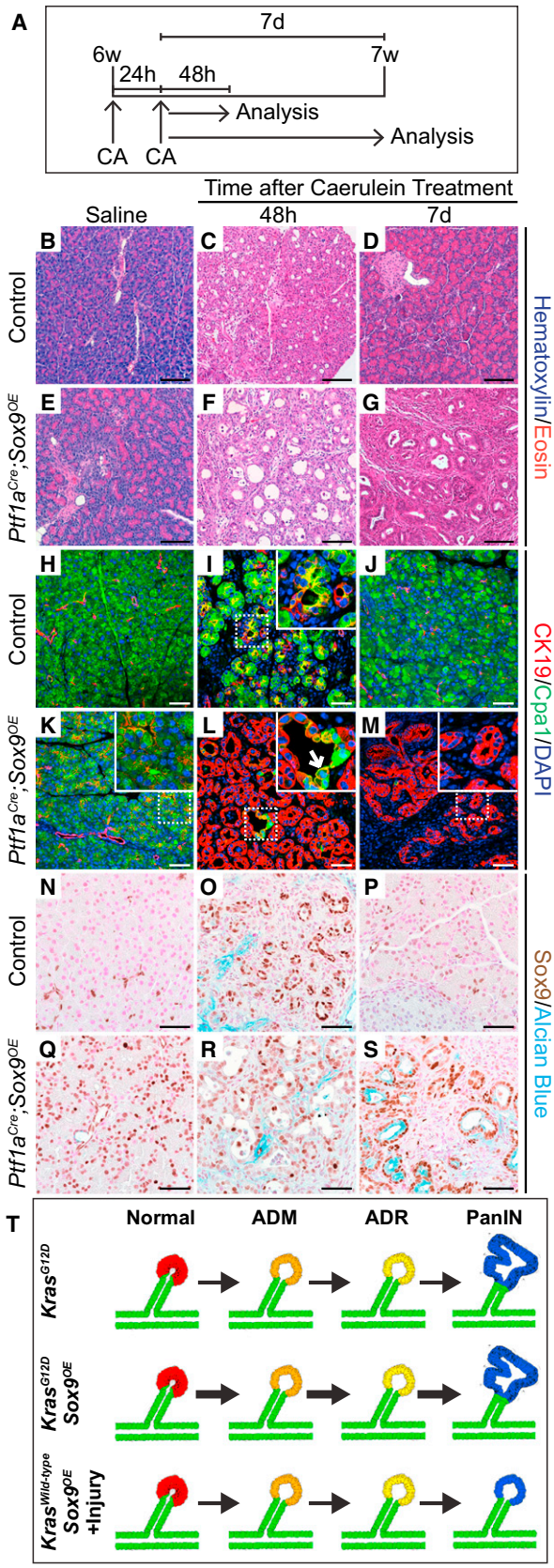

Figure 6. *Sox9* Promotes Persistent ADR and Formation of Mucinous Metaplastic Lesions after Acute Pancreatitis

(A) Six-week-old *Ptf1a*^{Cre};*Sox9*^{OE} and control mice were treated with two sets of caerulein (CA) or saline injections on consecutive days and analyzed 48 hr (h) or 7 days (d) later. Saline-treated mice were analyzed at 21 days.

(B–G) H&E staining reveals persistent ADM in *Ptf1a*^{Cre};*Sox9*^{OE} mice (G).

(H–M) Co-immunofluorescence staining for CK19 and Cpa1 shows a few CK19^{+}Cpa1^{+} (L, arrow) 48 hr after CA and mainly CK19^{+}Cpa1^{-} cells after 7 days (M) in *Ptf1a*^{Cre};*Sox9*^{OE} mice.

(N–S) Immunohistochemistry for Sox9 and Alcian blue staining shows Sox9^{+}Alcian blue^{+} mucinous metaplastic lesions in *Ptf1a*^{Cre};*Sox9*^{OE} mice (S) but not in control mice (P) 7 days after CA.

(T) Schematic summarizing the phenotypes of *Sox9* misexpressing mice in the presence and absence of *Kras*^{G12D} or acute pancreatitis. w, weeks. Scale bars: 100 μm (B–G) and 50 μm (H–S).

See also Figure S4.

6P). Two days after caerulein administration, *Ptf1a*^{Cre};*Sox9*^{OE} mice displayed more severe ductal metaplasia than control mice (Figures 6C and 6F) with numerous CK19^{+}Cpa1^{-} and Sox9^{+} cell clusters (Figures 6L and 6R). After 7 days, acinar morphology was not restored and CK19^{+}Cpa1^{-} ductal structures characteristic of ADR persisted (Figures 6E–6G, 6K–6M, and 6Q–6S). These findings show that *Sox9* misexpression is sufficient to promote reprogramming of acinar cells into a persistent duct-like state after pancreatic injury. Interestingly, a subset of the persistent ductal structures that arose from cells expressing the *Sox9*^{OE} transgene were Sox9^{+}Alcian blue^{+} (Figures S4A–S4G and 6S). These lesions displayed morphologic similarity to mucinous lesions observed in a chronic pancreatitis model (Strobel et al., 2007) with little cellular atypia and low amounts of acidic mucins compared to Kras^{G12D}-induced PanINs. Since acute pancreatitis alone is not sufficient to induce mucinous duct-like lesions, our data suggest that persistent expression of Sox9 in acinar cells in the context of tissue injury can initiate a cell state with some characteristics of mucinous PDA precursor lesions (Figure 6T).

Sox9 Is Not Absolutely Required for Injury-Induced Acinar-to-Ductal Metaplasia but Is Necessary for Further Progression into PanINs

Deletion of *Sox9* in the presence of oncogenic *Kras* completely blocked *Kras*^{G12D}-mediated changes in pancreas morphology, including the development of ADM and PanINs (Figures 4E–4Q). However, it remains unclear whether pancreatic injury can still induce ADM and premalignant lesions in the absence of *Sox9*. To address this question, we deleted *Sox9* in acinar cells and examined pancreata for ADM after caerulein treatment (Figure S4H). As expected, control mice exhibited transient ADM characterized by ectopic Sox9 and CK19 expression in acinar cells 2 days after caerulein treatment (Figures S4J, S4P, and S4V, arrows). Similar lesions devoid of Sox9 were found in caerulein-treated *Ptf1a*^{CreER};*Sox9*$^{f/f}$ mice (Figures 4M, 4S, and 4Y, arrows), suggesting that Sox9 activity is not absolutely required to initiate ADM. In both control and *Sox9*-deleted mice, areas of ADM were replaced by normal acinar tissue after 7 days (Figures S4I, S4K, S4L, S4N, S4O, S4Q, S4R, S4T, S4U, S4W, S4X, and S4Z). These data suggest that pancreatic injury can induce ADM-initiating cues independent of *Sox9*.

The finding that pancreatitis causes ADM even in the absence of *Sox9* raises the question of whether *Sox9*-deleted acinar cells can undergo ADR and form PanINs if expression of oncogenic

Kras is combined with pancreatic injury. To first examine whether *Sox9* is necessary for $Kras^{G12D}$-mediated ADR, we deleted *Sox9* and activated $Kras^{G12D}$ expression in $Ptf1a^{CreER}$;$Kras^{G12D}$;$Sox9^{f/f}$ mice at 3 weeks of age and induced acute pancreatitis 3 weeks later (Figures 7A and S5A). Because Kras had only been active for 6 weeks, PanINs were still rare in $Ptf1a^{CreER}$;$Kras^{G12D}$;$Sox9^{+/+}$ mice in the absence of caerulein (Figure 7G). Caerulein induced widespread formation of $Sox9^{+}$ ADM in $Ptf1a^{CreER}$;$Sox9^{+/+}$ and $Ptf1a^{CreER}$;$Kras^{G12D}$;$Sox9^{+/+}$ mice within 2 days after treatment (Figures 7B, 7C, 7G, 7H, S5B, S5C, S5E, and S5F). Notably, in *Sox9*-deleted $Ptf1a^{CreER}$;$Kras^{G12D}$;$Sox9^{f/f}$ pancreata, $Sox9^{-}$ duct-like structures were still present (Figures 7L, 7M, S5H, and S5I, arrows), confirming our previous observation that *Sox9* is not absolutely required for injury-induced ADM. As expected, ADM was transient in the absence of $Kras^{G12D}$ and the ductal structures were replaced by $Cpa1^{+}$ acini after 21 days (Figures 7B, 7D, 7E, S5B, and S5D). In contrast, Kras-active $Ptf1a^{CreER}$;$Kras^{G12D}$;$Sox9^{+/+}$ mice displayed persistent $Sox9^{+}$ ADM (Figures 7I and S5G, arrows), $CK19^{+}Cpa1^{-}$ duct-like structures (Figure 7J, arrow), as well as numerous $Sox9^{+}$ lesions with morphologic characteristics of PanINs (Figures 7J, 7K, and S5G, arrowheads). Significantly, *Sox9* deletion in the presence of oncogenic Kras abrogated caerulein-induced PanIN formation, while some $Sox9^{-}CK19^{+}Cpa1^{-}$ duct-like lesions persisted (Figures 7N, 7O, and S5J, arrows). Consistent with these findings, numerous Alcian $blue^{+}$ cells were detected in $Ptf1a^{CreER}$;$Kras^{G12D}$;$Sox9^{+/+}$ mice, but virtually none in $Ptf1a^{CreER}$;$Kras^{G12D}$;$Sox9^{f/f}$ mice (Figures 7F, 7K, 7P, and 7Q). Remaining Alcian $blue^{+}$ lesions in $Ptf1a^{CreER}$;$Kras^{G12D}$;$Sox9^{f/f}$ mice were $Sox9^{+}$ (Figures S5K–S5M) and therefore escaped recombination. Together, these findings show that pancreatic injury can, at least partially, overcome the block in ADM caused by *Sox9* inactivation in Kras-active acinar cells, but cannot induce PanINs in the absence of *Sox9* (Figure 7R). Thus, *Sox9* is critically required for reprogramming of acini into PanINs.

DISCUSSION

The Cellular Origin of PanINs

Our study demonstrates that acinar cells exhibit a much higher propensity to form PanINs after oncogenic mutation of *Kras* than ductal or CACs. This finding was surprising, because PDA has been suggested to originate from CACs due to shared molecular features between PanINs and CACs. Notably, although exceedingly low in frequency, PanINs were observed after *Sox9CreER*-mediated $Kras^{G12D}$ activation. Since the *Sox9CreER* transgene also induces recombination in a small number of acinar cells, one possibility is that these rare PanINs originated from acinar cells that recombined the $Kras^{G12D}$ allele. However, we observed that the PanINs were predominantly associated with large pancreatic ducts, which argues against an acinar origin. A similar association of PanINs with large ducts has been described in $CK19^{CreER}$;$Kras^{G12D}$ mice, a model in which recombination is mainly induced in large ducts and not in small ducts or CACs (Ray et al., 2011). Together, these observations suggest that large pancreatic ducts, but not CACs, can give rise to PanINs, albeit at an extremely low frequency.

The location of PanINs close to large ducts points to a possible involvement of pancreatic duct glands in PanIN formation. Pancreatic duct glands are small blind-ended pouches within the larger pancreatic ducts that express embryonic progenitor markers, proliferate in response to pancreatitis, and display some metaplastic features similar to PanINs even in the absence of oncogenic mutations (Strobel et al., 2010). These features may render pancreatic duct glands susceptible to transformation by oncogenic Kras. The scarcity of pancreatic duct glands within the organ could explain why despite targeting of duct glands by the *Sox9CreER* transgene (Kopp et al., 2011), PanIN frequency was extremely low in *Sox9CreER*;$Kras^{G12D}$ mice. Of note, because recombination was only induced in 12% of all $Sox9^{+}$ cells by our tamoxifen regimen, the duct glands may not have been targeted in every mouse, which is consistent with the absence of PanINs in a subset of *Sox9CreER*;$Kras^{G12D}$ mice. At present, very little is known about the biological role of pancreatic duct glands, but their possible involvement in PDA initiation warrants further investigation.

Our finding that ductal and CACs do not readily form PanINs in response to oncogenic Kras raises the question of whether the ductal/CAC compartment is generally refractory to oncogenic transformation. In addition to activating mutations in *KRAS*, loss-of-function mutations in the tumor suppressors TP53, CDKN2A, or PTEN have also been found in PDA (Feldmann et al., 2007; Kanda et al., 2012; Ying et al., 2011). Notably, *Pten* loss results in rapid formation of invasive carcinoma, which is preceded by significant expansion of CACs (Stanger et al., 2005). This suggests that CACs, ductal cells and acinar cells may have the potential to initiate invasive carcinoma, but that each cellular context may require a different repertoire of genetic alterations for tumor initiation. Cell-specific induction of different oncogenic mutations in mice may define morphologically and molecularly distinct tumors, which may help identify human PDA subtypes that respond differently to therapeutic intervention.

Duct-Associated Genes Orchestrate the Emergence of Premalignant Lesions from Acinar Cells

Our cell tracing studies show that the predominant mechanism by which $Kras^{G12D}$ induces PanINs is to initiate a gene expression program similar to pancreatic ducts in acinar cells. We further show that the transcription factor Sox9 promotes, and is required for, PanIN formation from the acinar cell compartment. Recent studies have revealed a role for *Sox9* in maintaining ductal cell morphology and regulating duct-specific genes (Delous et al., 2012; Manfroid et al., 2012; Shih et al., 2012), suggesting that Sox9 might have a similar function during acinar cell conversion into PanINs. Consistent with this notion, we found that Sox9 induces *CK19* expression and promotes ADR in the presence of $Kras^{G12D}$ or pancreatic injury. Furthermore, a role for *Sox9* in conferring certain ductal characteristics to cells has recently been demonstrated in a model of surgically-induced pancreatitis (Prevot et al., 2012). While *Sox9* promotes ADM and ADR in gain-of-function experiments, our results show that tissue injury can still, to some extent, induce ADM from *Sox9*-deficient acinar cells. This suggests that other factors can compensate for Sox9 during injury-induced ADM. One candidate is the duct-specific transcription factor Hnf6, which is

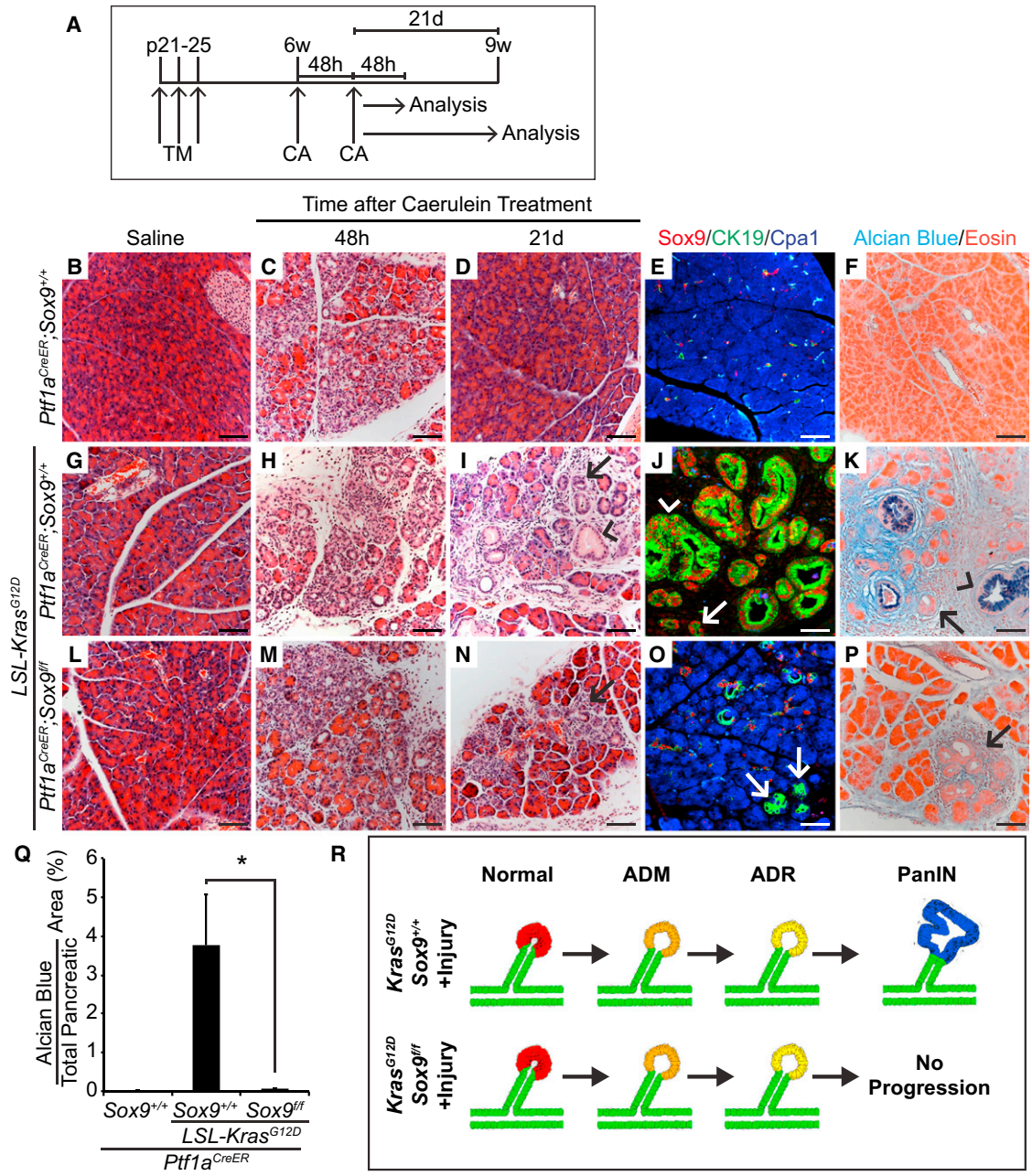

Figure 7. *Sox9*-Deficient Acinar Cells Expressing Kras^{G12D} Can Undergo Persistent ADR after Acute Pancreatitis, but Do Not Progress into PanINs

(A) *Ptf1a*^{CreER};*Sox9*$^{+/+}$, *Ptf1a*^{CreER};*LSL-Kras*^{G12D};*Sox9*$^{+/+}$ and *Ptf1a*^{CreER};*LSL-Kras*^{G12D};*Sox9*$^{f/f}$ mice were injected with tamoxifen (TM) at postnatal day (p) 21, 23, and 25. At 6 weeks (w) of age, mice were treated with two sets of caerulein (CA) or saline injections on alternating days and analyzed 48 hr (h) or 21 days (d) later.

(B–D, G–I, and L–N) H&E staining shows persistent ADM in *Ptf1a*^{CreER};*LSL-Kras*^{G12D};*Sox9*$^{+/+}$ and to a lesser extent also in *Ptf1a*^{CreER};*LSL-Kras*^{G12D};*Sox9*$^{f/f}$ mice (I and N, arrows). PanINs are only present in *Ptf1a*^{CreER};*LSL-Kras*^{G12D};*Sox9*$^{+/+}$ mice (I), arrowhead).

(E, J, and O) Co-immunofluorescence staining for CK19, Cpa1, and Sox9 reveals CK19^{+}Cpa1^{-} duct-like cell clusters in *Ptf1a*^{CreER};*LSL-Kras*^{G12D} mice in the presence and absence of *Sox9* (J and O, arrows).

(F, K, and P) Alcian blue and eosin staining shows PanINs in *Ptf1a*^{CreER};*LSL-Kras*^{G12D};*Sox9*$^{+/+}$ mice (K), but not in *Ptf1a*^{CreER};*LSL-Kras*^{G12D};*Sox9*$^{f/f}$ mice (P). Arrows in K and P point to ADM and arrowheads in J and K to PanINs.

(Q) Quantification of Alcian blue^{+} pancreatic area 21 days after CA (n = 4–5).

(R) Schematic summarizing the phenotype observed in *Sox9* loss-of-function experiments in the presence of *Kras*^{G12D} and acute pancreatitis. Values are shown as mean ± SEM. *p < 0.05. Scale bars: 50 μm.

See also Figure S5.

induced in acinar cells by pancreatic injury and is both necessary and sufficient for ADM (Prevot et al., 2012). In the absence of *Sox9*, however, Hnf6 is less efficient in inducing CK19 (Prevot et al., 2012), suggesting synergy between Hnf6 and Sox9 during ductal conversion of acinar cells. Different from Sox9, Hnf6 expression is not maintained in PanINs and PDA (Prevot et al., 2012). Therefore, only Sox9 expression is sustained in PanINs, providing a possible explanation for why Sox9 is absolutely required for PanIN formation.

Acinar-derived duct-like lesions and pancreatic ducts display similar molecular and morphological features, yet PanINs emerge more readily from acinar-derived duct-like cells than ductal cells. This implies that duct-like lesions differ from native pancreatic ducts. The transcription factors Sox9, Hnf6, and Hes1 are not only markers for pancreatic ductal cells, but are also expressed in multipotent progenitors of the developing pancreas (Jacquemin et al., 2003; Miyamoto et al., 2003; Seymour et al., 2007), raising the question of whether ADM is truly ductal in nature or more closely resembles embryonic progenitors. Previous studies have suggested that ADM lesions are similar to immature embryonic progenitor-like cells because they express Pdx1, Nestin, and Hes1 (Jensen et al., 2005; Miyamoto et al., 2003; Shi et al., 2012; Song et al., 1999). However, multipotent progenitor markers, such as Hnf1b and Nkx6.1 (Schaffer et al., 2010; Solar et al., 2009), are not present in acinar-derived duct-like cells (Jensen et al., 2005; Prevot et al., 2012) indicating that these cells may resemble an acinar-committed yet still immature Nestin-positive progenitor cell (Carrière et al., 2007; Esni et al., 2004). Comparative transcriptome analysis of these different native and transformed cell populations will shed light on the molecular differences between these populations and could provide clues as to why PanINs readily emerge from acinar cells, but not ducts, in response to oncogenic Kras.

The Role of Acinar-to-Ductal Metaplasia in the Initiation of Pancreatic Neoplasia

Our finding that PanINs predominantly originate from acinar cells identifies the transition of acinar cells into a duct-like state as an important early event in tumor initiation. In addition to induction of ductal genes, destabilization of the acinar cell phenotype appears to also promote ADM and PanINs, as evidenced by an acceleration in $Kras^{G12D}$-mediated ADM and PanIN formation after deletion of the acinar-restricted transcription factor *Mist1* (Shi et al., 2009, 2012). This suggests that the observed synergy between oncogenic Kras and *Sox9* misexpression or pancreatic injury in PanIN initiation might be a result of each condition increasing acinar cell plasticity. Therefore, known risk factors for PDA, such as chronic pancreatitis or genetic variants of acinar-specific genes (Li et al., 2012; Lowenfels et al., 1993, 1997), may increase PDA risk by rendering acinar cells more plastic and reducing the threshold for ADM. It is important to note that a direct lineage relationship between ADM and PanINs has yet to be formally demonstrated and the possibility remains that ADM lesions do not directly transition into PanINs. However, it is clear that both ADM and PanIN lesions arise from acinar cells (Guerra et al., 2007; Morris et al., 2010) and that reducing ADM formation through inhibition of the EGFR pathway or overexpression of pro-acinar genes reduces $Kras^{G12D}$-induced PanINs (Ardito et al., 2012; Navas et al., 2012; Shi et al., 2012). This suggests that pathways critical for ADM are also necessary for PanIN formation.

Our results imply that therapeutic targeting of signaling pathways involved in ductal reprogramming of acinar cells could prevent PDA initiation. Previous studies have demonstrated that the EGFR, Hedgehog and Notch signaling pathways promote ADM and PanIN formation (De La O et al., 2008; Fendrich et al., 2008; Miyamoto et al., 2003; Pasca di Magliano et al., 2006; Rajurkar et al., 2012; Siveke et al., 2007). Interestingly, these pathways are known to be upstream regulators of *Sox9* expression in multiple organs (Bien-Willner et al., 2007; Haller et al., 2012; Ling et al., 2010; Meier-Stiegen et al., 2010; Muto et al., 2009; Zong et al., 2009). Moreover, Notch signaling has recently been shown to control *Sox9* expression and induce ductal genes in the pancreas (Delous et al., 2012; Manfroid et al., 2012; Shih et al., 2012). Therefore, it is possible that Sox9 is the critical effector of Notch during PanIN induction. Consistent with this notion, inhibition of Notch signaling in the presence of oncogenic Kras reduced PanIN formation (Plentz et al., 2009), similar to *Sox9* inactivation in our current study. However, it remains to be examined how inputs from different signaling pathways converge on Sox9 to promote PanIN initiation. Our findings now pave the way for future studies exploring whether the inhibition of acinar cell plasticity could have therapeutic applications in the prophylaxis of PDA in high-risk individuals.

EXPERIMENTAL PROCEDURES

Mouse Procedures

All animal experiments described herein were approved by the University of California, San Diego and San Francisco Institutional Animal Care and Use Committees. The sources for mouse strains as well as genotyping and glucose measurement strategies are described in the Supplemental Experimental Procedures. Tamoxifen (Sigma-Aldrich) was dissolved in corn oil and administered subcutaneously at 5 mg/40 g per injection. Mice were injected with caerulein (50 μg/kg diluted in saline; Sigma-Aldrich) or saline on two alternating days once every hour for 6 hours each day (used in experiments with $Kras^{G12D}$ mice) or on two consecutive days once every hour for 8 hours each day (used in experiments in absence of $Kras^{G12D}$ allele) (Morris et al., 2010).

Histology, Immunohistochemical and Immunofluorescence Analysis

Paraffin-embedded or frozen sections were subjected to hematoxylin (Mayers or Harris formulations), eosin, Alcian blue, nuclear fast red (Vector Labs), immunohistochemical or immunofluorescence staining as described (Morris et al., 2010; Seymour et al., 2007, 2008). Detailed procedures for histologic and morphometric analyses, as well as a list of primary and secondary antibodies can be found in the Supplemental Experimental Procedures.

Statistical Analysis

P values were calculated using the two-tailed Student's t test with the GraphPad Prism or Excel software.

SUPPLEMENTAL INFORMATION

Supplemental Information includes five figures, one table, and Supplemental Experimental Procedures and can be found with this article online at http://dx.doi.org/10.1016/j.ccr.2012.10.025.

ACKNOWLEDGMENTS

We thank Nissi Varki (UCSD Cancer Center, Histopathology Core), Cecilia Austin, Jimmy Chen, Nancy Rosenblatt, Sangho Yu, and Kai En Tang for

expert technical assistance and Andrew Lowy and members of the Sander and Hebrok laboratories for discussions and comments on the manuscript. For mouse lines and antibodies, we would like to thank David Tuveson, (UK Cambridge Research Institute; *Kras*^{G12D} mice), Gerd Scherer (University of Freiburg; *Sox9*^{flox} mice), and Chrissa Kioussi (Oregon State University; anti-GFP antibody). Microscopy was supported by resources from the UCSF Diabetes and Endocrinology Research Center (DERC). This work was supported by NIH-R01DK078803 to M.S., NIH-R01CA112537 to M.H., NIH-F32CA136124 to J.L.K., and DFG-FI1719/1-1 to G.V.F.

Received: July 26, 2012
Revised: October 1, 2012
Accepted: October 30, 2012
Published online: November 29, 2012

REFERENCES

Aguirre, A.J., Bardeesy, N., Sinha, M., Lopez, L., Tuveson, D.A., Horner, J., Redston, M.S., and DePinho, R.A. (2003). Activated Kras and Ink4a/Arf deficiency cooperate to produce metastatic pancreatic ductal adenocarcinoma. Genes Dev. *17*, 3112–3126.

Ardito, C.M., Grüner, B.M., Takeuchi, K.K., Lubeseder-Martellato, C., Teichmann, N., Mazur, P.K., Delgiorno, K.E., Carpenter, E.S., Halbrook, C.J., Hall, J.C., et al. (2012). EGF Receptor Is Required for KRAS-Induced Pancreatic Tumorigenesis. Cancer Cell *22*, 304–317.

Bien-Willner, G.A., Stankiewicz, P., and Lupski, J.R. (2007). SOX9cre1, a cis-acting regulatory element located 1.1 Mb upstream of SOX9, mediates its enhancement through the SHH pathway. Hum. Mol. Genet. *16*, 1143–1156.

Brembeck, F.H., Schreiber, F.S., Deramaudt, T.B., Craig, L., Rhoades, B., Swain, G., Grippo, P., Stoffers, D.A., Silberg, D.G., and Rustgi, A.K. (2003). The mutant K-ras oncogene causes pancreatic periductal lymphocytic infiltration and gastric mucous neck cell hyperplasia in transgenic mice. Cancer Res. *63*, 2005–2009.

Carrière, C., Seeley, E.S., Goetze, T., Longnecker, D.S., and Korc, M. (2007). The Nestin progenitor lineage is the compartment of origin for pancreatic intraepithelial neoplasia. Proc. Natl. Acad. Sci. USA *104*, 4437–4442.

Carrière, C., Young, A.L., Gunn, J.R., Longnecker, D.S., and Korc, M. (2009). Acute pancreatitis markedly accelerates pancreatic cancer progression in mice expressing oncogenic Kras. Biochem. Biophys. Res. Commun. *382*, 561–565.

Cornish, T.C., and Hruban, R.H. (2011). Pancreatic Intraepithelial Neoplasia. Surgical Pathology Clinics *4*, 523–535.

De La O, J.P., and Murtaugh, L.C. (2009). Notch and Kras in pancreatic cancer: at the crossroads of mutation, differentiation and signaling. Cell Cycle *8*, 1860–1864.

De La O, J.P., Emerson, L.L., Goodman, J.L., Froebe, S.C., Illum, B.E., Curtis, A.B., and Murtaugh, L.C. (2008). Notch and Kras reprogram pancreatic acinar cells to ductal intraepithelial neoplasia. Proc. Natl. Acad. Sci. USA *105*, 18907–18912.

Delous, M., Yin, C., Shin, D., Ninov, N., Debrito Carten, J., Pan, L., Ma, T.P., Farber, S.A., Moens, C.B., and Stainier, D.Y.R. (2012). Sox9b is a key regulator of pancreaticobiliary ductal system development. PLoS Genet. *8*, e1002754.

Desai, B.M., Oliver-Krasinski, J., De Leon, D.D., Farzad, C., Hong, N., Leach, S.D., and Stoffers, D.A. (2007). Preexisting pancreatic acinar cells contribute to acinar cell, but not islet beta cell, regeneration. J. Clin. Invest. *117*, 971–977.

Esni, F., Stoffers, D.A., Takeuchi, T., and Leach, S.D. (2004). Origin of exocrine pancreatic cells from nestin-positive precursors in developing mouse pancreas. Mech. Dev. *121*, 15–25.

Feldmann, G., Beaty, R., Hruban, R.H., and Maitra, A. (2007). Molecular genetics of pancreatic intraepithelial neoplasia. J. Hepatobiliary Pancreat. Surg. *14*, 224–232.

Fendrich, V., Esni, F., Garay, M.V., Feldmann, G., Habbe, N., Jensen, J.N., Dor, Y., Stoffers, D., Jensen, J., Leach, S.D., and Maitra, A. (2008). Hedgehog signaling is required for effective regeneration of exocrine pancreas. Gastroenterology *135*, 621–631.

Gidekel Friedlander, S.Y., Chu, G.C., Snyder, E.L., Girnius, N., Dibelius, G., Crowley, D., Vasile, E., DePinho, R.A., and Jacks, T. (2009). Context-dependent transformation of adult pancreatic cells by oncogenic K-Ras. Cancer Cell *16*, 379–389.

Goldstein, A.S., Huang, J., Guo, C., Garraway, I.P., and Witte, O.N. (2010). Identification of a cell of origin for human prostate cancer. Science *329*, 568–571.

Guerra, C., Schuhmacher, A.J., Cañamero, M., Grippo, P.J., Verdaguer, L., Pérez-Gallego, L., Dubus, P., Sandgren, E.P., and Barbacid, M. (2007). Chronic pancreatitis is essential for induction of pancreatic ductal adenocarcinoma by K-Ras oncogenes in adult mice. Cancer Cell *11*, 291–302.

Habbe, N., Shi, G., Meguid, R.A., Fendrich, V., Esni, F., Chen, H., Feldmann, G., Stoffers, D.A., Konieczny, S.F., Leach, S.D., and Maitra, A. (2008). Spontaneous induction of murine pancreatic intraepithelial neoplasia (mPanIN) by acinar cell targeting of oncogenic Kras in adult mice. Proc. Natl. Acad. Sci. USA *105*, 18913–18918.

Haller, R., Schwanbeck, R., Martini, S., Bernoth, K., Kramer, J., Just, U., and Rohwedel, J. (2012). Notch1 signaling regulates chondrogenic lineage determination through Sox9 activation. Cell Death Differ. *19*, 461–469.

Heiser, P.W., Cano, D.A., Landsman, L., Kim, G.E., Kench, J.G., Klimstra, D.S., Taketo, M.M., Biankin, A.V., and Hebrok, M. (2008). Stabilization of beta-catenin induces pancreas tumor formation. Gastroenterology *135*, 1288–1300.

Hezel, A.F., Kimmelman, A.C., Stanger, B.Z., Bardeesy, N., and Depinho, R.A. (2006). Genetics and biology of pancreatic ductal adenocarcinoma. Genes Dev. *20*, 1218–1249.

Hingorani, S.R., Petricoin, E.F., Maitra, A., Rajapakse, V., King, C., Jacobetz, M.A., Ross, S., Conrads, T.P., Veenstra, T.D., Hitt, B.A., et al. (2003). Preinvasive and invasive ductal pancreatic cancer and its early detection in the mouse. Cancer Cell *4*, 437–450.

Hingorani, S.R., Wang, L., Multani, A.S., Combs, C., Deramaudt, T.B., Hruban, R.H., Rustgi, A.K., Chang, S., and Tuveson, D.A. (2005). Trp53R172H and KrasG12D cooperate to promote chromosomal instability and widely metastatic pancreatic ductal adenocarcinoma in mice. Cancer Cell *7*, 469–483.

Jacquemin, P., Lemaigre, F.P., and Rousseau, G.G. (2003). The Onecut transcription factor HNF-6 (OC-1) is required for timely specification of the pancreas and acts upstream of Pdx-1 in the specification cascade. Dev. Biol. *258*, 105–116.

Jensen, J.N., Cameron, E., Garay, M.V., Starkey, T.W., Gianani, R., and Jensen, J. (2005). Recapitulation of elements of embryonic development in adult mouse pancreatic regeneration. Gastroenterology *128*, 728–741.

Kanda, M., Matthaei, H., Wu, J., Hong, S.M., Yu, J., Borges, M., Hruban, R.H., Maitra, A., Kinzler, K., Vogelstein, B., and Goggins, M. (2012). Presence of somatic mutations in most early-stage pancreatic intraepithelial neoplasia. Gastroenterology *142*, 730–733.

Kopp, J.L., Dubois, C.L., Schaffer, A.E., Hao, E., Shih, H.P., Seymour, P.A., Ma, J., and Sander, M. (2011). Sox9+ ductal cells are multipotent progenitors throughout development but do not produce new endocrine cells in the normal or injured adult pancreas. Development *138*, 653–665.

Li, D., Duell, E.J., Yu, K., Risch, H.A., Olson, S.H., Kooperberg, C., Wolpin, B.M., Jiao, L., Dong, X., Wheeler, B., et al. (2012). Pathway analysis of genome-wide association study data highlights pancreatic development genes as susceptibility factors for pancreatic cancer. Carcinogenesis *33*, 1384–1390.

Ling, H., Sylvestre, J.R., and Jolicoeur, P. (2010). Notch1-induced mammary tumor development is cyclin D1-dependent and correlates with expansion of pre-malignant multipotent duct-limited progenitors. Oncogene *29*, 4543–4554.

Lowenfels, A.B., Maisonneuve, P., Cavallini, G., Ammann, R.W., Lankisch, P.G., Andersen, J.R., Dimagno, E.P., Andrén-Sandberg, A., and Domellöf, L.; International Pancreatitis Study Group. (1993). Pancreatitis and the risk of pancreatic cancer. N. Engl. J. Med. *328*, 1433–1437.

Lowenfels, A.B., Maisonneuve, P., DiMagno, E.P., Elitsur, Y., Gates, L.K., Jr., Perrault, J., and Whitcomb, D.C.; International Hereditary Pancreatitis Study

Group. (1997). Hereditary pancreatitis and the risk of pancreatic cancer. J. Natl. Cancer Inst. *89*, 442–446.

Manfroid, I., Ghaye, A., Naye, F., Detry, N., Palm, S., Pan, L., Ma, T.P., Huang, W., Rovira, M., Martial, J.A., et al. (2012). Zebrafish sox9b is crucial for hepatopancreatic duct development and pancreatic endocrine cell regeneration. Dev. Biol. *366*, 268–278.

Meier-Stiegen, F., Schwanbeck, R., Bernoth, K., Martini, S., Hieronymus, T., Ruau, D., Zenke, M., and Just, U. (2010). Activated Notch1 target genes during embryonic cell differentiation depend on the cellular context and include lineage determinants and inhibitors. PLoS ONE *5*, e11481.

Miyamoto, Y., Maitra, A., Ghosh, B., Zechner, U., Argani, P., Iacobuzio-Donahue, C.A., Sriuranpong, V., Iso, T., Meszoely, I.M., Wolfe, M.S., et al. (2003). Notch mediates TGF alpha-induced changes in epithelial differentiation during pancreatic tumorigenesis. Cancer Cell *3*, 565–576.

Morris, J.P., 4th, Cano, D.A., Sekine, S., Wang, S.C., and Hebrok, M. (2010). Beta-catenin blocks Kras-dependent reprogramming of acini into pancreatic cancer precursor lesions in mice. J. Clin. Invest. *120*, 508–520.

Muto, A., Iida, A., Satoh, S., and Watanabe, S. (2009). The group E Sox genes Sox8 and Sox9 are regulated by Notch signaling and are required for Müller glial cell development in mouse retina. Exp. Eye Res. *89*, 549–558.

Navas, C., Hernández-Porras, I., Schuhmacher, A.J., Sibilia, M., Guerra, C., and Barbacid, M. (2012). EGF receptor signaling is essential for k-ras oncogene-driven pancreatic ductal adenocarcinoma. Cancer Cell *22*, 318–330.

Pasca di Magliano, M., Sekine, S., Ermilov, A., Ferris, J., Dlugosz, A.A., and Hebrok, M. (2006). Hedgehog/Ras interactions regulate early stages of pancreatic cancer. Genes Dev. *20*, 3161–3173.

Plentz, R., Park, J.S., Rhim, A.D., Abravanel, D., Hezel, A.F., Sharma, S.V., Gurumurthy, S., Deshpande, V., Kenific, C., Settleman, J., et al. (2009). Inhibition of gamma-secretase activity inhibits tumor progression in a mouse model of pancreatic ductal adenocarcinoma. Gastroenterology *136*, 1741–1749.

Prevot, P.P., Simion, A., Grimont, A., Colletti, M., Khalaileh, A., Van den Steen, G., Sempoux, C., Xu, X., Roelants, V., Hald, J., et al. (2012). Role of the ductal transcription factors HNF6 and Sox9 in pancreatic acinar-to-ductal metaplasia. Gut *61*, 1723–1732.

Rajurkar, M., De Jesus-Monge, W.E., Driscoll, D.R., Appleman, V.A., Huang, H., Cotton, J.L., Klimstra, D.S., Zhu, L.J., Simin, K., Xu, L., et al. (2012). The activity of Gli transcription factors is essential for Kras-induced pancreatic tumorigenesis. Proc. Natl. Acad. Sci. USA *109*, E1038–E1047.

Ray, K.C., Bell, K.M., Yan, J., Gu, G., Chung, C.H., Washington, M.K., and Means, A.L. (2011). Epithelial tissues have varying degrees of susceptibility to Kras(G12D)-initiated tumorigenesis in a mouse model. PLoS ONE *6*, e16786.

Rovira, M., Scott, S.G., Liss, A.S., Jensen, J., Thayer, S.P., and Leach, S.D. (2010). Isolation and characterization of centroacinar/terminal ductal progenitor cells in adult mouse pancreas. Proc. Natl. Acad. Sci. USA *107*, 75–80.

Schaffer, A.E., Freude, K.K., Nelson, S.B., and Sander, M. (2010). Nkx6 transcription factors and Ptf1a function as antagonistic lineage determinants in multipotent pancreatic progenitors. Dev. Cell *18*, 1022–1029.

Seymour, P.A., Freude, K.K., Tran, M.N., Mayes, E.E., Jensen, J., Kist, R., Scherer, G., and Sander, M. (2007). SOX9 is required for maintenance of the pancreatic progenitor cell pool. Proc. Natl. Acad. Sci. USA *104*, 1865–1870.

Seymour, P.A., Freude, K.K., Dubois, C.L., Shih, H.P., Patel, N.A., and Sander, M. (2008). A dosage-dependent requirement for Sox9 in pancreatic endocrine cell formation. Dev. Biol. *323*, 19–30.

Shi, G., Zhu, L., Sun, Y., Bettencourt, R., Damsz, B., Hruban, R.H., and Konieczny, S.F. (2009). Loss of the acinar-restricted transcription factor Mist1 accelerates Kras-induced pancreatic intraepithelial neoplasia. Gastroenterology *136*, 1368–1378.

Shi, G., Direnzo, D., Qu, C., Barney, D., Miley, D., and Konieczny, S.F. (2012). Maintenance of acinar cell organization is critical to preventing Kras-induced acinar-ductal metaplasia. Oncogene. Published online June 4, 2012. http://dx.doi.org/10.1038/onc.2012.210.

Shih, H.P., Kopp, J.L., Sandhu, M., Dubois, C.L., Seymour, P.A., Grapin-Botton, A., and Sander, M. (2012). A Notch-dependent molecular circuitry initiates pancreatic endocrine and ductal cell differentiation. Development *139*, 2488–2499.

Siveke, J.T., Einwächter, H., Sipos, B., Lubeseder-Martellato, C., Klöppel, G., and Schmid, R.M. (2007). Concomitant pancreatic activation of Kras(G12D) and Tgfa results in cystic papillary neoplasms reminiscent of human IPMN. Cancer Cell *12*, 266–279.

Solar, M., Cardalda, C., Houbracken, I., Martín, M., Maestro, M.A., De Medts, N., Xu, X., Grau, V., Heimberg, H., Bouwens, L., and Ferrer, J. (2009). Pancreatic exocrine duct cells give rise to insulin-producing beta cells during embryogenesis but not after birth. Dev. Cell *17*, 849–860.

Song, S.Y., Gannon, M., Washington, M.K., Scoggins, C.R., Meszoely, I.M., Goldenring, J.R., Marino, C.R., Sandgren, E.P., Coffey, R.J., Jr., Wright, C.V., and Leach, S.D. (1999). Expansion of Pdx1-expressing pancreatic epithelium and islet neogenesis in transgenic mice overexpressing transforming growth factor alpha. Gastroenterology *117*, 1416–1426.

Stanger, B.Z., Stiles, B., Lauwers, G.Y., Bardeesy, N., Mendoza, M., Wang, Y., Greenwood, A., Cheng, K.H., McLaughlin, M., Brown, D., et al. (2005). Pten constrains centroacinar cell expansion and malignant transformation in the pancreas. Cancer Cell *8*, 185–195.

Strobel, O., Dor, Y., Alsina, J., Stirman, A., Lauwers, G., Trainor, A., Castillo, C.F., Warshaw, A.L., and Thayer, S.P. (2007). In vivo lineage tracing defines the role of acinar-to-ductal transdifferentiation in inflammatory ductal metaplasia. Gastroenterology *133*, 1999–2009.

Strobel, O., Rosow, D.E., Rakhlin, E.Y., Lauwers, G.Y., Trainor, A.G., Alsina, J., Fernández-Del Castillo, C., Warshaw, A.L., and Thayer, S.P. (2010). Pancreatic duct glands are distinct ductal compartments that react to chronic injury and mediate Shh-induced metaplasia. Gastroenterology *138*, 1166–1177.

Visvader, J.E. (2011). Cells of origin in cancer. Nature *469*, 314–322.

Ying, H., Elpek, K.G., Vinjamoori, A., Zimmerman, S.M., Chu, G.C., Yan, H., Fletcher-Sananikone, E., Zhang, H., Liu, Y., Wang, W., et al. (2011). PTEN is a major tumor suppressor in pancreatic ductal adenocarcinoma and regulates an NF-κB-cytokine network. Cancer Discov *1*, 158–169.

Zhu, L., Shi, G., Schmidt, C.M., Hruban, R.H., and Konieczny, S.F. (2007). Acinar cells contribute to the molecular heterogeneity of pancreatic intraepithelial neoplasia. Am. J. Pathol. *171*, 263–273.

Zong, Y., Panikkar, A., Xu, J., Antoniou, A., Raynaud, P., Lemaigre, F., and Stanger, B.Z. (2009). Notch signaling controls liver development by regulating biliary differentiation. Development *136*, 1727–1739.

Cancer Cell
Article

Pharmacologic Inhibition of MALT1 Protease by Phenothiazines as a Therapeutic Approach for the Treatment of Aggressive ABC-DLBCL

Daniel Nagel,[1] Stefani Spranger,[3] Michelle Vincendeau,[1] Michael Grau,[4] Silke Raffegerst,[3] Bernhard Kloo,[1] Daniela Hlahla,[1] Martin Neuenschwander,[5] Jens Peter von Kries,[5] Kamyar Hadian,[2] Bernd Dörken,[6] Peter Lenz,[4] Georg Lenz,[6] Dolores J. Schendel,[3] and Daniel Krappmann[1,*]

[1]Research Unit Cellular Signal Integration
[2]Assay Development and Screening Platform
Helmholtz Zentrum München–German Research Center for Environmental Health, Institute of Molecular Toxicology and Pharmacology, Ingolstädter Landstrasse. 1, 85764 Neuherberg, Germany
[3]Helmholtz Zentrum München–German Research Center for Environmental Health, Institute of Molecular Immunology and Immune Monitoring Platform, Marchioninistrasse 25, 81377 Munich, Germany
[4]Department of Physics, Philipps-University Marburg, Renthof 5, 35032 Marburg, Germany
[5]Leibniz-Institut für Molekulare Pharmakologie, Robert-Roessle-Strasse 10, 13125 Berlin, Germany
[6]Department of Hematology, Oncology and Tumorimmunology, Molecular Cancer Research Center, Charité–University Medicine Berlin, Augustenburger Platz 1, Forum 4, 13353 Berlin, Germany
*Correspondence: daniel.krappmann@helmholtz-muenchen.de
http://dx.doi.org/10.1016/j.ccr.2012.11.002

SUMMARY

Proteolytic activity of the mucosa-associated lymphoid tissue lymphoma translocation protein-1 (MALT1) paracaspase is required for survival of the activated B cell subtype of diffuse large B cell lymphoma (ABC-DLBCL). We have identified distinct derivatives of medicinal active phenothiazines, namely mepazine, thioridazine, and promazine, as small molecule inhibitors of the MALT1 protease. These phenothiazines selectively inhibit cleavage activity of recombinant and cellular MALT1 by a noncompetitive mechanism. Consequently, the compounds inhibit anti-apoptotic NF-κB signaling and elicit toxic effects selectively on MALT1-dependent ABC-DLBCL cells in vitro and in vivo. Our data provide a conceptual proof for a clinical application of distinct phenothiazines in the treatment of ABC-DLBCL.

INTRODUCTION

Upon antigenic stimulation, mucosa-associated lymphoid tissue lymphoma translocation protein-1 (MALT1) is a key mediator of upstream NF-κB signaling to control lymphocyte activation, survival, and differentiation (Hailfinger et al., 2009a; Thome, 2008). Together with CARMA1 (also known as CARD11) and BCL10, MALT1 assembles the CBM complex that bridges proximal antigen receptor signaling events to the IκB kinase (IKK) complex, the gatekeeper of the canonical NF-κB pathway (Scheidereit, 2006). Upon T cell antigen receptor (TCR)/CD28 costimulation, MALT1 acts as a protein scaffold that recruits other critical signaling molecules like TRAF6, caspase 8, and A20 to the CBM complex (Thome, 2008). Furthermore, covalent ubiquitin modifications in MALT1 catalyzed by the E3 ligase TRAF6 facilitate the association of two downstream protein kinase complexes, TAB2-TAK1 and NEMO-IKKα/β, which ultimately leads to IKK activation (Oeckinghaus et al., 2007).

In addition to its scaffolding function, MALT1 contains a paracaspase domain that displays high homology to caspases from mammals and metacaspases from plants and fungi (Uren et al., 2000). Like metacaspases, MALT1 cleaves substrates

Significance

Cleavage activity of the mucosa-associated lymphoid tissue lymphoma translocation protein-1 (MALT1) paracaspase contributes to the oncogenic potential of MALT1 in MALT lymphoma and ABC-DLBCL, the latter representing one of the most aggressive lymphoma entities. We identified small molecular compounds belonging to the class of phenothiazines as potent and selective inhibitors of the MALT1 protease. MALT1 inhibition by phenothiazines selectively kills ABC-DLBCL in vitro and in vivo, revealing their potency in achieving target-directed treatment of MALT1-dependent lymphoma. Phenothiazines have been widely used as antipsychotic drugs even in long-term treatment of schizophrenia and psychosis. Thus, well-defined toxicity, pharmacokinetics, and pharmacodynamics can facilitate clinical trials for an off-label use of these compounds in ABC-DLBCL therapy.

after arginine residues, indicating that the enzymatic cleavage activity is quite distinct from caspases, which in general require an aspartate at the P1 position (Vercammen et al., 2004). MALT1 proteolytic activity is induced upon TCR/CD28 costimulation, which promotes cleavage of the substrates BCL10, A20, CYLD, and RelB (Coornaert et al., 2008; Hailfinger et al., 2011; Rebeaud et al., 2008; Staal et al., 2011). Inhibition of MALT1 protease activity by the antagonistic tetrapeptide Z-VRPR-FMK, which was originally designed as an inhibitor of metacaspases in plants, impairs optimal NF-κB activation and interleukin-2 (IL-2) production in T cells (Düwel et al., 2009; Rebeaud et al., 2008). Similarly, mutation of the catalytic cysteine 464 renders MALT1 proteolytically inactive and also impairs IL-2 production after complementation of MALT1-deficient T cells (Düwel et al., 2009). These results indicate that small molecule inhibitors that selectively target MALT1 protease activity may be promising candidates for clinical use in T cell-dependent immune diseases, such as allergic inflammation or autoimmunity.

A tumor-promoting role of MALT1 has been found in a subset of diffuse large B cell lymphoma (DLBCL) and MALT lymphoma (Ngo et al., 2006). By gene expression profiling, DLBCL can be classified into distinct entities and the most abundant subtypes are the ABC-DLBCL and the germinal center B cell-like (GCB-) DLBCL (Alizadeh et al., 2000; Rosenwald and Staudt, 2003; Rosenwald et al., 2002; Savage et al., 2003; Wright et al., 2003). Based on the gene expression signature, the ABC-DLBCL subtype originates from B lymphocytes stimulated through their B cell antigen receptor (BCR). With a 5-year survival rate of 35%, patients with ABC-DLBCL have the worst prognosis, reflecting the aggressive clinical behavior of ABC-DLBCL cells (Lenz et al., 2008b). The hallmark of ABC-DLBCL, but not GCB-DLBCL, cells is the constitutive activation of the NF-κB signaling pathway (Alizadeh et al., 2000; Davis et al., 2001). Congruent with this, a recent genetic study of the DLBCL revealed the preferential association of gene alterations in the NF-κB and BCL6-BLIMP1 axis in ABC-DLBCL and in BCL2 and MYC in GCB-DLBCL, suggesting that anti-apoptotic NF-κB signaling is indeed critical for ABC-DLBCL survival (Pasqualucci et al., 2011). While some ABC-DLBCL patients carry oncogenic CARMA1 mutations (Lenz et al., 2008a), the majority of ABC-DLBCL is characterized by chronic active BCR signaling and in ~20% of the cases activating mutations in the BCR proximal regulator CD79A and CD79B are found (Davis et al., 2010). Consistent with a requirement for BCR signaling, an RNA interference screen identified CARMA1, BCL10, or MALT1 as critical regulators of NF-κB activation, and survival and growth of ABC-DLBCL (Ngo et al., 2006). Furthermore, inhibition of MALT1 proteolytic activity by Z-VRPR-FMK inhibits NF-κB-dependent gene expression and exerts toxic effects specifically in ABC-DLBCL cells (Ferch et al., 2009; Hailfinger et al., 2009b). MALT1 paracaspase activity also contributes to the pathogenesis of MALT lymphoma that is characterized by the translocation t(11;18)(q21;q21), which creates a fusion between the C terminus of MALT1, including the paracaspase domain, and the N terminus of IAP2 (API2-MALT1) (Isaacson and Du, 2004). The paracaspase domain of API2-MALT1 fusion protein catalyzes the cleavage of NIK and thereby enhances noncanonical NF-κB activation, which confers apoptosis resistance (Rosebeck et al., 2011). Thus, specific small molecule inhibitors against the MALT1 paracaspase could be beneficial for the treatment of lymphoma associated with deregulated MALT1 activity, such as ABC-DLBCL and MALT lymphoma.

The peptide Z-VRPR-FMK provided an initial hint that MALT1 inhibition is a feasible strategy for interfering with survival of ABC-DLBCL cells in vitro. However, due to poor pharmacologic properties, Z-VRPR-FMK needs to be administered in very high concentrations to exert effects on cells and antagonistic peptides in general are not adequate for clinical applications. The goal of this study was to identify small molecule inhibitors for pharmacologic inhibition of the MALT1 protease and to determine the effects of these MALT1 inhibitors on ABC-DLBCL proliferation and survival in vitro and in vivo.

RESULTS

Identification of Phenothiazine Derivatives as Selective MALT1 Protease Inhibitors

To identify small molecular weight compounds that could inhibit MALT1 protease activity, we purified recombinant GSTMALT1 from *Escherichia coli* to establish an in vitro protease cleavage assay suitable for high throughput screening (HTS). GSTMALT1 was incubated for 1 hr at 30°C in the presence of 50 μM of the tetrapeptide substrate Ac-LRSR-AMC, which is derived from the MALT1 cleavage site in the C terminus of BCL10 (Rebeaud et al., 2008). Proteolytic activity was determined by measuring the increase of fluorescence that is emitted after cleavage and the accompanying release of the fluorophore AMC (Figures 1A and 1B). MALT1-catalyzed cleavage of Ac-LRSR-AMC is evident from a robust increase in fluorescence intensity over time. As expected, mutation of the conserved cysteine (C453A) in the paracaspase domain of MALT1 (Isoform B) completely abolished MALT1 catalytic activity (Figure 1B). As expected, the tetrapeptide Z-VRPR-FMK blocked MALT1 cleavage activity at low nanomolar concentrations (Figure 1B; Figure S1A available online). In contrast, the potent caspase inhibitory peptide Ac-DEVD-CHO effectively blocked caspase 8 activity at picomolar concentrations, but only marginally reduced MALT1 activity when used at concentrations up to 200 μM (Figures S1B–S1D).

We screened approx. 18,000 compounds of the ChemBioNet collection (Lisurek et al., 2010) using the assay format depicted in Table S1. The primary screen was conducted by measuring the increase in AMC fluorescence in a 384 half-well format over an assay time of 20 min in the presence of 10 μM of each compound (see Supplemental Experimental Procedures). Dose-response assays were performed for secondary hit validation and selectivity on MALT1 was determined by comparing the influence on caspase 8 activity. These analyses yielded 15 hits, corresponding to ~0.08% of the primary screen. When examining the structure of the 15 hits, we noticed that three of the most efficient and selective compounds (Figure S1E, compounds A, B, and C) are derivatives of the tricyclic phenothiazine that contains two outer benzene rings linked by nitrogen and sulfur atoms in the inner ring. Also the heterocyclic core found in compound D displays high structural similarities to phenothiazine, whereby the nitrogen is replaced by carbon. These initial results suggested that certain phenothiazine derivatives (PD) may act as MALT1 inhibitors. Moreover, at 50 μM, all four compounds were reducing MALT1 protease activity to less than 10%, but

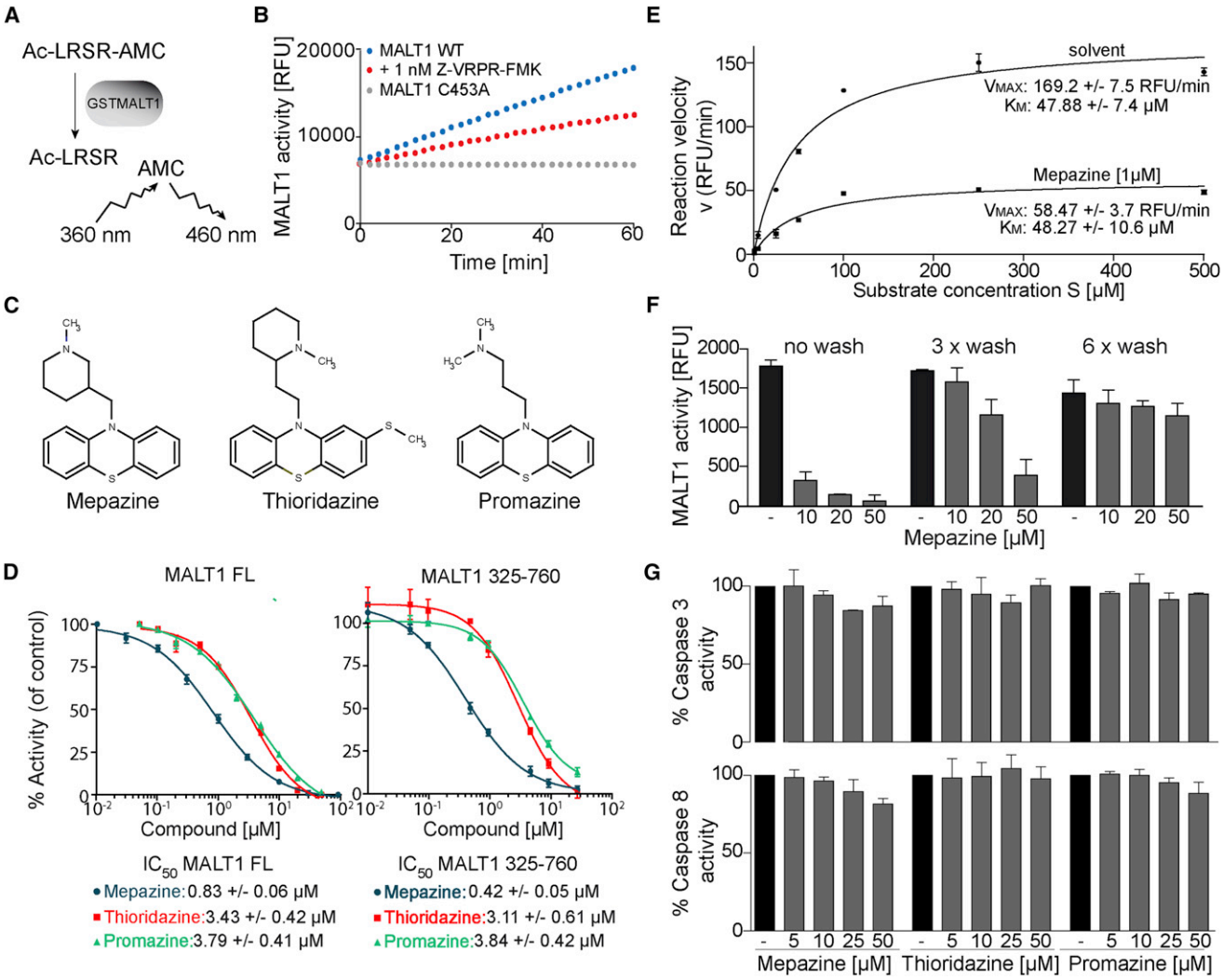

Figure 1. Selective MALT1 Inhibition by Mepazine, Thioridazine, and Promazine

(A) A schematic representation of the MALT1 protease assay for HTS. Cleavage of the fluorophore AMC by GSTMALT1 from the fluorogenic substrate Ac-LRSR-AMC results in an increase of fluorescence.

(B) Purified recombinant GSTMALT1 from bacterial expression was incubated for 1 hr at 30°C with 50 µM of Ac-LRSR-AMC and the proteolytic activity was determined by measuring the increase of AMC fluorescence. Graph shows a representative of at least five independent experiments.

(C) Chemical structures of the three inhibitory compounds.

(D) Dose-response curves and IC_{50} values for mepazine, thioridazine, and promazine.

(E) Michaelis-Menten kinetics was determined by increasing the concentration of Ac-LRSR-AMC substrate in the absence or presence of 1 µM mepazine.

(F) GSTMALT1 coupled to glutathione sepharose beads was treated with mepazine (10, 20, or 50 µM) for 30 min. MALT1 activity was assayed after washing the beads for 0, 3, or 6 times before cleavage reaction was started (mean ± SD; n = 3).

(G) Cleavage of human recombinant caspase 3 and caspase 8 against Ac-DEVD-AMC as substrate (mean ± SD; n = 3).

See also Figure S1 and Table S1.

caspase 8 activity was hardly affected even at the highest inhibitor concentration, indicating that the four PD display a high selectively for MALT1 (Figure S1F). We also tested the core phenothiazine scaffold and found that it inhibited MALT1 activity in a dose-dependent manner (Figure S1G). Notably, our initial results implied that only the modifications of compound A seemed to significantly improve the inhibitory potential of the phenothiazine backbone toward MALT1, suggesting that distinct phenothiazines could be promising candidates as selective MALT1 inhibitors.

Mepazine, Thioridazine, and Promazine Act as Potent and Selective MALT1 Paracaspase Inhibitors

We obtained 26 commercially available PD, to test their inhibitory potential (Figure S1H). Whereas most compounds (12–26) had no or only very weak inhibitory potential (IC_{50} > 20 µM), eight compounds (4–11) inhibited MALT1 activity with an IC_{50} roughly between 5 and 20 µM. Only three PD had an IC_{50} below 5 µM. Thus, only a small subset of PD was capable of efficiently inhibiting MALT1. The three most potent compounds represent promazine, thioridazine, and mepazine, the

latter initially identified in the screening (Figure 1C). To define the inhibitory potential, we determined exact IC_{50} values for each compound on recombinant full length (FL) GSTMALT1 and an enzymatically active MALT1 fragment encompassing amino acids 325 to 760 that contained the paracaspase and C-terminal Ig-like (Ig3) domains (Figure 1D). Mepazine was most effective in inhibiting GSTMALT1 FL and GSTMALT1 325-760 with IC_{50} values of 0.83 and 0.42 μM, respectively. Also thioridazine and promazine showed a dose-dependent inhibition of GSTMALT1 FL and GSTMALT1 325-760, but the IC_{50} values were approximately 4-fold (GSTMALT1 FL) or 8-fold (GSTMALT1 325-760) higher when compared to mepazine. In contrast, promethazine (compound 18 in Figure S1H), a drug still being used in the treatment of certain psychiatric disorders and highly related to the three active PD, did not cause any significant MALT1 inhibition at concentrations up to 20 μM. These results indicate a high degree of specificity in MALT inhibition even within the group of PD.

To test the mode of action, we determined the effect of mepazine in Michaelis-Menten kinetics on the basis of the fluorogenic MALT1 cleavage assay (Figure 1E). GSTMALT1 FL displayed a V_{MAX} of ~170 RFU/min and the Michaelis-Menten constant (K_M) was calculated to ~48 μM, which is in the range of what has been determined previously (Hachmann et al., 2012). Addition of mepazine at a concentration around the IC_{50} (1 μM) strongly decreased the V_{MAX} to ~58 RFU/min while the K_M of 48 μM was not altered. Mepazine and other phenothiazines do not contain reactive groups. However, to confirm that mepazine acts as a noncovalent reversible inhibitor, we performed washout experiments using GSTMALT1 attached to glutathione sepharose beads (Figure 1F). Again, mepazine inhibited MALT1 cleavage activity, but several cycles of washing the GSTMALT1 beads resulted in complete loss of inhibition even at the highest concentration of the compound (50 μM). Thus, the effects of mepazine on MALT1 enzymatic activity revealed a noncompetitive and reversible mode of MALT1 inhibition by phenothiazines.

Next we assayed the effects of PD on caspases, which are structurally the closest relatives of MALT1 in mammals (Uren et al., 2000). Importantly, all three PD did not significantly inhibit caspase 3 or caspase 8 activity, even at concentrations up to 50 μM (Figure 1G), reflecting the selectivity of the compounds as MALT1 inhibitors.

Phenothiazines Inhibit MALT1 Activity and IL-2 Induction in T Cells

As MALT1 protease activity is required for T cell responses, we determined the effects of PD on MALT1 activity and IL-2 production in T cells. We performed a MALT1 cleavage assay after immunoprecipitation (IP) of the protein from Jurkat T cells. Cells were left untreated or incubated for 3 hr with 10 μM of mepazine or thioridazine and subsequently left unstimulated or stimulated with anti-CD3/CD28. MALT1 protease activity was almost undetectable in the absence of stimulation and peaked at 30–60 min after CD3/CD28 treatment. Addition of either mepazine or thioridazine resulted in a strong reduction of MALT1 protease activity in stimulated Jurkat T cells at all time points (Figure 2A). Mepazine and thioridazine incubation also caused a severe reduction in PMA/Ionomycin (P/I)-stimulated MALT1 protease activity in Jurkat T cells (Figure S2A). To confirm that both phenothiazines were inhibiting MALT1 activity inside the cells, we monitored MALT1 cleavage of RelB after stimulation of Jurkat T cells (Figure 2B). RelB cleavage product RelBΔ could be detected when Jurkat T cells were incubated with proteasome inhibitor MG132 prior to P/I stimulation to prevent degradation of the unstable RelB truncation (Hailfinger et al., 2011). As evident from decreased RelBΔ levels and a parallel increased expression of full-length RelB, mepazine and thioridazine impaired RelB cleavage in a dose-dependent manner (Figure 2B). Similar to the situation with recombinant MALT1, mepazine was more efficient in inhibiting cellular MALT1 cleavage activity and significantly reduced the appearance of RelBΔ between 2 and 5 μM, whereas thioridazine was effective above 5 μM.

To determine the impact of MALT1 inhibition by PD on T cell activation, we measured secreted IL-2 amounts by ELISA after P/I or anti-CD3/CD28 stimulation of Jurkat T cells in the presence or absence of mepazine or thioridazine. Both compounds led to a decrease of IL-2 levels in the media of PD-treated cells after T cell activation (Figure 2C). To verify that the inhibitory potential of PD was also detectable in primary T cells, we isolated and purified murine CD4- positive Th1 T cells and measured *IL-2* mRNA induction by qPCR and IL-2 protein levels by ELISA after anti-CD3/CD28 coligation in the presence or absence of 5 and 10 μM of mepazine or thioridazine (Figures 2D and S2B). Both *IL-2* mRNA induction and protein expression were reduced in a dose-dependent manner. Finally, we used primary human peripheral blood mononuclear cells (PBMCs) from three donors to evaluate whether inhibition of MALT1 activity also promoted a decreased IL-2 production in primary human T cells (Figure 2E). Congruent with the previous results, mepazine and thioridazine treatment led to a significant decrease of IL-2 secretion in PBMCs of all three donors.

Phenothiazines Inhibit MALT1 Activity and Induction of NF-κB Target Genes in ABC-DLBCL Cells

Coinciding with a constitutive cleavage of MALT1 substrates, we previously showed enhanced MALT1 protease activity as a characteristic feature of all ABC-DLBCL cells (Kloo et al., 2011). To determine the effect of phenothiazines on cellular MALT1 activity, ABC-DLBCL cells were treated for 4 hr with 5 or 10 μM of mepazine, thioridazine, and promazine. We performed an anti-MALT1 IP and MALT1 protease activity was determined by adding the substrate AC-LRSR-AMC to the precipitates. All three PD inhibited MALT1 protease activity from ABC-DLBCL cells in a dose-dependent manner (Figure 3A). The inhibition after partial MALT1 IP purification suggested that binding of PD promotes MALT1 to adopt an inactive conformation inside the cells. Even though inhibition of cellular MALT1 activity varied depending on the individual cell lines and the compounds, in general, mepazine had the strongest effects and MALT1 activity was reduced by at least 75% in all ABC-DLBCL cells at 10 μM. Treatment of thioridazine and promazine significantly inhibited cellular MALT1 activity and in agreement with in vitro IC_{50} data the effects of both inhibitors were in general weaker compared to mepazine.

Next, we asked whether MALT1 inhibition by the two strongest compounds, mepazine and thioridazine, would also prevent MALT1 substrate cleavage in ABC-DLBCL cells. RelB was shown to counteract anti-apoptotic activity of the NF-κB factors RelA and c-Rel and its cleavage to RelBΔ by MALT1 releases

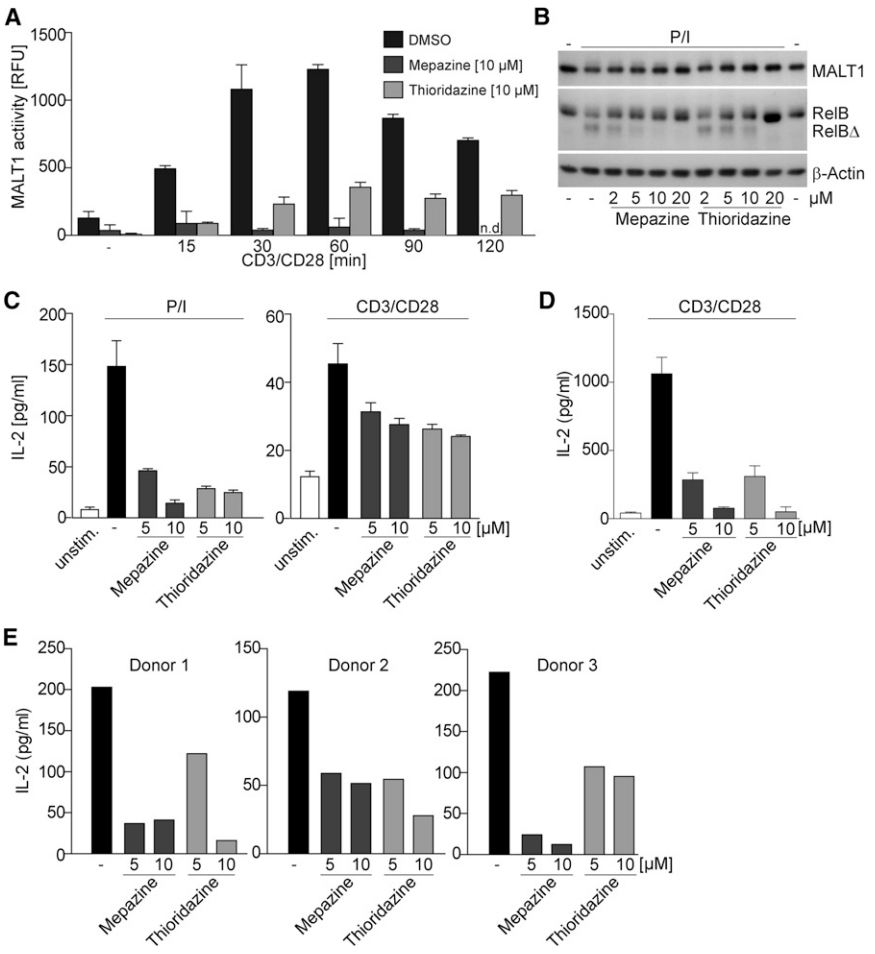

Figure 2. Mepazine and Thioridazine Impair MALT1-Mediated T Cell Activation

(A) Jurkat T cells were untreated or incubated for 3 hr with 10 μM of mepazine or thioridazine and then treated with anti-CD3/CD28 as indicated. Proteolytic activity after immunoprecipitation of MALT1 was determined by fluorogenic protease assay (mean ± SD; n = 3).

(B) Jurkat T cells were treated with solvent, mepazine, or thioridazine for 3 hr prior to 1 hr MG132 incubation. Afterward, cells were stimulated with P/I for 30 min. RelB and RelBΔ were analyzed by western blot. Blots show a representative of at least three independent experiments.

(C) IL-2 secretion was measured by ELISA after P/I or anti-CD3/CD28 stimulation of Jurkat T cells for 20 hr in the presence or absence of mepazine or thioridazine (mean ± SD; n = 3).

(D) Primary murine $CD4^+$ T cells were treated with mepazine or thioridazine and stimulated with anti-CD3/CD28 antibodies for 20 hr and then analyzed for IL-2 secretion (mean ± SD; n = 3).

(E) Primary human PBMCs from three donors were treated with mepazine and thioridazine for 3 hr before induction with anti-CD3/CD28 for 20 hr. Extracellular IL-2 levels were measured by ELISA (mean ± SD; n = 3).

See also Figure S2.

ABC-DLBCL cells from this negative regulation (Hailfinger et al., 2011). The inherently unstable RelB cleavage product (RelBΔ) was detected in ABC-DLBCL cells HBL1, OCI-Ly3, and TMD8 after addition of the proteasome inhibitor MG132 (Figure 3B). When the cells were treated for 4 hr with 2, 5, or 10 μM of mepazine or thioridazine, the appearance of RelBΔ cleavage product was inhibited and full-length RelB was stabilized in a dose-dependent manner. Correlating with the previous results on recombinant and cellular MALT1 inhibition, mepazine was more effective than thioridazine in inhibiting RelB cleavage. These results provided clear evidence that mepazine and thioridazine were effectively inhibiting constitutive cellular MALT1 cleavage activity in ABC-DLBCL cells.

In the ABC-DLBCL cell line HBL1, a MALT1 expression signature was generated using the covalently attached antagonistic tetrapeptide inhibitor Z-VRPR-FMK (Hailfinger et al., 2009b). To gain insight into whether PD exerted similar cellular effects, we determined gene expression profiles in HBL1 cells after different incubation times with mepazine, which most strongly inhibited MALT1 in previous assays (Figure 3C). When we compared the expression signature after administration of mepazine to the expression profile after Z-VRPR-FMK incubation, we observed a significant overlap in the genes that are downregulated in response to both treatments. In fact both the antagonistic tetrapeptide and the pharmacologic compound mepazine inhibited many genes quite rapidly and showed significant effects already after 6 hr of incubation, which further indicated that both inhibitors were exerting these cellular effects by acting through MALT1 inhibition. The weaker effects noted with mepazine after 12 and 24 hr are most likely due to the fact that, in contrast to Z-VRPR-FMK, the PD is inhibiting MALT1 in a noncovalent and reversible manner. As expected, we also observed differences in the two expression profiles, which were most likely related to MALT1-independent off-target effects of either Z-VRPR-FMK or mepazine.

Because MALT1 activity was shown to contribute to NF-κB activation and target gene expression in ABC-DLBCL cells (Ferch et al., 2009; Hailfinger et al., 2009a), we also determined if mepazine treatment impaired NF-κB target gene expression in HBL1 cells (Figure 4A). For this analysis, we compared relative changes in the gene expression after increasing times of treatment with mepazine in HBL1 cells by genome-wide expression arrays to an NF-κB expression signature generated after incubation with the highly specific IKKβ inhibitor MLN120B (Kloo et al., 2011). Mepazine significantly decreased the overall expression as well as the proportion of NF-κB target genes in the signature, clearly indicating that MALT1 inhibition by mepazine, just like Z-VRPR-FMK, suppressed activation of the NF-κB pathway in ABC-DLBCL cells.

To verify the effects of mepazine in other ABC-DLBCL cells, we monitored protein expression of selected NF-κB target genes that are known to possess critical functions for ABC-DLBCL biology (Figures 4B and 4C). One-time mepazine treatment led to a dose-dependent decrease of anti-apoptotic BCL-XL and FLIP-L proteins (Figure 4B). Furthermore, ABC- or GCB-DLBCL

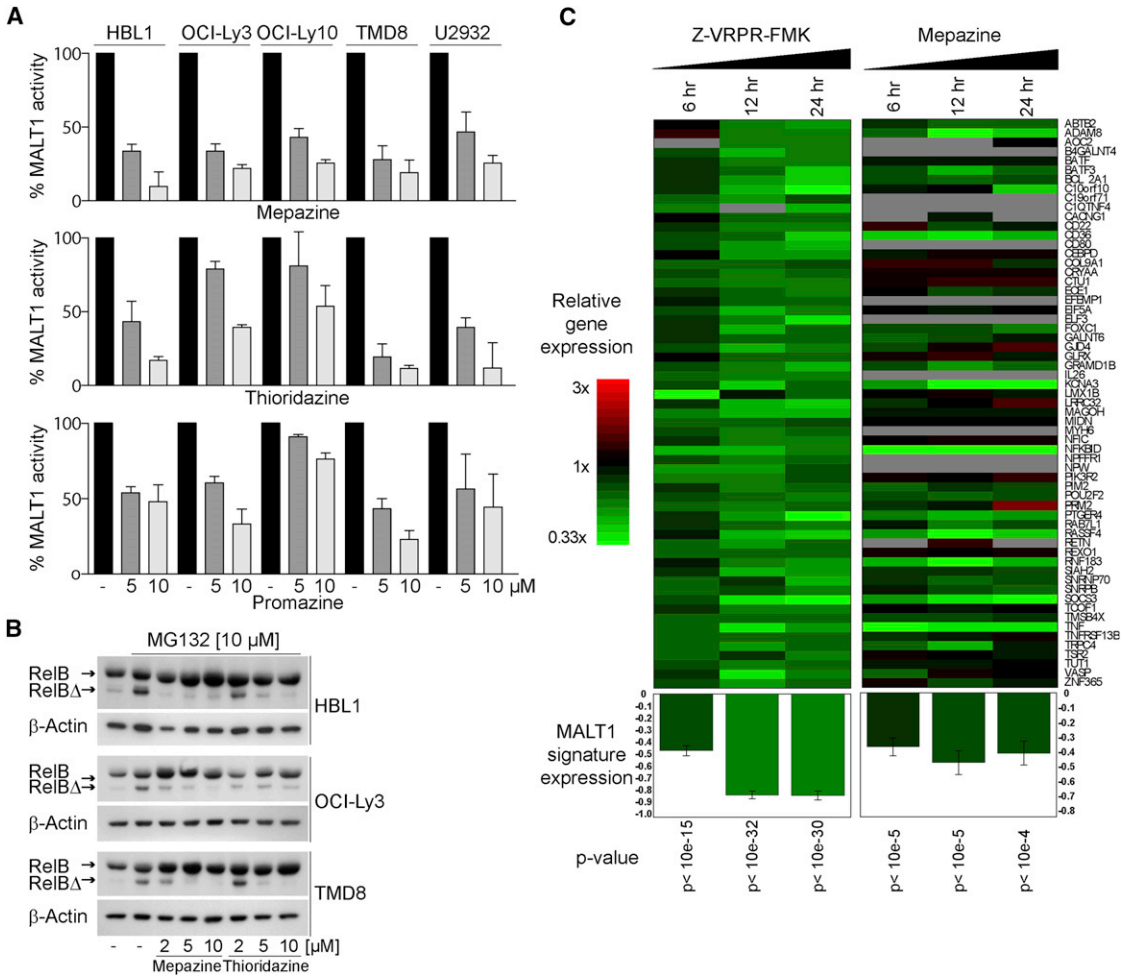

Figure 3. PD Treatment Impairs MALT1 Activity in ABC-DLBCL Cells

(A) Cellular MALT1 activity in ABC-DLBCL was analyzed after 4 hr incubation with mepazine, thioridazine, or promazine (mean ± SD; n = 3).

(B) Cells were treated with solvent, mepazine, or thioridazine for 4 hr prior to 1 hr MG132 incubation. RelB and RelBΔ were analyzed via western blot. Blots show a representative of at least three independent experiments.

(C) Gene expression profiling of the ABC-DLBCL cell line HBL1 after treatment with peptide Z-VRPR-FMK or mepazine (20 μM) for 6, 12, and 24 hr. Gene expression changes were assessed by DNA microarrays and are depicted according to the color scale shown. A gene was selected as dependent on MALT1 activity if Z-VRPR-FMK decreased gene expression by at least 33% after all three inhibition time points. This gene expression signature was subsequently applied to expression data following treatment with mepazine. Error bars depict standard error of the mean. Statistical significance of the decrease in the MALT1 signature average in each treated sample was verified by paired t test.

cells were treated with 10 μM mepazine for 20 hr and secretion of the NF-κB-regulated cytokines IL-6 and IL-10 was determined by ELISA (Figure 4C). Whereas GCB-DLBCL cells expressed low amounts of IL-6 or IL-10, ABC-DLBCL cells secreted both cytokines albeit to variable extents, reflecting heterogeneity among the different cell lines. Mepazine did not affect expression of IL-6 and IL-10 in GCB-DLBCL cells.

Selective Toxicity and Induction of Apoptosis by Phenothiazines in ABC-DLBCL Cells

Because the three PD efficiently inhibited MALT1 protease activity in vitro and in vivo, we tested their effect on the viability of ABC-DLBCL cells. As a control we used three GCB-DLBCL cell lines, BJAB, Su-DHL-6, and Su-DHL-4 that were previously shown to be independent of MALT1 proteolytic activity for their growth and survival (Ferch et al., 2009). We measured cytotoxic effects by MTT assays after 2 days of incubation after one-time compound treatment using increasing concentrations of mepazine, thioridazine, and promazine (Figure 5A). All compounds caused a decrease of cell viability in the ABC-DLBCL cells HBL1, OCI-Ly3, U2932, and TMD8, without significantly affecting GCB-DLBCL cells. Furthermore, we determined cell viability by cell counting after 4 days of incubation in response to a singular compound treatment (Figure 5B). Congruent with the MTT assay, the PD also decreased the overall number of viable ABC-DLBCL cells. Again, the reduced viability was much more pronounced in ABC-DLBCL cells, while GCB-DLBCL cell viability was only slightly impaired at the highest concentration of the compounds. Consistent with the results obtained in the cellular MALT1 cleavage assay, in general promazine had the

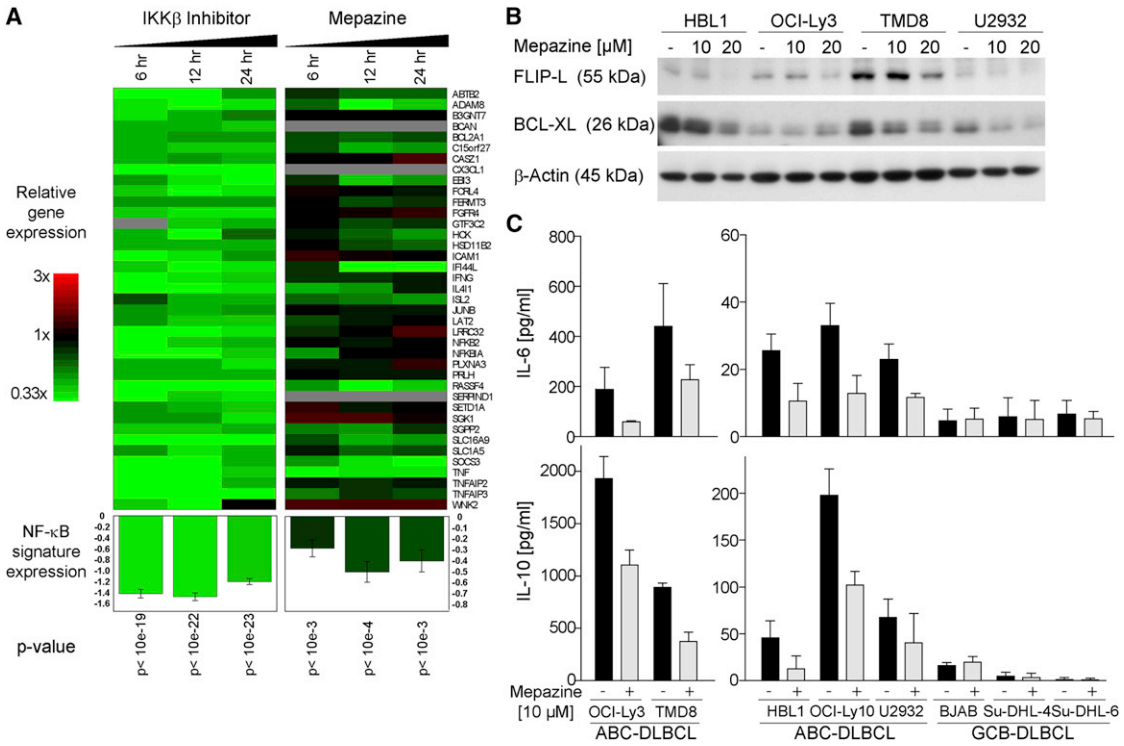

Figure 4. Mepazine Treatment Impairs NF-κB Target Gene Expression in ABC-DLBCL Cells

(A) Gene expression profiling of the ABC-DLBCL cell line HBL1 after treatment with mepazine (see Figure 3) was compared to the NF-κB gene signature generated after administration of the specific IKKβ inhibitor MLN120B. The significance of the decrease in the NF-κB signature average in each treated sample was verified by paired t test.

(B) Expression of NF-κB target genes BCL-XL and FLIP-L in ABC-DLBCL cells after mepazine treatment. Protein amounts were examined after 20 hr of treatment using the indicated concentrations by western blot. Data show a representative of three independent experiments.

(C) ABC- and GCB-DLBCL cells were treated with mepazine for 20 hr and the levels of secreted IL-6 and IL-10 were analyzed via ELISA (mean ± SD; n = 3).

mildest effects on the viability of the ABC-DLBCL cells. To validate that the decrease in viability of ABC-DLBCL cells is linked to the administration of distinct PD that act as MALT1 inhibitors, we treated DLBCL cells with promethazine (Figure S3A). Despite its close structural relation to promazine, promethazine did not inhibit MALT1 protease activity at concentrations up to 20 μM (see compound 18 in Figure S1H). Indeed, promethazine did not significantly inhibit viability of ABC- or GCB-DLBCL cells after 4 days of treatment, providing further evidence that the cellular effects of mepazine, thioridazine, and promazine were dependent on their ability to inhibit MALT1.

To demonstrate that decreased viability of ABC-DLBCL cells after PD treatment is linked to MALT1-dependent NF-κB inhibition, we infected HBL1 cells with a lentivirus expressing the constitutively active mutant IKKβ SS176/180EE (caIKKβ) and simultaneously GFP (Figure 5C). GFP-expressing cells were sorted by FACS, yielding caIKKβ or mock-infected populations of more than 95% GFP-positive cells. caIKKβ expression was verified by western blotting (Figure S3B). As expected, the viability of mock-infected HBL1 cells was strongly reduced in response to increasing doses of mepazine or thioridazine. In contrast, caIKKβ−expressing cells were resistant to the incubation of the PD. Thus, augmented IKKβ signaling counteracts the toxicity of PD, providing further evidence that PD are acting upstream of IKKβ through MALT1 inhibition.

For efficient anticancer drugs it is required that they exert toxic effects by enhancing cell death to eradicate the tumor cells. Therefore, we determined whether mepazine, as the most potent MALT1 inhibitor, affected viability of ABC-DLBCL cells by enhancing apoptosis (Figure 5D). To this end, DLBCL cells were treated for 5 days with 15 μM mepazine and apoptotic cells were identified by FACS as AnnexinV-PE positive and 7-AAD-negative cells. Mepazine provoked an enhanced apoptotic rate in all ABC-DLBCL cells, while apoptosis was not increased in the two GCB-DLBCL control cells. Thus, PD are selectively toxic to ABC-DLBCL cells and toxicity is at least partially due to enhanced apoptosis in the affected lymphoma cells, revealing a potential use of mepazine and structurally related compounds for ABC-DLBCL therapy.

Mepazine and Thioridazine Impede Growth of ABC-DLBCL In Vivo

We determined whether mepazine and thioridazine could also exert effects on lymphoma growth in vivo in a murine DLBCL xenogeneic tumor model. For this purpose, the ABC-DLBCL cell line OCI-Ly10 and the GCB-DLBCL cell line Su-DHL-6 were injected as subcutaneous xenografts into NOD/scid IL-2Rg^{null} (NSG) mice (Figure 6A). Both tumor cell lines were engrafted simultaneously on opposite flanks of individual mice. Starting 1 day after injection, the mice were treated by

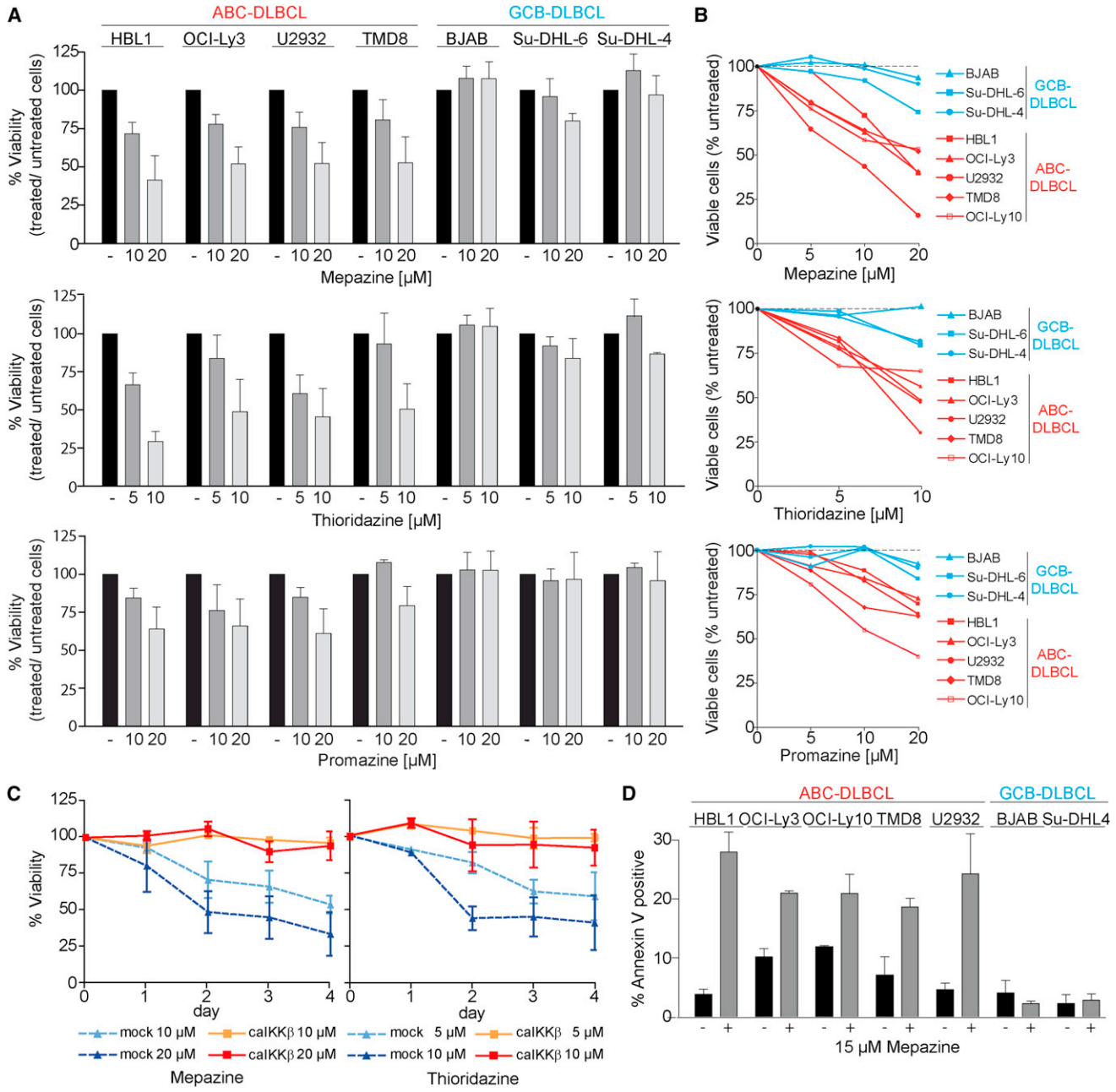

Figure 5. PD Are Selectively Toxic to ABC-DLBCL Cells

(A) ABC-DLBCL cell lines (HBL1, OCI-Ly3, U2932, TMD8) and GCB-DLBCL cell lines (BJAB, Su-DHL-6, Su-DHL-4) were treated with indicated concentrations of mepazine, thioridazine, or promazine (single treatment) for 2 days and their viability was subsequently analyzed with a MTT cytotoxicity test (mean ± SD; n = 3).

(B) Viability of cells treated with mepazine, thioridazine, or promazine (single dose treatment) for 4 days was determined by trypan blue exclusion counting of living cells. Data represent the mean of three independent experiments.

(C) HBL1 cells were lentivirally transduced to co-express calKKβ along with GFP or GFP alone (mock). GFP-positive cells were sorted via FACS and treated at day 0 with the indicated concentrations of mepazine or thioridazine. Cells were treated for 4 days and viable cells were counted by trypan blue exclusion every day during the treatment. Values represent the relative cell numbers compared to the untreated controls (mean ± SD; n = 3).

(D) ABC-DLBCL and GCB-DLBCL cell lines were treated for 5 days with 15 μM mepazine. Apoptotic cells were identified by FACS analysis as AnnexinV-PE positive and 7-AAD negative cells (mean ± SD; n = 3).

See also Figure S3.

intraperitoneal (i.p.) administration of solvent or either mepazine (16 mg/kg) or thioridazine (12 mg/kg). In control-treated mice, massive tumors grew from both DLBCL cell lines within 3 weeks of transplantation. Daily administration of mepazine or thioridazine strongly impaired the expansion of the ABC-DLBCL cell line OCI-Ly10. In contrast, both PD completely failed to exert

any inhibitory effects on the progression of the GCB-DLBCL cell line Su-DHL-6 in the same animals. To ascertain that mepazine and thioridazine are not only impeding growth in the initiation phase of xenografted OCI-Ly10 cells, but are also affecting grown tumors, we allowed OCI-Ly10 and Su-DHL-6 xenografted tumors to grow to ~75 mm^2 before treatment (Figure 6B). Again, mepazine and thioridazine strongly reduced the progression of OCI-Ly10 tumors while having no effect on the growth of Su-DHL-6 tumors in this setting. Thus, PD are in fact able to inhibit growth of a preformed ABC-DLBCL tumor.

Thioridazine is orally available in humans and pharmacokinetic (PK) studies led to a consensus therapeutic range between 200 and 2000 ng/ml in the blood of patients (Baumann et al., 2004). To determine if the concentrations of thioridazine in the blood of NSG mice after i.p. injection are not exceeding this therapeutic window, we measured serum concentrations in NSG mice after 0, 1, 2, 6, and 24 hr in response to acute dosing of 12 mg/kg thioridazine. Thioridazine concentrations between 170 and 270 ng/ml were measured 1 hr after dosing and the levels rapidly decreased thereafter (Figure 6C). After 24 hr, thioridazine levels were below the detection limit (20 ng/ml).

To show that mepazine and thioridazine were acting directly on the tumor cells, we determined the induction of apoptosis in the tumor tissue. Transplanted tumors were removed at the end of the treatment period (21 days; see Figure 6A) and apoptotic cells were visualized by TUNEL staining on sections of the tumor tissue (Figure 6D). Congruent with the selective in vivo toxicity, mepazine or thioridazine treatment increased the number of apoptotic cells in the xenografted ABC-DLBCL cell line OCI-Ly10, while no induction of apoptosis was observed in the in GCB-DLBCL cell line Su-DHL-6. Furthermore, constitutive cleavage of the MALT1 substrate RelB was impaired after mepazine and thioridazine treatment in specimens of xenografted OCI-Ly10 tumors, revealing that also in mice the compounds were indeed acting by inhibiting MALT1 activity in the tumor cells (Figure 6E). Thus, the murine tumor model provided evidence that MALT1 inhibition by phenothiazines selectively kills MALT1-dependent DLBCL in vivo and indicates a potential therapeutic benefit for use of the known compounds in ABC-DLBCL therapy.

DISCUSSION

In this study, we have identified PD as small molecule inhibitors that effectively and selectively inhibit proteolytic activity of recombinant and cellular MALT1. Importantly, only a distinct subset of PD inhibited MALT1, with the best inhibitory activity found for mepazine, thioridazine, and promazine, three known organic compounds that have been in clinical use as antipsychotic or sedative drugs. All three PD interfered with inducible MALT1 activity in activated T cells and constitutive activity in ABC-DLBCL cells. Furthermore, mepazine and thioridazine caused impaired T cell activation as well as reduced viability that was selective for the ABC subtype of DLBCL, processes that were shown to be critically dependent on MALT1 activity (Düwel et al., 2009; Ferch et al., 2009; Hailfinger et al., 2009b). In addition, both compounds were inhibiting MALT1 activity and selectively inducing apoptosis and thereby reducing growth of ABC-DLBCL in a preclinical DLBCL xenotransplantation model. Thus, cellular and in vivo data underscore the effectiveness of PD as pharmacologic MALT1 inhibitors and suggest their potential clinical application for ABC-DLBCL therapy.

MALT1 is the only human paracaspase with very distinct properties when compared to mammalian caspases (Hachmann et al., 2012), revealing that specific inhibitors are clearly promising drug candidates for selective inactivation of the MALT1 oncogenic activity. Selectivity is critical, because impairment of apoptosis through caspase inhibition would certainly trigger adverse effects detrimental for lymphoma therapy. Indeed, all PD tested displayed a high preference for MALT1 and did not impair the initiator caspase 8 and the executioner caspase 3. Congruently, mepazine and thioridazine were able to induce apoptotic cell death in MALT1-dependent ABC-DLBCL.

Michaelis-Menten kinetics and wash-out experiments revealed that mepazine does not directly affect substrate binding to the catalytic center of MALT1 in a competitive manner, but rather acts as a noncompetitive and reversible inhibitor. Because all PD inhibit activity of a catalytically active MALT1 fragment that spans the paracaspase and C-terminal Ig3 domain to a similar extent as the full length protein, they apparently exert allosteric effects within the active paracaspase domain. The recent elucidation of the crystal structure of the MALT1 paracaspase and Ig3 domains in its free form and bound to the tetrapeptide inhibitor indicates that substrate binding causes a substantial structural reorganization to achieve an active protease (Wiesmann et al., 2012; Yu et al., 2011). Mepazine and thioridazine inhibit constitutive activity of recombinant MALT1, suggesting that PD bind within the paracaspase-Ig3 region of MALT1 and thereby possibly counteract the structural rearrangement required to maintain the active confirmation. Also inside the cells, PD act directly on the MALT1 paracaspase, as indicated by impaired cleavage of the substrate RelB. Furthermore, the inhibitory effect on MALT1 is also evident from the inhibition of MALT1 activity in in vitro protease assays after IP of cellular MALT1. Thus, in T cells PD are apparently maintaining MALT1 in an inactive conformation that is resistant to activation by upstream pathways. Furthermore, the inhibition of constitutive MALT1 activity in ABC-DLBCL cells even after IP purification suggests that in the ABC-DLBCL cells PD are in fact forcing the active MALT1 protease into an inactive conformation. Mepazine and thioridazine are most likely causing cellular MALT1 to adopt a structure reminiscent to the inactive enzyme prior to stimulation. In fact, these results on cellular MALT1 inhibition are compatible with the noncompetitive, allosteric mode of inhibition that PD exert on recombinant MALT1. Taken together, our recombinant and cellular data underscore the efficacy and selectivity of PD as small molecule MALT1 inhibitors.

In cells, the strong inhibition of cellular MALT1 activity after relatively short PD incubation times clearly indicated that the substances were directly affecting MALT1 protease. Mepazine was ~4- to 6-fold more effective than thioridazine in inhibiting recombinant MALT1 and it was also more effective in cells, indicating that cellular uptake, compound stability, and cellular concentration may be in a similar range. Different PD have been or are still in clinical use, reflecting that the phenothiazine scaffold seems to be a privileged structure to obtain in vivo effects. Interestingly, toxicity tests on ABC-DLBCL cells

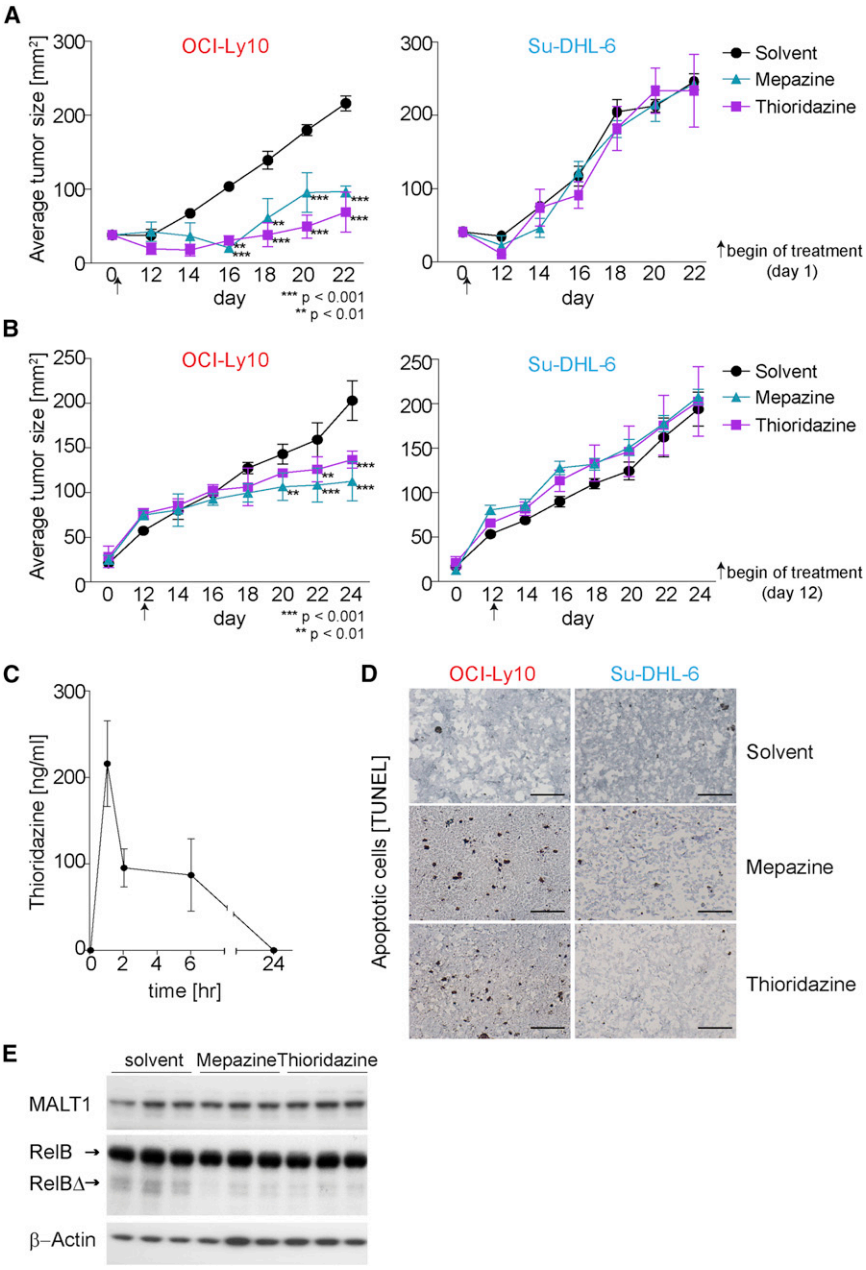

Figure 6. Mepazine and Thioridazine Interfere with Growth and Induce Apoptosis in ABC-DLBCL Cell Line OCI-Ly10 In Vivo

(A) Transplantation of OCI-Ly10 or Su-DHL-6 cells resuspended in matrigel into the flanks of NSG mice was carried out on day 0. Tumor size was determined by caliper measurement. Intraperitoneal administration of solvent, mepazine (400 μg/day) or thioridazine (300 μg/day) was started 24 hr after transplantation and given continuously every 24 hr for the entire treatment period. Statistical analysis was performed using a two-way Anova test (mean ± SD; n = 3).

(B) Mice were treated as in (A) but administration of compounds was started on day 12 after xenotransplantation when tumors were grown to ~75 mm^2 (mean ± SD; n = 3).

(C) Thioridazine concentrations were measured in the serum 0–24 hr after i.p. injection (12 mg/kg) by HPLC (mean ± SD; n = 3).

(D) Apoptosis was determined on tumor sections (experiment in A) by TUNEL staining after 22 days of treatment. Pictures show staining of representative tumor sections (scale bar 100 μm).

(E) RelB and RelBΔ were detected in extracts of OCI-Ly10 tumor specimens by western blotting 22 days after transplantation (experiment in A). Blots show results from three mice treated with solvent, mepazine, or thioridazine.

revealed some differences in the effects of thioridazine to mepazine. In fact, differential side effects of PD may synergize with MALT1 inhibition to exert the toxic effect on ABC-DLBCL cells. In this context, thioridazine has been reported to inhibit PI3K-PDK1-AKT signaling in ovarian cancer cells (Choi et al., 2008; Rho et al., 2011). Constitutive AKT phosphorylation is a common feature of DLBCL cells, independent of their classification. We observed some effects of thioridazine on AKT phosphorylation (data not shown), which may account for an augmentation of thioridazine toxicity. However, as GCB-DLBCL cells, which also show constitutive PI3K-AKT signaling (Kloo et al., 2011) and are resistant to thioridazine, MALT1 inhibition is clearly the primary cause for the cellular toxicity in this setting. We recently demonstrated that PI3K-PDK1 contributes to enhanced MALT1 activity in the two ABC-DLBCL cell lines HBL1 and TMD8 that carry oncogenic mutations in the BCR signaling adaptor CD79B (Kloo et al., 2011). Clearly, thioridazine did not only affect survival of HBL1 and TMD8 cells, but also was toxic to all MALT1-dependent ABC-DLBCL, again indicating that its primary target is MALT1. Nevertheless, concomitant inhibition of PI3K-AKT may add to the effects of thioridazine on MALT1.

The important clinical potential of the three PD identified and analyzed in this study stems from the fact that all have been used formerly in trials or in the clinic as antipsychotic or sedative drugs. This activity in this setting is thought to be based primarily on their ability to function as dopamine D2 receptor antagonists (Seeman et al., 1976). Mepazine, the most effective MALT1 inhibitor, has been evaluated as an antipsychotic and tranquilizing drug under the brand name Pacatal in the late 1950s and early 1960s. Whereas some clinical investigations provided evidence for antipsychotic effects, other studies failed to do so (Sarwer-Foner and Koranyi, 1957; Whittier et al., 1960). Some side effects were reported after mepazine treatment, including a reduction of asthma attacks, indicating potential immunosuppressive activity (Sarwer-Foner and Koranyi, 1957). Thioridazine (brand name Mellaril/Melleril) is still commercially available, but is reserved for the treatment of schizophrenic patients who do not respond to other antipsychotic drugs. Thioridazine is also

considered to be beneficial for other medical applications because it exerts toxic effects on different cancer cell lines (Rho et al., 2011; Zhelev et al., 2004). In addition, thioridazine is considered as a candidate drug for the treatment of tuberculosis or malaria, but the reasons for its antimicrobial and antiparasitic actions are currently unknown (van Soolingen et al., 2010; Weisman et al., 2006). Promazine (brand name Sparine), which displayed the weakest toxicity for MALT1-dependent ABC-DLBCL, is still used to treat restless behavior.

Comparative analysis of pharmacokinetic (PK) profiles in rodents and humans further support the possibility for a potential off-label clinical use of thioridazine to treat ABC-DLBCL. We measured thioridazine levels of 170–270 ng/ml in the serum of NSG mice 1 hr after treatment, which is congruent with previous single dose PK studies after i.p. injection (10 mg/kg) in rats (Daniel et al., 1997). The concentrations obtained in rodents are within the range of peak concentrations reported in humans (130–650 ng/ml) 1–4 hr after oral uptake of 100 mg thioridazine (Chakraborty et al., 1989; Shvartsburd et al., 1984). However, whereas in humans considerable concentrations of thioridazine are still present even after 1 day, the drug is undetectable in rodents after 24 hr (see Figure 6C; Daniel et al., 1997). A dose of 10–12 mg/kg in rodents corresponds to ~800 mg for an adult. Given these relatively high doses, PK studies clearly demonstrate a much faster metabolism of thioridazine in rodents compared to humans. Congruently, in rats 2 weeks of chronic i.p. injection (10 mg/kg twice daily) led to plasma concentrations of thioridazine that peaked at ~750 ng/ml and declined to ~90 ng/ml over 24 hr (Daniel et al., 1997). The recommended therapeutic range of thioridazine in humans has been set to steady state levels of 200–2,000 ng/ml in the plasma of patients treated for psychiatric disorders (Baumann et al., 2004). These data reveal that the thioridazine levels that are effective in killing xenografted ABC-DLBCL tumors after i.p. injection in mice are within the range or even below the therapeutic window that can be achieved after oral administration of thioridazine in humans. Thus, the PK profile lends support to a possible clinical off-label use of PD in ABC-DLBCL therapy.

The identification of mepazine, thioridazine, and promazine as three small molecule inhibitors of MALT1 opens potential additional therapeutic uses. The inhibitory action of PD on T cell activation indicates a potential immunosuppressive effect of MALT1 inhibition that needs to be further explored, but adverse effects of PD that have mostly terminated a long-term antipsychotic use are certainly not tolerated for an application as immunosuppressants. However, a restricted short-term usage of mepazine or thioridazine for treatment of patients with aggressive lymphoma that depends on MALT1 proteolytic activity and is resistant to current therapeutic protocols can be envisioned. The overall 5-year survival rate of 35% for patients with ABC-DLBCL emphasizes the urgent clinical need for alternative treatment options (Lenz et al., 2008b). The increase in apoptosis as well as the decrease in tumor growth of the ABC-DLBCL cell line OCI-Ly10 in response to mepazine or thioridazine treatment in mice underscores the potency of these drugs. Thioridazine is still on the market and the xenotransplantation model as well as PK profile suggests that a daily administration of up to 800 mg, which is the maximal permitted oral dosage in psychotic patients, could have beneficial effects in patients with ABC-DLBCL. A combinatorial therapy could be possible, because the reduced expression of prosurvival factors after MALT1 inhibition by PD could sensitize ABC-DLBCL tumor cells for chemotherapy-induced apoptosis. Besides the differential ABC- and GCB-DLBCL classification, further diagnostic markers to identify patients with lymphoma who would most likely benefit from MALT1 inhibition by PD are certainly required. In addition, effectivity and selectivity of MALT1 inhibition by PD can be optimized by medicinal chemistry programs to yield a more potent and possibly selective drug for the treatment of MALT lymphoma or ABC-DLBCL.

EXPERIMENTAL PROCEDURES

Cell Culture and Reagents

DLBCL cell lines (except OCI-Ly10) were cultured in RPMI 1640 medium (Invitrogen) supplemented with 20% FCS and 100 U/ml penicillin/streptomycin. OCI-Ly10 was cultured in IMDM (Invitrogen) with 20% human plasma, penicillin/streptomycin and 50 μM β-mercaptoethanol. Jurkat T cells were cultured like DLBCL cells with 10% FCS. The isolation of PBMCs from heparin-treated (1000 U/ml) whole blood was done with Lymphoprep according to manufacturer (Axis-shield). Isolation of murine $CD4^+$ T cells was performed with T-cell-specific Dynabeads (Invitrogen) and they were cultured in Jurkat medium and 50 μM β-mercaptoethanol. Stimulation of Jurkat T cells, PBMCs, and mouse $CD4^+$ T cells was either initiated by the addition of phorbol 12-myristate 13-acetate (PMA; 200 ng/ml) and ionomycin (I; 300 ng/ml) (both Calbiochem) or by hCD3/hCD28 and mIgG1/mIgG2a antibodies (BD Biosciences). The use of PBMC from healthy donors in this study was approved by the Ethics Board of the Medical Faculty of the Ludwig-Maximilians-University Munich, Germany and donors gave informed consent.

Z-VRPR-FMK (Alexis Biochemicals), mepazine acetate (Chembridge), promazine hydrochloride, thioridazine hydrochloride, promethazine hydrochloride (all Sigma Aldrich), and all other PD tested (Chembridge or Sigma) were solved in DMSO. Antibodies used were BCL-XL (Cell Signaling), MALT1 (H300, Santa Cruz), c-FLIP (Alexis Biochemicals), β-Actin (I-19, Santa Cruz), and RelB (Cell Signaling).

Recombinant and Endogenous Protease Cleavage Assays

Recombinant GSTMALT1 was purified from *E. coli* and all cleavage assays were in 384-well microplates format using 200 ng of GSTMALT1 and 50 μM of the substrate Ac-LRSR-AMC. Cleavage activity was determined by the increase of AMC fluorescence measured in Synergy 2 Microplate Reader (Biotek). Reversible inhibition was determined after coupling of 300 ng GSTMALT1 to glutathione sepharose and subsequent wash out of the compounds. Cleavage of human caspase 3 (BioVision) and caspase 8 (Cayman Chemical) was assayed accordingly against Ac-DEVD-AMC as substrate using 50 and 250 pg of protein, respectively. Activity of endogenous MALT1 in the absence or presence of inhibitors was determined after MALT1 IP as described earlier (Kloo et al., 2011).

Real-Time RT-PCR and ELISA

Synthesis of cDNA was performed with DNA-free RNA samples (RNeasy Mini Kit, QIAGEN) by reverse transcription with random hexamers and Superscript II (Invitrogen) according to the manufacturer's protocol and real-time PCR was performed using LC 480 SybrGreen PCR mix on a LC 480 Lightcycler system (Roche). RNA was normalized by β-Actin mRNA. Primers are shown in Supplemental Experimental Procedures.

Human and murine IL-2 (BenderMed Systems), IL-6, and IL-10 ELISAs (Immunotools) were performed according to the manufacturer's protocols.

Gene Expression Profiling

Gene expression profiling was performed for the ABC-DLBCL cell line HBL1 after treatment with DMSO or 20 μM of mepazine for the indicated time points. RNA extraction using RNeasy Mini Kit (QIAGEN) and analysis of whole-genome Agilent 4 × 44K gene expression arrays (Agilent Technologies) was performed following the manufacturer's protocol. Signals from either

DMSO-treated (labeled with Cy3) or mepazine-treated (labeled with Cy5) HBL1 cells were compared. We applied a previously developed MALT1 and NF-κB target gene signature to the gene expression data (Hailfinger et al., 2009b; Kloo et al., 2011). Genes that were significantly downregulated were determined by paired t test ($p < 0.05$).

Viability, MTT, and Apoptosis Assays

Viability of DLBCL cell lines was analyzed with a cell count assay of trypan blue-stained cells after 4 days and by MTT (3-4,5-dimethylthiazol-2-yl-2,5-diphenyltetrazoliumbromid) cytotoxicity test after 2 days of inhibitor treatment in comparison to DMSO-treated cells. Reduction of MTT to formazan was measured at 450 nm with a μQuant microplate spectrophotometer (Biotek). Apoptosis rates were determined with PE-Annexin V staining of $7AAD^-$ cells (BD PharMingen) by FACS (LSRII, BD). Data were analyzed using FlowJo software (Treestar). TUNEL assay was performed on frozen 5 μm DLBCL tumor tissue sections with the DEAD End colorimetric TUNEL system kit according to the manufacturer's protocol (Promega). Tissue sections were stained with H&E and images were taken on a Zeiss Axioplan microscope.

Lentiviral Transduction

Constitutively active Flag-IKKβ (caIKKβ) mutant (SS176, 180EE) and GFP were linked by a cotranslational processing site T2A (Hadian et al., 2011) and introduced into pLVTHM plasmid. Infection into HBL1 cells was performed as described earlier (Wiznerowicz and Trono, 2003). After 1 week in culture, HBL1 cells were sorted by FACS yielding more than 95% GFP-positive HBL1 cells. Viability of cells in response to phenothiazine treatment was determined by counting of trypan blue staining.

In Vivo Tumor Cell Engraftment, Treatment of Mice, and PK Thioridazine

All experiments were approved by the Bavarian State authorities (file no. 115-09) according to the legal regulations for animal experimentation. Tumors were engrafted in 6- to 8-week-old female NOD.Cg-*Prkdc*^{scid} *Il2rg*^{tm1Wjl}/SzJ (NSG) mice by subcutaneous injection of 4×10^6 tumor cells (OCI-Ly10 or SU-DHL-6) resuspended in matrigel (BD). Both tumors were engrafted simultaneously on opposite flanks of individual mice, with three mice for each treatment group. Intraperitoneal administration of solvent, mepazine, or thioridazine was started 1 or 12 days after transplantation and given continuously every 24 hr thereafter. We used a daily application dose of 300 μg thioridazine and 400 μg mepazine per animal (25 g), corresponding to approximately 12 mg/kg and 16 mg/kg, respectively. The tumor size was measured every other day after visual appearance using a caliper and calculated as square millimeters (length × width). Mice were sacrificed when the SU-DHL-tumor size was above 250 mm^2. Statistical data were analyzed with a two-way Anova test.

For the pharmacokinetic study of thioridazine, NSG mice were i.p. injected with a single dose of 300 μg. For each indicated time-point three mice were treated and blood serum concentrations of thioridazine were determined via HPLC by standardized diagnostic protocol (MVZ Dortmund).

ACCESSION NUMBERS

The GEO database accession number for the raw data for expression profiling is GSE39741.

SUPPLEMENTAL INFORMATION

Supplemental Information includes three figures, one table, and Supplemental Experimental Procedures and can be found with this article online at http://dx.doi.org/10.1016/j.ccr.2012.11.002.

ACKNOWLEDGMENTS

We thank Martin Göttlicher for helpful discussion, Bernhard Frankenberger for advice on animal welfare issues, and Stephan Mathas for providing caIKKβ. This work was supported by a grant from the German Cancer Society and the Life Science Foundation to D.K. G.L. was supported by the German Research Foundation, the German Cancer Society, the Else-Kröner-Fresenius Stiftung, and the Berliner Krebsgesellschaft e.V. A patent for the clinical use of phenothiazines in MALT1-dependent diseases has been submitted to the European patent office.

Received: May 21, 2011
Revised: September 14, 2012
Accepted: November 2, 2012
Published: December 10, 2012

REFERENCES

Alizadeh, A.A., Eisen, M.B., Davis, R.E., Ma, C., Lossos, I.S., Rosenwald, A., Boldrick, J.C., Sabet, H., Tran, T., Yu, X., et al. (2000). Distinct types of diffuse large B-cell lymphoma identified by gene expression profiling. Nature *403*, 503–511.

Baumann, P., Hiemke, C., Ulrich, S., Eckermann, G., Gaertner, I., Gerlach, M., Kuss, H.J., Laux, G., Müller-Oerlinghausen, B., Rao, M.L., et al.; Arbeitsgemeinschaft fur neuropsychopharmakologie und pharmakopsychiatrie. (2004). The AGNP-TDM expert group consensus guidelines: therapeutic drug monitoring in psychiatry. Pharmacopsychiatry *37*, 243–265.

Chakraborty, B.S., Midha, K.K., McKay, G., Hawes, E.M., Hubbard, J.W., Korchinski, E.D., Choc, M.G., and Robinson, W.T. (1989). Single dose kinetics of thioridazine and its two psychoactive metabolites in healthy humans: a dose proportionality study. J. Pharm. Sci. *78*, 796–801.

Choi, J.H., Yang, Y.R., Lee, S.K., Kim, S.H., Kim, Y.H., Cha, J.Y., Oh, S.W., Ha, J.R., Ryu, S.H., and Suh, P.G. (2008). Potential inhibition of PDK1/Akt signaling by phenothiazines suppresses cancer cell proliferation and survival. Ann. N Y Acad. Sci. *1138*, 393–403.

Coornaert, B., Baens, M., Heyninck, K., Bekaert, T., Haegman, M., Staal, J., Sun, L., Chen, Z.J., Marynen, P., and Beyaert, R. (2008). T cell antigen receptor stimulation induces MALT1 paracaspase-mediated cleavage of the NF-kappaB inhibitor A20. Nat. Immunol. *9*, 263–271.

Daniel, W.A., Syrek, M., Mach, A., Wójcikowski, J., and Boksa, J. (1997). Pharmacokinetics of thioridazine and its metabolites in blood plasma and the brain of rats after acute and chronic treatment. Pol. J. Pharmacol. *49*, 439–452.

Davis, R.E., Brown, K.D., Siebenlist, U., and Staudt, L.M. (2001). Constitutive nuclear factor kappaB activity is required for survival of activated B cell-like diffuse large B cell lymphoma cells. J. Exp. Med. *194*, 1861–1874.

Davis, R.E., Ngo, V.N., Lenz, G., Tolar, P., Young, R.M., Romesser, P.B., Kohlhammer, H., Lamy, L., Zhao, H., Yang, Y., et al. (2010). Chronic active B-cell-receptor signalling in diffuse large B-cell lymphoma. Nature *463*, 88–92.

Düwel, M., Welteke, V., Oeckinghaus, A., Baens, M., Kloo, B., Ferch, U., Darnay, B.G., Ruland, J., Marynen, P., and Krappmann, D. (2009). A20 negatively regulates T cell receptor signaling to NF-kappaB by cleaving Malt1 ubiquitin chains. J. Immunol. *182*, 7718–7728.

Ferch, U., Kloo, B., Gewies, A., Pfänder, V., Düwel, M., Peschel, C., Krappmann, D., and Ruland, J. (2009). Inhibition of MALT1 protease activity is selectively toxic for activated B cell-like diffuse large B cell lymphoma cells. J. Exp. Med. *206*, 2313–2320.

Hachmann, J., Snipas, S.J., van Raam, B.J., Cancino, E.M., Houlihan, E.J., Poreba, M., Kasperkiewicz, P., Drag, M., and Salvesen, G.S. (2012). Mechanism and specificity of the human paracaspase MALT1. Biochem. J. *443*, 287–295.

Hadian, K., Griesbach, R.A., Dornauer, S., Wanger, T.M., Nagel, D., Metlitzky, M., Beisker, W., Schmidt-Supprian, M., and Krappmann, D. (2011). NF-κB essential modulator (NEMO) interaction with linear and lys-63 ubiquitin chains contributes to NF-κB activation. J. Biol. Chem. *286*, 26107–26117.

Hailfinger, S., Rebeaud, F., and Thome, M. (2009a). Adapter and enzymatic functions of proteases in T-cell activation. Immunol. Rev. *232*, 334–347.

Hailfinger, S., Lenz, G., Ngo, V., Posvitz-Fejfar, A., Rebeaud, F., Guzzardi, M., Penas, E.M., Dierlamm, J., Chan, W.C., Staudt, L.M., and Thome, M. (2009b).

Essential role of MALT1 protease activity in activated B cell-like diffuse large B-cell lymphoma. Proc. Natl. Acad. Sci. USA *106*, 19946–19951.

Hailfinger, S., Nogai, H., Pelzer, C., Jaworski, M., Cabalzar, K., Charton, J.E., Guzzardi, M., Décaillet, C., Grau, M., Dörken, B., et al. (2011). Malt1-dependent RelB cleavage promotes canonical NF-kappaB activation in lymphocytes and lymphoma cell lines. Proc. Natl. Acad. Sci. USA *108*, 14596–14601.

Isaacson, P.G., and Du, M.Q. (2004). MALT lymphoma: from morphology to molecules. Nat. Rev. Cancer *4*, 644–653.

Kloo, B., Nagel, D., Pfeifer, M., Grau, M., Düwel, M., Vincendeau, M., Dörken, B., Lenz, P., Lenz, G., and Krappmann, D. (2011). Critical role of PI3K signaling for NF-kappaB-dependent survival in a subset of activated B-cell-like diffuse large B-cell lymphoma cells. Proc. Natl. Acad. Sci. USA *108*, 272–277.

Lenz, G., Davis, R.E., Ngo, V.N., Lam, L., George, T.C., Wright, G.W., Dave, S.S., Zhao, H., Xu, W., Rosenwald, A., et al. (2008a). Oncogenic CARD11 mutations in human diffuse large B cell lymphoma. Science *319*, 1676–1679.

Lenz, G., Wright, G., Dave, S.S., Xiao, W., Powell, J., Zhao, H., Xu, W., Tan, B., Goldschmidt, N., Iqbal, J., et al.; Lymphoma/Leukemia Molecular Profiling Project. (2008b). Stromal gene signatures in large-B-cell lymphomas. N. Engl. J. Med. *359*, 2313–2323.

Lisurek, M., Rupp, B., Wichard, J., Neuenschwander, M., von Kries, J.P., Frank, R., Rademann, J., and Kühne, R. (2010). Design of chemical libraries with potentially bioactive molecules applying a maximum common substructure concept. Mol. Divers. *14*, 401–408.

Ngo, V.N., Davis, R.E., Lamy, L., Yu, X., Zhao, H., Lenz, G., Lam, L.T., Dave, S., Yang, L., Powell, J., and Staudt, L.M. (2006). A loss-of-function RNA interference screen for molecular targets in cancer. Nature *441*, 106–110.

Oeckinghaus, A., Wegener, E., Welteke, V., Ferch, U., Arslan, S.C., Ruland, J., Scheidereit, C., and Krappmann, D. (2007). Malt1 ubiquitination triggers NF-kappaB signaling upon T-cell activation. EMBO J. *26*, 4634–4645.

Pasqualucci, L., Trifonov, V., Fabbri, G., Ma, J., Rossi, D., Chiarenza, A., Wells, V.A., Grunn, A., Messina, M., Elliot, O., et al. (2011). Analysis of the coding genome of diffuse large B-cell lymphoma. Nat. Genet. *43*, 830–837.

Rebeaud, F., Hailfinger, S., Posevitz-Fejfar, A., Tapernoux, M., Moser, R., Rueda, D., Gaide, O., Guzzardi, M., Iancu, E.M., Rufer, N., et al. (2008). The proteolytic activity of the paracaspase MALT1 is key in T cell activation. Nat. Immunol. *9*, 272–281.

Rho, S.B., Kim, B.R., and Kang, S. (2011). A gene signature-based approach identifies thioridazine as an inhibitor of phosphatidylinositol-3′-kinase (PI3K)/AKT pathway in ovarian cancer cells. Gynecol. Oncol. *120*, 121–127.

Rosebeck, S., Madden, L., Jin, X., Gu, S., Apel, I.J., Appert, A., Hamoudi, R.A., Noels, H., Sagaert, X., Van Loo, P., et al. (2011). Cleavage of NIK by the API2-MALT1 fusion oncoprotein leads to noncanonical NF-kappaB activation. Science *331*, 468–472.

Rosenwald, A., and Staudt, L.M. (2003). Gene expression profiling of diffuse large B-cell lymphoma. Leuk. Lymphoma *44*(*Suppl 3*), S41–S47.

Rosenwald, A., Wright, G., Chan, W.C., Connors, J.M., Campo, E., Fisher, R.I., Gascoyne, R.D., Muller-Hermelink, H.K., Smeland, E.B., Giltnane, J.M., et al.; Lymphoma/Leukemia Molecular Profiling Project. (2002). The use of molecular profiling to predict survival after chemotherapy for diffuse large-B-cell lymphoma. N. Engl. J. Med. *346*, 1937–1947.

Sarwer-Foner, G.J., and Koranyi, E.K. (1957). The clinical investigation of pacatal in open psychiatric settings. Can. Med. Assoc. J. *77*, 450–459.

Savage, K.J., Monti, S., Kutok, J.L., Cattoretti, G., Neuberg, D., De Leval, L., Kurtin, P., Dal Cin, P., Ladd, C., Feuerhake, F., et al. (2003). The molecular signature of mediastinal large B-cell lymphoma differs from that of other diffuse large B-cell lymphomas and shares features with classical Hodgkin lymphoma. Blood *102*, 3871–3879.

Scheidereit, C. (2006). IkappaB kinase complexes: gateways to NF-kappaB activation and transcription. Oncogene *25*, 6685–6705.

Seeman, P., Lee, T., Chau-Wong, M., and Wong, K. (1976). Antipsychotic drug doses and neuroleptic/dopamine receptors. Nature *261*, 717–719.

Shvartsburd, A., Nwokeafor, V., and Smith, R.C. (1984). Red blood cell and plasma levels of thioridazine and mesoridazine in schizophrenic patients. Psychopharmacology (Berl.) *82*, 55–61.

Staal, J., Driege, Y., Bekaert, T., Demeyer, A., Muyllaert, D., Van Damme, P., Gevaert, K., and Beyaert, R. (2011). T-cell receptor-induced JNK activation requires proteolytic inactivation of CYLD by MALT1. EMBO J. *30*, 1742–1752.

Thome, M. (2008). Multifunctional roles for MALT1 in T-cell activation. Nat. Rev. Immunol. *8*, 495–500.

Uren, A.G., O'Rourke, K., Aravind, L.A., Pisabarro, M.T., Seshagiri, S., Koonin, E.V., and Dixit, V.M. (2000). Identification of paracaspases and metacaspases: two ancient families of caspase-like proteins, one of which plays a key role in MALT lymphoma. Mol. Cell *6*, 961–967.

van Soolingen, D., Hernandez-Pando, R., Orozco, H., Aguilar, D., Magis-Escurra, C., Amaral, L., van Ingen, J., and Boeree, M.J. (2010). The antipsychotic thioridazine shows promising therapeutic activity in a mouse model of multidrug-resistant tuberculosis. PLoS ONE *5*, 5.

Vercammen, D., van de Cotte, B., De Jaeger, G., Eeckhout, D., Casteels, P., Vandepoele, K., Vandenberghe, I., Van Beeumen, J., Inzé, D., and Van Breusegem, F. (2004). Type II metacaspases Atmc4 and Atmc9 of Arabidopsis thaliana cleave substrates after arginine and lysine. J. Biol. Chem. *279*, 45329–45336.

Weisman, J.L., Liou, A.P., Shelat, A.A., Cohen, F.E., Guy, R.K., and DeRisi, J.L. (2006). Searching for new antimalarial therapeutics amongst known drugs. Chem. Biol. Drug Des. *67*, 409–416.

Wiesmann, C., Leder, L., Blank, J., Bernardi, A., Melkko, S., Decock, A., D'Arcy, A., Villard, F., Erbel, P., Hughes, N., et al. (2012). Structural determinants of MALT1 protease activity. J Mol Biol. *149*, 4–21.

Whittier, J.R., Klein, D.F., Levine, G., and Weiss, D. (1960). Mepazine (pacatal): clinical trial with placebo control and psychological study. Psychopharmacology (Berl.) *1*, 280–287.

Wiznerowicz, M., and Trono, D. (2003). Conditional suppression of cellular genes: lentivirus vector-mediated drug-inducible RNA interference. J. Virol. *77*, 8957–8961.

Wright, G., Tan, B., Rosenwald, A., Hurt, E.H., Wiestner, A., and Staudt, L.M. (2003). A gene expression-based method to diagnose clinically distinct subgroups of diffuse large B cell lymphoma. Proc. Natl. Acad. Sci. USA *100*, 9991–9996.

Yu, J.W., Jeffrey, P.D., Ha, J.Y., Yang, X., and Shi, Y. (2011). Crystal structure of the mucosa-associated lymphoid tissue lymphoma translocation 1 (MALT1) paracaspase region. Proc. Natl. Acad. Sci. USA *108*, 21004–21009.

Zhelev, Z., Ohba, H., Bakalova, R., Hadjimitova, V., Ishikawa, M., Shinohara, Y., and Baba, Y. (2004). Phenothiazines suppress proliferation and induce apoptosis in cultured leukemic cells without any influence on the viability of normal lymphocytes. Phenothiazines and leukemia. Cancer Chemother. Pharmacol. *53*, 267–275.

Cancer Cell
Article

MALT1 Small Molecule Inhibitors Specifically Suppress ABC-DLBCL In Vitro and In Vivo

Lorena Fontan,[1,2,5,11] Chenghua Yang,[3,11,12] Venkataraman Kabaleeswaran,[3,6,7] Laurent Volpon,[8] Michael J. Osborne,[8] Elena Beltran,[5] Monica Garcia,[1,2] Leandro Cerchietti,[1] Rita Shaknovich,[1,4] Shao Ning Yang,[1] Fang Fang,[1,2] Randy D. Gascoyne,[9] Jose Angel Martinez-Climent,[5] J. Fraser Glickman,[10] Katherine Borden,[8] Hao Wu,[3,6,7,*] and Ari Melnick[1,2,*]

[1]Division of Hematology and Medical Oncology
[2]Department of Pharmacology
[3]Department of Biochemistry
[4]Division of Immunopathology, Department of Pathology
Weill Cornell Medical College, New York, NY 10021, USA
[5]Division of Oncology, Center for Applied Medical Research, University of Navarra, 31008 Pamplona, Navarra, Spain
[6]Program in Cellular and Molecular Medicine, Children's Hospital Boston, Boston, MA 02115, USA
[7]Department of Biological Chemistry and Molecular Pharmacology, Harvard Medical School, Boston, MA 02115, USA
[8]Institute for Research in Immunology and Cancer, University of Montreal, Montreal QC H3C 3J7, Canada
[9]Centre for Lymphoid Cancer, BC Cancer Agency, Vancouver, BC V5Z 1L3, Canada
[10]High-Throughput Screening Resource Center, The Rockefeller University, New York, NY 10065, USA
[11]These authors contributed equally to this work
[12]Present address: Department of Molecular Pharmacology and Chemistry, Sloan-Kettering Institute, New York, NY 10021, USA
*Correspondence: hao.wu@childrens.harvard.edu (H.W.), amm2014@med.cornell.edu (A.M.)
http://dx.doi.org/10.1016/j.ccr.2012.11.003

SUMMARY

MALT1 cleavage activity is linked to the pathogenesis of activated B cell-like diffuse large B cell lymphoma (ABC-DLBCL), a chemoresistant form of DLBCL. We developed a MALT1 activity assay and identified chemically diverse MALT1 inhibitors. A selected lead compound, MI-2, featured direct binding to MALT1 and suppression of its protease function. MI-2 concentrated within human ABC-DLBCL cells and irreversibly inhibited cleavage of MALT1 substrates. This was accompanied by NF-κB reporter activity suppression, c-REL nuclear localization inhibition, and NF-κB target gene downregulation. Most notably, MI-2 was nontoxic to mice, and displayed selective activity against ABC-DLBCL cell lines in vitro and xenotransplanted ABC-DLBCL tumors in vivo. The compound was also effective against primary human non-germinal center B cell-like DLBCLs ex vivo.

INTRODUCTION

Non-Hodgkin's lymphoma (NHL) is the seventh most frequent cancer (Siegel et al., 2012). Diffuse large B cell lymphoma (DLBCL) is the most common subtype of NHL, accounting for ~25% of all lymphoma cases (Swerdlow et al., 2008). Gene expression profiling allowed subclassification of DLBCL into distinct molecular subtypes, including germinal center B cell-like (GCB) DLBCL, activated B cell-like (ABC) DLBCL, and primary mediastinal B cell lymphoma (PMBL) (Alizadeh et al., 2000; Rosenwald et al., 2003). These subtypes differ significantly in their spectrum of recurrent somatic mutations, dependence on different signaling pathways, and response to current standard therapies (Lenz et al., 2008b; Wright et al., 2003). Patients with the GCB subtype have a significantly better overall survival compared to those with the ABC subtype (Alizadeh et al., 2000;

Significance

MALT1 is a unique paracaspase protein that transduces aberrant oncogenic signaling in ABC-DLBCL. This manuscript reports the development of a constitutively activated form of MALT1 that enabled a screen for small molecule inhibitors. This led to identification of MI-2, an irreversible MALT1 protease inhibitor, which is a lead compound with nanomolar activity in cell-based assays and selective activity against ABC-DLBCLs. Importantly, we show that MALT1 inhibitors kill ABC-DLBCLs in vitro and in vivo, are nontoxic to animals, and also suppress primary human non-GCB-DLBCL specimens. Hence, we demonstrate that MALT1 is a bona fide therapeutic target and provide a lead compound that forms the basis of a class of therapeutic agents for B cell lymphomas.

Rosenwald et al., 2002). Improved therapies are needed for all DLBCLs but most urgently for ABC-DLBCLs, which are the most chemoresistant.

ABC-DLBCL is characterized by its reliance on the oncogenic activation of the NF-κB pathway through several different mechanisms. These mostly involve somatic mutations in molecules participating in signaling downstream of the B cell receptor (BCR), including activating mutations of *CARMA1/CARD11* (Lenz et al., 2008a) and *CD79A/B* (Davis et al., 2010), homozygous deletion/inactivating mutations of *TNFAIP3/A20* (Compagno et al., 2009; Honma et al., 2009), and activating mutations of *MYD88* downstream of the Toll-like receptor (Ngo et al., 2011). CARMA1 forms part of the CARMA1-BCL10-MALT1 (CBM) complex and mediates NF-κB activation downstream of the B cell receptor, T cell receptor (Ruefli-Brasse et al., 2003; Ruland et al., 2003), and ITAM-coupled natural killer cell receptors (Gross et al., 2008). The MALT1 (mucosa-associated lymphoid tissue lymphoma translocation 1) subunit is the active signaling component of the CBM complex (Lucas et al., 2001) and features protease activity that cleaves and inactivates inhibitors of the NF-κB signaling pathway such as TNFAIP3/A20 (Coornaert et al., 2008), CYLD (Staal et al., 2011), and RELB (Hailfinger et al., 2011) or the BCL10 protein (Rebeaud et al., 2008), indirectly activating NF-κB signaling. *MALT1* translocations, including t(11;18)(q21;q21), which produces an *API2-MALT1* fusion, and t(14;18)(q32;q21), which results in the *IGH-MALT1* translocation, are detected in up to 55% of MALT-type lymphomas (Farinha and Gascoyne, 2005). These translocations lead to overexpression of *MALT1* and, in the case of the *API2-MALT1* translocation, constitutive activation of the pathway (Dierlamm et al., 1999; Sanchez-Izquierdo et al., 2003; Streubel et al., 2003). Constitutive expression of MALT1 in mice induces a disease that is similar to MALT lymphomas in humans, and induces ABC-like DLBCLs in a p53-null background (Vicente-Dueñas et al., 2012). *MALT1* has not been found mutated or translocated in DLBCL but is gained along with *BCL2*, and this low-copy-number amplification is associated with an ABC-DLBCL phenotype (Dierlamm et al., 2008). Moreover, ABC-DLBCL cell lines have been shown to be dependent on MALT1 catalytic activity (Ferch et al., 2009; Hailfinger et al., 2009; Ngo et al., 2006).

MALT1 is a paracaspase, which is related to the caspase (cysteine-*asp*artic prote*ases*) family of proteases but cleaves after Arg residues instead of Asp (Rebeaud et al., 2008). *MALT1* is the only gene encoding paracaspase in the human genome. MALT1-null animals display defects in B and T cell function but are otherwise healthy (Ruefli-Brasse et al., 2003; Ruland et al., 2003). These factors suggest that MALT1-targeted therapy would likely be well tolerated with little or manageable toxicity. Consequently, MALT1 represents a potentially important therapeutic target for ABC-DLBCL and MALT lymphoma.

RESULTS

Biochemical Screening Identifies Low Molecular Weight Inhibitors of MALT1 Proteolytic Activity

We reasoned that MALT1 small molecule inhibitors might be useful chemical tools for studying MALT1 biology and treating MALT1-addicted tumors. However, full length MALT1 and its paracaspase domain (amino acids 340–789) are naturally present in physiological solutions as a monomer, which has very low proteolytic activity. Caspases generally must homodimerize for maximal catalytic activity (Pop et al., 2006; Walker et al., 1994; Yin et al., 2006), and accordingly the recently reported structures of the paracaspase domain of MALT1 in complex with a peptide inhibitor are dimeric (Wiesmann et al., 2012; Yu et al., 2011). In order to generate catalytically active MALT1 for an effective assay to screen for inhibitors, we biochemically engineered a recombinant form of MALT1 (340–789) fused with a leucine zipper dimerization motif (LZ-MALT1), which promotes its dimerization and activation (Figure 1A). We developed a MALT1 activity assay using the MALT1 substrate peptide LRSR linked to the fluorogen AMC (7-amino-4-methylcoumarin). Cleavage of the Ac-LRSR-AMC substrate by MALT1 resulted in release of AMC and a fluorescent signal.

The optimal conditions for high-throughput screening were determined by systematic variation of the concentrations of the enzyme and the substrate in a two-dimensional grid. Fluorescence measurements were taken every 45 s for 60 min. The measurements were plotted as a function of time. Conditions with a linear relationship between fluorescence and time were considered appropriate for screening. Quality was assessed using the Z′ factor, a coefficient reflective of the dynamic range of the assay and variance of the data (Zhang et al., 1999), calculated by the formula $Z'\ \text{factor} = 1 - 3 \times (\sigma_p + \sigma_n)/(|\mu_p - \mu_n|)$, where $\sigma_{p/n}$ is the standard deviation for positive and negative control and $\mu_{p/n}$ is the mean for positive and negative control. The Z′ factor for this screen was 0.738, which is within the optimal range 0.5–1 (Zhang et al., 1999). A total of 46,464 compounds was screened (see Supplemental Experimental Procedures available online). Using 40% inhibition as a threshold, 324 candidate compounds were selected for validation in a concentration-response assay (Figure 1B). Of these, 19 compounds (Figure S1A) were selected for further validation based on their biochemical activity (half-maximal inhibitory concentration [IC_{50}] < 20 μM; Figure 1C).

Candidate Inhibitors Selectively Suppress ABC-DLBCL Cell Lines and MALT1 Catalytic Activity

MALT1 activity plays an important role in selectively maintaining proliferation of ABC-DLBCL cell lines (Ngo et al., 2006). Accordingly, ABC- and GCB-DLBCL cell lines present differential sensitivity to MALT1 cleavage inhibition by the peptide Z-VRPR-FMK (Ferch et al., 2009; Hailfinger et al., 2009; Rebeaud et al., 2008). To determine whether candidate small molecules display a similar profile, two ABC-DLBCL cell lines, HBL-1 and TMD8, and one GCB-DLBCL cell line, OCI-Ly1, were exposed to increasing concentrations of the 19 selected molecules. Cell proliferation was measured 48 hr after exposure to a single dose of compound using an ATP-based metabolic luminescent assay (summarized in Figure 1C). Three compounds consistently induced significant selective dose-dependent suppression of ABC-DLBCL cells (MI-2, $p < 0.0001$; MI-4, $p = 0.006$; MI-11, $p < 0.0001$; regression extra sum-of-squares F test; Figures 1C and S1B). Hence, these compounds were active in cells, selective for ABC-DLBCLs, and lack nonspecific cellular toxicity. MI-6 and MI-15 also showed differential inhibition of ABC-DLBCL cells but did not reach statistical significance.

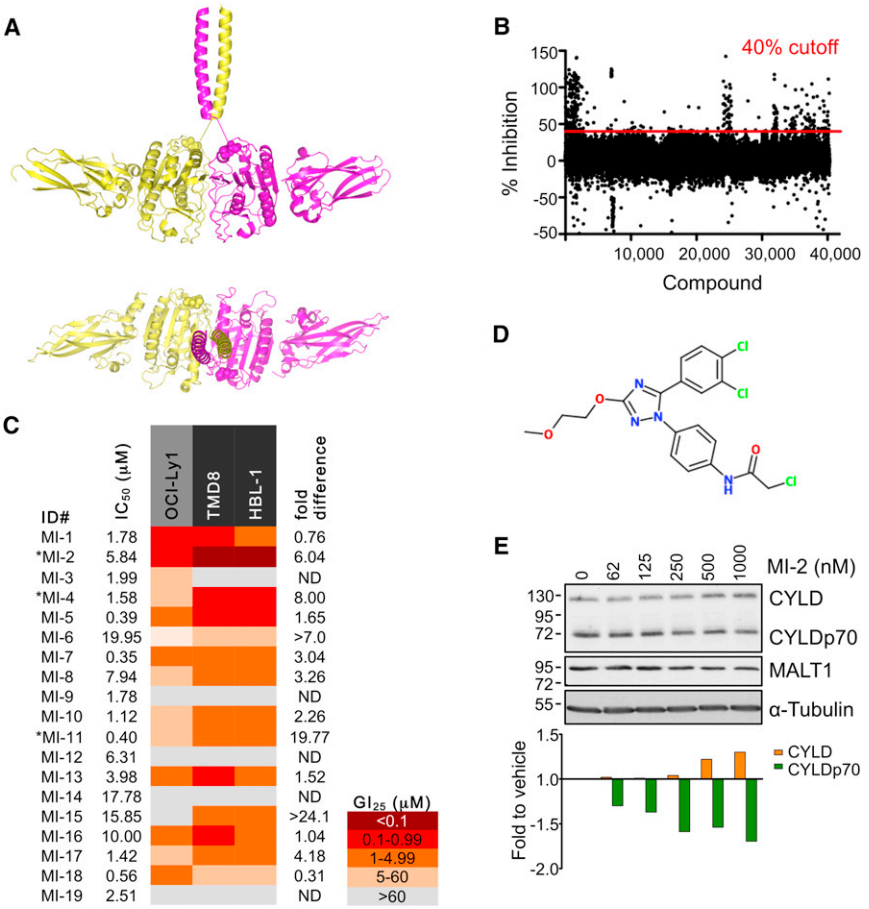

Figure 1. Identification of MALT1 Small Molecule Inhibitors

(A) Dimeric LZ-MALT1 representation showing LZ-MALT1 monomers in yellow and magenta. Met338 is shown as a sphere model. The model was generated using the MALT1 structure (Protein Data Bank [PDB] ID code 3UOA) and LZ structure (PDB ID code 2ZTA).

(B) Represented is the % inhibition for each of the compounds assayed at 12.5 μM. Cutoff was 40% inhibition.

(C) Summary table of IC_{50} and GI_{25} results for screening hits. Experiments were performed three times in triplicate. Fold difference = OCI-Ly1 GI_{25}/average GI_{25} for the MALT1-dependent cell lines. *Significant dose-dependent suppression of proliferation in ABC-DLBCL, regression extra sum-of-squares F test.

(D) MI-2 structure.

(E) MALT1 cleavage of CYLD inhibition by MI-2 in HBL-1 cells at 24 hr studied by western blot. α-tubulin, and loading control. Densitometry values were normalized to α-tubulin and are relative to vehicle-treated cells. The representative result is from three experiments.

See also Figure S1.

Compound MI-2 was the most potent in cell-based assays, with 25% growth-inhibitory concentration (GI_{25}) values in the high-nanomolar range. MI-2 (Figure 1D) was therefore next assayed for inhibition of MALT1-mediated substrate cleavage in lymphoma cells. HBL-1 cells were treated with increasing concentrations of MI-2 for 24 hr and cleavage of the MALT1 target protein CYLD was measured by western blotting and densitometry. MI-2 caused a dose-dependent decrease in MALT1-mediated cleavage, noted by an increase in the uncleaved CYLD protein and a decrease in the cleaved form of the protein (Figure 1E). MI-2 was selective as a MALT1 paracaspase inhibitor, because it displayed little activity against the structurally related caspase family members caspase-3, -8, and -9 (Figure S1C). Moreover, MI-2 did not inhibit caspase-3/7 activity or apoptosis in cell-based assays at concentrations that suppress MALT1 (Figures S1D–S1F). Hence, MI-2 is a potential lead compound as a therapeutic MALT1 inhibitor.

MI-2 Analogs Display MALT1-Inhibitory Activity

To establish whether compound MI-2 represented a potential scaffold for development of MALT1 inhibitors, we compared MI-2 with other chemical compounds in silico to identify potential analogs. A total of 704 analog compounds from available libraries with similarity score ≥70% (Tanimoto similarity functions) was screened by LZ-MALT1 fluorescence assay. Nineteen analogs displaying equal or higher activity than MI-2 were selected (Figure 2A). Five analogs with biochemical IC_{50}s within a similar range as MI-2 were selected for further characterization in cell-proliferation assays (Figures 2B and 2C). All five analogs (MI-2A1–5) exhibited the same trend toward selective suppression of the ABC-DLBCL cell lines, with GI_{25} concentrations in the micromolar range (Figure 2C). Two analog compounds with no LZ-MALT1-inhibitory activity in vitro (MI-2A6 and -7) used as chemical controls had no effect on cell proliferation over the same dose range (Figure S2). The five active MI-2 analogs were assayed for inhibition of MALT1 cleavage of CYLD. All five compounds, administered at 5 μM for 8 hr, showed cleavage inhibition similar to the Z-VRPR-FMK MALT1 blocking peptide (50 μM) used as positive control (Figure 2D), although MI-2 itself remained the most potent compound. Collectively, the conservation of MALT1 inhibitor activity in vitro and in cell-based assays among chemically related compounds points toward the suitability of MI-2 and its analogs as lead compound inhibitors of MALT1.

MI-2 Directly Binds and Irreversibly Inhibits MALT1

We next investigated whether MI-2 directly bound to MALT1 or indirectly affected MALT1 activity, for example through binding to the LZ region of the fusion protein. Heteronuclear single-quantum coherence (HSQC) nuclear magnetic resonance (NMR) spectroscopy was used to characterize the binding of MI-2 to the paracaspase domain of MALT1 (residues 329–728). As MI-2 was titrated in, resonances corresponding to the unbound state of MALT1 decreased in intensity, while another set of resonances corresponding to the MALT1-MI-2 complex gradually appeared (Figure 3A). This pattern of chemical shift changes is characteristic of slow exchange on the NMR

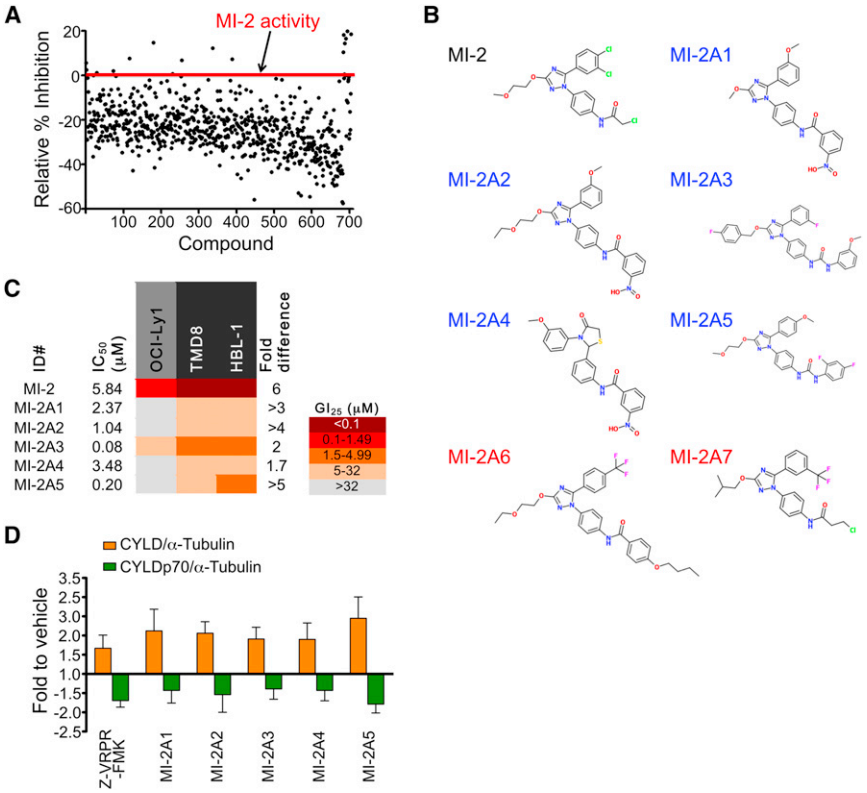

Figure 2. MI-2 Analogs Display Similar MALT1-Inhibition Activity

(A) Seven hundred and four compounds with over 70% homology to MI-2 were screened. Compounds with equal or higher activity than MI-2 were selected.

(B) Structures of the MI-2 analog compounds assayed in cell growth-inhibition experiments. Blue, active analogs; red, inactive analogs.

(C) IC_{50} and GI_{25} values for the selected analogs assayed in HBL-1, TMD8, and OCI-Ly1 cells. Experiments were performed three times in triplicate. Fold difference = OCI-Ly1 GI_{25}/average GI_{25} for the MALT1-dependent cell lines.

(D) CYLD cleavage was studied in HBL-1 cells treated with 5 μM analog compound or 50 μM Z-VRPR-FMK for 8 hr. Densitometry results were normalized to α-tubulin and fold change-to-vehicle ratios were calculated. Results are mean ± SEM of three independent experiments.

See also Figure S2.

timescale and is indicative of a robust interaction between MALT1 and MI-2. In contrast, NMR spectroscopy studies showed no evidence of binding by the inactive analogs MI-2A6 and MI-2A7 (Figure 3B).

Because MI-2 contains a reactive chloromethyl amide, we investigated whether MI-2 could modify MALT1 covalently using liquid chromatography-mass spectrometry (LC-MS). As shown in Figure 3C, MALT1 paracaspase domain (329–728) presented a major peak at 55,988.4 Da. Upon incubation with the compound MI-2, the major peak of MALT1 was shifted to 56,407.5 Da, an increase of 419.1 Da. This corresponds to addition of MI-2 minus the chloride group, indicating that MI-2 can bind covalently to MALT1 and potentially act as an irreversible inhibitor. Because the chloromethyl amide group is not conserved in the active MI-2 analogs (Figure 2B), it is most likely the common chemical scaffold in the MI-2 series that provides specificity to MALT1. Notably, LC-MS performed with MI-2 and the MALT1 active site mutant C464A revealed markedly reduced covalent binding, suggesting that the active site C464 residue is the main target of modification by MI-2 (Figure 3C). To further explore the potential mode of binding of MI-2 to the MALT1 paracaspase domain, we employed molecular docking using AutoDock 4.2 (Morris et al., 2009). The crystal structure of MALT1 (Wiesmann et al., 2012; Yu et al., 2011) was kept as a rigid body while allowing conformational flexibility of MI-2. The final results were ranked on the predicted binding free energy and the cluster size for each docking conformation. The top five poses were selected, all of which had similar docking scores with slight changes in their orientations. As shown for the first top hit, MI-2 appears to bind the active site cleft with its chloromethyl group close to the active site C464 in the paracaspase domain (Figures 3D and S3A), consistent with a covalent-bond formation between these two groups. Collectively, the data suggest that MI-2 engages and irreversibly binds the MALT1 active site.

To examine whether MI-2 inhibition of MALT1 is consistent with irreversible binding kinetics, LZ-MALT1 was preincubated with different concentrations of MI-2 for 5–80 min followed by addition of the substrate Ac-LRSR-AMC to determine enzymatic activity (Figures 3E and S3B). Notably, the percent MALT1 inactivation increased with time, reaching plateaus near the end of the test, consistent with covalent and irreversible inhibition. Inhibition was concentration dependent, with higher concentrations showing greater inactivation and faster rates of saturation. In contrast, the active MI-2 analog MI-2A2, which does not have the chloromethyl amide group, showed no evidence of cumulative inhibition of MALT1, consistent with reversible inhibition. It should be noted that MI-2 reached close to 100% inhibition, whereas MI-2A2 with a lower IC_{50} only reached ~50% inhibition (Figure 3E). The irreversible kinetics might contribute to the more potent effects of MI-2 in cell-based assays versus its analogs that lack the chloromethyl amide group and only bind reversibly, as has been noted in the case of peptidyl halomethyl ketone protease inhibitors (Powers et al., 2002).

MI-2 Inhibits MALT1 Functions in ABC-DLBCL Cell Lines

Having confirmed MI-2 as a lead compound, we next explored its effects on MALT1 signaling in ABC-DLBCL cells. We first examined the impact of MI-2 on cleavage of additional MALT1 substrates such as A20, BCL10, and RELB. Because these proteins are directed to proteasomal degradation after cleavage (Coornaert et al., 2008; Hailfinger et al., 2011; Rebeaud et al., 2008), we used the proteasome inhibitor MG-132 to facilitate visualization of cleavage products (Figure 4A). HBL-1 and

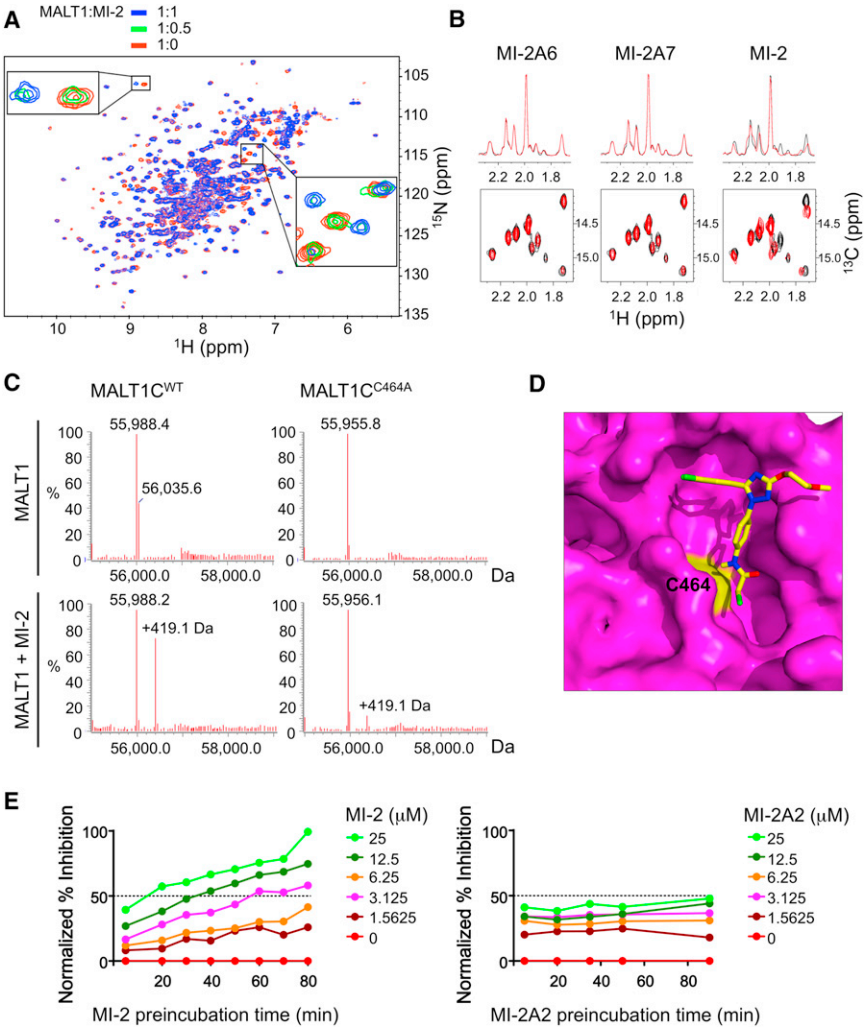

Figure 3. MI-2 Directly Interacts with and Irreversibly Inhibits MALT1

(A) Superposition of the ^{1}H-^{15}N HSQC spectrum of the apo-MALT1 (red) with the MALT1-MI-2 complex (blue) at a molar ratio of 1:1. The expanded regions highlight interacting residues in the slow-exchange regime on the NMR timescale (intermediate 1:0.5 MALT1:MI-2 ratio is shown in green).

(B) One-dimensional (top) and two-dimensional (bottom) ^{1}H-^{13}C HSQC NMR spectra of MALT1 (329–728) without (black) and with compounds MI-2A6, MI-2A7, and MI-2 (red).

(C) LC-MS for MALT1^{WT} and MALT1^{C464A} (amino acids 329–728) with and without MI-2.

(D) Docked MI-2 (in stick model) on the MALT1 paracaspase domain (in surface representation). MALT1 is shown in magenta with C464 in yellow. MI-2 is shown with carbons in yellow, oxygens in red, nitrogens in blue, and chlorines in green.

(E) LZ-MALT1 was preincubated with the indicated concentrations of MI-2 or MI-2A2 (0–25 μM) for different durations (5–90 min) before Ac-LRSR-AMC was added. The graphs represent normalized % inhibition compared to preincubation time. See also Figure S3.

TMD8 cell lines were exposed to either MI-2 (2 μM) or vehicle for 30 min followed by 5 μM MG-132 for an additional 1 (lanes 2 and 3) or 2 hr (lanes 4 and 5) in order to allow cleaved forms of MALT1 substrates to accumulate during exposure to MI-2. As expected, MG-132 exposure revealed the accumulation of A20, BCL10, and RELB cleavage products due to the constitutive activity of MALT1 in these DLBCL cells. However, exposure to MI-2 diminished the abundance of cleaved forms and/or increased the abundance of full-length proteins, consistent with the loss of MALT1 enzymatic activity (Figure 4A).

MALT1 mediates c-REL translocation to the nucleus following BCR stimulation (Ferch et al., 2007). Therefore, HBL-1 cells were exposed to 200 nM MI-2, 50 μM Z-VRPR-FMK (positive control), or vehicle for 24 hr, followed by c-REL flow cytometry of whole cells or isolated nuclei. Both MI-2 and Z-VRPR-FMK reduced nuclear c-REL to a similar extent, without affecting whole-cell levels of this protein (Figure 4B). To further confirm this result, we also performed western blots for c-REL and p65 in nuclear extracts of HBL-1 and TMD8 cells treated for 24 hr with GI_{50} concentrations of MI-2 (200 nM for HBL-1 and 500 nM for TMD8). In both cell lines, exposure to MI-2 caused a clear reduction of nuclear c-REL whereas it did not affect p65 levels (Figure 4C). This selectivity toward c-REL had also been previously shown in MALT1 knockout mice and after MALT1 cleavage inhibition by the MALT1 blocking peptide Z-VRPR-FMK (Ferch et al., 2007, 2009; Hailfinger et al., 2011).

Antigen receptor-mediated NF-κB signaling partly depends on MALT1 activity (Ruefli-Brasse et al., 2003; Ruland et al., 2003). Hence, we tested the effect of MI-2 on attenuating NF-κB activation induced by phorbol 12-myristate 13-acetate (PMA)/ionomycin, which mimics BCR activation and activates MALT1-dependent cleavage (Coornaert et al., 2008; Rebeaud et al., 2008). First, 293T cells were transfected with the NF-κB reporter vector $(NF\text{-}\kappa B)_5$-luc2CP-pGL4 (harboring five copies of the NF-κB consensus-response element and a destabilized firefly luciferase) and TK-pRL control together with plasmids expressing BCL10 and either MALT1^{WT} or MALT1^{C464A} (inactive mutant). Exposure to PMA/ionomycin significantly increased luciferase activity in 293T cells when MALT1^{WT} was transfected, but not with the mutant MALT1^{C464A}. Pretreatment with MI-2 significantly inhibited NF-κB induction by PMA/ionomycin stimulation similarly to Z-VRPR-FMK, whereas it did not significantly affect that of MALT1^{C464A} (Figure 4D). HBL-1 cells are reported to exhibit chronic active B cell receptor signaling with consequent NF-κB activation (Davis et al., 2010). HBL-1 was transfected with the reporter construct $(NF\text{-}\kappa B)_5$-luc2CP-pGL4 and TK-pRL control. Treatment with MI-2 promoted a 20% and 50% reduction in NF-κB reporter activity at 8 and 24 hr, respectively. A similar result was observed for Z-VRPR-FMK (50 μM) (Figure 4E). This reduction in NF-κB reporter activity was significant at 24 hr for MI-2 and the blocking peptide Z-VRPR-FMK.

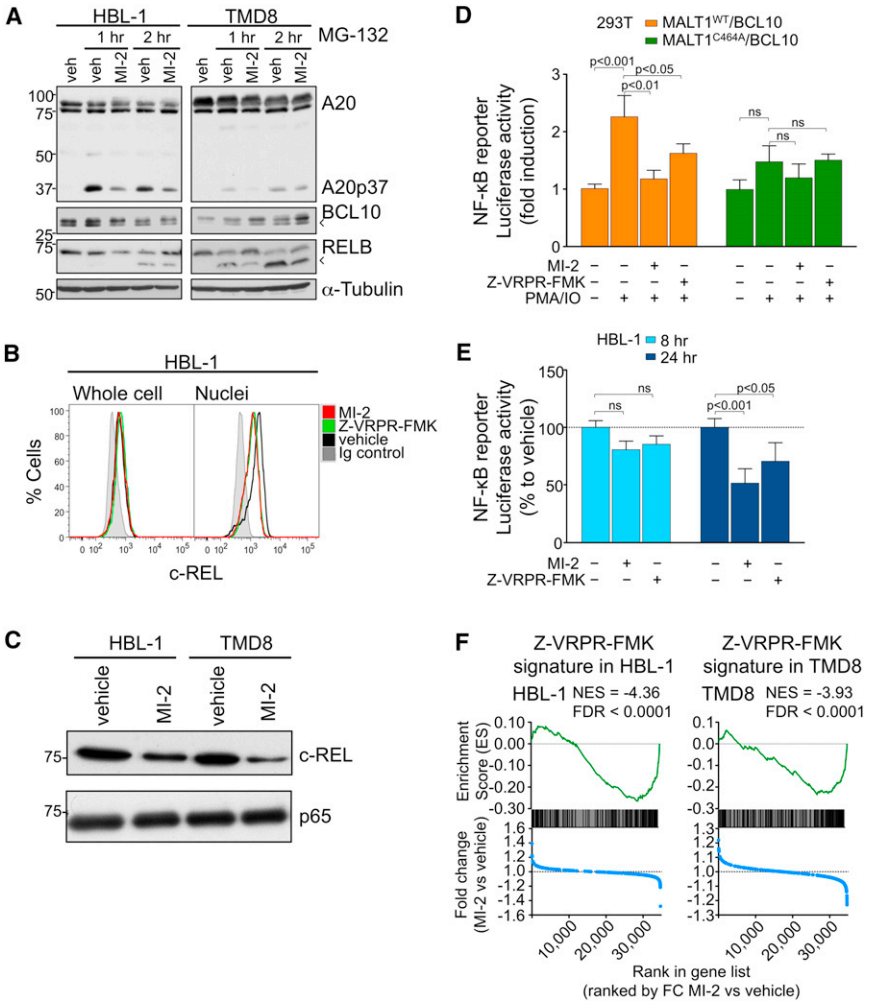

Figure 4. MI-2 Inhibits MALT1 Signaling in DLBCL Cells

(A) Western blots for A20, RELB, and BCL10 after 30 min pretreatment with 2 μM MI-2 or vehicle, followed by proteasome inhibitor MG-132 (5 μM) treatment for 1 or 2 hr in HBL-1 and TMD8. Arrowheads indicate cleavage products.

(B) Flow cytometry for c-REL whole cells or isolated nuclei from HBL-1 cells treated with 200 nM MI-2, 50 μM Z-VRPR-FMK, or vehicle for 24 hr.

(C) c-REL and p65 protein expression in nuclear extracts of HBL-1 and TMD8 cells treated for 24 hr with 200 or 500 nM MI-2, respectively.

(D) NF-κB reporter assays in 293T cells transfected with the indicated expression constructs. Cells were treated for 30 min with 2 μM MI-2, 50 μM Z-VRPR-FMK, or vehicle followed by PMA/ionomycin for 2 hr. The y axis represents luciferase fold induction relative to vehicle-treated cells, normalized to internal control. Statistics, ANOVA, Bonferroni posttest.

(E) NF-κB reporter assays in HBL-1 cells treated with 200 nM MI-2, 50 μM Z-VRPR-FMK, or vehicle for 8 and 24 hr. The y axis represents % luciferase activity relative to vehicle-treated cells, normalized to internal control. Statistics, ANOVA, Bonferroni posttest.

(F) Enrichment of Z-VRPR-FMK-downregulated genes after MI-2 treatment in HBL-1 and TMD8 cells using GSEA. Normalized enrichment score (NES) and false discovery rate (FDR) values are indicated. Top: enrichment score versus relative position of ranked genes (green tracing); bottom: fold change (FC) MI-2/vehicle versus relative position of ranked genes (blue tracing). Experiments were performed in triplicate unless otherwise specified. Data are mean ± SEM.

See also Figure S4.

The impact of MI-2 on NF-κB signaling was further characterized by gene expression profiling. For these experiments, the HBL-1 and TMD8 cell lines were treated with GI_{50} concentrations of MI-2 (HBL-1, 200 nM; TMD8, 500 nM) or 50 μM Z-VRPR-FMK for 8 hr, and RNA was extracted for gene expression studies using oligonucleotide microarrays. Z-VRPR-FMK was previously shown to attenuate the NF-κB signature in ABC-DLBCL cell lines (Hailfinger et al., 2009). MI-2 would be expected to exhibit a similar profile. For this study, we assigned Z-VRPR-FMK signatures by capturing the top 200 downregulated genes by Z-VRPR-FMK treatment compared to vehicle for each cell line. We next performed gene set enrichment analysis (GSEA) of this Z-VRPR-FMK signature against the differential expression of all genes preranked by fold change between MI-2- and vehicle-treated cells for each cell line. The Z-VRPR-FMK signature was significantly enriched among genes downregulated after MI-2 treatment for both cell lines (Figure 4F). GSEA was next performed using two independent ABC-DLBCL NF-κB gene expression signatures derived from either OCI-Ly3 and OCI-Ly10 or HBL-1 cell lines. We observed significant enrichment of these NF-κB gene sets among genes downregulated after MI-2 treatment in both cell lines (Figure S4). Collectively, these data suggest that MI-2 suppresses NF-κB activity induced by MALT1, similar to the effect observed with Z-VRPR-FMK.

MI-2 Selectively Suppresses MALT1-Dependent DLBCL Cell Lines

To further explore the spectrum of MI-2-mediated MALT1-inhibition effects, we turned to a larger panel of six ABC-DLBCL and two GCB-DLBCL cell lines (Table S1). Endogenous MALT1 activity was evaluated by western blotting for A20, BCL10, and CYLD, and NF-κB activation by phospho-IκB-α and total IκB-α (Figure S5A). Dependence on MALT1 proteolytic activity for proliferation was tested by 50 μM Z-VRPR-FMK treatment for 48 hr (Figure S5B). As expected, the two GCB-DLBCL cell lines (OCI-Ly7 and OCI-Ly1) did not display evidence of MALT1 or NF-κB signaling and did not respond to Z-VRPR-FMK. The U2932 and HLY1 ABC-DLBCL cell lines harbor mutations in TAK1 and A20, which activate NF-κB signaling downstream of MALT1. Hence, these two cell lines displayed relatively little response to Z-VRPR-FMK. In contrast, the ABC-DLBCL cells HBL-1, TMD8, OCI-Ly3, and OCI-Ly10 displayed evidence of MALT1 activity and inhibition of proliferation by Z-VRPR-FMK, indicating that these four cell lines are MALT1 dependent.

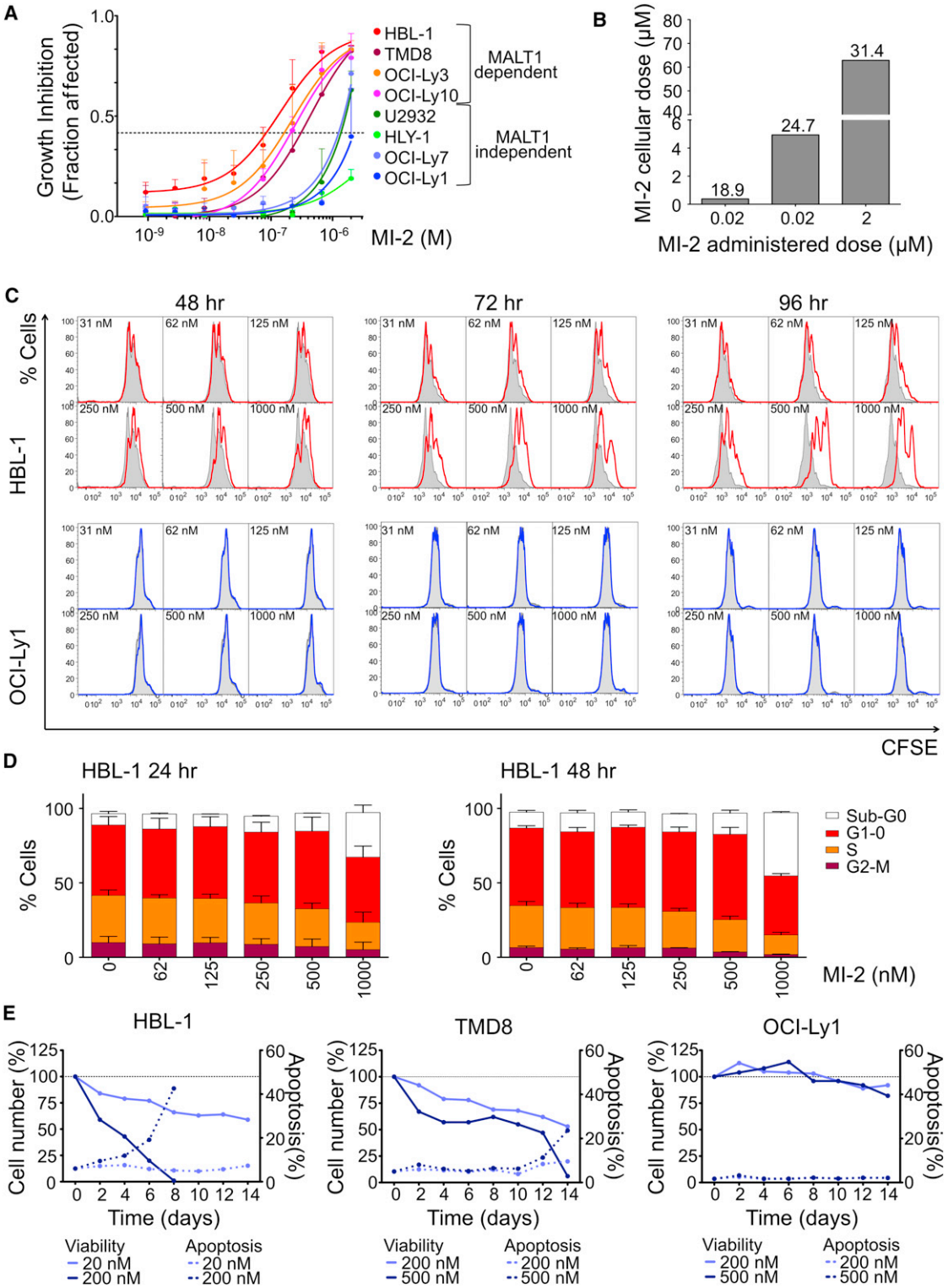

Figure 5. MI-2 Inhibits Cell Proliferation of MALT1-Dependent DLBCL Cells

(A) Dose-effect graphical representation for eight DLBCL cell lines exposed to MI-2 for 48 hr. Data are mean ± SEM of three independent experiments performed in triplicate.

(B) Intracellular MI-2 concentration determined by LC-MS in HBL-1 cells treated for 2 hr. The y axis represents MI-2 intracellular concentration. The x axis represents administered dose of MI-2. Fold-change accumulation in cells is indicated.

(C) CFSE dilution assay in HBL-1 and OCI-Ly1 cells after treatment with MI-2 for 48, 72, and 96 hr. Cells (2×10^4) were measured; $DAPI^-$ cells were gated for analysis.

All eight cell lines were exposed to increasing concentrations of MI-2 (single dose) and cell proliferation was measured at 48 hr using an ATP-based metabolic luminescent assay (Figure 5A). Growth inhibition by MI-2 was selective for MALT1-dependent cell lines, whereas the ABC-DLBCL MALT1-independent cell lines, U2932 and HLY-1, and the two GCB-DLBCL cell lines were resistant. The GI_{50} for MI-2 in HBL-1, TMD8, OCI-Ly3, and OCI-Ly10 cells was 0.2, 0.5, 0.4, and 0.4 μM, respectively, which is lower than its IC_{50} in vitro (Figure 1). This is likely explained by the irreversible binding of MI-2 to MALT1 as shown in Figure 3, but could also be due to intracellular accumulation of the compound. Indeed, we observed an 18- to 30-fold increase in MI-2 intracellular concentration in experiments where HBL-1 cells were exposed to 0.02, 0.2, or 2 μM MI-2 for 2 hr and washed three times and MI-2 was measured by LC-MS (Figure 5B). The intracellular concentration in the 0.2 μM MI-2-treated cells was 5 μM, similar to the calculated in vitro IC_{50} (Figure 5B). To determine the kinetics of accumulation of free drug, we measured the intracellular concentration of MI-2 at the GI_{50} concentration of 0.2 μM at 30 min and 2, 6, 12, 24, and 48 hr (Figure S5C). By 12 hr, there was virtually no detectable free MI-2 within the cells. However, after exposure of HBL-1 cells to increasing concentrations of a single dose of MI-2, recovery of cells only started to become evident after 48 hr (of the 0.2 μM dose level; Figure S5D). These data suggest that the potent biological effects of MI-2 are due at least in part to its irreversible binding to MALT1 aided by its tendency to concentrate in cells.

To explore in more detail the biological effects of MALT1 inhibition, HBL-1, TMD8, OCI-Ly10, and the GCB-DLBCL cell line OCI-Ly1 were treated with increasing concentrations of MI-2. Cell proliferation was examined using the 5-(and 6)-carboxyfluorescein diacetate succinimidyl ester (CFSE) dilution assay by flow cytometry on viable cells at 48, 72, and 96 hr. MI-2 substantially inhibited proliferation in HBL-1, TMD8, and OCI-Ly10 whereas it did not affect OCI-Ly1 (Figures 5C and S5E). Using BrdU incorporation-DAPI (4′,6-diamidino-2-phenylindole) staining and flow cytometry to assess the cell cycle, it was evident that MI-2 induced a dose-dependent decrease in S phase, with a reciprocal increment in the proportion of cells in G1-0 and sub-G0 (Figure 5D). To determine whether MALT1 inhibitors induced apoptosis, the ABC-DLBCL cell lines HBL-1 and TMD8 were treated daily with MI-2 at their respective GI_{25} and GI_{50}, and the control OCI-Ly1 cell line at the higher doses was used for TMD8. Trypan blue exclusion and apoptosis assessed by Annexin V^+ $DAPI^-$ flow cytometry was measured every 48 hr for a period of 14 days. Whereas MI-2 had no effect on OCI-Ly1 cells, it profoundly suppressed both HBL-1 and TMD8 cells, with the former exhibiting earlier and higher abundance of apoptotic cells (Figure 5E). Using the more sensitive caspase-3/7 cleavage assay, we observed evidence of dose-dependent apoptosis within 48 hr in both ABC-DLBCL cell lines (Figure S5F). Hence, MI-2 powerfully suppresses the growth and survival of ABC-DLBCL cell lines.

Compound MI-2 Is Nontoxic to Animals

To determine its suitability as a MALT1 lead compound for in vivo studies, we examined whether MI-2 induced toxic effects in mice. Five C57BL/6 mice were exposed to daily intraperitoneal (IP) administration of increasing doses of MI-2 ranging from 0.05 to 25 mg/kg over the course of 10 days to a cumulative dose of 51.1 mg/kg, and another five mice were exposed to vehicle only (5% DMSO, n = 5) (Figure 6A, toxicity 1). There was no evidence of lethargy, weight loss (Figure 6B, toxicity 1), or other physical indicators of sickness. To ascertain whether the maximal administered dose of 25 mg/kg is safe in a 14 day schedule, we exposed ten mice to daily IP administration of 25 mg/kg of MI-2 over 14 days to a cumulative dose of 350 mg/kg, using as controls five mice injected with vehicle only (Figure 6A, toxicity 2). Five mice were sacrificed after the 14 day course of MI-2 administration (together with the five controls) and the other five mice were sacrificed after a 10 day washout period to assess delayed toxicity. No toxic effects or other indicators of sickness, including weight loss (Figure 6B, toxicity 2) or tissue damage (macroscopic or microscopic), were noted (Figure 6C). Brain, heart, lung, liver, kidney, bowel, spleen, thymus, and bone marrow tissues were examined. Bone marrow was normocellular with trilineage maturing hematopoiesis. Myeloid-to-erythroid ratio was 4–5:1. Megakaryocytes were normal in number and distribution. There was no fibrosis or increased number of blasts or lymphocytes. Complete peripheral blood counts, biochemistry, and liver function tests were normal (Table S2), These studies established the safety of MI-2 for use in antilymphoma efficacy studies.

MI-2 Suppresses Human ABC-DLBCL Xenografts and Primary Human DLBCLs Ex Vivo

In order to determine whether MI-2 could suppress DLBCLs in vivo, we engrafted HBL-1 and TMD8 (MALT1-dependent) and OCI-Ly1 (MALT1-independent) DLBCL cells into the right flank region of nonobese diabetic/severe combined immunodeficiency (NOD-SCID) mice. Once tumors reached an average of 120 mm^3 in volume, mice were randomized to receive IP injection of MI-2 25 mg/kg/day or vehicle (5% DMSO). Animals were sacrificed 24 hr after the 14th injection. Remarkably, MI-2 profoundly suppressed the growth of both the TMD8 and HBL-1 ABC-DLBCL xenografts versus vehicle, whereas it had no effect on the growth of OCI-Ly1 tumors (Figure 7A). The fact that OCI-Ly1 tumors were unaffected suggests that MI-2 activity is due to its effects on lymphoma cells rather than the host microenvironment. Histological examination using the TUNEL assay to detect apoptotic cells showed a significant increase in apoptotic cells in MI-2-treated HBL-1 and TMD8 xenografts relative to vehicle but not in OCI-Ly1 xenografts (Figures 7B and S6A). We also observed a significant decrease in proliferation as measured by Ki-67 staining in HBL-1 and TMD8 xenografts compared to vehicle, but observed no difference in OCI-Ly1 xenografts (Figures 7C and S6B). To evaluate the effect

(D) BrdU pulse-labeled HBL-1 cells treated for 24 and 48 hr with MI-2 were analyzed by flow cytometry. The graph shows the % of cells for each cell-cycle phase for vehicle and each of the concentrations assayed. Data are mean ± SD of two independent experiments.
(E) Apoptosis time course in cell lines treated with MI-2 every 24 hr. Cells were counted using trypan blue and apoptosis was assessed by Annexin V^+ $DAPI^-$ every 48 hr for a period of 14 days. Left y axis, % cell number relative to vehicle for each time point. Right y axis, % apoptotic cells for each time point.
See also Table S1 and Figure S5.

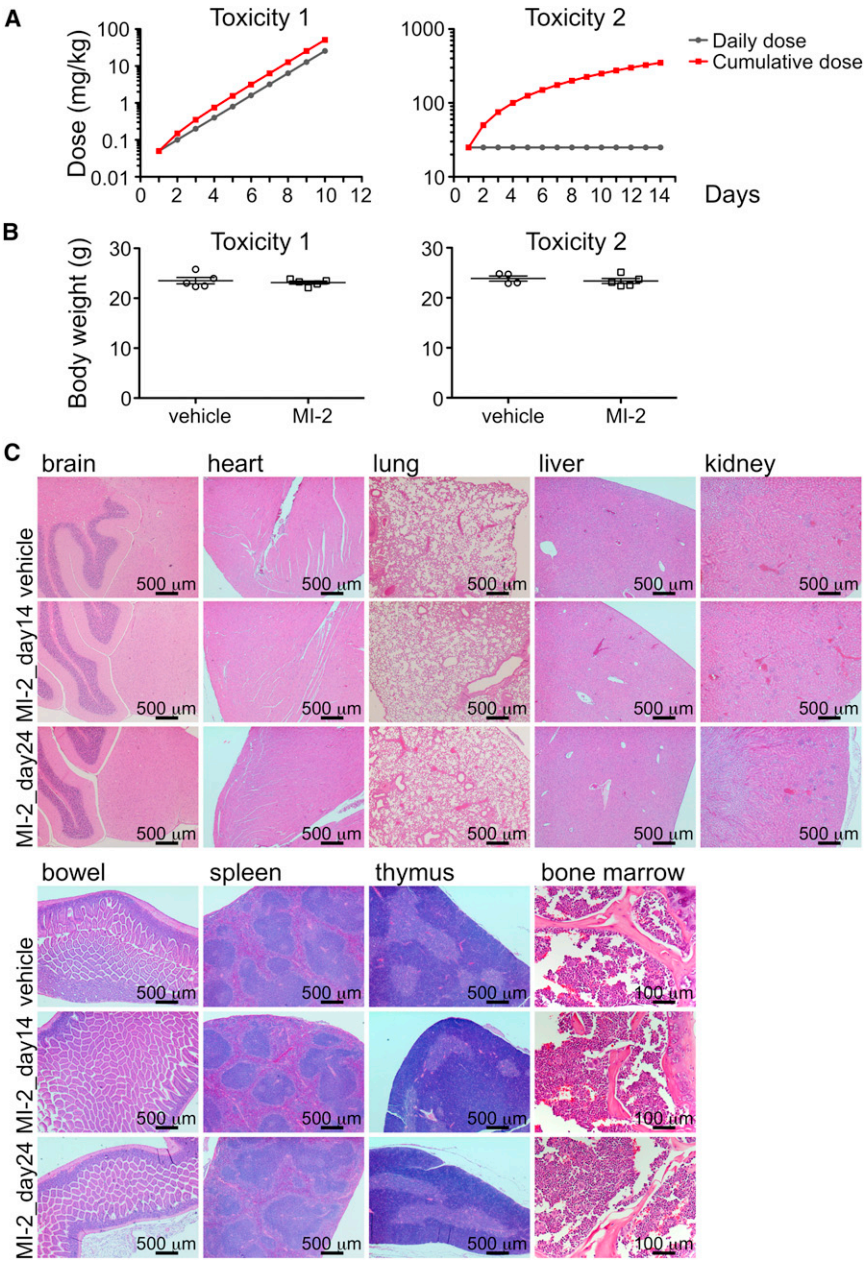

Figure 6. MI-2 Is Nontoxic to Animals

(A) Dose scheme for toxicity 1 (increasing daily dose) and toxicity 2 (same daily dose) experiments show daily and cumulative doses for each experiment.

(B) The y axis depicts mean ± SEM body weight of animals studied in both the incremental and cumulative dose schemes. Toxicity 1, $p = 0.59$ t test; toxicity 2, $p = 0.52$ t test.

(C) H&E staining for the indicated tissues in animals treated with vehicle, MI-2 25 mg/kg daily for 14 days, or MI-2 25 mg/kg daily for 14 days followed by a 10 day washout.

See also Table S2.

of MI-2 treatment on NF-κB signaling in xenografts, c-REL immunofluorescence was performed in paraffinized tumor sections. Consistent with data shown in Figures 4B and 4C, MI-2-treated tumors exhibited reduced c-REL nuclear protein (Figures 7D and S6C). Therefore, the MI-2 small-molecule MALT1 inhibitor specifically suppresses proliferation, survival, and NF-κB activity in ABC-DLBCLs in vivo in a lymphoma cell-autonomous manner.

Finally, to determine whether MI-2 could also suppress primary human DLBCLs, we obtained single-cell suspensions from lymph node biopsies of five DLBCL patients for whom their GCB versus non-GCB status could be ascertained by immunohistochemistry using the Hans criteria (Hans et al., 2004), as a surrogate for GCB versus ABC classification. Lymphoma cells were isolated and exposed to 0.8 μM MI-2 or vehicle in four replicates. After 48 hr exposure, cell number and viability were determined using trypan blue. Notably, two of the non-GCB cases responded to MI-2 ($p = 0.04$ and 0.003 versus vehicle), whereas none of the GCBs did (Figure 7E). One of the non-GCB cases did not respond to MI-2; perhaps this case was not accurately classified by Hans's criteria. Overall, these studies indicate that therapeutic targeting of MALT1 using the MI-2 small-molecule inhibitor has powerful suppressive effects on human ABC-DLBCL cells and warrants translation for use in clinical trials.

DISCUSSION

CBM complex signaling is constitutively active in a subset of ABC-DLBCLs due to somatic mutations of various genes leading to constitutive MALT1 signaling and NF-κB activation (Davis et al., 2010). The catalytic activity of MALT1 is well defined and involves substrate features such as peptide length and amino acid composition and position (Hachmann et al., 2012). Purified MALT1 is not very active in solution, because it is present as a monomer instead of its active dimeric form. Dimerization can be induced by high-salt concentrations, 1 M sodium citrate (Boatright et al., 2003). However, these high-salt conditions are nonphysiological and unsuitable for screening physiologically relevant small-molecule inhibitors. Use of a constitutively dimeric form of MALT1 enabled us to screen and identify potential inhibitors. Among these, MI-2 was found to be a potent, selective, and irreversible MALT1 inhibitor, analogous to protease inhibitor drugs such as telaprevir against the NS3/4A protease of hepatitis C virus (Klibanov et al., 2011), the proteasome inhibitor carfilzomib (Genin et al., 2010), and others (Powers et al., 2002). Although the peptide inhibitor Z-VRPR-FMK has been useful as a research tool, it is not suitable as a MALT1 therapeutic agent given its relatively large size, charge,

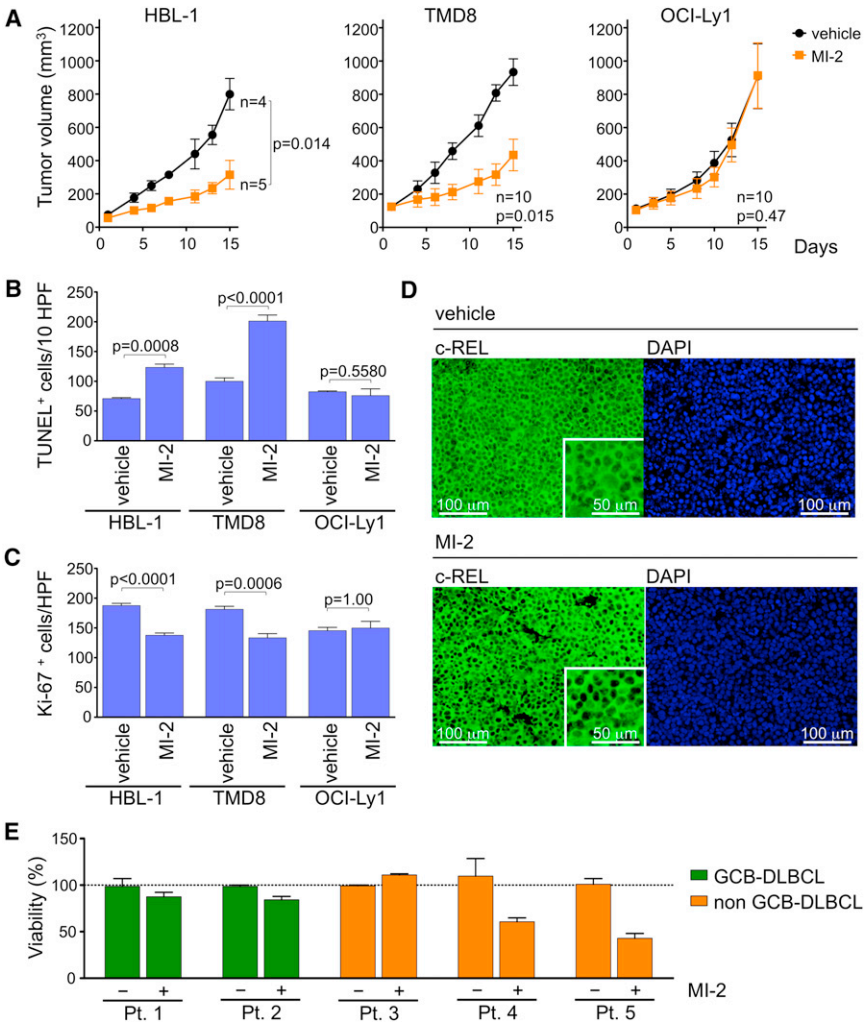

Figure 7. MI-2 Suppresses ABC-DLBCLs In Vivo and Primary Human DLBCL Ex Vivo

(A) Tumor growth curve for HBL-1, TMD8, and OCI-Ly1 xenografts in NOD-SCID mice treated with 25 mg/kg/day MI-2 or the same volume of vehicle for 14 consecutive days. Statistics, paired t test.

(B) TUNEL$^+$ staining in histologic sections of HBL-1, TMD8, and OCI-Ly1 xenografts. The y axis represents the number of TUNEL$^+$ cells per ten high-power fields (HPFs; n = 5 tumors/treatment, n = 3 for HBL-1). Statistics, t test.

(C) Ki-67 immunohistochemistry staining of xenografted HBL-1, TMD8, and OCI-Ly1 tumor sections. The y axis represents Ki-67$^+$ cells per high-power field (5 HPFs/tumor for n = 5 where analyzed for each treatment, n = 3 for HBL-1). Statistics, t test.

(D) Immunohistochemical detection of c-REL in sections from HBL-1 xenografts exposed to MI-2 or vehicle. Insets are 2× digital amplification. Representative image of three HPFs analyzed for n = 3 tumors stained for each treatment.

(E) Viability assays were performed in quadruplicate in primary human DLBCL patient samples treated for 48 hr with 0.8 μM MI-2 or vehicle. The y axis represents % of viable cells normalized to vehicle. Data are presented as mean ± SEM for all panels.

See also Figure S6.

and consequent lower cell permeability. Accordingly, MI-2 displayed superior activity in cell-based assays with excellent cell penetration and indeed featured high concentration within cells, and yet was still highly selective for MALT1 versus other caspases. Notably, a selective and irreversible small-molecule inhibitor of the tyrosine kinase BTK, PCI-32765 (ibrutinib), is currently under clinical development in patients with B cell non-Hodgkin's lymphoma (Honigberg et al., 2010). Irreversibility of MI-2 may provide pharmacokinetic advantages. As ABC-DLBCLs have chronically active BCR signaling, prolonged suppression of MALT1 cleavage would likely be necessary for maximal antilymphoma activity. Using an irreversible inhibitor, activity will only return when new enzyme is synthesized. This may allow drugs to be effective at a lower plasma concentration, thus reducing dosing level and frequency, limiting the requirement for a long plasma half-life without compromising efficacy, and minimizing potential toxic effects related to prolonged exposure to circulating drugs. Indeed, our detailed studies indicated that MI-2 was nontoxic in animals. This result is consistent with the fact that MALT1 is the only paracaspase in humans and that MALT1-deficient mice are relatively healthy (Ruefli-Brasse et al., 2003; Ruland et al., 2003).

Chronic activation of the BCR pathway in ABC-DLBCL is mediated by several different mechanisms, many of them upstream of MALT1. ABC-DLBCL is addicted to this pathway and is often specifically addicted to MALT1 cleavage activity (Ferch et al., 2009; Hailfinger et al., 2009; Ngo et al., 2006). Notably, MI-2 selectively killed ABC-DLBCL cell lines with CD79A/B, CARMA1, and/or MYD88 mutations but not those occurring in proteins downstream of MALT1, including those with A20 homozygous deletion or TAK1 mutation. These findings underline the importance of targeted resequencing of recurrently mutated alleles in lymphoma for the rational deployment of targeted therapeutics. Although the full spectrum of lymphomas that can be targeted with MALT1 inhibitors is not fully clear yet, using an ex vivo system we were able to show that primary human non-GCB-DLBCL specimens are also addicted to MALT1 and are suppressed by MI-2.

As single agents are generally not curative and rapidly generate resistance (Misale et al., 2012), there is a growing interest in combinatorial-targeted therapy. Rational combination of MALT1 cleavage inhibition could include a combination with tyrosine kinase inhibitors targeting the Src family (dasatinib, saracatinib, bosutinib, and KX01), SYK (fostamatinib disodium), or BTK (PCI-32765). These drugs would likely synergize with MALT1 cleavage inhibition of NF-κB by further inhibiting BCR signaling, including mitogen-activated protein kinases and phosphatidylinositol 3-kinase (Lim et al., 2012). Protein kinase C (PKC) inhibition would also be a potentially beneficial

combination, as it could further inhibit the NF-κB pathway, including those activities dependent on MALT1 but independent of its proteolytic activity. The PKC inhibitor sotrastaurin, in clinical trials for prevention of transplantation rejection and treatment of psoriasis (Manicassamy, 2009; Matz et al., 2011), has been recently shown to inhibit growth of ABC-DLBCL xenografted tumors (Naylor et al., 2011), pointing to its potential use as an antilymphoma therapy for this lymphoma subtype. ABC-DLBCLs also feature BCL6 translocation, SPI-B amplification, or PRDM1 deletion or mutation (Lenz and Staudt, 2010). BCL6 inhibitors promote apoptosis and cell-cycle arrest through release of critical checkpoint genes (Cerchietti et al., 2009, 2010a; Polo et al., 2004). Combination of MI-2 and BCL6 inhibitors would thus suppress two critical pathways in ABC-DLBCLs (BCL6 and NF-κB), potentially leading to therapeutic synergy. Taken together, the results reported here identify MI-2 as a lead compound targeting MALT1 and demonstrate the significance, safety, and efficacy of MALT1 as a therapeutic target and MI-2 as a therapeutic agent for the treatment of aggressive non-Hodgkin's lymphomas that are both dependent on NF-κB signals and resistant to conventional chemotherapeutic regimens.

EXPERIMENTAL PROCEDURES

Detailed experimental procedures are presented in Supplemental Experimental Procedures.

High-Throughput Screening for MALT1 Proteolytic Activity Inhibitors

Ac-LRSR-AMC was used as substrate and reactions were measured with excitation/emission wavelengths of 360/465 nm. Two time points were measured for each reaction to eliminate false positives due to compound autofluorescence. The final percent inhibition was calculated with the formula $\{[\text{fluorescence}_{\text{test compound (T2}-\text{T1)}} - \text{fluorescence}_{\text{neg ctrl (T2}-\text{T1)}}]/[\text{fluorescence}_{\text{pos ctrl (T2}-\text{T1)}} - \text{fluorescence}_{\text{neg ctrl (T2}-\text{T1)}}]\} \times 100$, where Z-VRPR-FMK (300 nM) was used as positive control and buffer only as negative control. The positive hits were validated in concentration-response experiments within a dose range of 0.122–62.5 μM to determine IC_{50} of the compounds. Activity was validated using recombinant full-length wild-type MALT1.

Growth-Inhibition Determination

Cell proliferation was determined by ATP quantification using a luminescent method (CellTiter-Glo; Promega) and trypan blue dye exclusion. Standard curves for each cell line were calculated by plotting the cell number (determined using trypan blue) against their luminescence values, and cell number was calculated accordingly. Cell viability in drug-treated cells was normalized to their respective controls (fractional viability), and results are given as 1-fractional viability. CompuSyn software (Biosoft) was used to determine GI_{25} and GI_{50} values.

Mouse Xenograft Experiments

Eight-week-old male SCID NOD.CB17-Prkdc^{scid}/J mice were purchased from Jackson Laboratories and housed in a clean environment. Mice were subcutaneously injected with low-passage 10^7 human HBL-1, TMD8, or OCI-Ly1 cells in 50% Matrigel. Treatment was initiated when tumors reached an average size of 120 mm^3. MI-2 was reconstituted in DMSO and stored at −80°C until used and was administered by intraperitoneal injection. Tumor volume was monitored by digital calipering three times a week and calculated using the formula (smallest diameter^2 × largest diameter)/2. All procedures involving animals followed National Institutes of Health protocols and were approved by the Animal Institute Committee of the Weill Cornell Medical College of Cornell University.

Primary Cells

Patient-deidentified tissues were obtained in accordance with the guidelines and approval of the University of Navarra Institutional and Weill Cornell Medical College Review Boards. Only discarded leftover tissue after diagnosis was rendered was utilized for research, in agreement with institutional review board protocol. Patient samples were processed as previously described (Cerchietti et al., 2010b). Briefly, single-cell suspensions from lymph node biopsies were obtained by physical disruption of tissues followed by cell-density gradient separation. Cell number and viability were determined by trypan blue exclusion. Primary DLBCL cells were cultured in 96-well plates. Cells were grown in RPMI medium with 20% FBS supplemented with antibiotics for 48 hr. Cells were exposed to 0.8 μM MI-2 (1 μM for Pt.2) or control (DMSO) in quadruplicate. After 48 hr of exposure, viability was determined by using trypan blue (Sigma). All samples were normalized to their own replicate control.

ACCESSION NUMBERS

The Gene Expression Omnibus accession number for the expression microarray data reported in this paper is GSE40003.

SUPPLEMENTAL INFORMATION

Supplemental Information includes six figures, two tables, and Supplemental Experimental Procedures and can be found with this article online at http://dx.doi.org/10.1016/j.ccr.2012.11.003.

ACKNOWLEDGMENTS

We thank Paulus Erbel, Martin Renatus, and Nicola Hughes (Novartis Institutes for BioMedical Research, Basel, Switzerland) for mass spectrometry, NMR experiments, and advice; Beatriz Bellosillo (H. del Mar, Barcelona, Spain) and Miguel A. Piris (Hospital Marques de Valdecillas, Santander, Spain) for providing lymphoma samples; and Ermelinda Damko, Liwei Wang, Qi Qiao, and Jennifer Ishii for technical assistance. L.F. is supported by the Spanish Ministry of Science Fellowship "Sara Borrell." C.Y. was supported by the Irvington Institute Postdoctoral Fellowship Program of the Cancer Research Institute. H.W. and A.M. are supported by Leukemia and Lymphoma Society Translational Research Program 6210-12. A.M. is a Burroughs Wellcome Clinical Translational Scientist and is supported by the Chemotherapy Foundation and the Beverly and Raymond Sackler Center for Physical and Biomedical Sciences.

Received: August 8, 2012
Revised: October 26, 2012
Accepted: November 12, 2012
Published: December 10, 2012

REFERENCES

Alizadeh, A.A., Eisen, M.B., Davis, R.E., Ma, C., Lossos, I.S., Rosenwald, A., Boldrick, J.C., Sabet, H., Tran, T., Yu, X., et al. (2000). Distinct types of diffuse large B-cell lymphoma identified by gene expression profiling. Nature *403*, 503–511.

Boatright, K.M., Renatus, M., Scott, F.L., Sperandio, S., Shin, H., Pedersen, I.M., Ricci, J.E., Edris, W.A., Sutherlin, D.P., Green, D.R., and Salvesen, G.S. (2003). A unified model for apical caspase activation. Mol. Cell *11*, 529–541.

Cerchietti, L.C., Yang, S.N., Shaknovich, R., Hatzi, K., Polo, J.M., Chadburn, A., Dowdy, S.F., and Melnick, A. (2009). A peptomimetic inhibitor of BCL6 with potent antilymphoma effects in vitro and in vivo. Blood *113*, 3397–3405.

Cerchietti, L.C., Ghetu, A.F., Zhu, X., Da Silva, G.F., Zhong, S., Matthews, M., Bunting, K.L., Polo, J.M., Farès, C., Arrowsmith, C.H., et al. (2010a). A small-molecule inhibitor of BCL6 kills DLBCL cells in vitro and in vivo. Cancer Cell *17*, 400–411.

Cerchietti, L.C., Hatzi, K., Caldas-Lopes, E., Yang, S.N., Figueroa, M.E., Morin, R.D., Hirst, M., Mendez, L., Shaknovich, R., Cole, P.A., et al. (2010b). BCL6

repression of EP300 in human diffuse large B cell lymphoma cells provides a basis for rational combinatorial therapy. J. Clin. Invest. *120*, 4569–4582.

Compagno, M., Lim, W.K., Grunn, A., Nandula, S.V., Brahmachary, M., Shen, Q., Bertoni, F., Ponzoni, M., Scandurra, M., Califano, A., et al. (2009). Mutations of multiple genes cause deregulation of NF-κB in diffuse large B-cell lymphoma. Nature *459*, 717–721.

Coornaert, B., Baens, M., Heyninck, K., Bekaert, T., Haegman, M., Staal, J., Sun, L., Chen, Z.J., Marynen, P., and Beyaert, R. (2008). T cell antigen receptor stimulation induces MALT1 paracaspase-mediated cleavage of the NF-κB inhibitor A20. Nat. Immunol. *9*, 263–271.

Davis, R.E., Ngo, V.N., Lenz, G., Tolar, P., Young, R.M., Romesser, P.B., Kohlhammer, H., Lamy, L., Zhao, H., Yang, Y., et al. (2010). Chronic active B-cell-receptor signalling in diffuse large B-cell lymphoma. Nature *463*, 88–92.

Dierlamm, J., Baens, M., Wlodarska, I., Stefanova-Ouzounova, M., Hernandez, J.M., Hossfeld, D.K., De Wolf-Peeters, C., Hagemeijer, A., Van den Berghe, H., and Marynen, P. (1999). The apoptosis inhibitor gene API2 and a novel 18q gene, MLT, are recurrently rearranged in the t(11;18)(q21;q21) associated with mucosa-associated lymphoid tissue lymphomas. Blood *93*, 3601–3609.

Dierlamm, J., Murga Penas, E.M., Bentink, S., Wessendorf, S., Berger, H., Hummel, M., Klapper, W., Lenze, D., Rosenwald, A., Haralambieva, E., et al.; Deutsche Krebshilfe Network Project "Molecular Mechanisms in Malignant Lymphomas". (2008). Gain of chromosome region 18q21 including the MALT1 gene is associated with the activated B-cell-like gene expression subtype and increased BCL2 gene dosage and protein expression in diffuse large B-cell lymphoma. Haematologica *93*, 688–696.

Farinha, P., and Gascoyne, R.D. (2005). Molecular pathogenesis of mucosa-associated lymphoid tissue lymphoma. J. Clin. Oncol. *23*, 6370–6378.

Ferch, U., zum Büschenfelde, C.M., Gewies, A., Wegener, E., Rauser, S., Peschel, C., Krappmann, D., and Ruland, J. (2007). MALT1 directs B cell receptor-induced canonical nuclear factor-κB signaling selectively to the c-Rel subunit. Nat. Immunol. *8*, 984–991.

Ferch, U., Kloo, B., Gewies, A., Pfänder, V., Düwel, M., Peschel, C., Krappmann, D., and Ruland, J. (2009). Inhibition of MALT1 protease activity is selectively toxic for activated B cell-like diffuse large B cell lymphoma cells. J. Exp. Med. *206*, 2313–2320.

Genin, E., Reboud-Ravaux, M., and Vidal, J. (2010). Proteasome inhibitors: recent advances and new perspectives in medicinal chemistry. Curr. Top. Med. Chem. *10*, 232–256.

Gross, O., Grupp, C., Steinberg, C., Zimmermann, S., Strasser, D., Hannesschläger, N., Reindl, W., Jonsson, H., Huo, H., Littman, D.R., et al. (2008). Multiple ITAM-coupled NK-cell receptors engage the Bcl10/Malt1 complex via Carma1 for NF-κB and MAPK activation to selectively control cytokine production. Blood *112*, 2421–2428.

Hachmann, J., Snipas, S.J., van Raam, B.J., Cancino, E.M., Houlihan, E.J., Poreba, M., Kasperkiewicz, P., Drag, M., and Salvesen, G.S. (2012). Mechanism and specificity of the human paracaspase MALT1. Biochem. J. *443*, 287–295.

Hailfinger, S., Lenz, G., Ngo, V., Posvitz-Fejfar, A., Rebeaud, F., Guzzardi, M., Penas, E.M., Dierlamm, J., Chan, W.C., Staudt, L.M., and Thome, M. (2009). Essential role of MALT1 protease activity in activated B cell-like diffuse large B-cell lymphoma. Proc. Natl. Acad. Sci. USA *106*, 19946–19951.

Hailfinger, S., Nogai, H., Pelzer, C., Jaworski, M., Cabalzar, K., Charton, J.E., Guzzardi, M., Décaillet, C., Grau, M., Dörken, B., et al. (2011). Malt1-dependent RelB cleavage promotes canonical NF-κB activation in lymphocytes and lymphoma cell lines. Proc. Natl. Acad. Sci. USA *108*, 14596–14601.

Hans, C.P., Weisenburger, D.D., Greiner, T.C., Gascoyne, R.D., Delabie, J., Ott, G., Müller-Hermelink, H.K., Campo, E., Braziel, R.M., Jaffe, E.S., et al. (2004). Confirmation of the molecular classification of diffuse large B-cell lymphoma by immunohistochemistry using a tissue microarray. Blood *103*, 275–282.

Honigberg, L.A., Smith, A.M., Sirisawad, M., Verner, E., Loury, D., Chang, B., Li, S., Pan, Z., Thamm, D.H., Miller, R.A., and Buggy, J.J. (2010). The Bruton tyrosine kinase inhibitor PCI-32765 blocks B-cell activation and is efficacious in models of autoimmune disease and B-cell malignancy. Proc. Natl. Acad. Sci. USA *107*, 13075–13080.

Honma, K., Tsuzuki, S., Nakagawa, M., Tagawa, H., Nakamura, S., Morishima, Y., and Seto, M. (2009). TNFAIP3/A20 functions as a novel tumor suppressor gene in several subtypes of non-Hodgkin lymphomas. Blood *114*, 2467–2475.

Klibanov, O.M., Williams, S.H., Smith, L.S., Olin, J.L., and Vickery, S.B. (2011). Telaprevir: a novel NS3/4 protease inhibitor for the treatment of hepatitis C. Pharmacotherapy *31*, 951–974.

Lenz, G., and Staudt, L.M. (2010). Aggressive lymphomas. N. Engl. J. Med. *362*, 1417–1429.

Lenz, G., Davis, R.E., Ngo, V.N., Lam, L., George, T.C., Wright, G.W., Dave, S.S., Zhao, H., Xu, W., Rosenwald, A., et al. (2008a). Oncogenic CARD11 mutations in human diffuse large B cell lymphoma. Science *319*, 1676–1679.

Lenz, G., Wright, G.W., Emre, N.C., Kohlhammer, H., Dave, S.S., Davis, R.E., Carty, S., Lam, L.T., Shaffer, A.L., Xiao, W., et al. (2008b). Molecular subtypes of diffuse large B-cell lymphoma arise by distinct genetic pathways. Proc. Natl. Acad. Sci. USA *105*, 13520–13525.

Lim, K.H., Yang, Y., and Staudt, L.M. (2012). Pathogenetic importance and therapeutic implications of NF-κB in lymphoid malignancies. Immunol. Rev. *246*, 359–378.

Lucas, P.C., Yonezumi, M., Inohara, N., McAllister-Lucas, L.M., Abazeed, M.E., Chen, F.F., Yamaoka, S., Seto, M., and Nunez, G. (2001). Bcl10 and MALT1, independent targets of chromosomal translocation in MALT lymphoma, cooperate in a novel NF-κB signaling pathway. J. Biol. Chem. *276*, 19012–19019.

Manicassamy, S. (2009). Sotrastaurin, a protein kinase C inhibitor for the prevention of transplant rejection and treatment of psoriasis. Curr. Opin. Investig. Drugs *10*, 1225–1235.

Matz, M., Naik, M., Mashreghi, M.F., Glander, P., Neumayer, H.H., and Budde, K. (2011). Evaluation of the novel protein kinase C inhibitor sotrastaurin as immunosuppressive therapy after renal transplantation. Expert Opin. Drug Metab. Toxicol. *7*, 103–113.

Misale, S., Yaeger, R., Hobor, S., Scala, E., Janakiraman, M., Liska, D., Valtorta, E., Schiavo, R., Buscarino, M., Siravegna, G., et al. (2012). Emergence of KRAS mutations and acquired resistance to anti-EGFR therapy in colorectal cancer. Nature *486*, 532–536.

Morris, G.M., Huey, R., Lindstrom, W., Sanner, M.F., Belew, R.K., Goodsell, D.S., and Olson, A.J. (2009). AutoDock4 and AutoDockTools4: automated docking with selective receptor flexibility. J. Comput. Chem. *30*, 2785–2791.

Naylor, T.L., Tang, H., Ratsch, B.A., Enns, A., Loo, A., Chen, L., Lenz, P., Waters, N.J., Schuler, W., Dörken, B., et al. (2011). Protein kinase C inhibitor sotrastaurin selectively inhibits the growth of CD79 mutant diffuse large B-cell lymphomas. Cancer Res. *71*, 2643–2653.

Ngo, V.N., Davis, R.E., Lamy, L., Yu, X., Zhao, H., Lenz, G., Lam, L.T., Dave, S., Yang, L., Powell, J., and Staudt, L.M. (2006). A loss-of-function RNA interference screen for molecular targets in cancer. Nature *441*, 106–110.

Ngo, V.N., Young, R.M., Schmitz, R., Jhavar, S., Xiao, W., Lim, K.H., Kohlhammer, H., Xu, W., Yang, Y., Zhao, H., et al. (2011). Oncogenically active MYD88 mutations in human lymphoma. Nature *470*, 115–119.

Polo, J.M., Dell'Oso, T., Ranuncolo, S.M., Cerchietti, L., Beck, D., Da Silva, G.F., Prive, G.G., Licht, J.D., and Melnick, A. (2004). Specific peptide interference reveals BCL6 transcriptional and oncogenic mechanisms in B-cell lymphoma cells. Nat. Med. *10*, 1329–1335.

Pop, C., Timmer, J., Sperandio, S., and Salvesen, G.S. (2006). The apoptosome activates caspase-9 by dimerization. Mol. Cell *22*, 269–275.

Powers, J.C., Asgian, J.L., Ekici, O.D., and James, K.E. (2002). Irreversible inhibitors of serine, cysteine, and threonine proteases. Chem. Rev. *102*, 4639–4750.

Rebeaud, F., Hailfinger, S., Posevitz-Fejfar, A., Tapernoux, M., Moser, R., Rueda, D., Gaide, O., Guzzardi, M., Iancu, E.M., Rufer, N., et al. (2008). The proteolytic activity of the paracaspase MALT1 is key in T cell activation. Nat. Immunol. *9*, 272–281.

Rosenwald, A., Wright, G., Chan, W.C., Connors, J.M., Campo, E., Fisher, R.I., Gascoyne, R.D., Muller-Hermelink, H.K., Smeland, E.B., Giltnane, J.M., et al.; Lymphoma/Leukemia Molecular Profiling Project. (2002). The use of molecular

profiling to predict survival after chemotherapy for diffuse large-B-cell lymphoma. N. Engl. J. Med. *346*, 1937–1947.

Rosenwald, A., Wright, G., Leroy, K., Yu, X., Gaulard, P., Gascoyne, R.D., Chan, W.C., Zhao, T., Haioun, C., Greiner, T.C., et al. (2003). Molecular diagnosis of primary mediastinal B cell lymphoma identifies a clinically favorable subgroup of diffuse large B cell lymphoma related to Hodgkin lymphoma. J. Exp. Med. *198*, 851–862.

Ruefli-Brasse, A.A., French, D.M., and Dixit, V.M. (2003). Regulation of NF-κB-dependent lymphocyte activation and development by paracaspase. Science *302*, 1581–1584.

Ruland, J., Duncan, G.S., Wakeham, A., and Mak, T.W. (2003). Differential requirement for Malt1 in T and B cell antigen receptor signaling. Immunity *19*, 749–758.

Sanchez-Izquierdo, D., Buchonnet, G., Siebert, R., Gascoyne, R.D., Climent, J., Karran, L., Marin, M., Blesa, D., Horsman, D., Rosenwald, A., et al. (2003). MALT1 is deregulated by both chromosomal translocation and amplification in B-cell non-Hodgkin lymphoma. Blood *101*, 4539–4546.

Siegel, R., Naishadham, D., and Jemal, A. (2012). Cancer statistics, 2012. CA Cancer J. Clin. *62*, 10–29.

Staal, J., Driege, Y., Bekaert, T., Demeyer, A., Muyllaert, D., Van Damme, P., Gevaert, K., and Beyaert, R. (2011). T-cell receptor-induced JNK activation requires proteolytic inactivation of CYLD by MALT1. EMBO J. *30*, 1742–1752.

Streubel, B., Lamprecht, A., Dierlamm, J., Cerroni, L., Stolte, M., Ott, G., Raderer, M., and Chott, A. (2003). T(14;18)(q32;q21) involving IGH and MALT1 is a frequent chromosomal aberration in MALT lymphoma. Blood *101*, 2335–2339.

Swerdlow, S.H., Campo, E., Harris, N.L., Jaffe, E.S., Pileri, S.A., Stein, H., Thiele, J., and Vardiman, J.W. (2008). World Health Organization Classification of Tumours of Haematopoietic and Lymphoid Tissues (Lyon: IARC Press).

Vicente-Dueñas, C., Fontán, L., Gonzalez-Herrero, I., Romero-Camarero, I., Segura, V., Aznar, M.A., Alonso-Escudero, E., Campos-Sanchez, E., Ruiz-Roca, L., Barajas-Diego, M., et al. (2012). Expression of MALT1 oncogene in hematopoietic stem/progenitor cells recapitulates the pathogenesis of human lymphoma in mice. Proc. Natl. Acad. Sci. USA *109*, 10534–10539.

Walker, N.P., Talanian, R.V., Brady, K.D., Dang, L.C., Bump, N.J., Ferenz, C.R., Franklin, S., Ghayur, T., Hackett, M.C., Hammill, L.D., et al. (1994). Crystal structure of the cysteine protease interleukin-1β-converting enzyme: a (p20/p10)2 homodimer. Cell *78*, 343–352.

Wiesmann, C., Leder, L., Blank, J., Bernardi, A., Melkko, S., Decock, A., D'Arcy, A., Villard, F., Erbel, P., Hughes, N., et al. (2012). Structural determinants of MALT1 protease activity. J. Mol. Biol. *419*, 4–21.

Wright, G., Tan, B., Rosenwald, A., Hurt, E.H., Wiestner, A., and Staudt, L.M. (2003). A gene expression-based method to diagnose clinically distinct subgroups of diffuse large B cell lymphoma. Proc. Natl. Acad. Sci. USA *100*, 9991–9996.

Yin, Q., Park, H.H., Chung, J.Y., Lin, S.C., Lo, Y.C., da Graca, L.S., Jiang, X., and Wu, H. (2006). Caspase-9 holoenzyme is a specific and optimal procaspase-3 processing machine. Mol. Cell *22*, 259–268.

Yu, J.W., Jeffrey, P.D., Ha, J.Y., Yang, X., and Shi, Y. (2011). Crystal structure of the mucosa-associated lymphoid tissue lymphoma translocation 1 (MALT1) paracaspase region. Proc. Natl. Acad. Sci. USA *108*, 21004–21009.

Zhang, J.H., Chung, T.D., and Oldenburg, K.R. (1999). A simple statistical parameter for use in evaluation and validation of high throughput screening assays. J. Biomol. Screen. *4*, 67–73.

Cancer Cell
Article

The EphA2 Receptor Drives Self-Renewal and Tumorigenicity in Stem-like Tumor-Propagating Cells from Human Glioblastomas

Elena Binda,[1,*] Alberto Visioli,[1] Fabrizio Giani,[1] Giuseppe Lamorte,[2] Massimiliano Copetti,[3] Ken L. Pitter,[4] Jason T. Huse,[5] Laura Cajola,[6] Nadia Zanetti,[6] Francesco DiMeco,[7,8] Lidia De Filippis,[1] Annunziato Mangiola,[9] Giulio Maira,[9] Carmelo Anile,[9] Pasquale De Bonis,[9] Brent A. Reynolds,[10] Elena B. Pasquale,[11] and Angelo L. Vescovi[1,3,6,*]
[1]Department of Biotechnology and Biosciences, University of Milan Bicocca, 20126 Milan, Italy
[2]IRCSS Casa Sollievo della Sofferenza, c/o Istituto Mendel, 00198 Rome, Italy
[3]IRCSS Casa Sollievo della Sofferenza, Opera di San Pio da Pietralcina, 71013 S. Giovanni Rotondo (FG), Italy
[4]Weill Cornell Graduate School of Medical Sciences, New York, NY 10065, USA
[5]Department of Pathology, Memorial Sloan-Kettering Cancer Center, New York, NY 10065, USA
[6]StemGen SpA, 20126 Milan, Italy
[7]National Neurological Institute "C. Besta", 20133 Milan, Italy
[8]Department of Neurosurgery, John Hopkins University, Baltimore, MD 21287, USA
[9]Institute of Neurosurgery, Catholic University of the Sacred Heart, 00168 Rome, Italy
[10]Evelyn F. and William L. McKnight Brain Institute, Program in Stem Cell Biology and Regenerative Medicine, The University of Florida, Ganesville, FL 32610-0015, USA
[11]Sanford-Burnham Medical Research Institute, La Jolla, CA 92037, USA
*Correspondence: elena.binda@unimib.it (E.B.), vescovi@tin.it (A.L.V.)
http://dx.doi.org/10.1016/j.ccr.2012.11.005

SUMMARY

In human glioblastomas (hGBMs), tumor-propagating cells with stem-like characteristics (TPCs) represent a key therapeutic target. We found that the EphA2 receptor tyrosine kinase is overexpressed in hGBM TPCs. Cytofluorimetric sorting into EphA2^{High} and EphA2^{Low} populations demonstrated that EphA2 expression correlates with the size and tumor-propagating ability of the TPC pool in hGBMs. Both ephrinA1-Fc, which caused EphA2 downregulation in TPCs, and siRNA-mediated knockdown of *EPHA2* expression suppressed TPCs self-renewal ex vivo and intracranial tumorigenicity, pointing to EphA2 downregulation as a causal event in the loss of TPCs tumorigenicity. Infusion of ephrinA1-Fc into intracranial xenografts elicited strong tumor-suppressing effects, suggestive of therapeutic applications.

INTRODUCTION

Human glioblastoma multiforme (hGBM) is the most malignant among gliomas. Because of their very heterogeneous cellular, genetic, epigenetic, and molecular make-up (Maher et al., 2001), hGBMs have a dismal prognosis and almost inevitably recur (Krex et al., 2007; Chen et al., 2012).

Recent findings have demonstrated the existence of a subpopulation of hGBM cells, called cancer stem cells, whose idiosyncratic properties make them resilient to standard therapies. First identified in acute myeloid leukemia (Bonnet and Dick, 1997), cancer stem cells, better defined as tumor-propagating cells (TPCs; Kelly et al., 2007), have been isolated from a variety of solid tumors (Ponti et al., 2005; Ricci-Vitiani et al., 2009; Buzzeo et al., 2007). TPCs with both stem cell characteristics and tumor-initiation and propagation ability have now emerged as key players in hGBM pathogenesis (Hadjipanayis and Van Meir, 2009; Galli et al., 2004).

Significance

Identification and characterization of key regulatory mechanisms in TPCs are crucial for the development of specific therapies for hGBMs. We show that TPCs overexpress EphA2 in hGBMs, which underpins their inherent ability to maintain an undifferentiated state, supporting their self-renewal and tumorigenicity. EphA2 abundance provides a measure of the stem-like potential and tumor-propagating ability of TPCs from hGBMs. Thus, high EphA2 levels can be used to enrich TPCs by cell sorting. EphrinA1-Fc ligand-induced downregulation or siRNA-mediated knockdown of *EPHA2* expression both cause loss of self-renewal as well as induce differentiation and loss of tumor-initiating capacity in hGBM TPCs. Sustained intracranial infusion of ephrinA1-Fc under settings that resemble putative therapeutic conditions elicits effective antitumorigenic activity.

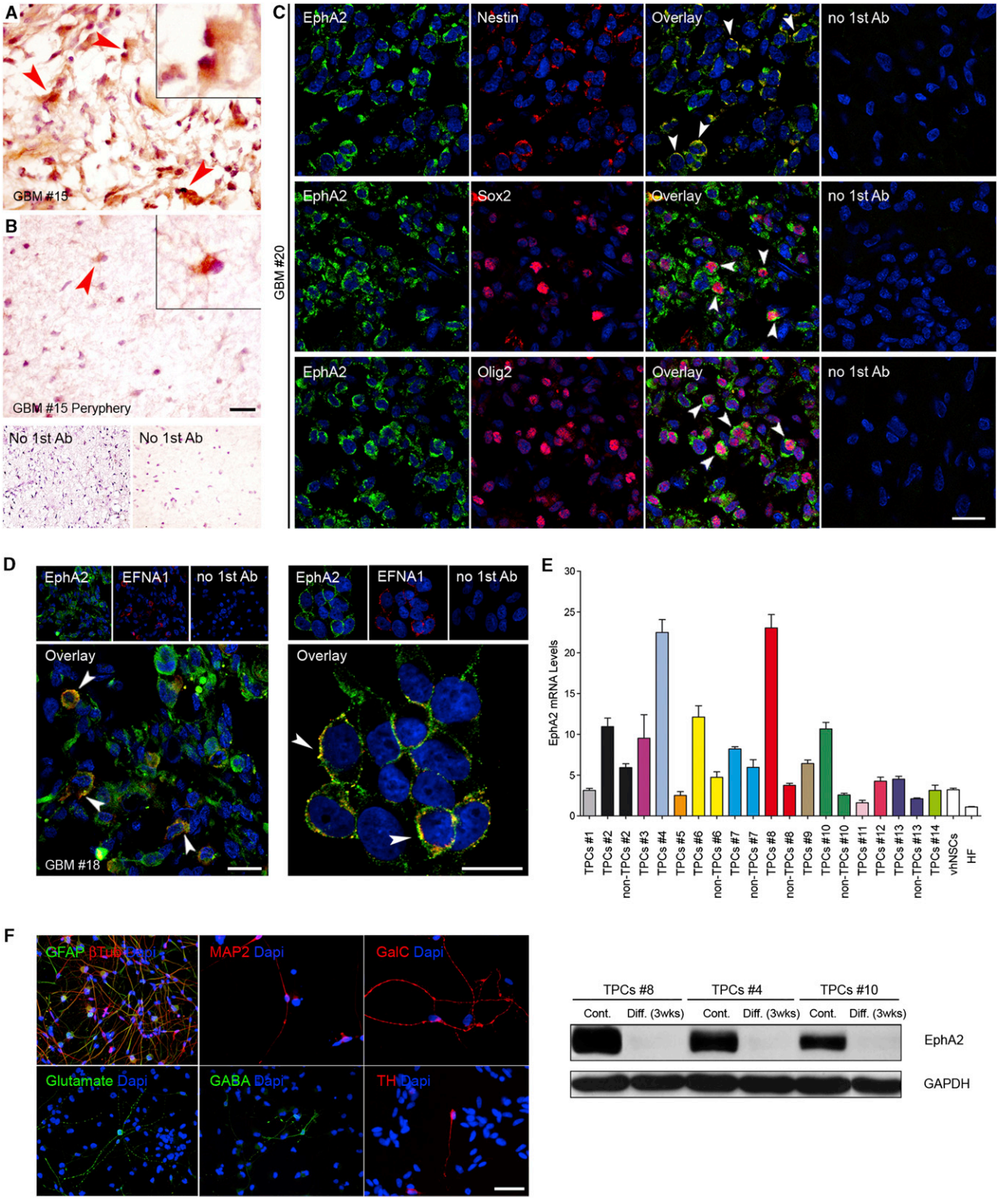

Figure 1. The EphA2 Receptor in Human Glioblastoma Tissues and TPCs

(A and B) Example of strong and frequent EphA2 immunoreactivity (brown) in the tumor core (A, arrows) as compared to infrequent, weaker labeling in the periphery (B) of the same hGBM specimen (six hGBMs yielded similar results). Insets: higher magnification. Bottom: no primary antibody. Blue, hematoxylin counterstain. Scale bar, 20 μm. See also Figures S1A–S1C.

While the origin and nature of hGBM TPCs remain to be unraveled, alterations of G1 arrest regulatory pathways in Nestin- or GFAP-positive cells can cause the onset of high-grade gliomas (Alcantara Llaguno et al., 2011). Thus, hGBM TPCs might derive from the transformation of neural stem cells or their transit amplifying precursor progeny (Alcantara Llaguno et al., 2009; Vescovi et al., 2006). Oligodendroglial precursors might also be the cell of origin in some hGBMs (Sukhdeo et al., 2011). The peculiar characteristics of TPCs encompass a relative quiescent nature, unlimited self-renewal, the clonal capacity to found a tumor (Galli et al., 2004), and resistance to conventional and multimodal treatments (Bao et al., 2006).

Owing to their stem-like nature, TPCs might be regulated by the same cues that control the activity of normal neural precursors and stem cells (NSCs). In fact, pathways that impinge on self-renewal and cell fate in normal NSCs are also active in brain tumors (Alcantara Llaguno et al., 2011; Dell'Albani, 2008). Also, therapeutic agents targeting Wnt, Hedgehog, or Notch deplete the TPC population in hGBMs (Takebe et al., 2011), and tumor suppressor genes can regulate TPC self-renewal (Zheng et al., 2008). The connection of TPCs with NSCs is reinforced by the discovery that critical effectors of NSC activity in the brain stem cell niche, such as bone morphogenetic proteins, suppress the growth of hGBM TPCs, enforcing their differentiation into astroglia (Lee et al., 2008; Piccirillo et al., 2006; Zhang et al., 2006). Another key regulator in the adult NSC niche, nitric oxide, can also drive TPC proliferation in hGBMs (Eyler et al., 2011).

Eph receptor tyrosine kinases and their ephrin ligands influence central nervous system development, stem cell niches, and cancer cells (Goldshmit et al., 2006; Genander and Frisén, 2010; Pasquale, 2010). Deregulation of the Eph receptor/ephrin system is associated with acquisition of tumorigenic properties, tumor growth, angiogenesis, and metastasis in human cancers. In particular, EphA2 receptor is overexpressed in many human epithelial malignancies and hGBMs, where it can promote proliferation and invasiveness through mechanisms that are not well understood and may be independent of ephrin ligand binding (Wykosky and Debinski, 2008; Miao et al., 2009; Pasquale, 2010; Gopal et al., 2011; Nakada et al., 2011; Miao and Wang, 2012). High EphA2 expression also correlates with tumor stage, progression, and patient survival (Wykosky et al., 2005; Liu et al., 2006; Wang et al., 2008; Miao et al., 2009; Li et al., 2010; Wu et al., 2011).

In this study, we investigated the putative regulatory role and function of the EphA2 receptor in TPCs from hGBMs.

RESULTS

High EphA2 Expression in hGBMs and Their TPCs

Analysis of hGBM surgery specimens showed high EphA2 mRNA expression as compared to other EphA and EphB receptors (Figure S1A available online). Real-time PCR (qPCR) revealed how EphA2 mRNA levels were up to 100-fold higher in hGBMs than in normal human brain tissue, as compared to a 10-fold upregulation in low-grade gliomas, epitheliomas, and primitive neuroectodermal tumors (Figure S1B).

Strong EphA2 immunoreactivity was found in many cells of the non-necrotic hGBM core (Figure 1A) versus a few positive cells in the tumor periphery (Figure 1B) and normal brain (Figure S1C). Accordingly, immunolabeling of hGBM tissues showed coexpression of EphA2 and antigens of normal and transformed neural precursors, namely Nestin, Sox2, and Olig2 (Fatoo et al., 2011; Ligon et al., 2007) (Figure 1C). In contrast, the signal for ephrinA1, an EphA2 preferred ligand (Wykosky et al., 2008; Miao et al., 2009), was variable in intensity and distribution in the hGBM core and undetectable in the periphery (Figure S1C).

We also found high EphA2 mRNA and protein levels in cells acutely dissociated from hGBMs or cultured as neurospheres and enriched for the putative TPC markers SSEA-1 or CD44 (Figures S1D–S1F). Analysis of hGBM TPCs confirmed this overexpression (Figure 1E), which was from 2- to 300-fold that of their original hGBM tissue (Figure S1G). EphA2 and ephrinA1 were detected in both hGBMs and their TPCs (Figure 1D). Notably, EphA2 was heavily downregulated when TPCs were differentiated, losing stemness and tumorigenicity (Piccirillo et al., 2006; Zhang et al., 2006) (Figure 1F), reinforcing a correlation between high EphA2 levels and the TPC state.

EphA2 mRNA levels in individual TPC neurosphere cultures also correlated with their specific growth kinetics (Figures S1H and S1I), i.e., with their self-renewal activity (Rietze and Reynolds, 2006), and with *EPHA2* gene copy number at the 1p36.12 locus ($p < 0.0001$) (Figures S1H and S1J).

Enriching for Cells with Enhanced Tumor-Propagating Ability Based on EphA2 Expression

To reinforce the correlation between EphA2 enhanced levels and the TPC state we FACS-sorted acutely isolated hGBM cells into two distinct pools, expressing either high ($EphA2^{High}$) or low ($EphA2^{Low}$) EphA2 levels, and then assessed their in vitro clonogenicity and intracranial tumorigenic capacity. As expected, the $EphA2^{High}$ fraction contained more clonogenic cells than the $EphA2^{Low}$ fraction (Figure 2A) and mice implanted with $EphA2^{High}$ cells showed a higher mortality (median survival 4 months) than those receiving $EphA2^{Low}$ cells (median survival 7 months) (Figure 2B). Limiting dilution intracranial transplantation using acutely dissociated $EphA2^{High}$ and $EphA2^{Low}$ cells (Figures S2A–S2C) confirmed that high EphA2 levels are a hallmark of TPCs and can be used for their enrichment. In addition, when primary hGBM cells were sorted based on their combined expression of EphA2 and the putative TPC antigen SSEA-1 (Figures 2C and 2D), intracranial tumorigenicity was significantly

(C) Immunolabeling of hGBM tissue shows that cells positive for the putative neural stem cell markers Nestin, Sox2, or Olig2 (red) coexpress (arrows) the EphA2 receptor (green; five hGBMs yielded similar results). Scale bar, 20 μm.
(D) Coexpression of EphA2 (green) and ephrinA1 (red) on the surface of cells in hGBM tissues (left) and TPC cultures (right). Arrows mark examples of coexpression (yellow). Scale bars, 10 μm.
(E) Higher EphA2 expression as detected by qPCR in cultured TPCs from the core (TPCs; n = 14 independent cultures) versus cells from the periphery of the same hGBM (non-TPCs; n = 6 independent cultures; Student's t test, p = 0.017). Controls: vhNSCs and human fibroblasts (HF). Error bars: SEM. See also Figures S1D–S1J.
(F) TPCs differentiated by mitogen starvation show upregulation of astroglial (GFAP), oligodendroglial (GalC), and neuronal (β-Tub, MAP2, tyrosine hydroxylase [TH], glutamate, and GABA) markers (left), while losing EphA2 expression (right). Scale bar, 20 μm

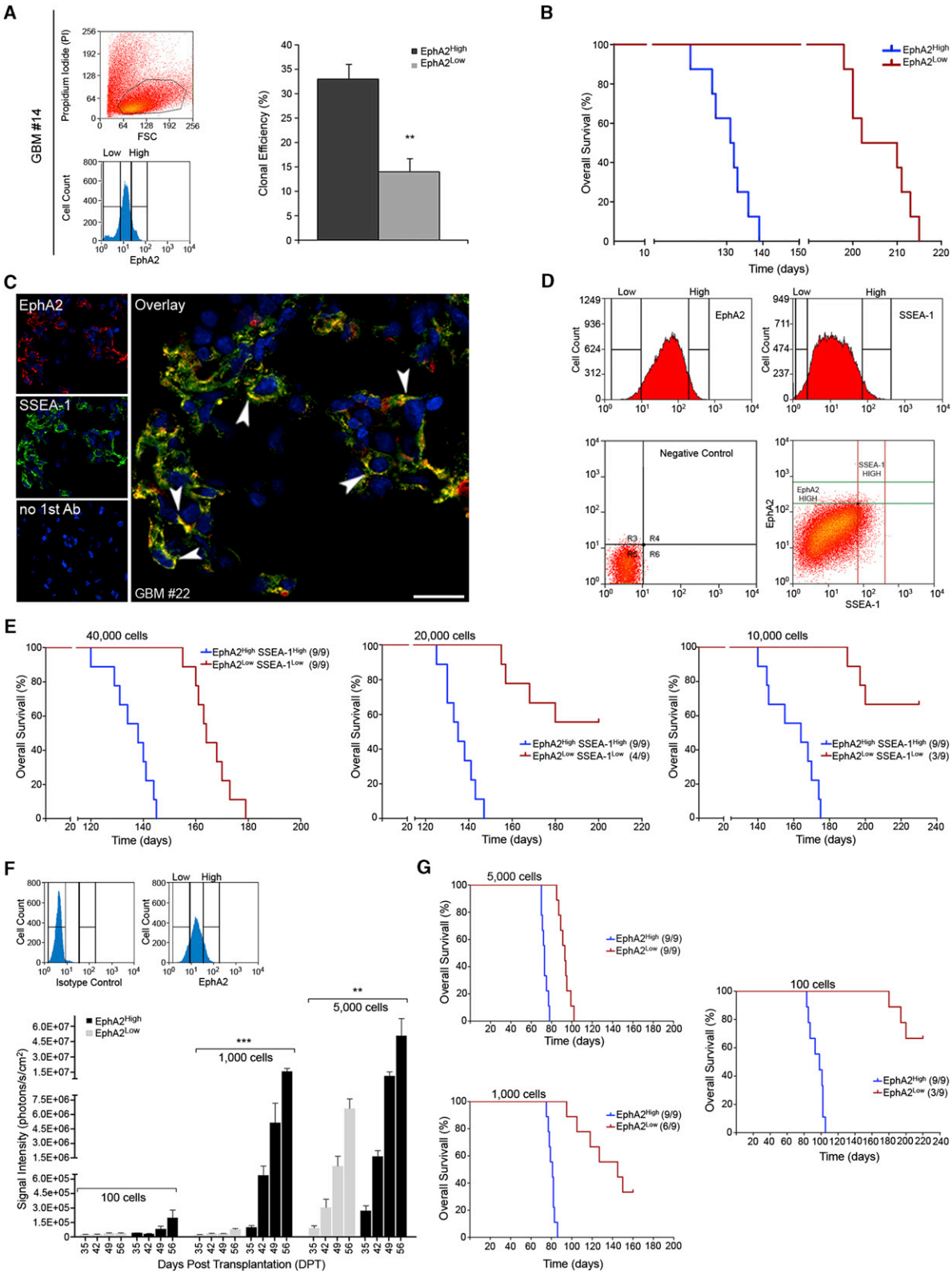

Figure 2. Enrichment of the Stem-like Tumorigenic Pool Based on EphA2 Levels

(A) Viable (propidium iodide negative) tumor cells acutely isolated from hGBM specimens (top left) were sorted into EphA2^{High} and EphA2^{Low} fractions (bottom left). The EphA2^{High} fraction displayed higher clonogenic index than the EphA2^{Low} fraction (right) (n = 4 tumors). Error bars: SEM; **p = 0.0004 for EphA2^{High} versus EphA2^{Low} by Student's t test.

higher in EphA2^{High} SSEA-1^{High} than in EphA2^{Low} SSEA-1^{Low} cells (Figure 2E). Similar results were obtained with EphA2^{High} CD44^{High} and EphA2^{Low} CD44^{Low} cells (Figures S2D–S2F). By applying the extreme limiting dilution analysis approach, we were able to show that the frequency of tumor-initiating cells (TICs) was always significantly higher in cell fractions with an increased EphA2 expression, alone or in combination with SSEA-1 or CD44 (Figure S2G). Finally, when EphA2^{High} and EphA2^{Low} cultured TPCs were assayed for intracranial tumorigenicity in a limiting dilution assay, as few as 100 EphA2^{High} cells established large gliomas in 60 days, as compared to a minimum requirement of 5,000 cells when using EphA2^{Low}, below which level tumorigenicity was negligible, even after 7 months (Figures 2F and 2G).

EphrinA1-Fc Downregulates EphA2 and Inhibits TPC Growth and Expression of Neural Stem Markers

Due to the emerging correlation between high EphA2 expression and TPC state, we used ephrinA1-Fc (a soluble ephrinA1 dimer fused to Fc) to downregulate EphA2 (Wykosky et al., 2005; Liu et al., 2007) and examined its effects on hGBM TPCs. A dose-dependent EphA2 downregulation ensued, which peaked at ephrinA1-Fc concentrations of 1–5 μg/ml, producing up to 90% receptor depletion (Figure S3A). EphrinA1-Fc induced a negligible EphA2 downregulation both in cells derived from the hGBM periphery (non-TPCs)—bearing stem-like features but negligible tumorigenicity (Piccirillo et al., 2009)—and v-myc-immortalized, non-transformed hNSCs (vhNSCs; De Filippis et al., 2007) (Figure 3A). Immunofluorescence assays confirmed EphA2 loss in both acutely isolated and cultured TPCs upon ephrinA1-Fc treatment (Figure 3B).

TPCs acutely isolated from hGBM specimens adhered to the dish when treated with ephrinA1-Fc, losing their capacity to grow and to generate stable TPC lines in the neurosphere assay (Figures 3C, 3D, and 3G), an effect also seen in 14 established TPC cultures (Figures 3E–3G, S3B, and S3C). In contrast, ephrinA1-Fc had negligible effects on non-TPCs (Figure 3H) and vhNSCs (Figure 3I). Hence, ephrinA1-Fc dowregulates EphA2 and hinders the expansive growth of cells that possess both stem cell characteristics and tumor-propagating ability.

EphrinA1-Fc Depletes the TPC Pool, Inhibits Self-Renewal, and Induces Astroglial Differentiation

The effects of ephrinA1-Fc suggested that it might inhibit the expansion of the TPC pool. This was emphasized by the ability of ephrinA1-Fc to downregulate both EphA2 and the neural precursor markers Nestin, Sox2, or Olig2 (Figure 3J) that are coexpressed in TPC spheroids. Also, FACS analysis showed loss of the putative TPC markers SSEA-1, CD44 and CD133 (Dell'Albani, 2008; Fatoo et al., 2011) (Figure S3D), but not of BMI-1 (Fatoo et al., 2011). Finally, ephrinA1-Fc depleted the TPC side population (SP), thought to comprise stem-like cells (Fukaya et al., 2010) (Figure S3E).

To confirm depletion of the TPC stem-like pool by ephrinA1-Fc, we measured self-renewal ability in a clonogenic assay, whereby single cells from acutely dissociated or from established TPC lines were plated in single wells by automated FACS and grown as neurospheres. EphrinA1-Fc drastically decreased clonogenicity in TPCs but not in non-TPCs, slightly increasing vhNSC clonogenicity (Figure 4A). Loss of self-renewal was not caused by changes in cell cycling (Figure 4B) or viability (Figure 4C). Notably, ephrinA1-Fc induced a marked, time-dependent upregulation of the astroglial antigen GFAP, without affecting the neuronal βIII tubulin and oligodendroglial GalC markers (Figure 4D). Thus, ephrinA1-Fc hinders self-renewal in TPCs in a non-cytotoxic way and increases astroglial differentiation.

Molecular Regulation of TPCs Stemness by EphA2

We studied the molecular events underlying the changes induced in hGBM TPCs by ephrinA1-Fc. EphrinA1-Fc transiently increased EphA2 tyrosine phosphorylation, in a dose-dependent manner, causing a strong and persistent downregulation of EphA2 expression (Figure 4E). We also observed marked ERK phosphorylation, which returned to basal levels after 24 hr, a moderate increases in Akt and FAK phosphorylation (Figure 4E, bottom panels), and reorganization of the actin cytoskeleton (Figures 4F–4J).

Altogether, this suggested that EphA2 expression sustains TPC self-renewal and that receptor loss played a causal role in the depletion of the hGBM stem-like pool. To prove this, we used a mixture of siRNAs to assess the effects of direct EphA2 downregulation (Figure 5A). *EPHA2* silencing caused changes consistent with loss of stemness and increased differentiation, ie, (1) loss of clonogenicity (Figure 5B) and amplification rate (Figure 5C), (2) downregulation of putative stem cell markers (Figure 5E), and (3) increased GFAP expression (Figure 5F). These changes were quite similar to those induced by ephrinA1-Fc (Figures 3G, 3J, 4A, and 4D). Per se, EphA2 downregulation activated ERK in TPCs, as shown by a prominent increase in its phosphorylation (Figures 5F and 5G). Feeble Akt and FAK activation were detected. Furthermore, when EphA2 levels began to

(B) Intracranial transplantation of 6 x 10^4 EphA2^{High} or EphA2^{Low} cells confirmed the much higher tumor-propagating capacity of the former (MC test, log-rank $p < 0.0001$ for EphA2^{High} versus EphA2^{Low}; n = 8).

(C) Confocal images show widespread colocalization (arrowheads; yellow) of EphA2 (red) and SSEA-1 (green) in hGBM tissue. Scale bar, 20 μm.

(D) Cells from the same hGBM were sorted and gated according to EphA2 and SSEA-1 levels.

(E) Kaplan-Meier survival curves show that mice receiving intracranially 2 × 10^4 and 1 × 10^4 EphA2^{High} SSEA-1^{High} purified TPCs die earlier (median survival: 135 and 164 days, respectively) than mice receiving EphA2^{Low} SSEA-1^{Low} cells (56% and 67% survival at 200 days, respectively). MC and GBW tests, log-rank $p < 0.0001$ EphA2^{High} SSEA-1^{High} versus EphA2^{Low} SSEA-1^{Low}; n = 9). Survival was also shorter when implanting 4 × 10^4 EphA2^{High} SSEA-1^{High} as compared to EphA2^{Low} SSEA-1^{Low} TPCs. See also Figure S2.

(F) Limiting dilution intracranial transplant of cultured, luciferase-tagged TPCs sorted into EphA2^{High} and EphA2^{Low} pools (top). Light emission imaging analysis (bottom; 5,000, 1,000, and 100 cells per mouse) shows a higher tumor-initiating ability of EphA2^{High} versus EphA2^{Low} TPCs. Error bars, SEM; ***$p < 0.0001$, **$p = 0.002$, EphA2^{High} versus EphA2^{Low}.

(G) Kaplan-Meier analysis shows that mice receiving EphA2^{High} TPCs die earlier than mice receiving EphA2^{Low} cells (MC and GBW tests, log-rank $p < 0.0001$ EphA2^{High} versus EphA2^{Low}; n = 9).

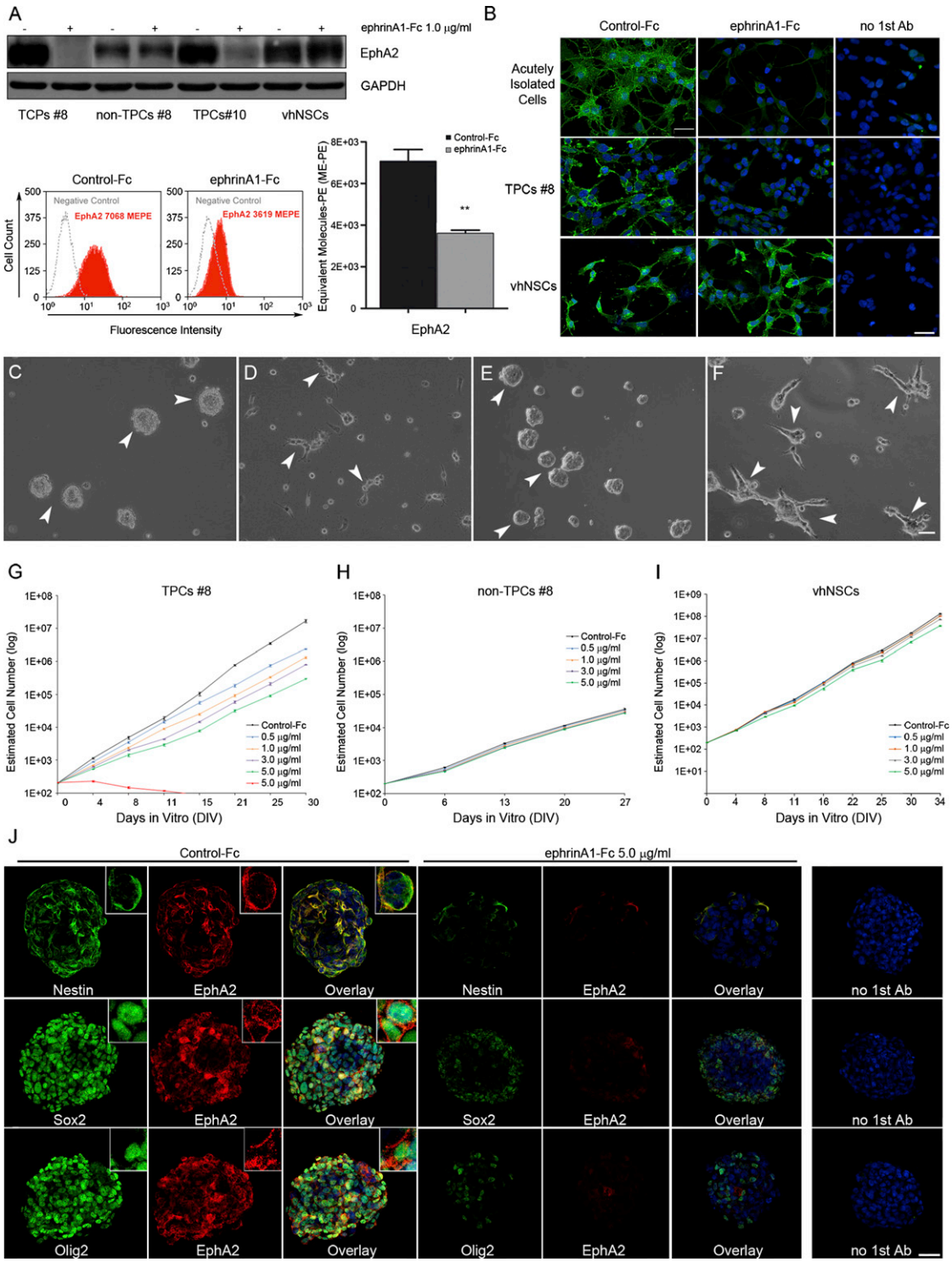

Figure 3. EphA2 Downregulation by EphrinA1-Fc Inhibits In Vitro Proliferation and Depletes the Stem Cell-like Pool in hGBM TPCs

(A) (Top) Cells were treated with ephrinA1-Fc for 24 hr. EphA2 was heavily downregulated in TPCs but not vhNSCs and non-TPCs. (Bottom) FACS analysis and flow cytometry quantitative data showing EphA2 downregulation in TPCs based on equivalent molecules of phycoerythrin (ME-PE) (n = 10 independent cultures); error bars, SEM; **p < 0.005 by Student's t test. See also Figure S3A.

(B) EphrinA1-Fc (5 μg/ml for 24 hr) downregulates EphA2 expression in TPCs acutely isolated from patients or from neurospheres (TPCs no. 8 shown as an example), but not in vhNSCs. Scale bar, 20 μm.

(C–F) EphrinA1-Fc (5 μg/ml for 48 hr) triggers obvious morphologic changes (arrowheads) in acutely isolated TPCs (C, control; D, treated) or serially subcultured TPC neurospheres (E, control; F, treated), promoting cell adhesion. Scale bar, 50 μm.

normalize, due to the elapsing effect of siRNAs transfection (Figure 5A, arrow), TPCs growth and ERK phosphorylation also began to normalize (Figures 5C, arrow, and 5F). siRNA-mediated knockdown of *EPHA2* expression in vhNSCs also inhibited growth (Figure 5D), in contrast to ephrinA1-Fc treatment, which neither inhibited growth nor downregulated EphA2 in these cells (Figures 3A, 3B, and 3I). Transduction of TPCs with individual *EPHA2* siRNA, and rescue with a siRNA-resistant *EPHA2* construct, confirmed these effects as the result of the EphA2 mRNA knockdown (Figure 5G). Importantly, inhibition of ERK activation partially rescued loss in clonogenicity as induced by *EPHA2* siRNA, implicating ERK activation in the loss of TPC stemness, as caused by EphA2 downregulation (Figure 5H).

Notably, EphA2 phosphorylation on Serine897 (Ser897) promotes oncogenic activities of the receptor that do not depend on its interaction with ephrin ligands (Miao et al., 2009). We detected a strong signal for Ser897-phosphorylated EphA2 in the hGBM core and in TPCs but not in the hGBM periphery, non-TPCs or vhNSCs (Figure 6A). Furthermore, treatment with high doses of soluble monomeric EphA2 extracellular domain that block endogenous EphA2-ephrin interaction did not affect GFAP levels or ERK activity in TPCs (Figure 6B). Thus, the effects of EphA2 in TPCs appear to be independent from activation by endogenous ephrinA ligands.

EphrinA1-Fc and EPHA2 Silencing by siRNAs Suppress TPC Tumorigenicity In Vivo

The main effect of ephrinA1-Fc treatment or siRNA-mediated *EPHA2* silencing is the depletion of the tumorigenic hGBM TPC pool, which ought to reduce their tumorigenic capacity in vivo. To examine the in vivo effects of ephrinA1-Fc, we used three experimental paradigms. hGBM TPCs were (1) treated with ephrinA1-Fc in culture prior to transplantation (pre-treatment), (2) treated starting immediately after transplantation (co-treatment), or (3) allowed to establish sizeable tumors before beginning treatment with ephrinA1-Fc (post-treatment). All three protocols were evaluated in a subcutaneous xenograft model. Furthermore, pre- and post-treatment protocols were also evaluated in an intracranial (orthotopic) xenograft model (Galli et al., 2004; Piccirillo et al., 2006).

When TPCs were injected subcutaneously, ephrinA1-Fc inhibited growth in all three protocols (Figure 7A). Similar results were obtained with the more complex, yet clinically more relevant, orthotopic model. In the intracranial hGBM model, tumor growth was greatly reduced in the pre-treatment settings, as shown by quantitative imaging of luciferase-tagged hGBM TPCs (luc-TPCs; Figures 7B left panels, 7C left, 7E, and 7F) and by the increase in overall survival (Figure 7C, right). Importantly, ephrinA1-Fc infusion into the brain for 14 days by means of osmotic mini-pumps also effectively suppressed the growth of well pre-established hGBMs (Figures 7B middle and right panels, 7D left, 7G, and 7H). Kaplan-Meier analysis revealed a median survival of 130 days for mice receiving ephrinA1-Fc versus 72 days for controls, infused with Fc (Figure 7D, right)—confirming the therapeutic efficacy of ephrinA1-Fc administration.

Immunohistochemistry confirmed that EphA2, which was high in TPC-derived, control intracranial hGBMs (Figure S4A), strongly downregulated upon ephrinA1-Fc infusion (Figure S4B). Control tumors contained numerous malignant cells (Figure S4C), whereas ephrinA1-Fc-treated ones contained few neoplastic cells and many more differentiated elements (Figure S4D). Accordingly, ephrinA1-Fc-treated tumors embodied a lower percentage of mitotic cells (Figures S4E and S4F) and were significantly less vascularized than Fc-treated controls (2-fold reduction in total vascular area, with less and smaller blood vessels; Figures S4G and S4H and data not shown).

To determine if decreasing EphA2 receptor levels was sufficient to inhibit hGBM tumorigenicity, we analyzed the effects of siRNAs-mediated *EPHA2* silencing on the in vivo tumor-propagating ability of luc-TPCs, in comparison with luc-TPCs treated with control-siRNAs or untreated ones. Knockdown of endogenous *EPHA2* suppressed the growth of TPC-derived intracranial tumors (Figure 7I, top) and substantially increased overall survival (Figure 7I, bottom).

Given the prominent involvement of EphA2 in the pathogenic mechanisms of hGBMs documented above, we analyzed the TCGA data set (Network, 2008) for relative EphA2 mRNA expression in hGBM subcategories (Verhaak et al., 2010). We found that the classical and mesenchymal subtypes had the highest EphA2 expression (Figure 8). In addition, when the mesenchymal or proneural subtypes were divided into two groups based on median EphA2 expression, high EphA2 expression trended with poor patient survival (mesenchymal: 10.9 versus 15.03 months, $p = 0.0415$ Mantel-Cox [MC], $p = 0.0215$ Gehan-Breselow-Wilcoxon [GBW]; proneural: 9.9 versus 16.73 months, $p = 0.2026$ MC test, $p = 0.0411$ GBW test). There was no significant correlation between EphA2 and patient survival in the neural and classical subtypes.

DISCUSSION

We describe a specific role for the EphA2 receptor in the pathogenesis of hGBMs. We report how enhanced EphA2 expression is a property of the TPCs in these cancers and show a causal relationship between high EphA2 expression and the capacity of these cells to expand their pool size and form hGBMs. Accordingly, high levels of EphA2 expression can be used to enrich for TPCs by FACS. Furthermore, treatment with a soluble form of the EphA2 ligand, ephrinA1-Fc, hinders the self-renewal ability of hGBM TPCs causing a drastic loss in their capacity to establish and propagate hGBM phenocopies subcutaneously or intracranially. We demonstrate that EphA2 receptor downregulation is a causal event in the suppression of the tumor-propagating

(G–I) Acutely isolated TPCs cannot establish stable TPC primary lines if exposed to ephrinA1-Fc (G, red line), which also inhibits steady growth in pre-established TPCs (G); $p < 0.0001$ versus Control-Fc. Negligible inhibition of ephrinA1-Fc was observed in non-TPCs (H) and vhNSCs (I) ($p < 0.005$ versus Control-Fc; TPCs no. 8 and non-TPCs no. 8 are shown as representative examples); error bars, SEM. See also Figures S3B and S3C.

(J) Coexpression of EphA2 (red) with the putative stem antigens Nestin, Sox2, or Olig2 (green) in TPC spheroids treated for 24 hr with Control-Fc or ephrinA1-Fc. EphrinA1-Fc nearly abolishes expression of both EphA2 and the stem antigens. Insets: higher magnification. Scale bar, 40 μm. See also Figures S3D and S3E.

Unless otherwise indicated, the data are representative of three independent experiments giving similar results.

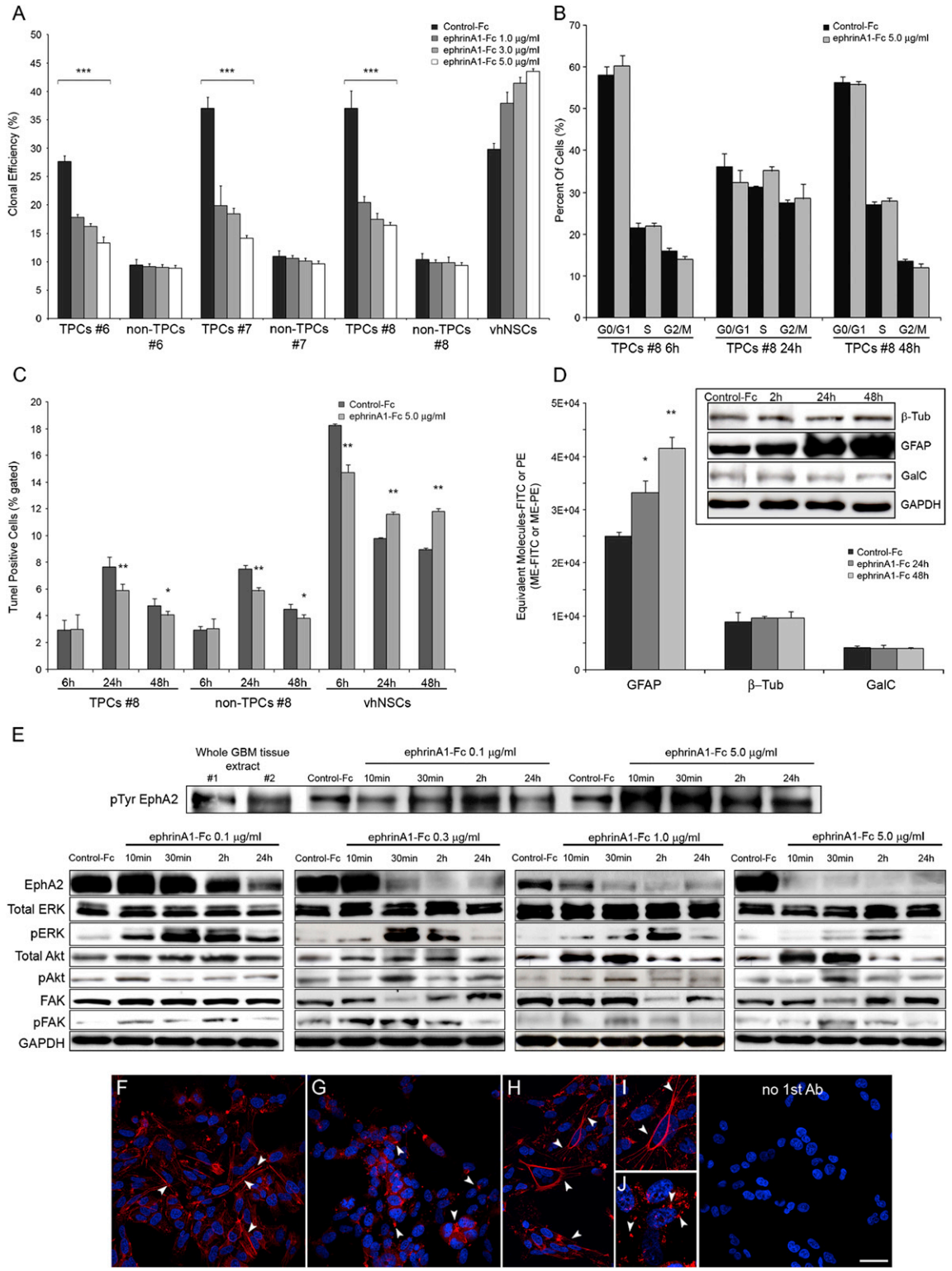

Figure 4. EphrinA1-Fc Inhibits TPC Self-Renewal by Inducing a Differentiated Phenotype

(A) Clonogenic assays show a dose-dependent inhibition of self-renewal by ephrinA1-Fc in TPCs but not in non-TPCs and vhNSCs; error bars, SEM; ***$p < 0.0001$ versus Control-Fc cells.

(B) Up to 5 μg/ml ephrinA1-Fc does not alter TPC cell cycling, as determined by FACS analysis of BrdU incorporation; error bars: SEM.

(C) Cytofluorimetric Tunel analysis shows no induction of apoptosis in TPCs or non-TPCs treated with ephrinA1-Fc; error bars: SEM; **$p < 0.005$, *$p < 0.05$ versus Control-Fc.

capacity of TPCs. Intracranial administration of ephrinA1-Fc causes EphA2 downregulation in hGBM orthotopic xenografts, significantly hindering their growth and expansion in the brain, even if these tumors are established ahead of ephrinA1-Fc administration.

Aberrant expression of Eph receptors has been reported in various cancers, including gliomas, and correlates with malignancy (Wykosky and Debinski, 2008; Pasquale, 2010; Nakada et al., 2011; Miao and Wang, 2012). In our survey of 12 hGBM specimens, we found EphA2 to be the most upregulated of the Eph receptors. This is consistent with the EphA2 overexpression previously reported in most high-grade human gliomas, which correlates with poor prognosis (Wykosky et al., 2005; Liu et al., 2006; Wang et al., 2008; Miao et al., 2009; Li et al., 2010; Wu et al., 2011), suggesting a role for EphA2 in the pathogenesis of hGBMs.

While studies with glioma cell lines have implicated EphA2 in cell growth and invasiveness (Wykosky et al., 2005; Liu et al., 2006, 2007; Miao et al., 2009; Li et al., 2010; Gopal et al., 2011), the identity and nature of the actual target cells in the patients' own GBM remain unclear. In addition, the cellular functions affected by EphA2, the regulatory mechanisms underpinning EphA2′s actions in hGBMs pathophysiology, and the possibility of manipulating this system to suppress glioma growth are not well characterized. hGBMs contain subpopulations of cells that act as stem-like TPCs, which have now been proven to be crucial therapeutic targets (Chen et al., 2012). We found that the EphA2 receptor is coexpressed with neural precursor markers in hGBMs, being concentrated in regions rich in TPCs. Furthermore, hGBM cell preparations enriched in TPCs display enhanced EphA2 levels which, conversely, are low in low-grade gliomas (Figure S1B) that contain few TPCs (Galli et al., 2004). Altogether, these findings suggest that high EphA2 levels are a distinguishing feature of hGBM TPCs.

Conclusive evidence to this idea came from fractionating TPCs into $EphA2^{Low}$ and $EphA2^{High}$ populations, also in combination with high levels of the putative TPC markers. The highest tumorigenic potential was associated with high EphA2 or combined, high EphA2 SSEA-1 or EphA2 CD44 expression. Thus, in vitro and in vivo limiting dilution experiments show that high EphA2 expression can be exploited to obtain preparations highly enriched in TPCs, which are capable of establishing intracranial hGBMs by injection of as few as 100 cells.

Overexpression of EphA2 in TPCs suggests a role for this receptor in hGBM pathogenesis. A first indication that EphA2 might drive the expansion of the TPC pool came from the significant correlation between the rate of self-renewal of multiple TPC preparations and their EphA2 mRNA levels and *EPHA2* gene copy number. This was reinforced by the fact that EphA2 expression decreases dramatically when hGBM TPCs lost their stemness upon differentiation.

To verify the role of EphA2 in TPC self-renewal and amplification, we first perturbed EphA2 by using the ephrinA1-Fc ligand (Noblitt et al., 2004; Lee et al., 2011; Khodayari et al., 2011). This treatment decreased the proliferation of both acutely isolated and of serially subcultured hGBM TPCs, was coupled to the failure of primary hGBM TPCs to generate stably expanding lines and caused both loss of expansion capacity and clonogenic ability in well-established TPC cultures.

The ephrinA1-Fc action was associated to decreased expression of putative hGBM TPC antigens (such as Olig2, Nestin, Sox2, CD133, CD44, and SSEA-1), occurred in the absence of detectable changes in cell cycle or apoptosis and produced increased astroglial differentiation and the depletion of the chemoresistant SP. Notably, these effects were specific to TPCs, since stem-like cells from the same tumors but lacking tumor-propagating ability (non-TPCs) and nontransformed neural stem cells (vhNSCs) were resilient to ephrinA1-Fc administration. Thus, in vitro exposure to ephrinA1-Fc leads to the depletion of those stem-like cancer cells that are responsible for hGBM initiation, growth, and recurrence after therapy.

EphrinA1-Fc caused prolonged EphA2 downregulation in TPCs, suggesting a critical role for this phenomenon in this ligand's tumor suppressor activities. Although ephrin Ligands trigger Eph receptor tyrosine phosphorylation and activation, thereby eliciting complex downstream signaling, they also cause Eph receptor downregulation (Wykosky et al., 2005; Liu et al., 2007; Pasquale, 2010). We observed only negligible inhibition of TPC clonogenicity (less than 10%; data not shown) at the lower ephrinA1-Fc concentrations tested, which induced strong intracellular signaling but limited EphA2 downregulation. Conversely, at higher ephrinA1-Fc concentrations, signaling was weaker, but EphA2 downregulation, inhibition of TPC clonogenicity and growth were much more evident. Indeed, while signaling was transient and returned to basal levels within 24 hr, the inhibition of TPC tumorigenicity and EphA2 downregulation persisted well beyond 24 hr. The importance of EphA2 downregulation was further supported by the observation that in vhNSCs ephrinA1-Fc failed to both induce EphA2 downregulation and inhibit cell growth and self-renewal. Furthermore, siRNA-mediated knockdown of *EPHA2* expression closely mimicked the effects of ephrinA1-Fc on TPC self-renewal, expansion, differentiation in vitro, and tumorigenic ability in vivo. Interestingly, *EPHA2* expression knockdown also inhibited the growth and self-renewal of the "ephrinA1-Fc-resilient" vhNSCs. Therefore, EphA2 downregulation alone can inhibit TPC tumor-propagating activity although it remains possible that ephrinA1-Fc-induced EphA2 signaling may also contribute

(D) Quantitative FACS analysis shows a time-dependent increase in equivalent molecules of fluorescein (ME-FITC) for astroglial GFAP but not neuronal βIII tubulin (β-Tub) or oligodendroglial GalC markers in ephrinA1-Fc-treated TPCs; error bars, SEM; *p = 0.0095, **p = 0.0005 versus Control-Fc. (Inset) Western blotting confirms a marked, time-dependent increase in GFAP under the same settings.

(E) (Top) Tyrosine phosphorylation of EphA2 immunoprecipitated from whole hGBM lysates and from TPCs treated with ephrinA1-Fc. (Bottom) Western blots for EphA2, ERK, Akt and FAK (Tyr397) expression and phosphorylation in TPCs treated with increasing ephrinA1-Fc concentrations over a 24 hr time course. Lower ephrinA1-Fc concentrations preferentially stimulate signaling, higher ones more rapidly downregulate the receptor.

(F–J) (F) TPCs spread on Cultrex show an organized actin cytoskeleton and F-actin assembled in stress fibers (arrows). Typical ring-like actin bundles are seen at higher magnification (H and I; arrowheads). (G and J) EphrinA1-Fc-treatment (5 μg/ml for 5 min) causes TPC elongation and actin concentration at cell-cell junctions (arrowhead). Scale bar, 20 μm.

Unless otherwise indicated, the data are representative of three independent experiments giving similar results.

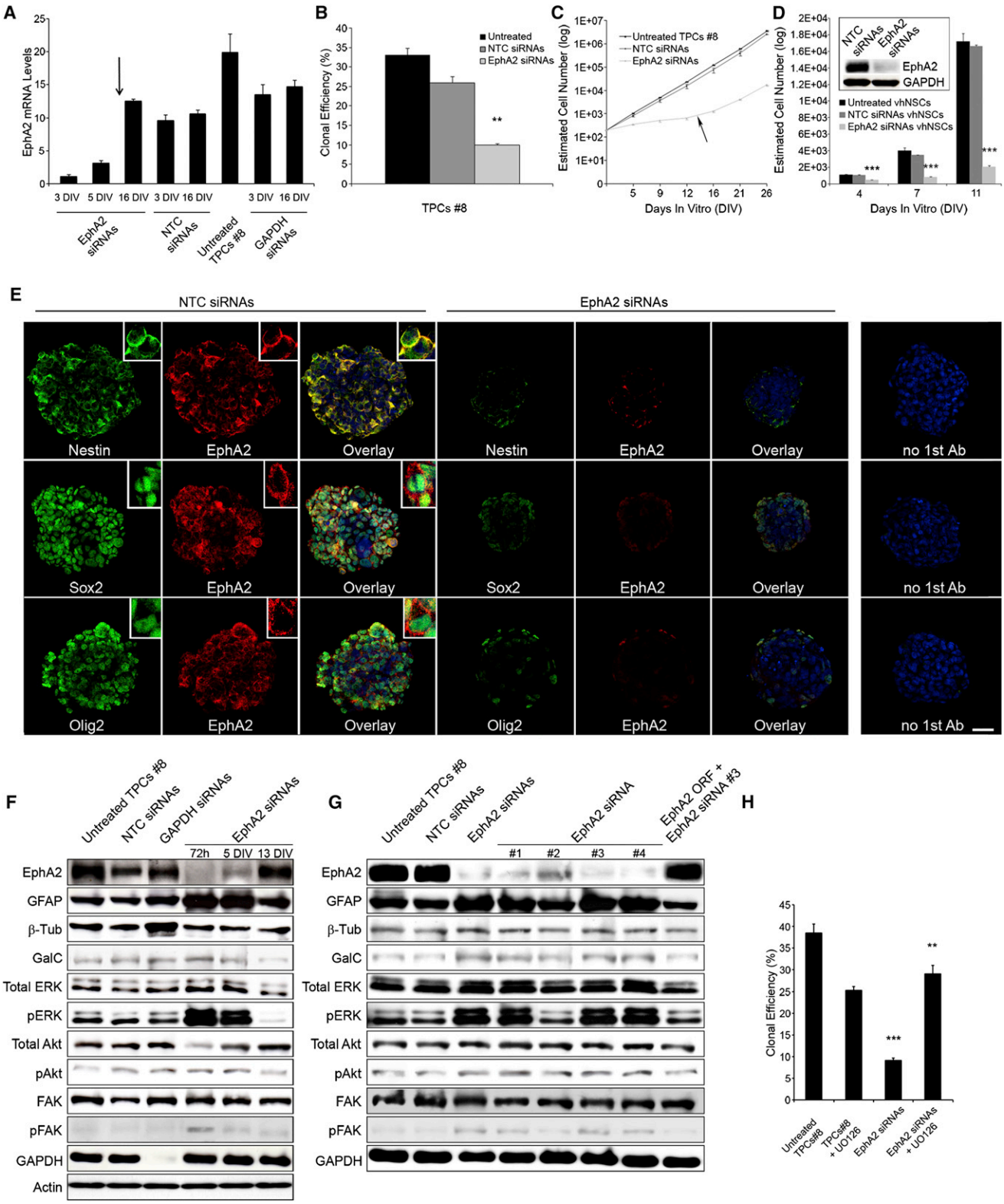

Figure 5. *EPHA2* siRNA Knockdown in hGBM TPCs Inhibits Self-Renewal and Increases Differentiation, Concomitant with ERK and Akt Activation

(A) TPCs were treated with an *EPHA2* siRNA pool, non-targeting control (NTC) or *GAPDH* control pool siRNAs. Three days post-transfection, only the *EPHA2* siRNAs caused a substantial decrease in EphA2 mRNA, as detected by qPCR. Between 12 and 16 days post-transfection (DIV), EphA2 levels began to normalize (arrow); error bars, SEM.

to the suppression of TPC tumorigenicity (Wykosky and Debinski, 2008; Nakada et al., 2011; Miao and Wang, 2012). Thus, EphA2 is prominently expressed in TPCs and is required for sustained self-renewal and expansion of this tumor-propagating cell pool in hGBMs.

The depletion of the TPC stem-like pool induced by ephrinA1-Fc treatment and EphA2 downregulation seems to arise from increased cell differentiation. First, loss of the undifferentiated state is demonstrated by the depletion of Sox2, Olig2, Nestin, CD133, CD44, and SSEA-1, as well as the increased expression of the astroglial marker GFAP, as induced by both ephrinA1-Fc and knockdown of *EPHA2* expression. Second, both manipulations also inhibit the typical undifferentiated stem-like functions of TPCs, such as self-renewal and extensive amplification capacity. Given the unchanged cell cycling and death rate, these data imply that ephrinA1-Fc and EphA2 downregulation cause the loss of undifferentiated functional and antigenic properties as well as the acquisition of a more mature cell phenotype by TPCs.

The activities of EphA2 in hGBM TPCs appear to involve unconventional ephrin-independent activities of EphA2, which are not yet well understood but may also involve crosstalk with other signaling systems (Miao et al., 2009; Pasquale, 2010; Gopal et al., 2011; Miao and Wang, 2012). This is supported by the prominent phosphorylation of EphA2 at the Ser897 residue (Miao et al., 2009) that we detected in the TPC-enriched core but not the periphery of hGBMs, and in cultured TPCs but not non-TPCs or vhNSCs. Phosphorylation of EphA2 Ser897 by Akt is known to promote EphA2′s oncogenic activities independently of ephrin binding, and in fact interaction of EphA2 with ephrinA1 inhibits phosphorylation at this site (Miao et al., 2009). Consistent with a role of EphA2 in TPCs that does not depend on activation by endogenous ephrins, using the soluble EphA2 extracellular domain to block EphA2-ephrin interaction did not affect GFAP levels or ERK activation in TPCs. In contrast, *EPHA2* siRNA-mediated knockdown depleted the stem cell pool concomitantly with ERK, suggesting that this pathway may mediate the effects of EphA2. This was confirmed by using the ERK inhibitor UO126, which re-established self-renewal ability in TPCs with downregulated EphA2 expression. This suggests that ERK can promote differentiation in TPCs that have lost EphA2 expression.

The hindrance of self-renewal capacity induced by ephrinA1-Fc predicts that this ligand will lessen the ability of TPCs to establish tumors in vivo. In fact, a 48 hr exposure to soluble ephrinA1-Fc reduced the capacity of TPCs to establish hGBM phenocopies, both subcutaneously and intracranially. A similar effect was observed when we implanted TPCs subcutaneously and began ephrinA1-Fc infusion either at the same time or after sizeable tumors had been established. Treatment of intracranial tumors with ephrinA1-Fc significantly reduced the tumor mass, vascularization, and proliferation and dramatically decreased EphA2 levels. When *EPHA2* expression in TPCs was knocked down with siRNAs, intracranial tumorigenicity was nearly abolished. Thus, EphA2 is critical to maintain TPC properties and plays a pivotal role in the pathogenesis of hGBMs in the brain, as driven by TPCs.

Our findings are consistent with previous studies suggesting that EphA2 expression correlates with malignancy in hGBMs (Liu et al., 2006; Wang et al., 2008; Li et al., 2010; Wu et al., 2011). Hence, we examined the relationship between EphA2 expression and patient survival in relation to the recent stratification of hGBMs into different subtypes (Verhaak et al., 2010). We found that EphA2 is most highly expressed in the classical and mesenchymal groups and that, at least in the mesenchymal subtype, patients with EphA2 levels above the median trended toward poorer survival. This trend was also present and statistically significant in the proneural subtype, although this subtype has lower mean levels of EphA2 than the mesenchymal and classical ones. The correlation with poor survival in these two groups further underscores the importance of EphA2 expression in aggressive tumor behavior, which may be more relevant in the mesenchymal and proneural hGBM subtypes.

We were able to drastically inhibit the growth of pre-existing orthotopic hGBM xenografts under experimental conditions that mimic those needed for experimental human therapy, such as protracted delivery through intra-parenchymal infusion. This supports the value of devising anti-GBM therapies that harness the Eph/ephrin system to target the TPC compartment. Hence, the concept emerges of impinging in non-toxic fashion on specific molecular targets, such as EphA2, to tackle the subset of tumor cells that plays the most critical role in hGBM pathogenesis.

We show that a signaling system that is operational in the neural stem cell niche also regulates self-renewal and tumorigenicity in hGBM TPCs, in agreement with previous observations (Ying et al., 2011). Eph receptors and ephrins regulate the migration, survival, proliferation, cell fate and differentiation of neural precursors during development (Goldshmit et al., 2006; Genander and Frisén, 2010). In the adult, such activities persist in stem cell niches, including those of the adult central nervous

(B) siRNA-mediated knockdown of *EPHA2* expression causes loss of TPC clonogenicity; error bars, SEM; $^{**}p < 0.005$ EphA2 versus NTC siRNAs.
(C) TPC growth decrease is concomitant with siRNA-mediated EphA2 downregulation and normalizes when EphA2 levels begin recover (arrow); error bars, SEM; $p < 0.0001$ *EPHA2* siRNAs versus NTC.
(D) siRNA-mediated EphA2 downregulation decreased vhNSCs growth; error bars, SEM; $^{***}p < 0.0001$ *EPHA2* siRNAs versus NTC. Inset: western blot for EphA2 upon *EPHA2* siRNA treatment.
(E) Confocal analysis shows that siRNA-mediated EphA2 downregulation in TPC spheroids is associated with depletion of putative stem markers, as compared to NTC-treated spheroids (NTC siRNAs). Insets: magnification. Scale bar, 40 μm.
(F and G) Western blot analysis show increased GFAP but not β-Tub or GalC levels in TPCs treated with *EPHA2* siRNAs versus NTC or *GAPDH* siRNAs (F). ERK phosphorylation is also strongly increased concomitant with EphA2 downregulation, with more prominent effects at 72 hr than at 5 days, when EphA2 levels begin to recover. (G) Representative western blot showing that only the siRNA sequences that effectively reduce EphA2 expression increase GFAP expression and activate ERK. An *EPHA2* construct lacking the 3′UTR sequence targeted by *EPHA2* siRNA no. 3 was used to transfect TPCs in a control rescue experiments.
(H) The reduced TPC clonogenicity caused by knockdown of *EPHA2* expression was partially restored by 10 μM UO126, which inhibits ERK; error bars, SEM; $^{***}p < 0.0001$, $^{**}p < 0.005$ versus untreated TPCs.
Unless otherwise stated, data are representative of three independent experiments giving similar results.

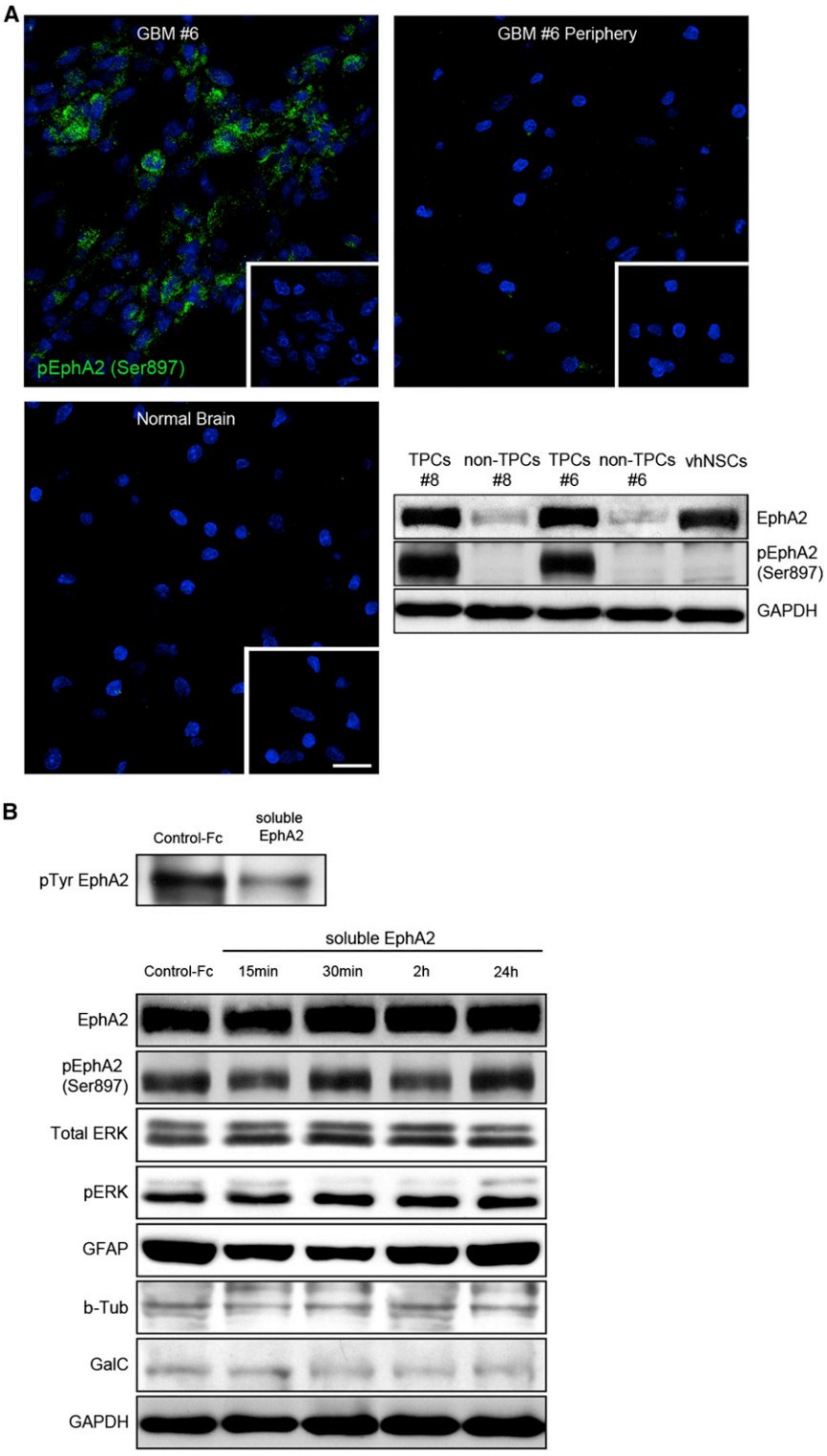

Figure 6. EphA2 Does Not Appear to be Activated by Ephrins in hGBM

TPC is phosphorylated on Ser897 in hGBM and treatment with the soluble EphA2 extracellular domain to inhibit ephrin binding to endogenous EphA2 does not affect TPC signaling pathways.

(A) Top: EphA2 is constitutively phosphorylated on Ser897 in the core of hGBMs (left) but not in the periphery of hGBMs (center) or normal brain (right). Bottom: EphA2 is highly phosphorylated on Ser897 in hGBM TPCs but not non-TPCs or vhNSCs. EphA2 Ser897 phosphorylation suggests ephrin-independent oncogenic activities.

(B) Representative western blots showing that treatment of TPCs with 10 μg/ml EphA2 extracellular domain to inhibit possible interactions with endogenous ephrin ligands does not affect GFAP levels or ERK phosphorylation as compared to Fc protein used as a control.

Data are representative of three independent experiments giving similar results.

system, although our understanding of Eph/ephrin regulatory functions in adult neurogenesis remains limited. Since other Eph receptors besides EphA2 are expressed in adult neural stem cell niches (Goldshmit et al., 2006; Genander and Frisén, 2010), by using agents that selectively target EphA2 we may be able to target stem-like cells in hGBMs without affecting the normal brain stem cell population.

These findings emphasize the importance of approaches that exploit fundamental similarities in the physiology of normal neural stem cells and their stem-like, tumor-propagating counterpart in brain tumors (Vescovi et al., 2006). Such approaches can make use of the wealth of information derived from studies on regulatory systems in normal neural stem cells to identify candidate effectors capable to affect TPCs, thus helping to design more effective and specific anti-GBM therapies.

EXPERIMENTAL PROCEDURES

Primary Culture, Culture Propagation, Population Analysis, and Cloning

Adult hGBM, low-grade gliomas, ependimomas, PNET tissues, and normal human brain samples were obtained and classified according to the World Health Organization guidelines. All of the tumors were banked in accordance with research ethics board approval from the Institute of Neurosurgery, Catholic University of the Sacred Heart (Prot. RBAP10KJC5) and patients gave informed consent prior to surgery. hGBM non-necrotic core and periphery tissues were dissected and digested in a papain solution (Worthington Biochemical, Lakewood, NJ, USA). Primary stem-like tumor-propagating cells (acutely isolated cells) were plated in NeuroCult NS-A medium (StemCell Technologies, Vancouver, BC, Canada) containing 20 ng/ml of epidermal- and 10 ng/ml of fibroblast-growth factor (Peprotech, Rocky Hill, NJ, USA) (culture medium; Galli et al., 2004). EphA2 was stimulated with ephrinA1-Fc (R&D Systems, Minneapolis, MN, USA) for the indicated concentrations and times. Mouse monoclonal IgG1 isotype (R&D Systems) was used as control. For population analysis, clonogenic assays and differentiation

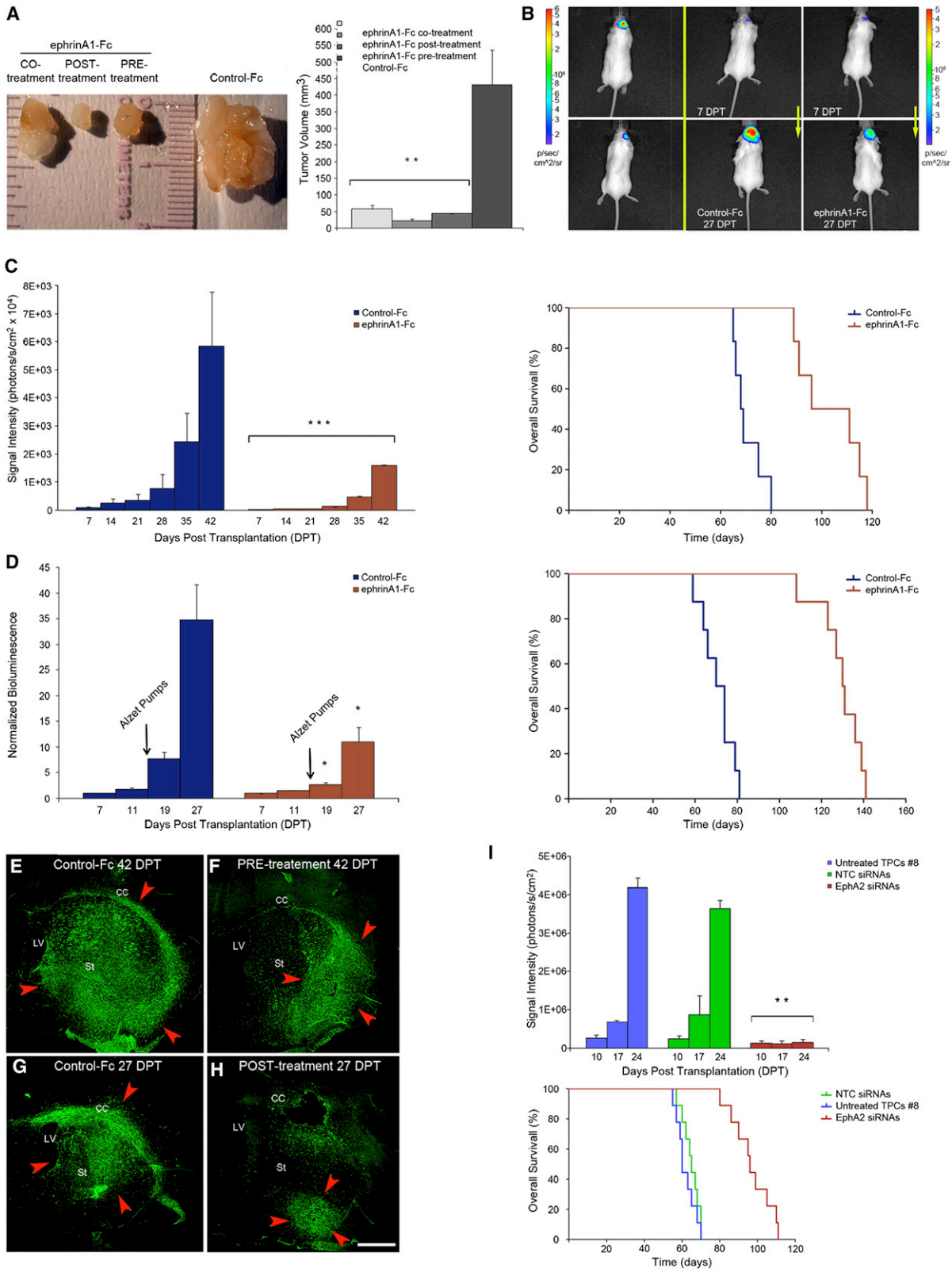

Figure 7. EphA2 Downregulation by EphrinA1-Fc or by siRNA-Mediated Knockdown Inhibits TPC Tumorigenicity in Immunodeficient Mice

(A) Treating TPCs with ephrinA1-Fc (5 μg/ml for 48 hr) prior to subcutaneous implantation (PRE-treatment) lessens their tumor-initiating capacity (left). Similar results were obtained by coinjecting TPCs and ephrinA1-Fc (CO-treatment) or injecting ephrinA1-Fc (10 μg/day) around the tumor starting 11 days after cell

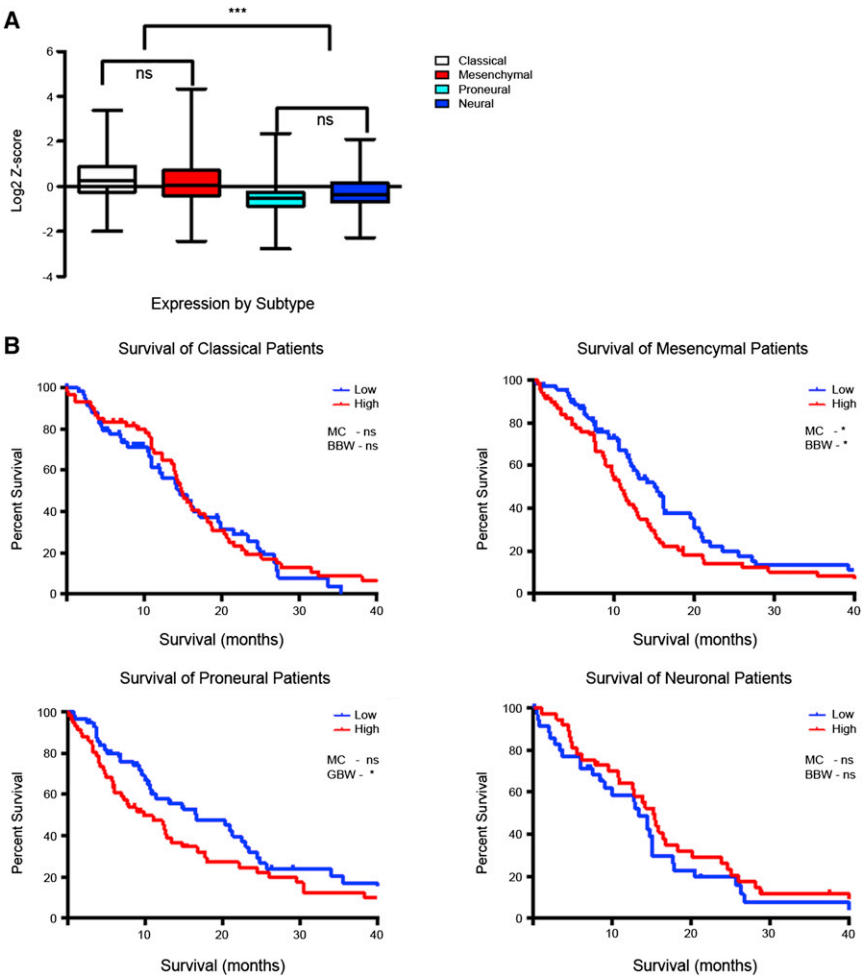

Figure 8. EphA2 Is Differentially Expressed in GBM Subtypes, and Its Abundance Correlates with Patient Survival

(A) Relative EphA2 mRNA expression in the four GBM subtypes of the TCGA data set. (***p < 0.0001 by ANOVA; n = 495).

(B) Kaplan-Meier survival curves for the classical, mesenchymal, proneural, and neural subtypes. High and low expression are defined as above and below the median expression value for each subtype, log-rank p values were determined by MC and GBW tests.

experiments see the matching section in the Supplemental Experimental Procedures.

Statistical Analysis for the Correlation

Growth curves were analyzed with a hierarchical linear model for repeated-measurements to assess trend over time (Diggle et al., 1994; Singer and Willett, 2003). Log-transformed cell number was considered as outcome. Association with EphA2 mRNA expression levels and *EPHA2* copy number were assessed including them into the statistical models (Figures S1H–S1J). A spatial power correlation type was used to account for unequally spaced time occasions during the experiment (Singer and Willett, 2003). Unless indicated otherwise, comparisons between ephrinA1-Fc (also with different doses) treated cells and Control-Fc-treated cells were carried out with a hierarchical linear model for repeated-measurements. The p values less than 0.05 were considered statistically significant. All analyses were performed using SAS Statistical Package Release 9.1 (SAS Institute, Cary, NC, USA) or GraphPad Prism.

Evaluation of Tumorigenicity by Subcutaneous or Orthotopic Implantation

Tumorigenicity was studied by TPCs subcutaneous or orthotopic injections (Galli et al., 2004). All animal procedures were conducted in accordance with the Guidelines for the Care and Use of Laboratory Animals and were approved by the Institutional Animal Care and Use Committees (IACUCs) at the University of Milan Bicocca. See the matching section in the Supplemental Experimental Procedures for details.

Molecular Analysis

TCGA data analysis was performed as described by Squatrito et al., 2010; survival and expression data were based on clinical TCGA data and relative

transplant (POST-treatment). (Right) Volumes of subcutaneous tumors 35 days after TPCs injection. Histograms, mean volume ± SEM; **p = 0.0002 versus Control-Fc mice, n = 6.

(B) Imaging of luciferase-tagged TPCs (luc-TPCs) injected into the brain of *Scid/bg* mice. After 42 days, untreated TPCs established larger tumors (vehicle, top left) than ephrinA1-Fc PRE-treated TPCs (bottom left). Luc-TPC tumors established for 7 days (7 DPT, top center) grew quickly when a mini-pump delivered Control-Fc for 14 days starting at 11 days post-transplant (27 DPT, bottom center). In contrast, tumor growth was markedly inhibited by ephrinA1-Fc (top and bottom right panels).

(C) (Left) Quantitative analysis of luc-TPC signals for the PRE-treatment intracranial transplants. Histograms, mean ± SEM; ***p < 0.0001 versus Control-Fc mice; n = 6. (Right) Kaplan-Meier survival curves showing that mice receiving ephrinA1-Fc-treated TPCs have a significant longer life span than mice injected with Control-Fc cells (MC and GBW tests, log-rank p = 0.0005 and 0.0013 respectively; n = 9).

(D) (Left) Quantitative time course analysis of the luc-TPC signal for POST-treatment paradigm (arrows mark the time of mini-pumps implantation). Histograms, mean ± SEM; *p < 0.05 versus Fc-treated mice; n = 8. (Right) Kaplan-Meier survival curves are shown (MC and GBW tests, log-rank p < 0.0001 and p = 0.0002 versus Control-Fc mice; n = 9).

(E–H) Mouse brain sections immunolabeled for luciferase show that tumors established from luc-TPCs PRE-treated with Control-Fc (E) spread through the brain parenchyma more than those established from cells PRE-treated with ephrinA1-Fc (F) at 42 DPT. Similarly, ephrinA1-Fc infused into the brain for 2 weeks starting 11 days after tumor establishment (H) inhibits the growth of luc-TPC tumors more than Control-Fc (G). Arrowheads mark the edges of the tumors. CC, corpus callosum; LV, lateral ventricle; St, striatum. See also Figure S4. Scale bar, 1 mm.

(I) Loss of intracranial tumorigenicity in luc-TPCs treated with *EPHA2* siRNAs for 72 hr prior to transplantation as compared to NTC siRNA-treated or untreated TPCs. Tumor growth was monitored by quantitative imaging analysis (top). Histograms, mean ± SEM; ***p < 0.0001 *EPHA2* siRNAs versus NTC; n = 6. (Bottom) Kaplan-Meier survival analysis. Mice receiving *EPHA2* siRNA-transfected TPCs die significantly later than those receiving untreated TPCs or TPCs transfected with non-targeting control siRNAs (MC and GBW tests, log-rank p < 0.0001 versus NTC siRNAs treatment; n = 9).

mRNA expression obtained from the TCGA data portal (http://cancergenome.nih.gov/dataportal/data/about) and the MSKCC cBio Genome Data Analysis Portal (http://cbio.mskcc.org/gdac-portal/index.do), respectively. Tumor subtype classification was previously described (Verhaak et al., 2010). Relative mRNA results are based on relative distribution of the expression values for diploid tumor samples and were subjected to statistical analysis by one-way ANOVA (GraphPad Prism v5.0 software). Survival curves were analyzed using the Kaplan-Meier method, with groups compared by respective median survival of number of days taken to reach 50% morbidity; log-rank p value was measured using both MC and GBW tests.

SUPPLEMENTAL INFORMATION

Supplemental Information includes four figures and Supplemental Experimental Procedures and can be found with this article online at http://dx.doi.org/10.1016/j.ccr.2012.11.005.

ACKNOWLEDGMENTS

This research was supported by grants from the McDonnell Foundation (220020207), AIRC (IG-10141), MIUR (RBAP10KJC5 and RF-INN-2008-1220368), and NIH (P01CA138390). We thank Lucia Sergisergi for providing the luciferase lentivirus.

Received: August 4, 2011
Revised: January 31, 2012
Accepted: November 13, 2012
Published: December 10, 2012

REFERENCES

Alcantara Llaguno, S., Chen, J., Kwon, C.H., Jackson, E.L., Li, Y., Burns, D.K., Alvarez-Buylla, A., and Parada, L.F. (2009). Malignant astrocytomas originate from neural stem/progenitor cells in a somatic tumor suppressor mouse model. Cancer Cell *15*, 45–56.

Alcantara Llaguno, S.R., Chen, Y., McKay, R.M., and Parada, L.F. (2011). Stem cells in brain tumor development. Curr. Top. Dev. Biol. *94*, 15–44.

Bao, S., Wu, Q., McLendon, R.E., Hao, Y., Shi, Q., Hjelmeland, A.B., Dewhirst, M.W., Bigner, D.D., and Rich, J.N. (2006). Glioma stem cells promote radioresistance by preferential activation of the DNA damage response. Nature *444*, 756–760.

Bonnet, D., and Dick, J.E. (1997). Human acute myeloid leukemia is organized as a hierarchy that originates from a primitive hematopoietic cell. Nat. Med. *3*, 730–737.

Buzzeo, M.P., Scott, E.W., and Cogle, C.R. (2007). The hunt for cancer-initiating cells: a history stemming from leukemia. Leukemia *21*, 1619–1627.

Chen, J., Li, Y., Yu, T.S., McKay, R.M., Burns, D.K., Kernie, S.G., and Parada, L.F. (2012). A restricted cell population propagates glioblastoma growth after chemotherapy. Nature *488*, 522–526.

De Filippis, L., Lamorte, G., Snyder, E.Y., Malgaroli, A., and Vescovi, A.L. (2007). A novel, immortal, and multipotent human neural stem cell line generating functional neurons and oligodendrocytes. Stem Cells *25*, 2312–2321.

Dell'Albani, P. (2008). Stem cell markers in gliomas. Neurochem. Res. *33*, 2407–2415.

Diggle, P., Liang, K.Y., and Zeger, S.L. (1994). Analysis of Longitudinal Data (New York: Clarendon Press).

Eyler, C.E., Wu, Q., Yan, K., MacSwords, J.M., Chandler-Militello, D., Misuraca, K.L., Lathia, J.D., Forrester, M.T., Lee, J., Stamler, J.S., et al. (2011). Glioma stem cell proliferation and tumor growth are promoted by nitric oxide synthase-2. Cell *146*, 53–66.

Fatoo, A., Nanaszko, M.J., Allen, B.B., Mok, C.L., Bukanova, E.N., Beyene, R., Moliterno, J.A., and Boockvar, J.A. (2011). Understanding the role of tumor stem cells in glioblastoma multiforme: a review article. J. Neurooncol. *103*, 397–408.

Fukaya, R., Ohta, S., Yamaguchi, M., Fujii, H., Kawakami, Y., Kawase, T., and Toda, M. (2010). Isolation of cancer stem-like cells from a side population of a human glioblastoma cell line, SK-MG-1. Cancer Lett. *291*, 150–157.

Galli, R., Binda, E., Orfanelli, U., Cipelletti, B., Gritti, A., De Vitis, S., Fiocco, R., Foroni, C., Dimeco, F., and Vescovi, A. (2004). Isolation and characterization of tumorigenic, stem-like neural precursors from human glioblastoma. Cancer Res. *64*, 7011–7021.

Genander, M., and Frisén, J. (2010). Ephrins and Eph receptors in stem cells and cancer. Curr. Opin. Cell Biol. *22*, 611–616.

Goldshmit, Y., McLenachan, S., and Turnley, A. (2006). Roles of Eph receptors and ephrins in the normal and damaged adult CNS. Brain Res. Brain Res. Rev. *52*, 327–345.

Gopal, U., Bohonowych, J.E., Lema-Tome, C., Liu, A., Garrett-Mayer, E., Wang, B., and Isaacs, J.S. (2011). A novel extracellular Hsp90 mediated co-receptor function for LRP1 regulates EphA2 dependent glioblastoma cell invasion. PLoS ONE *6*, e17649.

Hadjipanayis, C.G., and Van Meir, E.G. (2009). Tumor-initiating cells in malignant gliomas: biology and implications for therapy. J. Mol. Med. *87*, 363–374.

Kelly, P.N., Dakic, A., Adams, J.M., Nutt, S.L., and Strasser, A. (2007). Tumor growth need not be driven by rare cancer stem cells. Science *317*, 337.

Khodayari, N., Mohammed, K.A., Goldberg, E.P., and Nasreen, N. (2011). EphrinA1 inhibits malignant mesothelioma tumor growth via let-7 microRNA-mediated repression of the RAS oncogene. Cancer Gene Ther. *18*, 806–816.

Krex, D., Klink, B., Hartmann, C., von Deimling, A., Pietsch, T., Simon, M., Sabel, M., Steinbach, J.P., Heese, O., Reifenberger, G., et al.; German Glioma Network. (2007). Long-term survival with glioblastoma multiforme. Brain *130*, 2596–2606.

Lee, H.Y., Mohammed, K.A., Peruvemba, S., Goldberg, E.P., and Nasreen, N. (2011). Targeted lung cancer therapy using ephrinA1-loaded albumin microspheres. J. Pharm. Pharmacol. *63*, 1401–1410.

Lee, J., Son, M.J., Woolard, K., Donin, N.M., Li, A., Cheng, C.H., Kotliarova, S., Kotliarov, Y., Walling, J., Ahn, S., et al. (2008). Epigenetic-mediated dysfunction of the bone morphogenetic protein pathway inhibits differentiation of glioblastoma-initiating cells. Cancer Cell *13*, 69–80.

Li, X., Wang, L., Gu, J.W., Li, B., Liu, W.P., Wang, Y.G., Zhang, X., Zhen, H.N., and Fei, Z. (2010). Up-regulation of EphA2 and down-regulation of EphrinA1 are associated with the aggressive phenotype and poor prognosis of malignant glioma. Tumour Biol. *31*, 477–488.

Ligon, K.L., Huillard, E., Mehta, S., Kesari, S., Liu, H., Alberta, J.A., Bachoo, R.M., Kane, M., Louis, D.N., Depinho, R.A., et al. (2007). Olig2-regulated lineage-restricted pathway controls replication competence in neural stem cells and malignant glioma. Neuron *53*, 503–517.

Liu, D.P., Wang, Y., Koeffler, H.P., and Xie, D. (2007). Ephrin-A1 is a negative regulator in glioma through down-regulation of EphA2 and FAK. Int. J. Oncol. *30*, 865–871.

Liu, F., Park, P.J., Lai, W., Maher, E., Chakravarti, A., Durso, L., Jiang, X., Yu, Y., Brosius, A., Thomas, M., et al. (2006). A genome-wide screen reveals functional gene clusters in the cancer genome and identifies EphA2 as a mitogen in glioblastoma. Cancer Res. *66*, 10815–10823.

Maher, E.A., Furnari, F.B., Bachoo, R.M., Rowitch, D.H., Louis, D.N., Cavenee, W.K., and DePinho, R.A. (2001). Malignant glioma: genetics and biology of a grave matter. Genes Dev. *15*, 1311–1333.

Miao, H., and Wang, B. (2012). EphA receptor signaling—complexity and emerging themes. Semin. Cell Dev. Biol. *23*, 16–25.

Miao, H., Li, D.Q., Mukherjee, A., Guo, H., Petty, A., Cutter, J., Basilion, J.P., Sedor, J., Wu, J., Danielpour, D., et al. (2009). EphA2 mediates ligand-dependent inhibition and ligand-independent promotion of cell migration and invasion via a reciprocal regulatory loop with Akt. Cancer Cell *16*, 9–20.

Nakada, M., Hayashi, Y., and Hamada, J. (2011). Role of Eph/ephrin tyrosine kinase in malignant glioma. Neuro-oncol. *13*, 1163–1170.

Network, C.G.A.R.; Cancer Genome Atlas Research Network. (2008). Comprehensive genomic characterization defines human glioblastoma genes and core pathways. Nature *455*, 1061–1068.

Noblitt, L.W., Bangari, D.S., Shukla, S., Knapp, D.W., Mohammed, S., Kinch, M.S., and Mittal, S.K. (2004). Decreased tumorigenic potential of EphA2-overexpressing breast cancer cells following treatment with adenoviral vectors that express EphrinA1. Cancer Gene Ther. *11*, 757–766.

Pasquale, E.B. (2010). Eph receptors and ephrins in cancer: bidirectional signalling and beyond. Nat. Rev. Cancer *10*, 165–180.

Piccirillo, S.G., Reynolds, B.A., Zanetti, N., Lamorte, G., Binda, E., Broggi, G., Brem, H., Olivi, A., Dimeco, F., and Vescovi, A.L. (2006). Bone morphogenetic proteins inhibit the tumorigenic potential of human brain tumour-initiating cells. Nature *444*, 761–765.

Piccirillo, S.G., Combi, R., Cajola, L., Patrizi, A., Redaelli, S., Bentivegna, A., Baronchelli, S., Maira, G., Pollo, B., Mangiola, A., et al. (2009). Distinct pools of cancer stem-like cells coexist within human glioblastomas and display different tumorigenicity and independent genomic evolution. Oncogene *28*, 1807–1811.

Ponti, D., Costa, A., Zaffaroni, N., Pratesi, G., Petrangolini, G., Coradini, D., Pilotti, S., Pierotti, M.A., and Daidone, M.G. (2005). Isolation and in vitro propagation of tumorigenic breast cancer cells with stem/progenitor cell properties. Cancer Res. *65*, 5506–5511.

Ricci-Vitiani, L., Fabrizi, E., Palio, E., and De Maria, R. (2009). Colon cancer stem cells. J. Mol. Med. *87*, 1097–1104.

Rietze, R.L., and Reynolds, B.A. (2006). Neural stem cell isolation and characterization. Methods Enzymol. *419*, 3–23.

Singer, J.D., and Willett, J.B. (2003). Applied Longitudinal Data Analysis: Modeling Change and Event Occurrence (Oxford: Oxford University Press).

Squatrito, M., Brennan, C.W., Helmy, K., Huse, J.T., Petrini, J.H., and Holland, E.C. (2010). Loss of ATM/Chk2/p53 pathway components accelerates tumor development and contributes to radiation resistance in gliomas. Cancer Cell *18*, 619–629.

Sukhdeo, K., Hambardzumyan, D., and Rich, J.N. (2011). Glioma development: where did it all go wrong? Cell *146*, 187–188.

Takebe, N., Harris, P.J., Warren, R.Q., and Ivy, S.P. (2011). Targeting cancer stem cells by inhibiting Wnt, Notch, and Hedgehog pathways. Nat. Rev. Clin. Oncol. *8*, 97–106.

Verhaak, R.G., Hoadley, K.A., Purdom, E., Wang, V., Qi, Y., Wilkerson, M.D., Miller, C.R., Ding, L., Golub, T., Mesirov, J.P., et al.; Cancer Genome Atlas Research Network. (2010). Integrated genomic analysis identifies clinically relevant subtypes of glioblastoma characterized by abnormalities in PDGFRA, IDH1, EGFR, and NF1. Cancer Cell *17*, 98–110.

Vescovi, A.L., Galli, R., and Reynolds, B.A. (2006). Brain tumour stem cells. Nat. Rev. Cancer *6*, 425–436.

Wang, L.F., Fokas, E., Bieker, M., Rose, F., Rexin, P., Zhu, Y., Pagenstecher, A., Engenhart-Cabillic, R., and An, H.X. (2008). Increased expression of EphA2 correlates with adverse outcome in primary and recurrent glioblastoma multiforme patients. Oncol. Rep. *19*, 151–156.

Wu, N., Zhao, X., Liu, M., Liu, H., Yao, W., Zhang, Y., Cao, S., and Lin, X. (2011). Role of microRNA-26b in glioma development and its mediated regulation on EphA2. PLoS ONE *6*, e16264.

Wykosky, J., and Debinski, W. (2008). The EphA2 receptor and ephrinA1 ligand in solid tumors: function and therapeutic targeting. Mol. Cancer Res. *6*, 1795–1806.

Wykosky, J., Gibo, D.M., Stanton, C., and Debinski, W. (2005). EphA2 as a novel molecular marker and target in glioblastoma multiforme. Mol. Cancer Res. *3*, 541–551.

Wykosky, J., Palma, E., Gibo, D.M., Ringler, S., Turner, C.P., and Debinski, W. (2008). Soluble monomeric EphrinA1 is released from tumor cells and is a functional ligand for the EphA2 receptor. Oncogene *27*, 7260–7273.

Ying, M., Wang, S., Sang, Y., Sun, P., Lal, B., Goodwin, C.R., Guerrero-Cazares, H., Quinones-Hinojosa, A., Laterra, J., and Xia, S. (2011). Regulation of glioblastoma stem cells by retinoic acid: role for Notch pathway inhibition. Oncogene *30*, 3454–3467.

Zhang, Q.B., Ji, X.Y., Huang, Q., Dong, J., Zhu, Y.D., and Lan, Q. (2006). Differentiation profile of brain tumor stem cells: a comparative study with neural stem cells. Cell Res. *16*, 909–915.

Zheng, H., Ying, H., Yan, H., Kimmelman, A.C., Hiller, D.J., Chen, A.J., Perry, S.R., Tonon, G., Chu, G.C., Ding, Z., et al. (2008). p53 and Pten control neural and glioma stem/progenitor cell renewal and differentiation. Nature *455*, 1129–1133.

EMT and MET in Metastasis: Where Are the Cancer Stem Cells?

Thomas Brabletz[1,*]
[1]Department of General and Visceral Surgery, Comprehensive Cancer Center and BIOSS Centre for Biological Signalling Studies, University of Freiburg Medical Center, Hugstetter Str. 55, 79106 Freiburg, Germany
*Correspondence: thomas.brabletz@uniklinik-freiburg.de
http://dx.doi.org/10.1016/j.ccr.2012.11.009

Activation of epithelial-mesenchymal transition (EMT) is important for cancer cell dissemination. Two papers in this issue of *Cancer Cell* (Ocaña and colleagues and Tsai and colleagues) support the concept that the reversal of EMT is necessary for efficient metastatic colonization. Moreover, although EMT has been associated with stemness properties, one study indicates that they are not necessarily linked.

Metastasis is responsible for more than 90% of cancer associated mortality; therefore, the clinical need to prevent or target metastasis is great. For distant metastasis, primary tumor cells must invade, disseminate through blood vessels, seed at the distant site, and colonize to macrometastases. De-differentiation through aberrant activation of the embryonic program "epithelial-mesenchymal transition" (EMT) was shown to strongly enhance cancer cell motility and dissemination (Thiery et al., 2009). Moreover, gene expression patterns in human cancers indicated that de-differentiated cancer cells combine EMT properties with a stem-cell like phenotype, leading to the concept of "migrating cancer stem cells" as the basis of metastasis (Brabletz et al., 2005). A direct molecular link between EMT and stemness was demonstrated by seminal findings that EMT activators, such as Twist1, can co-induce EMT and stemness properties (Mani et al., 2008; Morel et al., 2008), thereby linking the EMT and cancer stem cell concept (Dalerba et al., 2007). However, metastases of the most common human cancers (well- to moderately-differentiated carcinomas) often show a re-differentiation in the sense of a mesenchymal-epithelial (re-)transition (MET). Consequently, transient de-differentiation (EMT)- re-differentiation (MET) processes were proposed to be a driving force of metastasis (Brabletz et al., 2001). But why do metastases re-differentiate? Invasive, de-differentiated cancer cells were shown to be growth arrested, and proliferation was detected in re-differentiated metastasis, leading to the proposal that EMT must be reversed in order to allow growth and colonization (Brabletz et al., 2001). This is supported by the fact that EMT-inducing transcription factors can directly inhibit proliferation (Thiery et al., 2009). Although many clinical reports fostered the concept of transient EMT-MET switches in metastasis, there are only a few experimental proofs (e.g., Chaffer et al., 2006; Korpal et al., 2011). Two papers in this issue of *Cancer Cell* support the role of an EMT in dissemination and the need of a MET for efficient metastasis.

In the first report, Tsai et al. (2012, in this issue of *Cancer Cell*) used an elegant mouse model for skin cancer in which metastatic squamous cell carcinomas were induced by topic application of the carcinogens DBMA and TPA and the expression of Twist1 was selectively induced in keratinocytes by docycycline. Oral application of doxycycline induced Twist1 in all cancer cells, irrespective of their localization (primary tumor, circulating or disseminated tumor cells, or metastasis), therefore modeling "irreversible" Twist1/EMT activation. In contrast, topical application of doxycycline only induced Twist1 in the primary skin tumors, and Twist1 expression is shut down in disseminated tumor cells ("reversible" Twist1/EMT activation). Twist1 activation in both conditions (compared to uninduced controls) increased the number of circulating tumor cells and tumor cells extravasated to the lung, supporting the role of EMT in dissemination. However, the number of metastases in the "reversible" Twist1-model was higher than that in the "irreversible" Twist1-model. Moreover, the authors demonstrated that downregulation of Twist1 in metastases was associated with increased proliferation and reversal of an EMT-associated growth arrest. In summary, this study clearly supports the role of an EMT in dissemination and the necessity of a subsequent MET for colonization and macrometastasis (Figure 1A). Twist1 downregulation was shown to be important to overcome EMT-associated growth arrest, but reactivation of proliferation is likely not the only reason for a MET in metastasis. Recently, it was shown that, while re-differentiation induced by expression of miR-200 is required for metastatic colonization in a xenograft model, miR-200 also directly targets SEC23A, which stimulates the secretion of metastasis-suppressive proteins (Korpal et al., 2011).

The second study by Ocana et al. (2012, in this issue of *Cancer Cell*) also supports the role of EMT for dissemination and the necessity to revert EMT for metastasis. But, surprisingly, the features of the newly discovered EMT activator "paired-related homeobox transcription factor 1" (Prrx1) make the underlying molecular links more complex. In contrast to other EMT-activators, Prrx1 suppresses stemness traits, raising again the questions of where and which are the cancer stem cells. The authors detected Prrx1 as an additional EMT inducer activating delamination from the primitive streak in chicken embryos. Prrx1 is coexpressed and cooperates with Twist1 in inducing all EMT features relevant for

dissemination, such as migration and invasion. In a xenograft model using human BT-549 breast cancer cells (coexpressing Prrx1 and Twist1), a knockdown of both factors (but not of Twist1 alone!) increased lung metastasis after tail vein injection, but not in an orthotopic setting. Importantly, in contrast to the study by Tsai et al. (2012), depletion of Twist1 alone had no effect, indicating that Prrx1 is not only cooperating with Twist1, but is also dominating its function. The big surprise came when the authors analyzed stemness and tumor-initiating features: Prrx1 decreased stemness features and knockdown of Prrx1 in BT-549-increased mammosphere formation, self renewal capacity, and the fraction of $CD24^{low}/CD44^{high}$ cancer stem cells. Of note, increased stemness was associated with maintained proliferation capacity. This is in contrast to stemness induced by other EMT activators (Twist1 alone, Snail1, Snail2, and ZEB1), which are associated with a growth arrest. Strikingly, the presence of Twist1 was not necessary for the stemness features, because combined depletion of both Prrx1 and Twist1 had the same effect. Conversely, overexpression of Prxx1 in another undifferentiated breast cancer cell line MDA-MB-231 (expressing ZEB1 but neither Prrx1 nor Twist) also suppressed stemness features, indicating that ZEB1-associated stemness can also be inhibited. Finally, by analyzing published data sets, the authors could show that high expression of Prrx1 (often associated with Twist1 expression) in breast and the squamous type of lung cancer is associated with a good prognosis and increased metastasis-free survival. These results are of high relevance for cancer biology because they not only support the model of an EMT/MET switch in metastasis, but they also identify a potentially new mechanism allowing metastatic colonization by uncoupling stemness from EMT and growth arrest in favor of a parallel maintenance of a stemness, MET, and proliferation phenotype (Figure 1B). In this context, the study mechanistically supports a concept where cancer stem cells either can be embedded in the epithelial mass of benign precoursors, primary tumors, or metastases (stationary cancer stem cells) or linked to EMT/motility in invading, disseminating, growth-arrested tumor cells (migrating cancer stem cells) initially proposed from the analyses of colon cancer (Brabletz et al., 2005) (Figure 1).

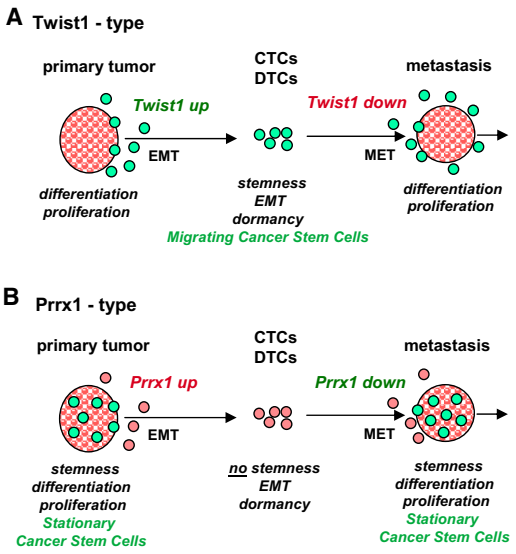

Figure 1. EMT and MET in Metastasis: Where Are the Cancer Stem Cells?

Models and consequences deduced from the papers by Tsai et al. (2012) and by Ocana et al. (2012) are shown.

(A) Data by Tsai et al. (2012) support the concept that upregulation of an EMT activator (e.g., Twist1) in invasive cells of the primary tumor induces dissemination. A downregulation of the EMT inducer and a subsequent redifferentiation (MET) at the distant site is necessary to allow colonization and macrometastasis. Because Twist1 also induces stemness properties and a growth arrest, putative cancer stem cells are mobile but nonproliferating (migrating cancer stem cells; green indicates stemness phenotype and activation).

(B) The EMT activator Prrx1, newly identified by Ocana et al. (2012), suppresses stemness properties in the EMT and dissemination state. Prrx1 must be downregulated to activate stemness properties and allow colonization. Thus, putative cancer stem cells are not mobile but embedded in the epithelial tumor mass both in the primary tumor and metastases (stationary cancer stem cells). Both types of metastasis require an EMT for dissemination and a MET for colonization. The most important difference is that in the Prrx1-type EMT, growth arrest and stemness are uncoupled, favoring the parallel maintenance of a MET, proliferation, and stemness phenotype.

However, these data on Prxx1 raise a lot of new questions, particularly in the context of publications on Twist1, e.g., by Tsai et al. (2012).

How do Twist and Prrx1 interact at a molecular level and how does Prrx1 inhibit the stemness-inducing but not the EMT-inducing function of Twist1 (and potentially other EMT inducers like Snail1 and ZEB1)?

How does the loss of Prrx1 induce stemness in (re-)differentiated epithelial cancer cells, which also downregulate Twist1?

What is the role of Prxx1 in physiological stem cell biology? Does it distinguish between stationary and migrating stem cells? Are these mutually exclusive modes of stemness? Is the Twist1-mode or the Prrx1-mode (Figure 1) more relevant for human cancer metastasis?

In which (cancer) cells and tissues is Prrx1 expressed and potentially controlling other EMT inducers (see BT549 versus MDA-MB-231; different areas during primitive streak delamination)?

In summary, both papers experimentally support the need of a re-differentiation (MET) for the colonization and metastasis of differentiated carcinomas and show that one reason is the EMT-associated growth arrest. This has a clinical impact for future therapeutic strategies against metastasis. Inducing differentiation and targeting EMT alone might be counterproductive by activating proliferation of disseminated cells; it should be combined with therapy against cycling cells, e.g., with a standard chemotherapy. In addition, inhibiting MET, thereby maintaining dormancy and/or directly targeting the stem cell phenotype, wherever it is located, could be a promising strategy.

ACKNOWLEDGMENTS

T.B. is funded by the Deutsche Forschungsgemeinschaft (SFB850/B2, SFB992/C06 and DFG BR1399/6-1).

REFERENCES

Brabletz, T., Jung, A., Reu, S., Porzner, M., Hlubek, F., Kunz-Schughart, L.A., Knuechel, R., and Kirchner, T. (2001). Proc. Natl. Acad. Sci. USA *98*, 10356–10361.

Brabletz, T., Jung, A., Spaderna, S., Hlubek, F., and Kirchner, T. (2005). Nat. Rev. Cancer *5*, 744–749.

Chaffer, C.L., Brennan, J.P., Slavin, J.L., Blick, T., Thompson, E.W., and Williams, E.D. (2006). Cancer Res. *66*, 11271–11278.

Dalerba, P., Cho, R.W., and Clarke, M.F. (2007). Annu. Rev. Med. *58*, 267–284.

Korpal, M., Ell, B.J., Buffa, F.M., Ibrahim, T., Blanco, M.A., Celià-Terrassa, T., Mercatali, L., Khan, Z., Goodarzi, H., Hua, Y., et al. (2011). Nat. Med. *17*, 1101–1108.

Mani, S.A., Guo, W., Liao, M.-J., Eaton, E.N., Ayyanan, A., Zhou, A.Y., Brooks, M., Reinhard, F., Zhang, C.C., Shipitsin, M., et al. (2008). Cell *133*, 704–715.

Morel, A.P., Lièvre, M., Thomas, C., Hinkal, G., Ansieau, S., and Puisieux, A. (2008). PLoS ONE *3*, e2888.

Ocana, O.H., Corcoles, R., Fabra, A., Moreno-Bueno, G., Acloque, H., Vega, S., Barrallo-Gimeno, A., Cano, A., and Nieto, M.A. (2012). Cancer Cell *22*, this issue, 709–724.

Thiery, J.P., Acloque, H., Huang, R.Y., and Nieto, M.A. (2009). Epithelial-mesenchymal transitions in development and disease. Cell *139*, 871–890.

Tsai, J.H., Donaher, J.L., Murphy, D.A., Chau, S., and Yang, J. (2012). Cancer Cell *22*, this issue, 725–736.

Disputed Paternity: The Uncertain Ancestry of Pancreatic Ductal Neoplasia

Anirban Maitra[1,3] and Steven D. Leach[2,3,*]
[1]Department of Pathology
[2]Department of Surgery and the McKusick-Nathans Institute of Genetic Medicine
[3]The Sol Goldman Center for Pancreatic Cancer Research
Johns Hopkins University, Baltimore, MD 21205, USA
*Correspondence: stleach@jhmi.edu
http://dx.doi.org/10.1016/j.ccr.2012.11.015

In this issue of *Cancer Cell*, Kopp and colleagues report that pancreatic ductal cells are largely refractory to the induction of pancreatic neoplasia. Whereas a rare ductal subpopulation may still prove capable of neoplastic transformation, these findings refocus attention on acinar and other non-ductal cell types as initiators of this deadly neoplasm.

While malignant tumors of the pancreas can display a variety of histologic forms, the term "pancreatic cancer" is usually synonymous with a pathological diagnosis of pancreatic ductal adenocarcinoma (PDAC). As its name implies, PDAC has long been presumed to arise from pancreatic ductal epithelial cells. Along with its noninvasive precursor, pancreatic intraepithelial neoplasia (PanIN), these tumors typically display a distinctly duct-like histology, and express markers of ductal differentiation. As demonstrated for other tumor types, however, tumor histology is often misleading in determining tumor lineage, and work from Kopp et al. (2012) published in this issue of *Cancer Cell* reinforces the disputed paternity of pancreatic "ductal" neoplasia.

Initial clues suggesting that non-ductal cells might serve as effective cells of origin for pancreatic ductal neoplasia were provided by studies involving transgenic misexpression of individual oncogenes under the regulation of non-ductal promoter elements, in which a subset of resulting tumors displayed histologic resemblance to adult ductal epithelium (Sandgren et al., 1991). However, these similarities were ultimately proven to be only skin-deep, as additional studies of PanIN and PDAC revealed activation of transcriptional programs typically observed in embryonic pancreatic epithelium, but not in differentiated duct cells (Miyamoto et al., 2003; Park et al., 2011).

With the advent of autochthonous mouse models of pancreatic neoplasia, more recent studies have interrogated individual pancreatic cell types for the ability to generate PanIN, based upon Cre/lox-mediated activation of oncogenic *Kras*. Initial seminal work in this arena utilized either *Pdx1*^{Cre} or *Ptf1a*^{Cre} alleles to activate *Kras* in embryonic pancreatic progenitor cells (Aguirre et al., 2003; Hingorani et al., 2003). While these studies demonstrated that embryonic activation of oncogenic *Kras* effectively initiated pancreatic ductal neoplasia, they provided considerably less information regarding the capacity of individual adult cell lineages to similarly serve as effective cells of origin. Based on the availability of appropriate Cre driver lines, this adult capacity was first interrogated in pancreatic acinar cells. Using either a Nestin-Cre driver to activate oncogenic *Kras* in exocrine progenitor cells and their acinar cell descendants (Carrière et al., 2007) or a variety of inducible Cre lines to activate *Kras* in adult acinar cells (De La O et al., 2008; Guerra et al., 2007; Habbe et al., 2008), these studies provided strong evidence that acinar cells could indeed serve as effective biologic parents for pancreatic ductal neoplasia. In these studies, the ability of adult acinar cells to generate PanIN was dramatically accelerated in the context of associated pancreatitis, a known risk factor for the human disease. Additional studies suggested that a permissive inflammatory microenvironment could broadly bestow PanIN-parenting capabilities, as even insulin-expressing cells

A New "Brew" of MALT1 Inhibitors

Ryan M. Young[1] and Louis M. Staudt[1,*]
[1]Metabolism Branch, Center for Cancer Research, National Cancer Institute, National Institutes of Health, 9000 Rockville Pike, Bethesda, MD 20892, USA
*Correspondence: lstaudt@mail.nih.gov
http://dx.doi.org/10.1016/j.ccr.2012.11.011

The activated B cell-like (ABC) subtype of diffuse large B cell lymphoma (DLBCL) is an aggressive lymphoma that is addicted to NF-κB signaling through the CARD11-BCL10-MALT1 complex. In this issue of *Cancer Cell*, Nagel and colleagues and Fontan and colleagues describe MALT1 inhibitors suitable for clinical use that are selectively toxic to this malignancy.

Aberrant activation of NF-κB is a feature shared by many human lymphomas due to the ability of NF-κB to promote tumor survival. In particular, constitutive NF-κB activity is a hallmark of the ABC DLBCL subtype. This DLBCL subtype is the most recalcitrant to current immunochemotherapy regimens, due in part to the anti-apoptotic properties of NF-κB activity. Hence, targeted therapeutic agents that shut down NF-κB in ABC DLBCL are urgently needed.

ABC DLBCL tumors subvert normal B cell signaling pathways to activate NF-κB by acquiring somatic mutations that activate and/or amplify their signaling output (Figure 1). An RNA interference screen identified a central role for CARD11, BCL10, and MALT1 in the pathogenesis of ABC DLBCL cell lines (Ngo et al., 2006). These three signaling effectors form the "CBM" complex, which serves as a signaling scaffold that recruits TRAF6, TAK1, and the IKK complex to activate the IκB kinase β (IKKβ) and stimulate NF-κB through the "classical" pathway. In 10% of ABC DLBCL cases, somatic mutations affecting the coiled-coil domain of CARD11 spontaneously induce the formation of the CBM complex and NF-κB activity (Lenz et al., 2008). Other ABC DLBCL lymphomas lack CARD11 mutations but, nevertheless, rely upon wild-type CARD11 to activate NF-κB and sustain survival (Ngo et al., 2006). These ABC DLBCL tumors rely upon a "chronic active" form of BCR signaling to engage CARD11 and the NF-κB pathway (Davis et al., 2010). ABC DLBCLs with wild-type CARD11 die upon knockdown or pharmacologic inhibition of any component of the BCR signaling cascade (Davis et al., 2010). Recurrent mutations in the BCR subunits CD79B and CD79A occur in roughly one fifth of ABC DLBCL cases, providing genetic evidence that chronic active BCR signaling is important in ABC DLBCL pathogenesis (Davis et al., 2010).

BCR pathway inhibitors are currently being investigated in clinical trials to evaluate their efficacy against ABC DLBCL and other forms of B cell lymphoma. These inhibitors chiefly target either BCR proximal kinases, such as BTK and SYK, or the phosphatidylinositol 3-kinase pathway that emanates from the BCR. Promising responses have been observed, including complete and partial responses to the BTK inhibitor ibrutinib in ABC DLBCL. However, experiments in cell lines suggest that these upstream BCR pathway inhibitors will be unable to treat tumors that harbor oncogenic CARD11 mutations, necessitating alternative therapies for these patients.

The recently described proteolytic activity of MALT1 provides a new target for therapeutic development (reviewed in McAllister-Lucas et al., 2011). The caspase-like domain of MALT1 cleaves substrates following arginine residues, unlike conventional caspase that cleave after aspartate residues. MALT1 cleaves and disables A20 (TNFAIP3) and CYLD, both negative regulators of NF-κB, thereby potentiating NF-κB signaling. Based on these results in normal lymphocytes, two groups demonstrated that MALT protease activity is required for NF-κB activity and survival of ABC DLBCL cells (Ferch et al., 2009; Hailfinger et al., 2009). A peptide inhibitor of MALT1 paracaspase activity was toxic to ABC DLBCL cell lines, but not to models of other lymphoma subtypes. In theory, MALT1 should make an excellent therapeutic target. First, MALT1 knockout mice are defective in T and B cell activation but are otherwise healthy. Second, the paracaspase domain of MALT1 is unique within the human genome, suggesting that a MALT1 inhibitor might not cause significant off-target side effects.

In this issue of *Cancer Cell*, Nagel et al. (2012) and Fontan et al. (2012) report the discovery of small molecule inhibitors of MALT1 that represent a new class of lymphoma therapeutics. Both studies utilized in vitro MALT1 protease assays in high-throughput screens of small molecule libraries, yielding inhibitors of MALT1 activity at low micromolar concentrations in vitro. In a library of drugs approved for human use, Nagel et al. (2012) identified three phenothiazines, a class of antipsychotic drugs, which inhibit MALT1 paracaspase activity and kill ABC DLBCL cells. The doses necessary to inhibit the growth of ABC DLBCL xenografts were equivalent to those achieved when humans are given these drugs, suggesting that they could be used off-label in clinical trials soon. While phenothizines may be tolerated for short term chemotherapy, their long-term use will be limited by the already known side effects characteristic of this drug class, for example tardive dyskinesia. Fontan et al. (2012) discovered a novel small molecule, termed MI-2, that notably inhibited MALT1 by forming a covalent linkage in the active site. Although traditional drug development has shied away from irreversible inhibitors because of potential crossreactivity and immunogenicity, they afford outstanding pharmacodynamic properties. Indeed, the hepatitis C NS3/4A protease inhibitor Telaprevir and the proteasome inhibitor Carfilzomib are both irreversible. Likewise, the unusual potency of ibrutinib in many lymphoid

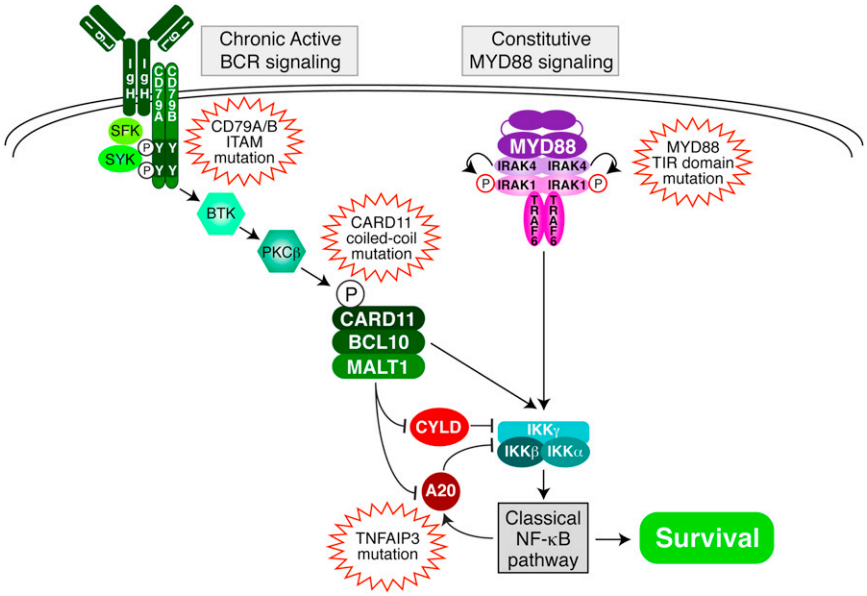

Figure 1. Role of MALT1 in Signaling to NF-κB in ABC DLBCL
Two prominent pathways leading to NF-κB activation in ABC DLBCL are shown: chronic active BCR signaling and constitutive MYD88 signaling. MALT1 plays a key role in the BCR pathway in two ways. First, as a component of the CBM complex with CARD11 and BCL10, MALT1 helps recruit and activate IκB kinase (IKK). Second, MALT1 protease activity potentiates NF-κB signaling by cleaving and inactivating two negative regulators of IKK, A20 (TNFAIP3), and CYLD. Recurrent mutations in ABC DLBCL tumors that cause or intensify NF-κB activity are shown.

malignancies may be due to its covalent attachment to BTK. While MI-2 is a lead compound that may require further optimization, it is notable that mice treated with MI-2 did not have detectable physiological, histological, or biochemical signs of toxicity.

Clinical trials with correlative studies will be needed to determine the lymphoma phenotypes and genotypes that are best suited to MALT1-directed therapy. While the BCR pathway inhibitor ibrutinib is showing promising activity in clinical trials, it is too early to know what mechanisms of resistance may develop. From this perspective, we cannot really have too many targeted therapies, especially ones that have few if any side effects. An important niche not addressed by the BCR pathway inhibitors would be the ~10% of ABC DLBCL tumors with CARD11 mutations. MALT1 inhibitors might also be potentially useful in some cases of germinal center B cell-like (GCB) subtype of DLBCL, since CARD11 mutations occur in ≈5% of these tumors and are associated with elevated NF-κB activity compared to the majority of GCB DLBCLs (Lenz et al., 2008). Gastric MALT lymphomas with a t(11;18) translocation may be another venue because this translocation creates a fusion oncoprotein composed of protein interaction domains from c-IAP2 and the MALT1 paracaspase domain that is proteolytically active (McAllister-Lucas et al., 2011). Germline CARD11 coiled-coil domain mutations have recently been identified in families with a congenital B lymphocytosis, which can progress to chronic lymphocytic leukemia. MALT1 inhibitors could prove useful in this setting if they can be tolerated long-term without side effects (Snow et al., 2012). Finally, it should be noted that a second prominent signaling pathway can activate NF-κB in ABC DLBCL via the signaling adaptor MYD88. Recurrent somatic mutations of MYD88 occur in 39% of ABC DLBCLs, with one particularly potent point mutant, MYD88 L265P, occurring in 29% of cases (Ngo et al., 2011). Some ABC DLBCLs have both MYD88 L265P and CD79B mutations (Ngo et al., 2011), and cell line models of such cases rely on MALT1 for survival (Fontan et al., 2012). However, other ABC DLBCLs only have MYD88 mutations and are not dependent upon BCR signaling (Ngo et al., 2011), and these do not respond to MALT1 inhibition (Fontan et al., 2012). Thus, the optimum deployment of MALT1 inhibitors awaits a precise definition of which ABC DLBCL tumors rely upon BCR signaling through MALT1 for survival.

REFERENCES

Davis, R.E., Ngo, V.N., Lenz, G., Tolar, P., Young, R.M., Romesser, P.B., Kohlhammer, H., Lamy, L., Zhao, H., Yang, Y., et al. (2010). Nature *463*, 88–92.

Ferch, U., Kloo, B., Gewies, A., Pfänder, V., Düwel, M., Peschel, C., Krappmann, D., and Ruland, J. (2009). J. Exp. Med. *206*, 2313–2320.

Fontan, L., Yang, C., Kabeleeswaran, V., Volpon, L., Osborne, M.J., Beltran, E., Garcia, M., Cerchietti, L., Shaknovich, R., Yang, S.N., et al. (2012). Cancer Cell *22*, this issue, 812–824.

Hailfinger, S., Lenz, G., Ngo, V., Posvitz-Fejfar, A., Rebeaud, F., Guzzardi, M., Penas, E.M., Dierlamm, J., Chan, W.C., Staudt, L.M., and Thome, M. (2009). Proc. Natl. Acad. Sci. USA *106*, 19946–19951.

Lenz, G., Davis, R.E., Ngo, V.N., Lam, L., George, T.C., Wright, G.W., Dave, S.S., Zhao, H., Xu, W., Rosenwald, A., et al. (2008). Science *319*, 1676–1679.

McAllister-Lucas, L.M., Baens, M., and Lucas, P.C. (2011). Clin. Cancer Res. *17*, 6623–6631.

Nagel, D., Spranger, S., Vincendeau, M., Grau, M., Raffegerst, S., Kloo, B., Hlahla, D., Neuenschwander, M., von Kries, J.P., Hadian, K., et al. (2012). Cancer Cell *22*, this issue, 825–837.

Ngo, V.N., Davis, R.E., Lamy, L., Yu, X., Zhao, H., Lenz, G., Lam, L.T., Dave, S., Yang, L., Powell, J., and Staudt, L.M. (2006). Nature *441*, 106–110.

Ngo, V.N., Young, R.M., Schmitz, R., Jhavar, S., Xiao, W., Lim, K.H., Kohlhammer, H., Xu, W., Yang, Y., Zhao, H., et al. (2011). Nature *470*, 115–119.

Snow, A.L., Xiao, W., Stinson, J.R., Lu, W., Chaigne-Delalande, B., Zheng, L., Pittaluga, S., Matthews, H.F., Schmitz, R., Jhavar, S., et al. (2012). J. Exp. Med. *209*, 2247–2261.

metaplasia (ADM) do, indeed, harbor *KRAS* mutations identical to those observed in adjacent PanIN (Shi et al., 2009). These findings might be consistent with *KRAS* mutations arising in either acinar cells themselves or in areas of ADM, with subsequent rapid progression to PanIN.

Assuming that these findings are indeed relevant to the human disease, what are the ramifications of the current findings? Certainly, they suggest that future chemoprevention strategies might be best targeted at early events in acinar rather than ductal cells; blocking acinar cell activation of *Sox9* now joins Notch pathway inhibition and maintenance of *Mist1* expression as examples of such approaches. In addition, these findings underscore an increasingly recognized disconnect between *Kras* mutations and Kras activity. Along these lines, it will be fascinating to determine the presumably epigenetic determinants underlying the differential responsiveness to oncogenic *Kras* observed in acinar and ductal cell types; manipulating such determinants may convert acinar cells into less capable parents, hopefully eliminating PanIN from the pancreatic family tree.

REFERENCES

Aguirre, A.J., Bardeesy, N., Sinha, M., Lopez, L., Tuveson, D.A., Horner, J., Redston, M.S., and DePinho, R.A. (2003). Genes Dev. *17*, 3112–3126.

Carrière, C., Seeley, E.S., Goetze, T., Longnecker, D.S., and Korc, M. (2007). Proc. Natl. Acad. Sci. USA *104*, 4437–4442.

De La O, J.P., Emerson, L.L., Goodman, J.L., Froebe, S.C., Illum, B.E., Curtis, A.B., and Murtaugh, L.C. (2008). Proc. Natl. Acad. Sci. USA *105*, 18907–18912.

Gidekel Friedlander, S.Y., Chu, G.C., Snyder, E.L., Girnius, N., Dibelius, G., Crowley, D., Vasile, E., DePinho, R.A., and Jacks, T. (2009). Cancer Cell *16*, 379–389.

Guerra, C., Schuhmacher, A.J., Cañamero, M., Grippo, P.J., Verdaguer, L., Pérez-Gallego, L., Dubus, P., Sandgren, E.P., and Barbacid, M. (2007). Cancer Cell *11*, 291–302.

Habbe, N., Shi, G., Meguid, R.A., Fendrich, V., Esni, F., Chen, H., Feldmann, G., Stoffers, D.A., Konieczny, S.F., Leach, S.D., and Maitra, A. (2008). Proc. Natl. Acad. Sci. USA *105*, 18913–18918.

Hingorani, S.R., Petricoin, E.F., Maitra, A., Rajapakse, V., King, C., Jacobetz, M.A., Ross, S., Conrads, T.P., Veenstra, T.D., Hitt, B.A., et al. (2003). Cancer Cell *4*, 437–450.

Kopp, J.L., von Figura, G., Mayes, E., Liu, F.F., Dubois, C.L., Morris, J.P., Pan, F.C., Akiyama, H., Wright, C.V.E., Jensen, K., et al. (2012). Cancer Cell *22*, this issue, 737–750.

Miyamoto, Y., Maitra, A., Ghosh, B., Zechner, U., Argani, P., Iacobuzio-Donahue, C.A., Sriuranpong, V., Iso, T., Meszoely, I.M., Wolfe, M.S., et al. (2003). Cancer Cell *3*, 565–576.

Park, J.Y., Hong, S.M., Klimstra, D.S., Goggins, M.G., Maitra, A., and Hruban, R.H. (2011). Appl. Immunohistochem. Mol. Morphol. *19*, 444–449.

Sandgren, E.P., Quaife, C.J., Paulovich, A.G., Palmiter, R.D., and Brinster, R.L. (1991). Proc. Natl. Acad. Sci. USA *88*, 93–97.

Shi, C., Hong, S.M., Lim, P., Kamiyama, H., Khan, M., Anders, R.A., Goggins, M., Hruban, R.H., and Eshleman, J.R. (2009). Mol. Cancer Res. *7*, 230–236.

Chemokine to the Rescue: Interleukin-8 Mediates Resistance to PI3K-Pathway-Targeted Therapy in Breast Cancer

Robert T. Abraham[1,*]
[1]Oncology Research, Pfizer Worldwide Research and Development, 10777 Science Center Drive, CB3/1376, San Diego, CA 92121, USA
*Correspondence: robert.abraham@pfizer.com
http://dx.doi.org/10.1016/j.ccr.2012.11.012

Adaptive resistance to PI3K-mTOR inhibitors potentially limits the clinical antitumor activities of these agents. In this issue of *Cancer Cell*, Britschgi and coworkers show that certain tumors acquire resistance to PI3K-mTOR inhibitors through activation of a JAK2-dependent pathway, leading to interleukin-8 secretion.

More than 25 years have passed since the discovery of phosphoinositide 3-kinase (PI3K) as an oncoprotein-associated enzymatic activity. The term "PI3K" in this context designates the Class I subset of phosphoinositide kinases (comprising the α, β, γ, and δ isoforms), which convert phosphatidylinositol-4,5-bisphosphate to the bioactive second messenger phosphatidylinositol-3,4,5-trisphosphate (Vanhaesebroeck et al., 2012). These PI3Ks are activated, directly or indirectly, by a variety of cell surface receptors that include receptor tyrosine kinases (RTKs) and G protein-coupled receptors. Several cardinal alterations elicited by PI3K activation include changes in cell proliferation, survival, migration, and metabolism, and are highly aligned with the "hallmarks of cancer" discussed by Hanahan and Weinberg (2011). Indeed, inappropriate activation of the PI3K pathway has been observed in a remarkably broad array of human cancers. Nested within this pro-oncogenic signaling network are two pivotal protein serine-threonine kinases, AKT (also termed protein kinase B) and mTOR, both of which represent druggable targets, like PI3K itself. This combination of biological relevance and pharmacological tractability rendered the PI3K pathway an irresistible target for cancer drug discovery. The ensuing efforts in

medicinal chemistry delivered a treasure trove of PI3K pathway inhibitors, and a stunning number (25–30) of these compounds are now in various stages of late preclinical or clinical development.

The unprecedented level of pharmaceutical investment in PI3K pathway inhibitors was based on expectations that these agents would exert broad-based inhibitory effects on tumor growth and progression. Unfortunately, single-agent therapy with PI3K pathway inhibitors has, with few exceptions, failed to deliver on the promise of breakthrough antitumor activity in the clinical setting. Adaptive drug resistance has emerged as an important mechanism whereby cancer cells limit the therapeutic activities of these inhibitors (Bagrodia et al., 2012). Recent studies indicate that pharmacological disruption of PI3K signaling engages a multiplicity of compensatory responses that restore signal flux to a level that maintains the oncogenic phenotype. An intriguing report by Britschgi et al. (2012) in this issue of *Cancer Cell* adds to this compendium of resistance mechanisms by demonstrating that certain tumors acquire resistance to PI3K pathway-targeted therapies by elaborating a pro-inflammatory chemokine that not only drives drug resistance, but also leads to a more invasive, metastatic phenotype for the cancer cells.

Britschgi et al. (2012) focused their studies on triple-negative breast cancer (TNBC), a tumor type differentiated from other breast cancer subtypes by the absence of receptors for HER2, progesterone, and estrogen. TNBC is a highly aggressive disease with a poor response to current therapies. Evidence that the PI3K pathway is commonly activated in TNBC has raised hope that PI3K pathway-targeted agents might significantly alter the therapeutic landscape for this disease (Ibrahim et al., 2012). Britschgi et al. (2012) examined the phosphorylation states of specific signaling proteins during acute ($\leq$20 hr) exposure of TNBC-like cell lines to BEZ235, a dually-active PI3K/mTOR inhibitor. An unanticipated finding was that BEZ235 exposure stimulated tyrosine phosphorylation of the JAK2 kinase and its substrate, the STAT5 transcription factor. The JAK kinase family consists of four members, which are typically (but not exclusively) activated by cytokine and chemokine receptors (Seavey and Dobrzanski, 2012). The activated JAKs, in turn, phosphorylate one or more of the seven STAT family proteins, thereby stimulating their nuclear translocation and transactivating functions. BEZ235 treatment triggered selective modification of JAK2 and STAT5, indicating that this drug provoked specific rather generalized activation of JAK-STAT signaling in these TNBC cell lines (Britschgi et al., 2012). Further experiments revealed that BEZ235 stimulated the expression of mRNA transcripts encoding interleukin-8 (IL-8) and the subsequent secretion of this chemokine by the drug-treated cells. The expression of IL-8 receptor CXCR1 was also increased during BEZ235 exposure, establishing an autokine-acting chemokine signaling pathway in the drug-treated TNBC cells.

Exploration of the mechanism underlying BEZ235-induced JAK2-STAT5 activation uncovered a biphasic response. The early (0–8 hr after drug treatment) increase in JAK2-STAT5 activation was linked to upregulation of the IR/IGF-1R signaling pathway. This finding is consistent with previous observations that inhibition of the PI3K-AKT axis of the PI3K signaling network stimulates a FOXO transcription factor-dependent homeostatic response leading to upregulation of receptors that strongly activate PI3K, such as the RTKs IR/IGF1R and MET (Chakrabarty et al., 2012; Muranen et al., 2012). The initial wave of JAK2/STAT5 signaling stimulated the expression and secretion of IL-8, which then acted through the CXCR1 receptor to drive a second wave of JAK2-STAT5 activity. Thus, inhibition of PI3K/mTOR sets in motion a sequence of events that culminate in a self-amplifying autocrine loop involving the IL-8-CXCR1-JAK2-STAT5 signaling cascade. The unanticipated increase in IL-8 signaling provoked by PI3K/mTOR inhibition was at least partially responsible for limiting the inhibitory effects of BEZ235 on AKT activity, cancer cell survival in vitro, and tumor growth in vivo. Moreover, these results may have broader clinical implications, in that IL-8 is recognized as a significant tumor progression factor through its pleiotropic activities related to cancer stem cells, angiogenesis, and metastasis (Waugh and Wilson, 2008). Hence, it is conceivable that treatment of TNBC with PI3K/mTOR inhibitors could to lead to worsened patient outcomes related to enhanced intratumoral IL-8 activity.

Although these findings place an additional obstacle in the path to successful implementation of PI3K pathway-targeted therapies, they also present a therapeutic opportunity, in that the IL8-dependent adaptive response is amenable to pharmacologic intervention (for example with drugs that target JAK2) (Seavey and Dobrzanski, 2012). Indeed, Britschgi et al. (2012) demonstrated that combination therapy with a JAK2 kinase inhibitor increased the antiproliferative and cytocidal activities of BEZ235 in vitro and augmented the antitumor activity of BEZ235 in mouse xenograft studies. Furthermore, the authors observed that circulating tumor cell numbers in mice bearing highly metastatic breast tumors, which were only marginally reduced by the PI3K/mTOR inhibitor, were dramatically suppressed by treatment with a JAK2 inhibitor, both in the absence and presence of BEZ235. The authors further noted that CXCR1 expression was heterogeneous in these tumor cell populations and presented evidence that the most highly CXCR1-positive cells were enriched for both tumor-initiating and metastatic behaviors. The results support a clinically testable combination strategy involving PI3K-mTOR and JAK2 inhibitors in TNBC and in other tumors in which suppression of PI3K signaling provokes a compensatory increase in IL8 production.

This study underscores the robustness of the adaptive network that strives to maintain homeostatic signal flux through the PI3K pathway in cancer cells. Previously described mechanisms of PI3K inhibitor resistance can be characterized as "vertical"; for example, inhibition of PI3K-α elicits a homeostatic response, such as increased expression of IR/IGF1R, which aims to restore PI3K-α activity (Figure 1). The adaptive response uncovered by Britschgi et al. (2012) adds a chemokine-dependent "horizontal" element to the existing array of PI3K inhibitor resistance mechanisms. The more sobering news might be that this adaptive response confers not only drug resistance, but also a more aggressive phenotype on TNBC cells.

This study raises several questions for future investigation. First, given that IL-8

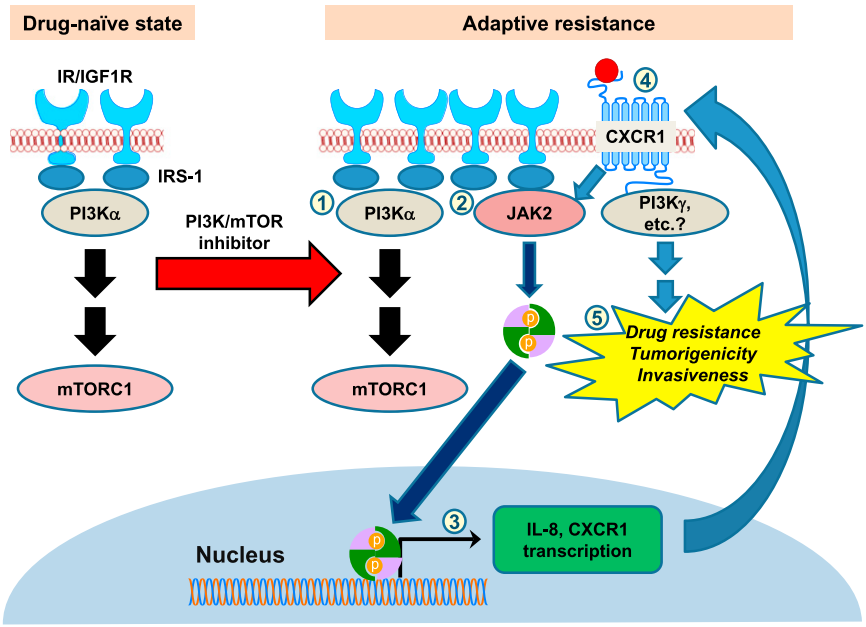

Figure 1. Acquisition of Resistance to PI3K/mTOR Inhibitors through Compensatory Activation of the JAK2-STAT5 Pathway

Triple-negative breast cancer cells drive signaling through the PI3K/mTOR pathway via activation of receptor tyrosine kinases, such as insulin receptors and insulin-like growth factor-1 receptors (IR/IGF-1R). Treatment with a PI3K-mTOR inhibitor triggers a biphasic adaptive resistance response. In the initial phase of this response, the cells upregulate expression of IR/IGF-1R and IRS-1 (1), which stimulates a compensatory increase in PI3K-α activity (vertical resistance), together with IRS-1-dependent activation of the JAK2-STAT5 pathway (2). STAT5 translocates to the nucleus and stimulates transcription of the genes encoding interleukin-8 (IL-8) and the IL-8 receptor, CXCR1 (3). The secretion of IL-8 establishes a self-amplifying, autocrine and/or paracrine chemokine loop that might activate a different PI3K isoform, PI3K-γ (4), and propagates JAK2-STAT5 activation, leading to horizontal drug resistance and increased tumorigenicity and invasiveness in TNBC cell populations (5).

signals through a GPCR, it would be interesting to learn whether the IL-8-dependent adaptive response involves a switch from PI3K-α to the GPCR-associated PI3K-γ isoform (Figure 1). Second, PI3K/mTOR inhibitors stimulate autophagy, which was recently shown to support the secretion of IL-8 and other pro-inflammatory cytokines through an unconventional secretory pathway (Deretic et al., 2012). If IL-8 release from drug-treated TNBC cells is attributable to unconventional secretion, then this mechanism of adaptive resistance might be susceptible to combination therapy with an autophagy inhibitor. Finally, and most importantly, we need to understand more fully the actual contributions of IL-8 to PI3K/mTOR inhibitor resistance in human TNBC patients, as well the roles of drug-induced IL-8 release in adaptive drug resistance in other human cancers.

REFERENCES

Bagrodia, S., Smeal, T., and Abraham, R.T. (2012). Pigment Cell Melanoma Res. *25*, 819–831.

Britschgi, A., Andraos, R., Brinkhaus, H., Klebba, I., Romanet, V., Müller, A., Murakami, M., Radimerski, T., and Bentires-Alj, M. (2012). Cancer Cell *22*, this issue, 796–811.

Chakrabarty, A., Sánchez, V., Kuba, M.G., Rinehart, C., and Arteaga, C.L. (2012). Proc. Natl. Acad. Sci. USA *109*, 2718–2723.

Deretic, V., Jiang, S., and Dupont, N. (2012). Trends Cell Biol. *22*, 397–406.

Hanahan, D., and Weinberg, R.A. (2011). Cell *144*, 646–674.

Ibrahim, Y.H., García-García, C., Serra, V., He, L., Torres-Lockhart, K., Prat, A., Anton, P., Cozar, P., Guzmán, M., Grueso, J., et al. (2012). Cancer Discov *2*, 1036–1047.

Muranen, T., Selfors, L.M., Worster, D.T., Iwanicki, M.P., Song, L., Morales, F.C., Gao, S., Mills, G.B., and Brugge, J.S. (2012). Cancer Cell *21*, 227–239.

Seavey, M.M., and Dobrzanski, P. (2012). Biochem. Pharmacol. *83*, 1136–1145.

Vanhaesebroeck, B., Stephens, L., and Hawkins, P. (2012). Nat. Rev. Mol. Cell Biol. *13*, 195–203.

Waugh, D.J., and Wilson, C. (2008). Clin. Cancer Res. *14*, 6735–6741.

Chaffer, C.L., Brennan, J.P., Slavin, J.L., Blick, T., Thompson, E.W., and Williams, E.D. (2006). Cancer Res. *66*, 11271–11278.

Dalerba, P., Cho, R.W., and Clarke, M.F. (2007). Annu. Rev. Med. *58*, 267–284.

Korpal, M., Ell, B.J., Buffa, F.M., Ibrahim, T., Blanco, M.A., Celià-Terrassa, T., Mercatali, L., Khan, Z., Goodarzi, H., Hua, Y., et al. (2011). Nat. Med. *17*, 1101–1108.

Mani, S.A., Guo, W., Liao, M.-J., Eaton, E.N., Ayyanan, A., Zhou, A.Y., Brooks, M., Reinhard, F., Zhang, C.C., Shipitsin, M., et al. (2008). Cell *133*, 704–715.

Morel, A.P., Lièvre, M., Thomas, C., Hinkal, G., Ansieau, S., and Puisieux, A. (2008). PLoS ONE *3*, e2888.

Ocana, O.H., Corcoles, R., Fabra, A., Moreno-Bueno, G., Acloque, H., Vega, S., Barrallo-Gimeno, A., Cano, A., and Nieto, M.A. (2012). Cancer Cell *22*, this issue, 709–724.

Thiery, J.P., Acloque, H., Huang, R.Y., and Nieto, M.A. (2009). Epithelial-mesenchymal transitions in development and disease. Cell *139*, 871–890.

Tsai, J.H., Donaher, J.L., Murphy, D.A., Chau, S., and Yang, J. (2012). Cancer Cell *22*, this issue, 725–736.

Disputed Paternity: The Uncertain Ancestry of Pancreatic Ductal Neoplasia

Anirban Maitra[1,3] and Steven D. Leach[2,3,*]
[1]Department of Pathology
[2]Department of Surgery and the McKusick-Nathans Institute of Genetic Medicine
[3]The Sol Goldman Center for Pancreatic Cancer Research
Johns Hopkins University, Baltimore, MD 21205, USA
*Correspondence: stleach@jhmi.edu
http://dx.doi.org/10.1016/j.ccr.2012.11.015

In this issue of *Cancer Cell*, Kopp and colleagues report that pancreatic ductal cells are largely refractory to the induction of pancreatic neoplasia. Whereas a rare ductal subpopulation may still prove capable of neoplastic transformation, these findings refocus attention on acinar and other non-ductal cell types as initiators of this deadly neoplasm.

While malignant tumors of the pancreas can display a variety of histologic forms, the term "pancreatic cancer" is usually synonymous with a pathological diagnosis of pancreatic ductal adenocarcinoma (PDAC). As its name implies, PDAC has long been presumed to arise from pancreatic ductal epithelial cells. Along with its noninvasive precursor, pancreatic intraepithelial neoplasia (PanIN), these tumors typically display a distinctly duct-like histology, and express markers of ductal differentiation. As demonstrated for other tumor types, however, tumor histology is often misleading in determining tumor lineage, and work from Kopp et al. (2012) published in this issue of *Cancer Cell* reinforces the disputed paternity of pancreatic "ductal" neoplasia.

Initial clues suggesting that non-ductal cells might serve as effective cells of origin for pancreatic ductal neoplasia were provided by studies involving transgenic misexpression of individual oncogenes under the regulation of non-ductal promoter elements, in which a subset of resulting tumors displayed histologic resemblance to adult ductal epithelium (Sandgren et al., 1991). However, these similarities were ultimately proven to be only skin-deep, as additional studies of PanIN and PDAC revealed activation of transcriptional programs typically observed in embryonic pancreatic epithelium, but not in differentiated duct cells (Miyamoto et al., 2003; Park et al., 2011).

With the advent of autochthonous mouse models of pancreatic neoplasia, more recent studies have interrogated individual pancreatic cell types for the ability to generate PanIN, based upon Cre/lox-mediated activation of oncogenic *Kras*. Initial seminal work in this arena utilized either *Pdx1*^{Cre} or *Ptf1a*^{Cre} alleles to activate *Kras* in embryonic pancreatic progenitor cells (Aguirre et al., 2003; Hingorani et al., 2003). While these studies demonstrated that embryonic activation of oncogenic *Kras* effectively initiated pancreatic ductal neoplasia, they provided considerably less information regarding the capacity of individual adult cell lineages to similarly serve as effective cells of origin. Based on the availability of appropriate Cre driver lines, this adult capacity was first interrogated in pancreatic acinar cells. Using either a Nestin-Cre driver to activate oncogenic *Kras* in exocrine progenitor cells and their acinar cell descendants (Carrière et al., 2007) or a variety of inducible Cre lines to activate *Kras* in adult acinar cells (De La O et al., 2008; Guerra et al., 2007; Habbe et al., 2008), these studies provided strong evidence that acinar cells could indeed serve as effective biologic parents for pancreatic ductal neoplasia. In these studies, the ability of adult acinar cells to generate PanIN was dramatically accelerated in the context of associated pancreatitis, a known risk factor for the human disease. Additional studies suggested that a permissive inflammatory microenvironment could broadly bestow PanIN-parenting capabilities, as even insulin-expressing cells

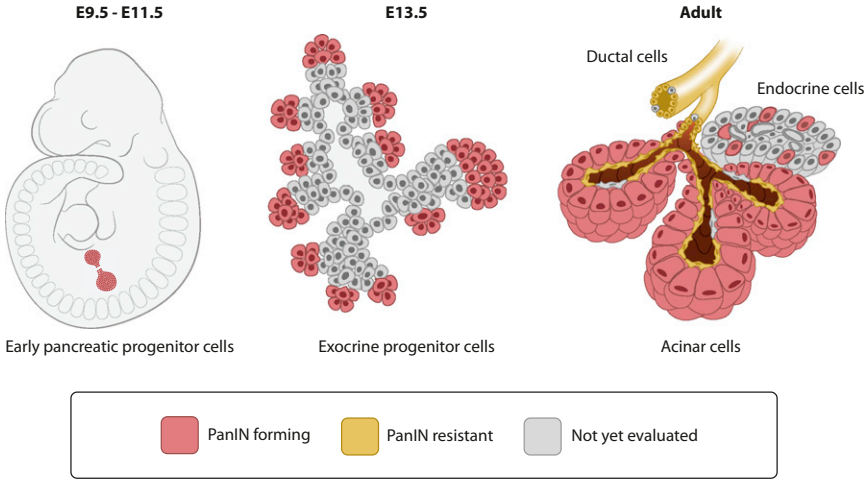

Figure 1. Competence of Individual Pancreatic Cell Types to Generate Pancreatic Intraepithelial Neoplasia in Response to Oncogenic *Kras* Activation

(A) *Kras* activation in early pancreatic progenitor cells and their progeny leads to effective pancreatic intraepithelial neoplasia (PanIN) initiation.

(B) *Kras* activation in later exocrine-dedicated progenitor cells and their acinar cell progeny also results in PanIN.

(C) *Kras* activation in differentiated acinar cells, but not the most common ductal epithelial lineage, leads to effective PanIN initiation. In an inflammatory microenvironment, insulin-expressing endocrine cells can also generate PanIN. Low-abundance pancreatic ductal/centroacinar subpopulations may still remain to be evaluated as effective cells of origin. Red indicates cell types capable of forming PanIN; yellow indicates cells resistant to PanIN; and gray indicates known and potentially unknown cell populations still unevaluated.

were shown to be capable of generating PanIN in the context of associated pancreatitis (Gidekel Friedlander et al., 2009).

Ironically, these studies demonstrating that pancreatic ductal neoplasia could be generated from a variety of non-ductal cell types were all completed prior to a similar definitive evaluation in actual ductal epithelial cells. However, a long-awaited detailed glimpse at the parental capacities of the ductal epithelial lineage is now available. In this new study, Kopp et al. (2012) directly compare the efficiency of PanIN formation following cell type-specific activation of oncogenic *Kras* in the acinar lineage using a *Ptf1a*^{CreER} line and in the ductal/centroacinar lineage using a *Sox9*^{CreER} line. For both lines, postnatal tamoxifen administration induced recombination in a similar proportion of target cells. Similar to prior studies using other acinar cell-specific Cre driver lines, the authors observed potent induction of PanIN lesions in *Ptf1a*^{CreER}; *Kras*^{G12D} mice, an effect that was further accelerated by concomitant pancreatitis. However there was minimal-to-no PanIN induction in *Sox9*^{CreER}; *Kras*^{G12D} mice, even in the presence of pancreatitis. Even when discrepant PanIN frequencies were normalized based on the greater abundance of acinar cells, the difference in PanIN-generating capabilities between the two lineages remained striking, with acinar cells at least 100-fold more effective than ductal/centroacinar cells in generating PanIN. In addition, the authors demonstrated that, within the acinar lineage, *Sox9* itself was required for efficient PanIN induction, and that *Sox9* overexpression enhanced both pancreatitis-associated metaplasia and *Kras*-induced PanIN formation within the acinar lineage.

Together, these comprehensive studies demonstrate that, while differentiated acinar cells are fully capable of generating PanIN through requisite *Kras*-induced *Sox9* activation, ductal and centroacinar cells already expressing *Sox9* are dramatically resistant to *Kras*-induced neoplastic transformation. In conjunction with prior studies, these findings lead to the startling recognition that the predominant *Sox9*-expressing ductal epithelial lineage represents the only pancreatic epithelial lineage evaluated to date that is unable to efficiently generate PanIN (Figure 1).

Before entirely disqualifying ductal and centroacinar cells from consideration as capable PanIN parents, it is necessary to consider a broad number of remaining questions and possibilities. First, it must be recognized that, while *Sox9* appears to be expressed in a substantial majority of pancreatic ductal and centroacinar cells, there is considerable heterogeneity in gene expression along the ductal epithelial tree, and the distinct possibility remains that PanIN can effectively originate from a subpopulation of *Sox9*-negative ductal epithelial cells. In addition, the study by Kopp et al. (2012) relied on tamoxifen-induced recombination in only 12% of all *Sox9*-expressing cells. As acknowledged by the authors, this fraction, when further reduced by a less than uniform response to *Kras* even among competent cell types, means that rare *Sox9*-expressing cells (i.e., centroacinar cells) might not have been effectively interrogated in large numbers; perhaps these cells account for the rare PanIN lesion observed in these mice. In spite of these caveats, it remains difficult to escape the authors' primary conclusion that the predominant ductal lineage in adult mouse pancreas remains largely refractory to *Kras*-mediated transformation.

While it is tempting to extend these findings to the human disease, appropriate caution is warranted. In particular, the current experimental paradigm only evaluates what can happen, i.e., the competence of individual adult murine cell types to generate PanIN in response to oncogenic *Kras*, as opposed to what actually does happen under conditions of spontaneous or carcinogen-induced human *KRAS* mutations. Certainly, murine PanIN induced by *Kras* activation in either embryonic pancreas or in adult acinar cells seems to bear exquisite resemblance to human PanIN, both histologically and with respect to gene expression patterns. However, prior analysis of *KRAS* sequences in acinar cells adjacent to human PanIN failed to identify mutant alleles (Shi et al., 2009), suggesting that acinar cell *KRAS* mutations are either extremely rare or rapidly induce metaplastic or neoplastic conversion to a non-acinar morphology. On the other hand, cells with features of acinar differentiation can often be identified in human PanIN, and a subset of acinar to ductal

metaplasia (ADM) do, indeed, harbor *KRAS* mutations identical to those observed in adjacent PanIN (Shi et al., 2009). These findings might be consistent with *KRAS* mutations arising in either acinar cells themselves or in areas of ADM, with subsequent rapid progression to PanIN.

Assuming that these findings are indeed relevant to the human disease, what are the ramifications of the current findings? Certainly, they suggest that future chemoprevention strategies might be best targeted at early events in acinar rather than ductal cells; blocking acinar cell activation of *Sox9* now joins Notch pathway inhibition and maintenance of *Mist1* expression as examples of such approaches. In addition, these findings underscore an increasingly recognized disconnect between *Kras* mutations and Kras activity. Along these lines, it will be fascinating to determine the presumably epigenetic determinants underlying the differential responsiveness to oncogenic *Kras* observed in acinar and ductal cell types; manipulating such determinants may convert acinar cells into less capable parents, hopefully eliminating PanIN from the pancreatic family tree.

REFERENCES

Aguirre, A.J., Bardeesy, N., Sinha, M., Lopez, L., Tuveson, D.A., Horner, J., Redston, M.S., and DePinho, R.A. (2003). Genes Dev. *17*, 3112–3126.

Carrière, C., Seeley, E.S., Goetze, T., Longnecker, D.S., and Korc, M. (2007). Proc. Natl. Acad. Sci. USA *104*, 4437–4442.

De La O, J.P., Emerson, L.L., Goodman, J.L., Froebe, S.C., Illum, B.E., Curtis, A.B., and Murtaugh, L.C. (2008). Proc. Natl. Acad. Sci. USA *105*, 18907–18912.

Gidekel Friedlander, S.Y., Chu, G.C., Snyder, E.L., Girnius, N., Dibelius, G., Crowley, D., Vasile, E., DePinho, R.A., and Jacks, T. (2009). Cancer Cell *16*, 379–389.

Guerra, C., Schuhmacher, A.J., Cañamero, M., Grippo, P.J., Verdaguer, L., Pérez-Gallego, L., Dubus, P., Sandgren, E.P., and Barbacid, M. (2007). Cancer Cell *11*, 291–302.

Habbe, N., Shi, G., Meguid, R.A., Fendrich, V., Esni, F., Chen, H., Feldmann, G., Stoffers, D.A., Konieczny, S.F., Leach, S.D., and Maitra, A. (2008). Proc. Natl. Acad. Sci. USA *105*, 18913–18918.

Hingorani, S.R., Petricoin, E.F., Maitra, A., Rajapakse, V., King, C., Jacobetz, M.A., Ross, S., Conrads, T.P., Veenstra, T.D., Hitt, B.A., et al. (2003). Cancer Cell *4*, 437–450.

Kopp, J.L., von Figura, G., Mayes, E., Liu, F.F., Dubois, C.L., Morris, J.P., Pan, F.C., Akiyama, H., Wright, C.V.E., Jensen, K., et al. (2012). Cancer Cell *22*, this issue, 737–750.

Miyamoto, Y., Maitra, A., Ghosh, B., Zechner, U., Argani, P., Iacobuzio-Donahue, C.A., Sriuranpong, V., Iso, T., Meszoely, I.M., Wolfe, M.S., et al. (2003). Cancer Cell *3*, 565–576.

Park, J.Y., Hong, S.M., Klimstra, D.S., Goggins, M.G., Maitra, A., and Hruban, R.H. (2011). Appl. Immunohistochem. Mol. Morphol. *19*, 444–449.

Sandgren, E.P., Quaife, C.J., Paulovich, A.G., Palmiter, R.D., and Brinster, R.L. (1991). Proc. Natl. Acad. Sci. USA *88*, 93–97.

Shi, C., Hong, S.M., Lim, P., Kamiyama, H., Khan, M., Anders, R.A., Goggins, M., Hruban, R.H., and Eshleman, J.R. (2009). Mol. Cancer Res. *7*, 230–236.

Chemokine to the Rescue: Interleukin-8 Mediates Resistance to PI3K-Pathway-Targeted Therapy in Breast Cancer

Robert T. Abraham[1,*]
[1]Oncology Research, Pfizer Worldwide Research and Development, 10777 Science Center Drive, CB3/1376, San Diego, CA 92121, USA
*Correspondence: robert.abraham@pfizer.com
http://dx.doi.org/10.1016/j.ccr.2012.11.012

Adaptive resistance to PI3K-mTOR inhibitors potentially limits the clinical antitumor activities of these agents. In this issue of *Cancer Cell*, Britschgi and coworkers show that certain tumors acquire resistance to PI3K-mTOR inhibitors through activation of a JAK2-dependent pathway, leading to interleukin-8 secretion.

More than 25 years have passed since the discovery of phosphoinositide 3-kinase (PI3K) as an oncoprotein-associated enzymatic activity. The term "PI3K" in this context designates the Class I subset of phosphoinositide kinases (comprising the α, β, γ, and δ isoforms), which convert phosphatidylinositol-4,5-bisphosphate to the bioactive second messenger phosphatidylinositol-3,4,5-trisphosphate (Vanhaesebroeck et al., 2012). These PI3Ks are activated, directly or indirectly, by a variety of cell surface receptors that include receptor tyrosine kinases (RTKs) and G protein-coupled receptors. Several cardinal alterations elicited by PI3K activation include changes in cell proliferation, survival, migration, and metabolism, and are highly aligned with the "hallmarks of cancer" discussed by Hanahan and Weinberg (2011). Indeed, inappropriate activation of the PI3K pathway has been observed in a remarkably broad array of human cancers. Nested within this pro-oncogenic signaling network are two pivotal protein serine-threonine kinases, AKT (also termed protein kinase B) and mTOR, both of which represent druggable targets, like PI3K itself. This combination of biological relevance and pharmacological tractability rendered the PI3K pathway an irresistible target for cancer drug discovery. The ensuing efforts in